
UNIVERSITÀ
DEGLI STUDI
DI BRESCIA

*DIPARTIMENTO DI INGEGNERIA MECCANICA E INDUSTRIALE*

*DOTTORATO DI RICERCA IN INGEGNERIA MECCANICA E INDUSTRIALE*

---

*settore scientifico disciplinare* ING/IND-09

*CICLO XXXVII*

---

# *THERMOPHYSICAL CHARACTERISATION OF INNOVATIVE WORKING FLUIDS FOR CLOSED THERMODYNAMIC CYCLES*

*Dottorando:*
*MICHELE DONINELLI*

*SUPERVISORE:*
*PROF. GIOELE DI MARCOBERARDINO*

# *ABSTRACT*

This research focuses on the thermophysical characterization of innovative working fluids intended to operate in high-temperature closed thermodynamic cycles. The identification and study of pure and mixed innovative working fluids aim to enhance the performance of thermodynamic cycles for both electrical and thermal energy production. This study aligns with the decarbonization goals of the industrial and energy sectors, exploring the advancement of key technologies such as Organic Rankine Cycles (ORC), high-temperature heat pumps (HTHP), and innovative power cycles for concentrated solar power (CSP) systems, which are essential for achieving these objectives.

In this context, silicon tetrachloride ($SiCl_4$) is proposed in the literature for the first time as a working fluid for high-temperature power cycles. Compared to conventional ORC fluids, which are limited by thermal stability to a maximum operating temperature of approximately 300°C, $SiCl_4$ can maintain thermochemical stability beyond 650°C. This opens up new possibilities for heat recovery from high-temperature industrial exhaust gases and enhances the efficiency of biomass or solar power plants. Thermodynamic evaluations highlight the potential of this fluid to increase the efficiency of Rankine cycles by up to 10 percentage points compared to current organic fluids.

In parallel, fluorobenzene has been proposed as an innovative fluid for both ORC and HTHP applications due to its favourable environmental profile (with near-zero GWP and zero ODP). Thermal stability tests show a degradation rate of fluorobenzene of less than 5% per year at a temperature of 350°C, placing it among the few thermally stable organic fluids at temperatures above 300°C. Unlike the conventional thermal stability tests performed at the Fluid Testing Laboratory at the University of Brescia, the methodology was revised to simulate the presence of a non-condensable gas (NCG) removal system to verify its behaviour under real operating conditions. The results suggest that, with an efficient NCG management system, fluorobenzene can operate without issues at 350°C. Due to its high critical temperature (286°C) and medium molecular complexity, fluorobenzene can be efficiently employed in HTHP applications with a condensation temperature around 200°C.

The experimental characterization of the identified working fluids extends beyond thermal stability testing to include volumetric properties. In fact, while the thermodynamic properties of pure fluids are typically well-described by conventional equations of state (such as cubic equations), mixture behaviour often requires regression of specific parameters within these equations based on experimental data to improve predictive accuracy.

For this reason, a significant part of the research was dedicated to measuring experimental data for vapor-liquid equilibrium (VLE) and density for $CO_2$ mixtures, using an isochoric apparatus developed at the Fluid Testing Laboratory of the University of Brescia. This apparatus was validated with known literature mixtures and subsequently used to obtain missing VLE data. The volumetric characterization was completed with VLE and density measurements for $CO_2$+$SiCl_4$ and $CO_2$+$C_2Cl_4$, conducted during a research period at the Centre for Energy Environment Processes (CEEP) at Mines Paris PSL, in Fontainebleau, France.

The analysis of $CO_2$-based mixtures as working fluids is aimed at exploring their applicability in transcritical cycles for HTHP (around 200°C) and for power cycles in CSP plants with central receivers (above 550°C). Among the analysed mixtures, $CO_2$+$SiCl_4$ showed a 4.2% increase in electrical output compared to pure $CO_2$, in next-generation CSP plants scneario. VLE data of the mixture were measured using a variable-volume PVT apparatus, allowing for precise calibration of the equation of state and achieving an average absolute deviation (AAD%) of 0.68% from experimental data. Density data were collected using a vibrating tube densimeter (VTD), which enabled more accurate characterization of the mixture. A specific configuration of the VTD was developed to effectively measure the mixture density, establishing a procedure that could serve as a standard for future studies on mixtures with significantly different volatilities. An innovative method also allowed additional bubble points (VLE) to be obtained through the densimeter, which matched measurements taken with the PVT apparatus.

The $CO_2$+$C_2Cl_4$ mixture, studied for HTHP applications, demonstrated a low thermal decomposition rate up to 230-250°C, sufficient for providing sensible heat below 200°C. Thermodynamic analysis indicates that the $CO_2$+$C_2Cl_4$ mixture offers a favourable balance between performance and compression ratios when sensible heat is needed up to 200°C, and low-temperature process heat is available. Density data obtained from the vibrating tube densimeter were used to refine the thermodynamic model.

The thesis is structured as a collection of scientific articles organized by research areas, including: Part 1, dedicated to the characterization of pure fluids for high-temperature cycles; Part 2, focused on the experimentation of $CO_2$ mixtures; Part 3, which explores models for estimating transport properties, such as viscosity and thermal conductivity; and Part 4, concluding with systemic analyses and techno-economic assessments of the proposed solutions, including considerations for design and annual system operation.

# *SOMMARIO*

Questa ricerca si focalizza sulla caratterizzazione termofisica di fluidi di lavoro innovativi, destinati ad operare in cicli termodinamici chiusi ad alte temperature. L'identificazione, e lo studio, di fluidi di lavoro puri e/od in miscela innovativi è mirata al miglioramento delle prestazioni di cicli termodinamici per la produzione di energia elettrica e termica. Lo studio si colloca nell'ambito della decarbonizzazione dei settori industriale ed energetico, esplorando il potenziamento di tecnologie chiave come i cicli Rankine a fluido organico (ORC), le pompe di calore ad alta temperatura (HTHP) e cicli di potenza innovativi per sistemi a concentrazione solare (CSP), fondamentali per il raggiungimento di questi obiettivi.

In questo contesto, è stato proposto per la prima volta in letteratura il tetracloruro di silicio ($SiCl_4$) come fluido di lavoro per cicli di potenza ad alta temperatura. Rispetto ai fluidi ORC convenzionali, limitati dalla stabilità termica ad operare a temperature massime di circa 300°C, il $SiCl_4$ è in grado di mantenere stabilità termochimica oltre 650°C, aprendo nuove possibilità per il recupero di calore da fonti come i gas esausti industriali ad alta temperatura e per l'efficientamento di centrali a biomassa o solari. Valutazioni termodinamiche evidenziano la capacità da parte di questo fluido di incrementare l'efficienza dei cicli Rankine fino al 10 punti percentuali rispetto ai fluidi organici attuali.

In parallelo, il fluorobenzene è stato proposto come fluido innovativo sia per cicli ORC e HTHP, grazie al suo profilo ambientale positivo (GWP quasi nullo e ODP pari a zero). Test di stabilità termica evidenziano un tasso di degradazione del fluorobenzene entro il 5% annuo ad una temperatura di 350°C, posizionandosi tra i pochi fluidi organici termicamente stabili oltre 300°C. Contrariamente al convenzionale test di stabilità termica presso il Laboratorio dei Test dei Fluidi dell'Università degli Studi di Brescia, la metodologia è stata revisionata per simulare la presenza di un sistema di rimozione dei gas non condensabili (NCG), per verificarne il comportamento in reali condizioni operative. I risultati suggeriscono che, con un sistema di gestione NCG efficiente, il fluorobenzene possa operare senza problematiche ad una temperatura di 350°C. Grazie alla sua elevata temperatura critica (286°) e una complessità molecolare media, il fluorobenzene può essere impiegato in modo efficiente in HTHP con temperatura di condensazione intorno a 200°C.

La caratterizzazione sperimentale dei fluidi di lavoro identificati non si limita al test di stabilità termica, bensì sono state misurate anche proprietà volumetriche dei fluidi. Infatti, se da un lato le proprietà termodinamiche dei fluidi puri sono tipicamente ben descritte da equazioni di stato convenzionali quali le cubiche, nel caso di miscele è necessario regredire determinati parametri delle equazioni di stato sulla base di dati sperimentali per migliorare la predittività.

Per questo motivo un'importante parte della ricerca è stata dedicata alla misurazione di dati sperimentali di equilibrio liquido-vapore (VLE) e densità per miscele di $CO_2$ tramite un apparato isocoro sviluppato presso il Laboratorio di Test dei Fluidi dell'Università di Brescia, durante questo lavoro, validato con miscele note in letteratura e poi utilizzato per ottenere dati VLE mancanti in letteratura. La caratterizzazione volumetrica è stata completata con misure VLE e di densità di

$CO_2$+$SiCl_4$ e $CO_2$+$C_2Cl_4$, eseguite durante il periodo trascorso presso il Centre for Energy Environment Processes (CEEP) di Mines Paris PSL, in Fontainebleau (Francia).

L'analisi delle miscele a base di $CO_2$ come fluido di lavoro è finalizzata ad esplorarne l'applicabilità in ciclo transcritico per HTHP (intorno 200°C) e per cicli di potenza in impianti a concentrazione solare (CSP) con ricevitore centrale (sopra 550°C).

Tra le miscele analizzate, la $CO_2$+$SiCl_4$ ha mostrato un incremento di produzione elettrica del 4.2% rispetto alla $CO_2$ pura. Le proprietà di equilibrio liquido-vapore (VLE) sono state misurate con un apparato PVT a volume variabile, consentendo di calibrare con accuratezza l'equazione di stato ed ottenendo una deviazione media assoluta (AAD%) dello 0.68% rispetto ai dati sperimentali. Dati di densità sono stati misurati tramite un densimetro a tubo vibrante (VTD), che ha permesso di caratterizzare meglio la miscela. Una particolare configurazione del VTD è stata sviluppata per poter misurare in modo efficace la densità della miscela, e tale procedura può essere considerata come standard per futuri lavori su miscele i cui componenti han volatilità molto diverse. Inoltre, una procedura innovativa ha permesso di ottenere ulteriori punti di bolla (VLE) attraverso il densimetro, i quali erano in accordo con le misure effettuate con l'apparato PVT.

La miscela $CO_2$+$C_2Cl_4$, studiata per applicazioni HTHP, ha rivelato un basso tasso di decomposizione termica fino a 230-250°C, sufficiente per fornire calore sensibile sotto 200°C. L'analisi termodinamica dimostra che la miscela $CO_2$+$C_2Cl_4$ presenta un equilibrio favorevole tra performance e rapporti di compressione, quando è richiesto calore sensibile fino a 200°C ed è disponibile calore di processo di bassa temperatura. Dati di densità ottenuti al densimetro a tubo vibrante sono stati utilizzati per migliorare il modello termodinamico.

La tesi, strutturata come una raccolta di articoli scientifici organizzati per aree di ricerca, include: Parte 1, dedicata alla caratterizzazione dei fluidi puri per cicli ad alta temperatura; Parte 2, focalizzata sulla sperimentazione delle miscele di $CO_2$; Parte 3, che approfondisce i modelli per la stima delle proprietà di trasporto, come viscosità e conducibilità termica; e Parte 4, che conclude con analisi sistemiche e valutazioni tecno-economiche delle soluzioni proposte, includendo considerazioni sul design e sull'operatività annuale del sistema.

*Io proprio vorrei che gli uomini responsabili della cultura e dell'insegnamento ricordassero che noi italiani dobbiamo toglierci di dosso questo complesso di inferiorità che ci hanno insegnato, ovvero che gli italiani sono bravi letterati, bravi poeti, bravi cantanti, bravi suonatori di chitarra, brava gente, ma non hanno le capacità della grande organizzazione industriale. Ricordatevi, amici di altri paesi: sono le cose che hanno fatto credere a noi e che ora insegnano anche a voi. Tutto ciò è falso e noi ne siamo un esempio. Dovete avere fiducia in voi stessi, nelle vostre possibilità, nel vostro domani; dovete formarvelo da soli questo vostro domani. Ma per fare questo è necessario studiare, imparare, conoscere i problemi.*

*Enrico Mattei, in un discorso del 1961*

# *TABLE OF CONTENTS*

# *Chapter 1 - Introduction and research objectives*

## 1.1 Challenges in high-temperature thermodynamic cycles

Historically, power production in industrialized countries has been dominated by thermal power plants, such as steam Rankine cycles and open-cycle gas turbines. These technologies rely on high-grade heat sources, typically derived from the combustion of fossil fuels, to achieve acceptable efficiencies that make them economically attractive.

The European Union's commitment to achieving climate neutrality by 2050 [1] is a cornerstone of its energy policy, driving the development of advanced energy conversion technologies that are both efficient and sustainable. This strategy underscores the critical need to reduce $CO_2$ emissions across multiple sectors, including power generation, industry, transportation, and residential use. Within this framework, the energy conversion and industrial sectors are particularly significant, as they account for over 60% of total $CO_2$ emissions [2]. To address these challenges, waste heat recovery (WHR), the integration of renewable energy sources (RES), and the decarbonization of industrial thermal demand have been identified as key enabling technologies, offering three distinct pathways to reduce the carbon footprint of energy conversion systems and industrial processes, all of which are explored throughout this thesis.

As mentioned, one promising approach within the decarbonization strategy is the exploitation of waste heat from power plants and industrial processes. This heat, which is often discarded to the environment, represents a valuable energy resource that can be harnessed to improve overall system efficiency of industrial systems and reduce $CO_2$ emissions. the state of the art is the organic Rankine cycle (ORC) technology, that is unrivalled for low-medium high temperature heat sources typically from 120°C to 450°C [3]. Closed ORC power cycles can be suitable for the heat recovery from flue gases of industrial processes and gas turbines, but they also play an important market position with renewable sources such as geothermal and biomass.

As stated by Macchi [4], the selection of the working fluid is the most important step in determining the success of an ORC, as the thermodynamic properties of the working fluid directly affect the efficiency in the exploitation of the sensible heat source, the operating conditions, and the turbomachines efficiency. The working fluid selection provides the ORC systems the adequate flexibility and efficiency in adapting to different heat sources and sinks. A fundamental aspect of this selection, when high-grade heat is available, is the thermal stability of the working fluid, which sets a limit on the maximum operating temperature of the thermodynamic cycle and is closely linked to its thermal-to-electric efficiency. A working fluid can be defined thermally stable, at a certain temperature level, if its chemical structure maintain integrity after prolonged exposure, without undergoing dissociation or isomerization reactions. Exceeding a fluid's thermal stability threshold can lead to decomposition, resulting in engine malfunctions due to the accumulation of reaction products, reduced heat transfer efficiency, increased operational costs from fluid refills, and potential fouling or erosion of system components. Currently, ORCs are constrained by the thermal stability limits of organic fluids, which typically cap their maximum operating temperature slightly

above 300°C [5]. Only a limited number of organic fluids can maintain the integrity of their chemical bonds at temperatures superior to 300°C, with notable examples including cyclic hydrocarbons like cyclopentane and toluene [6][7]. These fluids are among the few capable of withstanding elevated temperatures without significant degradation, making them suitable for higher temperature applications within the constraints of organic fluid stability. This restricts the applicability of ORC systems in scenarios where heat sources at elevated temperature are available.

On the other hand, conventional steam Rankine cycles, which can operate at higher temperatures, are often not the best option for low power output applications (below 5-10 $MW_{el}$) due to high specific capital cost, layout complexity, low heat recovery efficiency due to high latent heat of evaporation, and poor partial load performance (especially at medium-low turbine inlet temperature due to blade erosion issues). Macchi and Astolfi [8] describe the 5–20 $MW_{el}$ range as a "grey zone" where neither ORC nor steam technology clearly dominates, though ORC is gaining traction due to its simpler design, better part-load performance, and lower maintenance costs. In this zone, Supercritical $CO_2$ ($sCO_2$) could be considered as an alternative, but it requires complex system layout (such as recompression) [9] to optimize the thermal efficiency, operates at high pressures (above 200 bar), and presents challenges in control, making it less practical for small-scale applications. Moreover, $sCO_2$ cycles present large internal heat recovery, reducing the capability of cooling the heat source, i.e. the heat recovery efficiency.

From this overview, it appears clear that there is need to research for innovative working fluids. Papapetrou et al. [10] estimate the EU's waste heat potential at 300 TWh/year, with over 40% above 500°C, mainly in cement, iron, and steel industries. Efficient heat recovery in such cases could benefit from thermally stable fluids, as stated by Colonna et al. [5], which can operate at 500–600°C in stainless steel environment. Thermally stable fluids capable to reach or, eventually, overcome the thermal stability threshold (300–350°C) of state-of-the-art organic fluids could exploit more efficiently high-temperature heat sources that are characterized by a thermal power ranging from tens of kW to few MW, where conventional steam Rankine cycles are not the best techno-economical solution.

The development of innovative fluids with enhanced thermal stability could expand the market applicability of ORCs in both biomass and concentrated solar power (CSP), enabling more efficient and cost-effective energy conversion in a wider range of renewable energy contexts. In fact, ORC is the state-of-the-art technology in small-scale (0.5-5 $MW_{el}$) combined heat and power (CHP) plants fuelledwith solid biomass, even if not able to fully exploit the temperature potential deriving from biomass combustion. Easy-accessible feed-in-tariff, especially for electrical output below 1 $MW_{el}$, promoted the installation of many biomass-fired ORC systems coupled with district heating networks starting from the 90's [11][12]. Despite the substantial incentives and the benefit of working with a dispatchable renewable source, biomass plants have shown minimal improvement in the levelized cost of electricity production, when compared to other renewable energy sources like solar or wind. This stagnation primarily stems from the unique characteristics of biomass-fired plants, which entail significant capital costs associated with biomass boilers and abatement systems, power units, and operational expenses (biomass cost). Progress in enhancing the efficiency of biomass-driven ORCs has been limited, resulting in low electrical efficiencies, typically around 15% for CHP plants [13]. As attested by Swierzewski and Kalina [14], the profitability of biomass-fired ORC CHP

units in retrofitting district heating plants is low, subject to market volatility and financial assistance, with feasible projects averaging a 12-year discounted payback period. Improving the electrical efficiency of CHP-ORC plants with innovative working fluids is a pathway to increase the economic perfor mance of such systems.

While ORC still represents a well-established solution for biomass, their role in concentrated solar power (CSP) is limited only to a limited portfolio of existing plants ranging from few $kW_{el}$ to few $MW_{el}$ where they are competitive with steam Rankine cycles. Solar-ORC technologies include flat plate collectors, vacuum tube collectors, compound parabolic collectors, parabolic trough collectors, and linear Fresnel reflectors [15]. The relatively low electrical efficiency of ORC makes them more attractive when combined heat and power are required. In fact, one of the biggest installations is the hybrid solar-biomass driven ORC plant in Brønderslev Forsyning, which provides 3.8 $MW_{el}$ and thermal power for the local district heating network.

The increase of use of solar energy is within the objectives of the long-term EU strategy to be climate neutral by 2050 and of the RePowerEU plan [16]. The deployment of renewable electricity in the EU to date has primarily been driven by support schemes. In 2019, this support covered 89% of the total electricity produced from wind and 83% by solar photovoltaic (PV) [17]. According to an IEA report [18], the amount of renewable energy capacity added to energy systems around the world grew by 50% in 2023, reaching almost 510 gigawatts (GW), with solar PV accounting for three-quarters of additions worldwide. However, when variable RES like wind and solar increase their penetration in electricity markets, their production has to be curtailed more often due to overproduction, system inflexibility or grid congestion [19]. In a context where the curtailment becomes relevant, Manzolini et al.[20] overcame the levelized cost of electricity (LCOE) concept, as the it is based on the assumption that power generation remains constant through the years, proposing the actual cost of electricity (ACOE) as new index. According to their study, CSP has the lowest curtailment due to the use of the thermal energy storage (TES) that enables the decoupling between renewable source availability and electricity generation and/or connection to the grid.

Even if parabolic through collector is the most adopted technology worldwide [21], solar thermal tower (or central receiver) is the most considered for upcoming installations due to higher overall efficiency. For example, at this time, Cosin Solar Technology company has active CSP tower projects totalling 1 $GW_{el}$ that will be finalized within the next few years. These CSP tower systems adopt molten nitrate salts as heat carrier and thermal storage medium (up to round 565°C), and subcritical steam-Rankine cycle as power block operating at maximum temperature of 540-550°C. The Levelized Cost of Electricity (LCOE) of CSP plants has been decreasing over the past several years, going from the 0.393 $/kWh of 2010 to 0.117$/kWh in 2023, as reported by the International Renewable Energy Agency (IRENA) [22].

However, there is need for further improvement to increase the competitiveness of CSP plants in comparison with other thermal power plants. In this direction, many research is devoted to the application of $sCO_2$ as next-generation working fluid. $sCO_2$ recompressed Brayton cycles are particularly advantageous for their high efficiency due to exploitation of real gas effects, compactness, and potential for significant cost reductions (high power density). Studies indicate that $sCO_2$ cycles can offer approximately 18% cost savings compared to conventional steam Rankine cycles at maximum cycle temperatures around 550°C, highlighting their potential as a more

economical alternative. To advance the development of $sCO_2$ cycles, many projects have been launched around the globe. The Southwest Research Institute (SwRI) received 169 million $ to demonstrate the feasibility of $sCO_2$ cycles by building the STEP demo plant [23]. In 2024, the project achieved full operational speed of its turbine at 27,000 RPM, operating at 500C and 250 bar, generating 4 $MW_{el}$ of grid-synchronized power. The aim of SwRI is to turn the STEP demo plant into the final recompression configuration in 2025 reaching 10 $MW_{el}$ production. Commercial scale 8 $MW_{el}$ (EPS100 model) $sCO_2$ power block is achieved in U.S. by Echogen company for waste heat recovery applications [24]. In Europe, the H2020 SOLARSCO2OL project is aimed at developing a $sCO_2$ power block in order to reduce the LCOE of CSP plants below 0.1$/kWh [25].

Dry cooling in hot environments, such as locations of CSP plants, entails minimum cycle temperatures as high as 50°C, and this drastically reduces the $sCO_2$ cycle efficiency due lower leveraging of real gas effects during the compression step. To solve this issue, innovative $CO_2$-based mixtures with higher critical temperature dopants have been proposed in literature as a viable choice to turn the supercritical Brayton cycle into a transcritical Rankine [26][27]. The capability of the $CO_2$ mixture to perform liquid compression even in environments with high ambient temperatures improves the overall system efficiency and reduces the cost of electricity production. Moreover, $CO_2$-based mixtures simplify the cycle layout as they can typically efficiently work in a simple recuperated cycle compared to pure $sCO_2$, which typically requires a more complex (and costly) recompression layout.

The H2020 SCARABEUS project [28] has been at the forefront of exploring various dopants for $CO_2$ mixtures, focusing on fluids with superior thermal stability, crucial for operation in state-of-the-art central receiver plants (550°C) or next-generation plants (700°C). These dopants, including molecules like Titanium Tetrachloride ($TiCl_4$) [29], are selected for their ability to maintain thermo-chemical stability at elevated temperatures, representing a significant step forward compared to the unconventional fluids currently used in ORC engines. The research and testing of these dopants marks an advancement over current technologies, paving the way for more robust and efficient energy conversion systems capable of operating at higher thermal thresholds. Starting from 2021, the H2020 Desolination project [30], in which a substantial part of this thesis is framed, continued to investigate the use of $CO_2$ binary mixture as working fluid in CSP plants. In the latter project, the heat rejection unit of the $CO_2$-based cycle is exploited to feed a desalination unit [31][32]. The project experimentally investigated additional dopants with high thermal stability, yielding results that could also be applied in the ORC field. A demonstration plant of the Desolination concept is going to be installed in Riyad in the next few years [33].

In addition to WHR and the increased use of renewable sources, as mentioned, industrial high-temperature heat pumps (HTHP) have recently gained significant attention for their role in the decarbonisation pathway. In particular, HTHP could be effective in decarbonising the industrial heat demand in hard-to-abate sectors, especially those with substantial heat requirements above 100°C, such as pulp and paper, food and beverage, and chemical industries. According to Naegler et al. [34], in 2012, the final energy demand for heat across all EU28 member states accounted for 2077 PJ below 100°C, 2214 PJ in the 100-400°C range, and 3859 PJ above 400°C. Steam generation constitutes approximately 40% of industrial process heating demand in Europe, highlighting the critical need for efficient and sustainable heat generation technologies. HTHP have the potential to

replace conventional steam boilers fuelled by fossil sources, reducing greenhouse gas emissions and enhancing energy efficiency [35]. However, the deployment of HTHPs is limited by the availability of suitable refrigerants that combine high-temperature capabilities with low Global Warming Potential (GWP). Historically, heat pumps have relied on hydrofluorocarbons (HFCs) and, more recently, hydrofluoroolefins (HFOs) as refrigerants. In line with EU climate objectives and F-Gas regulations, the industry is transitioning towards alternative refrigerants with reduced GWP.

One promising candidate for high-temperature applications is HFO-1336mzz(Z) [36][37], which offers a high critical temperature (171.3°C), low GWP, and zero ozone depletion potential, making it a practical and sustainable choice for HTHPs. However, challenges remain in finding suitable working fluids for sink temperatures above 160°C, as many conventional refrigerants face limitations in low critical temperature, thermal stability, and compressor design due to excessive pressure ratios. In these high-temperature ranges, there is a need to explore new refrigerants or fluid mixtures that do not fall under F-Gas or PFAS restrictions, which are anticipated to be more stringent in the near future. The development and testing of innovative working fluids for HTHPs, along with further research into their thermal stability and material compatibility, are essential steps toward enhancing the performance and applicability of these systems in the industrial sector.

This research of this thesis focuses on both pure fluids and dopants for $CO_2$ binary mixtures in transcritical thermodynamic cycles, working in HTHP and high-temperature power cycles. The methodology of the research work is detailed in the next Section. The identification process involves a comprehensive screening of the most promising working fluids based on their intrinsic characteristics and thermodynamic efficiency, as determined through detailed modelling across various cycle layouts. Thermal stability assessment is conducted using well-established static isochoric method. The volumetric behaviour of $CO_2$ mixtures is experimentally assessed through both traditional methods and a newly developed setup - within this research - at the Fluid Test Laboratory of the University of Brescia. This integrated approach ensures that the selected fluids not only meet the performance requirements of high-temperature power cycles but also advance the experimental understanding of $CO_2$ mixture thermodynamics, while pushing the thermal stability limits of current working fluids.

## 1.2 Research methodology

This section outlines the research methodology, summarizing the key activities as follows:

- Identification of potential working fluids (both pure and $CO_2$ mixtures) with advanced thermal stability and efficiency.
- Design of a new experimental apparatus for volumetric testing of mixtures, focusing on vapor-liquid equilibrium (VLE) measurements.
- Experimental thermal stability testing using a static isochoric method.
- Experimental measurement of the volumetric behavior of $CO_2$ mixtures.
- Refinement of equations of state (EoS) based on volumetric testing to accurately describe the thermodynamic behavior of $CO_2$ mixtures.
- Modelling of transport properties for the selected working fluid.
- Thermodynamic cycle analysis in Aspen Plus software [38] using the optimised EoS;
- Design of cycle components.

The core focus of this research is the identification of innovative working fluids. Since the ongoing advancements in turbomachinery and heat exchangers are constrained by practical manufacturing limitations, the choice of working fluid becomes a crucial variable for optimizing any thermodynamic cycle. As shown in Figure 1, identifying the working fluid is the first step that drives all subsequent modelling and experimental activities.

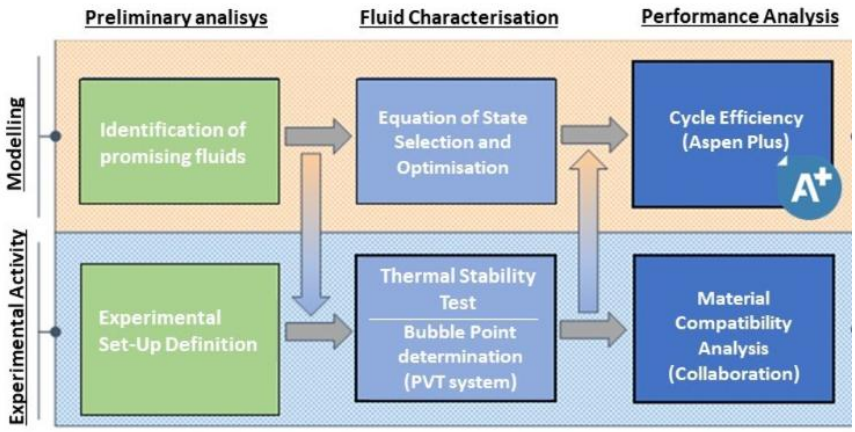


*Figure 1. Overview of the research methodology: starting with the identification of working fluids and the design of a new experimental setup at the Fluid Test Laboratory to determine vapor-liquid equilibrium conditions of mixtures, followed by experimental testing of the selected fluids for thermal stability and volumetric properties (Pressure-Volume-Temperature-Composition data). The process concludes with thermodynamic cycle calculations after tuning the Equation of State (EoS) based on experimental data, with material compatibility analysis conducted, when necessary, in collaboration with the Metal Labs at the University of Brescia.*

After selecting the most promising fluids, it is crucial to experimentally evaluate their thermal stability to establish the maximum operating temperature. The following section outlines the static isochoric method used in this study for the thermal stability test. Determining the maximum operating temperature is the first step in assessing the fluid's suitability for specific applications, such as high-temperature power cycles or heat pumps.

To achieve realistic assessment of the cycle performance, accurate prediction of thermodynamic properties of the working fluid is an essential step. A detailed literature review will support the selection and development of optimized equations of state (EoS) applicable for calculating the thermophysical properties of both pure fluids and mixtures. In case of mixtures, experimental vapor-liquid equilibrium (VLE) data are required to regress the binary interaction parameters of the selected EoS. Experimental VLE data are essential for capturing the non-ideal behavior of mixtures and refining EoS models. Without such data, binary interaction parameters are often assumed to be zero, leading to inaccuracies in the prediction of the thermodynamic properties of the mixture, especially the phase boundaries.

Accordingly, the experimental work conducted within this work can be divided into two main activities: i) thermal stability test; ii) volumetric measurements of $CO_2$ mixtures, i.e. VLE and density data.

A new experimental setup has been designed and validated as part of this research to measure VLE conditions of $CO_2$ mixture at the Fluid Test Laboratory of the University of Brescia. Moreover, in

collaboration with the Centre for Energy Environment Processes (CEEP) at Mines Paris PSL, additional VLE and density measurements have been performed using more conventional methods.

Following the identification and experimental characterization of the fluids, their performance in thermodynamic cycles, such as power cycles or heat pumps, is analysed using Aspen Plus software [39]. The results of this analysis guide the subsequent design and optimization of cycle components. For the components design, it is necessary to characterize not only the thermodynamic properties but also the transport properties, such as viscosity and thermal conductivity.

The following sub-sections will outline the key principles guiding the main activities illustrated in Figure 2.

### 1.2.1 Identification on Innovative Working Fluids

The search for innovative working fluids focuses on identifying and developing solutions capable of operating at high temperatures, thereby enhancing thermal efficiency and reducing greenhouse gas emissions across various energy sectors. This Section explores the different categories of working fluids under investigation, highlighting their potential applications and the challenges associated with their development.

An ideal working fluid should have certain key characteristics:

- low toxicity
- zero ozone depletion potential (ODP), low global warming potential (GWP)
- market availability at low cost
- low viscosity and high thermal conductivity
- thermal stability, and material compatibility with common stainless steel
- compatibility with common lubricants
- not listed under international protocols that call for the phasing out of specific compound families from the market (such as PFAS compounds).
- good thermodynamic efficiency of the associated thermodynamic cycle over the heating and cooling temperature ranges of interest.

As mentioned, this work focuses on pure fluids or dopants for $CO_2$ mixtures to be operated in high temperature power cycles or heat pumps. While selecting a working fluid for high-temperature applications, the most fundamental aspect is thermal stability, important to avoid decomposition products across the cycle that can lead to component malfunctions, accumulation of non-condensable products as well as engine blockage. According to the different applications of interest for this research, there are three different thermal level that the identified working fluids must withstand or overcome:

The 550°C (and above) level of the CSP tower plants in which $CO_2$ mixtures are intended to operate as next-generation working fluid

The 300-350°C level of the state-of-the-art ORC field

The 150-160°C level of HTHP systems (still laboratory scale)

The identification of dopants whose chemical bonds are not subjected to extensive dissociation or isomerization reactions above 550°C (i.e. the state-of-the-art maximum temperature for CSP plants with nitrate salts) is a very challenging task. Therefore, it is necessary to prioritize the thermal stability aspect sacrificing the toxicological-environmental qualities of the working fluid. In fact, as mentioned, is it well-known that the maximum operating temperatures of organic fluids commercially employed in Organic Rankine Cycles (ORC) is below 300-350°C due to thermal stability issues [7]. For example, Siloxanes can be adopted in ORCs up to 260°C [40], with acceptable decomposition rates, while hydrocarbons can operate near 300°C [7] as maximum temperature. Most of refrigerants cannot be considered as $CO_2$ dopant in state-of-the art CSP tower plants since refrigerants chemically decompose at temperatures lower than 425°C [41] due to C-H bond cleavage. Moreover, refrigerants typically possess low critical temperature, while high critical temperature is desired to have a transcritical power cycle with condensation temperatures around 50°C. Similarly, in WHR sector, the critical temperature is crucial, as pure fluids with elevated critical temperatures are better suited to match high-temperature heat sources. In this sense, research on $CO_2$ dopants aligns closely with the development of pure working fluids for high-temperature ORC applications.

Within the Scarabeus and Desolination projects, the ambitious target of 550°C has been achieved by a few mixtures, though with some problematics. The $CO_2$ mixture with hexafluorobenzene ($C_6F_6$) was demonstrated to be thermally stable below 600°C [42] in an Inconel 625 alloy vessel after 100 hours thermal stresses. However, a metallographic study on the welds of the test vessel, exposed at the mixture at 550°C, revealed long cracks in the heat-affected zone (HAZ) of the welds [43]. As a result, $C_6F_6$ was phased out as a dopant candidate for the demonstrator plant in the Desolination project. Also titanium tetrachloride ($TiCl_4$) has been explored in recent years both as a potential $CO_2$ dopant [44] in the SCARABEUS project for 700°C applications, and as a pure fluid for high-temperature Rankine cycles [45]. Given that $TiCl_4$ is industrially oxidized at very high temperatures (1500-2000 K) to produce $TiO_2$ [46], its thermal stability at 700°C was initially assumed. Previous tests conducted in our Fluid Test Laboratory confirmed its stability up to 500°C in stainless steel [47], a notable improvement over other non-conventional fluid. However, its strong reactivity presents significant challenges for power plant applications. Additionally, $TiCl_4$'s extreme tendency to hydrolyse in contact with humid air complicates its use. Its high boiling point (136.4°C) would require sub-atmospheric conditions in the turbine, recuperator, and condenser for optimal system performance, which increases the risk of air infiltration and subsequent fluid hydrolysis.

In the case of $CO_2$+$TiCl_4$ mixture, the issue of air in-leakage is mitigated by high operating pressures (above 100 bar), but experimental vapor-liquid equilibrium (VLE) tests failed due to $TiCl_4$'s reactivity with materials. Consequently, $TiCl_4$ was excluded as a potential dopant for the Desolination project's demonstrator. In this direction, sulphur dioxide ($SO_2$) has been selected as potential dopant [48] for the demonstration plant of Desolination [49], after an extensive campaign of long-term material compatibility at the Fluid Test Laboratory and Metal Labs of the University of Brescia.

As part of this research, within the H2020 Desolination project framework, Silicon Tetrachloride ($SiCl_4$) has been proposed for the first time both as pure fluid for very-high temperature Rankine cycles (Chapter 2 and Chapter 9) [50] and as $CO_2$ dopant for transcritical CSP plants (Chapter 4) [51]. Experimental studies, presented in the next sections, showed that $SiCl_4$ remains stable even after prolonged exposure at 650°C in contact with stainless steel, providing a notable improvement over

other known fluid. According to reports, $SiCl_4$ remains thermally stable even at 1200°C and it is much less reactive than $TiCl_4$ [52], justifying the industrial interest. The lower normal boiling point (57°C), in comparison with $TiCl_4$, and its wide use in chemical industry poses less problematics related to its reactivity and its potential use as working fluid.

When approaching applications that -at state of the art- operates at lower temperatures (i.e., below 550°C) such as ORC and HTHP, it is possible to lower the thermo-chemical stability requisite and to better satisfy also toxicological and environmental characteristics. Hydrocarbons (HCs) have a favourable toxicological profile, in general, and exhibit varying levels of thermo-chemical stability based on their molecular structure. Cyclic hydrocarbons, such as cyclopentane and toluene, generally have higher activation energies and better stability compared to linear hydrocarbons. Fluorinated compounds, such as hydrofluorocarbons (HFCs), offer enhanced thermal stability due to their strong C-F bonds [56]. Historically, heat pumps have relied on HFCs and more recently on hydrofluoroolefins (HFOs) as refrigerants, but their low critical temperature does not fit the industrial requirement for high-temperature latent heat. The search for suitable refrigerants becomes increasingly complex as desired sink temperatures rise above 150-160°C. This range presents significant challenges due to the limitations in the low critical temperature of most conventional refrigerants, including HFOs, below 180°C. As a consequence, this range of sink temperatures can be covered by transcritical HTHP cycles operating with pure fluids or $CO_2$ mixtures [57,58]

The pursuit of suitable working fluids for delivering latent heat extends to complex hydrocarbons [59], such as cyclopentane, n-pentane, and isopentane, due to their high critical temperatures, making them viable candidates for the 160-200°C range. Among novel substances, fluorobenzene ($C_6H_5F$) is proposed in this research (Chapter 3) as a potential working fluid for both closed-loop HTHPs and ORC systems [60]. Fluorobenzene offers near-zero GWP and zero ODP, with a high critical temperature of 286°C, making it suitable subcritical HTHP beyond the capabilities of current low-GWP refrigerants. Unlike benzene, fluorobenzene has significantly lower toxicity. With a single fluorine atom, the fluid is not classifiable as a PFAS substance, making it an environmentally friendly and cost-effective alternative.

However, it must be noted that not only isothermal heat is required by processes, but also sensible high-temperature heat. For instance, the pressurized water loop of a district heating network (DHN) has a return temperature of 60°C and a supply temperature in the range 90-120°C depending on the ambient conditions and thermal losses in the DHN itself. In this case, a transcritical HTHP, with non-isothermal heat rejection, can better perform than a subcritical HTHP due to well matching the heat sink. In fact, $CO_2$ transcritical heat pumps are a commercially available solution [61]. The biggest $CO_2$ heat pump, consisting of three units of 44 $MW_{th}$ each, is under construction in Aalborg (Denmark) to serve the local DHN. In particular, the heat pump is fed by seawater at 2-3°C at the evaporator and rejects 98°C heat at the gas cooler. However, when low-grade waste heat is available (40-100°C), a $CO_2$ heat pump may not be the optimal choice due to $CO_2$'s low critical temperature (31°C), which forces the system to evaporate at low temperatures, leading to significant irreversibility production during heat transfer with the heat source. To address this, the present work explores the use of $CO_2$ binary mixtures with a high critical temperature dopant ($C_2Cl_4$ in particular) as a potential solution for enhancing the performance of the sensible heat pump (Chapter 5) [62].

### 1.2.2 Experimental characterisation: thermal stability

A fundamental aspect in the working fluid selection is thermal stability, as it determines the suitability of a working fluid to operate in a certain application and it is closely related to its efficiency. Even in case of HTHP systems, the compressor discharge temperature can reach values that necessitates the investigation of the thermo-chemical stability of the working fluid. This is particularly relevant when the working fluid complexity (number of atoms per molecule) is low, thus having low internal degrees of freedom and specific heat, which tends to overheat during compression.

A compound is defined thermally stable at a certain temperature level if its chemical bonds are not subjected to dissociation or isomerization reactions. The thermal decomposition of the working fluid involves a deviation of the engine behaviour from the design conditions, leading to malfunction and possible shutdown [63]. The primary concerns associated with the degradation of the power cycle's working fluid are: 1) the accumulation of liquid degradation products has the potential for altering the bulk fluid properties and thereby affecting heat transfer processes with a resultant loss in cycle efficiency, and 2) the accumulation of non-condensable gases results in a rise in turbine back pressure which ultimately results in a decrease in cycle efficiency and specific net-work; 3) the formation of solid particles which can contribute to the turbine's blade erosion.

In an inert environment, the thermal stability of a fluid is only dependent on the energy barriers of the bonds constituting the molecule. However, the presence of contaminants (oil, water, air, etc.) or the materials of the engine can act as catalyst of the decomposition process. For this reason, the thermal stability of working fluids should be tested in contact with common materials used for the manufacture of high-temperature components of the power block. Pyrolysis tests are usually performed, in literature, in inert quartz tubes and with low residence time (seconds), providing scarce information from a power plant point of view. For this reason, there is need for a method that accounts for the presence of manufacturing materials and with adequate residence time (hours) to appreciate the formation of degradation products.

Even if only a chemical analysis can quantify and recognize the decomposition products after a thermal stress, it is possible to detect the thermal degradation of a fluid in a semi-qualitative way through a change of physical properties. Blake et al. (1961, [64]) introduced an experimental thermal stability test based on the analysis of the pressure deviations during isothermal conditions; the method was used to investigate the thermal decomposition of 100 organic compounds and was used later by many authors. The principle behind Blake's approach is that the moles of decomposition products formed by molecular bond cleavage during the constant-temperature thermal stress, can be visualized as a pressure increase.

Since small degradation can lead to significative increase of the vapor pressure due to cleavage of the molecule into smaller and more volatile compounds, decomposition phenomena can be identified from relative variations of the vapor pressure after thermal stress compared to the same property of the virgin fluid. This concept is similar to that of Blake, but the deviation of vapor pressure due to presence of non-condensable products is more clearly evident even at smaller decomposition rates, especially at sub-atmospheric vapour pressures. The first experimental apparatus adopting this concept was developed by Angelino and Invernizzi [65], in order to evaluate the thermal stability of working fluids for ORCs. In the Fluids Test Laboratory facility at

Department of Mechanical and Industrial Engineering of the University of Brescia, this "static" experimental method is used to evaluate the thermal stability of the fluids. The experimental apparatus is described in [6] and shown in Figure 3. The virgin fluid sample of an arbitrarily fixed mass is inserted into a closed cylinder placed into a cryostat, and the vapor pressure is recorded during the permanence of the fluid at various temperature levels is considered as reference. After the measure of its reference vapour pressure, the fluid sample withstands different constant test temperatures at pre-set time intervals (typically from 80 to100 hours). After the permanence of the fluid sample at the test temperature, the vapour pressure curve is re-measured each time. Decomposition of the fluid is revealed by (i) any variation in the pressure recorded over time during the permanence of the sample at constant temperature; (ii) a difference in the vapour pressure compared to the reference isochoric line. Pasetti et al. [6] introduced a statistical analysis aimed at identifying those measured deviations of the vapor pressure that are clear sign of thermal decomposition of the fluid sample, thus not attributable to experimental uncertainties. Also, a pseudo-quantitative analysis was introduced for pure fluids consisting of the estimation of decomposition reaction rates. At low reduced temperatures, the mole fraction of gaseous decomposition fraction can be estimated as the deviation of the sample's vapor pressure due to presence of impurities [66]. Then, the rate of decomposition reaction (assumed unimolecular) can be regressed from the Arrhenius equation [6].

This "static" survey method is applicable to pure fluids as well as mixtures. However, in the case of mixtures, the reference curve is an equilibrium P-T curve which is a function of density, that is, of the amount of mixture loaded in the closed volume. According to this method, the $CO_2$ binary mixtures with $C_6F_6$ [42] and $C_6F_{14}$ [67] have been recently tested in the Fluid Test Laboratory.

The material of the sample cylinder and the test circuit is typically stainless steel, but it can be manufactured with other metal alloys used in the high-temperature components of the power plant. As an example, the $CO_2$+ $C_6F_6$ mixture has been tested in Inconel 625 environment, as $CO_2$ presents material compatibility issues above 450-500°C with stainless steel. However, fluorinated compounds strongly interact with Inconel 625 alloy in the heat affected zone of the welding at such temperatures [43]. For this reason, beyond the insights gained from the thermal stability test, metallographic analysis is crucial in identifying the compatibility between the fluid and the material, especially at temperature as high as 550°C.

In this research work, the static isochoric method has been applied to study the thermal stability of the proposed fluids: silicon tetrachloride ($SiCl_4$) in Chapter 2, fluorobenzene ($C_6H_5F$) in Chapter 3, and perchloroethylene ($C_2Cl_4$) in Chapter 5. Even in case of interest in $CO_2$ mixture with one of the mentioned dopants, it is decided to experimentally test the thermal stability of the pure working fluid, given the good thermal stability of $CO_2$. This choice is influenced by the characteristics of the aforementioned method, where deviations in vapor pressure become more noticeable under sub-atmospheric or near-atmospheric conditions. In the case of a $CO_2$ mixture, the test pressures are inherently higher, requiring a pressure transducer with a larger full-scale range. Consequently, the uncertainty in pressure measurement increases, making it difficult to accurately detect pressure deviations caused by the dopant decomposition. The testing of the sole dopant ensures a better understanding its integrity under prolonged thermal exposure.

In this work, a novel procedure has been introduced during the thermal stability test of fluorobenzene (Chapter 3) to account for the presence of the non-condensable gases (NCG) removal system in ORC real operating conditions. In fact, partial thermal decomposition of the working fluid in ORC systems is generally unavoidable under normal conditions. What is crucial, however, is that fluid degradation occurs at an acceptable rate—meaning only occasional partial refills are necessary—and that the decomposition products are primarily non-condensable gases. These gases tend to accumulate in the condenser shell but can be removed by the NCG removal system. Conversely, if the working fluid degrades into liquid products, its properties change over time, leading to operational issues. To address this, the proposed methodology includes successive thermal stresses with periodic aspiration to simulate the activation of the NCG removal system, followed by a final chemical analysis of the thermally stressed liquid to ensure that the fluid does not degrade into other liquid species, such as benzene.

### 1.2.3 Experimental characterisation: VLE and density of $CO_2$ mixtures

In general, the accurate knowledge of the phase boundaries of mixtures is crucial for the design and optimization of closed thermodynamic cycles working in direct or inverse Rankine cycles. The evaluation of the power cycle efficiency and reliable design conditions strongly depend on the accuracy of the equation of state (EoS) used to determine the thermodynamic properties of the mixture and its phase behaviour. It is well known that, in case of mixtures, the reliability of the EoS is improved when the binary interaction parameters of the EoS are regressed based on experimental vapour-liquid equilibrium (VLE) data. When these adjustable parameters are tuned on experimental VLE data, the phase boundaries of the mixture are better represented by the EoS, which is crucial from the power cycle point of view.

Generally, VLE data of mixtures are measured with conventional Pressure-Volume-Temperature (PVT) systems [68] and VLE apparatus [69]. In PVT systems, the mixture is transferred into a cell, whose volume is varied with an automated piston under isothermal conditions, and the bubble point is determined from the divergence of the volumetric behaviour in the liquid phase and the two-phase field. In VLE cells, instead, a small sample of fluid, from both liquid and vapour phases, is extracted, vaporized, and analysed with gas chromatography. To avoid dead volumes and large pressure drop within the cell, the adoption of a capillary rapid on-line sampling injector (ROLSI®) [70] become a practical standard for VLE cells. A VLE apparatus used for the measurement of $CO_2$ binary mixtures is well described in the experimental works of Coquelet and Valtz [71][72][73].

In collaboration with the Centre for Energy Environment Processes (CEEP) at Mines Paris PSL, a PVT cell has been utilized [74], to measure bubble points of a $CO_2$ mixture with $SiCl_4$ for high-temperature Rankine cycle application (Chapter 4). Moreover, in the same work, an innovative approach has been adopted to measure additional bubble points with a vibrating tube densimeter.

Additionally, an isochoric apparatus has been developed during this research work in the Fluid Test Laboratory of the University of Brescia [75], which is presented in Chapter 6. The experimental setup is designed to obtain bubble points of mixtures from the divergence of isochoric behaviour of the mixture between the two-phase VLE region and the single-phase liquid region. The apparatus implemented in our laboratory employs a methodology (isochoric) already established in the literature; however, the proposed isochoric system provides the advantage of a simplified procedure

and equipment, resulting in reduced cost. Two mixtures ($CO_2$+$C_6F_6$ and $CO_2$+$C_5H_{12}$), whose volumetric behaviour is well-known in literature, were selected to validate the proposed apparatus and procedure while VLE data on the blend $CO_2$+c-$C_4F_8$ are here measured for the first time in literature.

Not only VLE data have been measured of the $CO_2$+$SiCl_4$ mixture at CEEP but also liquid density data. Liquid density measurements of the $CO_2$+$SiCl_4$ and $CO_2$+$C_2Cl_4$ mixtures have been obtained at the CEEP by using a vibrating tube densimeter (VTD), which core is an Anton Paar DMA HPM, as described in literature [76]. It is important to highlight that the experimental setup used in this research [74], featuring a variable volume cell prior to venting the mixture, was specifically designed to measure the density of a binary mixture composed of two compounds with significantly different volatilities. In this setup, the volume can be adjusted using a manual hand pump. This layout can serve as a reference case study for future density measurements of $CO_2$ zeotropic mixtures.

### 1.2.4 Modelling of thermophysical properties

In general, the accurate knowledge of the phase boundaries of mixtures is crucial for the design and optimization of closed thermodynamic cycles working in direct or inverse Rankine cycles. The evaluation of the power cycle efficiency and reliable design conditions strongly depend on the accuracy of the equation of state (EoS) used to determine the thermodynamic properties of the mixture and its phase behaviour. It is well known that, in case of mixtures, the reliability of the EoS is improved when the binary interaction parameters of the EoS are regressed based on experimental vapour-liquid equilibrium (VLE) data. When these adjustable parameters are tuned on experimental VLE data, the phase boundaries of the mixture are better represented by the EoS, which is crucial from the power cycle point of view.

Reliable thermodynamic models are necessary to calculate the properties of binary mixtures along the thermodynamic regions of interest for the closed thermodynamic cycle. In the last decades, cubic EoS such as the Peng Robinson (PR) [77] and Soave-Redlich-Kwong (SRK) [78] have become consolidated choices, especially in the industry [79] [80].

The PR EoS [77], as expressed in Equation 1-7, is the most considered model - in this work - for the calculation of thermodynamic properties calculations of pure fluids and $CO_2$ mixtures, given its simplicity and robustness.

$$P = \frac{RT}{v-b} - \frac{\alpha a}{v(v+b)+b(v-b)} \tag{1}$$

where the alpha function adopted is in its original form [77]:

$$\alpha = \left[1 + k\left(1 - \sqrt{T_r}\right)\right]^2 \tag{2}$$

$$k = 0.37464 + 1.54226\omega - 0.26992\omega^2 \tag{3}$$

$$a = 0.45724\frac{R^2 T_{cr}^2}{P_{cr}} \tag{4}$$

$$b = 0.0778\frac{RT_{cr}}{P_{cr}} \tag{5}$$

Van der Waals mixing rules are then adopted to describe the binary mixture as follows:

$$a_m = \sum_{i=1}^{n_c}\sum_{j=1}^{n_c} x_i x_j \sqrt{a_{ii}a_{jj}}\left(1 - k_{ij}\right) \tag{6}$$

$$b_m = \sum_{i=1}^{n_c} x_i b_i \tag{7}$$

where the binary interaction parameter (BIP) $k_{ij}$=$k_{ji}$ must be fitted on VLE data to improve the accuracy of the EoS in the mixture description. The general formulation of the EoS contains a second BIP on the covolume term, in Eq. 7, but it is commonly neglected in literature.

The BIP regression is performed within the software ASPEN Properties v12 [81], using the maximum likelihood method as numerical optimization method. The Britt–Luecke algorithm [82] with Deming initialization method [83] is applied to regress the parameter. The Average Absolute Deviation percentage (AAD%) is selected as a metric to quantify the Equation of State (EoS) fitting capability for the experimental data. The BIP of the PR EoS has been regressed on the measured bubble points data in the work with the $CO_2$+$SiCl_4$ mixture [74], and its capability in predicting also liquid density data of the mixture has been assessed. In the research on the $CO_2$+$C_2Cl_4$ mixture, the composition range of interest for HTHP operation focused on $CO_2$ molar content above 95%, where the influence of the BIP on the estimated phase envelope is negligible. Therefore, only liquid density data were measured, and the BIP of the PR EoS was tuned to these data to enhance the model's overall predictive accuracy.

While a refined thermodynamic model is useful to assess the cycle operating conditions and performance, for the design of the components of the power block it is necessary to possess reliable models for transport properties. In particular, the dynamic viscosity and thermal conductivity are fluid properties related to momentum and heat transfer and are key properties for the determination of the heat transfer coefficients. Almost all the methods available to estimate the transport properties of dense pure fluids and mixtures are empirical or semi-theoretical [84]. The generic transport property $\pi$ is calculated as a sum of a "zero-density" property $\pi 0$ and a "residual property" $\Delta\pi$:

$$\pi(T,p) = \pi_0(T) + \Delta\pi(T,p) \tag{8}$$

The zero-density term can be calculated with methods that are derived from the rigorous kinetic theory of gases, whilst almost all the methods available to describe the residual property are empirical or semi-theoretical, with the corresponding-state (CS) based methods being the most applied. About the residual term, when the two components in the mixture are very different in size and shape, the CS approach tends to fail since the reference fluid cannot be "conformal" with both the components in the mixture. As highlighted in a work presented in Chapter 7 [85], the transport properties of $CO_2$ complex mixtures are potentially better described with the use of the relatively recent friction-theory models [86][87], which relies on an equation of state to describe the residual transport property of the mixture. The f-theory models can provide good results for mixtures even

if the optimization is carried out only on pure component experimental data: no binary interaction parameters are involved in the model. The same models have been used in MATLAB software for the calculation of the transport properties of $SiCl_4$ [88] as large discrepancy was found between experimental data and transport models available in Aspen Plus software. The tuned transport properties models are used in Chapter 9 for the design of the components of the $SiCl_4$ power block in biomass-fired CHP application.

## 1.3 Bibliography


[1] E. Commission, D.-G. for Climate Action, Going climate-neutral by 2050 – A strategic long-term vision for a prosperous, modern, competitive and climate-neutral EU economy, Publications Office, 2019. https://doi.org/doi/10.2834/02074.

[2] IEA, Europe Emissions, https://www.iea.org/regions/europe/emissions.

[3] E. Macchi, M. Astolfi, Organic Rankine Cycle (ORC) Power Systems: Technologies and Applications, 2016.

[4] E. Macchi, THE CHOICE OF WORKING FLUID: THE MOST IMPORTANT STEP FOR A SUCCESSFUL ORGANIC RANKINE CYCLE (AND AN EFFICIENT TURBINE) -ORC2013 keynote lecture, Rotterdam, 2013.

[5] P. Colonna, E. Casati, C. Trapp, T. Mathijssen, J. Larjola, T. Turunen-Saaresti, A. Uusitalo, Organic Rankine Cycle Power Systems: From the Concept to Current Technology, Applications, and an Outlook to the Future, J Eng Gas Turbine Power 137 (2015) 100801. https://doi.org/10.1115/1.4029884.

[6] M. Pasetti, C.M. Invernizzi, P. Iora, Thermal stability of working fluids for organic Rankine cycles: An improved survey method and experimental results for cyclopentane, isopentane and n-butane, Appl Therm Eng 73 (2014) 764–774. https://doi.org/10.1016/j.applthermaleng.2014.08.017.

[7] C.M. Invernizzi, P. Iora, G. Manzolini, S. Lasala, Thermal stability of n-pentane, cyclo-pentane and toluene as working fluids in organic Rankine engines, Appl Therm Eng 121 (2017) 172–179. https://doi.org/10.1016/j.applthermaleng.2017.04.038.

[8] E. Macchi, M. Astolfi, Organic Rankine Cycle (ORC) Power Systems: Technologies and Applications, 2016.

[9] V. Dostal, P. Hejzlar, M.J. Driscoll, High-performance supercritical carbon dioxide cycle for next-generation nuclear reactors, Nucl Technol 154 (2006) 265–282. https://doi.org/10.13182/NT154-265.

[10] M. Papapetrou, G. Kosmadakis, A. Cipollina, U. La Commare, G. Micale, Industrial waste heat: Estimation of the technically available resource in the EU per industrial sector, temperature level and country, Appl Therm Eng 138 (2018) 207–216. https://doi.org/10.1016/j.applthermaleng.2018.04.043.

[11] A. Duvia, M. Gaia, ORC plants for power production from biomass from 0.4 MWe to 1.5 MWe: technology, efficiency, practical experiences and economy, in: Proceedings of the 7th Holzenergie Symopsium, Zurich, 2002.

[12] I. Obernberger, P. Thonhofer, E. Reisenhofer, Description and evaluation of the new 1,000 kWel organic rankine cycle process integrated in the biomass CHP plant in Lienz, Austria, Euroheat and Power 10 (2002) 1–17.

[13] M. Tańczuk, R. Ulbrich, Implementation of a biomass-fired co-generation plant supplied with an ORC (Organic Rankine Cycle) as a heat source for small scale heat distribution system - A comparative analysis under Polish and German conditions, Energy 62 (2013) 132–141. https://doi.org/10.1016/j.energy.2013.09.044.

[14] M. Świerzewski, J. Kalina, Optimisation of biomass-fired cogeneration plants using ORC technology, Renew Energy 159 (2020) 195–214. https://doi.org/10.1016/j.renene.2020.05.155.

[15] D. Matuszewska, Solar Organic Rankine Cycle (ORC) Systems: A Review of Technologies, Parameters, and Applications, Energies (Basel) 17 (2024) 5106. https://doi.org/10.3390/en17205106.

[16] European Commission, RePowerEU, (2022). https://commission.europa.eu/strategy-and-policy/priorities-2019-2024/european-green-deal/repowereu-affordable-secure-and-sustainable-energy-europe_en (accessed October 28, 2024).

[17] Sebastian. Busch, Ruben. Kasdorp, Derck. Koolen, Arnaud. Mercier, Magdalena. Spooner, The development of renewable energy in the electricity market, Publications Office of the European Union, 2023.

[18] IEA, Renewables 2023, 2023. www.iea.org.

[19] J. López Prol, D. Zilberman, No alarms and no surprises: Dynamics of renewable energy curtailment in California, Energy Econ 126 (2023) 106974. https://doi.org/https://doi.org/10.1016/j.eneco.2023.106974.

[20] G. Manzolini, M. Binotti, G. Gentile, G. Picotti, L. Pilotti, M.E. Cholette, Actual cost of electricity: An economic index to overcome levelized cost of electricity limits, IScience 27 (2024). https://doi.org/10.1016/j.isci.2024.109897.

[21] A.H. Alami, A.G. Olabi, A. Mdallal, A. Rezk, A. Radwan, S.M.A. Rahman, S.K. Shah, M.A. Abdelkareem, Concentrating solar power (CSP) technologies: Status and analysis, International Journal of Thermofluids 18 (2023). https://doi.org/10.1016/j.ijft.2023.100340.

[22] IRENA, RENEWABLE POWER GENERATION COSTS IN 2023 EXECUTIVE SUMMARY, Abu Dhabi, 2024. www.irena.org.

[23] D.R. Douslin, R.T. Moore, J.P. Dawson, G. Waddington, The Pressure-Volume-Temperature Properties of Fluorobenzene1, J Am Chem Soc 80 (1958) 2031–2038. https://doi.org/10.1021/ja01542a001.

[24] T.J. Held, SUPERCRITICAL CO2 CYCLES FOR GAS TURBINE COMBINED CYCLE POWER PLANTS, in: Power Gen International, Las Vegas.

[25] SOLARSCO2OL Project, https://www.solarsco2ol.eu/ (accessed October 28, 2024).

[26] G. Manzolini, M. Binotti, D. Bonalumi, C. Invernizzi, P. Iora, CO2 mixtures as innovative working fluid in power cycles applied to solar plants. Techno-economic assessment, Solar Energy 181 (2019) 530–544. https://doi.org/10.1016/J.SOLENER.2019.01.015.

[27] C.J.N. Sánchez, A.K. da Silva, Technical and environmental analysis of transcritical Rankine cycles operating with numerous CO2 mixtures, Energy 142 (2018) 180–190. https://doi.org/10.1016/j.energy.2017.09.120.

[28] SCARABEUS, Supercritical Carbon dioxide/Alternative fluids Blends for Efficiency Upgrade of Solar power plants, (2019).

[29] M. Binotti, G. Di Marcoberardino, P. Iora, C. Invernizzi, G. Manzolini, Scarabeus: Supercritical carbon dioxide/alternative fluid blends for efficiency upgrade of solar power plants, AIP Conf Proc 2303 (2020). https://doi.org/10.1063/5.0028799.

[30] DESOLINATION – Sustainable desalination from Concentrated Solar Power., https://desolination.eu/.

[31] O.A. Terracciano, F. De Francesco, R. Brizzi, F. Annese, M. Doninelli, L. Putelli, M. Gelfi, An Advanced Desalination System with an Innovative CO2 Power Cycle Integrated with Renewable Energy Sources, in: 2023: p. D011S017R002. https://doi.org/10.2118/215993-MS.

[32] I.M. Carraretto, E. Morosini, R. Simonetti, M. Astolfi, M. Binotti, G. Manzolini, Thermal Desalination Through Forward Osmosis Coupled With CO2-Mixture Power Cycles for CSP Applications, SolarPACES Conference Proceedings 2 (2024). https://doi.org/10.52825/solarpaces.v2i.789.

[33] E. Morosini, M. Astolfi, M. Doninelli, P. Iora, D. Serret, J.-M. Hugo, G. Manzolini, Preliminary Characterization of the Desolination Project Demo Plant: Design and Off-Design Operability, in: 2024: p. V011T28A023. https://doi.org/10.1115/GT2024-127246.

[34] T. Naegler, S. Simon, M. Klein, H.C. Gils, Quantification of the European industrial heat demand by branch and temperature level, Int J Energy Res 39 (2015) 2019–2030. https://doi.org/https://doi.org/10.1002/er.3436.

[35] S. Klute, M. Budt, M. van Beek, C. Doetsch, Steam generating heat pumps – Overview, classification, economics, and basic modeling principles, Energy Convers Manag 299 (2024) 117882. https://doi.org/https://doi.org/10.1016/j.enconman.2023.117882.

[36] K. Kontomaris, HFO-1336mzz-Z: High Temperature Chemical Stability and Use as A Working Fluid in Organic Rankine Cycles, International Refrigeration and Air Conditioning Conference (2014) 10.

[37] J. Navarro-Esbrí, A. Mota-Babiloni, Experimental analysis of a high temperature heat pump prototype with low global warming potential refrigerant R-1336mzz(Z) for heating production above 155 °C, International Journal of Thermofluids 17 (2023). https://doi.org/10.1016/j.ijft.2023.100304.

[38] Aspen Technology Inc., Aspen Plus®, Version V12.1, (2022).

[39] Aspen Technology Inc., Aspen Plus®, Version V12.1, (2022).

[40] L. Keulen, S. Gallarini, C. Landolina, A. Spinelli, P. Iora, C. Invernizzi, L. Lietti, A. Guardone, Thermal stability of hexamethyldisiloxane and octamethyltrisiloxane, Energy 165 (2018) 868–876. https://doi.org/10.1016/j.energy.2018.08.057.

[41] G. Angelino, C. Invernizzi, Experimental investigation on the thermal stability of some new zero ODP refrigerants, International Journal of Refrigeration 26 (2003) 51–58. https://doi.org/10.1016/S0140-7007(02)00023-3.

[42] G. Di Marcoberardino, E. Morosini, D. Di Bona, P. Chiesa, C. Invernizzi, P. Iora, G. Manzolini, Experimental characterisation of CO2 + C6F6 mixture: Thermal stability and vapour liquid equilibrium test for its application in transcritical power cycle, Appl Therm Eng 212 (2022) 118520. https://doi.org/10.1016/j.applthermaleng.2022.118520.

[43] L. Putelli, G. Di Marcoberardino, M. Gelfi, C.M. Invernizzi, P.G. Iora, G. Manzolini, Preliminary Analysis of High-Temperature Corrosion of Metallic Alloys With CO2 and CO2-Based Working Mixtures for Power Plants Applications, in: 2022: p. V009T28A035. https://doi.org/10.1115/GT2022-84197.

[44] G. Manzolini, M. Binotti, D. Bonalumi, C. Invernizzi, P. Iora, CO2 mixtures as innovative working fluid in power cycles applied to solar plants. Techno-economic assessment, Solar Energy 181 (2019) 530–544. https://doi.org/10.1016/J.SOLENER.2019.01.015.

[45] C.M. Invernizzi, P. Iora, D. Bonalumi, E. Macchi, R. Roberto, M. Caldera, Titanium tetrachloride as novel working fluid for high temperature Rankine Cycles: Thermodynamic analysis and experimental assessment of the thermal stability, Appl Therm Eng 107 (2016) 21–27. https://doi.org/10.1016/j.applthermaleng.2016.06.136.

[46] R.H. West, R.A. Shirley, M. Kraft, C.F. Goldsmith, W.H. Green, A detailed kinetic model for combustion synthesis of titania from TiCl4, Combust Flame 156 (2009) 1764–1770. https://doi.org/https://doi.org/10.1016/j.combustflame.2009.04.011.

[47] C.M. Invernizzi, P. Iora, D. Bonalumi, E. Macchi, R. Roberto, M. Caldera, Titanium tetrachloride as novel working fluid for high temperature Rankine Cycles: Thermodynamic analysis and experimental assessment of the thermal stability, Appl Therm Eng 107 (2016) 21–27. https://doi.org/10.1016/j.applthermaleng.2016.06.136.

[48] E. Morosini, A. Ayub, G. di Marcoberardino, C.M. Invernizzi, P. Iora, G. Manzolini, Adoption of the CO2 + SO2 mixture as working fluid for transcritical cycles: A thermodynamic assessment with optimized equation of state, Energy Convers Manag 255 (2022). https://doi.org/10.1016/j.enconman.2022.115263.

[49] E. Morosini, M. Astolfi, M. Doninelli, P. Iora, D. Serret, J.-M. Hugo, G. Manzolini, Preliminary Characterization of the Desolination Project Demo Plant: Design and Off-Design Operability, in: 2024: p. V011T28A023. https://doi.org/10.1115/GT2024-127246.

[50] M. Doninelli, G. Di Marcoberardino, P. Iora, M. Gelfi, C.M. Invernizzi, G. Manzolini, Silicon Tetrachloride as innovative working fluid for high temperature Rankine cycles: Thermal Stability, material compatibility, and energy analysis, Appl Therm Eng 249 (2024) 123239. https://doi.org/10.1016/j.applthermaleng.2024.123239.

[51] M. Doninelli, E. Morosini, G. Di Marcoberardino, C.M. Invernizzi, P. Iora, M. Riva, P. Stringari, G. Manzolini, Experimental investigation of the CO2+SiCl4 mixture as innovative working fluid for power cycles: Bubble points and liquid density measurements, Energy 299 (2024). https://doi.org/10.1016/j.energy.2024.131197.

[52] United States. Bureau of Mines., Mineral Facts and Problems: 1985 Edition, Washington D.C., 1985.

[53] M. Pasetti, C.M. Invernizzi, P. Iora, Thermal stability of working fluids for organic Rankine cycles: An improved survey method and experimental results for cyclopentane, isopentane and n-butane, Appl Therm Eng 73 (2014) 764–774. https://doi.org/10.1016/j.applthermaleng.2014.08.017.

[54] V. Havens, D.R. Ragaller, Study of toluene stability for an Organic Rankine Cycle (ORC) space-based power system, in: 1988. https://api.semanticscholar.org/CorpusID:107906670.

[55] Q. Eppinga, S. Ganassin, J. Van Buijtenen, Application and operation of 40+ Triogen ORC plants, Energy Procedia 129 (2017) 684–691. https://doi.org/10.1016/j.egypro.2017.09.145.

[56] S. Lasala, C. Invernizzi, P. Iora, P. Chiesa, E. Macchi, Thermal Stability Analysis of Perfluorohexane, Energy Procedia 75 (2015) 1575–1582. https://doi.org/10.1016/j.egypro.2015.07.358.

[57] J. Spale, A. Hoess, I.H. Bell, D. Ziviani, Low-GWP Working Fluid Mixtures Screening for Industrial High Temperature Heat Pumps with Supply Temperature > 200 ° C Low-GWP Working Fluid Mixtures Screening for Industrial High Temperature Heat Pumps with Supply Temperature > 200 ° C, in: 20th International Refrigeration and Air Conditioning Conference at Purdue, 2024.

[58] J. Gómez-Hernández, R. Grimes, J. V. Briongos, C. Marugán-Cruz, D. Santana, Carbon dioxide and acetone mixtures as refrigerants for industry heat pumps to supply temperature in the range 150–220 oC, Energy 269 (2023). https://doi.org/10.1016/j.energy.2023.126821.

[59] G. Angelino, C. Invernizzi, General method for the thermodynamic evaluation of heat pump working fluids, International Journal of Refrigeration 11 (1988) 16–25. https://doi.org/10.1016/0140-7007(88)90007-2.

[60] M. Doninelli, G. Di Marcoberardino, I. Alessandri, C.M. Invernizzi, P. Iora, Fluorobenzene as new working fluid for high-temperature heat pumps and organic Rankine cycles: Energy analysis and thermal stability test, Energy Convers Manag 321 (2024) 119023. https://doi.org/https://doi.org/10.1016/j.enconman.2024.119023.

[61] L. Wolscht, K. Knobloch, E. Jacquemoud, P. Jenny, Dynamic simulation and experimental validation of a 35 MW heat pump based on a transcritical CO2 cycle, Energy 294 (2024) 130897. https://doi.org/https://doi.org/10.1016/j.energy.2024.130897.

[62] E. Morosini, M. Doninelli, G. Di Marcoberardino, P. Iora, M. Riva, P. Stringari, G. Manzolini, Analysis of the CO2 + C2Cl4 mixture in high temperature heat pumps: Experimental thermal stability, liquid densities and cycle simulations, Energy Convers Manag 322 (2024) 119145. https://doi.org/10.1016/j.enconman.2024.119145.

[63] O. Badr, S.D. Probert, P.W. O'Callaghan, Selecting a working fluid for a Rankine-cycle engine, Appl Energy 21 (1985) 1–42. https://doi.org/10.1016/0306-2619(85)90072-8.

[64] M.R.O. E. S. Blake, W. C. Hammann, J. W. Edwards, T. E. Reichard, Thermal Stability as a Function of Chemical Structure, J Chem Eng Data 6 (1961).

[65] C.M. Invernizzi, THERMAL STABILITY EVALUATION FOR RANKINE CYCLES WORKING FLUIDS: EXPERIMENTAL APPARATUS AND CALIBRATION RESULTS, La Termotecnica N. 4 (1990) 69–76.

[66] L.A. Weber, Criteria for establishing accurate vapour pressure curves, International Journal of Refrigeration 17 (1994) 117–122. https://doi.org/10.1016/0140-7007(94)90052-3.

[67] S. Lasala, C. Invernizzi, P. Iora, P. Chiesa, E. Macchi, Thermal Stability Analysis of Perfluorohexane, Energy Procedia 75 (2015) 1575–1582. https://doi.org/10.1016/j.egypro.2015.07.358.

[68] N. Juntarachat, A. Valtz, C. Coquelet, R. Privat, J.N. Jaubert, Experimental measurements and correlation of vapor-liquid equilibrium and critical data for the CO2 + R1234yf and CO2 + R1234ze(E) binary mixtures, International Journal of Refrigeration 47 (2014) 141–152. https://doi.org/10.1016/j.ijrefrig.2014.09.001.

[69] K. Djebaili, E. El Ahmar, A. Valtz, A.H. Meniai, C. Coquelet, Vapor-Liquid Equilibrium Data for the Carbon Dioxide (CO2) + 1,1,1,3,3-Pentafluorobutane (R365mfc) System at Temperatures from 283.15 to 337.15 K, J Chem Eng Data 63 (2018) 4626–4631. https://doi.org/10.1021/acs.jced.8b00683.

[70] P. Guilbot, A. Valtz, H. Legendre, D. Richon, Rapid on-line sampler-injector: A reliable tool for HT-HP sampling and on-line GC analysis, Analusis 28 (2000) 426–431. https://doi.org/10.1051/analusis:2000128.

[71] K. Djebaili, E. El Ahmar, A. Valtz, A.H. Meniai, C. Coquelet, Vapor-Liquid Equilibrium Data for the Carbon Dioxide (CO2) + 1,1,1,3,3-Pentafluorobutane (R365mfc) System at Temperatures from 283.15 to 337.15 K, J Chem Eng Data 63 (2018) 4626–4631. https://doi.org/10.1021/acs.jced.8b00683.

[72] H. Madani, A. Valtz, C. Coquelet, A.H. Meniai, D. Richon, (Vapor + liquid) equilibrium data for (carbon dioxide + 1,1-difluoroethane) system at temperatures from (258 to 343) K and pressures up to about 8 MPa, Journal of Chemical Thermodynamics 40 (2008) 1490–1494. https://doi.org/10.1016/j.jct.2008.06.002.

[73] N. Juntarachat, A. Valtz, C. Coquelet, R. Privat, J.N. Jaubert, Experimental measurements and correlation of vapor-liquid equilibrium and critical data for the CO2 + R1234yf and CO2 + R1234ze(E) binary mixtures, International Journal of Refrigeration 47 (2014) 141–152. https://doi.org/10.1016/j.ijrefrig.2014.09.001.

[74] M. Doninelli, E. Morosini, G. Di Marcoberardino, C.M. Invernizzi, P. Iora, M. Riva, P. Stringari, G. Manzolini, Experimental investigation of the CO2+SiCl4 mixture as innovative working fluid for power cycles: Bubble points and liquid density measurements, Energy 299 (2024) 131197. https://doi.org/10.1016/j.energy.2024.131197.

[75] University of Brescia, ERGO - Fluid Test Laboratory, https://ergo.unibs.it/research/fluid-test-laboratory

[76] M. Nazeri, A. Chapoy, A. Valtz, C. Coquelet, Fluid Phase Equilibria New experimental density data and derived thermophysical properties of carbon dioxide e Sulphur dioxide binary mixture ( CO 2 - SO 2 ) in

gas , liquid and supercritical phases from 273 K to 353 K and at pressures up to 42 MPa, Fluid Phase Equilib 454 (2017) 64–77. https://doi.org/10.1016/j.fluid.2017.09.014.

[77] D.Y. Peng, D.B. Robinson, A New Two-Constant Equation of State, Industrial and Engineering Chemistry Fundamentals 15 (1976) 59–64. https://doi.org/10.1021/i160057a011.

[78] G. Soave, Equilibrium constants from a modified Redlich-Kwong equation of state, Chem Eng Sci 27 (1972) 1197–1203. https://doi.org/10.1016/0009-2509(72)80096-4.

[79] J.S. Lopez-Echeverry, S. Reif-Acherman, E. Araujo-Lopez, Peng-Robinson equation of state: 40 years through cubics, Fluid Phase Equilib 447 (2017) 39–71. https://doi.org/10.1016/j.fluid.2017.05.007.

[80] A. Bertucco, M. Fermeglia, 50 years of Soave Equation of State (SRK): A source of inspiration for chemical engineers, Fluid Phase Equilib 566 (2023) 113678. https://doi.org/https://doi.org/10.1016/j.fluid.2022.113678.

[81] Aspen Technology Inc., Aspen Plus®, Version V12.1, (2022).

[82] H.I. Britt, R.H. Luecke, The estimation of parameters in nonlinear, implicit models, Technometrics 15 (1973) 233 – 247. https://doi.org/10.1080/00401706.1973.10489037.

[83] W.E. Deming, Statistical Adjustment of Data, Dover Publication Inc., New York, 1943.

[84] B.E. Poling, J.M. Prausnitz, The Properties of Gases and Liquids, 2001.

[85] M. Doninelli, G. Di Marcoberardino, On the design of recuperator for transcritical cycle adopting CO2-based mixture as working fluid: a focus on transport properties prediction, Energy Technology (2023). https://doi.org/10.1002/ente.202300677.

[86] S.E. Quiñones-Cisneros, C.K. Zéberg-Mikkelsen, E.H. Stenby, The friction theory (f-theory) for viscosity modeling, Fluid Phase Equilib 169 (2000) 249–276.

[87] S.E. Quiñones-Cisneros, S. Pollak, K.A.G. Schmidt, Friction Theory Model for Thermal Conductivity, J Chem Eng Data 66 (2021) 4215–4227. https://doi.org/10.1021/acs.jced.1c00400.

[88] M. Doninelli, G. Di Marcoberardino, P. Iora, M. Gelfi, C.M. Invernizzi, G. Manzolini, Silicon Tetrachloride as innovative working fluid for high temperature Rankine cycles: Thermal Stability, material compatibility, and energy analysis, Appl Therm Eng 249 (2024) 123239. https://doi.org/10.1016/j.applthermaleng.2024.123239.

# PART 1
# Pure working fluids characterisation

*The Part 1 deals with the novel pure working fluids that have been introduced by this research for the first time in literature. In particular, Chapter 2 will treat Silicon Tetrachloride as innovative working fluid for high-temperature Rankine cycles, comprising thermal stability test, material compatibility test, and energy analysis of the associated power cycle in different contexts. The thermophysical properties of $SiCl_4$ have also been discussed along with adequate models for their prediction. The research of Chapter 2 is partly funded by the project HICLOPS "High-medium temperature closed power cycles for waste heat recovery and renewable sources" - under the MUR Progetti di Rilevante Interesse Nazionale (PRIN) Bando 2022 under grant No 2022HMZ39A – and partly funded by DESOLINATION project – under the European Union's Horizon 2020 research and innovation programme under grant agreement No 101022686.*

*Chapter 3 will explore Fluorobenzene as novel working fluid demonstrating its suitability both for Organic Rankine Cycles and high-temperature heat pumps. An experimental campaign is conducted to determine the fluid degradation rate up to 350°C. The conventional thermal stability test has been included in a wider experimental framework to simulate the presence of a non-condensable gases removal system in real operating conditions. The research of Chapter 3 is partly funded by the project HICLOPS "High-medium temperature closed power cycles for waste heat recovery and renewable sources" - under the MUR Progetti di Rilevante Interesse Nazionale (PRIN) Bando 2022 under grant No 2022HMZ39A. The article is also partly funded by the project "COFFEE" under the National Recovery and Resilience Plan (PNRR), Mission 4 Component 2 Investment 1.3, Project title "Network 4 Energy Sustainable Transition – NEST" funded by the European Union – NextGenerationEU (Project Code PE0000021), Cascade call of the Spoke 5 "Energy Conversion".*

# *Chapter 2 - Silicon Tetrachloride as Innovative Working Fluid for High Temperature Cycles*

*THIS CHAPTER IS BASED ON THE ARTICLE: "SILICON TETRACHLORIDE AS INNOVATIVE WORKING FLUID FOR HIGH TEMPERATURE RANKINE CYCLES: THERMAL STABILITY, MATERIAL COMPATIBILITY, AND ENERGY ANALYSIS", PUBLISHED IN APPLIED THERMAL ENGINEERING, ELSEVIER, DOI: HTTPS://DOI.ORG/10.1016/J.APPLTHERMALENG.2024.123239*

**Abstract**

Silicon Tetrachloride ($SiCl_4$) is proposed as a new potential working fluid for high-temperature Rankine Cycles. The capability to overcome the actual thermal stability limit of fluids commercially employed in the state-of-the-art Organic Rankine Cycles (ORC) is demonstrated by static thermal stability and material compatibility tests. Experimental static test proves its thermo-chemical stability with a conventional stainless-steel alloy (AISI 316L) up to 650°C. A preliminary material compatibility analysis performed with optical microscope on the AISI 316L cylinder, after exposure of 300 hours to $SiCl_4$ at temperature higher than 550°C, confirms the potentiality of this fluid when coupled with high-grade heat sources. A thermodynamic analysis has been carried out accounting for the effect of operating conditions on the axial turbine efficiency. A comparison with fluids adopted in medium-high temperature ORCs is performed, evidencing that the proposed fluid could achieve more than +10% points as thermal efficiency gain compared to any commercial solutions when coupled with high-temperature sources such as solar, biomass, waste heat from industrial processes and prime movers. A 2 MW $SiCl_4$ cycle operating full-electric at 550°C reaches a thermal efficiency of 38%, exceeding values attainable by any other working fluid under similar conditions and power size.

## 2.1 Introduction

The EU net-zero emissions objective [1] requires an important expansion of the technologies adopted to exploit the available waste heat of industrial processes to reduce the primary energy consumption and the carbon footprint. Organic Rankine Cycle (ORC) is the leading technology in the field of waste heat recovery (WHR) from low-medium high temperature heat sources, typically from 120°C to 450°C [2]. The selection of the working fluid is a key task for the ORC design, making it flexible to each specific application with different heat source and heat sink. One of the main concern about the working fluid selection, especially when dealing with high temperature sources, is the thermal stability of organic fluids, which sets a constraint on the maximum operating temperature of the power cycle, strictly related to its thermodynamic efficiency. Thermal stability can be considered as the capability to preserve unchanged the physical properties of a fluid despite of heating. When a fluid is employed above its thermal stability limit, the activation energy required to break the weakest bond in the molecule is overcome and secondary products are formed. The chemical decomposition can cause engine malfunctions: (i) reaction products, that are typically light and incondensable compounds, can accumulate in the recuperator and the condenser, then reducing the available pressure ratio across the turbine; (ii) the heat transfer behaviour of the working fluid is negatively affected; (iii) the working fluid needs to be refilled and the products removed, increasing the operative costs; (iv) solid particles can be also produced causing fouling of the heat exchangers and erosion of the turbine blades.

To date, organic fluids employed in commercial ORC systems are limited to a maximum operating temperature of around 300°C which is representative of the practical limits of the hydrocarbon family [3] and siloxanes [4]. At such temperature level, thermal decomposition reaction is usually active for the two fluid families above mentioned but, in case the kinetic of the reaction is within acceptable values, a fluid refill every few years compensates for its degradation. In the next section, thermal stability studies on working fluids for ORC systems will be summarized to better address the significant issue of thermal stability.

However, according to Papapetrou et al. [5], the EU's total waste heat potential is 300 TWh/year, with over 40% available at temperatures exceeding 500°C (mainly cement, iron and steel sectors). This highlights the necessity to enhance the thermal capability of fluids adopted by the ORC technology, particularly in harnessing high-grade waste heat, to improve the thermal-to-electric conversion efficiency. The interest in a high conversion efficiency power block could arise in many different industrial sectors that normally produce high-temperature waste heat, in order to reduce the carbon footprint of industrial processes. An example could be the steel production by Electric Arc Furnaces, accounting for 28% of the worldwide steel production [6], where the off-gas (that is produced as a by-product of the process**)** is characterised by an average temperature of about 750 °C. Industrial waste heat, known for its high-grade heat content, is not the sole source; exhaust gases from gas turbines also commonly reach temperatures in the range of 550-600°C. Efficient heat recovery in these scenarios could be enhanced by employing a thermally stable working fluid. As stated by Colonna et al. [7], an ideal working fluid should remain thermally stable, when in contact with stainless steel, even at temperatures between 500 and 600°C. Furthermore, this consideration extends to various applications including concentrated solar power, pyrolysis processes, and biomass boilers.

Thermally stable fluids capable to overcome the thermal stability threshold (300-350°C) of state-of-the-art organic fluids could exploit more efficiently high-temperature heat sources that are characterized by a thermal power ranging from tens of kW to few MW, where conventional steam Rankine cycles are not the best techno-economical solution: they suffer from high capital costs, need for qualified personal to supervise the operations, low heat-recovery efficiency, as well as lower performance at part-load conditions [8]. Despite the mentioned drawbacks, they are largely considered for electrical power output above 2-5 $MW_{el}$ when there is high-grade heat available, as in medium-large biomass-fired plants [9]. Macchi and Astolfi referred to the 5-20 MW output range as the "steam vs. ORC grey zone" [2]. In this output range, there is no clear winner between the state-of-the-art ORC and steam technologies, although ORC is gaining market positions due to its simple layout and good performance at part-load, thus lowering maintenance cost as well as almost zero supervision personal costs.

In this "grey zone", also supercritical $CO_2$ ($sCO_2$) could play a role as potential working fluid, but it is not considered in this article for the following reasons: (i) $sCO_2$ Brayton cycles achieves good exploitation (cooling grade) of a sensible heat source only when a complex layout such as cascaded recuperative cycle (two turbines, two primary heat exchangers, two recuperators) is adopted [10]; (ii) the need of operating at near-critical conditions at the compressor intake to exploit the beneficial real gas effect with the associated risk of crossing the two-phase region [11]; (iii) the extremely high maximum cycle pressure (over 200 bar) compared to ORC (15-60 bar) and small-scale steam Rankine plants (60-90 bar); (iv) the design of the control system is particularly challenging especially in small scale power units (<0.5-5 $MW_{el}$) [12]. Echogen [13] manufactured the commercial EPS100 (8 MW nominal power output) heat recovery unit adopting $sCO_2$ with two turbines: one single-stage radial turbine drives the pump/compressor (2.7 MW shaft power) and one power turbine. However, when approaching lower power output, as in the EPS30 Echogen module (1.35 MW nominal output), such a complex architecture seems improbable to be adopted, and its declared thermal efficiency by catalogue is 18.8% when coupled with a heat source at 500°C, which is a value that can be overcome by commercial ORC systems at the same power output.

Given this premises, the aim of this work is to introduce a working fluid that is capable to fill this gap in the ORC technology and extend its market share. Silicon Tetrachloride ($SiCl_4$), or Tetra-chlorosilane, is proposed here for the first time as innovative working fluid for power production in a high-temperature Rankine cycles. $SiCl_4$ is an inorganic compound industrially involved in the production of solar grade silicon. Remarkable thermal stability was expected from this metal halide, as it is involved in high temperature processes. The pure $SiCl_4$ is reported to be stable even at 1200°C in the literature [14]. In the past, it was the product of the reaction of $SiO_2$ and chlorine at a temperature of 1300°C [15]. $SiCl_4$ is the main by-product of polycrystalline silicon production by the Siemens process adopted to obtain solar-grade silicon. It is estimated that around 18-20 tons of $SiCl_4$ are produced as by-product for each ton of poly-silicon [16]. Considering that the annual production of polysilicon is estimated to be around 1.65-1.7 million tons to date, it means that the annual yield of $SiCl_4$ as undesired by-product is more than 30 million tons per year. The great abundance of $SiCl_4$ reflects its availability in the market at a low cost. In the Siemens process, Silicon Tetrachloride is obtained as by-product of the $SiHCl_3$ pyrolysis, and it is necessary to reduce the $SiCl_4$ near 900°C with hydrogen or $H_2$-radicals to convert/recycle it into $SiHCl_3$ and increase the Si production [17].

Another pathway is the reutilization of the $SiCl_4$ by-product for the manufacturing of silica-based materials, for example fumed silica, optical fiber, ethyl silicate [18]; however, optical fiber level $SiCl_4$ requires extreme purity and must be further purified [19]. One of the key aspects of the production of solar-grade silicon is the effective recycle of $SiCl_4$, and this work open the path to another way to reutilize and make profit from by the polysilicon industry, in the circular economy point of view.

The identification of a new working fluid, starting from its interesting characteristics available in literature, has to be followed by a rigorous procedure that includes experimental test and modelling to confirm its good potentialities and expand the known database. Thus, the main goal of this work is to experimentally demonstrate the thermo-chemical capability of $SiCl_4$ and its material compatibility, and to provide preliminary indications about the performance gain achievable when using this working fluid compared to state-of-the-art ORC working fluids. Starting from a literature review on the maximum operating temperature of the conventional ORC working fluids, thermal stability, and material compatibility test with AISI 316L stainless steel have been performed to assess the $SiCl_4$ temperature threshold in realistic conditions. Furthermore, a comprehensive fluid characterisation has been carried out tuning the selected thermodynamic model and transport properties model with the available experimental data. The knowledge on the proper thermophysical properties models aims at providing all the necessary information to design the power cycles components adopting $SiCl_4$ working fluid. Eventually this work presents a preliminary estimate of the power cycle performance using the investigated fluid under various operating conditions and power outputs to highlight the benefits of its adoption in ORC cycle with respect to other conventional organic fluids.

## 2.2 Literature review on ORC working fluids thermal stability

The working fluid thermal stability poses a significant challenge for the lifetime and operability of the ORCs as well as for the power cycle performance. Over the last years, this temperature threshold have been investigated by different research groups for several fluid chemical classes such as hydrocarbons, refrigerants, and siloxanes. One of the main goal is to find out a specific working fluid that can withstand at temperature higher than 350-400 °C.

Pereira et al. [20] explored different methods for assessing the thermal stability of organic fluids, distinguishing between static and dynamic tests. The static isochoric method developed in our Fluid Test Laboratory of the University of Brescia by Invernizzi [21][22] is based on the concept that even a small breakdown of the fluid can cause an appreciable variation in vapor pressure determined by the partial pressure of decomposition products. This method involves measuring vapor pressure both before and after subjecting the fluid to thermal stress within a closed volume manufactured from carefully chosen material. This technique allows for the identification of degradation products, particularly when focusing on sub-atmospheric vapour pressures. Notably, in comparison to alternative methods, this approach offers the unique benefit of quantifying the actual impact of degradation products on vapor pressure. Consequently, it facilitates a comprehensive assessment of the influence of degradation products on important parameters, such as the pressure ratio across the turbine and subsequent effects on power output. During the past years, the static survey method

has been applied to several working fluids in our laboratory such as hydrocarbons [22][3], zero-ODP refrigerants [23], fluorinated alcohols [24], perfluorocarbons [25].

Table 1 summarises the thermal stability of different fluids potentially applicable for ORC applications, along with their critical parameters and normal boiling point (NBP).

Hydrocarbons (HC) exhibit variable levels of thermo-chemical stability based on their molecular structure. In general, cyclic hydrocarbons have a higher activation energy compared to linear ones. In fact, as a result of a previous study conducted in our laboratory, cyclopentane had a decomposition rate 20 times lower than n-pentane at 350°C [3]. While toluene and cyclopentane were found to have similar decomposition rate at 350°C, the decomposition rate of cyclopentane increases rapidly above 350°C, whereas toluene maintains an acceptable decomposition rate even up to 400°C. Despite that, cyclopentane is commonly used in commercial "high-temperature" ORC units below 300°C as bulk-temperature [26]. This standard approach provides a safety margin to significant molecular cleavage, also because most of the thermal degradation of the working fluid occurs within the thermal boundary layer that is at a temperature higher than the bulk. Toluene is acknowledged as one of the most thermally stable HC, with literature works supporting its low degradation rate up to 400°C [27][28]. However, in practice, toluene is applied in biomass-fired ORC units up to a maximum cycle temperature of 320°C (Triogen company [29]), in direct heat transfer mode.

Dai et al. [30] experimentally explored the thermal stability of n-pentane above 330°C proving that the pressure has no significant influence on the unimolecular decomposition reaction, where the rate of decomposition is mainly dependent on the temperature of the system.

Ginosar et al. [31] conducted tests on the thermal stability of cyclopentane at 240, 300, and 350 °C at 4.3 MPa in a glass-lined heated tube. Their findings suggest safe application in an ORC if the cycle maximum temperature is maintained below 300°C and air is excluded from the system. However, it is crucial to assess the thermal stability of a working fluid in contact with materials commonly employed in the high-temperature sections of a power plant, such as stainless steel or Inconel alloys. This evaluation is essential as the material can act as a catalyst for the unimolecular decomposition reaction.

Organic fluids containing the hydroxyl group (-OH) are characterized by even lower thermal stability compared to hydrocarbons as attested by previous experimental campaign on 2,2,2-trifluoroethanol ($C_2H_3F_3O$) and n-butanol ($C_4H_{10}O$). Appreciable decomposition was observed on the n-butanol sample following the initial thermal stress at 220°C. On the other hand, the rate of decomposition of trifluoroethanol at 300°C was found to be ten times lower than that of n-butanol, due to fluorine content stabilizing the molecule.

Hydrofluorocarbons (HFC) possess superior thermal stability compared to the HC counterpart due to high C-F bond energy. As a rule of thumb, the more the C-F bond compared to the C-H bonds present in the molecule the higher the thermal stability of the fluid, due to minor probability of collisions on the weakest bond. In fact, past investigation with the static survey method in our Fluid Test Lab proved that zero-ODP HFC refrigerants possess exceptionally high thermal stability limit [23]: 425°C for HFC-227ea, 400°C for HFC-23 and HFC-236fa, 350°C for HFC-143a and 300°C for HFC-245fa. Dai et al. [32] obtained similar results by measuring the fluoride ion concentration as a

product of the decomposition reaction: 400°C for HFC-236fa, 320°C for HFC-245fa. The thermal stability threshold of several refrigerants was also experimentally evaluated by Calderazzi and Colonna di Paliano [33] in a static isochoric setup, confirming the good thermo-chemical stability of fluorinated compounds: 368°C for HFC-134a ($C_2H_2F_4$) and 396°C for HFC-125 ($C_2HF_5$). On the other hand, they found poor results on chemical species containing C-I and S-F bonds: 102°C for R-1311 ($CF_3I$) and 204°C for R-7146 ($SF_6$). However, refrigerants possess relatively low critical temperature (below 150°C in most of the cases except for few compounds such as R133mzz(Z) with 171.3°C), then they are not suitable as working fluids in ORC systems coupled with very-high temperature heat sources, that is the main topic of this article. In fact, it is well known that the optimal working fluid to couple with a sensible heat source is one whose critical temperature is directly proportional to the temperature level of the source. For instance, Scaccabarozzi et al. [34] demonstrated that the optimal fluids for heat recovery from internal combustion engines have critical temperature in the range 65-85% of the heat source temperature. For this reason refrigerants are applied mostly in ORC systems driven by geothermal energy [35] and low-grade waste heat [36]. An important issue deriving from the thermal cracking of hydrofluorocarbons is that hydrofluoric acid (HF) is produced as degradation product [37].

Angelino and Invernizzi [38] proposed the adoption of cyclic polymethylsiloxanes in organic cycles proving that little degradation occurs even up to 400°C, and siloxanes are, to date, a commercial solution adopted in high-temperature ORC units, especially hexamethyldisiloxane (MM, $C_6H_{18}OSi$) and octamethyltrisiloxane (MDM, $C_8H_{24}O_2Si_3$) [39]. Keulen et al. [40], adopting the methodology proposed in our laboratory in conjunction with chemical analysis, determined that appreciable decomposition of MM and MDM was detectable at 240°C and 260°C respectively. However, from a practical perspective, what matters is not only that the degradation reaction is active at a certain temperature, but more importantly, the rate at which this reaction occurs. In fact, Preißinger et al. [41] demonstrated that MM has an annual degradation rate lower than 3.5% at 300°C. For this reason, in commercial units, MM is usually adopted up to a maximum cycle temperature around 300°C [26]. Wang et al. [42] studied the influence of MM thermal decomposition on the ORC system, leading to a decrease in net power and thermal efficiency but also in incomplete evaporation and acid corrosion in the evaporator. Siloxanes are commonly used in biomass-driven ORC, with thermal oil loop as heat carrier, at turbine inlet temperatures lower than 300°C [39].

The 400°C barrier as maximum cycle temperature can be approached, and eventually overcome, if hydrofluorocarbons rich in fluorine or totally perfluorinated compounds are considered as working fluids. As a drawback, the more the fluorine atoms the higher the global warming potential and cost. Perfluorohexane ($C_6F_{14}$) has been tested by Lasala et al. [25] in our Fluid Test Laboratory, in a mixture with carbon dioxide, and early signs of decomposition occurred after thermal stress at 400°C while at the previous thermal stress (350°C) no decomposition phenomena was observed. However, perfluorohexane has a high $GWP_{100\text{-}y}$ value equal to 9300, and there are some concerns about the material compatibility of perfluorinated compounds even with Inconel alloys [43].

One of the most significant results, in terms of thermal stability of working fluids for ORC, was obtained by Di Nanno et al. [44] from NASA, that patented the adoption of a mixture of fluorocarbons, pentafluorobenzene ($C_6HF_5$) and hexafluorobenzene ($C_6F_6$) [44], called RC-1 mixture, for WHR application, as no thermal decomposition occurred up to 468°C.

Recently, Titanium Tetrachloride ($TiCl_4$) was proposed by Invernizzi et al. [45] as working fluid for high-temperature Rankine cycles up to 500°C [45] and in binary mixtures with $CO_2$ for CSP application [46]. The main drawback related to the applicability of metal halides is the extremely high reactivity with water and moisture present in the air (hydrolysis) due to vacant d-orbitals. According to a previous experimental campaign carried out in our Fluid Test Laboratory, $TiCl_4$ resulted to be stable up to 500°C in stainless steel alloy, which is a significant improvement compared to other fluids. However, the extreme tendency of $TiCl_4$ to hydrolyse when in contact with humid air poses serious challenges for its application in power cycles as pure fluid: on one hand the high normal boiling point of $TiCl_4$ (136.4°C) leads to work in sub-atmospheric conditions in the turbine, recuperator, and condenser in order to have good system performance; on the other hand, a low minimum pressure level implies that the infiltration of air (and the consequent reaction with the fluid) in the system is hard to avoid. Eventually, in this work, another metal halide, $SiCl_4$, is investigated: the experimental procedure and results are reported in the next section.

From this overview, it becomes evident how challenging it is to enhance the thermal-to-electric efficiency of ORC systems when very-high temperature sources are available, given that the thermo-chemical stability of the working fluid remains the most limiting factor in the increment of the cycle maximum temperature.

*Table 1. Thermal stability threshold of different potential fluids for ORC applications*

| Fluid | Chemical Formula | Thermal Stability Threshold [°C] | Reference | Critical Temperature [°C] | Critical Pressure [bar] | NBP [°C] |
|---|---|---|---|---|---|---|
| R-1311 | $CF_3I$ | 102 | [33] | 122 | 40.4 | -22.5 |
| R-7146 | $SF_6$ | 204 | [33] | 45.5 | 37.6 | -63.9 |
| R-141b | $C_2H_3Cl_2F$ | 90 | [33] | 204.3 | 42.1 | -32 |
| HFC-245fa | $C_3F_5H_3$ | 300-320 | [23][32] | 154 | 36.5 | 15.3 |
| HFC-143a | $C_2H_3F_3$ | 350 | [23] | 72.7 | 37.6 | -47.6 |
| HFC-236fa | $C_3H_2F_6$ | 400 | [23] | 124.9 | 32 | -1.4 |
| HFC-23 | $CHF_3$ | 400 | [23] | 25.9 | 48.4 | -82 |
| HFC-227ea | $C_3HF_7$ | 425 | [23] | 103.5 | 29.5 | -17 |
| HFC-134a | $C_2H_2F_4$ | 368 | [33] | 101.1 | 40.7 | -26.3 |
| HFO-1336mzz(Z) | $C_4H_2F_6$ | 250-270 | [47][48] | 171.3 | 29 | 33.4 |
| HFO-1336mzz(E) | $C_4H_2F_6$ | 230-250 | [49] | 137.7 | 31.5 | 7.5 |
| HFO-1234ze(E) | $C_3H_2F_4$ | 180 | [50] | 109.4 | 36.4 | -19 |
| HFO-1234yf | $C_3F_4H_2$ | 170-200 | [35][37] | 95 | 33.8 | -29 |
| HFC-32 | $CH_2F_2$ | 250-270 | [49] | 78.1 | 58 | -51.7 |
| HFC-125 | $CH_2F_5$ | 396 | [33] | 66 | 35.9 | -48.5 |
| TFE | $C_2H_3F_3O$ | 250 | [24] | 227 | 48.3 | 74 |

| | | | | | | |
|---|---|---|---|---|---|---|
| n-butanol | $C_4H_{10}O$ | 220 | [24] | 289.8 | 43.7 | 118 |
| n-butane | $C_4H_{10}$ | 290 | [22] | 190 | 38 | -0.5 |
| Isopentane | $C_5H_{12}$ | 290 | [22] | 187.2 | 33.8 | 27.8 |
| Cyclopentane | $C_5H_{10}$ | 350 | [22][31] | 238.6 | 44.4 | 49.3 |
| n-pentane | $C_5H_{12}$ | 280-320 | [3][30][32] | 196.6 | 33.7 | 36.1 |
| Toluene | $C_7H_8$ | 400 | [3][27][28][51] | 320 | 41.1 | 110.6 |
| n-hexane | $C_6H_{14}$ | 260-280 | [52] | 234.7 | 30.3 | 68.7 |
| Perfluorohexane | $C_6F_{14}$ | 350-400 | [25] | 179.6 | 18.1 | 57.2 |
| Novec 649 | $C_6F_{12}O$ | 300 | [53] | 169 | 18.8 | 49 |
| Novec 4710 | $C_4F_7N$ | 300 | [54] | 112.9 | 25 | -4.7 |
| MM | $C_6H_{18}OSi_2$ | 300-320 | [41][40] | 246.7 | 19.4 | 100.5 |
| MDM | $C_8H_{24}O_2Si_3$ | 300-320 | [40] | 290.2 | 14.1 | 153 |
| Titanium Tetrachloride | $TiCl_4$ | 500 | [45] | 364.9 | 46.6 | 136.4 |
| **Silicon Tetrachloride** | **$SiCl_4$** | **> 650** | **This work** | **234.9** | **35.9** | **57** |

## 2.3 Thermal stability of $SiCl_4$ and material compatibility test

The thermal stability of $SiCl_4$ is experimentally assessed using the static survey method implemented in the Fluids Test Laboratory of the University of Brescia, as mentioned earlier. This approach relies on measuring the change of vapour pressure after thermal stress at constant temperature compared to the same property of the fresh fluid (not thermally stressed). The experimental apparatus and procedure implemented are well described in [22]. Nonetheless, for a more visual representation, the key components are illustrated in Figure 1 and summarized in Tables 2-3.

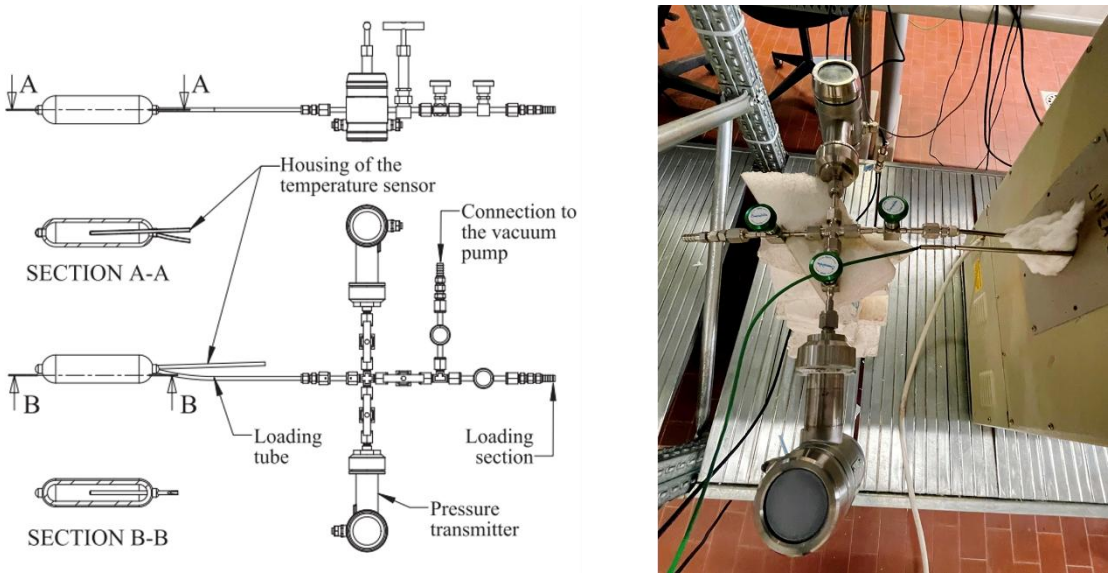


*Figure 1. schematization of the main components for thermal stability test (left), and system under thermal stress in a muffle furnace (right).*

The core of the system is the sample cylinder manufactured by Swagelok is AISI 316L, which is a material commonly adopted in power plants. As illustrated in Figure 1 (left), the cylinder features two welded connections: one for the loading tube, and the other one for the housing of the temperature probe (thermocouple), responsible for measuring the bulk fluid temperature. Two pressure transmitters have been used during the test: a low-pressure transmitter with adjustable full scale in the range 1-10 bar to measure the vapour pressure of the fluid with good accuracy, and one high-pressure transmitter (20-100 adjustable span) to monitor the pressure during the thermal stress in the muffle furnace. All the wetted parts of the system, including the pressure transmitters, are manufactured in AISI 316. When the fluid is subjected to thermal stress in the muffle furnace, the valve adjacent to the low-pressure transmitter is closed to protect it from overpressure, and the pressure is recorded only with the high-pressure transmitter.

*Table 2. Equipment for thermal stability testing.*

| Type | Manufacturer | Model | Characteristics |
|---|---|---|---|
| Sample cylinder | Swagelok | - | Internal Volume 150 $cm^3$<br>Material AISI 316L |
| Needle valves | Swagelok | SS-4H-V13 | - |
| Vacuum pump | Dami Cosmos | MP90DEVV | $P_{min}$ 1 mbar |
| Scale | Mettler-Toledo | MS12002TS | FS: 12.2 kg – Accuracy 0.1 g |
| Thermostatic bath | Julabo | Julabo FP 40 | -45/150°C - Resolution 0.1°C |

*Table 3. Instruments for thermal stability testing.*

| Type | Manufacturer | Model | Measurement range | Accuracy |
|---|---|---|---|---|

| | | | | |
|---|---|---|---|---|
| Pressure transmitter 1 | Keller | Klay 2000-SAN | 0..10 bar* | 0.1 % of full-scale |
| Pressure transmitter 2 | Keller | Klay 2000-SAN | 0..100 bar* | 0.1 % of full-scale |
| Thermocouple | Tersid | Type K | -200-1270 °C | Tolerance class I |

**Adjustable span (1-10 bar for transmitter 1, 20-100 bar for transmitter 2)*

The thermal stability test involves the following steps: (i) evacuation of the system using a vacuum pump; (ii) introduction of a pre-defined mass of fluid into the cylinder; (iii) placement of the cylinder vertically in a thermostatic bath for measuring the reference vapor pressure of the fresh fluid within a predetermined temperature range; (iv) horizontal placement of the system in a muffle furnace for a 100-hours thermal stress at a selected constant temperature; (v) after the thermal stress, returning the system to the thermostatic bath to measure vapor pressure within the same temperature range as the reference test; (vi) repeating the process by placing the system in the muffle furnace for another thermal stress at a higher temperature; (vii) iteratively repeating steps (v) to (vi) until the desired temperature level in the muffle furnace is reached. The test concludes when either the target temperature is achieved during the thermal stress or when a significant divergence in volumetric behavior of the fluid is noticed compared to the reference behaviour. The most relevant steps of the methodology are also represented in Figure 2.

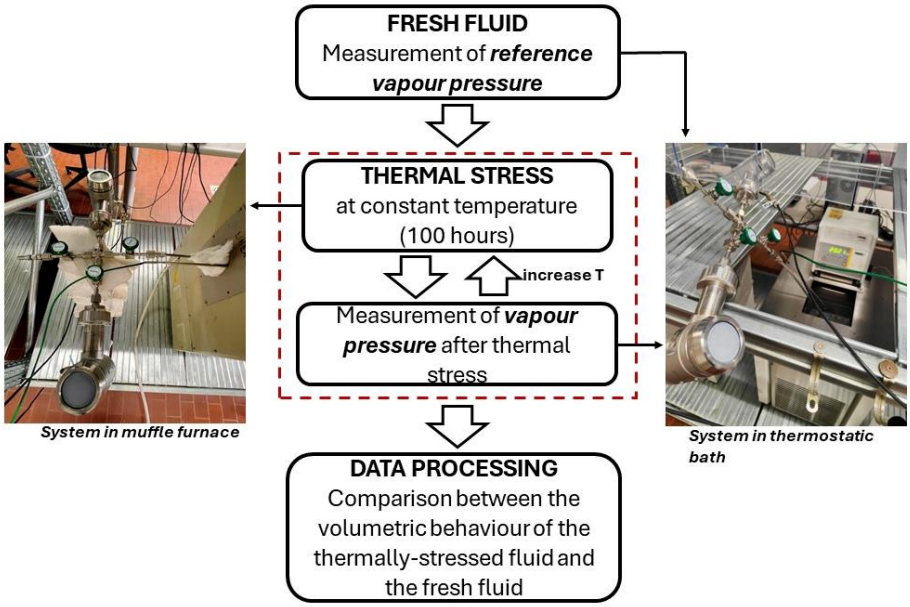


*Figure 2. Schematization of the methodology adopted for the thermal stability test.*

The supplier of the fluid is Merck, and the declared purity is higher than 99%. A sample of 22 grams of liquid $SiCl_4$ has been charged in the cylinder with fixed volume of 150 $cm^3$.

As already discussed in previous works [3][24], signs of degradation phenomena are more evident at sub-atmospheric vapour pressure condition, where the partial pressure of light and volatile

decomposition products noticeably increases the pressure deviation with respect to the fresh fluid. Consequently, given $SiCl_4$'s normal boiling point around 57°C, the reference vapor pressure ("REF" in Figure 3) was measured from 0-50°C with 10°C intervals.

The sample fluid experienced five consecutive stress tests in the muffle furnace at temperature from 450 °C to 650°C, with steps of 50°C. The test concluded at 650°C even if no thermal breakdown of the fluid was observed in order to avoid possible system overpressure occurring at higher temperatures. At the end of each 100-hours stress test, the saturation pressure curve was measured and compared with that of the fresh fluid (reference volumetric behaviour) in order to detect possible signs of decompositions. The vapour pressures measured after each 100-hours thermal stress and the one of the reference fresh fluid are reported in Figure 3.

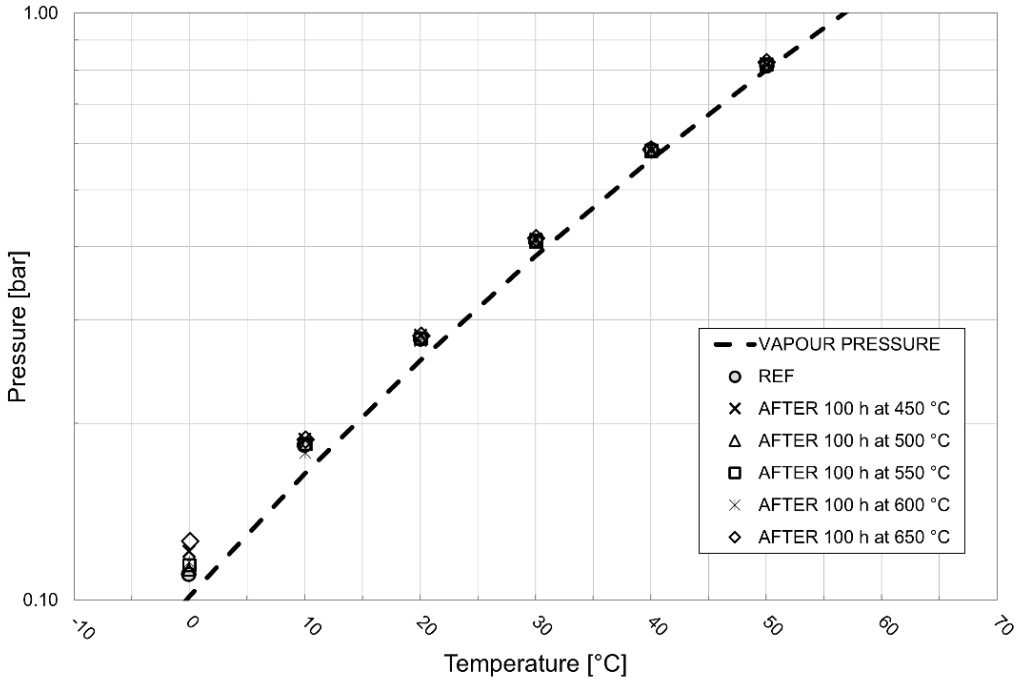


*Figure 3. Saturation pressures of $SiCl_4$ after different 100-hours thermal stress test from 450°C to 650 °C (50°C step) compared with the reference values ("REF") and the simulated vapour pressure (dashed line) with Peng Robinson EoS (logarithmic scale).*

From Figure 3, it is possible to conclude that the pure $SiCl_4$ in AISI 316L is stable up to 650°C as no vapour pressure deviations are appreciable. Unlike previous tests on different fluids for ORC applications conducted in our laboratory, no post processing of the data, such as the calculation of the rate of unimolecular decomposition [3], was feasible since no pressure deviations higher than the instrumental uncertainty were measured. Looking at the application point of view, the outstanding result obtained up to 650°C with a relatively low-cost material, compared to nickel-based alloys or other special metals, is very promising and proves the high potentialities of this fluid in high-temperature applications. Based on current investigation, $SiCl_4$ can be safely utilized up to a bulk temperature of 650°C without experiencing degradation. This temperature threshold aligns well with the thermal requirements of next-generation CSP plants [55], for example.

Another important aspect, for the commercialization of an ORC cycle with a new working fluid, is the material compatibility (especially at the maximum operating temperature). For this reason, a

preliminary medium term thermal stability and material compatibility test of 300 hours in AISI 316L was carried out at 550°C, a temperature level compatible with several high-temperature applications (e.g. solar, biomass, waste heat, etc.). After the thermal stress, the thermal stability has been verified in comparison with the reference vapour pressure line: no signs of degradation of the fluid have been detected, and the vessel has been cut and analysed in cross-section by means of an optical microscope to assess the interactions between the metal and the fluid.

The microstructural analysis to evaluate the interaction produced by the prolonged contact with the high-temperature atmosphere of $SiCl_4$ has been performed by means of a Reichert-Jung MeF3 optical microscope equipped with Leica qWin software for image analysis at Metal Labs of the University of Brescia [56]. The optical microscope analysis (Figure 4) shows that the interaction between the AISI 316L cylinder walls and $SiCl_4$ is weak both in the base-metal and in the heat-affected zone (HAZ) of the welding. Only in one welding sample a crack was detected (Figure 4-d), but it should be a pre-existing defect as already noticed in other non-stressed cylinders. The wall surface appears slightly jagged because of the coarse internal finishing. Eventually, this analysis gives encouraging results for the applicability of the fluid at 550°C in AISI 316L.

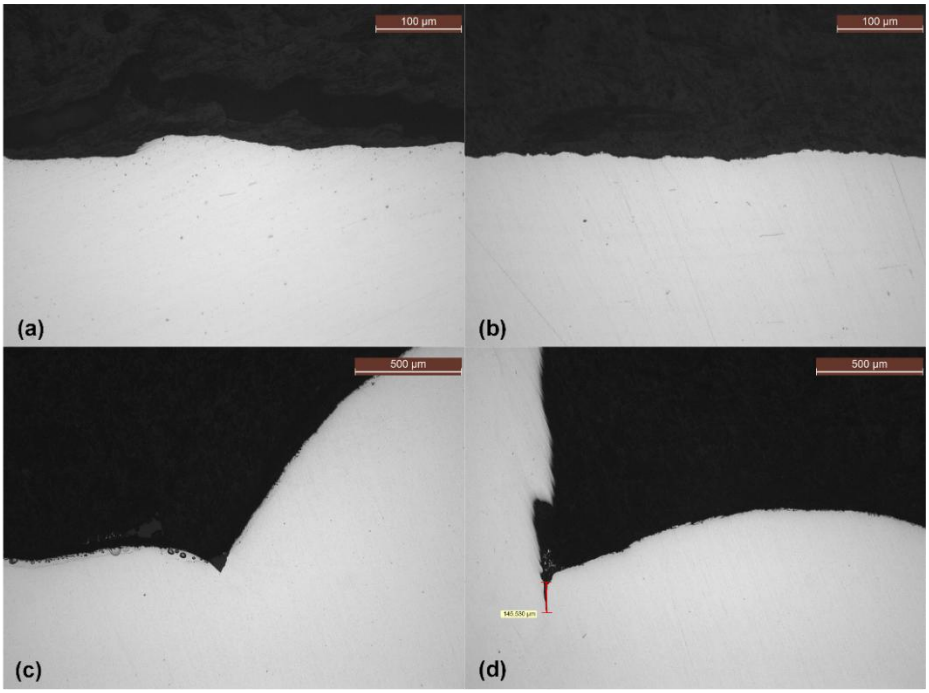


*Figure 4. Optical analysis results on the base-metal (a,b) and HAZ (c,d) after exposition for 300 hours at 550°C in $SiCl_4$ atmosphere.*

## 2.4 Silicon Tetrachloride: characteristics and thermophysical properties

Silicon Tetrachloride ($SiCl_4$) is a non-flammable metal halide that, at ambient conditions, is a colourless liquid. $SiCl_4$ possesses zero Ozone Depletion Potential (ODP) and Global Warming Potential (GWP), it is non-carcinogenic and non-flammable, and it is relatively low cost since it is widely produced as by-product in the silicon industry.

The normal boiling point of $SiCl_4$ (around 57°C) allows to operate the system above ambient pressure at reasonably low condensing temperatures, avoiding air in-leakage phenomena. For instance,

achieving sub-atmospheric condensation (and air infiltration) is practically not feasible for Titanium Tetrachloride since its normal boiling point is 136.4°C. Thus, cogeneration solutions where the fluid is condensed at 100°C are particularly attractive for $SiCl_4$, with minimum cycle pressure of 3.34 bar which eliminate the risks of air infiltrations and the need of a vacuum pump followed by a fluid recovery unit, while condensing $TiCl_4$ at 100°C in combined heat and power (CHP) applications requires 0.32 bar as minimum cycle pressure. Moreover, $SiCl_4$ is much less water-reactive than $TiCl_4$, as reported in the literature [57] and qualitatively confirmed by our laboratory experience. It is possible to conclude that $SiCl_4$ appears to be less problematic: it is necessary to guarantee a good degree of vacuum, paying attention during the phase when the circuit is being charged, to avoid contact with moisture in the air, then during the entire plant lifetime the reactivity with water becomes a marginal problem operating above ambient pressure.

The main thermodynamic properties of $SiCl_4$ are listed in Table 4.

*Table 4. Thermodynamic properties of Silicon Tetrachloride.*

| Parameter | Units | Value |
|---|---|---|
| Critical Temperature [58] | °C | 234.9 |
| Critical Pressure [58] | bar | 35.9 |
| Normal Boiling Point [59][60] | °C | 56.63/57.6 |
| Melting Point[b] | °C | -68 |
| Saturated Liquid Density (20°C) [61] | $kg/m^3$ | 1480 |
| Pitzer Acentric Factor[b] | - | 0.224 |
| Critical Compressibility Factor $Z_c$[b] | - | 0.271 |
| Molar Mass | g/mol | 169.9 |
| Pitzer Acentric Factor $\omega$[b] | - | 0.224 |
| Molecular Complexity parameter $\sigma$[a] | - | 1.37 |

[a] *Calculated according to Equation (1).* [b] *According to NIST Database in Aspen Plus V12 [62]*

$SiCl_4$ is a non-polar molecule, thus only London dispersion forces dominates the intermolecular interactions. The apparently anomalous low normal boiling point of $SiCl_4$ (around 57°C), compared to other tetrahalides such as $CCl_4$ (121°C), $CBr_4$ (189.5°C), and $TiCl_4$ (136.4°C), is due to its large molar volume [63]. The large molar volume entails a high molecular radius between molecules and then weak intermolecular forces.

The low critical pressure (35.9 bar) allows for the application of the fluid in transcritical conditions, that could be advantageous for the coupling with a high-temperature sensible heat source. In fact, the critical pressure of the fluids adopted in the existing supercritical ORCs, reported in the public literature, exceeds the one of $SiCl_4$. As an example, in 2012, Turboden realized a 500 $kW_{el}$ prototype with supercritical R134a as working fluid ($P_c$ = 40.06 bar) [2] to improve the conversion efficiency in geothermal applications. In the same year, the Houston-based company TAS Energy delivered a 22 $MW_{el}$ supercritical power cycle using the same fluid for the Neal Hot Springs geothermal plant [64]. In 2012, a 7.5 $MW_{el}$ waste heat recovery ORC was installed at a natural gas pumping station working with supercritical butane ($P_c$ = 38 bar).

The high molecular weight entails low enthalpy drop in the turbine, with the benefit of requiring few turbine stages but the penalty of needing large internal heat recovery exchanger (recuperator). From the molecular complexity parameter, calculated accordingly to Eq. 1, it is possible to conclude that $SiCl_4$ is not a complex fluid, however it is an isentropic fluid, i.e. the slope of the saturation curve is nearly vertical in a temperature-specific entropy (T-s) diagram.

$$\sigma = \frac{T_{cr}}{R}\left[\frac{dS_{SV}}{dT}\right]_{T_{red}=0.7} \quad (1)$$

A reliable thermodynamic model is necessary to calculate the thermodynamic properties of the working fluid during the transformations in the closed power cycle. It is well recognized that the most important property for the thermodynamic assessment of a cycle that works at saturation conditions is the vapour pressure. Experimental vapour pressures of $SiCl_4$ are available in the NIST Database of Aspen Plus V12 from slightly above the melting point to the critical point. The Peng Robinson (PR) equation of state (EoS) in its original formulation [65], with parameters reported in Table 4, has been used for the thermodynamic cycle evaluation since it has an average absolute deviation (AAD) on the experimental vapour pressure data equal to 1.22%, in the temperature range from 40°C to the critical temperature. Figure 5 represents the experimental vapour pressure available in NIST Database and the simulated vapour-pressure curve with the PR EoS.

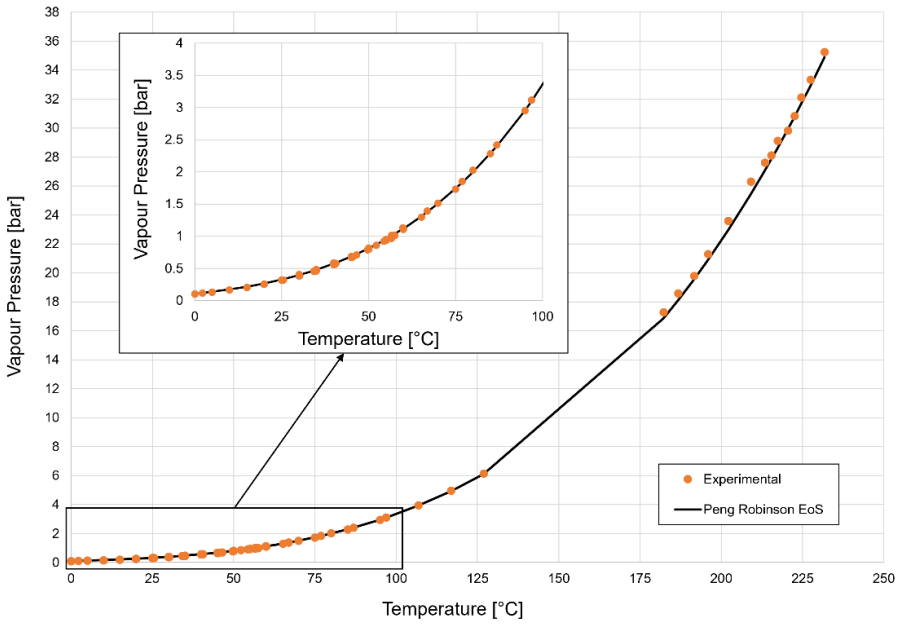


*Figure 5. Experimental vapour pressure (dots) vs simulated with PR EoS (solid line), with a focus on low temperatures.*

The work of Prat et al. [66] includes many correlations that fits experimental data for $SiCl_4$; in particular, their correlation for liquid density was found to fit very well the few available data in NIST database of Aspen Plus. In Aspen Plus environment, the Rackett equation has been used to determine the liquid density of the $SiCl_4$ since the AAD compared to the Prat correlation is 0.03%. A reliable liquid density model is necessary to perform the pump selection and design.

An eventual leak can be easily identified through a hydrochloric acid (HCl) detector, as a product of hydrolysis with humid air. In addition, there is much experience in handling silanes in the solar-grade polysilicon manufacturing, which could be useful for the required safety measures. According to the NFPA 704 Hazard Identification System, $SiCl_4$ is hazardous in terms of toxicity; as every chlorine-based gas, it is classified as a material that on short exposure could cause serious temporary or residual injury (Health Hazard 3). So, the fluid must be safely applied in a closed system with precautions on avoiding leakage in closed ambient, as it is an ORC which is inspected and tested in pressure against leaks during assembly. The toxicity is associated to formation of HCl when it comes in contact with humid ambient air. However, eventual necessary venting of the fluid (due to overpressure, maintenance, or flange leaking, for instance) can be totally neutralized through sodium hydroxide (NaOH) solution making this a secondary issue, as practiced in our laboratory experience. Caustic solution is the most common scrubbing liquid adopted for acid-gas control, such as HCl and $SO_x$, then probably already available at the power plant facility especially if furnaces are installed. In case of working fluid leakage, it is easy to detect by controlling the values of HCl.

Even if Silicon Tetrachloride is a hazardous compound, it is largely employed in the industrial field (especially in polysilicon, silica-based materials, and optical fiber productions) so there are many proven safety procedures and expertise. Silicon tetrachloride is not classified for environmental effects under the EU Globally Harmonized System (GHS).

### 2.4.1 Fine tuning of transport properties of $SiCl_4$

Considering using $SiCl_4$ as working fluid, it is important to assess not only thermodynamic but also transport properties. For heat exchangers design and rating, it is essential to possess reliable transport properties models for a wide range of operating conditions. This is particularly important when dealing with supercritical/transcritical cycles, where the fluid experience large variation in thermophysical properties. Moreover, in transcritical cycles, there is the need for models capable of describing transport properties along the high-pressure isobar, during the "transition" from liquid to supercritical gas, with continuity. A generic transport property is calculated as a sum of a "zero-density" property $\pi_0$ and a "residual property" $\Delta\pi$:

$$\pi(T, p) = \pi_0(T) + \Delta\pi(T, p) \tag{2}$$

The zero-density term $\pi_0$ can be calculated with methods that are derived from the rigorous kinetic theory of gases, whilst almost all the methods available to describe the residual property $\Delta\pi$ are empirical or semi-theoretical [67], with the corresponding-state (CS) based methods being the most applied. In an ORC, the turbine exhaust as well as the hot stream in the recuperator is constituted by a low-density superheated vapour whose transport properties are dominated by the "zero-density" term. In this fluid region, the associate error of the models, deriving from rigorous theory methods, is usually low (below 5% for most cases [67]).

On the other hand, in the dense regions as in high-pressure isobar, the residual term becomes predominant, and the property prediction is strongly influenced by the selected property model. For this reason, in this work a proper tuning of the friction-theory (f-theory) models for the description of the residual viscosity and thermal conductivity has been carried out in MATLAB [68]

environment. More information about the transport properties models can be found in the Supplementary Materials section.

In particular, the residual viscosity has been modelled with the general one-parameter friction theory model of Quiñones-Cisneros et al. [69] in conjunction with the PR EoS (using the parameters presented in Table 1). Particular relevance, in the fitting procedure, was given to available liquid data (i.e. high-density field). The correlation for the liquid viscosity of $SiCl_4$ provided by Prat [66], tuned on experimental data from 20°C to the normal boiling point, has been used, together with the experimental vapour viscosities from the NIST database in Aspen Plus® environment [62], for the optimisation of the f-theory general one-parameter viscosity model [69]. The critical characteristic viscosity of $SiCl_4$, which is a degree of freedom of the one-parameter f-theory model, has been optimized here to the value $\eta_{c,SiCl4} = 426.14$ μP to fit the available experimental viscosities of the fluid.

In the same way, the recent friction-theory model for thermal conductivity [70] has been optimized for $SiCl_4$. Available liquid and vapour thermal conductivity data [71][72] have been used to tune the coefficients needed for the property description. The coefficients retrieved using nonlinear data-fitting "lsqcurvefit" algorithm, in MATLAB's Optimization Toolbox, are reported in Table 5. The optimization procedure and the capability of the selected models to describe even complex systems are described in [73].

*Table 5. Fitted parameters of f-theory thermal conductivity model for $SiCl_4$.*

| **Compound** | $a_0$ | $a_1$ | $a_2$ | $b_0$ | $b_1$ | $b_2$ | $A_0$ | $B_0$ | $\Phi_c$ |
|---|---|---|---|---|---|---|---|---|---|
| $SiCl_4$ | -9.0261 | 0.1060 | -0.4060 | 11.2441 | 0.3683 | -0.4127 | 0.0012 | 0.2839 | 0 |

The two main transport properties models available in Aspen Plus environment, valid both for dense liquid and gas phases, are the TRAPP [74] and Chung-Lee-Starling [75] models: both the models make use of the CS approach for the calculation of the residual property. The comparison between the in-house optimized f-theory model and the above-mentioned models for the viscosity and thermal conductivity is reported in Figure 6 for the dense region (liquid phase).

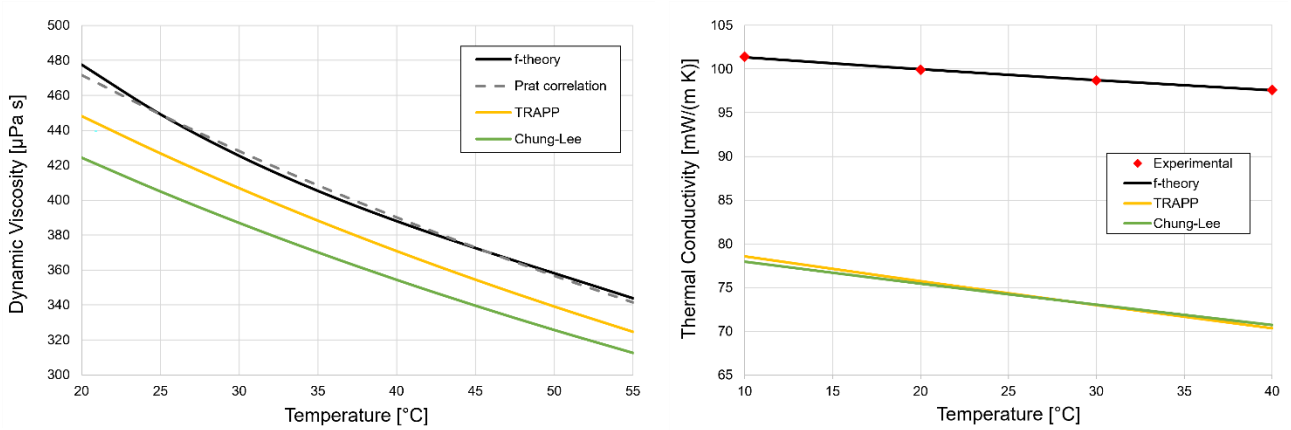


*Figure 6. Comparison between the optimized f-theory models for viscosity (left) and thermal conductivity (right), and other models available in commercial software for both liquid and vapour regions (TRAPP and Chung-Lee), with experimental saturated liquid thermal conductivities [71] (red dots) and Prat correlation [66] for viscosity which is tuned on experimental data.*

As highlighted by Figure 6, the optimized f-theory model for viscosity is the most appropriate for the transport property prediction in the dense phase. It was found an average absolute deviation (AAD) equal to 0.55% compared to the correlation of Prat for viscosity, which is tuned on experimental data. Since the experimental data referenced by Prat were not found in the open literature, we considered the Prat relation as reference for the viscosity. The methods available in Aspen Plus noticeably underestimate the thermal conductivity of liquid $SiCl_4$, which noticeably affect in a negative way the heat transfer coefficient calculation in the dense regions, i.e., the cold side of the recuperator and of the primary heat exchanger/evaporator as well as the liquid phase in the condenser. This is particularly evident if dealing with a supercritical fluid, whose behaviour is intermediate between a liquid and a gas.

Figure 7 shows the trend of the transport properties of $SiCl_4$ at supercritical pressure (60 bar), representative of potential operating condition in ORC system application. Even in this case, the TRAPP model appears to underestimate the thermal conductivity of the fluid compared to the optimized f-theory model, while the simulated viscosity values are aligned: the discontinuity of the TRAPP method is due to computational error of Aspen Plus software near the critical temperature. It is worth noting that the Reynolds number prediction is not affected much by the model selection, since similar viscosity is found, but the Prandtl number and, therefore, the heat transfer coefficient would be drastically underestimated in high-pressure conditions if TRAPP or Chung-Lee models are selected during the heat exchanger design.

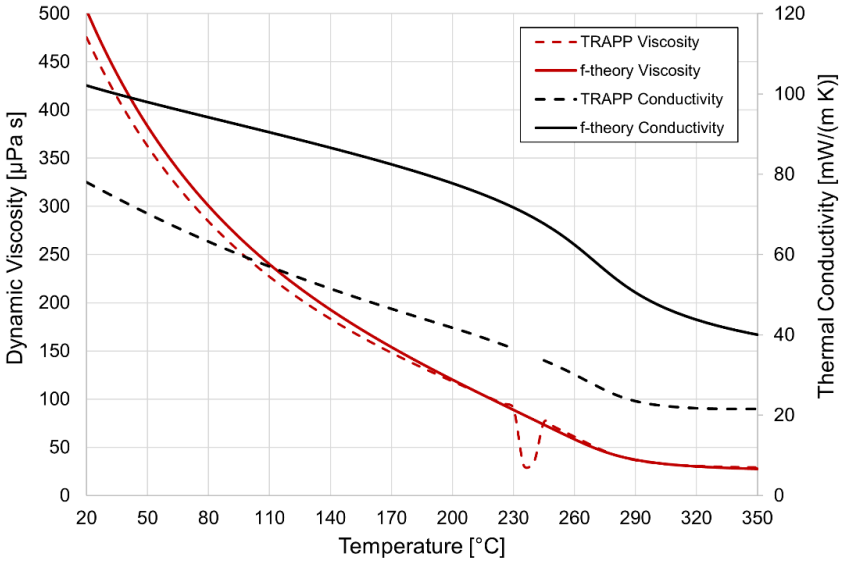


*Figure 7. Trend of transport properties along a supercritical isobar (60 bar) as predicted by the optimized f-theory model and by TRAPP model.*

## 2.5 Thermodynamic analysis of $SiCl_4$ power cycle

In the previous sections, the working fluid thermophysical properties and its thermal stability limits have been investigated. Here, a preliminary overview on the power cycle efficiency attainable with $SiCl_4$ as working fluid is performed in Aspen Plus v12 [62] using the PR EoS.

A typical ORC recuperative cycle layout is investigated, according to Figure 8. As regards the condensation pressure, a pressure slightly above the ambient pressure is adopted in this work to avoid air in-leakage phenomena. Moreover, a condensation above ambient pressure generally implies a reduction of volumetric flow rates, avoiding technical issues in the last turbine stage design. Although the fluid is not complex (see Table 2), the adoption of a recuperator to preheat the pumped liquid, by exploiting the thermal power available from the turbine exhaust, is essential to achieve good cycle efficiency due to a high turbine inlet temperature (TIT).

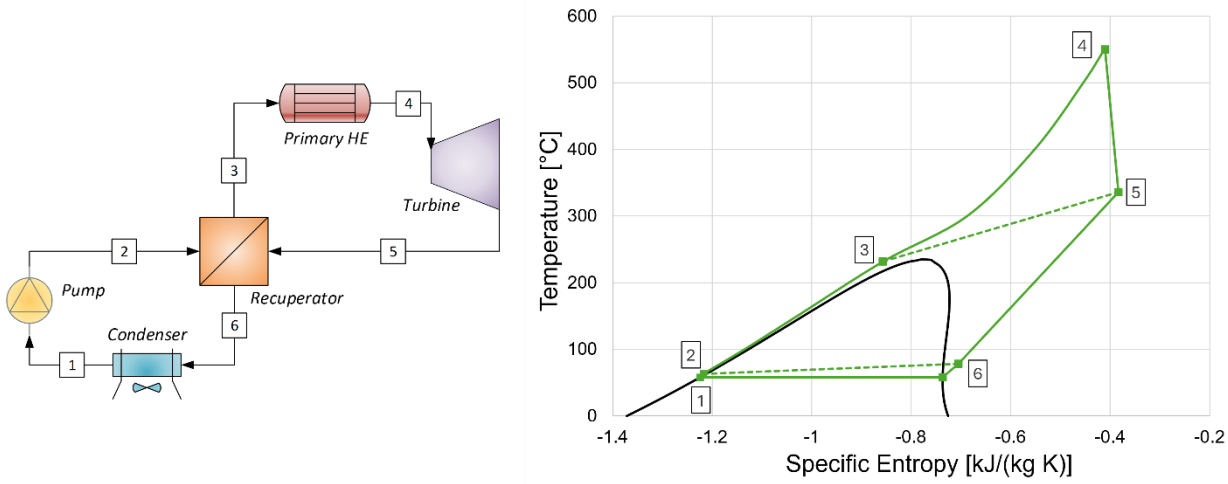


*Figure 8. Cycle layout (left) and temperature vs specific entropy diagram of $SiCl_4$ (right), considering TIT=550°C, $T_{min}$=58°C, and $P_{max}$=60 bar.*

The main assumptions and parameters of the cycle are reported in Table 6. To have a realistic picture of the potentiality of the proposed working fluid, the fluid machine efficiencies are set according to a conventional ORC size of 2 MW gross mechanical output (no electro-mechanical losses included).

*Table 6. $SiCl_4$ power cycle assumptions at design conditions.*

| **Parameters** | **Values** |
|---|---|
| Minimum Pressure | 1.05 bar |
| Minimum Temperature | 58 °C[a] |
| Turbine Inlet Temperature | 450 – 650 °C |
| $\Delta T_{min}$ Recuperator | 15 °C |
| Pressure Drop Recuperator (Hot/Cold side) | 1 % |
| Pressure Drop PHE and Condenser | 2 % |
| Turbine Isentropic Efficiency | calculated[b] |
| Pump Isentropic Efficiency | 65% |

[a] *No subcooling is considered.* [b] *from 3-stages correlation [76]*

The efficiency of the pump is set at 65%, a reasonable value [77] considering that high-head multi-stage pumps are required for the explored transcritical conditions. The turbine isentropic efficiency (total-to-static) has been evaluated in each different design condition according to the correlation of Astolfi and Macchi [76], which has been tuned on several ORC turbines/working fluids designed with their own Axtur code. According to the correlation, the turbine efficiency depends on the isentropic volumetric ratio $V_r=V_{out,is}/V_{in}$ and the size parameter $SP=V_{out,is}^{0.5}/\Delta h_{is}^{0.25}$. The volume expansion ratio was assumed by Macchi and Perdichizzi [78] in 1981 as a similarity parameter to reduce the impact of the working fluid, treating it as an ideal gas. They also noted that when extending efficiency data to turbines of markedly different sizes, non-similarity effects arise because

certain parameters cannot be proportionally scaled with the primary geometry. To counter the adverse impact on efficiency when reducing the size of the axial turbine beyond a specific threshold, they introduced the size parameter (SP): the efficiency experiences a drop of up to 9% when reducing it from 0.20 m to 0.01 m. The correlation for three-stage turbines has been implemented in Aspen Plus environment to evaluate, in each design point, the impact of the operating conditions on the turbine efficiency. The adopted procedure provides more reliable results than the commonly used approach based on constant isentropic efficiency of the turbine, especially for ORCs.

The cycle thermal efficiency, calculated as in Equation 3, is reported in Figure 9 at four different turbine inlet temperatures (in the 450-650°C range coherently with thermal stability test) as function of the maximum pressure. Considering that the critical pressure is 35.9 bar, both subcritical and transcritical conditions have been explored in Figure 9. The recuperator of the cycle is simulated by adopting 200 internal zones to account for large heat capacity variation along the supercritical isobar.

$$\eta_{th} = \frac{W_{Turbine} - W_{Pump}}{Q_{in}} = \frac{\dot{m}(h_4 - h_5) - \dot{m}(h_2 - h_1)}{\dot{m}(h_4 - h_3)} \tag{3}$$

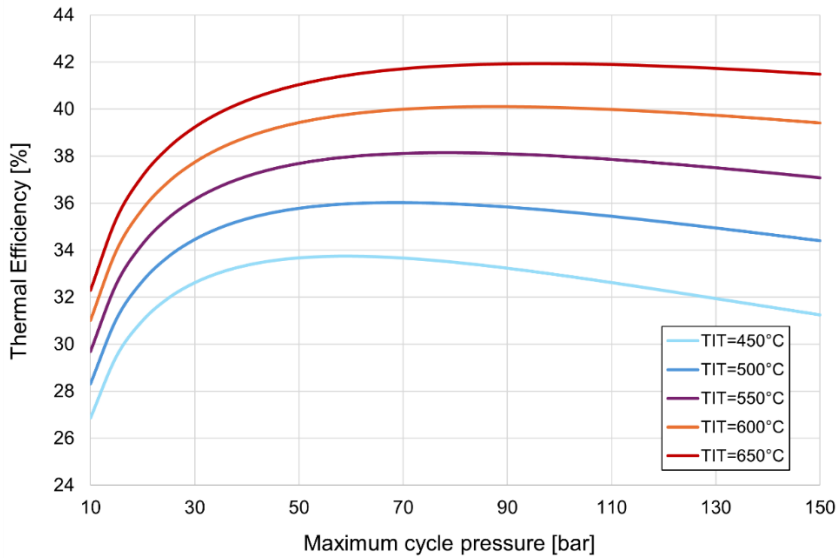


*Figure 9. Thermal efficiency of 2 $MW_{gross}$ $SiCl_4$ cycle as function of the maximum pressure at different TIT, with the assumptions of Table 3 ($P_{min}$=1.05 bar, $T_{min}$=58°C).*

The optimum maximum cycle pressure lies between 50 and 90 bar depending on the TIT. Considering the 550°C thermal level, which is compatible with several high temperature sources and indirect coupling with molten salts as heat transfer fluid (HTF), the optimal maximum pressure results to be 80 bar with an associated efficiency of 38.14%. However, there is a plateau of the thermal efficiency above a certain pressure level (around 50-60 bar). For this reason, in the following considerations we will consider 60 bar(a) as the design conditions, where the design efficiency is 38%. The selected operating conditions of the power block, according to Figure 8, are reported in detail in Tables 7-8.

*Table 7. Thermodynamic conditions of $SiCl_4$ cycle (Figure 8).*

| Streams | T [°C] | P [bar] | $x_{vap}$ [-] |
|---|---|---|---|
| **1** | 58 | 1.05 | 0 |
| **2** | 63.7 | 60 | 0 |
| **3** | 232.3 | 59.4 | 1 |
| **4** | 550 | 58.2 | 1 |
| **5** | 336.8 | 1.08 | 1 |
| **6** | 78.7 | 1.07 | 1 |

*Table 8. Summary of 2 $MW_{gross}$ $SiCl_4$ cycle design conditions (Table 7).*

| Parameters | units | Values |
|---|---|---|
| $\dot{m}$ | kg/s | 18.9 |
| $W_{pump}$ | kW | 122.2 |
| $W_{turbine}$ | kW | 2122.2 |
| $Q_{in,PHE}$ | kW | 5266.7 |
| $Q_{recuperator}$ | kW | 2868.2 |
| $Q_{condenser}$ | kW | 3266.8 |
| $UA_{recuperator}$ | kW/K | 66.3 |
| $\eta_{pump}$ | % | 65 |
| $\eta_{turbine}$ | % | 86.6 |
| $\eta_{th}$ | % | 38 |

At the abovementioned design conditions, the expansion volumetric ratio results 40.8, while the SP parameter is 0.12 m. A three stages expander is so a reasonable solution to distribute the volume flow variation along multiple stages. Following the correlation of Astolfi and Macchi, a turbine efficiency of 86.6% (as in Table 5) is found.

Furthermore, to broaden the overview regarding the performance of the thermodynamic cycle operating with $SiCl_4$, a sensitivity analysis on minimum temperature and plant size will be presented herein. In particular, condensation temperature is ranged from 30°C to 100°C to cover design conditions from water-cooling to cogeneration. In Figure 10, the resulting three-stages turbine and cycle efficiency are showed fixing the 2 MW gross mechanical output.

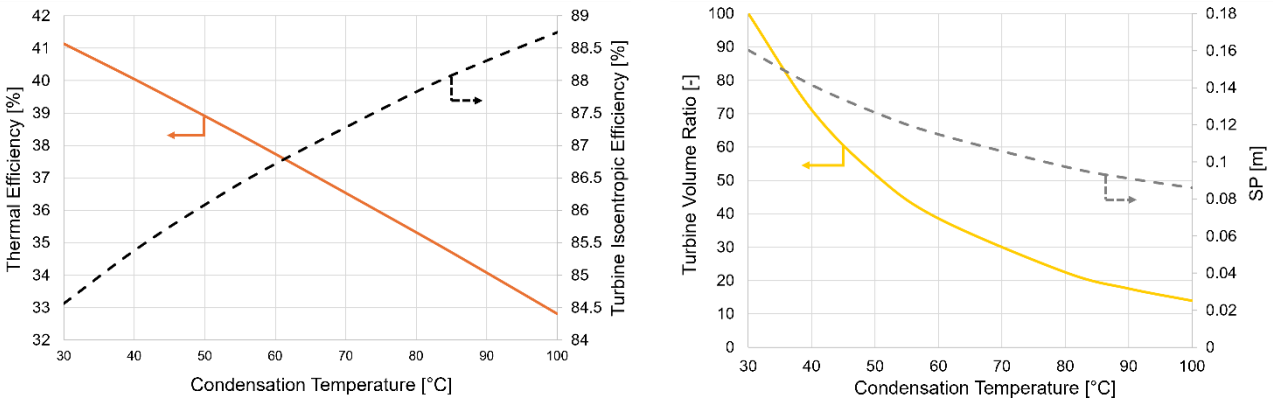


*Figure 10. Sensitivity on the cycle minimum temperature and its impact on the 2 $MW_{gross}$ $SiCl_4$ cycle and three-stages turbine efficiency (left) and three-stages turbine parameters (right), considering TIT=550°C and Pmax=60 bar.*

The design turbine efficiency increases with the increase of minimum cycle temperature due to the reduction of the volumetric ratio across the machine, given by the increase of saturation pressure in the condenser. On the other hand, at fixed output, by increasing the saturation pressure the turbine experiences a reduction of the size of the turbine (SP parameter in Figure 10-right) that enhances secondary losses, but this effect is not predominant compared to the beneficial reduction of the volumetric flow ratio. This analysis suggests the great potentiality of $SiCl_4$ in CHP mode, especially when the ORC is driven by high-grade heat. A thermal efficiency above 32.5% can be achieved by $SiCl_4$ when condensing at 100°C. This result is considerably higher than any value achieved by state-of-the-art ORCs in CHP application, where typical efficiency is in the range 16-19% [39][29].

In Figure 11, the effect of mass flow rate, thus power output, on the turbine efficiency is explored, at fixed pressure ratio (volumetric ratio). It can be noted, from Figure 11, that there is a threshold value (around 2 MW) below which the three-stage turbine efficiency drastically reduces. Figure 11 provides a good picture of the attainable efficiency in CHP applications, assuming a condensation temperature of 100°C: the gross cycle efficiency exceeds 33% for mechanical output above 4 MW adopting a three-stages turbine solution, which is a noticeable result. From this analysis, it is clear that the proposed fluid could potentially compete with steam Rankine cycles in CHP applications where high-grade heat is available.

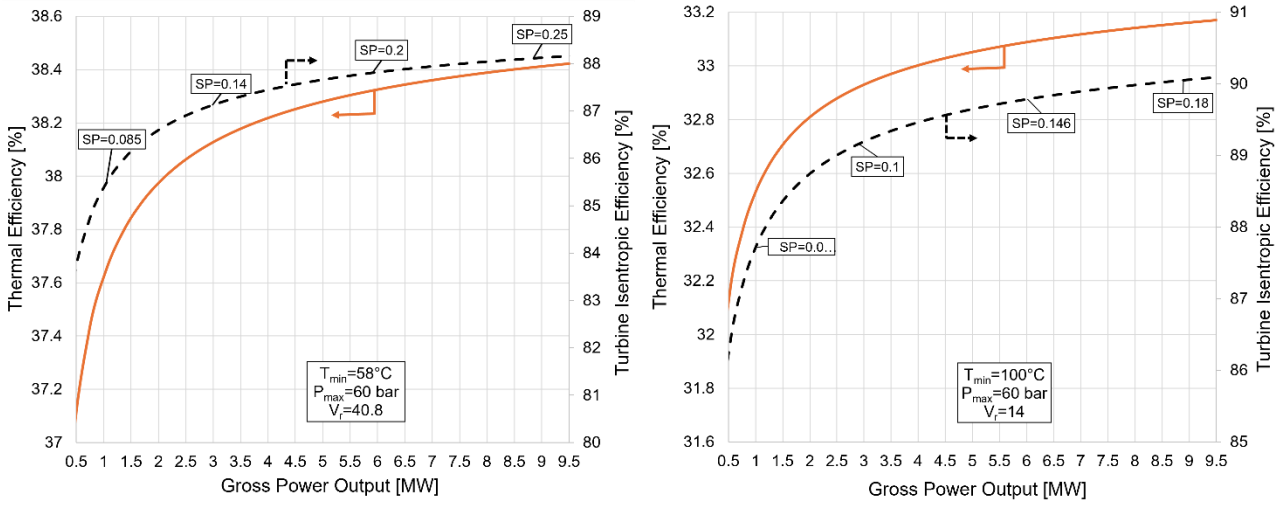


*Figure 11. impact of power size on the three-stage turbine efficiency and on the $SiCl_4$ cycle thermal efficiency, in scenarios of full-electric (left) and CHP (right).*

To highlight the benefits of adopting $SiCl_4$ as working fluid, a comparison between the investigated solution and other fluids for high-temperature (HT) ORC is performed. Steam Rankine cycles and $sCO_2$, as well as $CO_2$-based mixtures [79][80], are excluded from the analysis because the interest is here focused on the medium-low power size (from tens of kW to few MW power output).

A survey of working fluid commercially adopted for HT heat sources in ORC application and additional fluids proposed in literature, at research stage, is presented in Table 6 together with the maximum temperature at which the fluids can be applied without presence of degradation reaction or with acceptable decomposition rate. A review of commercially available ORC solutions for medium-high temperature applications can be found in the work of Vescovo [26] from Turboden company.

The maximum operating temperatures of the considered fluids serve as a practical threshold, as indicated in Table 9. This table reflects their thermal stability limit, incorporating a safety margin to account for potential hot spots and the thermal boundary layer. Epping et al. [29] reported the operating conditions of the toluene cycle as adopted by Tri-O-gen company, with minimum cycle temperature of 55°C and a TIT equal to 320°C. In fact, as result of a previous work [3] in our Fluid Test Lab, no significant degradation of toluene was found after 80-hours thermal stress at 325°C. It is worth to mention that the configuration adopted by Tri-O-gen consists into the combination of turbine, generator and pump running at high speed (25,000 rpm) without the need for a gearbox and shaft seals. A similar solution could be investigated also for $SiCl_4$ to guarantee a completely hermetic design due to its reactive nature.

As a matter of facts, 320°C stands as the highest temperature recorded in commercial ORC units, although Turboden [81] reports a newly developed unit operating up to approximately 400°C as its latest advancement.

*Table 9: List of high-temperature working fluids for ORC with their applicable bulk temperature limit and main characteristics.*

| Working Fluid | $T_{max}$ [°C] | Source | $T_{cr}$ [°C] | $P_{cr}$ [bar] | $P_{sat}$ @ 80°C [bar] | GWP | ODP | NFPA Health | NFPA Flammability |
|---|---|---|---|---|---|---|---|---|---|
| $SiCl_4$ | 650* | This work | 234.9 | 35.9 | 2 | ~0 | 0 | 3 | 0 |
| $TiCl_4$ | 500 | [45] | 364.9 | 46.6 | 0.15 | ~0 | 0 | 3 | 0 |
| Perfluorohexane | 400 | [25] | 179.6 | 18.1 | 2.07 | 9300 | 0 | 1 | 0 |
| Toluene | 320 | [82][3] | 320 | 41.1 | 0.37 | 3 | 0 | 2 | 3 |
| MM | 300 | [41] | 246.7 | 19.4 | 0.54 | ~0 | 0 | 2 | 4 |
| Cyclopentane | 275 | [22] | 239 | 45.1 | 2.5 | 5 | 0 | 1 | 3 |

**The investigation in this work proves 650°C, but further analysis could overcome this limit*

The thermal efficiency has been assessed as a function of the minimum cycle temperature in the range 50-100 °C, keeping the same assumptions on the turbomachines and heat exchangers, already defined in Table 3. A recuperated ORC layout with a fixed gross mechanical output of 2 MW have been considered. The fluids have been evaluated at maximum cycle temperatures considering the corresponding thermal stability limit, as reported in Table 9, and a maximum limit of 550 °C. The PR EoS has been used to perform the analysis in Aspen Plus environment.

In Figure 12, the performance of HT ORCs with the different fluids have been compared in applications with available high-grade heat (above 550°C), such as biomass, CSP, heat recovery from prime movers and from flue gases of industries and incinerators. For each condensation temperature, the maximum pressure which determine the best efficiency point has been considered. It is important to highlight that in the WHR sector thermal efficiency is not the only important parameter. The capability to efficiently cool the sensible heat source down to the minimum temperature limit (heat recovery factor) plays a significant role in the overall plant efficiency (i.e. the net power output divided by the maximum thermal power available from the sensible heat source). However, the heat recovery factor of an ORC plant can be significantly enhanced by adopting a split configuration [39], a practice commonly employed in CHP and WHR plants. Notably, the use of a split architecture can enhance the heat recovery efficiency of the Organic Rankine Cycle (ORC) without adversely affecting its thermal efficiency, within certain limits.

The sensitivity on the condensation temperature reflects different design conditions, from full electric to CHP mode. The comparison allows the reader to have a panoramic on the potential efficiency gain achievable with the proposed $SiCl_4$ in comparison with the commercially available solutions (solid lines) as well as with thermally stable fluids proposed at a research stage (dashed lines) in the past years. The performance of $SiCl_4$ cycle is also presented at a TIT equal to 500°C for comparison with $TiCl_4$, considering the latter fluid's maximum allowable temperature. As evident in Figure 12, $TiCl_4$ surpasses $SiCl_4$ in cogeneration applications, but the opposite occurs at low condensation temperatures due to large volume ratios across the turbine of $TiCl_4$.

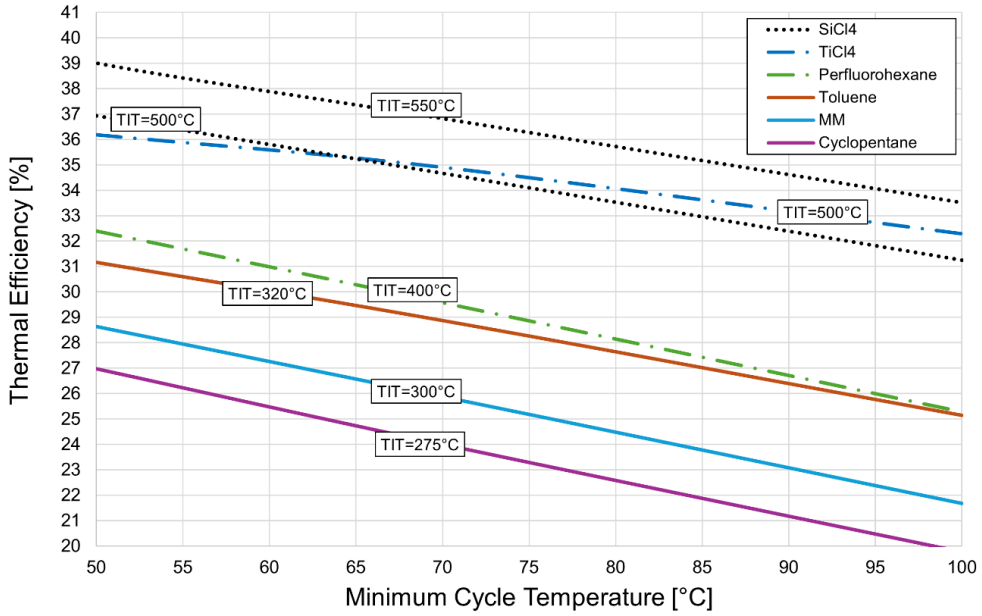


*Figure 12. Thermal efficiency of 2 $MW_{gross}$ HT-ORCs as function of the minimum cycle temperature in optimized conditions, when coupled with sources above 550°C. The dotted line represents the $SiCl_4$ cycle proposed, dashed lines represent fluids that have been proposed only at research stage, solid lines represent commercially adopted fluids. The fluids are simulated with TIT lower than 550°C and constrained by their thermal stability limit (Table 3).*

Considering the low efficiency reached by the state-of-the-art fluids (solid lines in Figure 12), in correspondence of high-temperature sources ORCs are unlikely to be adopted, at least for power output above 2-5 $MW_{el}$, where the specific cost and efficiency of steam cycles justify their choice. Instead, the results provided by this preliminary analysis prove the potentiality of $SiCl_4$ to be competitive with steam Rankine cycles for both low and high-power output.

Going into details, the differences among the different fluids under the identified optimal conditions are presented in Table 10 considering the case of 100°C condensation temperature, representative of a CHP plant.

*Table 10. characteristics of 2 $MW_{gross}$ HT-ORCs at 100°C minimum cycle temperature.*

| **Working Fluid** | **Optimal Cycle Maximum Pressure [bar]** | **$\dot{m}$ [kg/s]** | **$\Delta h_{is,turbine}$ [kJ/kg]** | **$V_{r,\ turbine}$ [-]** | **SP [m]** | **$\eta_{turbine}$** | **$\eta_{th}$** |
|---|---|---|---|---|---|---|---|
| $SiCl_4$ | 95* | 24.4 | 106.1 | 21.4 | 0.08 | 87.4 | 33.5 |
| $TiCl_4$ | 40 | 19.6 | 123.8 | 92.8 | 0.19 | 85.4 | 32.3 |
| Perfluorohexane | 75 | 64 | 44.1 | 19.2 | 0.11 | 88.6 | 25.3 |
| Toluene | 28 | 15.2 | 157.6 | 43.1 | 0.15 | 87.1 | 25.1 |
| MM | 24 | 32.5 | 75.8 | 31.3 | 0.17 | 88.2 | 21.7 |
| Cyclopentane | 40 | 21.5 | 113.2 | 10.6 | 0.09 | 89.4 | 19.7 |

**95 bar is the best efficiency point when condensing at 100°C, even if there is a plateau ($\eta_{th}$=33% is reached at 65 bar).*

Titanium Tetrachloride ($TiCl_4$) appears to be not suitable for a three-stage turbine solution since, condensing at 50°C, the volumetric ratio across the turbine overcome the value of 500 by evaporating above 35 bar. In fact, at 50°C condensing temperature, $TiCl_4$ has a saturation pressure equal to 0.043 bar, which poses challenges in the last turbine stage and condenser design. As reported in Table 7, the volumetric ratio reduces in CHP application, condensing at 100°C, but the minimum cycle pressure is still below the atmospheric one. As already mentioned, the extremely reactive nature of $TiCl_4$ with humid air, in conjunction with its high normal boiling point (136.4°C), poses serious question on its applicability in a power plant. Moreover, no analysis on material compatibility have been performed.

As indicated by the results presented in Table 10, the volumetric ratio of $SiCl_4$ is lower than that of MM. However, the lower turbine efficiency can be attributed to the lower size parameter, which is associated with the lower volumetric flow rate at the outlet.

$SiCl_4$ demonstrates the potential for a thermal efficiency gain of more than 10% compared to state-of-the-art fluids used in commercial high-temperature ORC (HT-ORC) units, surpassing a thermal efficiency of 38% in full-electric mode. This preliminary analysis highlights the promising capabilities of the proposed fluid, particularly in the presence of high-temperature heat sources.

## 2.6 Conclusions

Silicon Tetrachloride ($SiCl_4$) emerges as an innovative working fluid designed for very-high-temperature Rankine cycles. Experimental tests conducted in our Fluid Test Laboratory at the University of Brescia reveal the exceptional thermal stability of $SiCl_4$, surpassing the thermal capabilities of current state-of-the-art fluids utilized in Organic Rankine Cycle (ORC) systems. Notably, $SiCl_4$ demonstrates resilience under extreme conditions, exhibiting no signs of thermal degradation even at the maximum tested temperature of 650°C. State-of-the-art fluids used in ORC units are restricted to maximum operating temperatures below 300-350°C due to thermal stability thresholds. In contrast, the superior thermal capability of $SiCl_4$ makes it a promising solution for advancing high-temperature energy conversion systems.

Furthermore, going beyond the thermal stability test, an additional 300-hour thermal stress at 550°C, followed by detailed metallographic analysis, has uncovered promising results, suggesting mild interaction in terms of material compatibility between $SiCl_4$ and AISI 316L stainless steel. This underscores the practical viability of $SiCl_4$ in high-temperature applications.

In the context of employing $SiCl_4$ as the working fluid, an assessment of its thermophysical properties was conducted. While the PR EoS demonstrated adequacy from a thermodynamic standpoint, it was crucial to fine-tune transport property models within the MATLAB environment for an accurate representation of dynamic viscosity and thermal conductivity.

A preliminary thermodynamic analysis of the recuperated $SiCl_4$ cycle layout was conducted, considering the influence of operating conditions on turbine efficiency. The assessment of various design parameters affecting the thermal efficiency of the $SiCl_4$ cycle included condensation temperature, maximum pressure, and power output. Demonstrating feasibility, a 2 $MW_{gross}$ $SiCl_4$ cycle, condensing at 100°C in CHP application with a maximum temperature of 550°C, could achieve a thermal efficiency surpassing 33%. In full-electric application, the $SiCl_4$ cycle could reach a thermal

efficiency of 38%, exceeding values achievable by any other working fluid under similar conditions and power size.

The primary challenge linked to the use of this fluid is its reactivity with humid air, leading to the production of HCl, though in a milder way compared to $TiCl_4$. This presents operational difficulties, particularly in sustaining pressures above atmospheric levels to avoid air in-leakage. Nevertheless, the unusually low normal boiling point of $SiCl_4$ (57°C), in comparison to other tetrachlorides, facilitates operation at pressures above atmospheric. Moreover, any potential leak of working fluid can be easily identified using an HCl detector and neutralized with a sodium hydroxide (NaOH) solution.

In conclusion, $SiCl_4$ exhibits a potential +10% points gain in thermal efficiency compared to other ORC fluids used in high-temperature units, particularly when coupled with high-temperature sources (above 550°C) such as biomass, solar, prime movers, incinerators, and industrial flue gases. The preliminary results obtained in this article proves $SiCl_4$ as an appealing working fluid for enhancing the efficiency of high-temperature energy conversion systems.

**Nomenclature**

Acronyms

| | |
|---|---|
| AAD | Average Absolute Deviation |
| CHP | Combined Heat and Power |
| CS | Corresponding States |
| CSP | Concentrated Solar Power |
| EoS | Equation of State |
| EU | European Union |
| GWP | Global Warming Potential |
| HAZ | Heat Affected Zone |
| HT | High Temperature |
| HTF | Heat Transfer Fluid |
| NBP | Normal Boiling Point |
| NFPA | National Fire Protection Association |
| ODP | Ozone Depletion Potential |
| ORC | Organic Rankine Cycle |
| PHE | Primary Heat Exchanger |
| PR | Peng Robinson |
| REF | Reference Curve |
| Refprop | Reference Fluid Thermodynamic and Transport Properties |
| SP | Size Parameter, m |
| TIT | Turbine Inlet Temperature, °C |

| | |
|---|---|
| TRAPP | TRAnsport Property Prediction |
| WHR | Waste Heat Recovery |

Symbols

| | |
|---|---|
| $\Delta\pi$ | Residual property π |
| $\Delta h$ | Enthalpy Difference, kJ/kg |
| $\Delta T$ | Temperature Difference, °C |
| $\dot{m}$ | Mass flow rate, kg $s^{-1}$ |
| P | Pressure, bar |
| Q | Thermal duty, MW |
| R | Universal Gas Constant |
| s | Entropy, kJ $kg^{-1}$ $K^{-1}$ |
| T | Temperature |
| W | Mechanical work, MW |
| x | Fraction |
| Z | Compressibility factor, - |

Greek symbols

| | |
|---|---|
| $\eta_{th}$ | Cycle Thermal Efficiency, - |
| $\eta_{Turbine}$ | Turbine isentropic efficiency, - |
| $\eta_{Pump}$ | Pump isentropic efficiency, - |
| ω | Pitzer acentric factor, - |
| σ | Molecular Complexity Parameter, - |

Subscripts

| | |
|---|---|
| cr | Critical |
| ch | Channel |
| f | Friction term |
| in | Inlet |
| is | Isentropic |
| min | Minimum |
| max | Maximum |
| o | Zero-density |
| r | Ratio |
| red | Reduced |
| sat | Saturation |
| SV | Saturated Vapour |

| | |
|---|---|
| vap | Vapour |

Superscripts

| | |
|---|---|
| r | Residual |
| ref | Reference flud |

## 2.7 Bibliography


[1] E. Commission, D.-G. for Climate Action, Going climate-neutral by 2050 – A strategic long-term vision for a prosperous, modern, competitive and climate-neutral EU economy, Publications Office, 2019. https://doi.org/doi/10.2834/02074.

[2] E. Macchi, M. Astolfi, Organic Rankine Cycle (ORC) Power Systems: Technologies and Applications, 2016.

[3] C.M. Invernizzi, P. Iora, G. Manzolini, S. Lasala, Thermal stability of n-pentane, cyclo-pentane and toluene as working fluids in organic Rankine engines, Appl. Therm. Eng. 121 (2017) 172–179. https://doi.org/10.1016/j.applthermaleng.2017.04.038.

[4] G. Di Marcoberardino, C.M. Invernizzi, P. Iora, L. Arosio, M. Canavese, A. Lunghi, A. Mazzei, Thermal Stability and Thermodynamic Performances of Pure Siloxanes and Their Mixtures in Organic Rankine Cycles, Energies. 15 (2022) 1–20. https://doi.org/10.3390/en15103498.

[5] M. Papapetrou, G. Kosmadakis, A. Cipollina, U. La Commare, G. Micale, Industrial waste heat: Estimation of the technically available resource in the EU per industrial sector, temperature level and country, Appl. Therm. Eng. 138 (2018) 207–216. https://doi.org/10.1016/j.applthermaleng.2018.04.043.

[6] Worldsteel Association, Energy use in the steel industry, Worldsteel Assoc. Fact Sheet. (2013) 1–3.

[7] P. Colonna, E. Casati, C. Trapp, T. Mathijssen, J. Larjola, T. Turunen-Saaresti, A. Uusitalo, Organic Rankine Cycle Power Systems: From the Concept to Current Technology, Applications, and an Outlook to the Future, J. Eng. Gas Turbines Power. 137 (2015) 100801. https://doi.org/10.1115/1.4029884.

[8] B. Vanslambrouck, I. Vankeirsbilck, S. Gusev, M. De Paepe, Efficiency comparison between the steam cycle and the organic Rankine cycle for small scale power generation, Renew. Energy World Conf. Expo North Am. 32 (2012) 13.

[9] A. Guercio, R. Bini, Biomass-fired Organic Rankine Cycle combined heat and power systems, Elsevier Ltd, 2017. https://doi.org/10.1016/B978-0-08-100510-1.00015-6.

[10] M. Astolfi, D. Alfani, S. Lasala, E. Macchi, Comparison between ORC and CO2 power systems for the exploitation of low-medium temperature heat sources, Energy. 161 (2018) 1250–1261. https://doi.org/https://doi.org/10.1016/j.energy.2018.07.099.

[11] A. Romei, P. Gaetani, G. Persico, Computational fluid-dynamic investigation of a centrifugal compressor with inlet guide vanes for supercritical carbon dioxide power systems, Energy. 255 (2022) 124469. https://doi.org/10.1016/j.energy.2022.124469.

[12] M. Marchionni, M. Usman, L. Chai, S.A. Tassou, Inventory control assessment for small scale sCO2 heat to power conversion systems, Energy. 267 (2023) 126537. https://doi.org/10.1016/j.energy.2022.126537.

[13] T.J. Held, The 4th International Symposium - Supercritical CO2 Power Cycles September 9-10, 2014, Pittsburgh, Pennsylvania INITIAL TEST RESULTS OF A MEGAWATT-CLASS SUPERCRITICAL CO2 HEAT ENGINE, in: 2014. https://api.semanticscholar.org/CorpusID:204784180.

[14] United States. Bureau of Mines., Mineral Facts and Problems: 1985 Edition, Washington D.C., 1985.

[15] Y. Mochizuki, J. Bud, J. Liu, N. Tsubouchi, Production of Silicone Tetrachloride from Rice Husk by

Chlorination and Performance of Mercury Adsorption from Aqueous Solution of the Chlorinated Residue, ACS Omega. 5 (2020) 29110–29120. https://doi.org/10.1021/acsomega.0c03789.

[16] C. Cheng, C. Zhang, J. Jiang, E. Ma, J. Bai, J. Wang, Raman Spectroscopy Characterization of Dissolved Polysilicon Byproduct $SiCl_4$ in Ionic Liquids, J. Spectrosc. 2018 (2018) 2329189. https://doi.org/10.1155/2018/2329189.

[17] Y. Okamoto, M. Sumiya, Y. Nakamura, Y. Suzuki, Effective silicon production from SiCl4 source using hydrogen radicals generated and transported at atmospheric pressure, Sci. Technol. Adv. Mater. 21 (2020) 482–491. https://doi.org/10.1080/14686996.2020.1789438.

[18] Y. Wan, X. Zhao, D. Yan, D. Yang, Y. Li, S. Guo, Research and preparation of ultra purity silicon tetrachloride, AIP Conf. Proc. 1890 (2017). https://doi.org/10.1063/1.5005228.

[19] Y. Wan, X. Zhao, S. Guo, D. Yan, D. Yang, L. Wang, The preparation and detection of high purity silicon tetrachloride with optical fibres level, IOP Conf. Ser. Mater. Sci. Eng. 207 (2017). https://doi.org/10.1088/1757-899X/207/1/012018.

[20] J.S. Pereira, M. Santos, R. Mendes, J.C. André, J.B. Ribeiro, Thermal degradation assessment study of a direct vaporization ORC based micro-CHP system under close-to-real operating conditions, Appl. Therm. Eng. 214 (2022). https://doi.org/10.1016/j.applthermaleng.2022.118878.

[21] C.M. Invernizzi, THERMAL STABILITY EVALUATION FOR RANKINE CYCLES WORKING FLUIDS: EXPERIMENTAL APPARATUS AND CALIBRATION RESULTS, La Termotec. N. 4 (1990) 69–76.

[22] M. Pasetti, C.M. Invernizzi, P. Iora, Thermal stability of working fluids for organic Rankine cycles: An improved survey method and experimental results for cyclopentane, isopentane and n-butane, Appl. Therm. Eng. 73 (2014) 764–774. https://doi.org/10.1016/j.applthermaleng.2014.08.017.

[23] G. Angelino, C. Invernizzi, Experimental investigation on the thermal stability of some new zero ODP refrigerants, Int. J. Refrig. 26 (2003) 51–58. https://doi.org/10.1016/S0140-7007(02)00023-3.

[24] C. Invernizzi, M. Binotti, P. Bombarda, G. Di Marcoberardino, P. Iora, G. Manzolini, Water mixtures as working fluids in organic Rankine cycles, Energies. 12 (2019) 1–17. https://doi.org/10.3390/en12132629.

[25] S. Lasala, C. Invernizzi, P. Iora, P. Chiesa, E. Macchi, Thermal Stability Analysis of Perfluorohexane, Energy Procedia. 75 (2015) 1575–1582. https://doi.org/10.1016/j.egypro.2015.07.358.

[26] R. Vescovo, High temperature organic rankine cycle (HT-ORC) for cogeneration of steam and power, AIP Conf. Proc. 2191 (2019). https://doi.org/10.1063/1.5138886.

[27] R.L. Cole, J.C. Demirgian, J.W. Allen, Predicting toluene degradation in organic Rankine-cycle engines, in: United States, 1987. https://www.osti.gov/biblio/6414474.

[28] V. Havens, D.R. Ragaller, Study of toluene stability for an Organic Rankine Cycle (ORC) space-based power system, in: 1988. https://api.semanticscholar.org/CorpusID:107906670.

[29] Q. Eppinga, S. Ganassin, J. Van Buijtenen, Application and operation of 40+ Triogen ORC plants, Energy Procedia. 129 (2017) 684–691. https://doi.org/10.1016/j.egypro.2017.09.145.

[30] X. Dai, L. Shi, Q. An, W. Qian, Chemical kinetics method for evaluating the thermal stability of Organic Rankine Cycle working fluids, Appl. Therm. Eng. 100 (2016) 708–713. https://doi.org/10.1016/j.applthermaleng.2016.02.091.

[31] D.M. Ginosar, L.M. Petkovic, D.P. Guillen, Thermal Stability of Cyclopentane as an Organic Rankine Cycle Working Fluid, (2011) 4138–4144.

[32] X. Dai, L. Shi, Q. An, W. Qian, Thermal stability of some hydrofluorocarbons as supercritical ORCs working fluids, Appl. Therm. Eng. 128 (2018) 1095–1101. https://doi.org/10.1016/j.applthermaleng.2017.09.046.

[33] L. Calderazzi, P.C. di Paliano, Thermal stability of R-134a, R-141b, R-13I1, R-7146, R-125 associated with stainless steel as a containing material, Int. J. Refrig. 20 (1997) 381–389.

https://doi.org/https://doi.org/10.1016/S0140-7007(97)00043-1.

[34] R. Scaccabarozzi, M. Tavano, C.M. Invernizzi, E. Martelli, Comparison of working fluids and cycle optimization for heat recovery ORCs from large internal combustion engines, Energy. 158 (2018) 396–416. https://doi.org/https://doi.org/10.1016/j.energy.2018.06.017.

[35] C.M. Invernizzi, P. Iora, M. Preßinger, G. Manzolini, HFOs as substitute for R-134a as working fluids in ORC power plants: A thermodynamic assessment and thermal stability analysis, Appl. Therm. Eng. 103 (2016) 790–797. https://doi.org/10.1016/j.applthermaleng.2016.04.101.

[36] Y. Liang, J. Wu, Z. Sun, Y. Zhu, K. Ye, M. Dong, J. Lu, Thermodynamic and economic analysis of refrigerant mixture R290/R1234ze used in an ORC-EERC system for low temperature heat sources, Appl. Therm. Eng. 229 (2023) 120635. https://doi.org/https://doi.org/10.1016/j.applthermaleng.2023.120635.

[37] L. Xin, C. Liu, L. Tan, X. Xu, Q. Li, E. Huo, K. Sun, Thermal stability and pyrolysis products of HFO-1234yf as an environment-friendly working fluid for Organic Rankine Cycle, Energy. 228 (2021) 120564. https://doi.org/10.1016/j.energy.2021.120564.

[38] G. Angelino, C. Invernizzi, Cyclic Methylsiloxanes as Working Fluids for Space Power Cycles, J. Sol. Energy Eng. 115 (1993) 130–137. https://doi.org/10.1115/1.2930039.

[39] A. Salogni, D. Alberti, M. Metelli, R. Bertanzi, Operation and maintenance of a biomass fired - Organic Rankine Cycle - CHP plant: The experience of Cremona, Energy Procedia. 129 (2017) 668–675. https://doi.org/10.1016/j.egypro.2017.09.141.

[40] L. Keulen, S. Gallarini, C. Landolina, A. Spinelli, P. Iora, C. Invernizzi, L. Lietti, A. Guardone, Thermal stability of hexamethyldisiloxane and octamethyltrisiloxane, Energy. 165 (2018) 868–876. https://doi.org/10.1016/j.energy.2018.08.057.

[41] M. Preißinger, D. Brüggemann, Thermal stability of hexamethyldisiloxane (MM) for high-temperature Organic Rankine Cycle (ORC), Energies. 9 (2016). https://doi.org/10.3390/en9030183.

[42] W. Wang, X. Dai, L. Shi, Influence of thermal stability on organic Rankine cycle systems using siloxanes as working fluids, Appl. Therm. Eng. 200 (2022) 117639. https://doi.org/https://doi.org/10.1016/j.applthermaleng.2021.117639.

[43] L. Putelli, G. Di Marcoberardino, M. Gelfi, C.M. Invernizzi, P.G. Iora, G. Manzolini, Preliminary Analysis of High-Temperature Corrosion of Metallic Alloys With CO2 and CO2-Based Working Mixtures for Power Plants Applications, in: 2022: p. V009T28A035. https://doi.org/10.1115/GT2022-84197.

[44] L.R. Di Nanno, F.A. Di Bella, M.D. Koplow, An RC-1 organic Rankine bottoming cycle for an adiabatic diesel engine, 1983. https://ntrs.nasa.gov/citations/19840024236.

[45] C.M. Invernizzi, P. Iora, D. Bonalumi, E. Macchi, R. Roberto, M. Caldera, Titanium tetrachloride as novel working fluid for high temperature Rankine Cycles: Thermodynamic analysis and experimental assessment of the thermal stability, Appl. Therm. Eng. 107 (2016) 21–27. https://doi.org/10.1016/j.applthermaleng.2016.06.136.

[46] G. Manzolini, M. Binotti, D. Bonalumi, C. Invernizzi, P. Iora, CO2 mixtures as innovative working fluid in power cycles applied to solar plants. Techno-economic assessment, Sol. Energy. 181 (2019) 530–544. https://doi.org/10.1016/J.SOLENER.2019.01.015.

[47] K. Kontomaris, HFO-1336mzz-Z: High Temperature Chemical Stability and Use as A Working Fluid in Organic Rankine Cycles, Int. Refrig. Air Cond. Conf. (2014) 10.

[48] E. Huo, C. Liu, L. Xin, X. Li, X. Xu, Q. Li, S. Wang, C. Dang, Thermal stability and decomposition mechanism of HFO-1336mzz(Z) as an environmental friendly working fluid: Experimental and theoretical study, Int. J. Energy Res. 43 (2019) 4630–4643. https://doi.org/10.1002/er.4599.

[49] J. Liu, Y. Liu, C. Liu, L. Xin, W. Yu, Experimental and Theoretical Study on Thermal Stability of Mixture R1234ze(E)/R32 in Organic Rankine Cycle, J. Therm. Sci. 32 (2023) 1595–1613.

https://doi.org/10.1007/s11630-023-1790-2.

[50] M.Z. Irriyanto, H.S. Lim, B.S. Choi, A.A. Myint, J. Kim, Thermal stability and decomposition behavior of HFO-1234ze(E) as a working fluid in the supercritical organic Rankine cycle, J. Supercrit. Fluids. 154 (2019) 104602. https://doi.org/10.1016/j.supflu.2019.104602.

[51] Study of Toluene Stability for an Organic Rankine Cycle Space-Based Power System, (1988).

[52] X. Dai, L. Shi, Q. An, W. Qian, Screening of hydrocarbons as supercritical ORCs working fluids by thermal stability, Energy Convers. Manag. 126 (2016) 632–637. https://doi.org/https://doi.org/10.1016/j.enconman.2016.08.024.

[53] 3M Company, 3M™ Novec™ 649 Engineered Fluid, (2009) 8–11. www.3M.com/novec.

[54] L. Chen, B. Zhang, T. Yang, Y. Deng, X. Li, A.B. Murphy, Thermal decomposition characteristics and kinetic analysis of C4F7N/CO2 gas mixture, J. Phys. D. Appl. Phys. 53 (2019) 55502. https://doi.org/10.1088/1361-6463/ab56a0.

[55] M. Mehos, C. Turchi, J. Vidal, M. Wagner, Z. Ma, C. Ho, W. Kolb, C. Andraka, A. Kruizenga, Concentrating Solar Power Gen3 Demonstration Roadmap, Nrel/Tp-5500-67464. (2017) 1–140. https://doi.org/10.2172/1338899.

[56] Gruppo di Metallurgia - Università degli Studi di Brescia, https://metallurgia.unibs.it/.

[57] ARMY MATERIEL COMMAND ALEXANDRIA VA, ENGINEERING DESIGN HANDBOOK MILITARY PYROTECHNICS SERIES. PART ONE. THEORY AND APPLICATION, 1967.

[58] L.S. Toczylkin, C.L. Young, Vapour pressures of some liquids of quasi-spherical molecules near their critical points and the applicability of the principle of corresponding states, Aust. J. Chem. 30 (1977) 1591–1593. https://doi.org/10.1071/CH9771591.

[59] T. Rugina, L. Sacarescu, Isobaric vapor liquid equilibria for the binary systems dichloromethylsilane with chlorotrimethylsilane, dichlorodimethylsilane, trichloromethylsilane, or silicon tetrachloride, J. Chem. Eng. Data. 37 (1992) 143–145. https://doi.org/10.1021/je00006a003.

[60] R.O. Sauer, E.M. Hadsell, Azeotropes of Trimethylchlorosilane and Silicon Tetrachloride, J. Am. Chem. Soc. 70 (1948) 4258–4259. https://doi.org/10.1021/ja01192a512.

[61] T. Ruglna, L. Sacarescu, Isobaric Vapor-Liquid Equilibria for the Binary Systems (CH3)3SiCl, (CH3)2SiCl2, CH3SiCl3, or SiCl4, (1992) 143–145.

[62] Aspen Technology Inc., Aspen Plus®, Version V12.1, (2022).

[63] J.H. Hildebrand, Forces between Tetrahalide Molecules, J. Chem. Phys. 15 (2004) 727–736. https://doi.org/10.1063/1.1746306.

[64] S. Lecompte, E. Ntavou, B. Tchanche, G. Kosmadakis, A. Pillai, D. Manolakos, M. de Paepe, Review of experimental research on supercritical and transcritical thermodynamic cycles designed for heat recovery application, Appl. Sci. 9 (2019) 1–26. https://doi.org/10.3390/app9122571.

[65] D.Y. Peng, D.B. Robinson, A New Two-Constant Equation of State, Ind. Eng. Chem. Fundam. 15 (1976) 59–64. https://doi.org/10.1021/i160057a011.

[66] O.P. Prat, T. Cloitre, R.L. Aulombard, Thermal and mechanical properties of silicon tetrachloride (SiCl 4) and germanium tetrachloride (GeCl4) in their vapor and liquid phases, Chem. Vap. Depos. 13 (2007) 199–203. https://doi.org/10.1002/cvde.200604242.

[67] B.E. Poling, J.M. Prausnitz, The Properties of Gases and Liquids, 2001.

[68] The MathWorks Inc., MATLAB. (2022a).

[69] S.E. Quiñones-Cisneros, C.K. Zéberg-Mikkelsen, E.H. Stenby, One parameter friction theory models for viscosity, Fluid Phase Equilib. 178 (2001) 1–16. https://doi.org/10.1016/S0378-3812(00)00474-X.

[70] S.E. Quiñones-Cisneros, S. Pollak, K.A.G. Schmidt, Friction Theory Model for Thermal Conductivity, J. Chem. Eng. Data. 66 (2021) 4215–4227. https://doi.org/10.1021/acs.jced.1c00400.

[71] P.S. Ivannikov, I. V Litvinenko, I. V Radchenko, Thermal conductivity of liquid tetrachlorides, J. Eng. Phys. 23 (1972) 1397–1402. https://doi.org/10.1007/BF00834688.

[72] K.C. Hansen, C. Rungaroonthaikul, T.M. Aminabhavi, C.L. Yaws, Gaseous Thermal Conductivity of Silane, Dichlorosilane, Trichlorosilane, Tetrachlorosilane, and Tetrafluorosilane in the Temperature Range from 28 to 350 .degree.C, J. Chem. Eng. Data. 40 (1995) 15–17. https://doi.org/10.1021/je00017a003.

[73] M. Doninelli, G. Di Marcoberardino, On the design of recuperator for transcritical cycle adopting CO2-based mixture as working fluid: a focus on transport properties prediction, Energy Technol. (2023). https://doi.org/10.1002/ente.202300677.

[74] J.F. Ely, H.J.M. Hanley, A Computer Program for the Prediction of Viscosity and Thermal Conductivity in Hydrocarbon Mixtures, (1981).

[75] T.H. Chung, L.L. Lee, K.E. Starting, Applications of Kinetic Gas Theories and Multiparameter Correlation for Prediction of Dilute Gas Viscosity and Thermal Conductivity, Ind. Eng. Chem. Fundam. 23 (1984) 8–13. https://doi.org/10.1021/i100013a002.

[76] M. Astolfi, E. Macchi, Efficiency Correlations for Axial Flow Turbines Working With Non-Conventional Fluids, Asme Orc 2015. (2015) 1–12.

[77] C. Cho Khaing, A. Zaw Lynn, N. Nyi, Design of Multistage Centrifugal Pump Impeller for High Head Applications, Int. J. Latest Technol. Eng. VIII (2019) 115–120. www.ijltemas.in.

[78] E. Macchi, A. Perdichizzi, Efficiency Prediction for Axial-Flow Turbines Operating with Nonconventional Fluids, J. Eng. Power. 103 (1981) 718–724. https://doi.org/10.1115/1.3230794.

[79] M. Binotti, G. Di Marcoberardino, P. Iora, C. Invernizzi, G. Manzolini, Scarabeus: Supercritical carbon dioxide/alternative fluid blends for efficiency upgrade of solar power plants, AIP Conf. Proc. 2303 (2020). https://doi.org/10.1063/5.0028799.

[80] E. Morosini, M. Doninelli, D. Alfani, M. Astolfi, G. Di Marcoberardino, G. Manzolini, Analysis of the Potential of Co2 Based Mixtures To Improve the Efficiency of Cogenerative Waste Heat Recovery Power Plants, Conf. Proc. Eur. SCO2 Conf. (2023) 169–178. https://doi.org/10.17185/duepublico/77287.

[81] Turboden - ORC systems, https://www.turboden.com/products/2463/orc-system (accessed February 26, 2024).

[82] S. Ganassin, J.P. Van Buijtenen, C. Author, Small Scale Solid Biomass Fuelled Orc Plants for Combined Heat and Power, Proc. 3rd Int. Semin. ORC Power Syst. (2015) 1–9.

## 2.8 Supplementary materials

In this supplementary materials section, the main equations constituting the transport properties models implemented in MATLAB to describe the dynamic viscosity and thermal conductivity of Silicon Tetrachloride are reported. Additionally, we present the energy balances, solved in Aspen Plus V12 software, to evaluate the Rankine cycle working with Silicon Tetrachloride.

### 2.8.1 Transport properties models

The generic transport property $\pi$ is calculated as a sum of a "zero-density" property $\pi_0$ and a "residual property" $\Delta\pi$:

$$\pi(T,p) = \pi_0(T) + \Delta\pi(T,p) \quad (1)$$

The zero-density term can be calculated with methods that are derived from the rigorous kinetic theory of gases, whilst almost all the methods available to describe the residual property are empirical or semi-theoretical.

In this work, the Chung et al. model [1] is the kinetic-theory based method selected for the evaluation of viscosity (Eq. 2) and thermal conductivity (Eq. 3) of Silicon Tetrachloride in "zero-density" conditions.

| "Zero-density" viscosity | | "Zero-density" thermal conductivity | |
|---|---|---|---|
| $\mu_{i,0} = 40.785 \frac{F_C (M T)^{\frac{1}{2}}}{V_C^{\frac{2}{3}} \Omega^{(2,2)}}$ | (2) | $\frac{\lambda_{i,o} M}{\mu_{i,0} C_v} = \frac{3.75 \psi}{C_v/R}$ | (3) |

The residual transport property is treated instead by using the friction theory models for viscosity and thermal conductivity as described in the following section.

### 2.8.2 Friction Theory models for the residual viscosity and thermal conductivity

The residual dynamic viscosity of Silicon Tetrachloride has been calculated with the viscosity model developed by Quiñones-Cisneros et al. [2], as in the following quadratic form:

$$\Delta\eta = k_a p_a + k_r p_r + k_{rr} {p_r}^2 \quad (4)$$

where $k_a$, $k_r$, $k_{rr}$ are friction factors, obtained with mixing rules, related to the attractive (subscript "a") and repulsive (subscript "r) pressure terms. In the general one-parameter model, adopted in this work, the friction factors can be obtained only as function of a critical characteristic viscosity $\eta_{c,i}$ :

$$k_{j,i} = \frac{\eta_c \hat{k}_{j,i}}{P_{cr}} \quad (5)$$

while the reduced coefficient $\hat{k}_{j,i}$ depends only on the equation of state selected for the calculation of the attractive ($p_a$) and repulsive ($p_r$) pressure terms - see Table 2 of [2]. In Matlab, the Peng Robinson EoS as detailed in the following section is implemented. The critical characteristic viscosity, $\eta_c$ , has a physical explanation as the viscosity of the fluid at critical conditions. However, it is primarily utilized as a parameter to fit experimental data. This parameterization allows for the adjustment of the model based on available experimental results, ensuring better accuracy in representing the fluid's behavior. The critical characteristic viscosity of $SiCl_4$, has been tuned to the value $\eta_{c,SiCl4}$ = 426.14 μP to fit the available experimental viscosities of the fluid.

A one-parameter model for thermal conductivity is still lacking, so the friction theory model presented in [3] has been used with a second-order truncation:

$$\Delta\lambda = \lambda_c + \phi_{a,1} s_a + \phi_{a,2} {s_a}^2 + \phi_{r,1} s_r + \phi_{r,2} {s_r}^2 \quad (6)$$

where the attractive and repulsive residual entropy of the mixture has been computed with the PR EoS as detailed in the following section (implemented in a Matlab routine). The friction coefficients $\phi_{j,i}$ and the critical enhancement term $\lambda_c$ contain nine coefficients ($a_i$, $b_i$, $A_0$, $B_0$, $\phi_c$) that must be regressed on available experimental data in dense conditions (residual term). The regressed parameters on available experimental data of Silicon Tetrachloride are reported in the Section 4.1 of the article (Table 5).

### 2.8.3 Equations for power cycle evaluation

The computational tool adopted in this work for the simulations of the power cycle performances is Aspen Plus, a commercial software applied for modelling chemical processes and power cycles for several applications, which integrates mass and energy balances with dedicated equations of state as well as several specific component parameters starting from a component library or user-defined components model.

The original Peng Robinson EoS (Eq. 7-11) has been adopted by Aspen Plus to calculate the thermodynamic properties of $SiCl_4$ in the power cycle conditions. It has been also used to calculate thermodynamic properties required by the transport properties models.

$$P = \frac{RT}{v-b} - \frac{\alpha a}{v(v+b)+b(v-b)} \tag{7}$$

where the alpha function adopted is in its original form [4]:

$$\alpha = \left[1 + k\left(1 - \sqrt{T_r}\right)\right]^2 \tag{8}$$

$$k = 0.37464 + 1.54226\omega - 0.26992\omega^2 \tag{9}$$

$$a = 0.45724\frac{R^2 T_{cr}^2}{P_{cr}} \tag{10}$$

$$b = 0.0778\frac{RT_{cr}}{P_{cr}} \tag{11}$$

The power cycle architecture considered is also reported here, in Figure 1, to better reference the thermodynamic conditions.

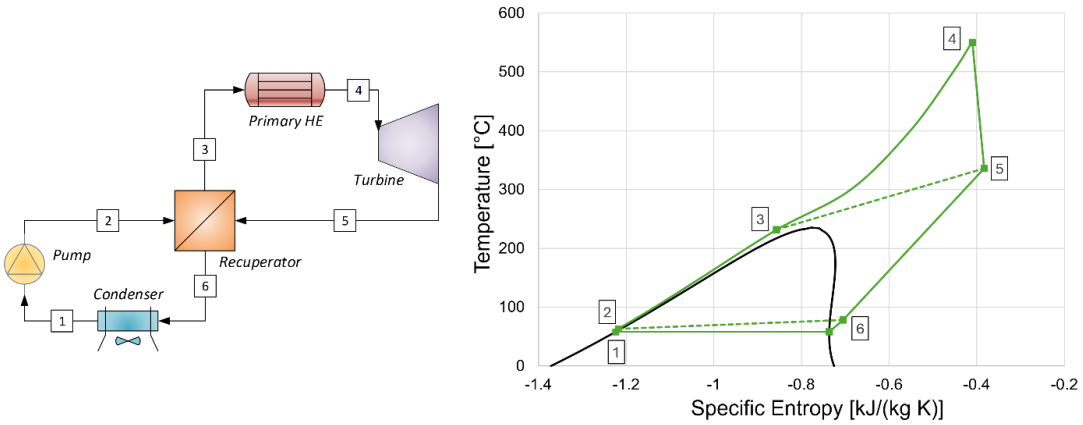


*Figure 1: Cycle layout (left) and temperature vs specific entropy diagram of $SiCl_4$ (right), considering TIT=550°C, $T_{min}$=58°C, and $P_{max}$=60 bar.*

The thermal efficiency of the cycle is computed as:

$$\eta_{th} = \frac{W_{Turbine} - W_{Pump}}{Q_{in}} = \frac{(h_4 - h_5) - (h_2 - h_1)}{(h_4 - h_3)} \tag{12}$$

where $W_{turbine}$ and $W_{pump}$ are mechanical power (no electro-mechanical losses) of the turbine and the pump respectively:

$$W_{Turbine} = \dot{m}(h_4 - h_5) = \dot{m}\left(h_4 - h_{5,is}\right)\eta_{turbine,is} \tag{13}$$

$$W_{Pump} = \dot{m}(h_2 - h_1) = \frac{\dot{m}(h_2 - h_1)}{\eta_{pump,is}} \tag{14}$$

where $\dot{m}$ is the mass flow rate of $SiCl_4$.

An internal code in Fortran language is included in the calculation of the power cycle to evaluate the isentropic efficiency of the turbine $\eta_{t,is}$ in each operating condition (pressure ratio, mass flow rate, inlet and outlet temperature, inlet and outlet density). This is performed by adding a routine that calculates the efficiency of the turbine as function of the volumetric ratio and the size parameter, as mentioned in the article.

A constant isentropic efficiency of 65% is used instead for the pump. The inlet conditions of the pump are assumed to be saturated liquid conditions at the assumed minimum cycle temperature (58°C for $SiCl_4$ in full-electric configuration). The minimum cycle pressure, accordingly, is computed by the EoS as the vapour pressure at the condensation temperature.

The recuperator is solved in Aspen Plus by dividing it into 200 internal zones, where the energy balance is solved in each zone and convergency is reached when the minimum temperature difference between the hot-side and the cold-side is the one imposed of 15°C. The heat transfer has been divided in many internal zones due to large heat capacity variation typically occurs in supercritical isobars when approaching the critical zone. The energy balance in the recuperator is:

$$Q_{rec} = \dot{m}(h_5 - h_6) = \dot{m}(h_3 - h_2) \quad (15)$$

where $Q_{rec}$ is the recuperator thermal power.

The energy balances on the primary heat exchanger and condenser are:

$$Q_{PHE} = \dot{m}(h_4 - h_3) \quad (16)$$

$$Q_{cond} = \dot{m}(h_6 - h_1) \quad (17)$$

All the energy balances are iteratively solved considering also the pressure drops as assumed in Table 6 of the article.

**Nomenclature**

| | |
|---|---|
| Acronyms | |
| EoS | Equation of state |
| PR | Peng Robinson EoS |
| Symbols | |
| $\Delta\pi_{residual}$ | Residual property π |
| h | Enthalpy, kJ/kg |
| ṁ | Mass flow rate, kg $s^{-1}$ |
| M | Molar mass, kg $kmol^{-1}$ |
| Q | Thermal duty, MW |
| ϱ | Density, kg $m^{-3}$ |
| s | Entropy, kJ $kg^{-1}$ $K^{-1}$ |
| T | Temperature |
| V | Molar Volume |
| W | Mechanical power, MW |
| Z | Compressibility factor, - |
| Greek symbols | |
| $\eta_{th}$ | Cycle thermal efficiency, - |

| | |
|---|---|
| $\eta_{Turbine}$ | Turbine isentropic efficiency, - |
| $\eta_{Pump,is}$ | Pump isentropic efficiency, - |
| $\omega$ | Pitzer acentric factor, - |

Subscripts

| | |
|---|---|
| a | Attractive |
| c | Critical |
| f | Friction term |
| o | Zero-density |
| r | Repulsive |

Superscripts

| | |
|---|---|
| r | Residual |

### 2.8.4 Bibliography of Supplementary Materials


[1] T.H. Chung, L.L. Lee, K.E. Starting, Applications of Kinetic Gas Theories and Multiparameter Correlation for Prediction of Dilute Gas Viscosity and Thermal Conductivity, Ind. Eng. Chem. Fundam. 23 (1984) 8–13. https://doi.org/10.1021/i100013a002.

[2] S.E. Quiñones-Cisneros, C.K. Zéberg-Mikkelsen, E.H. Stenby, One parameter friction theory models for viscosity, Fluid Phase Equilib. 178 (2001) 1–16. https://doi.org/10.1016/S0378-3812(00)00474-X.

[3] S.E. Quiñones-Cisneros, S. Pollak, K.A.G. Schmidt, Friction Theory Model for Thermal Conductivity, J. Chem. Eng. Data. 66 (2021) 4215–4227. https://doi.org/10.1021/acs.jced.1c00400.

[4] D.Y. Peng, D.B. Robinson, A New Two-Constant Equation of State, Ind. Eng. Chem. Fundam. 15 (1976) 59–64. https://doi.org/10.1021/i160057a011.

# *Chapter 3 - Fluorobenzene as novel working fluid*

*THIS CHAPTER IS BASED ON THE ARTICLE: "FLUOROBENZENE AS NEW WORKING FLUID FOR HIGH-TEMPERATURE HEAT PUMPS AND ORGANIC RANKINE CYCLES: ENERGY ANALYSIS AND THERMAL STABILITY TEST", PUBLISHED IN ENERGY CONVERSION AND MANAGEMENT, ELSEVIER, DOI: HTTPS://DOI.ORG/10.1016/J.ENCONMAN.2024.119023*


**Abstract**

Industrial high-temperature heat pumps and Organic Rankine Cycles play a pivotal role in reducing $CO_2$ emissions of the industrial sector. While several eco-friendly refrigerants have been explored for subcritical heat pumps below 150°C, above this threshold only a few fluids can be adopted.

In this article, fluorobenzene ($C_6H_5F$) is proposed for the first time as a versatile working fluid suitable for both HTHP and ORC systems. Notably, it possesses a near-zero Global Warming Potential, null Ozone Depletion Potential, low cost, and low toxicity. The thermo-chemical stability of fluorobenzene is experimentally investigated with an advanced procedure, simulating the presence of the non-condensable-gases removal system in real plant operating conditions. The yearly rate of unimolecular decomposition is estimated less than 4% at 350°C, and even after 400 hours of thermal stress no decomposition products have been detected in the liquid phase through Fourier Transform Infrared Spectroscopy.

In a direct heat exchange case study, coupled with exhaust gases at 390°C, fluorobenzene achieves a net power production higher than other commercial fluids adopted in high-temperature units. In subcritical two-stage throttling heat pump condensing at 180°C fluorobenzene shows a good Coefficient of Performance of 3.25 at 100°C temperature lift.


## 3.1 Introduction

In recent years, industrial high-temperature heat pumps (HTHP) have gained significant attention for their role in decarbonising the industrial heat demand. According to Naegler et al. [1], in 2012, the final energy demand for heat across all EU28 member states accounts for 2077 PJ below 100°C, 2214 PJ in the 100-400°C range, and 3859 PJ above 400°C. Steam generation constitutes approximately 40% of industrial process heating demand in Europe [2], representing the predominant heat requirement from 100°C up to 500°C. The near future may see conventional steam boilers [3], fuelled by fossil sources, being replaced with high-temperature heat pumps, particularly in industries like pulp and paper and food and beverage, due to their substantial heat demand up to 200°C [4].

Arpagaus et al. [5] provided for a comprehensive overview of high-temperature heat pumps, focusing on the temperature range below 150°C due to current technological limitations. They identified the shortage of refrigerants combining high-temperature capabilities with low Global Warming Potential (GWP) as one of the major obstacle to the wider adoption of the HTHP technology in industrial sectors.

The selection of an appropriate working fluid is a crucial aspect in designing a heat pump system, resulting in a compromise among several factors. In fact, an ideal working fluid should possess thermodynamic and physical adequate characteristics, thermo-chemical stability (no or limited degradation at the operating temperatures), safety (non-flammable, nontoxic, nonexplosive), market availability, environmental characteristics (low GWP and near-zero ODP), and compatibility with materials and lubricants in the compressor (if not oil-free).

Historically, heat pumps have relied on hydrofluorocarbons (HFCs) and, more recently, hydrofluoroolefins (HFOs) as refrigerants. In compliance with EU climate objectives, the F-Gas regulation anticipates the industry's transition to alternative refrigerants characterized by a reduced Global Warming Potential (GWP). HFC-245fa, possessing a zero Ozone Depletion Potential (ODP) and a high critical temperature of 154°C, was adopted in the past as a prevalent substitute for refrigerants like R114, R113, R123, and R500. Despite its widespread use, also in ORC systems, it's essential to acknowledge that HFC-245fa, with a Global Warming Potential ($GWP_{100\text{-}years}$) of 1030, is subject to phase-out requirements stipulated by pertinent regulations. Matheus-Royo et al. [6] assessed HCFO-1224yd(Z), HCFO-1233zd(E), and HFO-1336mzz(Z) as alternatives to HFC-245fa in high-temperature heat pumps, achieving a coefficient of performance (COP) of approximately 3 with a temperature lift (the difference between condensation and evaporation temperatures) of 70°C. They also developed a prototype with a heat sink temperature of 140°C using four low-GWP refrigerants [7]. a prototype that achieves heat sink temperature of 140°C adopting four low-GWP refrigerants. Sulaiman et al. [8] explored various low-GWP refrigerants for subcritical heat pumps with condensing temperatures up to 140°C. Carbon dioxide ($CO_2$) is one among the candidates for future high-temperature heat pumps [9], being operated in transcritical cycle with maximum (sensible) sink temperature around 130°C. Compressed carbon dioxide energy storage system (CCES) [10][11] can be integrated with $CO_2$ heat pumps to improve the round trip efficiency [11]. Liu et al. [12] also explored the use of $CO_2$ mixtures with R134a, R290, R600 and R601 to improve the efficiency of a pumped thermal energy storage by exploiting the temperature glide during the phase transition of the zeotropic mixtures.

HFO-1336mzz(Z) is being considered as an alternative to R-245fa in high-temperature, high-pressure (HTHP) applications. Notably, it's the only high critical temperature fluid (above 170°C) with low global warming and zero ozone depletion potential, making it a practical and sustainable choice for HTHP. The thermal stability limit of HFO-1336mzz(Z) has been investigated by Kontomaris et al. [13], assessing that the fluid is chemically stable up to 250°C, as HFC-245fa, suggesting its application in medium-low temperature ORC systems. Navarro-Esbrí and Mota-Babiloni [14] experimentally demonstrated that the fluid is capable to produce useful heat above 155°C, when coupled with a sensible heat source at 100°C.

In his review work, Arpagaus [5] indicated R1336mzz(Z), R718, R245fa, R1234ze(Z), R600, and R601 as suitable fluids to achieve high heat sink temperatures of up to 160°C. Also, Dai et al. [15] carried out techno-economic analysis considering R1234ze(Z) limiting to sink temperatures up to 120°C. However, above the 150-160°C delivery temperature, it is difficult to find suitable working fluids due to critical temperature, thermal stability , and compressor issues. Despite this, there is large industrial demand even above 160°C that should be covered by the HTHP technology. As an example, the chemicals sector in the U.S has around 62% of the heat demand in the temperature

range from 160 to 200°C [16], which is beyond the operative temperature limits of the mentioned refrigerants. HFOs could be applied in this temperature range in transcritical conditions which do not match well with most of the industrial heat demand being covered by high-quality steam production (isothermal). Moreover, there are some concerns about the thermal stability of some HFOs above 170°C. For instance, HFO-1234yf thermally degrades at 170°C [17], while the pyrolysis temperature of R1234ze(E) starts occurring around 230°C [18].

Few studies have been conducted about subcritical HTHPs delivering heat above 150°C, most of which deals with transcritical refrigerants [19][20] or subcritical zeotropic mixtures [21][22][23], that match well only with sensible sinks. A good overview of the industrial efforts about steam generating heat pumps condensing above such temperature threshold is presented in the work of Klute et al. [24]. The most considered solution to delivered high-temperature steam is to manufacture a cascaded cycle where the bottoming cycle is a closed-loop compression heat pump, and the top cycle is mechanical vapour recompression (MVR) producing high-pressure steam. As an example, a commercial solution [25] considers R1336mzzz(Z), R1224yd(Z), or R1233zd(E) as refrigerant for the bottoming cycle, equipped with centrifugal compressors.

The research of appropriate working fluids is even complicated by the restrictions that many fluids will face in the near future at least in Europe. According to the proposal of October 2022 of the European Council [26], from 1st January 2033 Split systems of a rated capacity of more than 12 kW based on fluorinated greenhouse gases with GWP of 150 or higher will be banned. Newly developed hydrofluoroolefins (HFOs) and hydrochlorofluoroolefins (HCFOs), given the low GWP, emerge as viable options for heat sinks below 160°C. However, it's important to note that anticipated EU restrictions on fluorinated olefins in the near future emphasize the pivotal significance of carefully choosing the working fluid.

In fact, in January 2023, the national authorities of the Netherlands, Germany, Sweden, Denmark and Norway submitted their Restriction Proposal to the European Chemicals Agency (ECHA). The proposal aims to restrict manufacturing, the placing on the market (including import) and the use of polyfluoroalkyl substances (PFAS) in Europe. The list covers over 10,000 substances, including Fluorinated gases (F-gases) and fluoropolymers that are used for heat pump equipment. As an example, 3M company will exit all PFAS manufacturing by the end of 2025. Structures subjectively considered to be PFAS were composed of either 30% or 40% fluorine, based on the fraction of the molecular formula excluding hydrogen atoms [27].

In this context, there is need to look for alternative working fluids that do not face F-Gas or PFAS restrictions. Especially in the temperature range above 160°C, a research gap about suitable refrigerants exists. Abedini et al. [28] underlined how suitable refrigerants for high temperature (up to 200°C) are not yet available, and for this reason they proposed binary mixtures as working fluid. However, mixtures deliver sensible heat, which is a niche market in the industry where heat is mostly required at constant temperature. The 160°C barrier is overcome by Turboden company, showcasing the possibility to deliver heat up to around 200°C, by adopting HCs as working fluids: cyclopentane, n-pentane, and isopentane are adopted in the 160-200°C temperature range due to high critical temperature. The necessity to shift from simple molecules (such as conventional refrigerants) to complex fluids (as highly-branched HCs), commonly used in ORC systems, in the context of HTHP approaching 200°C, was well anticipated by Angelino and Invernizzi [29] in 1987.

In this context, pure fluorobenzene ($C_6H_5F$) is proposed for the first time in this article as potential working fluid to be applied both in closed-loop HTHPs and ORC systems. With one single fluorine atom in the molecule, fluorobenzene is not classifiable as PFAS substance, according to the abovementioned classification. Moreover, it possesses near-zero GWP ($GWP_{100\text{-}years}$<<1), as reported by Burkholder et al. [30], and zero ODP, making it an environmental-friendly working fluid. Additionally, the exceptionally-high critical temperature (286°C) suits well the HTHP application, making it suitable to cover even the temperature range above 160°C where new-generation low-GWP refrigerants cannot cover in subcritical configuration. Unlike its hydrocarbon counterpart benzene, fluorobenzene has much lower toxicity. When compared to hexafluorobenzene ($C_6F_6$), instead, fluorobenzene is much cheaper (about 1/10th the cost of $C_6F_6$ for a quotation of around 1 kg quantity). The main thermophysical properties of fluorobenzene are presented in Table 1, such as molecular weight (MW), normal boiling point (NBP), but also density ($\varrho$), dynamic viscosity ($\eta$), thermal conductivity ($\lambda$), latent heat of vaporization ($\Delta h_{eva}$), surface tension ($\pi$), liquid heat capacity ($Cp_L$) experimentally available in literature at near ambient conditions (20°C).

*Table 1. Main thermophysical properties of fluorobenzene.*

| **Property** | MW | $\varrho$ (20°C) | NBP | $\lambda$ (20°C) | $\eta$ | $\Delta h_{eva}$ (20°C) | $\pi$ (20°C) | $Cp_L$ (20°C) |
|---|---|---|---|---|---|---|---|---|
| **Units** | kg mol$^{-1}$ | kg m$^3$ | °C | W m$^{-1}$ K$^{-1}$ | μPa s | MJ kmol$^{-1}$ | N m$^{-1}$ | MJ kmol$^{-1}$ K$^{-1}$ |
| **Value** | 0.961 | 1022.5 [31] | 84.7 [32] | 0.137 [33] | 585 [NIST Database] | 345.2 [34] | 0.0227 [35] | 0.146 [36] |

To confirm its potential application as working fluid, it is of fundamental importance to assess the thermo-chemical stability. In this paper, the consolidated static survey method adopted in the past for several ORC working fluids [37] and refrigerants [38] have been adopted. This method is particularly relevant since decomposition phenomena are detected from divergence of vapour pressure of the thermally stressed fluids in comparison with the fresh fluid, so it provides also useful indications about the fluid behaviour during system operation. The increase of vapour pressure due to the formation of decomposition products, constituted in prevalence of non-condensable-gases (NCG), reduces the available enthalpy drop across the turbine of an ORC reducing the overall performance [39]. A NCG removal system is commonly employed in ORC systems when dealing with sub-atmospheric condensation pressure at design conditions [40], i.e. with fluids characterized by high normal boiling point as it is fluorobenzene (86°C). The working fluid in the hot-well, affected by the presence of NCGs, is extracted though a vacuum pump and in the NCG removal system a gas treatment unit facilitates the recovery of a portion of the working fluid, which is then reintroduced into the power block [41].

In this article, compared to previous literature works, the thermal stability of the working fluid has been evaluated also simulating the presence of the NCG removal system in real ORC operations. The thermally stressed fluid is aspirated for a short time to remove the vapour phase in the test cylinder, and the vapour pressure of the fluid is evaluated and compared to the fresh fluid

behaviour. This test is finalized to prove that decomposition products are only in the vapour-phase and the fluid recirculated from the NCGs removal system into the power block maintains its physical and chemical properties unchanged. Additionally, this is also confirmed by a chemical analysis with Fourier-transform infrared spectroscopy (FTIR) on the liquid phase, after undergoing prolonged thermal test.

As the experimental campaign evidences a good thermo-chemical stability of fluorobenzene, degrading below 4% annually at 350°C, a case study considering its use in an ORC system directly coupled with industrial exhaust gases at 390°C is investigated. The exergy efficiency attainable with the adoption of fluorobenzene in this context is evaluated and compared with the few other organic fluids thermally stable at this temperature level. The specific application of direct heat exchange has been selected, compared to the more conventional indirect heat transfer through thermal oil loop, as fluid overheating (hot spot) and consequent decomposition are more likely to occur, especially during the transient operation of ORC at conditions of high heat flux [42].

The key novelty contributions of the present article can be summarized in:

- Pure fluorobenzene is presented for the first time as working fluid for HTHP and ORC systems.
- The thermal stability of fluorobenzene is experimentally investigated with a consolidated procedure.
- An advanced methodology has been developed to assess the thermal stability of the fluid simulating the presence of a NCG removal system in real ORC operation.
- A chemical analysis with FTIR methodology is performed on the thermally stressed fluorobenzene confirming no traces of degradation products in liquid phase.
- The annual degradation rate at 350°C of fluorobenzene is measured and compared to other high-temperature working fluids.
- The performance of fluorobenzene in subcritical HTHP delivering heat at 180°C (a thermal level poorly explored in the literature) is studied in different cycle architectures, providing useful insights about different working fluids.
- The efficiency gain deriving from the application of fluorobenzene in ORC in direct heat exchange with flue gases at 390°C, in comparison to other fluids commercially adopted in high-temperature ORC units.

## 3.2 Experimental investigation

### 3.2.1 Thermal stability test: setup and procedure

In this work, the consolidated static isochoric method developed by Invernizzi et al. [43] to evaluate the thermo-chemical stability of working fluids for Organic Rankine Cycles (ORC) has been adopted with the addition of a novel approach consisting of simulating the effects of NCG removal system as present in many commercial ORC systems.

The static survey method has been adopted in the Fluid Test Laboratory [44] with several working fluids in the past such as hydrocarbons [37][45], zero-ODP refrigerants [38], fluorinated alchols [46], perfluorocarbons [47], and $CO_2$ mixtures with perfluorocarbons [48]. It is based on the concept that even a small breakdown of the fluid can cause an appreciable rise in vapor pressure due to presence of decomposition products. In fact, due to prolonged exposure to thermal stress at a temperature

surpassing the activation energy barrier, the molecules undergo fragmentation into smaller, more volatile compounds. The identification of degradation phenomena is achieved through a comparative analysis of vapor pressure variations post thermal stress against the baseline of the fresh fluid (reference vapour pressure curve).

The experimental setup and procedure is well presented in the work of Pasetti et al. [37]. The specific setup used in this work is presented in Figure 1. The main component of the system is the sample cylinder ("A" in Figure 1), manufactured in AISI 316L, a material commonly employed in power plant components, whose internal volume is 150 $cm^3$. The tubes and valves illustrated are made of the same material. Consistent material choice for all components in the high-temperature sections is crucial, as it can potentially catalyse the decomposition reaction of the fluid.

Two pressure transducers are mounted in the systems to have high accuracy in the entire pressure measurement range. It is particularly important to have accuracy as much as possible in the pressure range where the reference vapour pressure is measured, and for this reason it is measured through a Klay 2000-SAN pressure transmitter ("PT1" in Figure 1) with adjustable span from 1 to 10 bar and accuracy of 0.1% of adjusted span. When the cylinder is placed in the muffle furnace for the 100-hour thermal stress, the valve "V2" in Figure 1 is closed to protect the low-pressure transmitter from overpressure. In that case, the pressure is recorded by using the high-pressure transmitter ("PT2" in Figure 1), a Klay 2000-SAN with adjustable span from 20 to 100 bar. A Tersid thermocouple (tolerance class I) is inserted into the cylinder through its welded housing ("B" in Figure 1). The main instruments, with related accuracy, are listed in Table 2.

The cylinder is loaded with 30 g of liquid fluorobenzene: the fluid is supplied by Merck [49] with a declared purity level above 99%.

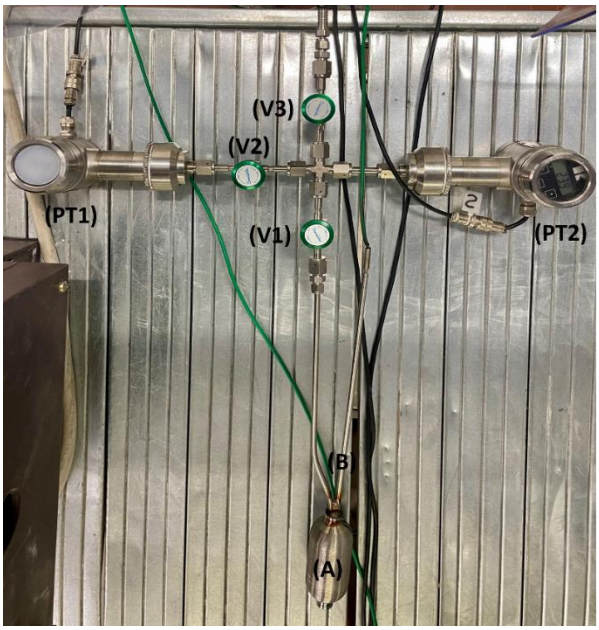


*Figure 1. Main components of the thermal stability test: the AISI 316L cylinder (A), the housing of the temperature probe (B), the low-pressure scale pressure transducer (PT1), the high-pressure scale pressure transducer (PT2), the main valve that closes the*

*cylinder from the rest of the circuit (V1), the valve which protects the PT1 from overpressure (V2), the valve that connects the circuit to the environment (vacuum pump/charging/venting).*

*Table 2. Instruments for thermal stability testing and related accuracy.*

| Type | Manufacturer | Model | Measurement range | Accuracy |
|---|---|---|---|---|
| Pressure transmitter 1 | Keller | Klay 2000-SAN | 0..10 bar* | 0.1 % of full-scale |
| Pressure transmitter 2 | Keller | Klay 2000-SAN | 0..100 bar* | 0.1 % of full-scale |
| Thermocouple | Tersid | Type K | -200-1270 °C | Tolerance class I |

**Adjustable span (1-10 bar for transmitter 1, 20-100 bar for transmitter 2)*

The static isochoric thermal stability test involves the following steps: (i) utilizing a vacuum pump to eliminate air and impurities; (ii) introducing a fresh fluid sample of arbitrary mass (but sufficient to have vapour-liquid equilibrium conditions) into the closed cylinder; (iii) placing the cylinder in a thermostatic bath to measure vapor pressure at various temperatures (establishing a reference curve); (iv) placing the cylinder horizontally in a muffle furnace to carry out a 100-hour constant-temperature stress test; (v) post thermal stress, re-evaluating vapor pressure within the same temperature range, as the reference curve, in the thermostatic bath; (vi) subjecting the fluid to a new thermal stress at a higher constant temperature; (vii) iterating the procedure until reaching the maximum test temperature.

There are various reasons to conclude the test at a certain temperature: i) after thermal stress at that temperature, the fluid decomposition appears significant (with high vapor pressure deviations); ii) there is practical interest in testing up to that temperature from an application perspective.

In this work, the decision to conclude the stability test was made upon reaching a thermal stress temperature of 350°C for the following reasons: i) it represents a thermal threshold at which the vast majority of organic fluids decompose at a high rate and are, for this reason, impractical for use, with a few exceptions such as cyclopentane and toluene [37]; ii) it is a thermal level compatible with multiple applications (high-temperature waste heat, concentrated solar power CSP, biomass); iii) the objective is not to subject the fluid to complete degradation but rather to assess its real applicability at 350°C by conducting further test as detailed in the following section.

### 3.2.2 Broadening the scope of the experimental investigation

In comparison to prior thermal stability investigations conducted in the Fluid Test Laboratory, the conventional methodology is here embedded within a broader framework, represented in Figure 2.

The 1st stage of the experimental campaign consists of the conventional thermal stability test, detailed in previous section, up to the defined limit of 350°C. In the 2nd stage, the fluid decomposition at the set temperature limit (350°C) is monitored over time with consecutive 100-hours thermal stress up to 300 hours. Concurrently, both at the beginning and at the end of this 2nd stage, verification is carried out to ensure that, following a brief aspiration (a few seconds with vacuum pump) of the

fluid into the cylinder after the 350°C thermal stress, its volumetric behaviour reverts to that of the fresh fluid. This procedure aims to identify any significant breakdown products in the liquid phase, ensuring confidence that any decomposition products formed in the high-temperature sections of the power block, subsequent to the removal of non-condensable gases, are completely eliminated. Consequently, upon reintroducing the recycled fluid from the NCG removal system, it retains its original thermophysical characteristics. This implies that the fluid at the pump does not appear affected by operating at 350°C as the turbine inlet temperature.

After this second stage, as in Figure 2, A chemical analysis on the thermally-stressed liquid after the "stage 2" was carried out to confirm the absence of decomposition products in the liquid phase. A Fourier-transform infrared spectroscopy (FTIR), using an Attenuated Reflection Setup (ATR, Everest Diamond-Thermo Nicolet) with a spectral resolution of 4 $cm^{-1}$, is used: the FTIR measurements were carried out by dropping 5 μL of liquid on a diamond ATR crystal. After the subtraction of the environmental background, the final spectrum was extracted as the average of 64 scans.

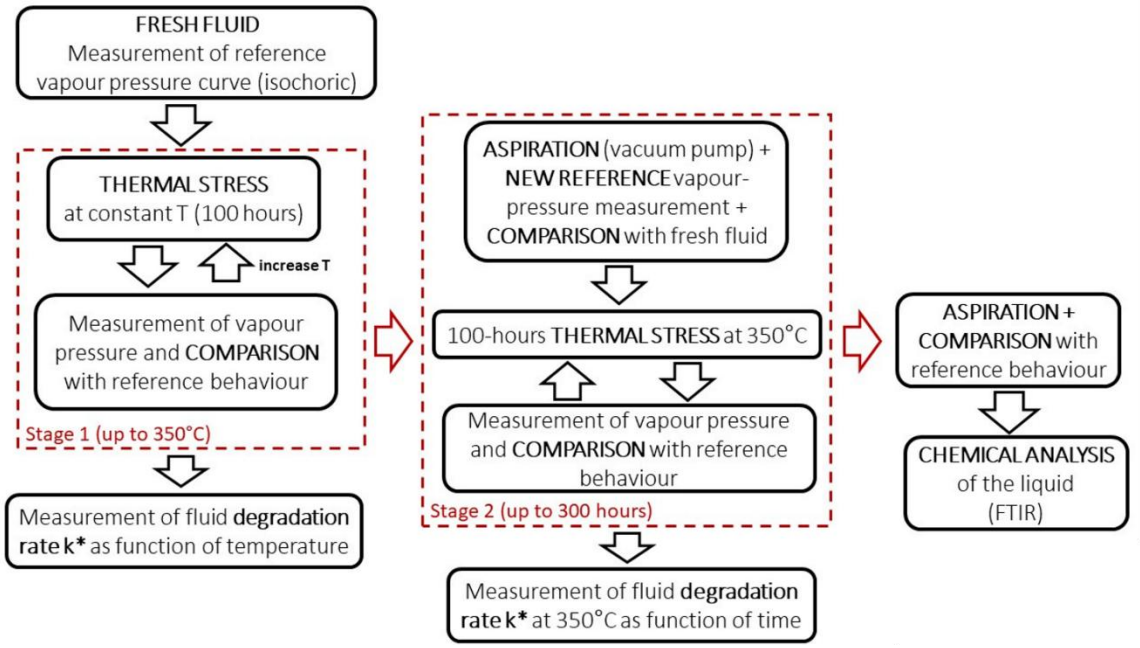


*Figure 2. Methodology adopted for the experimental investigation on fluorobenzene, comprising: i) at first stage, the consolidated static survey method for thermal stability testing up to 350°C; ii) at second stage, the evaluation of degradation phenomena at 350°C at 100-hours' time step up to 300 hours, with vapour aspiration to evaluate the presence of decomposition products in liquid phase; iii) the final evaluation of the thermally stressed liquid fluorobenzene with FTIR analysis after aspiration and check with reference curve.*

Despite qualitative indications about the thermal degradation of the fluid occurring in the 1st and 2nd stages are evident from Figures 3 and 4, a semi-quantitative index, the so-called quasi-constant rate of decomposition k* of the fluid, following the same methodology as explained in the work of Invernizzi et al. [45]. In the mentioned work, the authors measured the decomposition rate of n-pentane, cyclopentane and toluene after eighty hours thermal stress at varying temperatures. The same conceptual methodology is used in this work to calculate the decomposition rate $k^*$ of fluorobenzene, and to compare it with other fluids.

As stated in [45], the unimolecular decomposition typically manifests as an increase ($\Delta P_v$) in the vapor pressure of the sample fluid, especially appreciable under sub-atmospheric conditions. This article introduces two methodological differences, compared to [45], for determining the decomposition rate k*: (i) the rate k* following thermal stress at a specific temperature is calculated based on the $\Delta P_v$ at that temperature in relation to the preceding thermal stress (usually performed at a lower temperature), rather than comparing it to the vapor pressure of the reference fresh fluid. The adjustment is incorporated in this study to attribute the formation of decomposition products exclusively to the latest thermal stress (latest temperature), excluding the influence of previous thermal stresses carried out at different temperatures/conditions. This new approach is graphically addressed in Appendix, where the main equations for the calculation of k* are also presented.

As outcomes of the 1st stage of thermal stability testing, it is possible to evaluate the rate of decomposition of Fluorobenzene $k^*$ as function of temperature up to 350°C.

Slater's theory [29] suggests that a gas of polyatomic molecules acts as vibrating systems, dissociating when one internal coordinate exceeds a critical value tied to dissociation energy. The energy required for this dissociation, mainly driven by temperature, depends on the molecules' kinetic energy and collision force. Hence, the degradation rate (k*) of the working fluid is primarily influenced by the maximum temperature, however in this article the effect of the time on the kinetic of reaction has been investigated. In fact, the 2nd stage provides insights into the temporal evolution of the degradation rate k* specifically at 350°C.

### 3.3 Experimental results

The investigation focuses on measuring the reference vapor pressure below the normal boiling point of fluorobenzene (84.7°C) where the effect of non-condensable products are more noticeable at vapor pressures below atmospheric pressure. Specifically, the temperature range from 10°C to 80°C has been considered, with steps of 10°C (Figure 3).

The measured vapor pressure curve of the fresh fluorobenzene, assumed as reference in the experimental analysis, and the fluid behaviour after thermal stress test are shown in Figure 3. In the 1st stage, the sample fluid experienced four consecutive stress tests at temperature from 250 °C to 350°C. At the end of each 100-hours stress test, the saturation pressure curve was measured, and compared with that of the virgin fluid in order to detect possible signs of decompositions.

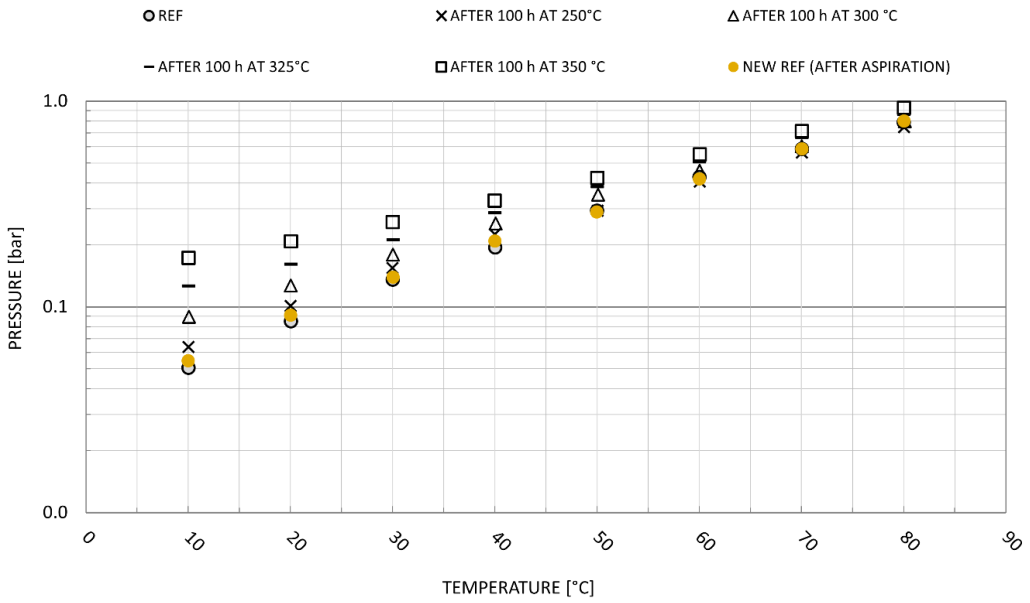


*Figure 3. Results of the 1st stage of thermal stability test on fluorobenzene, with the measured reference vapour pressure ("REF") and the vapour pressures measured subsequent 100-hours thermal stress at different temperatures (log scale); after the last 100 hours at 350°C, vacuum pump aspiration was performed and a new reference line ("NEW REF"), consistent with the previous one, was measured.*

For clarity purposes, uncertainties are not depicted on the graph because they would overlap with the data points, hindering a proper understanding of deviations of vapor pressure after different thermal stresses. There are two contributions of uncertainty related to each point in Figures 3-4: the instrumental uncertainty and the standard deviations. As the pressure transmitter is set at 1 bar full scale, its resulting accuracy is 1 mbar. Each set of (P, T) values is calculated as the arithmetic mean of the data recorded over a 15-minute period at steady-state conditions, encompassing approximately 180 acquisition samples. The resulting standard deviation $\sigma_P$ is within the instrumental uncertainty as the maximum standard deviation computed in 0.9 mbar. As the pressure transmitter is set at 1 bar full scale, its resulting accuracy is 1 mbar. The total uncertainty on the pressure values in Figure 3 and Figure 4 is typically below 2 mbar, then almost negligible, reaching 4 mbar as maximum value. In Appendix A it is possible to find the uncertainty of each measured point.

Fluorobenzene exhibits good thermal stability in the investigated temperature range (250-350°C), as the deviations against the reference vapour pressure curve does not increase exponentially with temperature, unlike many other organic fluids [37][46]. The increase in vapor pressure from one thermal stress to the next is linear, reaching a maximum value of 0.045 bar after thermal stress at 350°C. A semi-quantitative comparison with other fluids for ORCs will be presented in this section based on the quasi-constant rate of decomposition reaction $k^*$. The methodology adopted to calculate the k* parameter is detailed in the Appendix B. An example with toluene, in Appendix B, provides a clear indication of how the results of a thermal stability test translate into the estimate of the fluid degradation rate trend k*. Specifically, the example demonstrates that from the thermal stability results, it is evident when the fluid is undergoing significant degradation when vapour pressure deviations between successive stresses increases exponentially.

During the second stage of the experimental campaign, following the last 100-hours thermal stress conducted at 350°C during the first stage, a brief aspiration of the fluid using the vacuum pump (few seconds) is performed to simulate the NCG removal system typically present in an ORC system. Subsequently, the vapor pressure of the fluid is measured to establish a new reference curve ("NEW REF" in Figure 4) : the resulting trend, equal to the reference of the fresh sample, suggests that all thermal decomposition products are light and incondensable substances at the investigated temperature. On the other way around, substances dissolved in the liquid phase of the fluorobenzene would contribute to a change in the vapour pressure compared to the pure fresh fluid sample. The second stage aims at investigating the progression of degradation over time (up to 300 hours) with three additional 100-hours thermal stresses at the threshold value of 350°C.

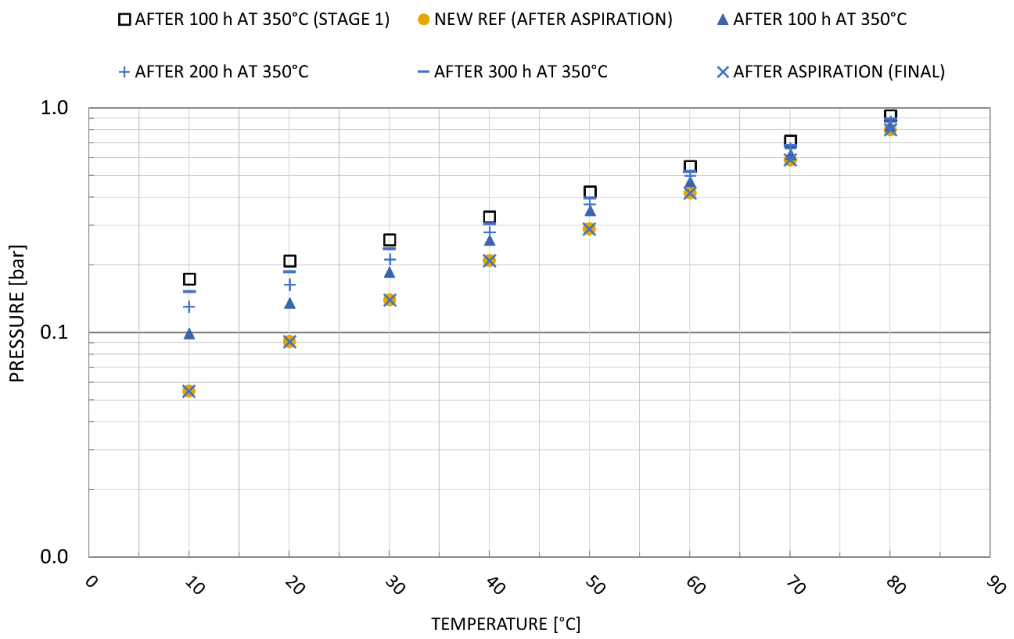


*Figure 4. Result of the 2nd stage of thermal stability test on fluorobenzene performed at 350°C for several hours (following stage 1 previously described); before starting the 2nd stage, aspiration with vacuum pump is performed and a new reference line is established ("NEW REF"). After 300 hours at 350°C the pressure of the system results to be lower than the values measured before aspiration after 100-hours stress at the same temperature (squares); in the end of the test, the final aspiration with vacuum pump determined the fluid sample to return to the reference behaviour of the fresh fluid.*

The 2nd stage of the thermal stability test confirms the low degradation rate of fluorobenzene at 350°C, reasonably supporting its suitability for use in closed power cycles operating at this thermal level. Indeed, after 300 cumulative hours of thermal stress at 350°C, the deviations from the reference curve are lower compared to the deviations measured at the end of the first stage at the same temperature, confirming the low rate of thermal decomposition reaction. Finally, the effect of the NCG removal system was simulated again by briefly aspirating with the vacuum pump and remeasuring the vapor pressure. The outcome of this procedure indicates that the fluid has returned to the volumetric behaviour of the fresh fluorobenzene, further confirming that thermal stress does not influence the liquid reintroduced into circulation after NCG removal system.

Eventually, to definitely prove this result, a FTIR analysis of the liquid phase at the end of the entire thermal stability test was conducted by ATR. As shown in Figure 5, the comparison between the FTIR spectra of fluorobenzene before (in blue) and after thermal stress (in red) does not reveal any significant difference: the two spectra are separated for clarity purposes shifting the red spectrum upwards (+0.4 absorbance units).

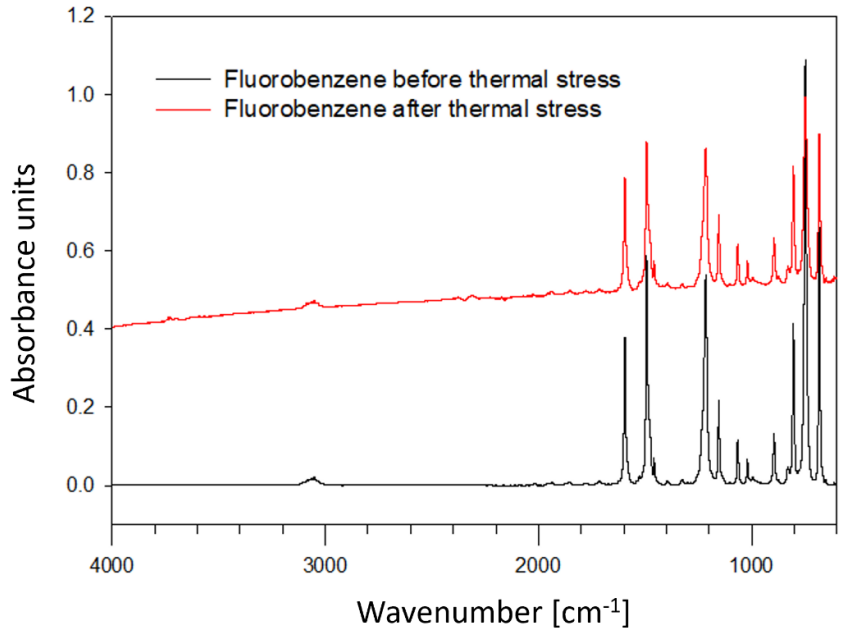


*Figure 5. ATR-FTIR spectra of fluorobenzene before (blue, reference from Aldrich Library: Fluorobenzene >99% ) and after (red) thermal stress; the two spectra are shifted upwards for clarity purposes.*

Eventually, Figure 6 show the rate of decomposition reaction $k^*$ as function of temperature and time (at 350°C), as outcomes of the 1st and 2nd stages of thermal stability testing. The semi-quantitative analysis provides indications on the velocity and the extent of the fluid degradation, but it is more useful to compare and classify the behaviour of different thermal-stressed working fluids.

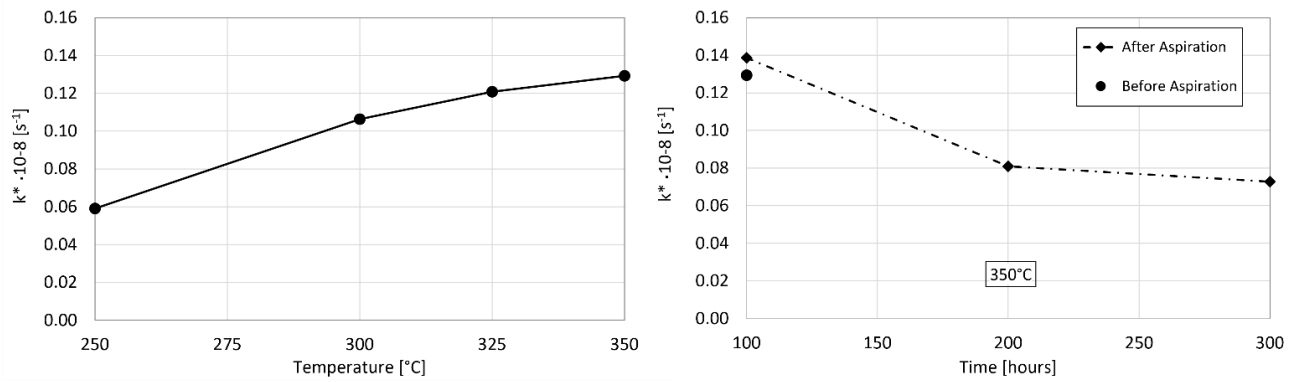


*Figure 6. Fluorobenzene degradation rate k* as function of temperature (left) from the 1st stage, and time (right) from the 2nd stage at 350°C thermal stress.*

At the end of the last thermal stress (350°C) of 1st stage of the campaign, the quasi-constant rate of decomposition is $0.13 \times 10^{-8}$ [$s^{-1}$] as evident from Figure 6, meaning 4% annual degradation of fluorobenzene at this temperature. Following aspiration and re-start with the 2nd stage (right side of Figure 6), the k* approaches $0.14 \times 10^{-8}$ [$s^{-1}$] after the first 100-hours at 350°C, that is a value coherent with that obtained at the same temperature during the 1st stage. The value is slightly higher, after 100 hours of the 2nd stage, because aspiration is performed at the end of the 1st stage: all the degradation products are removed from the system, and the reaction is then promoted as a consequence. For the same reason, in Figure 6 (on the right) the rate of decomposition appears to decrease with time at constant temperature (350°C): the accumulation of degradation products inhibits the unimolecular reaction (Le Châtelier's principle). For this reason, after prolonged thermal stress (300 hours) of fluorobenzene at 350°C, the decomposition rate stabilises at an asymptotic value of $0.0728 \times 10^{-8}$ $s^{-1}$.

It's noteworthy that the calculation of the k* parameter assumes that 1 mole of decomposition products is generated from 1 mole of fluid, as discussed in Pasetti et al. [37]. This assumption is conservative, as the breaking of molecular bonds more readily leads to the generation of multiple moles of products from a single mole of fluid. This implies that the reported results on the k* rate are likely overestimated and should be scaled according to the actual reaction stoichiometry. The comparison of fluorobenzene with other working fluids, investigated in the same laboratory under the same assumptions, is presented in Figure 7: these rates were determined using the same methodology outlined in the previous section and in Appendix B.

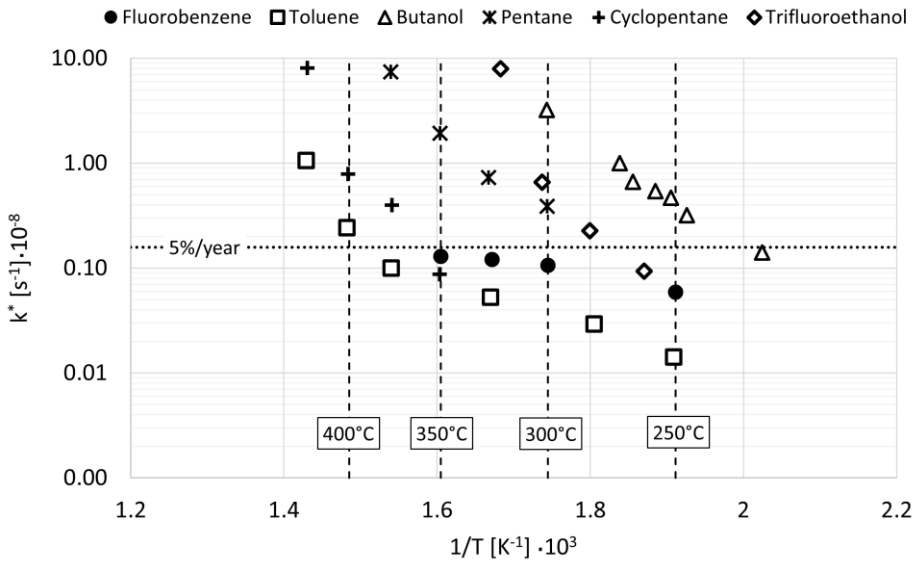


*Figure 7. Rate of unimolecular decomposition reaction of fluorobenzene at different temperatures in comparison with other fluids precedingly tested in our Fluid Test Laboratory with the same isochoric method [37].*

According to Figure 7, fluorobenzene (as well as toluene and cyclopentane) degrades by less than 5% per year at 350°C. Moreover, no exponential trend of k* (discussed in Appendix B) is noticeable from the results of fluorobenzene in the investigated temperature range. Further test, at higher temperature, could identify the temperature above which exponential trend of k* is noticeable. This

result is encouraging for the application of fluorobenzene in high-temperature ORC units, where the working fluid could be coupled with medium-high temperature sources in direct heat exchange.

## 3.4 Fluorobenzene as working fluid in ORC in direct heat exchange

Given the good thermal stability of fluorobenzene, demonstrated in the previous section, it is compared in this section with state-of-the-art fluids used in commercial high-temperature ORC units. Typically, high-temperature ORC units are fed by a thermal oil heat transfer loop, operating at maximum temperature of 300/310°C preventing thermal degradation of both the thermal oil itself and the organic fluid. This standard practice is common across various applications such as waste heat recovery (WHR) from electric arc furnaces [50], biomass boiler [51][52], CSP, as attested by ORC manufacturers [53][54].

However, in recent years, there has been growing interest in direct coupling with the heat source to enhance overall plant efficiency, as the indirect heat coupling limits the potential to cool down the heat source. Moreover, the direct heat transfer solution requires fewer components, reducing system complexity and capital cost. An example of direct heat exchange is Turboden's 0.7 $MW_{el}$ ORC unit, which recovers heat from 400°C exhaust gases from light fuel oil combustion at a steel rolling mill [55]. Another notable case is the 2 $MW_{el}$ ORC unit installed by Turboden in 2018 at Cementi Rossi (Piacenza, Italy) [56], where direct heat exchange was employed in a cement plant.

In direct heat coupling, even if the working fluid can be operated at turbine inlet temperature considerably lower than the heat source temperature, thermal cracking of the fluid is more likely to occur compared to the thermal oil case. This is primarily due to higher wall temperatures compared to conventional organic fluid-thermal oil heat exchanger, especially at high vapour quality conditions (low heat transfer coefficient). This condition may lead to potential hot spots and fluid degradation, especially within the thermal boundary layer. Therefore, when dealing with heat sources approaching 400°C, it is preferrable to adopt working fluids with low degradation rates up at 300-350°C. As a matter of facts, this requirement is met only by few working fluids, such as toluene, cyclopentane, siloxanes, and fluorobenzene. The mentioned fluids are reported in Table 3 along with their key characteristics, thermal stability threshold, and NFPA ratings.

In this section, a typical flue gas from a cement plant is considered as the heat source for evaluating the performance of fluorobenzene as an ORC working fluid. The key characteristics of this flue gas are delineated in Table 4. A flue gas with these characteristics is typical of a cement plant with 2100 tons of clinker per day [64]. Heat recovery from the flue gas is technically possible up to a minimum flue gas temperature of 100°C, according to the European Cement Research Academy (ECRA) [65]. The need for a minimum thermal draft in the stack and the risk of corrosion from condensation in filters and stacks restrict the recovery potential, allowing exploitation of exhaust gases only above a temperature threshold of 100°C. The considerations about the source can be generalized for many other exhaust gases deriving from other industrial applications, such as glass industry o stell mills. The results are, therefore, of general interest.

*Table 3. Thermal stability threshold of organic fluids for high-temperature ORC and main characteristics.*

| **Fluid** | **Formula** | **$T_{stability}$ [°C]** | **Reference** | **$T_{cr}$ [°C]** | **$P_{cr}$ [bar]** | **NBP [°C]** | **GWP** | **ODP** | **NFPA Health** | **NFPA Flammability** | **NFPA Reactivity** |
|---|---|---|---|---|---|---|---|---|---|---|---|
| Toluene | $C_7H_8$ | 400 | [45][57][58][59] | 320 | 41.1 | 110.6 | 3 | 0 | 2 | 3 | 2 |
| Cyclopentane | $C_5H_{10}$ | 350 | [37][60] | 238.6 | 44.4 | 49.3 | 5 | 0 | 1 | 3 | 1 |
| MM | $C_6H_{18}OSi_2$ | 300-320 | [61][62] | 246.7 | 19.4 | 100.5 | n.a. | 0 | 2 | 4 | 2 |
| **Fluorobenzene** | **$C_6H_5F$** | **350*** | **This work** | **287** | **45.5** | **84.7** | **<<1**[30] | **0** | **1** [63] | **3** | **0** |

**The investigation in this work extends up to 350°C, revealing low degradation rate.*

*Table 4. Heat source considered in this work.*

| **Parameters** | **Value** |
|---|---|
| Temperature [°C] | 390 |
| Pressure [bar] | 1.0132 |
| Volumetric Flow [$m^3/h$] | 359,000 |
| Minimum temperature [°C] | 100 |
| Available Exergy [MW] | 8.46 |
| Unavoidable Stack Loss [MW] | 0.78 |
| **Composition [% mol]** | |
| $N_2$ | 67.9 |
| $O_2$ | 6.0 |
| $CO_2$ | 18.67 |
| $H_2O$ | 7.33 |
| $NO_2$ | 0.03 |
| $SO_2$ | 0.01 |
| CO | 0.06 |

A recuperated layout of the ORC is considered, according to Figure 8. The recuperator is important not only to internally recover the heat available at the turbine outlet (increasing the cycle efficiency), but also to increase the temperature of the working fluid at the evaporator – or primary heat exchanger (PHE) - entrance (state "3"): this avoids the cooling of the flue gases below the minimum temperature limitation, in direct heat transfer. The power cycle architecture and a T-s diagram representative of the coupling with the heat source and sink is proposed in Figure 8. The assumptions adopted to calculate the power cycle conditions are reported in Table 5.

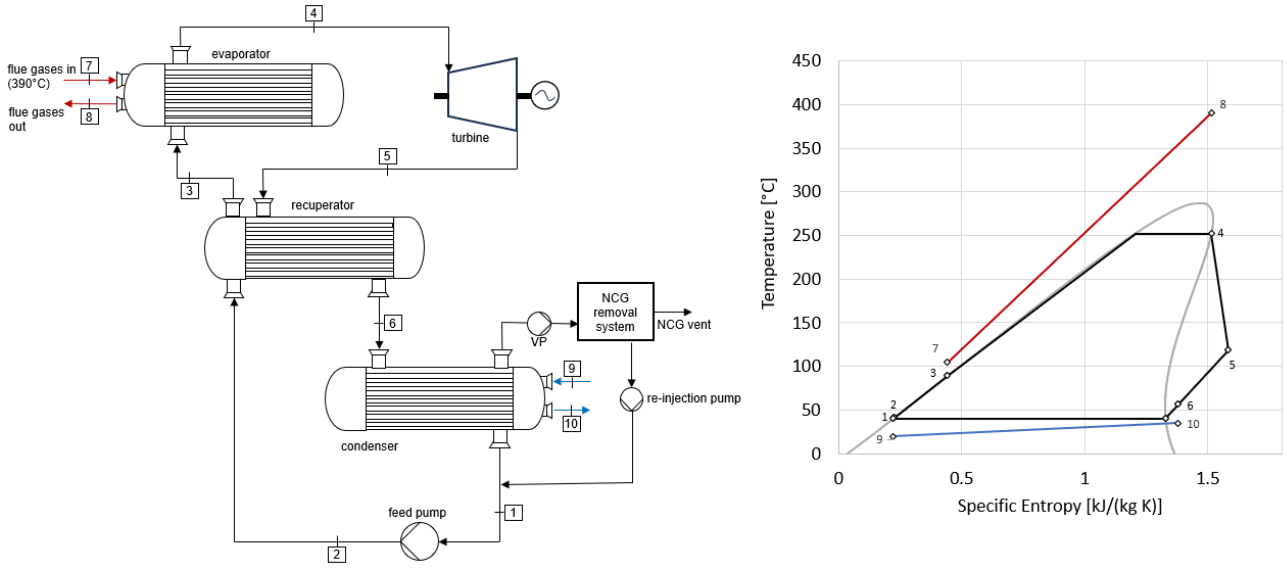


*Figure 8. ORC recuperated cycle layout (left) with direct heat exchange with the flue gases at 390°C and NCG removal system; T-s diagram of the saturated fluorobenzene cycle at 30 bar evaporation pressure (right).*

*Table 5. ORC modelling assumptions.*

| **Parameters** | **Values** |
|---|---|
| Minimum Temperature | 40 °C |
| Evaporation Pressure[a] | ≤ 0.9 $P_{cr}$ |
| Degree of Superheating | 0-50 °C |
| $\Delta T_{min}$ Recuperator | 15 °C |
| $\Delta T_{min}$ PHE | 15 °C |
| Pressure Drop Recuperator (Hot/Cold side) | 1 % |
| Pressure Drop PHE and Condenser | 2 % |
| Cooling Water In/Out Temperature | 20/35°C |
| Turbine Isentropic Efficiency ($\eta_{is,T}$) | calculated[b] |
| Pump Isentropic Efficiency ($\eta_{is,P}$) | 70% |

*[a]optimized; [b] from 3-stages axial turbine correlation [66] in each design condition*

The isentropic efficiency of the turbine is calculated in each operating condition with the correlation developed by Macchi and Astolfi [66] for three-stages axial turbines as function of a size parameter (SP) and the volumetric ratio ($V_r$). Only subcritical conditions ($P_{eva}$ < 0.9 $P_{cr}$) are considered as more attaining to commercial ORC units. Both saturated and superheated cycles (with a maximum of 50°C superheating) have been analysed. Energy and exergy balances are solved in Aspen Plus V12 software using the Peng Robinson EoS in its original form [67]. The main key performance indicators used are the net mechanical power output ($W_{net}$), the thermal efficiency ($\eta_{th}$), and the exergy efficiency ($\eta_{ex}$), defined as:

$$\dot{W}_{net} = \dot{W}_T - \dot{W}_P = \dot{m}_{wf}(h_4 - h_{5,is})\eta_{is,T} - \frac{\dot{m}_{wf}(h_{2,is} - h_1)}{\eta_{is,P}} \quad (1)$$

$$\eta_{th} = \frac{\dot{W}_{net}}{\dot{Q}_{PHE}} \quad (2)$$

$$\eta_{ex} = \frac{\dot{W}_{net}}{\dot{E}x_{source}} = \frac{\dot{W}_{net}}{\dot{m}_{hs}\, ex_{in}} \quad (3)$$

where $\dot{E}x_{source}$ represents the ideal power that can be extracted from the heat source when it is cooled down to the dead state temperature, i.e. the ambient temperature $T_0$ (considered 20°C). The exergy is calculated in each state point according to Equation 4:

$$ex_i = (h_i - h_0) - T_0(s_i - s_0) \quad (4)$$

The exergy balance is computed on each component in order to determine the distribution of the exergy destruction due to irreversibility generation, starting from the available exergy from the source (7.68 MW). An unavoidable exergy loss of 0.78 MW is constituted by the impossibility to cool the heat source down to a temperature lower than 100°C due to minimum stack temperature imposition (Table 4).

In Figure 9, the performance an ORC adopting fluorobenzene as working fluid are explored at varying evaporation pressure, considering a direct coupling with the sensible heat source at 390°C.

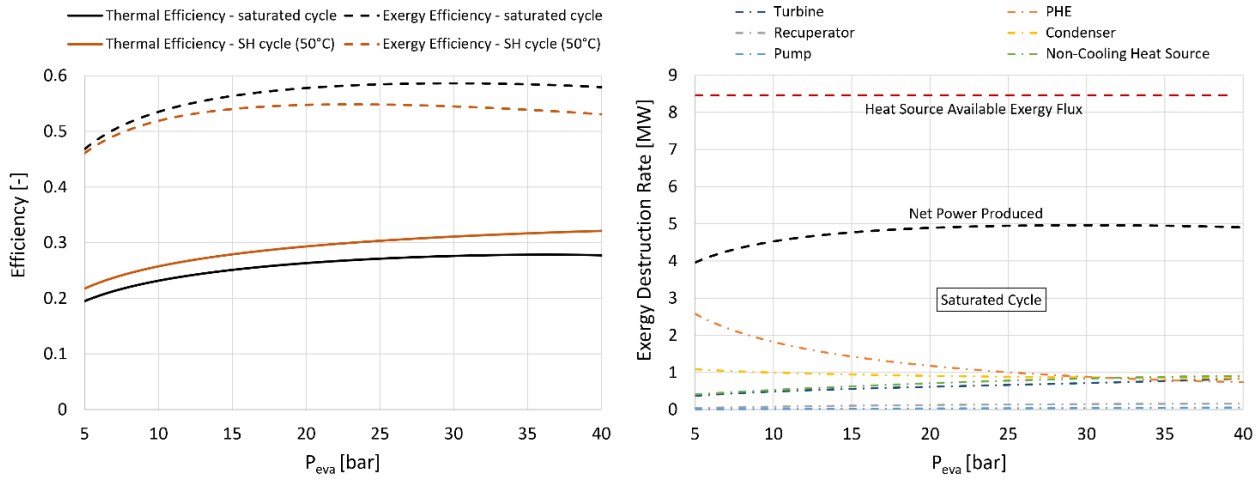


*Figure 9. Fluorobenzene saturated ORC directly coupled with sensible heat source at 390°C: thermal and exergy efficiency of both saturated and superheated cycle (left); heat source availability, net power production, and exergy destruction in power block components of the saturated cycle (right).*

Considering subcritical conditions, superheating is not profitable (Figure 9 – left) as it increases the turbine discharge temperature and, consequently, the temperature of the working fluid at the inlet of the PHE. This decreases the capability to cool the heat source, penalizing the net power

production. Considering a saturated cycle configuration, the exergy loss in the PHE reduces when the evaporation pressure increases (Figure 9 – right) as the temperature profiles of the heat source and the working fluids becomes closer. However, on the other hand, the losses in the turbine increase due to higher volumetric ratio across the turbine, which penalise its isentropic efficiency. Also, the exploitation of the heat source decreases (non-cooling contribution in Figure 9) at increased evaporation pressure. As a result, there is an optimal evaporation pressure around 30 bar for the saturated cycle (253°C evaporation temperature), at which point the net produced power is 4.96 MW, resulting in an exergy efficiency of 58.6%. The T-s diagram in Figure 8 reports the thermodynamic conditions which optimise the exergy efficiency of the cycle, and associated the state points of the fluorobenzene cycle are reported in Table 6.

*Table 6. Thermodynamic conditions of the fluorobenzene cycle at maximum power production conditions (i.e. maximum $\eta_{ex}$); state labels refers to the layout and T-s diagram of Figure 8.*

| State Point | T [°C] | P [bar] | ϱ [kg/m³] | h [kJ/kg] | s [kJ/kg/K] | x[-] |
|---|---|---|---|---|---|---|
| 1 | 40 | 0.207 | 1005.4 | 455.55 | 0.221 | 0 |
| 2 | 41.57 | 30 | 1003.5 | 459.79 | 0.226 | 0 |
| 3 | 89.49 | 29.7 | 942.3 | 533.06 | 0.443 | 0 |
| 4 | 252.29 | 29.11 | 106.4 | 1035.18 | 1.513 | 1 |
| 5 | 118.37 | 0.213 | 0.63 | 892.22 | 1.582 | 1 |
| 6 | 56.57 | 0.211 | 0.75 | 818.95 | 1.379 | 1 |

The best exergy efficiency condition (evaporating pressure, superheating degree) has been evaluated, in direct exchange with the same heat source at 390°C, also for the other organic fluids reported in Table 3, for comparison purposes. The results are reported in Table 7.

*Table 7. Results of ORCs in direct heat exchange with the flue gases detailed in Table 4, at maximum power output condition (best exergy efficiency condition).*

| Parameter | Fluorobenzene | Toluene | Cyclopentane | MM |
|---|---|---|---|---|
| **$\eta_{ex}$ [%]** | **58.64** | **58.1** | **55.2** | **46.76** |
| **$W_{net}$ [MW]** | **4.96** | **4.92** | **4.67** | **3.96** |
| $\dot{m}_{wf}$ [kg/s] | 35.76 | 30 | 32.54 | 49 |
| $T_7$ [°C] | 104.8 | 114 | 101 | 140.1 |
| $P_2$ [bar] | 30 | 15.5 | 40.5 | 12.5 |
| $T_{eva}$ [°C] | 253 | 246 | 229.5 | 216 |
| $P_{cond}$ [bar] | 0.21 | 0.08 | 0.75 | 0.12 |
| SH Degree [°C] | 0 | 0 | 11 | 0 |
| $V_{r,T}$ [-] | 159.1 | 184.3 | 65.9 | 141 |
| $SP_T$ [m] | 0.36 | 0.54 | 0.21 | 0.53 |
| $\eta_{is,T}$ [%] | 84.6 | 84.3 | 86.6 | 85.4 |

| | | | | |
|---|---|---|---|---|
| $W_T$ [MW] | 5.11 | 5 | 4.92 | 4.07 |
| $W_P$ [MW] | 0.15 | 0.08 | 0.25 | 0.12 |
| $Q_{PHE}$ [MW] | 17.96 | 17.4 | 18.19 | 15.8 |
| $Q_{Rec}$ [MW] | 2.62 | 3.02 | 2.72 | 8.24 |
| $Q_{Cond}$ [MW] | 13 | 12.48 | 13.52 | 11.86 |
| $UA_{rec}$ [MW/K] | 0.12 | 0.14 | 0.13 | 0.37 |
| $UA_{PHE}$ [MW/K] | 0.62 | 0.65 | 0.45 | 0.29 |
| $UA_{Cond}$ [MW/K] | 1.1 | 1.07 | 1.13 | 0.96 |

In direct heat exchange the net power produced, and then the exergy efficiency, of the fluorobenzene cycle is the highest among the fluids considered. The performance of fluorobenzene are similar to those of toluene. The low condensation pressure of toluene, however, results in higher volumetric flow rates at turbine outlet, posing more challenges in the last turbine stages, recuperator, and condenser.

In Table 7 are listed the UA products of the heat exchangers, which provide a comparative indication about the size of the heat exchangers. Regarding the recuperator, the fluids are similar except to the siloxane since its limited temperature drop across the turbine entails large internal heat recovery. The evaporator of the fluorobenzene cycle has similar UA value as the toluene cycle, while it is lower for cyclopentane: the latter has the optimal evaporation pressure near the critical one (at 0.9 $P_{cr}$ as the imposed limit), thus most of the heat is introduced in the cycle at variable temperature determining larger logarithmic mean temperature difference between the source and the working fluid. The siloxane, instead, has low UA value of the PHE as it evaporates at lower temperature, providing large temperature difference with the source.

In case of cyclopentane, even if the saturated cycle provides higher power production, a superheating degree of 11°C is found to be necessary to avoid excessive cooling of the heat source below the imposed limit of 100°C. On the contrary, MM is disadvantaged compared to other working fluids in direct exchange due to high molecular complexity entailing a small temperature drop across the turbine, and the related incapability to cool the flue gases due to large internal heat recovery ($Q_{rec}$ three times higher than other fluids -Table 7). In Figure 10, the fractional net power produced, and the exergy losses are reported for the various fluids. It is evident that MM has the highest exergy loss due to non-cooling of the flue gases. For this reason, MM should be considered in a split cycle architecture [68] to reduce the flue gases exhaust temperature. The large exergy losses in the recuperator of MM cycle are due to the highly regenerative nature of the fluid.

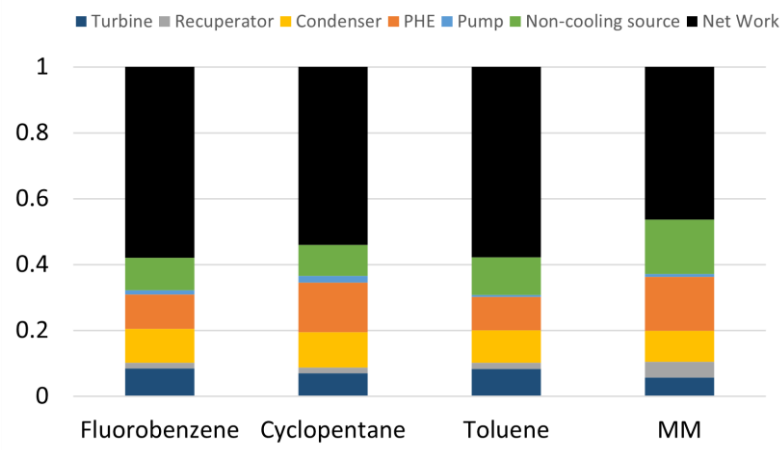


*Figure 10. Fraction of net power produced and exergy losses in each component starting from the available exergy of the flue gases.*

## 3.5 Fluorobenzene in high-temperature heat pump for 180°C heat delivery

This section provides a preliminary evaluation of subcritical HTHP performance using fluorobenzene as working fluid, focusing on a heat sink with a constant temperature of 180°C. The choice of this temperature level aligns with the earlier discussion in the Introduction section, which highlighted the limited availability of fluids suitable for subcritical closed-loop HTHP above 150-160°C and with the significant industrial heat demand up to 200°C for steam production. The analysis is extended to other working fluids that can be used in the same application in order to point out the benefits of the proposed solution.

As stated by Angelino and Invernizzi in 1987, <<*future high temperature fluids are more likely to be found among compounds having a complex molecular structure, recourse to the regenerative cooling of the liquid could become a procedure of general interest*>> [29]. The molecular complexity of a fluid can be expressed as in Equation 5, and it is proportional to the slope of the saturated vapour curve in the temperature-entropy diagram, measured at a reduced temperature of 0.7:

$$\sigma = \frac{T_{cr}}{R}\left[\frac{ds_{SV}}{dT}\right]_{T_{red}=0.7} \tag{5}$$

The investigated fluids, with critical temperature above 180°C, are reported in Table 8 along with their main characteristics such as the normal boiling point (NBP), the acentric factor (ω), the molecular complexity (σ) and the critical parameters ($T_{cr}$, $P_{cr}$). The thermodynamic properties are taken from Aspen Plus V12 [69].

*Table 8. Main characteristics of fluorobenzene and other low-GWP fluids potentially suitable for subcritical HTHP at 180°C sink temperature.*

| Compound | Formula | MW [g/mol] | σ [-] | $T_{cr}$ [°C] | $P_{cr}$ [bar] | ω [-] | NBP [°C] | $P_{sat}$ at 180°C [bar] |
|---|---|---|---|---|---|---|---|---|
| **Fluorobenzene** | **$C_6H_5F$** | **96.1** | **0.69** | **287** | **45.5** | **0.247** | **84.7** | **9.4** |
| Cyclopentane | $C_5H_{10}$ | 70.1 | 0.75 | 238.6 | 45.1 | 0.195 | 49.2 | 19.5 |

| | | | | | | | | |
|---|---|---|---|---|---|---|---|---|
| n-Pentane (R601) | $C_5H_{12}$ | 72.2 | 1.4 | 196.6 | 33.7 | 0.252 | 36.1 | 26.3 |
| Cyclohexane | $C_6H_{12}$ | 86.2 | 1.42 | 280.7 | 40.8 | 0.208 | 80.7 | 9.4 |
| Hexane | $C_6H_{14}$ | 86.2 | 1.71 | 234.5 | 30.3 | 0.301 | 68.7 | 13 |
| Heptane | $C_7H_{16}$ | 100.2 | 1.84 | 267.1 | 27.4 | 0.349 | 98.4 | 6.9 |
| Acetone | $C_3H_6O$ | 58.1 | -0.2 | 235 | 47 | 0.307 | 56.1 | 19.9 |
| Butanol | $C_4H_{10}O$ | 74.1 | 0.83 | 290 | 44.1 | 0.588 | 118.8 | 5.9 |
| Ethanol | $C_2H_6O$ | 46.1 | -3.14 | 240.9 | 61.4 | 0.644 | 78.3 | 19.7 |
| Methanol | $CH_3OH$ | 32 | -10.1 | 239.4 | 80.8 | 0.566 | 64.7 | 27.8 |

The saturation curves of the working fluids are reported in Figure 11 in the P-h diagram.

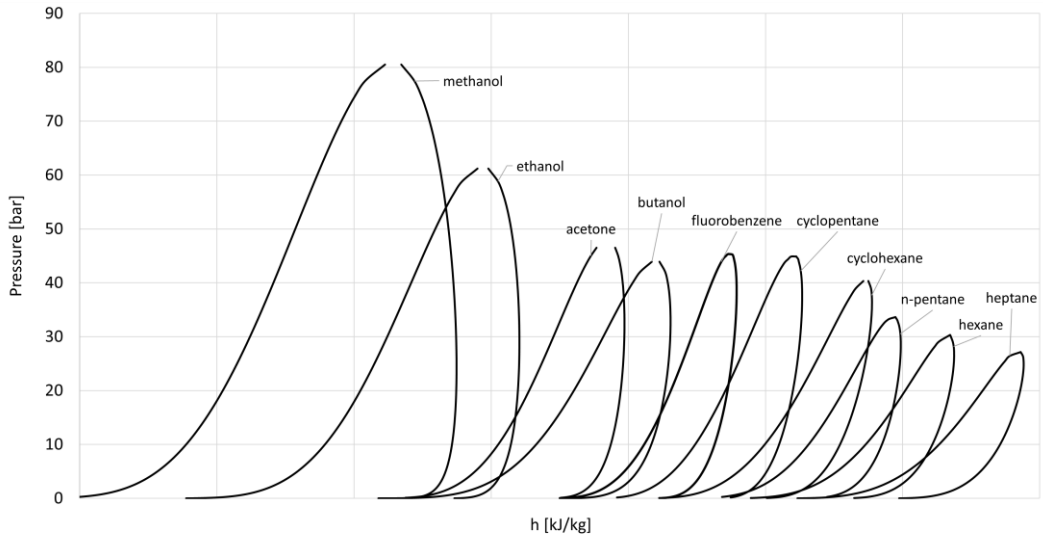


*Figure 11. Saturation curves of the working fluids considered for the subcritical HTHP in the pressure-specific enthalpy diagram.*

The key performance parameter of the HTHP is measured by the coefficient of performance (COP), which describes the ratio between supplied heat ($\dot{Q}_{sink}$) at the condenser and consumed power by the compressor ($\dot{W}_{comp}$):

$$COP = \frac{\dot{Q}_{sink}}{\dot{W}_{comp}} \quad (6)$$

The constraints and assumptions of the analysis are reported in Table 9. A maximum lift of 100°C (difference between $T_{cond}$ and $T_{eva}$) is considered, as it approaches the practical threshold for a two-stage centrifugal compressor. This limit is reached due to excessively high pressure ratios for the majority of refrigerants [70]. Then, the evaporation temperature is limited above 70°C, and the HTHP is considered to be thermally integrated with low-grade waste heat to be valorised (such as flue gases before stack). An isentropic efficiency of 75% is assumed for the compression step to allow a fair comparison among different working fluids, as in Abedini et al. [28]. Most of the correlations available in the literature are for volumetric compressors, while the focus here is on MW-scale industrial heat pumps, where centrifugal compressors are more likely to be adopted. However, in

Appendix C, results including the screw compressor efficiency of Ganesan and Eikevik [71] are presented, valuable for kW-scale HTHP. The pressure losses in the heat exchanger are neglected. The Peng Robinson EoS [67] is used in Aspen Plus V12, with the parameters in Table 8, to calculate the thermodynamic properties of the fluids and for the optimisation of the HTHP.

*Table 9. HTHP modelling assumptions.*

| **Parameters** | **Values** |
|---|---|
| Evaporation Temperature | 70-130°C |
| Condensation Temperature | 180°C |
| $\Delta T_{min}$ IHX | 10 °C |
| $\Delta P$ Heat Exchangers | neglected |
| Compression Isentropic Efficiency ($\eta_{is,C}$) | 75% |
| $\Delta T_{SH}$ at Compressor Inlet* | ≥ 2 °C |

**In regenerative cycles, the IHX should provide a proper degree of superheating to avoid condensation in the compressor*

As reported in Table 9, a minimum of 2°C of superheating at compressor inlet is assumed (for non-regenerated cycles). However, given the high critical temperature fluids considered in this analysis, the adoption of an internal heat exchanger (IHX) recuperator is necessary to provide an adequate degree of superheating at compressor inlet, which allows to avoid two-phase conditions inside the compressor [8]. Regeneration is necessary in case of complex fluid (elevate number of atoms in the molecule) possessing retrograde dew curve in the P-h diagram (Figure 11), such as most of high-critical temperature fluids. Therefore, the performance of the cycle improves and condensation within the compressors is prevented.

The IHX has negative impacts on fluids with low molecular complexity, resulting in: i) high temperature at compressor outlet due to low heat capacity; ii) associated risk of fluid thermal cracking; and iii) increased chances of compressor failure.

The regenerated HTHP architectures considered in this analysis are represented in Figure 12: a) one-stage throttling cycle; b) two-stage throttling cycle with regeneration in the lower portion of the cycle. In cycle (a), regeneration is carried out by subcooling the liquid at condenser outlet; in cycle (b), regeneration is performed between the vapour exhausted by the evaporator and the liquid before the last throttling, flashed at an intermediate pressure ($P_{int}$). The vapour compressed in the low pressure (LP) compressor of the HTHP type (b) is mixed with the vapour flashed at the same pressure: as a result, it is evident in Figure 12, that the discharge temperature after the high-pressure (HP) compression step is lower for cycle (b) at the same $\Delta T_{min}$ of the recuperator (IHX). The portion of the regenerative sub-cycle is determined by the intermediate pressure, which is determined through a proper optimization procedure for each fluid and temperature lift. Similar cycle architecture was also considered by Dong et al. [72].

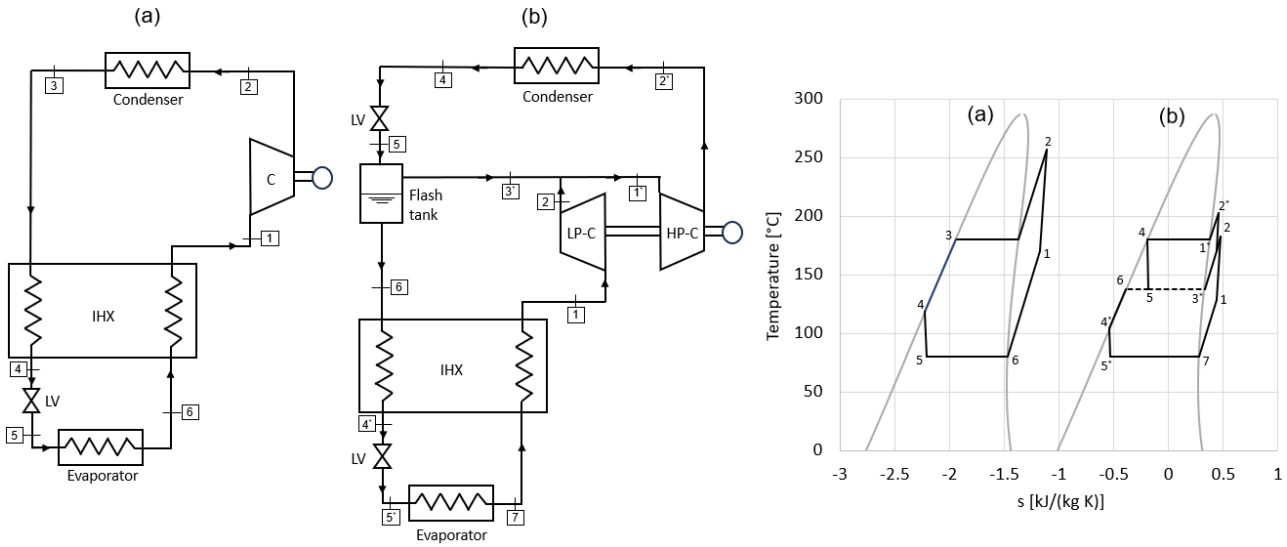


*Figure 12. Cycle architectures adopted for the subcritical 180°C HTHP; a) regenerative cycle with one-stage throttling; b) two-stage throttling with regeneration in the low-temperature portion; T-s diagram of the corresponding cycles using fluorobenzene at 100°C temperature lift at best COP conditions.*

The thermodynamic conditions of the fluorobenzene HTHP, according to the cycle architectures presented in Figure 12, are reported in Table 10 and Table 11 for 100°C temperature lift (evaporation temperature of 80°C).

*Table 10. Thermodynamic conditions of the fluorobenzene HTHP at 180°C delivery and 100°C temperature lift in configurations (a): state labels refers to the layout and T-s diagram of Figure 12.*

| State Point | T [°C] | P [bar] | ϱ [kg/m³] | h [kJ/kg] | s [kJ/kg/K] | x [-] |
|---|---|---|---|---|---|---|
| 1 | 170 | 0.87 | 2.3 | 962.3 | 1.629 | 1 |
| 2 | 256.7 | 9.36 | 22.6 | 1088 | 1.691 | 1 |
| 3 | 180 | 9.36 | 802.3 | 700 | 0.857 | 0 |
| 4 | 118.4 | 9.36 | 917.2 | 581.2 | 0.576 | 0 |
| 5 | 80 | 0.87 | 14.6 | 581.2 | 0.588 | 0.2 |
| 6 | 80 | 0.87 | 2.9 | 843.5 | 1.331 | 1 |

*Table 11. Thermodynamic conditions of the fluorobenzene HTHP at 180°C delivery and 100°C temperature lift in configurations (a) and (b): state labels refers to the layout and T-s diagram of Figure 12.*

| State Point | T [°C] | P [bar] | ϱ [kg/m³] | h [kJ/kg] | s [kJ/kg/K] | x [-] |
|---|---|---|---|---|---|---|
| 1 | 127.8 | 0.87 | 2.6 | 903.2 | 1.489 | 1 |
| 2 | 182.1 | 4 | 10.9 | 974.5 | 1.529 | 1 |
| 1* | 169.9 | 4 | 11.2 | 956 | 1.487 | 1 |
| 2* | 202.5 | 9.36 | 26.4 | 996.1 | 1.509 | 1 |

| | | | | | | |
|---|---|---|---|---|---|---|
| 3* | 137.8 | 4 | 12.3 | 909.8 | 1.379 | 1 |
| 4 | 180 | 9.36 | 802.3 | 700 | 0.857 | 0 |
| 5 | 137.8 | 4 | 41.8 | 700 | 0.868 | 0.29 |
| 6 | 137.8 | 4 | 883.8 | 616.1 | 0.665 | 0 |
| 4* | 104.3 | 4 | 936.6 | 556.5 | 0.513 | 0 |
| 5* | 80 | 0.87 | 23.3 | 556.5 | 0.518 | 0.12 |
| 7 | 80 | 0.87 | 2.9 | 843.5 | 1.331 | 1 |

It is important to emphasize that, in cycle (a), the reduction of the compressor discharge temperature can be only achieved by decreasing the design effectiveness of the recuperator (IHX). In general, the presence of an internal heat exchanger (IHX) increases the compressor discharge temperature, and there is a risk of thermal cracking for some fluids above 200°C. Furthermore, high discharge temperatures pose additional challenges in compressor design, although these aspects are beyond outside the scope of the present study.

The influence of recuperator size ($\Delta T_{min}$ in the IHX) on the COP and compressor discharge temperature in a one-stage throttling cycle ("a" in Figure 12) operating with fluorobenzene at 100°C temperature lift is illustrated in Figure 13. At 100°C lift, a minimum superheat (SH) of 21°C is necessary for fluorobenzene to prevent condensation in the compressor in a one-stage throttling cycle.

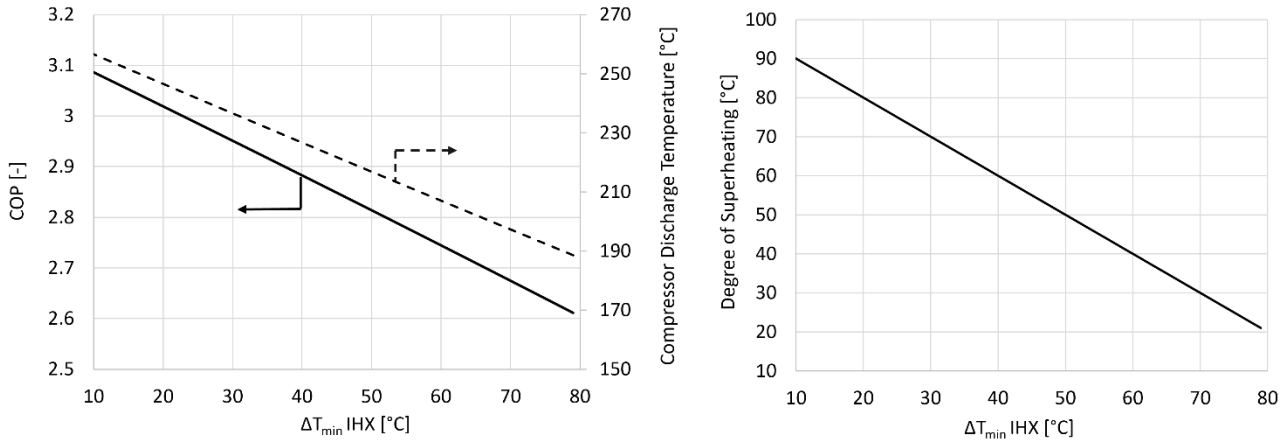


*Figure 13. Fluorobenzene HTHP one-stage throttling (type a) at 180°C condensation and 100°C lift (80°C evaporation): on the left, the impact of regeneration on the COP and compressor discharge temperature; on the right, the relation between ΔTmin in the IHX recuperator and the resulting degree of superheating at compressor inlet.*

The minimum degree of superheating (SH) necessary at the compressor inlet for various working fluids in a one-stage throttling cycle is illustrated in Figure 14. Acetone, methanol, and ethanol are not included in Figure 14 as they do not present condensation issues in the compressor, being the least complex fluids considered (the only fluids with negative complexity in Table 8).

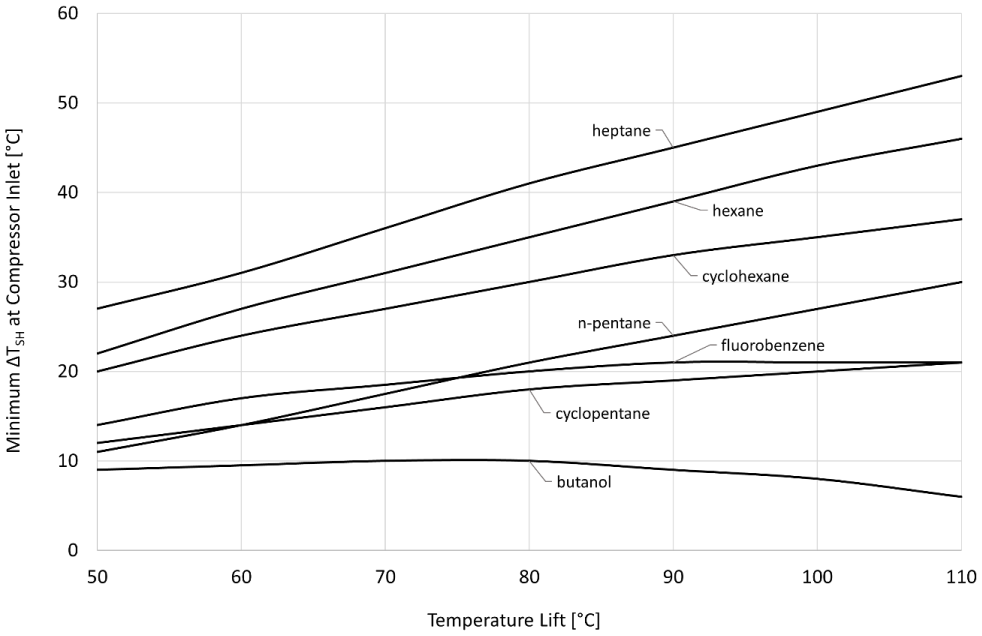


*Figure 14. Minimum Degree of Superheating requirements at compressor inlet for different working fluids in one-stage throttling HTHP, at 180°C condensing temperature, as function of temperature lift; methanol, ethanol and acetone do not face two-phase compression issues.*

It is evident that highly complex fluids such as heptane, hexane, and cyclohexane (with a pronounced retrograde saturation curve in P-h diagram) inherently requires a significant degree of superheating at compressor inlet. Therefore, a large recuperator is necessary to prevent the occurrence of a two-phase region during the compression step in single-stage throttling cycle.

The COP of the different potential working fluids delivering 180°C heat in single-stage throttling HTHP is reported in Table 12, considering a temperature lift of 100°C.

*Table 12. Results of subcritical HTHP at 180°C condensing temperature and 80°C evaporation temperature (100°C lift), in one-stage throttling (Figure 12-a).*

| **Fluids** | **COP** | **$\Delta T_{min}$ IHX [°C]** | **Compressor Discharge T [°C]** | **Risk of thermal cracking?** | **$\Delta h_{comp}$ [kJ/kg]** | **$\Delta h_{cond}$ [kJ/kg]** | **$\Delta h_{eva}$ [kJ/kg]** | **$\Delta h_{IHX}$ [kJ/kg]** | $\dot{Q}_{IHX}/\dot{Q}_{cond}$ |
|---|---|---|---|---|---|---|---|---|---|
| **Fluorobenzene** | **3.09** | **10** | **256.6** | **No** | **125.7** | **388** | **262.3** | **119** | **0.31** |
| Cyclopentane | 2.92 | 10 | 252 | **No** | 141.8 | 414.3 | 272.4 | 153.9 | 0.37 |
| Acetone | 2.87 | 10 | 287.8 | **n.a.** | 197.6 | 566.7 | 369.1 | 150.1 | 0.26 |
| Ethanol | 2.81 | 10 | 341.1 | **Yes** | 342.4 | 961.4 | 619.1 | 160.4 | 0.17 |
| Methanol* | 2.73 | - | 328.8 | **Yes** | 407.2 | 1109.2 | 702.1 | - | - |
| Butanol | 3.06 | 10 | 277.2 | **Yes** | 224.4 | 685.9 | 461.5 | 168.2 | 0.25 |
| Hexane | 2.9 | 10 | 231.3 | **n.a.** | 122.5 | 354.8 | 232.3 | 191.4 | 0.54 |
| Heptane | 3.03 | 10 | 226.9 | **n.a.** | 121.5 | 368.1 | 246.6 | 190.1 | 0.52 |
| n-Pentane | 2.55 | 10 | 238.8 | **No** | 124.5 | 317.2 | 192.6 | 194.3 | 0.61 |

| | | | | | | | | | |
|---|---|---|---|---|---|---|---|---|---|
| Cyclohexane | 3.08 | 10 | 240.7 | **n.a.** | 134.1 | 413.5 | 279.4 | 158.7 | 0.38 |

*[*]No IHX recuperator is used for this fluid as it has a negative impact on COP, and 2°C of superheating at evaporator outlet is assumed; n.a. stands for "not available" information about thermal stability.*

Fluorobenzene demonstrates the highest COP (3.09) at a 100°C lift, closely followed by cyclohexane (3.08) and butanol (3.06). Notably, fluids with higher critical temperature (Table 8) exhibit superior COP. Conversely, the lower performance of n-pentane cycle (COP of 2.55) can be attributed to its condensation temperature approaching the critical point, resulting in operation within an unfavourable reduced temperature region. For methanol, the least complex fluid ($\sigma$ = -10.1), regeneration adversely affects the COP in single-stage throttling cycle, leading to the exclusion of the IHX recuperator (2°C of superheating assumed at compressor inlet).

It should be noted that not only the COP, but also other factors affect the feasibility of a HTHP delivering heat at 180°C. The thermo-chemical integrity of the working fluid is a key factor to be considered, expect for working fluids with demonstrated stability at 300°C or above such as n-pentane and cyclopentane [45]. For instance, the butanol cycle's compressor discharge temperature is around 277°C if the IHX recuperator is operated with a 10°C pinch point. However, thermal decomposition of butanol is not negligible even at 220°C, as determined by our previous experimental campaign [46]. The same thermal stability is expected for other alcohols such as ethanol and methanol having the bonds in the alkyl chain. Therefore, a smaller recuperator should be adopted for butanol, resulting in reduced COP and compressor discharge temperature as a consequence. Similar thermal stability is expected for ethanol and methanol, given the similar molecular structure. For this reason, the feasibility of a fluid in HTHP delivering 180°C heat is assigned in Table 12 and Table 13 also by indicating whether thermal cracking of the organic fluid is likely to occur. In case of methanol, even although no IHX recuperator has been adopted due to its detrimental effect on COP, the low molecular complexity ($\sigma$=-10.1) results in high compressor overheating, likely exceeding the thermal stability limit. Consequently, methanol is deemed unsuitable for use in a single-stage throttling HTHP at the conditions explored in this work.

As a matter of facts, fluorobenzene and cyclohexane emerge as the most promising candidates for single-stage throttling HTHP at 180°C condensing temperature. Cyclohexane's high molecular complexity ($\sigma$=1.41) provides high vapour heat capacity, preventing compressor overheating and consequent superheating losses. However, the downside of cyclohexane's complexity is the need for significant degree of superheating at compressor inlet (refer to Figure 14) to avoid condensation within the compressor, posing challenges if the recuperator effectiveness decreases during off-design. On the other hand, fluorobenzene, with a moderate molecular complexity ($\sigma$=0.69), experiences more overheating in the compressor but requires fewer regeneration to avoid critical two-phase zones.

By adopting a two-stage throttling (cycle type "b" in Figure 12), a greater flexibility is introduced to optimise the cycle, primarily through the flash intermediate pressure (first throttling discharge pressure). This pressure level determines the portion of the sub-cycle with regeneration on the overall cycle, as well as the mass flow rates in the upper and lower sub-cycles. The low-pressure compressor (1-2 in Figure 12-b) elaborates lower mass flow rate than the high-pressure compressor

($1^*$-$2^*$ in Figure 12-b), depending on the mass vapour quality of the state point 5 (Figure 12– b) after the first throttling valve. The results of the different working fluid in two-stage-throttling architecture at 180°C delivery and 100°C temperature lift are presented in Table 13.

In comparison to the one-stage throttling cycle results, the HTHP with two-stage throttling demonstrates the potential for lower compressor discharge temperature and higher COP values. The ratio of the IHX thermal power to the delivered power at the condenser is lower in this case, as regeneration occurs only in the low-temperature sub-cycle. The mixing of flashed vapour with the vapour discharged by the low-pressure compressor reduces the compression work of the high-pressure compression stage. Fluids characterized by low heat capacity (molecular complexity), such as ethanol and methanol, the regenerative IHX has a detrimental effect on the performance and is therefore excluded from the analysis. This is because fluids with fewer internal degrees of freedom can only transfer additional energy input as translational movement, while complex fluids can distribute most of the energy across rotational and oscillating degree of freedom.

*Table 13. Results of subcritical HTHP at 180°C condensing temperature and 80°C evaporation temperature (100°C lift), in two-stage throttling (Figure 12-b).*

| **Fluids** | **COP** | **$P_{int,opt}$ [bar]** | **$\Delta T_{min}$ IHX [°C]** | **Compressor Discharge T [°C]** | **Risk of thermal cracking?** | **$\dot{m}_{LP}/\dot{m}_{HP}$ [-]** | **$\Delta h_{comp,LP}$ [kJ/kg]** | **$\Delta h_{comp,HP}$ [kJ/kg]** | **$\Delta h_{cond}$ [kJ/kg]** | **$\Delta h_{eva}$ [kJ/kg]** | **$\Delta h_{IHX}$ [kJ/kg]** | **$\dot{Q}_{IHX}/\dot{Q}_{cond}$** |
|---|---|---|---|---|---|---|---|---|---|---|---|---|
| **Fluorobenzene** | **3.25** | **4** | **10** | **202.5** | **No** | **0.72** | **71.4** | **40.1** | **296.4** | **287.3** | **59.9** | **0.14** |
| Cyclopentane | 3.1 | 9.5 | 10 | 198 | **No** | 0.64 | 81.4 | 41.6 | 289.9 | 308.5 | 77.5 | 0.17 |
| Acetone | 3.14 | 9 | 10 | 226.2 | **n.a.** | 0.7 | 111.1 | 60.8 | 433.6 | 422 | 77.2 | 0.13 |
| Ethanol* | 3.12 | 6.5 | - | 235.7 | **Yes** | 0.74 | 156.7 | 111.1 | 707 | 653 | - | - |
| Methanol* | 3.05 | 9.5 | - | 308 | **Yes** | 0.77 | 220.2 | 177 | 1062 | 929 | - | - |
| Butanol | 3.27 | 2 | 10 | 219.4 | **Yes** | 0.75 | 129.4 | 70.9 | 551 | 508.5 | 85.9 | 0.12 |
| Hexane | 3.06 | 7 | 10 | 185.9 | **n.a.** | 0.6 | 80.5 | 28.3 | 234.3 | 262.4 | 115 | 0.29 |
| Heptane | 3.15 | 3.5 | 10 | 183.1 | **n.a.** | 0.65 | 81 | 28.6 | 257.2 | 268 | 114.1 | 0.29 |
| n-Pentane | 2.79 | 16 | 10 | 192.1 | **No** | 0.48 | 85.4 | 23.2 | 179.8 | 239.5 | 125.9 | 0.34 |
| Cyclohexane | 3.21 | 4.5 | 10 | 191 | **n.a.** | 0.69 | 80.3 | 38.4 | 301.5 | 302.5 | 83.5 | 0.19 |

** No IHX* recuperator *is used for this fluid as it has a negative impact on COP, and 2°C of superheating at evaporator outlet is assumed.*

Among the considered fluids, butanol achieves the highest COP (3.27) in this cycle configuration. However, the compressor discharge temperature reaches approximately 220°C, leading to non-negligible thermal cracking of the fluid, then raising doubts about the feasibility of a butanol cycle under these conditions. Fluorobenzene follows closely with the second highest COP value (3.25). Cyclohexane has similar COP value (3.21), but the operability range of this fluid is very limited by the high molecular complexity of the fluid, which requires a $\Delta T_{min}$ of the IHX lower than 20°C (equivalent to a minimum superheating degree at LP compressor inlet of 42°C) to avoid condensation in the compressor. Consequently, there is high risk of compromising the compressor if the IHX recuperator effectiveness decreases during off-design conditions. In contrast, fluorobenzene does not encounter such limitations, as the $\Delta T_{min}$ of the IHX can increase up to 44°C without incurring two-phase compression. Given this feature and the high COP value (3.25) at 100°C lift, fluorobenzene emerges as a promising candidate for this application. The working fluids are compared in Appendix C, at 100°C temperature lift, also including a correlation for the compressor isentropic efficiency.

In the end, the results of different working fluids in the two-stage throttling HTHP cycle layout are represented in Figure 15 at varying temperature lift; the cycles are properly optimised in each condition. Ethanol, methanol, and butanol are omitted from Figure 15 as their compressor discharge temperature is excessive, as discussed, and are impractical for 180°C condensation temperature.

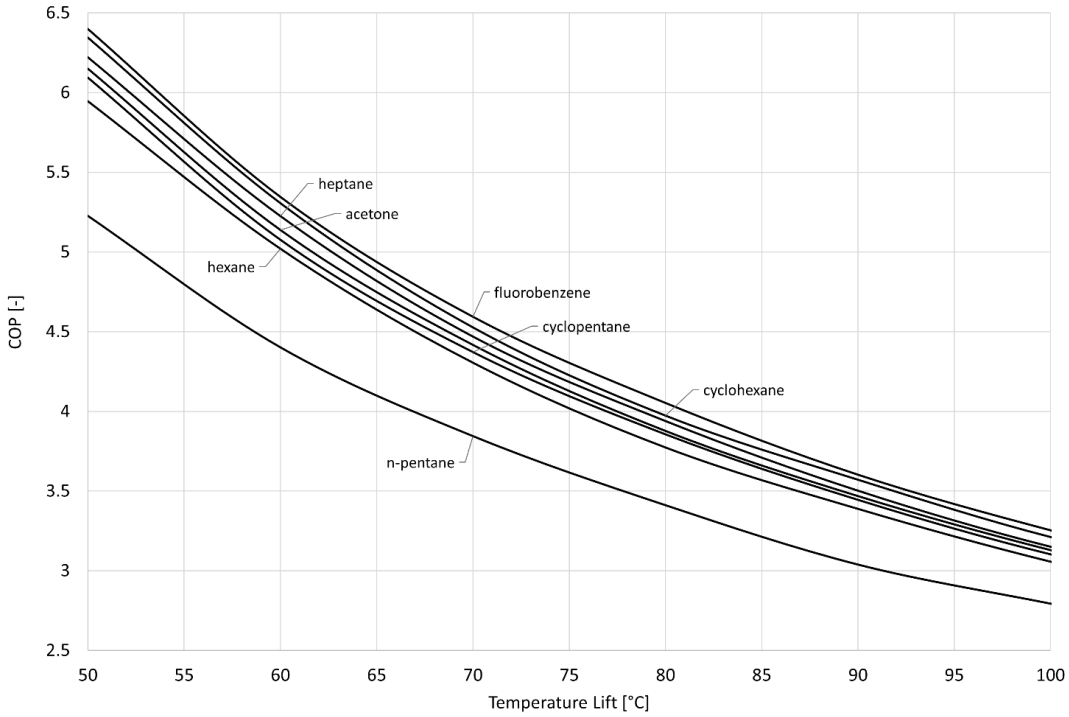


*Figure 15. COP of subcritical HTHP with different working fluids condensing at 180°C at varying temperature lift, in two-stage throttling architecture (Figure 12-b).*

In conclusion, fluorobenzene represents one of the most interesting working fluids, combining high COP values, no strict requirements for regeneration to avoid two-phase compression compared to

more complex fluids (cyclohexane, hexane, heptane), good thermo-chemical stability as demonstrated in the previous section, and high auto-ignition temperature (455°C).

## 3.6 Conclusions

Fluorobenzene is proposed for the first time as versatile working fluid for both Organic Rankine Cycles (ORC) and High-Temperature Heat Pumps (HTHP). The fluid possesses near zero GWP, zero ODP, and relatively low cost, and low toxicity compared to benzene. Moreover, fluorobenzene is not classifiable as PFAS substance, which are undergoing strict regulation in EU.

The thermo-chemical stability of fluorobenzene is experimentally tested in this study with a consolidated procedure in the Fluid Test Laboratory of the University of Brescia. Compared to past studies, the well-established static thermal stability method has been included in a broader framework in this work. The presence of a non-condensable-gases (NCG) removal system in commercial ORC has been simulated during the experimental campaign. The effect of time on the unimolecular decomposition reaction of the fluid has been assessed at constant temperature (350°C). As a result of the investigation, all degradation products appear in the vapour phase: after a brief aspiration of the fluid post thermal stress, the volumetric behaviour of the thermally-stressed fluorobenzene up to 350°C returned the reference behaviour of the fresh fluid. This result proves that, after aspiration of fluorobenzene in the hot-well of an ORC and the subsequent NCGs removal, the fluid recovered in the gas treatment unit and recirculated in the system maintains its physical properties unaltered. These results have been obtained not only by measuring the volumetric behaviour in laboratory, but also by a chemical analysis on the thermally-stressed fluid (after the thermal stability campaign) after prolonged thermal exposure at 350°C. The FTIR analysis on the liquid confirms that no substantial traces of any other degradation compound in the liquid phase.

The small degradation rate at 350°C poses fluorobenzene among the most thermally stable organic fluids, comparable with toluene and cyclopentane, adopted in high-temperature ORC units. Given the good thermal stability, fluorobenzene has been studied in direct heat exchange with a medium-high temperature source. In particular, flue gases available at 390°C have been considered. From 8.5 MW ideally available as exergy flux of the sensible heat source, the fluorobenzene cycle can produce about 5 MW as mechanical power output, reaching 58.6% exergy efficiency. The net power production of fluorobenzene surpasses that of other high-temperature ORC working fluids, although the production of toluene cycle is similar.

In high-temperature heat pump (HTHP) application, the performance of fluorobenzene have been studied in case of 180°C as heat delivery temperature, given the literature gap for subcritical heat pumps above 150/160°C. A cycle architecture with internal heat exchanger was found necessary to avoid two-phase states during the compression of the fluid, as it is for most of the high-critical temperature fluids considered in this study. The Coefficient of Performance of the fluorobenzene HTHP at 100°C temperature lift is 3.09 in one-stage throttling cycle and 3.25 in two-stage throttling architecture. Considering the efficiency of the compressor as a function of operating conditions (Appendix C), fluorobenzene emerges as the most efficient working fluid among those investigated. From this preliminary thermodynamic analysis, fluorobenzene represents one of the most promising working fluids for HTHP covering the heat demand in the temperature range near 200°C. In fact, as discussed in this article, fluorobenzene not only presents elevate COP values, but also it has no strict

requirements for regeneration to avoid two-phase compression compared to more complex fluids (cyclohexane, hexane, heptane), good thermo-chemical stability (as experimentally demonstrated), high critical temperature, and high auto-ignition temperature (455°C).

**Appendix A – Uncertainty of the experimental results**

The global uncertainty of the experimental vapour pressures measured during the thermal stability test are here reported. The total uncertainty of the pressure $u_P$ values is computed according to equation A1:

$$u_P = \sqrt{(\sigma_P)^2 + (u_{instrumental})^2} \quad \text{(A1)}$$

where $\sigma_P$ is the standard deviations of the measured pressure over 15 minutes recording with 180 sampling, and $u_{instrumental}$ is the contribution related to the accuracy of the pressure transmitter (in Table 1). The pressure transmitter has been operated at 1 bar full scale, and the resulting accuracy is 1 mbar.

The uncertainty related to each vapour pressure measurement presented in Figure 3 (stage 1) and 4 (stage 2) are reported below in Figures F1 and F2.

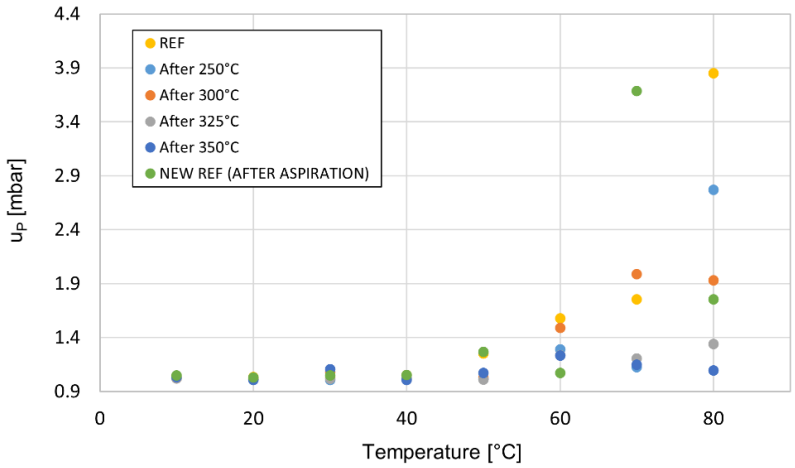


*Figure F1. Uncertainty of the vapour pressures measured during the 1st stage of experimental campaign (refer to Figure 3).*

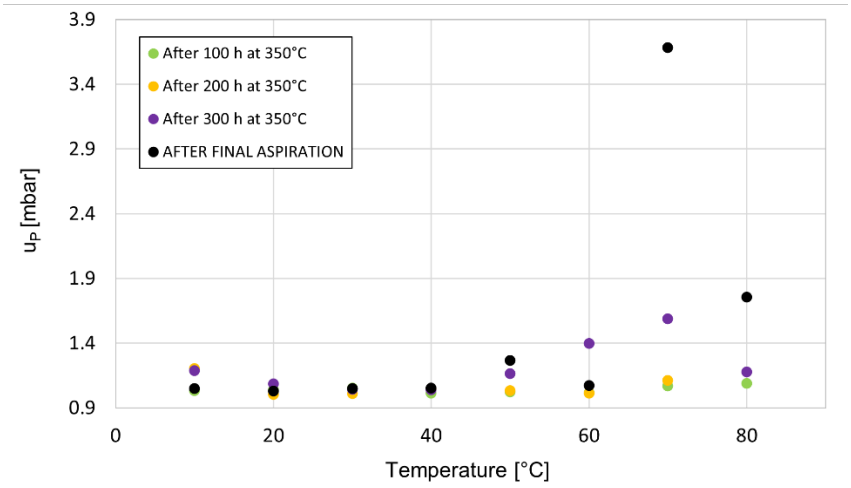


*Figure F2. Uncertainty of the vapour pressures measured during the 2nd stage of experimental campaign (refer to Figure 4).*

## Appendix B – Rate of unimolecular decomposition k* (new vs old approach)

The methodology adopted to calculate the quasi-constant rate of decomposition k* of a working fluid, following thermal stability test, is detailed in this section. Moreover, the main methodological differences between the approach adopted in this work and that used in past literature works are here described.

The equations (1-8) presented in a previous literature work [45] are used in this research, but with different approach. The main equations used for the calculation of k* are reported below for clarity purposes; please refer to the reference and nomenclature for the description of each term.

$$\frac{\ln(1-\bar{\beta})}{\Delta t} = -k^* \tag{A2}$$

$$\bar{\beta} = \frac{1}{N}\sum_{i=1}^{N} \frac{\Delta P_{v,i}}{P_{ref,i}} \frac{P_{vr,i}}{T_{vr,i}} z_{cr} \tag{A3}$$

As described in Equations A2 and A3, the k* is retrieved from the calculation of the term $\bar{\beta}$, that is proportional to the average value (over the N data points where the vapour pressure is calculated)

of each vapour pressure deviations ($\Delta P_{v,i}$) against the reference vapour pressure at the same temperature ($P_{v,i}$). Figure F3 illustrates the conceptual difference between this work and the previous literature works dealing with the calculation of k*: the pressure deviations resulting from a constant-temperature thermal stress are measured from the previous vapour pressure measured after the previous thermal stress. Instead, in previous works, the pressure deviations were calculated from the reference (fresh fluid) behaviour.

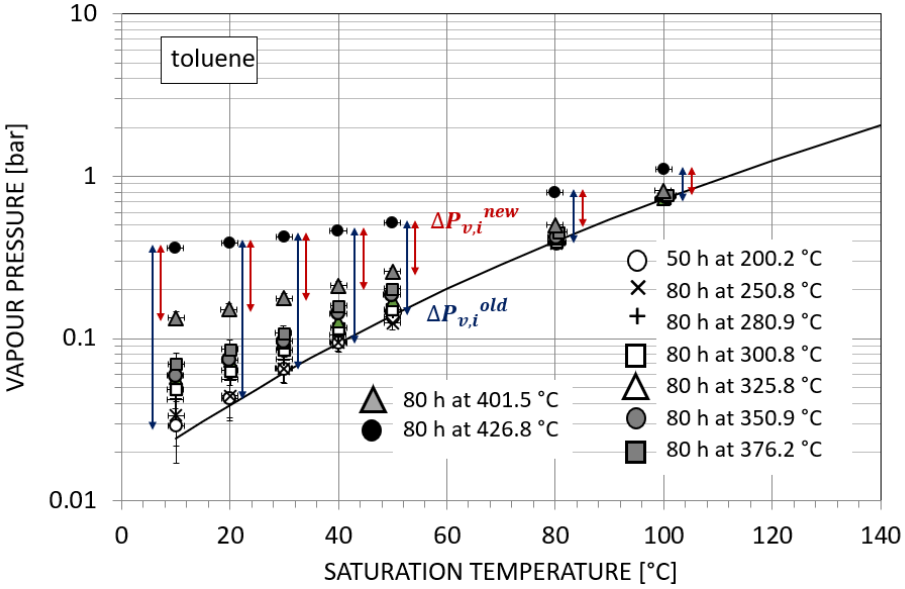


*Figure F3. Example of $\Delta P_{v,i}$ (Eq. A2) measurements for the calculation of k* at 427°C for toluene [45] with new approach compared to the old one: the vapour pressure increase resulting from a constant-temperature thermal stress is measured excluding the formation of degradation products due to preceding thermal stresses at lower temperatures.*

This conceptual shift, represented in Figure F3, has been considered as the formation of degradation products at a certain temperature is noticeable as a pressure increase compared to the vapour pressure measured before thermal stress. Then, the ($\Delta P_{v,i}$) arising from previous thermal stresses at lower temperatures are not accounted for the calculation of k* at a certain temperature: those $\Delta P_{v,i}$ must be allocated to the degradation occurring at lower temperatures.

From a qualitative standpoint, this new approach does not preclude the results described in previous works. The qualitative trend of k* does not change with methodology, as demonstrated in Figure F4 for toluene. In fact, when approaching temperatures at which fluid decomposition is relevant (above 400°C in Figure F3), the vapour pressure variations $\Delta P_{v,i}$ become high both considering as reference ($P_{rev,i}$) the vapour pressure measured after previous thermal stress (at lower temperature) or the fresh fluid vapour pressure (see Figure F3). The qualitative coherence is presented also in Figure F4: both approaches identifies a rapid increase of toluene degradation starting from temperatures above 370-390°C.

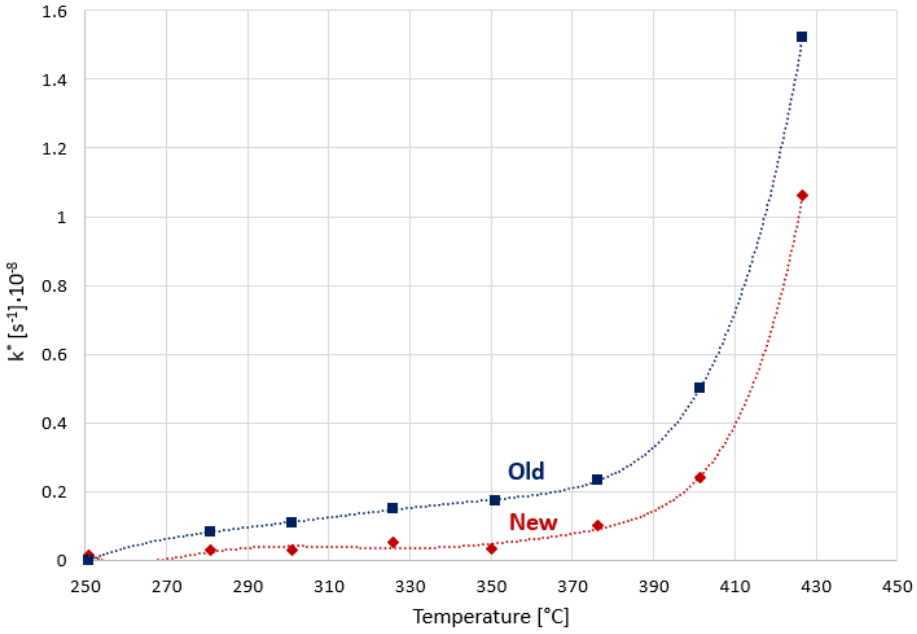


*Figure F4. resulting k* of toluene test [45] from the new approach adopted in this work and the previous one – the qualitative trend of fluid degradation is not affected by the methodology as the k* rapidly increases in the same temperature range (370-390°C).*

## Appendix C – HTHP results including compressor efficiency correlation

From the results of Section 4, it is evident that the most promising HTHP cycle configuration is the two-stage throttling cycle with regenerative cooling of the flashed liquid (Figure 12-b), at high temperature lift. The performance of such configurations are reevaluated in this Section introducing one major difference compared to the assumptions in Table 7: the compressors isentropic efficiency is not kept as a constant value, but a correlation is used. The correlation of Ganesan and Eikevik [71], as in Eq. A4, is used to determine the compressor isentropic efficiency as function of the pressure ratio:

$$\eta_{is,C} = -0.00000461\,x^6 + 0.00027131\,x^5 - 0.00628605\,x^4 + 0.07370258\,x^3 - 0.46054399\,x^2 + 1.40653347\,x - 0.87811477 \quad \text{(A4)}$$

where x is the pressure ratio across the single compressor. The volumetric efficiency of the compressor is fixed at the value 1 instead. The same approach has been adopted by Špale et al. [73] for the screening of different working fluids for a 100 kW high-temperature heat pump.

It must be noted that the correlation in Eq. A4 is representative of a screw compressor, thus valuable for applications where the compressor consumption does not exceed around 500 kW. The results in Section 4 are, instead, more representative of MW-scale industrial heat pumps adopting centrifugal compressors: the total pressure ratio can be spitted in several stages maintaining good efficiency at values in the 75-85% range [70].

The calculations here presented focus on a temperature lift of 100°C, i.e. the evaporation temperature of the working fluid is 80°C and the condensation temperature is kept 180°C. This allows a direct comparison with the previous results – with fixed compressor efficiency - of Table 13. These conditions are representative of the upgrading of waste heat or district heating network. The results are presented in Table T1.

*Table T1. Results of subcritical HTHP at 180°C condensing temperature and 80°C evaporation temperature (100°C lift), in two-stage throttling (Figure 12-b) considering the compressor isentropic efficiency as in Eq. A4.*

| **Fluids** | **COP** | **$P_{int,opt}$ [bar]** | **$\Delta T_{min}$ IHX [°C]** | **Compressor Discharge T [°C]** | **Risk of thermal cracking?** | **$\dot{m}_{LP}/\dot{m}_{HP}$ [-]** | **$\Delta h_{comp,LP}$ [kJ/kg]** | **$\Delta h_{comp,HP}$ [kJ/kg]** | **$\Delta h_{cond}$ [kJ/kg]** | **$\Delta h_{eva}$ [kJ/kg]** | **$\Delta h_{IHX}$ [kJ/kg]** | **$\dot{Q}_{IHX}/\dot{Q}_{cond}$** |
|---|---|---|---|---|---|---|---|---|---|---|---|---|
| **Fluorobenzene** | **3.17** | **3** | **10** | **191.5** | **No** | **0.65** | **55.6** | **51.9** | **278.2** | **294.5** | **44.2** | **0.1** |
| Cyclopentane | 2.93 | 8.5 | 10 | 196.8 | **No** | 0.6 | 73.5 | 53.9 | 287.3 | 315.8 | 70.6 | 0.14 |
| Acetone | 3.05 | 7 | 10 | 216.8 | **n.a.** | 0.64 | 88.4 | 79 | 413.7 | 435.5 | 58.9 | 0.1 |
| Ethanol* | 3.08 | 5 | - | 237.1 | **Yes** | 0.74 | 135.2 | 136.4 | 710.4 | 688 | - | - |
| Methanol* | 3.04 | 7.5 | - | 308.6 | **Yes** | 0.74 | 186.1 | 211.1 | 1063.2 | 960.3 | - | - |
| Butanol | 3.08 | 1.5 | 10 | 215.7 | **Yes** | 0.7 | 124.2 | 88.5 | 542.6 | 520 | 69.1 | 0.1 |
| Hexane | 2.75 | 7 | 10 | 191.1 | **n.a.** | 0.6 | 85.8 | 38.7 | 248.1 | 262.4 | 115 | 0.28 |
| Heptane | 2.78 | 3.5 | 10 | 190.9 | **n.a.** | 0.65 | 94.6 | 37.6 | 276.6 | 270.2 | 116.3 | 0.28 |
| n-Pentane | 2.46 | 14 | 10 | 189.5 | **No** | 0.41 | 76.2 | 38.6 | 171.5 | 101.8 | 110.4 | 0.26 |
| Cyclohexane | 3.05 | 4 | 10 | 189.4 | **n.a.** | 0.65 | 74.7 | 49.2 | 298 | 308.5 | 76.4 | 0.17 |

** No IHX recuperator is used for this fluid as it has a negative impact on COP, and 2°C of superheating at evaporator outlet is assumed.*

Even including the correlation of the compressor efficiency, fluorobenzene confirms its potentialities in HTHP delivering heat at 180°C at high temperature lift, having the highest COP compared with the other candidates in Table T1.

**Nomenclature**

Acronyms

| | |
|---|---|
| C | Compressor |
| COP | Coefficient of Performance, - |
| CSP | Concentrated Solar Power |
| EoS | Equation of State |
| EU | European Union |
| FTIR | Fourier-Transform Infrared Spettroscopy |
| GWP | Global Warming Potential |
| HP | High Pressure |
| HT | High Temperature |
| HTHP | High Temperature Heat Pump |
| HTF | Heat Transfer Fluid |
| LP | Low Pressure |
| MW | Molecular Weight |
| NBP | Normal Boiling Point |
| NCG | Non Condensable Gases |
| NFPA | National Fire Protection Association |
| ODP | Ozone Depletion Potential |
| ORC | Organic Rankine Cycle |
| PHE | Primary Heat Exchanger |
| PR | Peng Robinson |
| SP | Size Parameter, m |
| TIT | Turbine Inlet Temperature, °C |
| WHR | Waste Heat Recovery |

Symbols

| | |
|---|---|
| $\Delta h$ | Enthalpy Difference, kJ/kg |
| $\Delta T$ | Temperature Difference, K |

| | |
|---|---|
| $\Delta t$ | Time Difference, s |
| A | Area, $m^2$ |
| Cp | Specific Heat Capacity at Constant Pressure |
| $\dot{m}$ | Mass flow rate, kg $s^{-1}$ |
| N | Number of experimental data points |
| P | Pressure, bar |
| PT | Pressure Transmitter |
| $\dot{Q}$ | Thermal Power, MW |
| R | Gas Constant, kJ $kg^{-1}$ $K^{-1}$ |
| s | Specific Entropy, kJ $kg^{-1}$ $K^{-1}$ |
| T | Temperature, K |
| U | Global Heat Transfer Coefficient, W $m^2$ K |
| V | Volume, $m^3$ |
| $\dot{W}$ | Mechanical Power, MW |
| x | Mass Vapour Quality [-] |
| z | Compressibility factor, - |

Greek symbols

| | |
|---|---|
| $\eta_{th}$ | Cycle Thermal Efficiency, - |
| $\eta_{is,C}$ | Compressor isentropic efficiency, - |
| $\eta_{is,T}$ | Turbine isentropic efficiency, - |
| $\eta_{is,P}$ | Pump isentropic efficiency, - |
| $\omega$ | Pitzer acentric factor, - |
| $\rho$ | Density |
| $\sigma$ | Molecular Complexity Parameter, - |
| $\pi$ | Surface Tension |
| $\lambda$ | Thermal Conductivity |
| $\eta$ | Dynamic Viscosity |

Subscripts

| | |
|---|---|
| cr | Critical |
| comp | Compressor |
| el | Electrical |

| | |
|---|---|
| i | property relative to the i-th experimental point |
| in | Inlet |
| int | Intermediate |
| is | Isentropic |
| L | Liquid |
| min | Minimum |
| max | Maximum |
| r | Ratio |
| red | Reduced |
| sat | Saturation |
| SH | Superheating |
| SV | Saturated Vapour |
| th | Thermal |
| v | property relative to the saturated vapour |
| vap | Vapour |
| vr | reduced property relative to the saturated vapour |
| wf | Working Fluid |

## 3.7 Bibliography


[1] T. Naegler, S. Simon, M. Klein, H.C. Gils, Quantification of the European industrial heat demand by branch and temperature level, Int. J. Energy Res. 39 (2015) 2019–2030. https://doi.org/https://doi.org/10.1002/er.3436.

[2] M. Rehfeldt, T. Fleiter, F. Toro, A bottom-up estimation of the heating and cooling demand in European industry, Energy Effic. 11 (2018) 1057–1082. https://doi.org/10.1007/s12053-017-9571-y.

[3] G. Alarnaot Alarnaout, J. Navarro-Esbrí, A. Mota-Babiloni, Operational, economic, and carbon footprint feasibility of a moderately-high-temperature heat pump as an alternative to conventional boilers in various scenarios, Energy Convers. Manag. 309 (2024) 118424. https://doi.org/https://doi.org/10.1016/j.enconman.2024.118424.

[4] H. Jouhara, A. Żabnieńska-Góra, B. Delpech, V. Olabi, T. El Samad, A. Sayma, High-temperature heat pumps: Fundamentals, modelling approaches and applications, Energy. 303 (2024) 131882. https://doi.org/https://doi.org/10.1016/j.energy.2024.131882.

[5] C. Arpagaus, F. Bless, M. Uhlmann, J. Schiffmann, S.S. Bertsch, High temperature heat pumps: Market overview, state of the art, research status, refrigerants, and application potentials, Energy. 152 (2018) 985–1010. https://doi.org/10.1016/j.energy.2018.03.166.

[6] C. Mateu-Royo, J. Navarro-Esbrí, A. Mota-Babiloni, M. Amat-Albuixech, F. Molés, Thermodynamic analysis of low GWP alternatives to HFC-245fa in high-temperature heat pumps: HCFO-1224yd(Z), HCFO-1233zd(E) and HFO-1336mzz(Z), Appl. Therm. Eng. 152 (2019) 762–777. https://doi.org/10.1016/j.applthermaleng.2019.02.047.

[7] C. Mateu-Royo, J. Navarro-Esbrí, A. Mota-Babiloni, F. Molés, M. Amat-Albuixech, Experimental exergy and energy analysis of a novel high-temperature heat pump with scroll compressor for waste

heat recovery, Appl. Energy. 253 (2019) 113504. https://doi.org/10.1016/j.apenergy.2019.113504.

[8] A.Y. Sulaiman, D.F. Cotter, K.X. Le, M.J. Huang, N.J. Hewitt, Thermodynamic analysis of subcritical High-Temperature heat pump using low GWP Refrigerants: A theoretical evaluation, Energy Convers. Manag. 268 (2022) 116034. https://doi.org/https://doi.org/10.1016/j.enconman.2022.116034.

[9] L. Wolscht, K. Knobloch, E. Jacquemoud, P. Jenny, Dynamic simulation and experimental validation of a 35 MW heat pump based on a transcritical CO2 cycle, Energy. 294 (2024) 130897. https://doi.org/https://doi.org/10.1016/j.energy.2024.130897.

[10] J. Liu, Y. Zhang, S. Yin, Y. Zhang, X. Luo, Z. Liu, Economic and exergy transmission analysis of the gas-liquid type compressed CO2 energy storage system, Renew. Energy. 230 (2024) 120891. https://doi.org/https://doi.org/10.1016/j.renene.2024.120891.

[11] W. Xu, P. Zhao, N. Ma, A. Liu, J. Wang, Design and performance analysis of a combined cooling, heating and power system: Integration of an isobaric compressed CO2 energy storage and heat pump cycle, J. Energy Storage. 91 (2024) 112146. https://doi.org/10.1016/j.est.2024.112146.

[12] Z. Liu, Y. Zhang, Y. Zhang, C. Su, Performance of a high-temperature transcritical pumped thermal energy storage system based on CO2 binary mixtures, Energy. 305 (2024) 132300. https://doi.org/10.1016/j.energy.2024.132300.

[13] K. Kontomaris, HFO-1336mzz-Z: High Temperature Chemical Stability and Use as A Working Fluid in Organic Rankine Cycles, Int. Refrig. Air Cond. Conf. (2014) 10.

[14] J. Navarro-Esbrí, A. Mota-Babiloni, Experimental analysis of a high temperature heat pump prototype with low global warming potential refrigerant R-1336mzz(Z) for heating production above 155 °C, Int. J. Thermofluids. 17 (2023). https://doi.org/10.1016/j.ijft.2023.100304.

[15] B. Dai, X. Liu, S. Liu, D. Wang, C. Meng, Q. Wang, Y. Song, T. Zou, Life cycle performance evaluation of cascade-heating high temperature heat pump system for waste heat utilization: Energy consumption, emissions and financial analyses, Energy. 261 (2022) 125314. https://doi.org/https://doi.org/10.1016/j.energy.2022.125314.

[16] D.B. Fox, D. Sutter, J.W. Tester, The thermal spectrum of low-temperature energy use in the United States, Energy Environ. Sci. 4 (2011) 3731–3740. https://doi.org/10.1039/C1EE01722E.

[17] L. Xin, C. Liu, L. Tan, X. Xu, Q. Li, E. Huo, K. Sun, Thermal stability and pyrolysis products of HFO-1234yf as an environment-friendly working fluid for Organic Rankine Cycle, Energy. 228 (2021) 120564. https://doi.org/10.1016/j.energy.2021.120564.

[18] J. Liu, Y. Liu, C. Liu, L. Xin, W. Yu, Experimental and Theoretical Study on Thermal Stability of Mixture R1234ze(E)/R32 in Organic Rankine Cycle, J. Therm. Sci. 32 (2023) 1595–1613. https://doi.org/10.1007/s11630-023-1790-2.

[19] F. Schlosser, S. Zysk, T.G. Walmsley, L. Kong, B. Zühlsdorf, H. Meschede, Break-even of high-temperature heat pump integration for milk spray drying, Energy Convers. Manag. 291 (2023) 117304. https://doi.org/https://doi.org/10.1016/j.enconman.2023.117304.

[20] S. Li, Z. Zhao, Y. Zhang, H. Xu, W. Zeng, Experimental and numerical analysis of condensation heat transfer and pressure drop of refrigerant r22 in minichannels of a printed circuit heat exchanger, Energies. 13 (2020). https://doi.org/10.3390/en13246589.

[21] E. Obika, F. Heberle, D. Brüggemann, Thermodynamic analysis of novel mixtures including siloxanes and cyclic hydrocarbons for high-temperature heat pumps, Energy. 294 (2024) 130858. https://doi.org/https://doi.org/10.1016/j.energy.2024.130858.

[22] J. Liu, F. Zhou, N. Lyu, H. Fan, X. Zhang, Analysis of low GWP ternary zeotropic mixtures applied in high-temperature heat pump for waste heat recovery, Energy Convers. Manag. 292 (2023) 117381. https://doi.org/https://doi.org/10.1016/j.enconman.2023.117381.

[23] J. Liu, L. Zhou, Z. Lin, X. Zhang, Performance evaluation of low GWP large glide temperature zeotropic mixtures applied in air source heat pump for DHW production, Energy Convers. Manag. 274 (2022)

116457. https://doi.org/https://doi.org/10.1016/j.enconman.2022.116457.

[24] S. Klute, M. Budt, M. van Beek, C. Doetsch, Steam generating heat pumps – Overview, classification, economics, and basic modeling principles, Energy Convers. Manag. 299 (2024) 117882. https://doi.org/https://doi.org/10.1016/j.enconman.2023.117882.

[25] IEA, IEA Annex 58, "enertime - High Temperature Heat Pump," (2023). https://heatpumpingtechnologies.org/annex58/wp-content/uploads/sites/70/2022/07/hthpannex58enertimetechnologyv2.pdf (accessed March 1, 2024).

[26] General Secretariat of the Council Delegations, Proposal for a Regulation of the European Parliament and of the Council on fluorinated greenhouse gases, amending Directive (EU) 2019/1937 and repealing Regulation (EU) No 517/2014, Brussels, 2002.

[27] L.G.T. Gaines, G. Sinclair, A.J. Williams, A proposed approach to defining per- and polyfluoroalkyl substances (PFAS) based on molecular structure and formula, Integr. Environ. Assess. Manag. 19 (2023) 1333–1347. https://doi.org/10.1002/ieam.4735.

[28] H. Abedini, E. Vieren, T. Demeester, W. Beyne, S. Lecompte, S. Quoilin, A. Arteconi, A comprehensive analysis of binary mixtures as working fluid in high temperature heat pumps, Energy Convers. Manag. 277 (2023) 116652. https://doi.org/https://doi.org/10.1016/j.enconman.2022.116652.

[29] G. Angelino, C. Invernizzi, General method for the thermodynamic evaluation of heat pump working fluids, Int. J. Refrig. 11 (1988) 16–25. https://doi.org/10.1016/0140-7007(88)90007-2.

[30] J. Burkholder, O. Hondnebrog, B. McDonald, V.L. Orkin, V. Papadimitriou, D. Van Hoomissen, SUMMARY OF ABUNDANCES, LIFETIMES, ODPs, REs, GWPs, GTPs, (2023). https://tsapps.nist.gov/publication/get_pdf.cfm?pub_id=936562.

[31] J.E. Mills, THE INTERNAL HEAT OF VAPORIZATION., J. Am. Chem. Soc. 31 (1909) 1099–1130. https://doi.org/10.1021/ja01940a001.

[32] D.R. Douslin, R.T. Moore, J.P. Dawson, G. Waddington, The Pressure-Volume-Temperature Properties of Fluorobenzene1, J. Am. Chem. Soc. 80 (1958) 2031–2038. https://doi.org/10.1021/ja01542a001.

[33] L.P. Filippov, Liquid thermal conductivity research at Moscow University, Int. J. Heat Mass Transf. 11 (1968) 331–345. https://doi.org/https://doi.org/10.1016/0017-9310(68)90161-0.

[34] S.P. Verevkin, V.N. Emel'yanenko, M.A. Varfolomeev, B.N. Solomonov, K. V. Zherikova, Vaporization enthalpies of a series of the fluoro- and chloro-substituted methylbenzenes, Fluid Phase Equilib. 380 (2014) 67–75. https://doi.org/10.1016/j.fluid.2014.07.029.

[35] V. Desreux, A study of the parachor, Bull. Des Sociétés Chim. Belges. 44 (1935) 249–287.

[36] D.W. Scott, J.P. McCullough, W.D. Good, J.F. Messerly, R.E. Pennington, T.C. Kincheloe, I.A. Hossenlopp, D.R. Douslin, G. Waddington, Fluorobenzene: Thermodynamic Properties in the Solid, Liquid and Vapor States; A Revised Vibrational Assignment1, J. Am. Chem. Soc. 78 (1956) 5457–5463. https://doi.org/10.1021/ja01602a001.

[37] M. Pasetti, C.M. Invernizzi, P. Iora, Thermal stability of working fluids for organic Rankine cycles: An improved survey method and experimental results for cyclopentane, isopentane and n-butane, Appl. Therm. Eng. 73 (2014) 764–774. https://doi.org/10.1016/j.applthermaleng.2014.08.017.

[38] G. Angelino, C. Invernizzi, Experimental investigation on the thermal stability of some new zero ODP refrigerants, Int. J. Refrig. 26 (2003) 51–58. https://doi.org/10.1016/S0140-7007(02)00023-3.

[39] S. Wang, K. Li, W. Yu, C. Liu, Z. Guan, Effects of non-condensable gas on thermodynamic performance of transcritical organic Rankine cycle, Energy. 292 (2024) 130513. https://doi.org/https://doi.org/10.1016/j.energy.2024.130513.

[40] J. Li, G. Gao, P. Li, G. Pei, H. Huang, Y. Su, J. Ji, Experimental study of organic Rankine cycle in the presence of non-condensable gases, Energy. 142 (2018) 739–753. https://doi.org/10.1016/j.energy.2017.10.054.

[41] E. Macchi, M. Astolfi, Organic Rankine Cycle (ORC) Power Systems: Technologies and Applications, 2016.

[42] A. Benato, M.R. Kærn, L. Pierobon, A. Stoppato, F. Haglind, Analysis of hot spots in boilers of organic Rankine cycle units during transient operation, Appl. Energy. 151 (2015) 119–131. https://doi.org/10.1016/j.apenergy.2015.04.055.

[43] C.M. Invernizzi, THERMAL STABILITY EVALUATION FOR RANKINE CYCLES WORKING FLUIDS: EXPERIMENTAL APPARATUS AND CALIBRATION RESULTS, La Termotec. N. 4 (1990) 69–76.

[44] University of Brescia, ERGO - Fluid Test Laboratory, https://ergo.unibs.it/research/fluid-test-laboratory.

[45] C.M. Invernizzi, P. Iora, G. Manzolini, S. Lasala, Thermal stability of n-pentane, cyclo-pentane and toluene as working fluids in organic Rankine engines, Appl. Therm. Eng. 121 (2017) 172–179. https://doi.org/10.1016/j.applthermaleng.2017.04.038.

[46] C. Invernizzi, M. Binotti, P. Bombarda, G. Di Marcoberardino, P. Iora, G. Manzolini, Water mixtures as working fluids in organic Rankine cycles, Energies. 12 (2019) 1–17. https://doi.org/10.3390/en12132629.

[47] S. Lasala, C. Invernizzi, P. Iora, P. Chiesa, E. Macchi, Thermal Stability Analysis of Perfluorohexane, Energy Procedia. 75 (2015) 1575–1582. https://doi.org/10.1016/j.egypro.2015.07.358.

[48] G. Di Marcoberardino, C.M. Invernizzi, P. Iora, A. Ayub, D. Di Bona, P. Chiesa, M. Binotti, G. Manzolini, Experimental and analytical procedure for the characterization of innovative working fluids for power plants applications, Appl. Therm. Eng. 178 (2020) 115513. https://doi.org/10.1016/j.applthermaleng.2020.115513.

[49] Sigma Aldrich, https://www.sigmaaldrich.com/IT/it (accessed February 28, 2024).

[50] S. Lecompte, O.A. Oyewunmi, C.N. Markides, M. Lazova, A. Kaya, M. Van Den Broek, M. De Paepe, Case study of an organic Rankine cycle (ORC) for waste heat recovery from an electric arc furnace (EAF), Energies. 10 (2017) 1–16. https://doi.org/10.3390/en10050649.

[51] A. Salogni, D. Alberti, M. Metelli, R. Bertanzi, Operation and maintenance of a biomass fired - Organic Rankine Cycle - CHP plant: The experience of Cremona, Energy Procedia. 129 (2017) 668–675. https://doi.org/10.1016/j.egypro.2017.09.141.

[52] F. Capra, E. Martelli, Numerical optimization of combined heat and power Organic Rankine Cycles - Part B: Simultaneous design & part-load optimization, Energy. 90 (2015) 329–343. https://doi.org/10.1016/j.energy.2015.06.113.

[53] M. Gaia, 30 Years of Organic Rankine Cycle Development, First Int. Semin. ORC Power Syst. (2011) 29. http://orc2011.fyper.com/uploads/File/presentations3/30 Years of ORC development.pdf.

[54] enertime, ORC SOLUTIONS FOR INDUSTRY, (2023). https://www.enertime.com/assets/documents/fiche-orc_ind_7-2023_fr.pdf (accessed February 5, 2024).

[55] A. Foresti, Turboden : ORC Solutions for Cogeneration and District Heating, 2015.

[56] Turboden, Turboden ORC Technology Stands Out in Waste Heat Recovery Cement Plants, (2018). https://www.turboden.com/company/media/press/press-releases/2157/turboden-orc-technology-stands-out-in-waste-heat-recovery-cement-plants (accessed March 11, 2024).

[57] R.L. Cole, J.C. Demirgian, J.W. Allen, Predicting toluene degradation in organic Rankine-cycle engines, in: United States, 1987. https://www.osti.gov/biblio/6414474.

[58] V. Havens, D.R. Ragaller, Study of toluene stability for an Organic Rankine Cycle (ORC) space-based power system, in: 1988. https://api.semanticscholar.org/CorpusID:107906670.

[59] Study of Toluene Stability for an Organic Rankine Cycle Space-Based Power System, (1988).

[60] D.M. Ginosar, L.M. Petkovic, D.P. Guillen, Thermal Stability of Cyclopentane as an Organic Rankine Cycle Working Fluid, (2011) 4138–4144.

[61] M. Preißinger, D. Brüggemann, Thermal stability of hexamethyldisiloxane (MM) for high-temperature Organic Rankine Cycle (ORC), Energies. 9 (2016). https://doi.org/10.3390/en9030183.

[62] L. Keulen, S. Gallarini, C. Landolina, A. Spinelli, P. Iora, C. Invernizzi, L. Lietti, A. Guardone, Thermal stability of hexamethyldisiloxane and octamethyltrisiloxane, Energy. 165 (2018) 868–876. https://doi.org/10.1016/j.energy.2018.08.057.

[63] OSHA's Hazard Communication Standard, Safety Data Sheet - Fluorobenzene, 2019. https://www.agilent.com/cs/library/msds/STS-160-1_NAEnglish.pdf (accessed March 12, 2024).

[64] E.P.B. Júnior, M.D.P. Arrieta, F.R.P. Arrieta, C.H.F. Silva, Assessment of a Kalina cycle for waste heat recovery in the cement industry, Appl. Therm. Eng. 147 (2019) 421–437. https://doi.org/https://doi.org/10.1016/j.applthermaleng.2018.10.088.

[65] ECRA, Technical Report A-2016/1039: Evaluation of the energy performance of cement kilns in the context of co-processing, (2017) 53.

[66] M. Astolfi, E. Macchi, Efficiency Correlations for Axial Flow Turbines Working With Non-Conventional Fluids, Asme Orc 2015. (2015) 1–12.

[67] D.Y. Peng, D.B. Robinson, A New Two-Constant Equation of State, Ind. Eng. Chem. Fundam. 15 (1976) 59–64. https://doi.org/10.1021/i160057a011.

[68] A. Salogni, D. Alberti, M. Metelli, R. Bertanzi, Operation and maintenance of a biomass fired - Organic Rankine Cycle - CHP plant: The experience of Cremona, Energy Procedia. 129 (2017) 668–675. https://doi.org/10.1016/j.egypro.2017.09.141.

[69] Aspen Technology Inc., Aspen Plus®, Version V12.1, (2022).

[70] A. Jaatinen-Värri, J. Honkatukia, A. Uusitalo, T. Turunen-Saaresti, Centrifugal compressor design for high-temperature heat pumps, Appl. Therm. Eng. 239 (2024) 122087. https://doi.org/https://doi.org/10.1016/j.applthermaleng.2023.122087.

[71] P. Ganesan, T.M. Eikevik, New zeotropic CO2-based refrigerant mixtures for cascade high-temperature heat pump to reach heat sink temperature up to 180 °C, Energy Convers. Manag. X. 20 (2023). https://doi.org/10.1016/j.ecmx.2023.100407.

[72] Y. Dong, R. Wang, When and how to use cascade high temperature heat pump—Its multi-criteria evaluation, Energy Convers. Manag. 309 (2024) 118435. https://doi.org/https://doi.org/10.1016/j.enconman.2024.118435.

[73] J. Spale, A. Hoess, I.H. Bell, D. Ziviani, Low-GWP Working Fluid Mixtures Screening for Industrial High Temperature Heat Pumps with Supply Temperature > 200 ° C Low-GWP Working Fluid Mixtures Screening for Industrial High Temperature Heat Pumps with Supply Temperature > 200 ° C, in: 20th Int. Refrig. Air Cond. Conf. Purdue, 2024.

# PART 2
# Experimental characterisation of $CO_2$ mixtures

*The Part 2 of the thesis deals with the experimental investigation of $CO_2$ mixtures as advanced working fluid for power cycles and high-temperature heat pumps, with a focus on the measurement of volumetric properties.*

*Chapter 4 is dedicated to the analysis of the $CO_2$+$SiCl_4$ binary mixture as potential working fluid for high-temperature power cycles, given the outstanding thermal stability of $SiCl_4$ as explored in Part 1. Vapour-liquid equilibrium measurements, in particular bubble points, of the mixture are obtained using a PVT apparatus during the visiting PhD period at the Centre for Energy Environment Processes (CEEP) in Fontainebleau (France). Moreover, a vibrating tube densimeter has been used to measure liquid densities of the mixture, and to provide additional bubble point data through an innovative approach. The research is funded by DESOLINATION project.*

*Chapter 5 explores the use of the $CO_2$+$C_2Cl_4$ binary mixture as working fluid for high-temperature heat pumps adopting a transcritical cycle. Thermal stability of $C_2Cl_4$ is tested at the Fluid Test Laboratory of the University of Brescia, while liquid densities of the mixtures are measured during the visiting PhD period at the Centre for Energy Environment Processes (CEEP). The work is funded by HICLOPS and COFFEE projects.*

*Chapter 6 explores the new apparatus developed at Fluid Test Laboratory of the University of Brescia to test vapour-liquid equilibrium conditions of mixtures, with a focus on bubble points. The apparatus and methodology is validated by measuring two $CO_2$ binary mixtures whose phase behaviour is known from literature data, and bubble points of $CO_2$+c-$C_4F_8$ mixture are measured for the first time in literature.*

# *Chapter 4 - Investigation on $CO_2$+$SiCl_4$ mixture*

*THIS CHAPTER IS BASED ON THE ARTICLE: "EXPERIMENTAL INVESTIGATION OF THE $CO_2$+$SICL_4$ MIXTURE AS INNOVATIVE WORKING FLUID FOR POWER CYCLES: BUBBLE POINTS AND LIQUID DENSITY MEASUREMENTS", PUBLISHED IN ENERGY, ELSEVIER, DOI: HTTPS://DOI.ORG/10.1016/J.ENERGY.2024.131197*


**Abstract**

Supercritical $CO_2$ is recognized as a promising working fluid for next-generation of high temperature power cycles. Nevertheless, the use of $CO_2$ mixtures with heavier dopants is emerging as a promising alternative to supercritical $CO_2$ cycles in the recent years for air-cooled systems in hot environments. Accordingly, this work presents an experimental campaign to assess the thermodynamic behaviour of the $CO_2$+$SiCl_4$ mixture to be used as working fluid for high-temperature applications, conducted in the laboratories of CEEP Mines Paris PSL. At first, bubble conditions of the mixture are measured in a variable volume cell (PVT technique), then liquid densities are measured with a vibrating tube densimeter, for molar composition in the range between 70% and 90% of $CO_2$. The Peng Robinson EoS was fine-tuned on the bubble points obtained, resulting in a satisfactory accuracy level. Finally, a non-conventional methodology has been developed to measure bubble points with the vibrating tube densimeter, whose results are consistent with the VLE data obtained with the standard PVT technique. Thermodynamic analysis in next-generation concentrated solar power plant, at 700°C turbine inlet, confirms the mixture overcomes 50% thermal efficiency, providing +4.2% net electrical output over pure supercritical $CO_2$ at equal thermal power from the solar field.


## 4.1 Introduction

Starting from the theoretical conceptualization of supercritical $CO_2$ ($sCO_2$) power cycles attributed to Angelino [1] and Feher [2], a renewed and growing interest in this technology has been experienced in the last decade, especially to replace the state-of-the-art steam Rankine cycle in innovative categories of power generation systems. In particular, $sCO_2$ as working fluid is considered attractive in high-temperature applications such as nuclear [3], concentrated solar power (CSP) [4][5], hybrid plants [6], and high-temperature waste heat and heat recovery [7][8][9], mainly due to high thermodynamic efficiencies, also at part load conditions [10].

However, when considering applications with air-cooled heat rejection units (HRU) in environments with high average ambient temperatures, such as CSP locations, the effectiveness of $sCO_2$ cycles is negatively influenced by the higher compressibility factor of the $CO_2$ across the compression step, caused by the high compression inlet temperature (up to 50°C). High values of cycle minimum temperature can also be adopted for cogeneration purposes, in order to deliver heat to a thermal user such as for district heating networks [11] or thermal desalination plants [12].

For this reason, H2020 European-funded projects such as the SCARABEUS project [13] and the DESOLINATION project [14] identified a possible solution to increase the cycle efficiency by varying the working fluid itself: in this circumstance the working fluid remains liquid across the

whole compression step, entailing a low mechanical power consumption at any cycle minimum temperatures. To do so, $CO_2$-based mixtures are adopted in power cycles as working fluids: by mixing $CO_2$ with a dopant characterized by a high critical temperature it is possible to turn the supercritical cycle into a transcritical one. This solution can allow an increment of cycle efficiency with respect to $sCO_2$ cycles, especially when the cycle minimum temperature is as high as 50°C (with ambient temperatures around 35°C) [15]. The dopant molar fraction represents an additional degree of freedom of the power block which allows for the maximization of the electrical efficiency: depending on the specific dopant and power block layout the optimal mixture compositions can be found in the 70-90% range of $CO_2$ molar content [16]. For this reason, in this work, the $CO_2$ mixture is experimentally investigated in the above-mentioned composition range.

One of the most challenging factors that limits the widespread of the $sCO_2$ cycle technology is the design, manufacturing and operation of the main compressor: it must be designed to specifically work with $CO_2$ in near-critical conditions at its intake, where small temperature fluctuations can lead to non-negligible density variations and to the risk of the onset of liquid droplets as a consequence of the local acceleration near the blades leading edge [17].

On the other hand, the technological development of pumps operating with $CO_2$-based mixtures in liquid conditions theoretically appears as a minor technological challenge as attested by the pump manufactures involved in the H2020 DESOLINATION project [18]. Nevertheless, even if the compression of a liquid can be easier than a near-critical point compression of a supercritical fluid, a solid knowledge of the thermodynamic properties of the compressed flow is still necessary when innovative working fluids are considered (as binary mixtures with $CO_2$).

While selecting a $CO_2$-based mixture to be used as working fluid, a fundamental aspect in the dopant selection is its thermal stability, important to avoid decomposition products across the cycle that can lead to component malfunctions, accumulation of non-condensable products as well as engine blockage. The identification of fluids whose chemical bonds are not subjected to dissociation or isomerization reactions above 550°C (i.e. the state-of-the-art maximum temperature for CSP plants with solar salts) is a challenging task. In fact, is it well-known that the maximum operating temperatures of the fluids commercially employed in Organic Rankine Cycles (ORC) is below 300-350°C due to thermal stability issues [19]. For example, Siloxanes can be safely adopted in ORCs up to 260°C [20], with acceptable decomposition rates, while hydrocarbons can operate near 300°C [19] as maximum temperature. $CO_2$ binary mixtures with refrigerants have been studied by Sánchez and da Silva [21] for geothermal application, by Dai et al. [22] for low-grade heat conversion, as well as by Yao et al. [23] in medium-temperature waste heat recovery considering a maximum turbine inlet temperature of 360°C. However, most of refrigerants cannot be considered as $CO_2$ dopant in state-of-the art CSP tower plants since refrigerants chemically decompose at temperatures lower than 425°C [24] due to C-H bond cleavage. A $CO_2$+propane binary mixture was investigated by Ma et al. [25] and Niu et al. [26] in CSP application at 550°C turbine inlet temperature, presenting promising results at temperatures above the ones for conventional applications of propane.

Nevertheless, within the SCARABEUS and DESOLINATION frameworks, this ambitious target of 550°C has been reached by a handful of mixtures: for example, the $CO_2$ mixture with hexafluorobenzene ($C_6F_6$) was demonstrated to be thermally stable below 600°C [8] in an Inconel 625 alloy vessel for 100 hours.

Focusing strictly on CSP, the target for next-generation solar tower plants is set at operating with cycle maximum temperatures up to 700°C [27][28], posing further challenges on the identification of thermo-chemically stable dopants. In this direction, sulphur dioxide ($SO_2$) has been identified [29] within the SCARABEUS project as potential $CO_2$ dopant, and the associated efficiency gain compared to pure $CO_2$ is proved also by Tafur-Escanta et al. [30]. Also titanium tetrachloride ($TiCl_4$) has been considered in past years both as potential $CO_2$ dopant [31] in the SCARABEUS project, for the 700°C level, and as a pure fluid for high-temperature Rankine cycles [32]: since it is industrially oxidized at very-high temperatures (1500-2000 K) to produce $TiO_2$ [33], its thermal stability has been preliminary taken for granted in applications with maximum temperatures levels of 700°C.

Similarly to $TiCl_4$, Silicon Tetrachloride ($SiCl_4$) has the same tetrahedral structure and a remarkably high thermal stability, considering the various industrial processes where it is commonly adopted [34][35]. Both metal tetrachlorides are not flammable but they hydrolyse under exposure with humid air, decomposing in hydrochloric acid (HCl): nevertheless, the kinetic of the decomposition process is much slower in case of $SiCl_4$, as observed during the experimental tests presented in this work, justifying the interest in this fluid for industrial applications if compared to $TiCl_4$. Consequently, this work analyses the thermodynamic properties of the $CO_2$+$SiCl_4$ mixture, potentially to be adopted as working fluid for very-high temperature transcritical power cycles with high minimum temperature. Silicon Tetrachloride was produced in the past by reacting $SiO_2$ and chlorine at 1300°C [36]. According to reports, the pure form remains thermally stable even at 1200°C and it is much less reactive than $TiCl_4$ [37]. Approximatively 18-20 tons [38] of $SiCl_4$ are produced as by-product per ton of solar-grade silicon, reflecting the high market availability, the low cost, and the maturity of the industrial sector in handling this chemical component.

The objective of this research is to experimentally investigate the thermodynamic properties of the $CO_2$+$SiCl_4$ mixture as a novel working fluid for high-temperature power cycles. The primary aim is to assess the phase behaviour of the binary system, which is essential for determining thermodynamic conditions, designing components, and analysing off-design scenarios. Secondly, liquid density data of the mixture are necessary for future pump design and manufacturing.

The methodology involves conducting experimental studies to measure vapor-liquid equilibrium (VLE) data and liquid densities of the mixture. Two different apparatuses are employed: a Pressure-Volume-Temperature (PVT) apparatus for measuring bubble points and a vibrating tube densimeter (VTD) [39][40][41] for determining liquid densities across a wide pressure range.

Starting from the experimental data, an optimization procedure for a cubic Equation of State (EoS) is proposed. This involves fitting the binary interaction parameter (BIP) of the mixture using the Peng Robinson EoS [42], ensuring consistency across the different compositions measured.

Additionally, a non-conventional approach is developed to measure bubble points using vibrating tube densimeter. This approach provides data consistent with conventional method, validating the overall experimental methodology.

Finally, cycle calculations with fine-tuned EoS are performed to assess the performance of the $CO_2$+$SiCl_4$ mixture in next-generation CSP applications, at 700°C maximum cycle temperature. These calculations are part of the H2020 DESOLINATION project, aiming to assess the potential advantages of the mixture over pure $sCO_2$ in terms of cycle thermal efficiency.

## 4.2 Experimental campaign for mixture characterisation: methodology and measurements

### 4.2.1 PVT apparatus: bubble points measurements

The bubble points reported in this work for the $CO_2$+$SiCl_4$ mixture have been measured at the Centre for Energy Environment Processes (CEEP) of Mines Paris PSL in Fontainebleau, France, using the experimental apparatus previously presented by Neyrolles [43] and schematically reported in Figure 1: it includes a variable volume cell (PVT), used to measure bubble points of pressurized mixtures as an alternative to a conventional and more complex VLE cell, equipped with a composition analysis system.

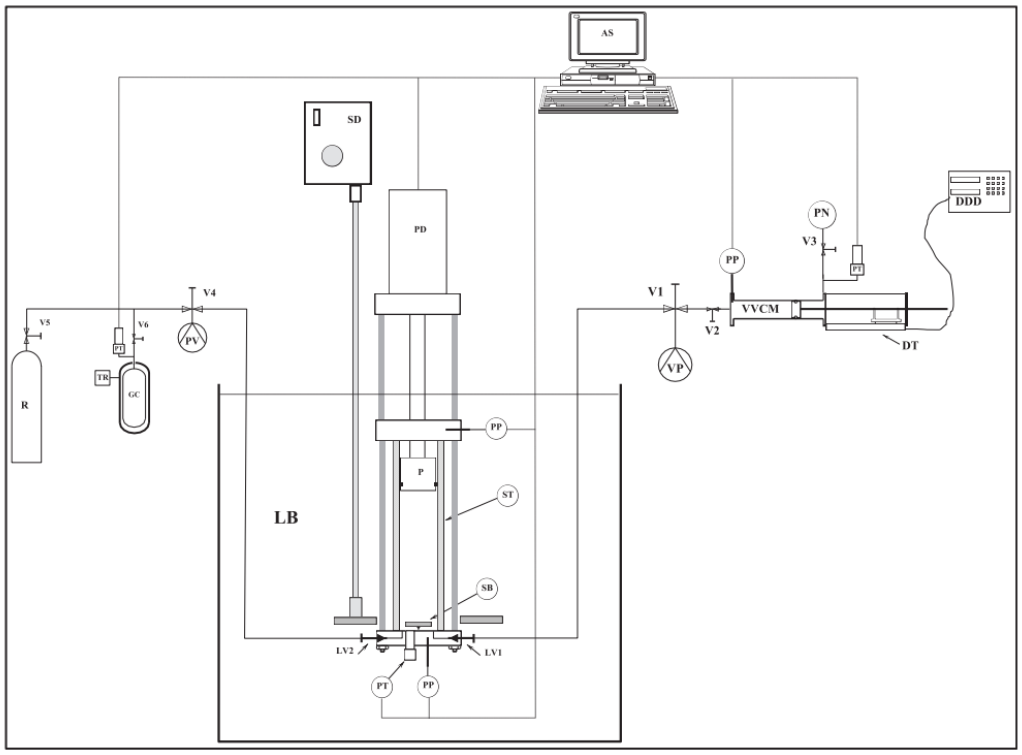


*Figure 1. Flow diagram of the apparatus. DDD: Digital Displacement Display; DT: Displacement Transducer; GC: Gas Cylinder; LB: Liquid Bath; LVi: Loading Valve; P: Piston; PD: Piston Monitoring; PN: Pressurized Nitrogen; PP: Platinum Probe; PT: Pressure Transducer; PV (VP): Vacuum Pump; R: Gas Reservoir; SD: Stirring Device; SB: Stirring Bar; ST: Sapphire Tube; TR: Thermal Regulator; Vi: Valve; VVCM: Variable Volume Cell with mechanical displacement of the piston. [43]*

An accurate description of the PVT test rig adopted is proposed by Neyrolles [43] and it is summarized in this work. The core of the apparatus is a variable volume equilibrium cell consisting of a sapphire tube held between two titanium flanges with suitable O-rings. The volume of the cell can be varied by controlling the position of a piston in the upper part of the cell. The piston position is controlled by a motorized lead screw actuator from Thomson®. A Kollmorgen controller is used to precisely control the downward climb of the piston in the cell. The pressure and the temperature, as well as the piston position, are monitored in continuous. A 100 Ω platinum thermoresistance (PT-

100) is adopted to measure the temperature in the lower part of the cell; the temperature sensor has been calibrated in comparison with a reference 25 Ω platinum probe (Tinsley, France), and the resulting accuracy is estimated to be ±0.03 K. The pressure is measured with a cryogenic miniature ruggedized Kulite pressure transducer placed at the bottom of the cell. The pressure transducer is calibrated with a precision pressure controller (Pace 5000 by Druck) in the range from 2 to 110 bar, and the resulting average accuracy was estimated to be ±26 mbar at the temperatures of interest. The measurements are carried out in isothermal conditions, since the cell is placed in a thermostatic water-based Tamson bath and the temperature set-point is guaranteed by a PID controller. The equilibrium conditions of the mixture in the cell are favoured by the presence of a corrosion-resistant magnetic stirrer placed at the cell bottom, which is controlled by an external agitator placed inside the bath. The mixture of $CO_2$ with $SiCl_4$ was vented under hood after neutralization into a water and Sodium Hydroxide (NaOH) solution to avoid the formation of HCl.

A detail of the variable volume cell can be visualized in Figure 2: the piston and the sapphire cell are visible in the centre, the two agitators (one inside the cell and the second one, the actuator, out of the cell) in the bottom.

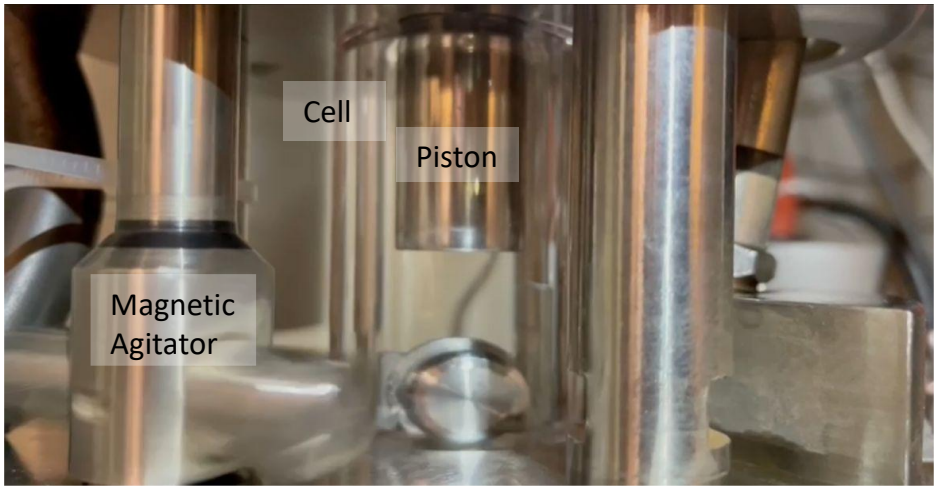


*Figure 2. High-pressure liquid mixture of $CO_2$+$SiCl_4$ after charging into the PVT cell, with agitation active.*

Figure 3 provides a better understading of the procedure adopted to identify each bubble point of the mixture with the PVT apparatus. At isothermal conditions, the position of the piston and the stabilized pressure inside the cell are recorded and plotted, as shown in Figure 3, for a particular mixture composition and bath temperature.

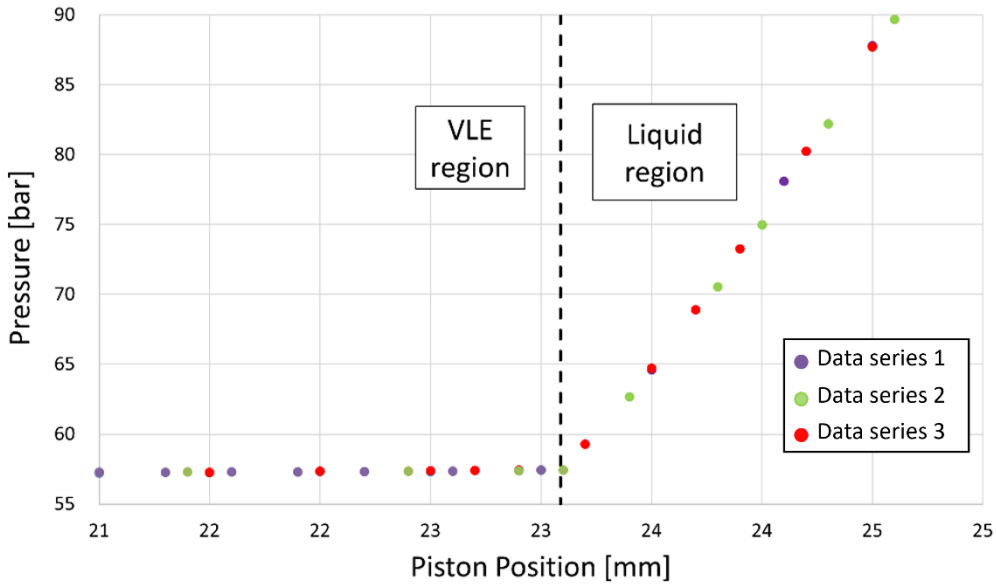


*Figure 3. PVT acquisitions for 80.2% molar $CO_2$+$SiCl_4$ at 35°C; different colours represent different series of measurements.*

The pressure variation measured in the cell is very significant if the mixture is at liquid conditions, where the mixture compressibility is very limited. On the other hand, in the VLE region, the pressure of the mixture is little sensitive to the volume variation because its effect on the pressure is compensated by the high compressibility of the gas phase. From the intersection of the two straight lines regressing the stabilized pressures as function of the piston displacement, detailing the pressure-volume behaviour of the mixture in both conditions (VLE and subcooled liquid), it is possible to determine the bubble pressure at the given fixed test temperature and mixture composition. Each bubble point (P,T,x) is experimentally evaluated at least three times in the PVT apparatus, both starting from the liquid and the VLE conditions: the different colours of the dots in Figure 3 represent different measurement series. Each point in Figure 3 represents a condition at which the piston position has been maintained fixed until the pressure is stabilized.

The experimental bubble points of the $CO_2$+$SiCl_4$ mixture are reported in Supplementary Materials and represented in Figure 4, taken in a composition range (80%-90%) that are of interest for the application of the mixture as working fluid in a transcritical power cycle. For each composition, the bubble pressure has been measured at four temperatures (35°C, 50°C, 60°C, 70°C). In particular, bubble pressures at 50°C and above are representative of bubble conditions at pump inlet of air-cooled power cycles in hot environments. The uncertainties on the temperature and the bubble pressure measured are reported together with the experimental values in Supplementary Materials.

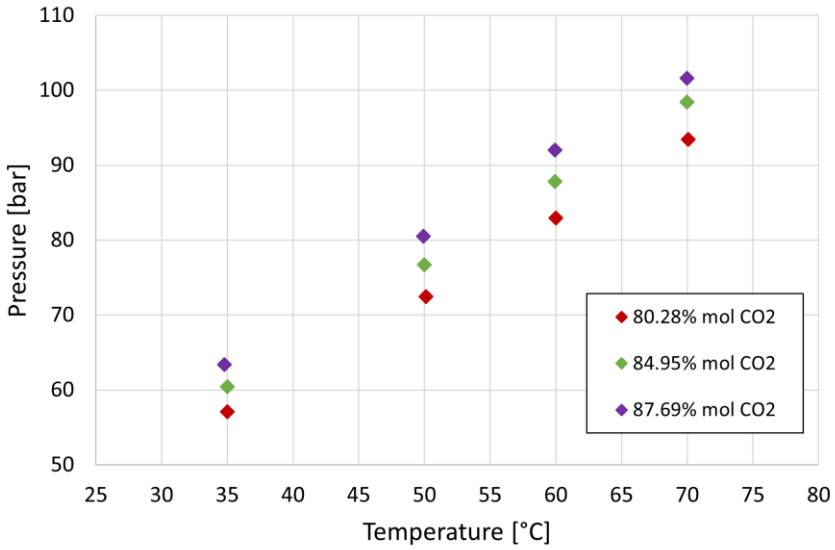


*Figure 4. Experimental bubble points for the mixture $CO_2$+$SiCl_4$.*

### 4.2.2 Vibrating Tube Densimeter

Liquid density measurements of the $CO_2$+$SiCl_4$ mixture have been obtained at the laboratory of the Centre for Energy Environment Processes (CEEP) of Mines Paris PSL by using a vibrating tube densimeter (VTD), which core is an Anton Paar DMA HPM, as described in literature [44]. The scheme of the apparatus is shown in Figure 5.

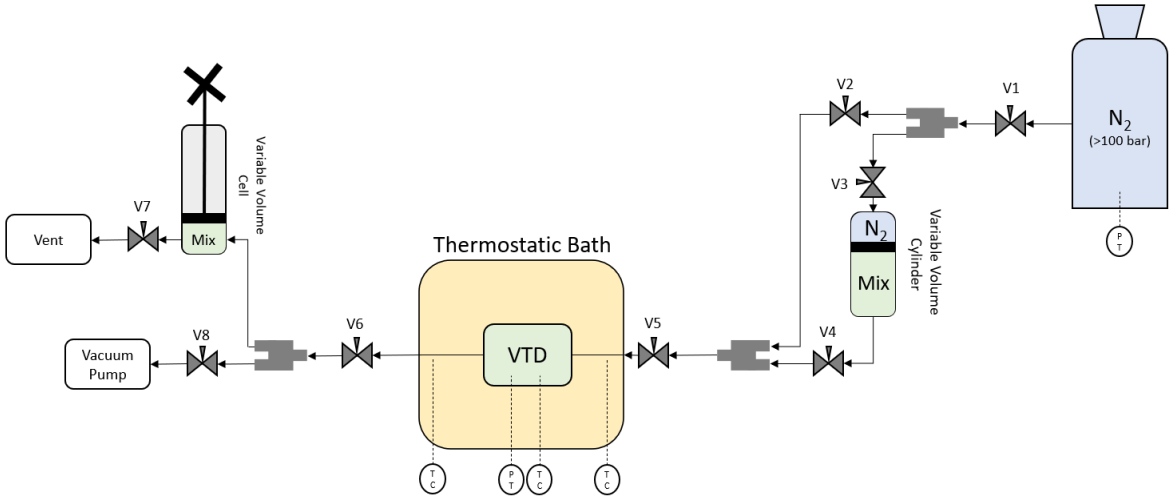


*Figure 5. schematization of the test-rig adopted with the vibrating tube densimeter.*

The measurement procedure consists in determining the density of the liquid mixture from the variation of the vibration period of a U-shaped tube when it is filled with the fluid with respect to when it is at vacuum conditions. In order to convert the vibration period into density values, the vibration period of the tube filled with a fluid with a known density must be measured in the same experimental apparatus to define a correlation between the vibration period and the density. As this

relation is temperature-dependent, this calibration must be carried out at each temperature of interest.

The VTD is immersed in a thermostatic liquid bath to maintain its temperature at a target value during the measurements. The operating range of the densimeter is from -10°C to 200°C in temperature, and over 1000 bar in pressure. The vibrating tube is made in Hastelloy, and its temperature is controlled by a heat transfer fluid flowing in a jacket with a temperature stability of 0.02°C. Additional information about the VTD adopted can be found in a previous literature work [39]. During the operation and before arriving at the bubble point condition, reached by expanding the fluid from subcooled liquid conditions, the temperature of the thermostatic bath is kept around 0.2°C lower than the heat transfer fluid flowing in the jacket of the densimeter, since the first bubble of $CO_2$-mixture must occur precisely into the vibrating tube.

A detail of the apparatus (the variable volume cylinder, the open thermostatic bath, and the pressure transducers of the VTD) is also proposed in Figure 6.

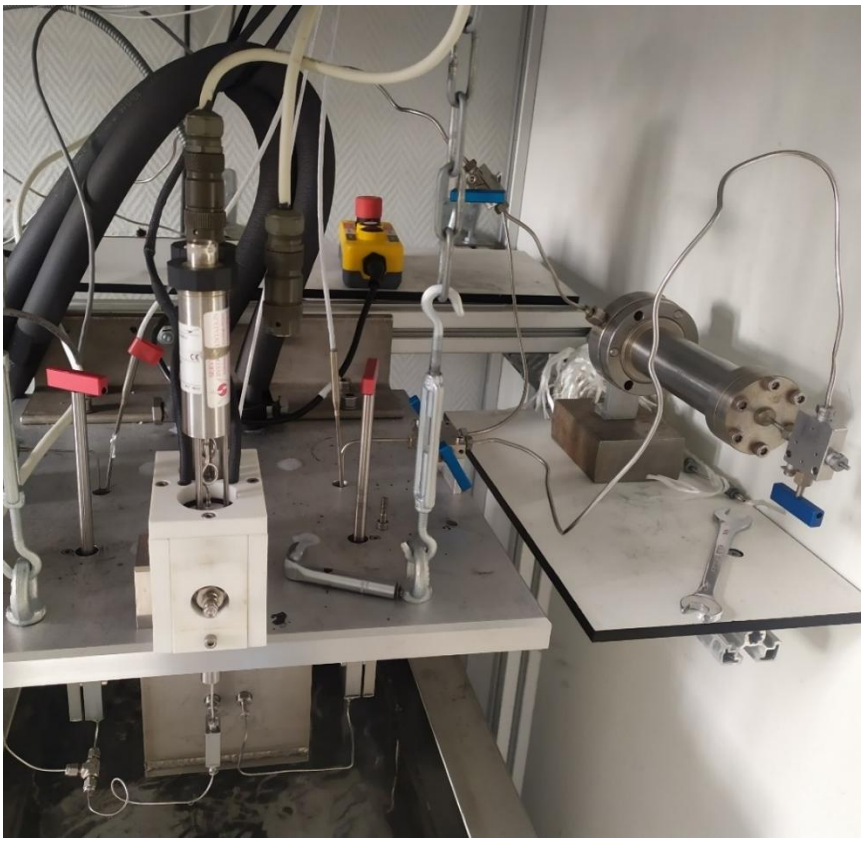

*Figure 6. Detail of the VTD apparatus, with the pressurized cylinder containing the mixture (on the right side), the red valves corresponding to the inlet/outlet valve of the VTD, the pressure transducers on the top, and the vibrating tube in its jacket above the free surface of the thermostatic bath.*

The variable volume cell at the outlet of the VTD has been added to manually modify the density (and the pressure) of the measured fluid in the vibrating tube, without influencing the mixture in the variable volume cylinder: the modification has been proposed specifically for mixtures, since it is crucial to definitively fix the composition of the measured fluid, for various pressure levels. Accordingly, the position of the piston of the variable volume cell is manually modified (with valve

V6 open) to match the pressure in the VTD to the desired value: once equilibrium is reached the valve V6 is closed and another acquisition can be carried out, at the same temperature but different pressure than the previous ones.

The described procedure is followed for each temperature at which measurements are carried out.

It is important to underline that the specific experimental set-up described in this work, with a variable volume cell before the venting of the mixture, is adopted to specifically measure the density of a binary mixture composed by two compounds with very different volatility. In this setup, the volume can be opportunely varied with a manual hip-pump. On the other hand, the most commonly adopted set-up to analyze the density of pure fluids or non-complex mixtures does not include the variable-volume cell at the VTD outlet (between V6 and the vent valve V7). With the conventional setup, after charging the mixture from high-pressure liquid conditions into the system, the vent valve (V7) is opened for a continuous evacuation (several seconds). This approach can be used because, when charging the pressurized mixture into the VTD at vacuum conditions, an initial flash is unavoidable: homogeneous mixture conditions are then reached by a continuous evacuation of the mixture through the vent valve. However, within this work it has been found out that subsequent sets of measurements of the same mixture (after venting it) were not repeatable due to a composition variation caused by the mixture flash after venting. For this reason, it was decided to collect the initial flash in the variable volume cell, instead of venting it out with the risk of compromising the mixture's composition inside the VTD.

### 4.2.3 VTD: liquid density measurements

Densities are determined by calibrating the vibrating tube period (τ) with the known density of pure carbon dioxide (adopted as reference fluid) at 40°C, 60°C and 80°C, with a linear correlation as reported in Equation 1:

$$\rho|_T = f\,(\tau)_T = A \cdot \tau + B \qquad (1)$$

To build the correlation of Equation 1 for each temperature, the results of the equation of state by Span and Wagner [45] have been assumed as reference values to be associated with the measured vibrating periods, computing the numerical values of A and B for each temperature investigated with a linear interpolation. The uncertainty range of the Span and Wagner EoS with respect to $CO_2$ density ranges from 0.03% to 0.05% at pressures up to 30 MPa and temperature up to 523 K.

Three compositions of the $CO_2$+$SiCl_4$ mixture have been tested in the VTD: the results are reported in Supplementary Materials and shown in Figure 7.

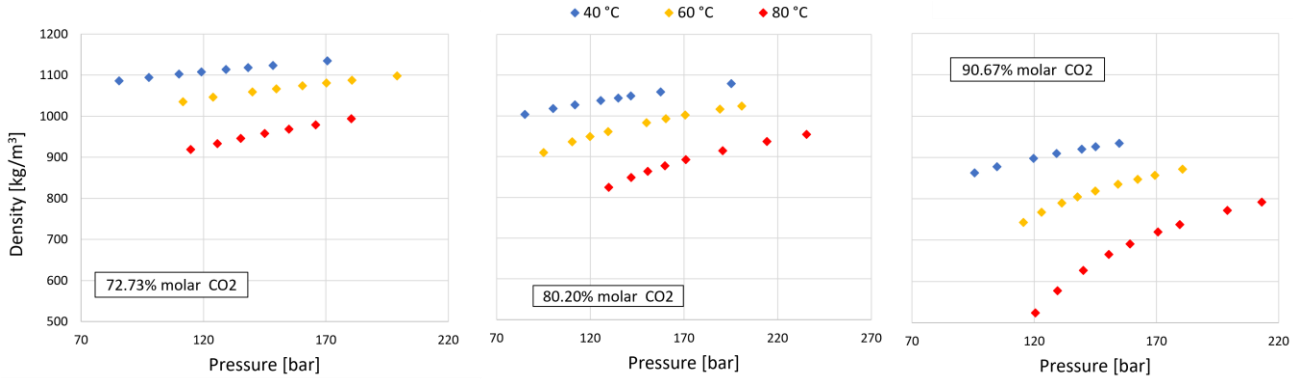


*Figure 7. experimental liquid densities of $CO_2$+$SiCl_4$ mixture at different compositions at three different temperatures.*

For each series of measurements, at isothermal conditions, the minimum pressure investigated was chosen around 20 bar above the expected bubble or dew pressure at the tested temperature, in order to avoid the onset of vapour-liquid conditions. In addition, by varying the volume of the variable volume cylinder (in Figure 5) with the hip-pump it was possible to investigate pressures above the one of the pressurized cylinder of the mixture.

### 4.2.4 VTD: bubble points measurements with innovative procedure

While analysing the $CO_2$+$SiCl_4$ mixture in the densimeter, a set of bubble points has been also determined with an innovative method. The operating principle that allows for the determination of the bubble condition using the VTD relies on the drastic variation of the oscillation period of the tube occurring while entering in the two-phase region starting from a condition of single-phase liquid at high pressure.

Two different procedures were adopted to reduce the pressure in the VTD and to approach the bubble pressure at isothermal conditions: both (i) by acting on the vent valve (V7 in Figure 5), and alternatively (ii) by increasing the available volume of the mixture through the hip-pump variable-volume at the outlet of the system. The main difference between the two techniques is that in the first case there is a continuous mass flow in the system, while in the second option the mass flow is intermittent due to discontinuous volume variation.

An example of the bubble onset identification by acting on the vent valve V7 is represented in Figure 8, monitoring the pressure and the vibrating tube oscillation period along the timespan considered. The pressure is reduced within the tube by around 0.05 bar per second, on average, controlling the needle valve at the vent. As the pressure reduces slowly down to the bubble condition at the set temperature, the oscillating period rapidly increases because of the formation of the vapour-phase that rapidly migrates towards the vent while the U-tube is enriched by the heavier liquid phase.

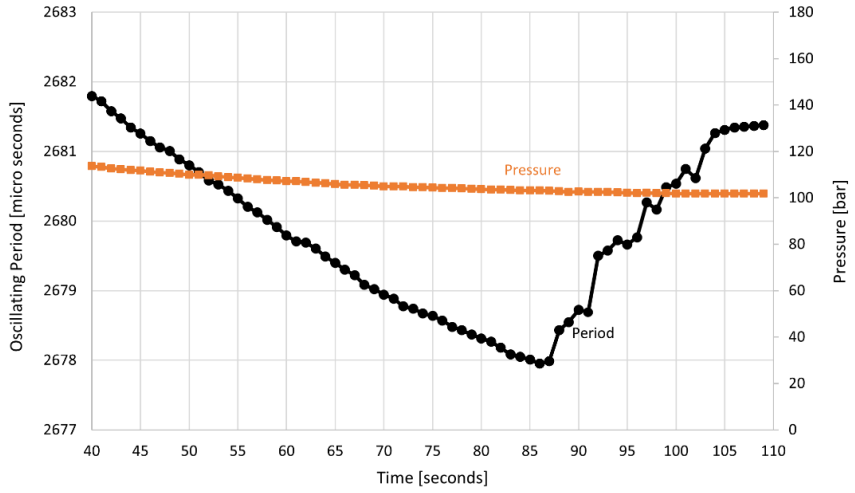


*Figure 8. Example of bubble point determination at the VTD acting on the vent valve.*

On the other hand, in Figure 9 is proposed the determination of the bubble point of the mixture using the second procedure (manual hip-pump).

In this case, the bubble point can be more easily visualised due to a drastic drop in the oscillating period: the formation of a less-dense vapour phase rich in $CO_2$ accumulates into the tube and the period decreases consequently. At the same time, the local pressure increases since the volume occupied by the vapour phase increases. After a few seconds, acting on the hip-pump, the vapour phase tends to migrate from the tube to the variable-volume at the tube outlet, located at a higher geodetic level. Finally, due to the migration of the vapour-phase outside the tube, the fluid inside the tube remains the liquid phase that is rich in the dense dopant ($SiCl_4$) and the period starts increasing again.

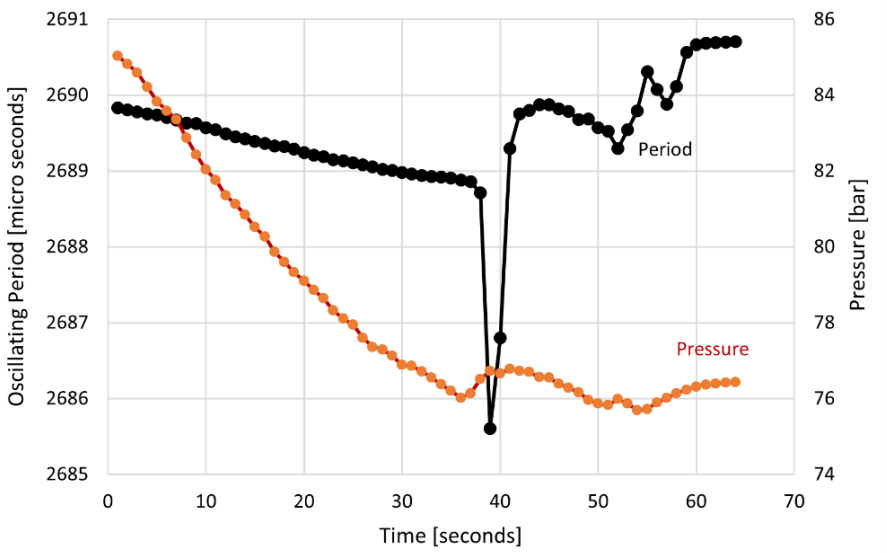


*Figure 9. Example of bubble point determination at the VTD acting on the manual hip-pump.*

The pressure reduction in the U-tube is less pronounced by using the vent valve than the hip-pump, resulting in a higher accuracy of the identified bubble pressure.

Even if the proposed approach strongly depends on the manual capacities of the operator dealing with the valve or the hip-pump, the collected data can also be treated in a semi-quantitative way by using the first or second derivative of the oscillating period against time. In particular, the bubble points at the VTD have been identified as stationary point or inflection point of the oscillating period, depending on the procedure used. An example of identification of the instant in which the first bubble forms within the U-tube can be found in Figure 10, where the bubble onset is presented as a stationary point of the oscillating period with respect to the sampling time.

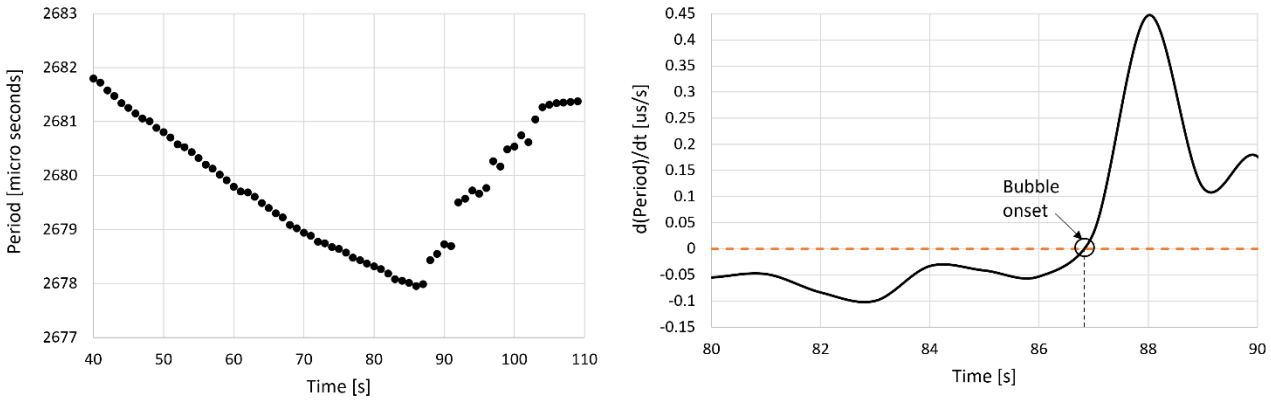


*Figure 10. Example of identification of the bubble point onset from the first derivative of the oscillating period against time.*

The bubble points obtained with the VTD apparatus are reported in Supplementary Materials. The consistency of these additional points is validated in the following section.

### 4.3 Modelling and Discussion

Reliable thermodynamic models are necessary to calculate the properties of binary mixtures along the thermodynamic regions of interest for the closed thermodynamic cycle. In the last decades, cubic EoS such as the Peng Robinson (PR) [42] and Soave-Redlich-Kwong (SRK) [46] have become consolidated choices, especially in the industry [47] [48]. Accordingly, in this work the original PR EoS [42] has been considered for a preliminary post-processing of the experimental data and thermodynamic analysis of the $CO_2$+$SiCl_4$ mixture. The PR EoS is expressed as in Eq. 2-6:

$$P = \frac{RT}{v-b} - \frac{\alpha a}{v(v+b)+b(v-b)} \tag{2}$$

where the alpha function adopted is in its original form [42]:

$$\alpha = \left[1 + k\left(1 - \sqrt{T_r}\right)\right]^2 \tag{3}$$

$$k = 0.37464 + 1.54226\omega - 0.26992\omega^2 \tag{4}$$

$$a = 0.45724 \frac{R^2 T_{cr}^2}{P_{cr}} \quad (5)$$

$$b = 0.0778 \frac{R T_{cr}}{P_{cr}} \quad (6)$$

Van der Waals mixing rules are then adopted to describe the binary mixture.

The EoS parameters of the chemical species studied in this work are reported in Table 1.

*Table 1. Parameters used in the EoS (default values in ASPEN [49] Properties).*

| Fluid | Critical temperature [°C] | Critical pressure [bar] | Pitzer's acentric factor ω [-] |
|---|---|---|---|
| $CO_2$ | 31.06 | 73.83 | 0.2236 |
| $SiCl_4$ | 233.85 | 35.9 | 0.2318 |

The binary interaction parameter (BIP) of the mixture has been regressed on the measured bubble points of the $CO_2$+$SiCl_4$ mixture. As a matter of fact, the accurate calibration of the EoS on VLE data is widely accepted in scientific literature as the best way to approach, at least at the first stage, the optimization of the EoS. The BIP regression is performed within the software ASPEN Properties v12 [49], using the maximum likelihood method as numerical optimization method. Even if bubble points have been obtained also with the VTD, the regression is carried out only considering the data measured with the PVT apparatus. In order to assess the accuracy in fitting the VLE properties, the average absolute deviation percentage (AAD%) was chosen as an index to quantify the accuracy of the EoS in representing the experimental data. The AAD is computed in this work as shown in Equation (7), where $P_{exp}$ is the measured pressure, $P_{calc}$ is the pressure calculated by using the EoS, and N is the number of experimental data considered:

$$AAD_{Pbubble}[\%] = \frac{100}{N} \cdot \sum_{i=1}^{n} \left| \frac{P_{exp} - P_{calc}}{P_{exp}} \right| \quad (7)$$

Table 2 reports the binary interaction parameter ($k_{ij}$) obtained by the data regression in ASPEN Plus v12 and the AAD% computed on the bubble pressure for each temperature, along with an overall average AAD% on all conditions. The Britt–Luecke algorithm [50] with Deming [51] initialization method was applied to regress the parameter.

*Table 2. Binary interaction parameter regressed and AAD% of the PR EoS for $CO_2$+$SiCl_4$ mixture.*

| EoS | $k_{ij}$ | AAD: bubble pressure | | | | |
|---|---|---|---|---|---|---|
| | | 35°C | 50°C | 60°C | 70°C | Global |
| PR | 0.06098 ±0.00338 | 0.57% | 0.56% | 0.56% | 1.00% | 0.68% |

The PR EoS with optimized binary interaction parameter can represent the VLE data of this mixture, obtained with PVT apparatus, with good precision, as indicated by the AAD%. In Figure 11, the experimental bubble data from this work are shown as diamonds, while the resulting VLE curves obtained by the PR EoS with the regressed BIP are shown as solid lines.

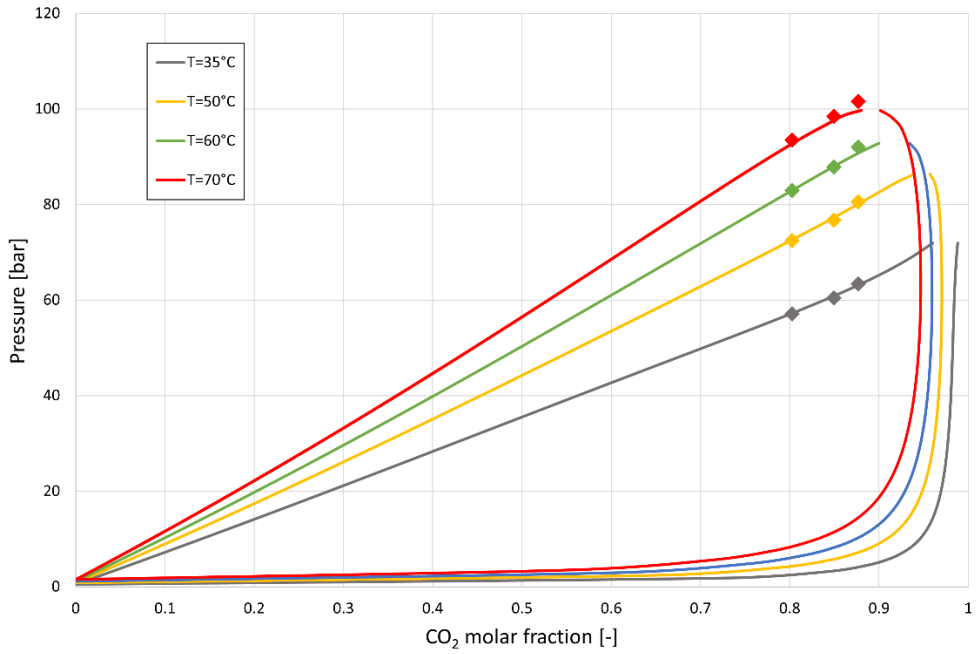


*Figure 11. Pressure-composition diagram of $CO_2$+$SiCl_4$ mixture with the optimised PR EoS (solid lines) at the four isothermal test conditions, dots represent the experimental data obtained in this work with the PVT apparatus.*

Another representation of the mixture two-phase behaviour is also possible in a pressure-temperature chart, as the one in Figure 12 for a $CO_2$ molar composition of 85%. A temperature glide of about 65 °C can be seen at 80 bars, while the critical point is far enough from the pump inlet operating conditions (slightly subcooled liquid at around 50-60 °C).

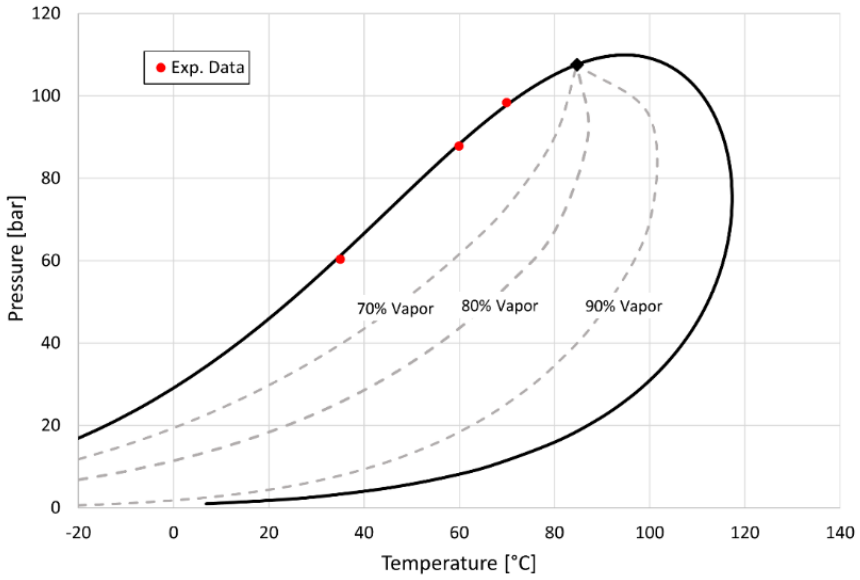


*Figure 12. Phase envelope of an 85% molar $CO_2$ mixture with $SiCl_4$; PR EoS calculations (solid line), calculated critical point (black dot), calculated vapor quality curves (dashed lines), and experimental bubble points (red dots).*

In Figure 13, the bubble points obtained using the densimeter (with the methodology shown in section 2.3.2) are reported as red dots on the phase envelopes corresponding to the experimental compositions (solid lines) calculated with the PR EoS optimised only on the bubble point data obtained using the PVT apparatus. On the left part of Figure 13, it is possible to visualize the consistency between the bubble points obtained with two different charges at almost the same composition (80.28% molar for the mixture tested at the PVT, 80.2% molar for the mixture tested at the VTD) with the two methodologies.

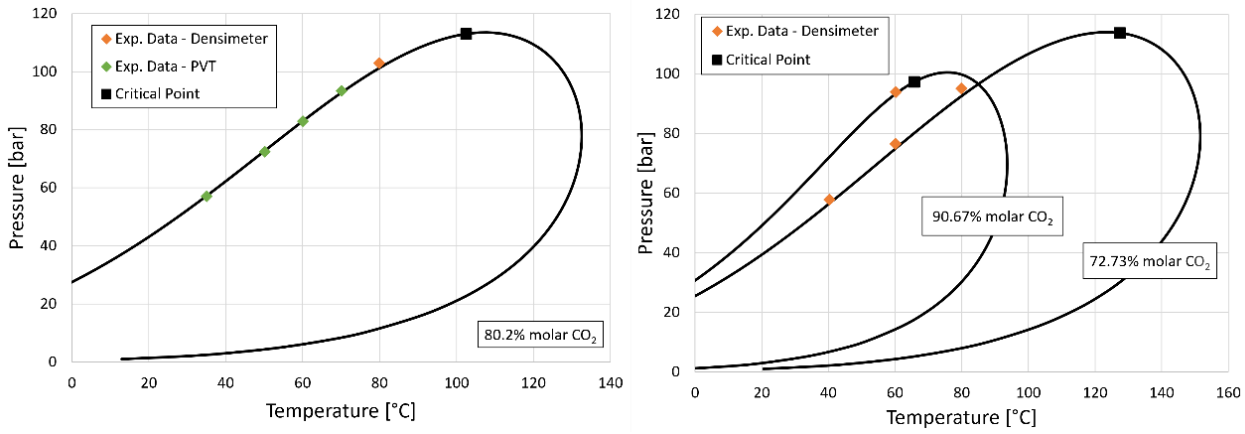


*Figure 13. P-T envelope curves of $CO_2$+$SiCl_4$ mixtures (solid lines) and critical points (black points) calculated with the optimized PR EoS, and experimental bubble points measured using the densimeter (red points) and the PVT (green points).*

As evident from Figure 13, the additional bubble points obtained using the VTD are consistent with those obtained with the rigorous PVT method and with the bubble lines computed using the PR EoS optimized only on the PVT data. The method proposed can be useful to have a preliminary

knowledge of vapour-liquid phase boundaries of multi-component systems without the requirement of expensive VLE dedicated apparatus, at least as a preliminary step.

The capability of the PR EoS with the regressed value of the BIP to predict the liquid densities of the mixture was tested, resulting in an AAD of 2.22%, considering all the data collected. The comparison between the optimized PR EoS and the experimental liquid densities of the mixture (Supplementary Materials and Figure 7) is presented in Table 3.

*Table 3. Average absolute deviation percent of the PR EoS with $K_{ij}$ against liquid densities of $CO_2$+$SiCl_4$ mixture.*

| | AAD [%] | | | |
|---|---|---|---|---|
| **$CO_2$ molar fraction %** | **40°C** | **60°C** | **80°C** | **Average** |
| 72.7% | 2.16 | 0.74 | 0.84 | 1.26 |
| 80.2% | 1.19 | 1.90 | 1.34 | 1.49 |
| 90.7% | 2.16 | 5.47 | 3.67 | 3.89 |

The PR EoS shows good agreement at higher $SiCl_4$ content (AAD=1.26% for 72.73% $CO_2$ molar content) while it underestimates the liquid densities at higher $CO_2$ molar content (AAD=3.89% for 90.67% $CO_2$ molar fraction). It must be noted that at 90.67% $CO_2$ molar fraction the calculated critical point is 64.4°C, and the higher deviations encountered at 60°C are probably attributed to near critical point conditions.

### 4.3.1 Comparison with previous literature works

In literature, other studies on this binary system are found and a comparison is proposed here, but a wider examination can be found in Supplementary Materials. In Figure 14, large deviations are present between the measured bubble points with the PVT apparatus and the data reported only in graphical form in Suleimenov [52].

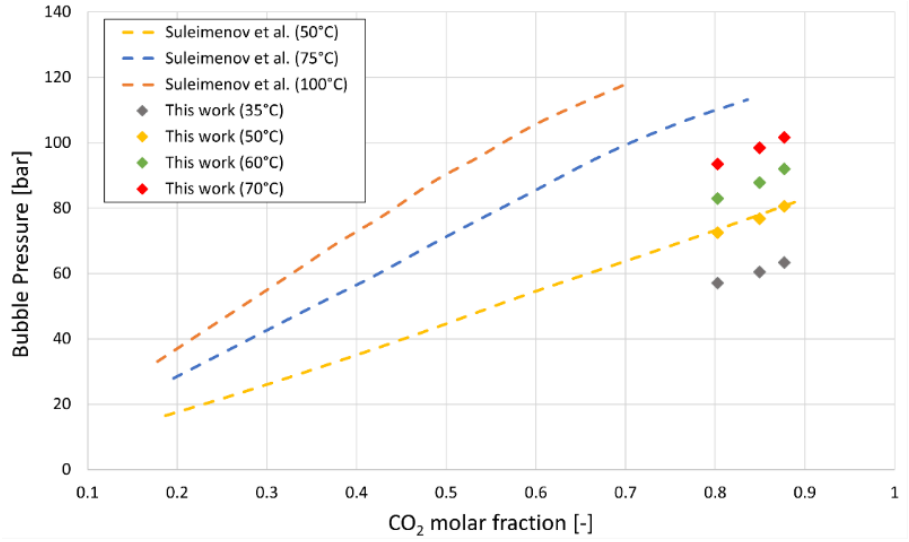


*Figure 14. Comparison between the bubble points measured in this work (dots) and the smoothed bubble line as reported by Suleimenov et al. [52] for the mixture $CO_2$+$SiCl_4$.*

The results from the Peng Robinson EoS with the binary interaction parameter regressed in this work have been compared with a second set of experimental data available in literature from Tolley's master thesis [53]. The graphical comparison between the EoS and Tolley data is reported in Figure 15, evidencing lack of agreement.

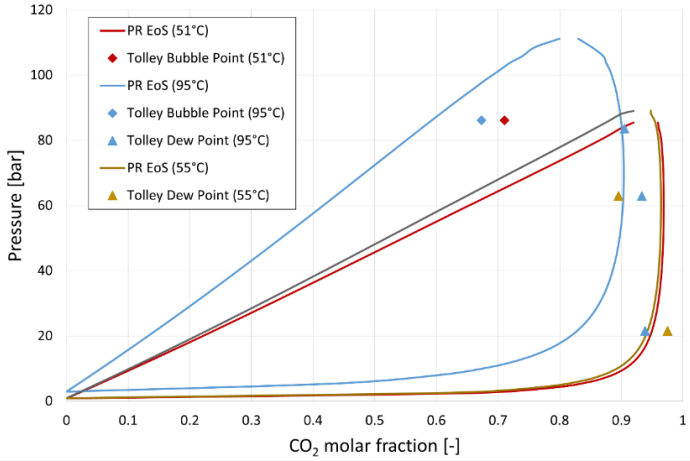


*Figure 15. Comparison between the PR EoS (solid lines) fitted with data obtained in this work and the experimental data reported in Tolley et al. [53].*

The comparison between the results of this work and those previously presented in literature evidenced large discrepancy, stressing the specific experimental investigation carried out for the $CO_2$+$SiCl_4$ mixture.

## 4.4 Preliminary analysis of $CO_2$+$SiCl_4$ power cycle in CSP context

This last section is dedicated to preliminary estimate the performance of the innovative $CO_2$+$SiCl_4$ mixture as working fluid for transcritical cycles for very high temperature CSP plants, justifying the interest in the experimental investigation proposed in this work. The EoS adopted to model the mixture and its BIP is the one proposed in this work in Table 2.

The cycle calculations consider a maximum temperature of 700°C, compatible with the expected thermal stability of the working fluid mixture and coherent with next-generation of central tower CSP plants. Such thermal level is also compatible with liquid HTFs to be adopted in high temperature external tubular receivers above 700°C, with sodium [54] or innovative mixtures [55] as HTF and innovative molten salts as storage fluids.

The thermodynamic cycle is simulated in Aspen Plus, considering the adoption of the $CO_2$+$SiCl_4$ mixture and $sCO_2$ in a recompression layout, which is the most effective layout for $sCO_2$ [56] due to balanced heat capacities in the recuperators. To evaluate the pure $sCO_2$ cycle, both the PR EoS and the Span-Wagner EoS [45] as implemented in REFPROP v10 [57] are used. The use of the PR EoS for both mixture and pure $sCO_2$ is necessary to fairly compare the two working fluids under the same thermodynamic model. The Span-Wagner EoS is also considered for the $sCO_2$ case as it is recognized to be the ad advanced and effective model to calculate the thermodynamic properties of $CO_2$. Compared to pure $sCO_2$, the $CO_2$+$SiCl_4$ mixture can benefit from liquid phase pumping instead of using the primary compressor, due to transcritical conditions. To solve the thermodynamic cycles some assumptions on the non-idealities of the components are used and reported in Table 3, according with previous literature work [29], and considered valid both for the $sCO_2$ cycle and the transcritical $CO_2$+$SiCl_4$ cycle. The cycle minimum temperature is assumed to be 50°C, representing an air-cooled design condition in hot-environments, typical of CSP plants.

The layout adopted for the mixture is reported in Figure 16, with the associated temperature-entropy (T-s) diagram of the $CO_2$+$SiCl_4$ mixture cycle considering a 92% $CO_2$ molar content. Referring to the recompression layout in Figure 16, the pre-heating section is divided into two recuperators, operating at different temperatures, i.e. low-temperature (LT) and high-temperature (HT) printed circuit heat exchangers (PCHEs), managing distinct mass flow rates to counterbalance the varying heat capacities of the $CO_2$-based fluid within the heat recovery process.

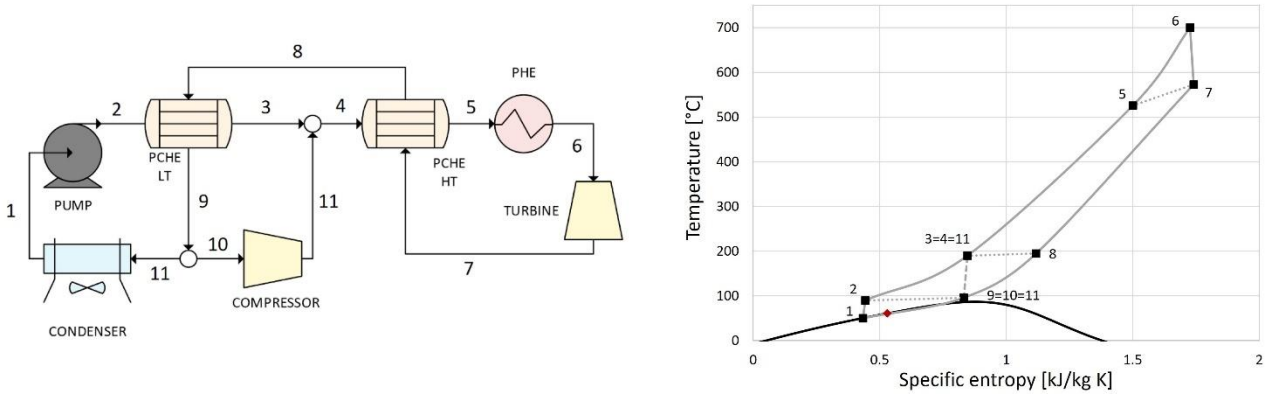


*Figure 16. Recompression power block layout (left side) for the transcritical $CO_2$+$SiCl_4$ mixture and associated T-s diagram (right side). The critical point of the mixture is represented as a red diamond in the T-s diagram. The internal heat recovery processes (LT and HT PCHE) is represented through dotted lines, while the re-compressor as dashed line.*

*Table 3. Power cycles assumptions and non-idealities for s$CO_2$ and $CO_2$ mixture cycles.*

| **Power Cycle Parameter** | **Value** |
|---|---|
| Turbine Inlet Temperature [°C] | 700 |
| Maximum Cycle Pressure [bar] | 250 |
| Cycle Minimum Temperature [°C] | 50 |
| Turbine / Compression Isentropic Efficiency [%] | 92 / 88 |
| PCHE Minimum Internal Temperature Difference [°C] | 5 |
| Condenser/ HRU Pressure loss [%] | 2 |
| PHE Pressure loss [%] | 2 |
| PCHE Pressure loss HP / LP [%] | 0.3/ 1.5 |
| Expander electro-mechanical efficiency [%] | 98 |
| Pump/Compressor electro-mechanical efficiency [%] | 98 |
| Fans (HRU) Electrical Consumption [$MW_{el}$] | 1% $Q_{HRU}$ |

The adoption of a transcritical power cycle in recompressed layout require the mixture to work in single-phase conditions at the exit of the low-temperature printed circuit heat exchanger recuperator (PCHE LT), points 9-10-11 in Figure 16, to provide dry conditions at the (secondary) compressor inlet. For this mixture and the conditions considered at the compression inlet, this is verified only for $CO_2$ molar content above 90% due to a reduction in the temperature glide occurring during the nearly isobaric condensation. A sensitivity test on the $CO_2$ molar fraction has been carried out from 90% to 100% $CO_2$, providing an overview of the effects of the mixture composition on the thermodynamic cycle efficiency, defined as in Equation 8.

$$\eta_{Cycle} = \frac{W_{Turbine} - W_{Main\ Pump/Compressor} - W_{Re-Compressor}}{Q_{PHE}} \quad (8)$$

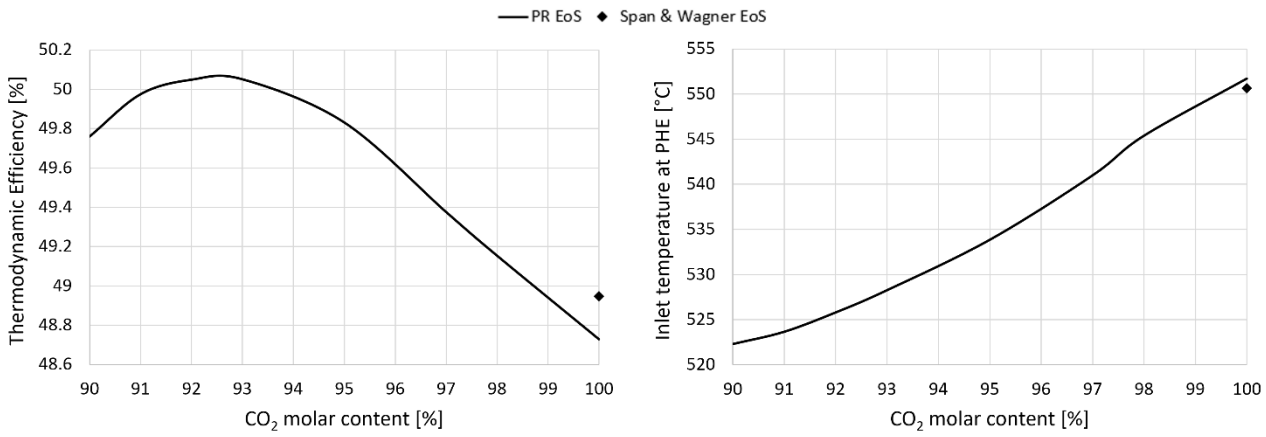


*Figure 17. thermodynamic cycle efficiency of $CO_2$+$SiCl_4$ and $Sco_2$ in recompressed layout (left), and temperature of the working fluid at the inlet of the PHE (right).*

As evident from Figure 17, the $CO_2$+$SiCl_4$ mixture outperforms pure $CO_2$ in thermodynamic efficiency: at around 92% $CO_2$ molar fraction, the 50% efficiency target is reached with the mixture in transcritical conditions, enabling around +1.3% efficiency point compared to pure $sCO_2$ (a relative deviation of around 2% in mechanical power at constant thermal input). The mixture does not only demonstrate an enhanced cycle efficiency with respect to the $sCO_2$ cycle, but it also allows a reduction of approximately 25°C of the temperature at the primary heat exchanger's inlet (PHE). As a result, it becomes possible to decrease the return temperature of the heat transfer fluid (HTF), subsequently reducing the parasitic electrical consumption of the HTF pump (having a lower mass flow rate at fixed thermal power).

Above 95% $CO_2$ molar fraction, the mixture works in supercritical conditions, as pure $sCO_2$, but the benefits of increasing the critical temperature are still present. In fact, even if the highest efficiency is identified at transcritical conditions (due to the low compression work at liquid conditions), the supercritical compression of the mixture at nearer critical conditions provides for better efficiency than pure $sCO_2$ (critical temperature 31°C). This is a consequence of the real gas effects, which are less pronounced in the case of $sCO_2$ due to the higher temperature difference between the compression inlet and the fluid critical point. The minimum pressure of the transcritical cycles working with the $CO_2$ mixture is the bubble pressure at pump inlet (50°C), while it is an optimised parameter in case of $sCO_2$ and for the mixture above 95% $CO_2$ molar content.

Considering the results of the innovative cycle at the optimized composition of 92% $CO_2$ molar, a comparison with the pure $sCO_2$ cycle is presented in Table 4, for a gross mechanical power of 100 MW. The comparison is presented in terms of both thermodynamic and electrical efficiency, considering the parasitic consumptions of the HTF pump, the auxiliary fans of an air-cooler at the heat rejection unit (HRU), and the electro-mechanical losses.

*Table 4. Performance of $CO_2$+$SiCl_4$ and $sCO_2$ power cycles at design conditions, for 100 MW gross mechanical output.*

| **Variable** | **$sCO_2$ Cycle** | **$CO_2$+$SiCl_4$ Cycle** |
|---|---|---|
| Plant layout | Recompressed | Recompressed |
| $CO_2$ molar fraction [-] | 1 | 0.92 |

| | | |
|---|---|---|
| Mass Flow Rate [kg/s] | 1086.3 | 1016 |
| Pump/Main Compressor Power [MW] | 28.6 | 19.7 |
| Recompressor Power [MW] | 18.2 | 15.6 |
| Turbine Power [MW] | 146.8 | 135.3 |
| Recuperator Thermal Power [MW] | 128.5 (LT) - 498 (HT) | 121.2 (LT) – 405.3 (HT) |
| PHE Thermal Power [MW] | 205.2 | 199.8 |
| HRU Thermal Power [MW] | 105.2 | 99.8 |
| UA LT PCHE Recuperator [MW/K] | 22.3 | 22.6 |
| UA HT PCHE Recuperator [MW/K] | 18.5 | 17 |
| Working fluid inlet PHE Temperature [°C] | 551.7 | 525.7 |
| **Thermodynamic Cycle Efficiency [%]** | **48.73** | **50.05** |
| Electromechanical losses [$MW_{el}$] | 3.3 | 3 |
| HRU Fan Consumption [$MW_{el}$] | 1.1 | 1 |
| HTF Pump Consumption [$MW_{el}$] | 1 | 0.8 |
| **Cycle Electric Efficiency [%]** | **46.1** | **48.1** |

In Table 4, the evaluation of the electrical consumption of the HTF pump as function of the temperature at the inlet of the PHE follows the methodology presented in a previous literature work [58], considering sodium as HTF and considering a solar multiple of the CSP plant from the literature of around 2.7, if adopting the thermodynamic cycles of this work in Table 4.

It can be noted that the net electrical efficiency of the mixture cycle results to be +2% efficiency points higher than pure $CO_2$, which is significant for the revenues and the economic performance of a CSP plant, and it represents an increment of around 4.2% in electric power at constant thermal input (considering the same solar plant).

## 4.5 Conclusions

In this work, experimental bubble points and liquid densities of a $CO_2$-rich mixture (more than 70% molar content) with $SiCl_4$ as dopant have been measured to assess the phase behaviour and volumetric behaviour of the mixture as potential working fluid in transcritical power cycles. The bubble point data obtained with a variable-volume PVT apparatus can be used in future works for calibrating proper equations of state and evaluating the cycle conditions, optimizing the performance. From a preliminary analysis, the Peng Robinson EoS with regressed BIP showed a good accuracy in representing the experimental bubble points (AAD of 0.68%), while acceptable deviations (AAD of 2.22%) are found with respect to the measured high-pressure liquid densities.

The particular set-up adopted for the vibrating tube densimeter resulted to be determinant for the measurement of the density of the $CO_2$+$SiCl_4$ mixture, characterized by large differences in volatility between the two components. As an innovative outcome of this work, the VTD was used not only to measure liquid densities of the mixture, but also to obtain additional bubble points. The bubble points acquired at VTD resulted to be consistent with those from the PVT test rig, as well as with the

thermodynamic model optimised only on the data from the PVT. This procedure can be adopted in the future to have preliminary information about the VLE conditions of a mixture.

The comparison with previous literature works highlighted the discrepancies of the data available in the literature, justifying even more the experimental campaign carried out here.

A preliminary thermodynamic analysis carried out with the optimized EoS demonstrates the potentiality of this mixture in comparison to pure $sCO_2$ in power cycles under the same assumptions and power block configuration (recompression layout), enabling a net electrical efficiency gain of around +2% points in a next-generation CSP tower plant with 700°C turbine inlet temperature. The mixture also allows for a reduction of approximately 25°C in the temperature at the primary heat exchanger's inlet, also decreasing the return temperature of the HTF, thereby mitigating the parasitic electrical losses resulting from HTF pump operations. Notably, the net electrical output of the $CO_2$+$SiCl_4$ mixture cycle in a CSP plant presents a +4.2% point increment over pure $CO_2$, under the same thermal power from the solar field, making a significant impact on the revenues and overall economic performance of a concentrated solar power plant.

**Nomenclature**

Acronyms

| | |
|---|---|
| AAD | Average Absolute Deviation |
| CSP | Concentrated solar power |
| EoS | Equation of state |
| HT | High Temperature |
| HTF | Heat Transfer Fluid |
| HRU | Heat Rejection Unit |
| LT | Low Temperature |
| ORC | Organic Rankine Cycle |
| PCHE | Printed Circuit Heat Exchanger |
| PHE | Primary Heat Exchanger |
| PR | Peng Robinson EoS |
| PVT | Pressure-Volume-Temperature |
| VLE | Vapour-Liquid Equilibrium |
| VTD | Vibrating Tubr Densimeter |

Symbols

| | |
|---|---|
| b | Covolume |
| P | Pressure, bar |
| ϱ | Density, kg $m^{-3}$ |
| Q | Thermal Power, MW |

| | |
|---|---|
| T | Temperature, °C |
| $v$ | Specific Volume |
| W | Mechanical Power, MW |

Greek symbols

| | |
|---|---|
| $\alpha$ | Alpha Function of the EoS |
| τ | Period, s |
| ω | Pitzer acentric factor, - |

Subscripts

| | |
|---|---|
| cr | Critical |
| el | Electrical |

## 4.6 Bibliography


[1] G. Angelino, Carbon Dioxide Condensation Cycles For Power Production, J. Eng. Power. 90 (1968) 287–295. https://doi.org/10.1115/1.3609190.

[2] E.G. Feher, The Supercritical Thermodynamic Power Cycle, Energy Convers. 8.2. (1968) 85–90.

[3] V. Dostal, P. Hejzlar, M.J. Driscoll, High-performance supercritical carbon dioxide cycle for next-generation nuclear reactors, Nucl. Technol. 154 (2006) 265–282. https://doi.org/10.13182/NT154-265.

[4] F. Crespi, D. Sánchez, J.M. Rodríguez, G. Gavagnin, A thermo-economic methodology to select sCO2 power cycles for CSP applications, Renew. Energy. 147 (2020) 2905–2912. https://doi.org/10.1016/j.renene.2018.08.023.

[5] M. Binotti, M. Astolfi, S. Campanari, G. Manzolini, P. Silva, Preliminary assessment of sCO2 cycles for power generation in CSP solar tower plants, Appl. Energy. 204 (2017) 1007–1017. https://doi.org/10.1016/j.apenergy.2017.05.121.

[6] A. Alenezi, L. Vesely, J. Kapat, Exergoeconomic analysis of hybrid sCO2 Brayton power cycle, Energy. 247 (2022) 123436. https://doi.org/10.1016/j.energy.2022.123436.

[7] G. Manente, F.M. Fortuna, Supercritical CO2 power cycles for waste heat recovery: A systematic comparison between traditional and novel layouts with dual expansion, Energy Convers. Manag. 197 (2019) 111777. https://doi.org/10.1016/j.enconman.2019.111777.

[8] S.A. Wright, C.S. Davidson, W.O. Scammell, Thermo-Economic Analysis of Four sCO2 Waste Heat Recovery Power Systems, 5th Int. Symp. - Supercrit. CO2 Power Cycles. (2016) 1–16. sco2symposium.com/papers2018/heat-exchangers/114_Paper.pdf.

[9] T. Gotelip, U. Gampe, S. Glos, Optimization strategies of different SCO2 architectures for gas turbine bottoming cycle applications, Energy. 250 (2022) 123734. https://doi.org/10.1016/j.energy.2022.123734.

[10] D. Alfani, M. Binotti, E. Macchi, P. Silva, M. Astolfi, sCO2 power plants for waste heat recovery: Design optimization and part-load operation strategies, Appl. Therm. Eng. 195 (2021) 117013. https://doi.org/10.1016/j.applthermaleng.2021.117013.

[11] E. Morosini, M. Doninelli, D. Alfani, M. Astolfi, G. Di Marcoberardino, G. Manzolini, Analysis of the Potential of Co2 Based Mixtures To Improve the Efficiency of Cogenerative Waste Heat Recovery Power Plants, Conf. Proc. Eur. SCO2 Conf. (2023) 169–178. https://doi.org/10.17185/duepublico/77287.

[12] M. Doninelli, E. Morosini, G. Gentile, L. Putelli, G. Di Marcoberardino, M. Binotti, G. Manzolini, Thermal desalination from rejected heat of power cycles working with CO2-based working fluids in

CSP application: A focus on the MED technology, Sustain. Energy Technol. Assessments. 60 (2023) 103481. https://doi.org/https://doi.org/10.1016/j.seta.2023.103481.

[13] M. Binotti, G. Di Marcoberardino, P. Iora, C. Invernizzi, G. Manzolini, Scarabeus: Supercritical carbon dioxide/alternative fluid blends for efficiency upgrade of solar power plants, AIP Conf. Proc. 2303 (2020). https://doi.org/10.1063/5.0028799.

[14] DESOLINATION – Sustainable desalination from Concentrated Solar Power., https://desolination.eu/.

[15] G. Di Marcoberardino, E. Morosini, G. Manzolini, Preliminary investigation of the influence of equations of state on the performance of CO2 + C6F6 as innovative working fluid in transcritical cycles, Energy. 238 (2022) 121815. https://doi.org/10.1016/j.energy.2021.121815.

[16] F. Crespi, P. de Arriba, D. Sánchez, A. Ayub, G. Di Marcoberardino, C. Invernizzi, G.S. Martínez, P. Iora, D. Di Bona, M. Binotti, G. Manzolini, Thermal Efficiency Gains Enabled by Using CO2 Mixtures in Supercritical Power Cycles, Energy. 238 (2021) 121899. https://doi.org/10.1016/j.energy.2021.121899.

[17] A. Romei, P. Gaetani, G. Persico, Computational fluid-dynamic investigation of a centrifugal compressor with inlet guide vanes for supercritical carbon dioxide power systems, Energy. 255 (2022) 124469. https://doi.org/10.1016/j.energy.2022.124469.

[18] O.A. Terracciano, F. De Francesco, R. Brizzi, F. Annese, M. Doninelli, L. Putelli, M. Gelfi, An Advanced Desalination System with an Innovative CO2 Power Cycle Integrated with Renewable Energy Sources, in: 2023: p. D011S017R002. https://doi.org/10.2118/215993-MS.

[19] C.M. Invernizzi, P. Iora, G. Manzolini, S. Lasala, Thermal stability of n-pentane, cyclo-pentane and toluene as working fluids in organic Rankine engines, Appl. Therm. Eng. 121 (2017) 172–179. https://doi.org/10.1016/j.applthermaleng.2017.04.038.

[20] L. Keulen, S. Gallarini, C. Landolina, A. Spinelli, P. Iora, C. Invernizzi, L. Lietti, A. Guardone, Thermal stability of hexamethyldisiloxane and octamethyltrisiloxane, Energy. 165 (2018) 868–876. https://doi.org/10.1016/j.energy.2018.08.057.

[21] C.J.N. Sánchez, A.K. da Silva, Technical and environmental analysis of transcritical Rankine cycles operating with numerous CO2 mixtures, Energy. 142 (2018) 180–190. https://doi.org/10.1016/j.energy.2017.09.120.

[22] B. Dai, C. Dang, M. Li, H. Tian, Y. Ma, Thermodynamic performance assessment of carbon dioxide blends with low-global warming potential (GWP) working fluids for a heat pump water heater, Int. J. Refrig. 56 (2015) 1–14. https://doi.org/10.1016/j.ijrefrig.2014.11.009.

[23] Y. Yao, L. Shi, H. Tian, X. Wang, X. Sun, Y. Zhang, Z. Wu, R. Sun, G. Shu, Combined cooling and power cycle for engine waste heat recovery using CO2-based mixtures, Energy. 240 (2022) 122471. https://doi.org/10.1016/j.energy.2021.122471.

[24] G. Angelino, C. Invernizzi, Experimental investigation on the thermal stability of some new zero ODP refrigerants, Int. J. Refrig. 26 (2003) 51–58. https://doi.org/10.1016/S0140-7007(02)00023-3.

[25] N. Ma, Z. Bu, Y. Fu, W. Hong, H. Li, X. Niu, An operation strategy and off-design performance for supercritical brayton cycle using CO2-propane mixture in a direct-heated solar power tower plant, Energy. 278 (2023) 127882. https://doi.org/10.1016/j.energy.2023.127882.

[26] X. Niu, N. Ma, Z. Bu, W. Hong, H. Li, Thermodynamic analysis of supercritical Brayton cycles using CO2-based binary mixtures for solar power tower system application, Energy. 254 (2022) 124286. https://doi.org/10.1016/j.energy.2022.124286.

[27] M. Mehos, C. Turchi, J. Vidal, M. Wagner, Z. Ma, C. Ho, W. Kolb, C. Andraka, A. Kruizenga, Concentrating Solar Power Gen3 Demonstration Roadmap, Nrel/Tp-5500-67464. (2017) 1–140. https://doi.org/10.2172/1338899.

[28] Y.L. He, Y. Qiu, K. Wang, F. Yuan, W.Q. Wang, M.J. Li, J.Q. Guo, Perspective of concentrating solar power, Energy. 198 (2020) 117373. https://doi.org/10.1016/j.energy.2020.117373.

[29] E. Morosini, A. Ayub, G. di Marcoberardino, C.M. Invernizzi, P. Iora, G. Manzolini, Adoption of the

CO2 + SO2 mixture as working fluid for transcritical cycles: A thermodynamic assessment with optimized equation of state, Energy Convers. Manag. 255 (2022). https://doi.org/10.1016/j.enconman.2022.115263.

[30] P. Tafur-Escanta, I. López-Paniagua, J. Muñoz-Antón, Thermodynamics analysis of the supercritical CO2 binary mixtures for Brayton power cycles, Energy. 270 (2023). https://doi.org/10.1016/j.energy.2023.126838.

[31] G. Manzolini, M. Binotti, D. Bonalumi, C. Invernizzi, P. Iora, CO2 mixtures as innovative working fluid in power cycles applied to solar plants. Techno-economic assessment, Sol. Energy. 181 (2019) 530–544. https://doi.org/10.1016/J.SOLENER.2019.01.015.

[32] C.M. Invernizzi, P. Iora, D. Bonalumi, E. Macchi, R. Roberto, M. Caldera, Titanium tetrachloride as novel working fluid for high temperature Rankine Cycles: Thermodynamic analysis and experimental assessment of the thermal stability, Appl. Therm. Eng. 107 (2016) 21–27. https://doi.org/10.1016/j.applthermaleng.2016.06.136.

[33] R.H. West, R.A. Shirley, M. Kraft, C.F. Goldsmith, W.H. Green, A detailed kinetic model for combustion synthesis of titania from TiCl4, Combust. Flame. 156 (2009) 1764–1770. https://doi.org/https://doi.org/10.1016/j.combustflame.2009.04.011.

[34] Y. Okamoto, M. Sumiya, Y. Nakamura, Y. Suzuki, Effective silicon production from SiCl4 source using hydrogen radicals generated and transported at atmospheric pressure, Sci. Technol. Adv. Mater. 21 (2020) 482–491. https://doi.org/10.1080/14686996.2020.1789438.

[35] Y. Wan, X. Zhao, D. Yan, D. Yang, Y. Li, S. Guo, Research and preparation of ultra purity silicon tetrachloride, AIP Conf. Proc. 1890 (2017). https://doi.org/10.1063/1.5005228.

[36] Y. Mochizuki, J. Bud, J. Liu, N. Tsubouchi, Production of Silicone Tetrachloride from Rice Husk by Chlorination and Performance of Mercury Adsorption from Aqueous Solution of the Chlorinated Residue, ACS Omega. 5 (2020) 29110–29120. https://doi.org/10.1021/acsomega.0c03789.

[37] United States. Bureau of Mines., Mineral Facts and Problems: 1985 Edition, Washington D.C., 1985.

[38] C. Cheng, C. Zhang, J. Jiang, E. Ma, J. Bai, J. Wang, Raman Spectroscopy Characterization of Dissolved Polysilicon Byproduct $SiCl_4$ in Ionic Liquids, J. Spectrosc. 2018 (2018) 2329189. https://doi.org/10.1155/2018/2329189.

[39] J.C. Thermodynamics, P. Stringari, G. Scalabrin, A. Valtz, D. Richon, Density measurements of liquid 2-propanol at temperatures between ( 280 and 393 ) K and at pressures up to 10 MPa, J. Chem. Thermodyn. 41 (2009) 683–688. https://doi.org/10.1016/j.jct.2008.12.014.

[40] P. Stringari, G. Scalabrin, D. Richon, F. Tecnica, C.E.P. Tep, C. Fre, R. Saint Honore, Compressed and Saturated Liquid Densities for the 2-Propanol + Water System, (2008) 1789–1795.

[41] P. Stringari, G. Scalabrin, D. Richon, C. Coquelet, Liquid Density and Bubble Pressure Measurements for the Propylene + 2-Propanol System, (2008) 1167–1174.

[42] D.Y. Peng, D.B. Robinson, A New Two-Constant Equation of State, Ind. Eng. Chem. Fundam. 15 (1976) 59–64. https://doi.org/10.1021/i160057a011.

[43] E. Neyrolles, A. Valtz, C. Coquelet, A. Chapoy, On the phase behaviour of the CO2 + N2O4 system at low temperatures, Chem. Eng. Sci. 258 (2022) 117726. https://doi.org/https://doi.org/10.1016/j.ces.2022.117726.

[44] M. Nazeri, A. Chapoy, A. Valtz, C. Coquelet, Fluid Phase Equilibria New experimental density data and derived thermophysical properties of carbon dioxide e Sulphur dioxide binary mixture ( CO 2 - SO 2 ) in gas , liquid and supercritical phases from 273 K to 353 K and at pressures up to 42 MPa, Fluid Phase Equilib. 454 (2017) 64–77. https://doi.org/10.1016/j.fluid.2017.09.014.

[45] R. Span, W. Wagner, A New Equation of State for Carbon Dioxide Covering the Fluid Region from the Triple-Point Temperature to 1100 K at Pressures up to 800 MPa, J. Phys. Chem. Ref. Data. 25 (1996) 1509–1596. https://doi.org/10.1063/1.555991.

[46] G. Soave, Equilibrium constants from a modified Redlich-Kwong equation of state, Chem. Eng. Sci. 27 (1972) 1197–1203. https://doi.org/10.1016/0009-2509(72)80096-4.

[47] J.S. Lopez-Echeverry, S. Reif-Acherman, E. Araujo-Lopez, Peng-Robinson equation of state: 40 years through cubics, Fluid Phase Equilib. 447 (2017) 39–71. https://doi.org/10.1016/j.fluid.2017.05.007.

[48] A. Bertucco, M. Fermeglia, 50 years of Soave Equation of State (SRK): A source of inspiration for chemical engineers, Fluid Phase Equilib. 566 (2023) 113678. https://doi.org/https://doi.org/10.1016/j.fluid.2022.113678.

[49] Aspen Technology Inc., Aspen Plus®, Version V12.1, (2022).

[50] H.I. Britt, R.H. Luecke, The estimation of parameters in nonlinear, implicit models, Technometrics. 15 (1973) 233 – 247. https://doi.org/10.1080/00401706.1973.10489037.

[51] W.E. Deming, Statistical Adjustment of Data, Dover Publication Inc., New York, 1943.

[52] O.M. Suleimenov, A.Z. Panagiotopoulos, T.M. Seward, Grand canonical Monte Carlo simulations of phase equilibria of pure silicon tetrachloride and its binary mixture with carbon dioxide, Mol. Phys. 101 (2003) 3213–3221. https://doi.org/10.1080/00268970310M.

[53] W.K. Tolley, Supercritical behavior of selected metal chlorides with carbon dioxide: A study of solubilities, solution densities, and excess enthalpies of mixing, 1990.

[54] T. Conroy, M.N. Collins, R. Grimes, Sodium receiver designs for integration with high temperature power cycles, Energy. 187 (2019) 115994. https://doi.org/10.1016/j.energy.2019.115994.

[55] G. Manzolini, G. Lucca, M. Binotti, G. Lozza, A two-step procedure for the selection of innovative high temperature heat transfer fluids in solar tower power plants, Renew. Energy. 177 (2021) 807–822. https://doi.org/10.1016/j.renene.2021.05.153.

[56] D. Alfani, M. Astolfi, M. Binotti, P. Silva, E. Macchi, Off-design performance of CSP plant based on supercritical CO2 cycles, AIP Conf. Proc. 2303 (2020) 130001. https://doi.org/10.1063/5.0029801.

[57] E. W. Lemmon and and Ian H. Bell and M. L. Huber and M. O. McLinden, NIST Standard Reference Database 23: Reference Fluid Thermodynamic and Transport Properties-REFPROP, Version 10.0, National Institute of Standards and Technology, (2018). https://doi.org/https://doi.org/10.18434/T4/1502528.

[58] E. Morosini, E. Villa, G. Quadrio, M. Binotti, G. Manzolini, Solar tower CSP plants with transcritical cycles based on CO2 mixtures: A sensitivity on storage and power block layouts, Sol. Energy. 262 (2023) 111777. https://doi.org/https://doi.org/10.1016/j.solener.2023.05.054.

## Supplementary Materials

### Mixture preparation

The mixture is prepared by weighing both pure components after charging them in a dedicated variable volume cylinder according to their relative volatility, starting from the heavier component to the lighter. $CO_2$ is the most volatile component, and it is stored in two-phase conditions in a gas bottle at ambient temperature (approximately 20 °C and 57 bar), while $SiCl_4$ is liquid at ambient temperature and pressure (normal boiling point around 57°C).

The $CO_2$ is supplied by Messer France SAS, with a purity of 99.995%, while the $SiCl_4$ is supplied by Tokyo Chemical Industry (TCI) with a certified purity above 98%.

A magnetic agitator is previously placed in the variable volume cylinder: it is used during the measurements to homogenize the composition of the mixture created. Then, a vacuum pump is

operated, up to a condition of around 5.5 Pa in the variable volume cylinder, measured with the Pirani vacuum gauge placed at its inlet. Particular attention is paid to the vacuum conditions inside the variable volume cylinder before injecting the silicon tetrachloride (dopant), since it is reactive with moisture present in the air. After vacuum is ensured, the empty charging cylinder is weighted.

Afterwards, the dopant is injected in the cylinder manually with a syringe through a sealing cap, avoiding the contamination with moisture in a dried air atmosphere glove box: the system is weighted again to measure the mass of the dopant entered in the volume, by difference with the previous value. Afterwards, the $CO_2$ is introduced not directly from its reservoir but trough an additional variable volume auxiliary cylinder that is filled with pressurized $CO_2$.

Once the mixture is prepared in the main variable volume cylinder, it is weighted again to compute by difference the mass of $CO_2$ in the mixture. Knowing the mass of both $CO_2$ and the dopant and their molecular mass, the molar composition of the mixture is determined. The system mass is measured with a Mettler Toledo CC3000 balance, with an accuracy of ±0.0001 g (six order of magnitude lower than the mass of the charged mixture), as an average of three subsequent measures.

The variable volume cylinder containing the prepared mixture is brought to the apparatus of interest (either the VTD or the P-V-T cell), where the piston is put in contact with the high-pressure nitrogen reservoir at a pressure higher than the expected bubble condition. An electromagnetic field is then created on the external surface of the cylinder to move the magnetic agitator, improving the mixing of the two components. After half an hour the homogeneity of composition is supposedly reached, with the mixture in the volume at liquid condition. Vacuum is created in the whole circuit of the test rig, before injecting for pressure difference the mixture from the charge to the measurement circuit.

**Comparison with previous literature works**

In Figure A1, a comparison is reported between the measured bubble points with the PVT apparatus and the data available in the literature, which are presented as smoothed bubble lines in Suleimenov [1]. Unfortunately, in the mentioned literature work, the numerical values of the densities measured and the experimental methodology are not detailed: these additional information are available in literature in another work of the same author but only in the form of an abstract [2]. In this abstract it is reported that the methodology used relies in a thermal conductivity detector (TCD) that quantifies the amount of $SiCl_4$ dissolved in the liquid and vapour phases sampled (around 20 microliters). Only the isothermal curves that are relevant for the comparison purpose are reported in Figure A1. The points measured within this work in the PVT apparatus at chapter 2.2 are in good agreement only with the bubble line at 50°C of Suleimenov, while large deviations seem existing when the isotherms at 75°C and 100°C are compared with the extrapolated trend of the bubble points obtained in this work. Since the experimental data available in the work of Suleimenov are presented only in graphical form, the curves in Figure A1 have been obtained by using a software for extracting numerical values form the original graphs.

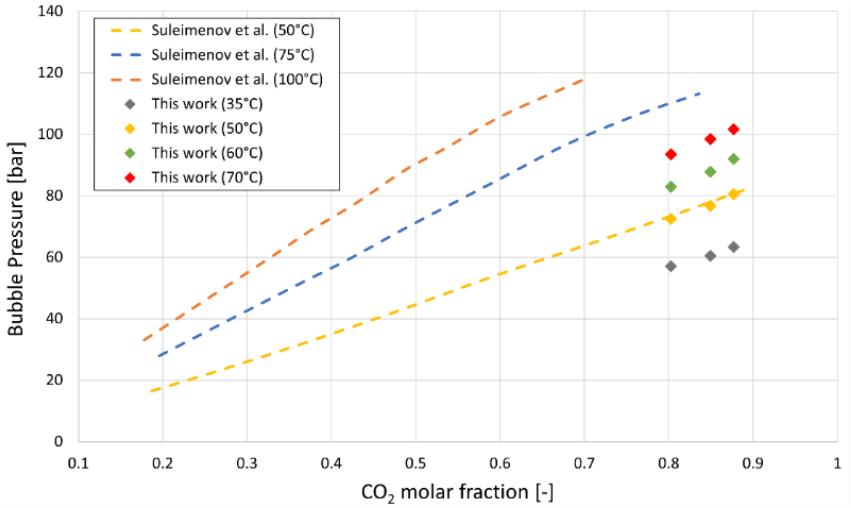


*Figure A1. Comparison between the bubble points measured in this work (dots) and the smoothed bubble line as reported by Suleimenov et al. [1] for the mixture $CO_2$+$SiCl_4$.*

The results from the Peng Robinson EoS with the binary interaction parameter regressed in this work have been compared with a second set of experimental data available in literature from Tolley's master thesis [3]. The data in Tolley have been obtained using a calorimeter, that is a different experimental approach with respect to the one of this work. The graphical comparison between the EoS and Tolley data is reported in Figure A2: the data from Tolley suggest a very small difference in the liquid composition at bubble conditions between 51°C (red dots) and 95°C (blue dots), clearly not consistent with the PR EoS calculations nor with the experimental data taken within this work.

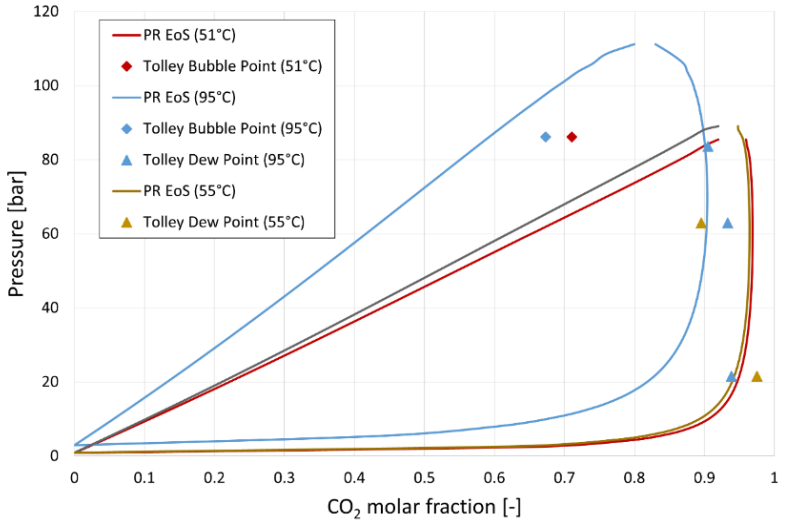


*Figure A2. Comparison between the PR EoS (solid lines) fitted with data obtained in this work and the experimental data reported in Tolley et al. [3].*

In conclusion, the comparison between the results of the present work and those previously presented in other literature works demonstrated the necessity of the specific experimental investigation carried out for the $CO_2$+$SiCl_4$ mixture.

**Uncertainty calculations**

The uncertainty on the physical quantity "X" is computed as in Equations E1-5, extended with a coverage factor of $k = 2$.

$$u_{Expanded}(X) = k \cdot \sqrt{(u_{Calibration}(X))^2 + (u_{Acquisition}(X))^2 + (u_{Repeatability}(X))^2 + (u_{Fitting}(X))^2} \quad \text{(E1)}$$

Where the contributions of the uncertainty are calculated as follows:

$$u_{Calibration}(X) = \max\big(Measured\ (X) - Reference\ (X)\big) \quad \text{(E2)}$$

$$u_{Acquisition}(X) = \sigma(X_{acquisited}) \quad \text{(E3)}$$

$$u_{Repeatability}(X) = \frac{\sigma(X_{measured})}{\sqrt{n}} \quad \text{(E4)}$$

The variable "X" can be either pressure, temperature, or density, depending on the apparatus.

For the PVT apparatus, only temperatures and pressures are measured, and their uncertainties reported. For the VTD, instead, uncertainties on temperatures, pressures and densities are given.

The contribution of the calibration in the uncertainty calculations is evaluated accounting for the calibration curve of the instrument compared with a reference value: it is 0.03 °C for the temperature and 0.02 bar for the pressure in any conditions considered in this work, while for the density it is 2.95 kg/m$^3$ at 40°C, 1.19 kg/m$^3$ at 60°C and 1.27 kg/m$^3$ at 80°C. The reference values are assumed as reference thermocouples and pressure transducers for temperature and pressure, respectively, while the value of density of the Span and Wagner EoS are assumed as reference for the calibration of the density, since the calibration of the VTD occurred with pure CO2 as reference fluid. The pressure transducer (PT) used for the measurement is a PAA-35HXTC (operating range up to 700 bar), and the temperature sensor (TC) are four-wire 100- Ω platinum resistance probes (Pt100). The reference pressure transducer used during calibration instead is a GE Sensing PACE 5000. During the measurements, the pressure and temperature were recorded thanks to the Agilent HP34970A data acquisition unit, while the period with the Anton Paar mPDS 5 transmitter.

The contribution of the acquisitions to the uncertainties is accounted according to the standard deviation of the variable, $\sigma(X_{acquisited})$, directly computed with the data acquisition unit, in a wide range of at least 60 acquisitions with a frequency of one acquisition per second.

Finally, the contribution of the repetition of each measurement to the final value reported (as an average) is accounted for the standard deviation of all the measured data $\sigma(X_{measured})$ divided by the square root of the number of data recorder at the same conditions (T,P,x).

While operating with the VTD, each thermodynamic condition (T,P,x) is measured only once, so the contribution of the repetition on the uncertainty is not considered. While operating the PVT cell,

since each bubble point is measured at least three times (as reported in section 2.2), the contribution of the repetition to the uncertainty of temperature and pressure is included.

Moreover, only for the PVT apparatus and only for the pressure measured (the bubble pressure), an additional contribution to the uncertainty ($u_{Fitting}(P_{bubble})$) is added to account for the imperfect fitting with a straight line of the experimental pressure-volume data, both for the VLE and the liquid region. Two bundles of parallel lines that include all points in VLE and liquid zone was created. The intersection of the upper straight lines of the two beams provides the maximum value of bubble pressure ($P_A$ in Figure A3) obtainable from the measured test points. The intersection of the lower lines of the two beams provides the minimum bubble pressure ($P_B$ in Figure A3) achievable. The error related to the identification of the bubble pressure, in isothermal conditions, is therefore quantifiable as:

$$u_{Fitting}(P_{bubble}) = P_A - P_B \tag{E5}$$

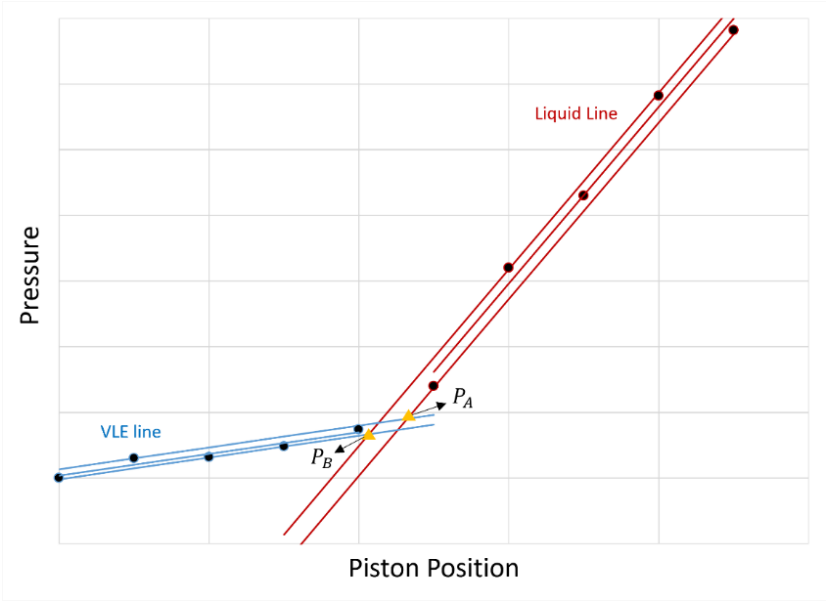


*Figure A3. qualitative graphical description of the methodology adopted to quantify the error contribution on the bubble pressure due to identification procedure ("fitting" term), where PA and PB represent respectively the maximum and minimum value of bubble pressure attainable by lines interception.*

The chosen method for calculating uncertainty of linear fitting is designed to exclude the contribution of uncertainty on the gradient of both the experimental liquid line and VLE (Vapor-Liquid Equilibrium) line. This decision is motivated by a desire to avoid an artificially high uncertainty value that arises from a more rigorous mathematical formulation. In fact, the high value resulting from the rigorous mathematical formulation of the uncertainty is considered misleading because it is attributed to the small number of experimental points recorded in the VLE region during each measurement series. In other words, the method is chosen not purely for mathematical accuracy but to better reflect the good repeatability observed experimentally. While the more rigorous mathematical formulation might be technically accurate, it could lead to an overestimation of uncertainty in the specific experimental context according to the considerations on, in one hand,

the limitations in the data collected in the VLE region and , in the other hand, the good consistency of the measurements over many repeated measurements.

**Experimental data of the $CO_2$+$SiCl_4$ mixture**

The bubble point data of the mixture $CO_2$+$SiCl_4$ measured using the PVT apparatus are reported in Table T1, where it is presented the liquid molar fraction of $CO_2$, the bubble temperatures and pressures along with their expanded uncertainties.

*Table T1. experimental bubble points for $xCO_2$+(1-x)$SiCl_4$ mixture with the PVT apparatus*

| **$CO_2$ Molar Fraction [%]** | **T [°C]** | **U(T) [°C]** | **P [bar]** | **U(P) [bar]** |
|---|---|---|---|---|
| 80.28% | 35.01 | 0.08 | 57.11 | 0.13 |
| | 50.11 | 0.07 | 72.46 | 0.29 |
| | 60.01 | 0.17 | 82.92 | 0.20 |
| | 70.09 | 0.11 | 93.44 | 0.08 |
| 84.95% | 35.02 | 0.09 | 60.41 | 0.25 |
| | 49.98 | 0.08 | 76.73 | 0.42 |
| | 59.93 | 0.09 | 87.82 | 0.31 |
| | 69.99 | 0.14 | 98.45 | 0.34 |
| 87.69% | 34.78 | 0.08 | 63.38 | 0.20 |
| | 49.92 | 0.09 | 80.53 | 0.32 |
| | 59.94 | 0.15 | 92.02 | 0.58 |
| | 69.97 | 0.14 | 101.59 | 0.38 |

The experimental liquid densities performed with the VTD are reported in Table T2 with the associated uncertainty.

*Table T2. experimental liquid densities ρ for $xCO_2+(1-x)SiCl_4$ mixture with VTD.*

| **$CO_2$ Molar Fraction [%]** | **Temperature [°C]** | **Pressure [bar]** | **Density [kg/m³]** | **U(T) [°C]** | **U(P) [bar]** | **U(Density) [kg/m³]** |
|---|---|---|---|---|---|---|
| 80.2 | 40.09 | 157.58 | 1058.6 | 0.06 | 0.05 | 5.9 |
| | | 141.64 | 1048.7 | 0.06 | 0.06 | 5.9 |
| | | 125.61 | 1037.9 | 0.06 | 0.05 | 5.9 |
| | | 100.24 | 1018.1 | 0.06 | 0.16 | 5.9 |
| | | 85.06 | 1003.8 | 0.06 | 0.14 | 5.9 |
| | | 111.88 | 1027.3 | 0.06 | 0.05 | 5.9 |
| | | 134.88 | 1044.1 | 0.06 | 0.04 | 5.9 |
| | | 195.18 | 1079.3 | 0.06 | 0.07 | 5.9 |
| 80.2 | 59.87 | 189.19 | 1016.2 | 0.06 | 0.05 | 2.4 |
| | | 170.74 | 1002 | 0.06 | 0.07 | 2.4 |
| | | 149.94 | 983.3 | 0.06 | 0.04 | 2.4 |
| | | 129.49 | 961.5 | 0.06 | 0.04 | 2.4 |
| | | 110.41 | 936.3 | 0.06 | 0.05 | 2.4 |
| | | 95.06 | 910 | 0.06 | 0.08 | 2.4 |
| | | 119.77 | 949.4 | 0.06 | 0.04 | 2.4 |
| | | 160.33 | 993 | 0.06 | 0.04 | 2.4 |
| | | 200.87 | 1024.4 | 0.06 | 0.06 | 2.4 |
| 80.2 | 79.9 | 235.43 | 954.6 | 0.06 | 0.05 | 2.5 |
| | | 214.33 | 937.5 | 0.06 | 0.05 | 2.5 |

| | | | | | | |
|---|---|---|---|---|---|---|
| | | 190.65 | 914.9 | 0.06 | 0.05 | 2.5 |
| | | 170.98 | 892.4 | 0.06 | 0.05 | 2.5 |
| | | 150.7 | 863.9 | 0.06 | 0.04 | 2.5 |
| | | 129.91 | 824.8 | 0.06 | 0.04 | 2.5 |
| | | 141.79 | 848.7 | 0.06 | 0.04 | 2.5 |
| | | 159.84 | 877.6 | 0.06 | 0.05 | 2.5 |
| 90.67 | 40.28 | 154.77 | 934.5 | 0.06 | 0.05 | 5.9 |
| | | 139.47 | 920.2 | 0.06 | 0.04 | 5.9 |
| | | 119.73 | 898.1 | 0.06 | 0.05 | 5.9 |
| | | 95.6 | 862.4 | 0.06 | 0.04 | 5.9 |
| | | 104.79 | 877.7 | 0.06 | 0.04 | 5.9 |
| | | 129.09 | 909.3 | 0.06 | 0.05 | 5.9 |
| | | 145.06 | 925.7 | 0.06 | 0.04 | 5.9 |
| 90.67 | 59.98 | 162.36 | 847.3 | 0.06 | 0.05 | 2.4 |
| | | 144.97 | 818.7 | 0.06 | 0.05 | 2.4 |
| | | 131.23 | 789.6 | 0.06 | 0.04 | 2.4 |
| | | 115.58 | 742.9 | 0.06 | 0.04 | 2.4 |
| | | 122.98 | 767.6 | 0.06 | 0.04 | 2.4 |
| | | 137.73 | 804.4 | 0.06 | 0.05 | 2.4 |
| | | 154.22 | 834.8 | 0.06 | 0.05 | 2.4 |
| | | 169.38 | 857.1 | 0.06 | 0.04 | 2.4 |
| | | 180.66 | 871.4 | 0.06 | 0.05 | 2.4 |

| | | | | | | |
|---|---|---|---|---|---|---|
| 90.67 | 79.9 | 213.13 | 792.1 | 0.06 | 0.04 | 2.5 |
| | | 199.03 | 772.1 | 0.06 | 0.08 | 2.5 |
| | | 170.59 | 719.3 | 0.06 | 0.05 | 2.5 |
| | | 150.55 | 665.6 | 0.06 | 0.04 | 2.5 |
| | | 140.01 | 626.8 | 0.06 | 0.05 | 2.5 |
| | | 120.52 | 523.8 | 0.06 | 0.04 | 2.5 |
| | | 129.5 | 577.6 | 0.06 | 0.04 | 2.5 |
| | | 159.12 | 690.9 | 0.06 | 0.04 | 2.5 |
| | | 179.58 | 737.9 | 0.06 | 0.04 | 2.5 |
| 72.73 | 40.29 | 148.34 | 1123.6 | 0.06 | 0.05 | 5.9 |
| | | 129.24 | 1113.4 | 0.06 | 0.11 | 5.9 |
| | | 110.01 | 1102.2 | 0.06 | 0.11 | 5.9 |
| | | 85.52 | 1086.1 | 0.06 | 0.12 | 5.9 |
| | | 97.73 | 1094.2 | 0.06 | 0.12 | 5.9 |
| | | 119.2 | 1107.6 | 0.06 | 0.05 | 5.9 |
| | | 138.2 | 1118.2 | 0.06 | 0.04 | 5.9 |
| | | 170.58 | 1134.5 | 0.06 | 0.05 | 5.9 |
| 72.73 | 59.95 | 199.09 | 1098.1 | 0.06 | 0.05 | 2.4 |
| | | 180.58 | 1087.3 | 0.06 | 0.06 | 2.4 |
| | | 160.48 | 1074.3 | 0.06 | 0.07 | 2.4 |
| | | 140 | 1059.4 | 0.06 | 0.05 | 2.4 |
| | | 111.67 | 1035.3 | 0.06 | 0.14 | 2.4 |

| | | | | | | |
|---|---|---|---|---|---|---|
| | | 123.98 | 1046.1 | 0.06 | 0.04 | 2.4 |
| | | 149.76 | 1066.6 | 0.06 | 0.05 | 2.4 |
| | | 170.26 | 1080.6 | 0.06 | 0.05 | 2.4 |
| 72.73 | 79.9 | 165.8 | 979.1 | 0.06 | 0.08 | 2.5 |
| | | 145.04 | 957.8 | 0.06 | 0.05 | 2.5 |
| | | 125.64 | 933.4 | 0.06 | 0.04 | 2.5 |
| | | 135.25 | 946.1 | 0.06 | 0.05 | 2.5 |
| | | 154.95 | 968.4 | 0.06 | 0.06 | 2.5 |
| | | 180.34 | 993.8 | 0.06 | 0.05 | 2.5 |
| | | 114.82 | 919.1 | 0.06 | 0.05 | 2.5 |

The additional bubble points measured with the VTD are reported in Table T3.

*Table T3. bubble points measured with the vibrating tube densimeter.*

| **$CO_2$ Molar Fraction [%]** | **T [°C]** | **P [bar]** |
|---|---|---|
| 82.2% | 79.89 | 102.92 |
| 90.67% | 60.25 | 93.90 |
| 72.73% | 40.33 | 57.80 |
| 72.73% | 60.18 | 76.52 |
| 72.73% | 79.90 | 95.13 |

## Bibliography of Supplementary Materials


[1] O.M. Suleimenov, A.Z. Panagiotopoulos, T.M. Seward, Grand canonical Monte Carlo simulations of phase equilibria of pure silicon tetrachloride and its binary mixture with carbon dioxide, Mol. Phys. 101 (2003) 3213–3221. https://doi.org/10.1080/00268970310M.

[2] O.M. Suleimenov, D. Banerjee, T.M. Seward, G. Gold, Vapour-Liquid Equilibrium Study of Silicon Tetrachloride-CO2 System, in: J. Conf. Abstr., 2000: p. 966.

[3] W.K. Tolley, Supercritical behavior of selected metal chlorides with carbon dioxide: A study of solubilities, solution densities, and excess enthalpies of mixing, 1990.

# *Chapter 5 - Analysis of $CO_2$+$C_2Cl_4$ mixture for HTHP*

*THIS CHAPTER IS BASED ON THE ARTICLE: "ANALYSIS OF THE $CO_2$+$C_2CL_4$ MIXTURE IN HIGH TEMPERATURE HEAT PUMPS: EXPERIMENTAL THERMAL STABILITY, LIQUID DENSITIES AND CYCLE SIMULATIONS", PUBLISHED IN ENERGY CONVERSION AND MANAGEMENT, ELSEVIER, DOI: HTTPS://DOI.ORG/10.1016/J.ENCONMAN.2024.119145*


**Abstract**

Transcritical heat pumps working with $CO_2$-based mixtures with a low-volatility dopant are found to achieve good performances in thermally integrated heat pumps, especially when sensible heat sources and heat sinks are considered. This paper introduces in literature tetrachloroethylene, $C_2Cl_4$, as $CO_2$-dopant for the mixture to be adopted as working fluid in high temperature heat pumps. To calibrate the thermodynamic model used in the cycle simulations, an experimental characterization on the mixture is proposed: liquid densities of the mixtures are measured, in a wide range of concentration, optimizing the binary interaction parameter of the Peng Robinson equation of state. Moreover, the thermal stability of pure $C_2Cl_4$ is experimentally evaluated, identifying the maximum allowable compressor outlet temperature between 200°C and 250°C, with a decomposition rate below 1%/year if the fluid is kept at temperatures around 200°C. Then, the potentialities of this very high temperature heat pump are assessed in spray dryer applications: a coefficient of performance around 3.38 is obtained for a conventional spray dryer plant, corresponding to 73% of second law efficiency, considering an air flow heated from ambient temperature to 200°C as the sink, while cooling the sensible heat source, available at 76°C, below 30°C. As term of comparison, the same system adopting propane, instead of the $CO_2$+$C_2Cl_4$ mixture, would achieve a coefficient of performance and second law efficiency of 2.94 and 64%, respectively.


## 5.1 Introduction

Within the heat pump research filed, fast-growing interest is given to very high temperature heat pumps (VHTHP) with maximum temperatures above 150°C, and high temperature heat pumps (HTHP) with maximum temperatures above 100°C [1,2], considered crucial to decarbonize many industrial sectors that may be otherwise "hard to abate" with respect to the carbon emissions [3,4]. As shown in literature by Chua [5], various industrial processes can be decarbonized with thermal power from HTHP, such as the paper, food or textile manufacturing, or the space heating in the civil sector with district heating networks.

When the system is analysed at component-level, according to a literature review from Arpagaus [6], screw compressors are largely adopted for HTHP, whereas oil-free centrifugal compressors are also mentioned for their importance in increasing the cycle efficiency [7]. Limiting the problems of the fluid contact with the lubricant oil, there are few solutions available on the market for temperature levels above 150°C exploiting refrigerants such as R-245fa or R-1336mzz(Z).

Detailed reviews are available in literature for screening refrigerants for HTHP [8]: in general, families of working fluids such as hydro-fluoro-olefins (HFO) and hydro-chloro-fluoro-olefins (HCFO) are considered as valid alternatives to hydro-fluoro-carbons (HFC) due to their limited global warming potential (GWP) and ozone depletion potential (ODP) effects [9].

Given the relatively low critical temperature of commercial refrigerants (the refrigerant with the highest critical temperature is R-1336mzz(Z), at 171°C), a paradigm shift from subcritical layouts to transcritical ones is necessary if the HTHP is coupled with high sink temperatures. As a matter of fact, carbon dioxide ($CO_2$) is one of the most considered working fluid for transcritical HTHP, as it is already a commercial solution for HTHP with cold sources at ambient temperature [10]. For example, a possible application for the recovery of low temperature heat sources with transcritical $CO_2$ heat pumps investigated in literature can be identified in the waste heat from data centers [11], available within the 25-35°C temperature range. Similarly, simple layouts of transcritical $CO_2$ heat pumps can be also exploited for the simultaneous space heating and cooling in the civil sector [12]. Nevertheless, due to the low critical temperature of $CO_2$ (31°C) cold sources at temperatures higher than 40-50°C would induce significant irreversibility in the evaporator of the transcritical HTHP: under this perspective, the use of $CO_2$ binary mixtures with a higher critical temperature allows for the optimal exploitation of low-grade sensible heat by tuning the temperature profile at the evaporator, minimizing the average temperature difference between the heat source and the working fluid.

The adoption of $CO_2$ mixtures as working fluids can play an important role to improve the HP coefficient of performance (COP) by exploiting sensible and low temperature heat sources, in the 70-90°C range, consistently above the $CO_2$ critical temperature: this category of HP, thermally integrated into a heat source at a temperature higher than the ambient one, can be in fact considered in waste heat upgrading processes. As the waste heat can be recovered from many applications [13], such as flue gases at the stack of conventional systems or waste by-product of industrial processes, at this low temperature range it is not always techno-economical advantageous to exploit the waste heat in a power cycle for electricity production [14]. According to reviews of waste heat availability in literature, a share of waste heat can be classified as technically recoverable but not interesting from an economical point of view, as proposed by Brückner [15]. In this context, thermally integrated heat pumps can also unlock the techno-economic potential that was originally not foreseen for a direct use of the available low temperature waste heat.

In addition to the effects of the heat source temperature profile on the HP, transcritical HTHP are proved to be effective also for applications with sensible heat sinks. This configuration of HTHP are studied in literature exploiting $CO_2$ as working fluid: Carnot batteries [16] (already developed by ABB [17], MAN-Energy Solutions [18] and Echogen [19]), advanced drying processes (as discussed in many literature works as by Abedini [20] and Vieren [21]), and high temperature pressurized water production useful both for industrial processes and for district heating are a few examples of possible applications. Regarding $CO_2$-mixtures, recent studies of HTHP with sensible heat sources evidenced promising configurations in terms of obtainable COP for various applications, such as thermally integrated Carnot batteries [22,23], upgrade of waste heat up to 90°C as proposed by Liu

[24] or low temperature drying processes as in the work of Dai, where the mixing of a dopant with $CO_2$ helps in reducing the cycle maximum pressure [25].

Among the many possible working fluids for this wide category of thermodynamic cycles, this work proposes tetrachloroethylene (i.e. $C_2Cl_4$, CAS number: 127-18-4) as dopant for $CO_2$ to be used in cycles with maximum temperatures up to around 250°C. Tetrachloroethylene is a non-flammable, non-reactive fluid with a limited toxicity level. It is liquid at ambient temperature, since its normal boiling point is 121°C, it can be put in contact with the skin without causing permanent damage and it has an aethereal odour that can be detected by humans at concentrations above 1 ppm (7 mg/m$^3$). It is cheap and it has plenty of commercial applications, such as being a dry-cleaning agent for textiles and an excellent solvent for organic materials: in fact, it is still massively produced and sold worldwide [26]. Its ODP approaches zero [27], as the compound is classified as a very short-lived substance, differently than other substances, like chlorofluorocarbons, that were banned by the Montreal protocol in 1987. The thermodynamic characteristics of the fluid are well known, and experimental data of this pure fluid are available in literature [28,29]. Nevertheless, even if $C_2Cl_4$ was historically present at high concentrations in dry-cleaning facilities in 1970s and 1980s (it was measured with average concentrations around 100 to 200 mg/m$^3$ in the 1980s in the US and Nordic European countries [30,31]), nowadays an accurate management of the leakages from the HTHP loop into the environment must be foreseen, considering that the fluid was categorized by the World Health Organization in 2017 as carcinogenic agent in class A2 (defined as "probably carcinogenic"). To do so, a series of technical solutions (such as dry gas seals for the turbomachinery leaks) are nowadays commonly adopted in the turbomachinery industry to avoid the dispersion of the working fluid in the external environment, allowing to deal with extremely problematic fluids.

$C_2Cl_4$ is considered of interest as dopant for a $CO_2$ mixture, since a very small amount of the dopant in the mixture (even below 1% on molar basis, i.e. below 5% on mass basis) is sufficient to drastically move the critical temperature of the resulting $CO_2$+$C_2Cl_4$ mixture above 70°C, allowing for large glides during the evaporation process, hence permitting favorable conditions for recovering heat from sensible sources. The dominant fraction of $CO_2$ in the mixture, finally, drastically reduces any effect related to the limited toxicity of the fluid and the GWP of the resulting working fluid.

Very few pieces of information are available in literature regarding $C_2Cl_4$ thermal stability, and no information about the thermodynamic behavior of the mixture can be found: according to a literature source the fluid starts decomposing within a narrow timespan below 400°C, determined experimentally by flowing vapors into quartz tube [32]. However, quartz tube is an inert environment, and the residence time considered in literature is too limited to understand the actual thermal resistance of the fluid, making the outcome of this test not relevant for real applications

Consequently, this work adopts a robust methodology to experimentally determine the fluid thermal stability, with the experimental procedure presented in literature [33], closing the research gap on the thermal stability of the selected fluid. In addition, in order to close the gap on the lack of available data for the $CO_2$+$C_2Cl_4$ mixture, a set of liquid densities of the mixture on the high-pressure region are collected: the data are exploited as a basis for a preliminary selection of the proper equation of state (EoS) for this mixture, necessary for the cycle calculations and the identification of

the HTHP performances. The methods developed in this work can be reproposed and extended in future works to other $CO_2$-mixtures with heavy dopants, characterized by a high normal boiling point, that can be of interest for the same application.

## 5.2 Methodology and overview of the work

The schematic of the full methodology adopted to assess the potentialities of the $CO_2$+$C_2Cl_4$ mixture as working fluid for VHTHP is depicted in Figure 1.

Experimental data on the specific mixture are necessary to have a preliminary characterization of the thermodynamic behavior of the fluid in a wide range of temperatures, pressures and compositions. In this work, an experimental campaign was carried out to measure liquid density of the mixture at high pressure and low temperature, using a validated methodology with a vibrating tube densimeter at the CTP experimental platform of Mines Paris, PSL University, Centre for Energy Environment Processes (CEEP), in Fontainebleau, France.

The measurement of the liquid densities of the mixture allowed the calibration of the Peng Robinson EoS, by fitting the binary interaction parameter on the collected experimental data. Focusing on the application of the mixture in HPs, an accurate characterization of the density across the whole range in temperatures and pressures can be valuable to have a confident characterization of the compressor volumetric ratio and the volumetric heating capacity of the cycle, two crucial parameters.

As a second step, it is important to define the maximum temperature at which the fluid can be operated. To do so, stability tests are conducted on $C_2Cl_4$, according to a validated methodology for pure fluids at the Fluid Test Laboratory of the University of Brescia (Italy): the $CO_2$-dopant is charged in a vessel and kept for one hundred hours at a predefined temperature, in an oven. Quantitative analyses are performed before and after the thermal stress, determining the eventual decomposition rate of the fluid. The simulations proposed in this work on HTHP will be coherent with the experimental campaign on thermal stability, in particular by limiting the maximum temperature of the working fluid in the HTHP at a value that leads to an almost negligible decomposition of the working fluid along the plant lifetime (below 2% per year).

Once the thermal stability analysis and the calibrated EoS are available, the modelling of the innovative VHTHP using $CO_2$+$C_2Cl_4$ as working fluid can start and the potentialities for a specific application assessed. In particular, the temperature range of both the sink and the source of the HP should be defined to identify the mixture composition which maximizes the COP. In addition, with respect to literature works on subcritical heat pumps with mixtures that present good performances in subcritical configurations with low temperature lifts [34], in this work excellent cycle performances are evidenced with large temperature lifts and in transcritical cycle configurations, closing this research gap.

Finally, a comparison between the HTHP performance proposed by the mixture and the one obtainable with conventional pure fluids for the same application is shown, fully demonstrating the interesting effectiveness of the innovative solution. The comprehensive analysis proposed to assess the potentialities of the innovative working fluid in commercial application can be extended and

applied to any other fluid and other conditions, providing a relevant contribution to the HTHP development.

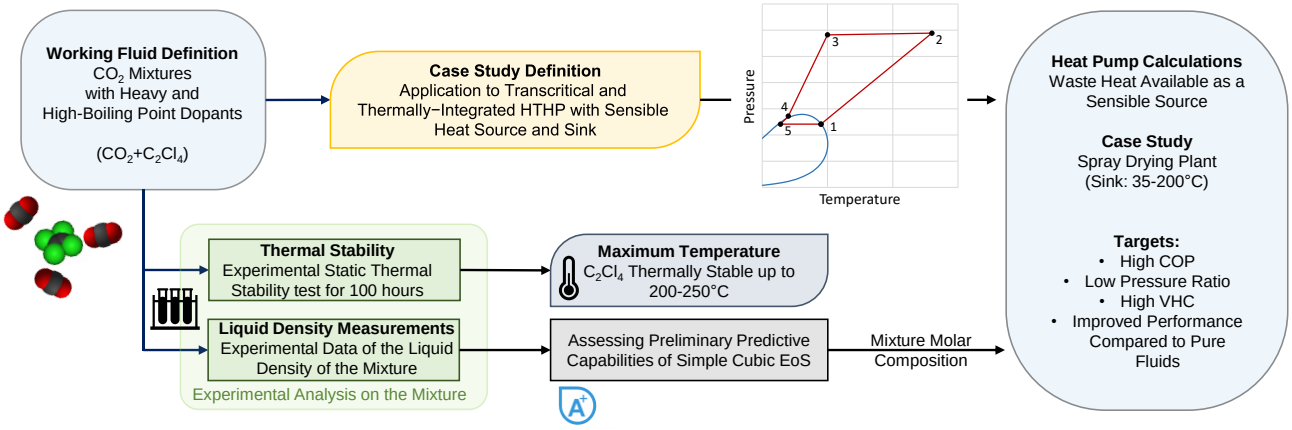


*Figure 1. Overview of the methodology adopted in this work*

## 5.3 Experimental analysis on the $CO_2$+$C_2Cl_4$ mixture liquid densities

Density measurements of the $CO_2$+$C_2Cl_4$ mixture have been obtained at the CTP experimental platform of Mines Paris, PSL University, Centre for Energy Environment Processes (CEEP), in Fontainebleau (France), through a Vibrating Tube Densimeter (VTD) manufactured by Anton Paar (model DMA HPM). The test rig is already described in literature by Nazeri [35] and presented by the authors of this work for the experimental analysis of a different $CO_2$-based mixture in literature [36]. The mixture is prepared in a variable volume cylinder by gravimetric method as described in supplementary materials.

The layout of the apparatus is depicted in Figure 2: the mixture is kept under pressure in liquid condition within the variable volume cylinder by a piston controlled with pressurized nitrogen. Afterwards, it flows into the VTD immersed into a thermostatic bath (opening the valves V4 and V5): when temperature and pressure reach equilibrium, the density can be measured. In order to modify the pressure of the fluid inside the VTD, a portion of liquid mixture can be accommodated in the variable volume cell, before the venting system, at constant temperature and composition. The uncertainties of the measured quantities (density, temperature and pressure) are computed as reported in supplementary materials, coherently with the use of the same VTD apparatus as reported in literature [36]. The thermostatic bath allows to keep a constant temperature along the measurements. A detailed description of the working principle of the measurements carried out in the VTD is reported in supplementary materials.

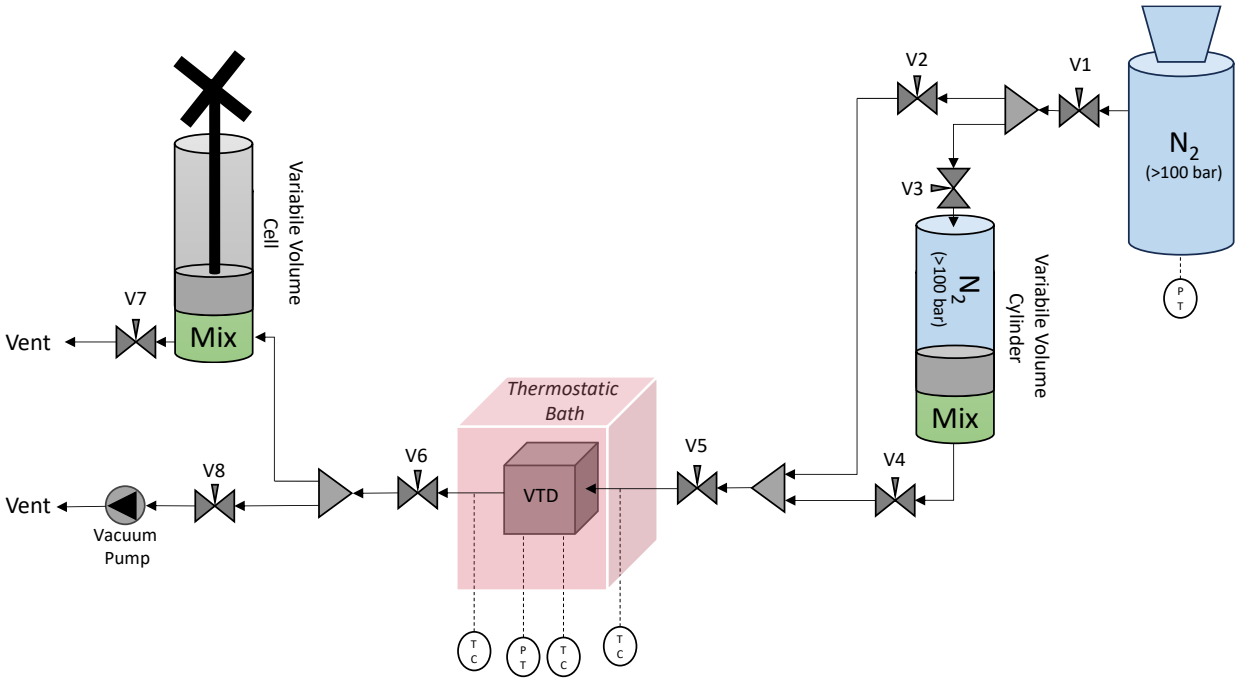


*Figure 2. Schematization of the test rig to measure the mixture liquid density*

The densities of the $CO_2$+$C_2Cl_4$ mixture are measured correlating the period of vibration of the tube ($\tau$) with the density of a reference fluid (pure $CO_2$ in this work) at 40°C, 60°C and 80°C (temperature conditions compatible with the thermostatic bath operative range), through a linear correlation as reported in Equation (1):

$$\rho|_T = f\,(\tau)_T = A \cdot \tau + B \tag{1}$$

To define the calibration curve of Equation (1), finding the numerical values of A and B at each temperature, a calibration of the VTD with pure $CO_2$ was carried out. The Span and Wagner reference EoS [37] is used for calculating the density of $CO_2$ at each measured temperature and pressure.

Density of the mixture has been measured from subcooled liquid down to a condition slightly above the bubble point, at each temperature. The results are graphically represented in Figure 3: composition with a molar fraction of $CO_2$ from around 70% to 93% have been measured. Measurements are reproduced in a narrow range of compositions (close to 70.4% molar in $CO_2$) with a different subsequent freshly charged mixtures to validate the experimental measurements. The coherency between the measured values of density at 70.47% and 70.31% molar content of $CO_2$ at two different temperatures confirms the consistency of the overall experimental procedure adopted for the preparation of the mixture. The experimental data collected and plotted in Figure 3 are gathered, along with the respective uncertainties, in Appendix A.

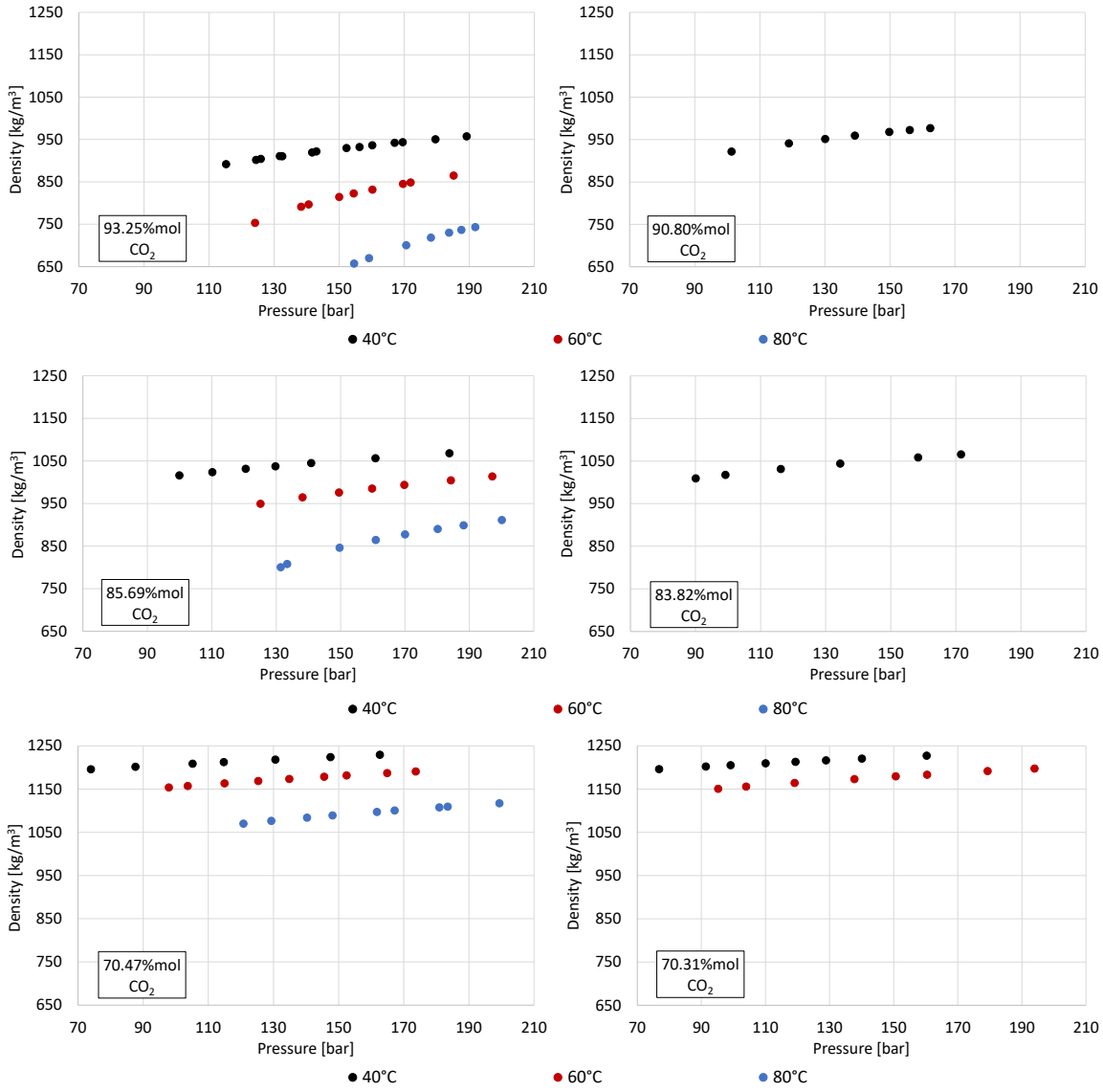


*Figure 3. Densities of the $CO_2$+$C_2Cl_4$ liquid mixture measured in the VTD proposed in this work*

## 5.4 Preliminary optimization of the Peng Robinson EoS on liquid densities

To preliminary estimate the performance of the selected mixture as working fluid in HTHP, an evaluation of the predictive behavior of the Peng Robinson EoS is presented in this work. The analysis is based on the fitting with the EoS of the experimental densities, as they are currently the only available set of experimental data in literature for this mixture.

The Peng Robinson EoS adopted for the simulations of this work is the one originally proposed in 1976 with the original Soave alpha function [38], embedded in ASPEN Plus v.11 [39], with Van der Waals mixing rules.

The binary interaction parameter (BIP), also known as $k_{ij}$ for cubic EoS, of the selected PR EoS for this mixture is therefore optimized by minimizing the average absolute deviation percentage (AAD%), proposed in Equation (2), between the density experimental data from this work and the computed values by the model.

$$AAD_{\rho_{mix}}[\%] = \frac{100}{N} \cdot \sum_{i=1}^{n} \left| \frac{\rho_{exp,mix} - \rho_{calc,mix}}{\rho_{exp,mix}} \right| \quad (2)$$

A sensitivity analysis is performed on the $k_{ij}$ of the EoS, varied between -0.1 and 0.25 and assumed as independent from the temperature. According to this preliminary binary interaction parameter optimization procedure, a value of $k_{ij} = 0.10$ is found to be corresponding to the lowest $AAD_{\rho_{mix}}$ (at about 2.2%), whereas the maximum deviation between the measured and computed density is 5.3%. The comparison between the predicted values of the PR EoS with $k_{ij} = 0.10$ and the experimental liquid density data is graphically shown in Appendix A, evidencing the very good match between the two sets of data.

Moreover, it has been found that the resulting value of the binary interaction parameter introduces no deviations in the phase envelope of the $CO_2$+$C_2Cl_4$ mixture for any $CO_2$ molar concentration above 95%, while at the same time providing a good approximation of its densities: in that composition range the cricondenbar of the mixture is over 95 bar and its cricondentherm higher than 85°C, not representing conditions of interest for the HTHP investigated in this study. Therefore, even if VLE data are theoretically necessary for a conclusive definition of the binary interaction parameter of the cubic EoS, in the composition range of interest in this work for this specific application the $k_{ij}$ does not influence the prediction of the VLE conditions for this mixture.

A more detailed evaluation of the EoS performances and a more accurate selection of the available EoS is considered out of the scope of this work, given the limited amount of available experimental data, but it can be carried out in future works, when experimental data on the VLE of the mixture will be collected. Under this future scenario, the thermodynamic models can be optimized through binary interaction parameters on those experimental data, providing a good approximation of the phase-behaviour for any mixture composition. In conclusion, to estimate the mixture properties (including the enthalpies and entropies of the mixture) when adopted in a thermodynamic cycle as proposed in Section 5 of this work, the PR EoS with a $k_{ij}$ of 0.10 is then preliminary adopted.

## 5.5 Thermal stability of Tetrachloroethylene

An experimental campaign to determine the thermal stability threshold of $C_2Cl_4$ is carried out in this work, which is an essential information for its application as working fluid in high-temperature applications, both for heat pumps and power cycles. $CO_2$ is excluded from the investigation due to its recognized stability at the temperatures of interest for the HTHP application. In particular, the analysis on the thermal stability allows to determine the allowable range of compressor outlet temperature (i.e. maximum temperature of the heat pump).

The methodology adopted to evaluate the thermal stability of $C_2Cl_4$ is a static isochoric method originally developed in the Fluid Test Laboratory of the University of Brescia [40], to assess the thermal stability of organic fluids adopted in Organic Rankine Cycles. The methodology assumes that even a small presence of thermal decomposition products, typically lighter and more volatile, can be identified by measuring the vapor pressure of the fluid after thermal stress. The partial pressure of non-condensable decomposition products can be recognized from the deviation of the measured fluid pressure from the vapor pressure of the fresh fluid (before thermal stress). This

deviation becomes notably evident when measuring sub-atmospheric or low values of the vapor pressure, and for this reason it was decided to exclusively test $C_2Cl_4$, rather than the overall mixture: decomposition products are more evident when testing $C_2Cl_4$, due to the fluid high boiling point (121°C), compared to vapor-liquid pressure conditions of a $CO_2$+$C_2Cl_4$ mixture.

The core of the experimental apparatus adopted for the thermal stability test is represented in Figure 4, while more details are outlined in the previous work of Pasetti [40]. The main component is the sample cylinder ("A") manufactured in AISI 316L by Swagelok, a material commonly utilized in high-temperature applications. To ensure precision across the measured pressure range, two pressure transducers are integrated into the system. The reference vapor pressure is measured using a Klay 2000-SAN pressure transmitter ("PT1" in Figure 4) with an adjustable span from 1 to 10 bar and an accuracy of 0.1% of the adjusted span. During the 100-hour thermal stress in the muffle furnace, the valve "V2" is kept closed to shield the low-pressure transmitter from overpressure. In this scenario, pressure is recorded using the high-pressure transmitter ("PT2" in Figure X), a Klay 2000-SAN with an adjustable span from 20 to 100 bar. A TC-Direct thermocouple (tolerance class I) is inserted into the cylinder through its welded housing ("B" in Figure 4).

The cylinder is initially loaded with a mass of liquid $C_2Cl_4$ of about 42 grams: the fluid is supplied by Merck, with a reported purity level exceeding 99%.


*Figure 4. Main components of the thermal stability test: the AISI 316L cylinder (A), the housing of the temperature probe (B), the low-pressure scale pressure transducer (PT1), the high-pressure scale pressure transducer (PT2), the main valve isolating the cylinder (V1), the valve protecting the PT1 from overpressure (V2), the valve connecting the circuit to the environment (V3). Figure adapted from authors previous work [41].*

The methodology to assess the thermal stability of $C_2Cl_4$ involves the following preliminary steps: (i) the evacuation of the system using a vacuum pump by opening valve V3, (ii) the introduction of the pure fluid into the cylinder, and (iii) the operation of the vacuum pump to remove air traces that may have entered the system. Afterwards, the cylinder is disposed vertically in a thermostatic bath

to measure the reference vapor pressure within a predetermined temperature range. Finally, the vessel is placed horizontally in the muffle furnace for a 100-hour thermal stress at a selected constant temperature: after the thermal stress, the system is replaced into the thermostatic bath to measure the fluid vapor pressure within the same temperature range of the reference test. The overview of the procedure followed is proposed in Figure 5.

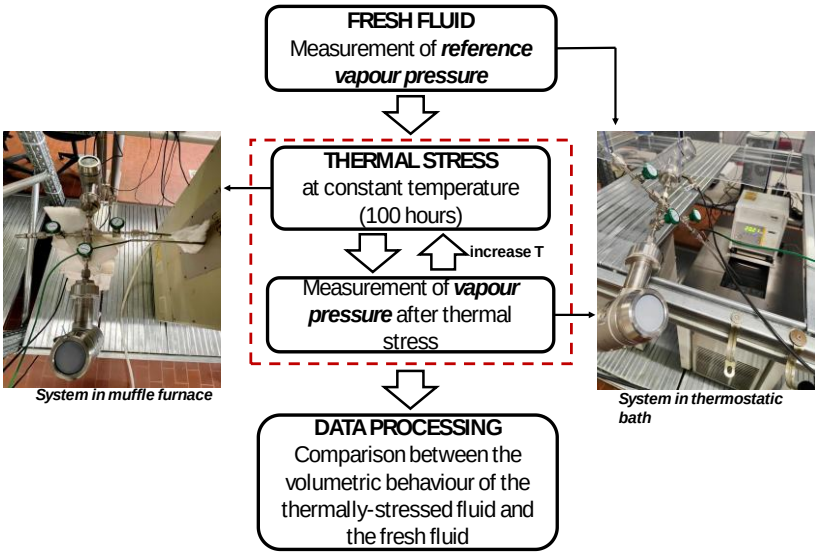


*Figure 5. Methodology adopted for the thermal stability test as already proposed in literature [41].*

If the fluid has not deteriorated after the thermal stress, the procedure can be repeated by placing again the cylinder in the furnace at a higher temperature: the test can be considered concluded when either a target temperature is achieved during the thermal stress or when a significant divergence in the behavior of the fluid is noticed compared to the reference behavior.

## 5.6 Results of the thermal stability analysis on tetrachloroethylene

For this fluid, the reference vapor pressure and the pressures measured along all thermal stresses are measured in the temperature range 60-120°C, to focus on sub-atmospheric conditions. Following the methodology described in the previous section, the experimental campaign consists of three thermal stresses from 200°C up to 300°C with a temperature step of 50 °C for the investigated fluid.

The results shown in Figure 6 indicate that, based on the deviation of the fluid behavior with respect to the reference condition, $C_2Cl_4$ can be considered thermally stable at 200°C, as pressure variations are insignificant compared to the reference vapor pressure. However, evidence of thermal degradation becomes apparent after exposure to thermal stress at 250°C, with substantial degradation observed in the final 100 hours at 300°C.

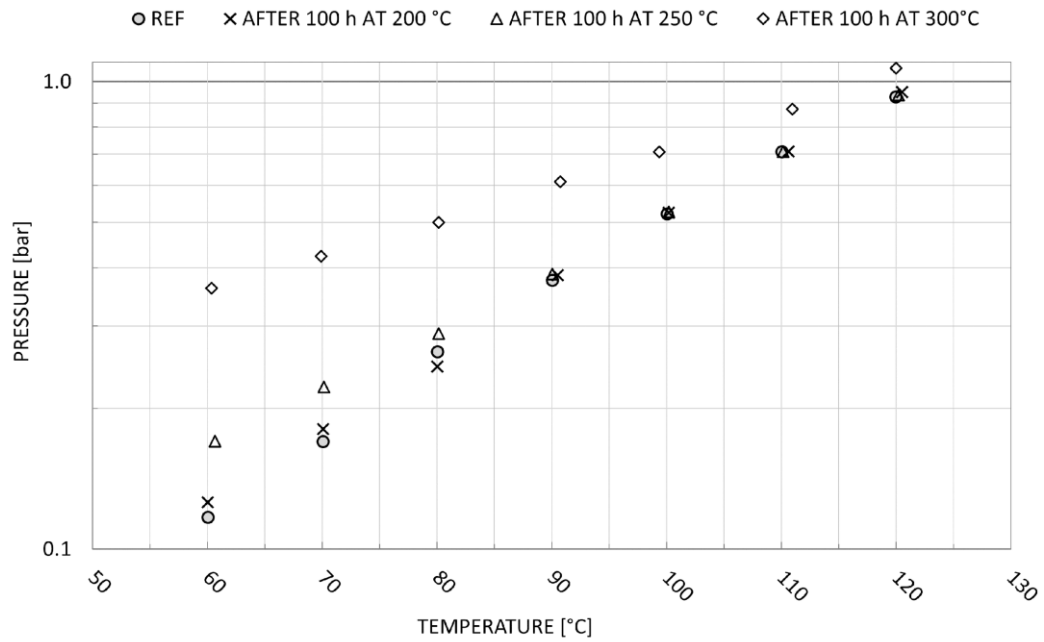


*Figure 6. Measured saturation pressure of $C_2Cl_4$ before ("REF") and after subsequent 100-hours thermal stress at different temperatures*

To better quantify the degradation of the fluid at different temperatures, the rate of unimolecular decomposition, $k^*$, has been calculated adopting the same methodology detailed in Invernizzi [42] (equations 1-8 of the reference work) and in the work of Doninelli [43], that is not reproposed for sake of brevity. The resulting value $k^*$ is defined and computed as the frequency of decomposition of the fluid investigated. From $k^*$ it can be also univocally computed the annual decomposition rate, expressed as percentage of $C_2Cl_4$ moles in the vessel that decomposes every year due to the high temperature conditions, under the assumption that the fluid remains at constant temperature for 8760 hours per year.

The calculated $k^*$ from the experimental data of the thermal stability stress and the associated annual degradation rate are presented in Figure 7, along with the associated error band.

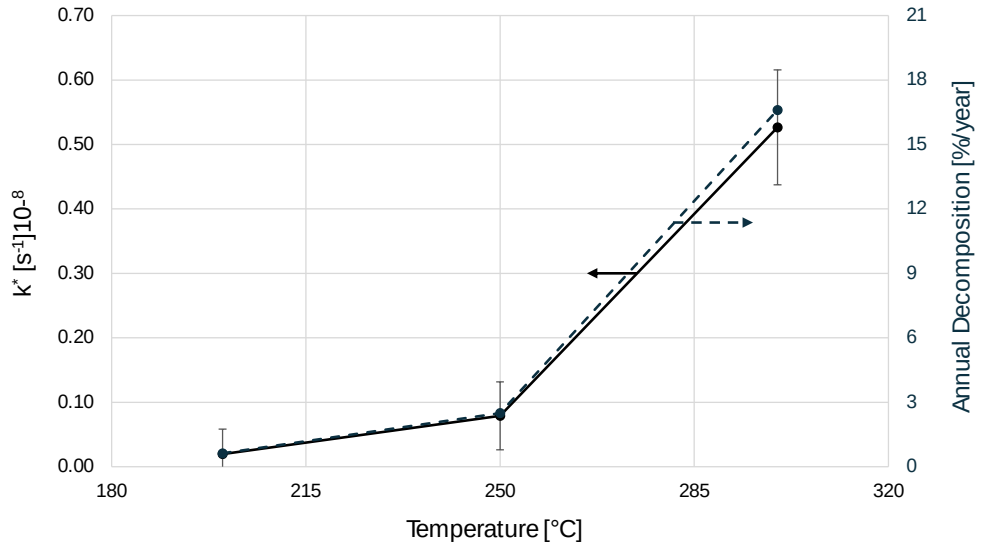


*Figure 7. Unimolecular decomposition rate k* (black solid line) at the investigated temperature range. Corresponding annual decomposition rate of the fluid (dark blue dotted line)*

To extend the analysis on the thermal stability of the fluid, in this work it is proposed also a comparative analysis between $C_2Cl_4$ and other already investigated fluids in literature under the same experimental setup and methodology [44]. Excluding fluids adopted in high-temperature ORC units (such as toluene, cyclopentane, pentane), the thermal stability of butanol and trifluoroethanol is reported in comparison with the stability of $C_2Cl_4$, as these two fluids are experimentally investigated in the literature work within a similar temperature range. The results of the comparison are underlined in Figure 8.

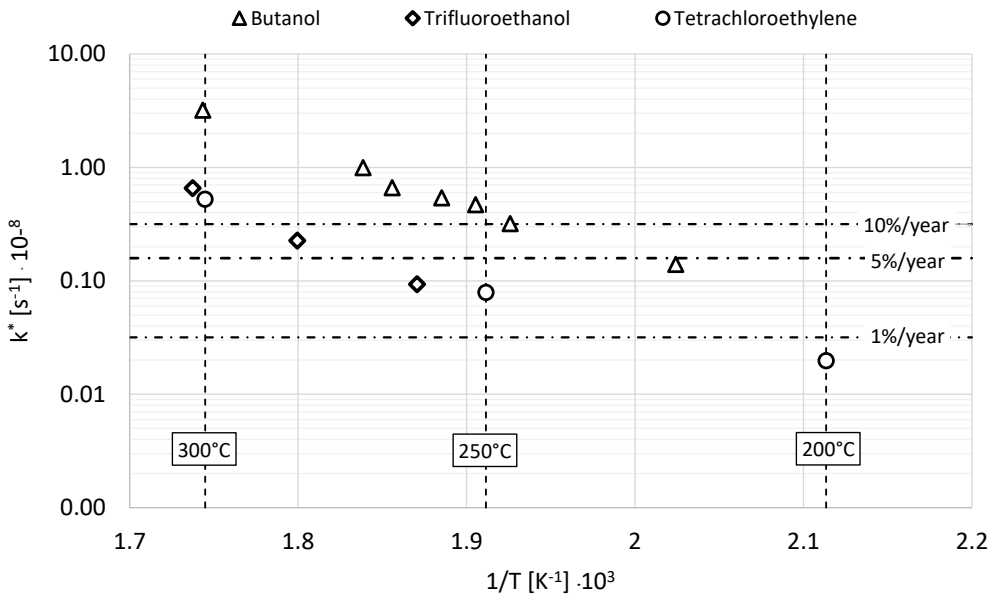


*Figure 8. Rate of decomposition of tetrachloroethylene compared to other fluids previously tested with the same methodology*

From the comparison presented in the figure, the degradation rate of tetrachloroethylene results to be similar to trifluoroethanol ($C_2H_3F_3O$) decomposition, and much lower that of butanol ($C_4H_{10}O$). At 250°C, the degradation rate of $C_2Cl_4$ is seven times lower than that of butanol.

From the results presented in this section, it is concluded to reasonably suggest using $C_2Cl_4$ up to a maximum application temperature in the range between 200 and 250°C.

## 5.7 Performance of the $CO_2$+$C_2Cl_4$ mixture for high temperature heat pumps

After the experimental characterization of the innovative $CO_2$-mixture, the performances of HTHP adopting this working fluid are evaluated in this chapter presenting a case study for a specific industrial application.

The performance of the mixture in a thermally integrated HTHP will be investigated for a spray drying plant, adopted mainly in the food industry and in other sectors, such as the chemical and pharmaceutical. As mentioned by Zühlsdorf [3], spray dryers in the food industry are typically in the MW-scale and are operated with a large number of equivalent hours. Spray dryers are used to turn liquid solutions (or slurry) into dried powders of the materials fed to the system. To do so, the feed is pressurized and atomized passing through nozzles, increasing the surface area per unit of volume: then, the flow is invested by hot air, evaporating the water.

Various literature studies identify the temperature range of the heat source and the sink for such application: a study of Wang [45] discussed a case study of spray drying plants in the dairy industry, where the waste heat is available at 76°C, released by the dryer itself, whereas hot thermal power must be produced to heat dry air from ambient conditions up to 200°C. Another case study described by Zühlsdorf [3] pointed at the temperature range of the sink to be between 60° to 210°C, whereas a literature work by Vieren [21] also investigated an HTHP with the same heat sink of Wang. Moreover, Schlosser investigated high temperature processes, including heat pumps, to provide heat to a spray dryer for the dairy industry, identifying the same target temperature range [46].

Considering the information available in literature, the cold source of the heat pump studied in this work is assumed to be the high-humidity air at the outlet of the drying process, at a temperature of 76°C according to the literature reference of Wang [45]. To ensure this target, the maximum temperature of the working fluid is set in this work at 210°C at compressor outlet, a value compatible with the experimental results of the thermal stability analysis, while the minimum temperature of the working fluid in the high-pressure HX is set at 60°C, enabling the heating of the ambient air at any reasonable value of ambient temperature. The calculations will be performed by maximizing the heat source exploitation, ensuring a target temperature difference of the heat source above 40°C, marking a difference between a heat pump based on mixtures with one adopting a pure fluid.

Once the heat source and sink are defined, these impose a set of boundary conditions on the cycle parameters. As a matter of fact, the cycle maximum pressure is determined by the compressor isentropic efficiency and the target value of its outlet temperature (210°C), and it is computed on a case-by-case basis. On the other hand, the minimum pressure of the system is evaluated at the dew point of the mixture for a compressor inlet temperature of 71°C, a value chosen to ensure a 5°C pinch point temperature difference with the cold source available at 76°C. As thoroughly discussed in

literature by Fu [47], the proposed configuration of heat pump for drying plants is extremely effective, since the heat source of the HTHP is the by-product at the outlet of the dryer itself, exploited in a closed-cycle process.

The calculations of the HTHP are carried out considering a non-recuperative transcritical cycle layout, chosen for its simplicity. The necessity to operate the cycle in transcritical conditions arises from two major factors: i) to reach high-pressures in the hot side, leading to a high reduced pressure (easily above 2), thus ensuring a near constant heat capacity of the working fluid across the gas cooler, avoiding problems related to the pinch-conditions in the high temperature heat rejection section, and ii) to recover most efficiently, boosting the cycle performance, the pressure difference from the high to low pressure side of the cycle using an expander operating only in single phase, avoiding any mechanical issue of the turbomachinery. Additionally, a transcritical heat pump also leads to very favorable trends of the main technical key parameters of the cycle, with a limited pressure ratio and volumetric ratio across the compressor, easing its manufacturing and operation even withstanding at very high nominal pressures.

Considering a non-recuperative layout, the HTHP can be characterized by the key performance parameters commonly defined and proposed in literature, reported in Equations (3) to (8):

$$COP = \frac{\dot{Q}_{SINK}}{\dot{W}_{Compressor} - \dot{W}_{Expander}} \tag{3}$$

$$\Delta T_{Heat\ Source}\ [°C] = T_1 - T_5 \tag{4}$$

$$PR_{Compressor} = \frac{P_2}{P_1} \tag{5}$$

$$VR_{Compressor} = \rho_2/\rho_1 \tag{6}$$

$$VHC\ \left[\frac{MJ}{m^3}\right] = \rho_1 \cdot (h_2 - h_3)_{SINK} \tag{7}$$

$$COP_{II\ Law} = \frac{COP}{COP_{Lorenz,mixture}} \tag{8}$$

While the thermal power and mechanical power across the HTHP components are defined as in Equations (9) to (11):

$$\dot{W}_{Compressor} = \dot{m} \cdot (h_2 - h_1) \tag{9}$$

$$\dot{W}_{Expander} = \dot{m} \cdot (h_3 - h_4) \tag{10}$$

$$\dot{Q}_{SINK} = \dot{m} \cdot (h_2 - h_3) \quad (11)$$

Finally, the main assumptions of the HTHP non-idealities simulated in this work with the $CO_2$+$C_2Cl_4$ mixture are proposed in Table 1: it is noticeable that the relatively high values of the isentropic efficiencies of the turbomachinery points to simulations for medium-to-large scale heat pump. In addition, for an intuitive representation of the results, the ideal coefficient of performance of the heat pump is computed in this work on the basis of the temperatures of the working fluid, making this value independent from the pinch between the $CO_2$-mixture and both the heat sink and the cold source. As mentioned in the table, the EoS used in this analysis on the $CO_2$+$C_2Cl_4$ mixture (hence for the calculation of the enthalpies and entropies of the mixture) is the Peng Robinson EoS, implemented as proposed in ASPEN Plus v.11 with the binary interaction parameter computed in this work. Analogously, also the HTHP is simulated in ASPEN Plus.

*Table 1. Characteristics and non-idealities of the transcritical HTHP of this work*

| Parameter | Assumption at Design |
|---|---|
| Compressor Isentropic Efficiency | 80 % |
| Expander Isentropic Efficiency | 80 % |
| Pressure drops at Sink HX (supercritical cooler) | 2 bar |
| Compressor Inlet | At Saturated Condition, at 71°C |
| Expander Outlet | At Saturated Condition |
| Electromechanical losses | Neglected |
| Equation of State | Peng Robinson ($k_{ij}$=0.1, as in this work) |
| Heat sink Temperature range | 35 - 200°C |
| Working fluid Temperature range across Sink HX (supercritical cooler) | 60 - 210°C |
| Heat source Temperature | 76°C |

To properly evaluate the technical performance and effectiveness of the system, the results of the innovative HTHP with the $CO_2$-mixture are compared with different HTHP adopting conventional working fluids. To do so, ten different pure fluids are considered, simulating the HTHP for the same application: n-pentane, R-134a, R-1234yf, R-1234ze, propane, iso-pentane, R-245fa, R-365mfc, R-236ea, R-236fa. The performance of these pure-fluids HTHP are evaluated with the EoS provided by Refprop v.10.0 [48]. The boundary conditions on the temperature range of both the heat sink and the heat source are the same as the one previously mentioned for the $CO_2$+$C_2Cl_4$ mixture HTHP, along with the cycle simple non-recuperative layout, and the main assumptions reported in Table 1, thus ensuring a fair comparison depending only on the thermodynamic of the working fluid selected. Similarly to this work, analogous simulations of transcritical HTHP with pure refrigerants and simple cycle layouts, heating air up to 200°C, have been already proposed by Zhao [49], even though

different boundary conditions were assumed, since in the literature work of Zhao it was assumed to thermally integrate the heat pump with an external heating network at 88°C, evaporating the refrigerants at 85°C.

Finally, for the calculations of the pure fluid HTHP, the compressor inlet temperature is univocally determined at 71°C, as for the $CO_2$-based heat pump, and the cycle maximum pressure is defined with the same methodology as for the mixture. The comparison is proposed at constant thermal power from the cold heat source, with different useful power to the dryer depending on the COP computed.

## 5.8 Case study results: HTHP with $CO_2$+$C_2Cl_4$ mixture for spray drying applications

The calculations of the HTHP with the $CO_2$+$C_2Cl_4$ mixture are carried out by finding the composition of the mixture that can ensure a large heat source exploitation, without compromising the system efficiency, fixing the compressor inlet temperature at 71°C: accordingly, a mass $CO_2$ content of the mixture of 96% is found (a value approximately corresponding to 99% on molar basis), ensuring a heat source cooling degree of 47°C (with an outlet temperature of the heat source of 29°C) and maximizing the heat introduction in the system. This specific condition is selected as the COP is maximized by presenting an expander outlet pressure, at saturated liquid, as close as possible to the cycle minimum pressure, therefore by minimizing the pressure difference in the expansion valve. Considering the HTHP with this molar composition of the fluid, the cycle minimum pressure is 62 bar and the maximum pressure 245 bar, with a compression pressure ratio of 3.93 and a volumetric ratio of 2.40. Different simulations, with a mixture mass composition richer in $CO_2$, above 96%, resulted in a glide not sufficiently extended to have saturated vapor conditions at 71°C, moving the compression inlet condition in the superheated region, compromising the COP. On the other hand, with a $CO_2$ mass content below 96%, the compression inlet pressure at saturated vapor increases over 62 bar and, in order to achieve the target compressor outlet temperature, the cycle maximum pressure would be higher than 250 bar, a technological threshold value adopted in literature. Secondly, in this circumstance with lower $CO_2$ content, the cold heat source exploitation is compromised, as the temperature difference at the evaporator decreases.

The investigated configuration of heat pump in this application is extremely promising: the COP of the cycle is computed to be 3.39 and the second law efficiency is around 74%, a very high value considering the 80% isentropic efficiency of the compression process. Finally, the VHC of the HTHP is computed at 36.2 MJ/m$^3$, proving the relevant compactness of the cycle, boosted by the reduced volumetric rates (with a density at compression inlet of 131 kg/m$^3$). According to a literature correlation for the estimation of the compressor efficiency proposed by Romei for s$CO_2$ cycles [50], extended in this work to the $CO_2$+$C_2Cl_4$ mixture as a highly $CO_2$-dominant working fluid, the isentropic efficiency assumed in this work at 80% for a radial compressor can be representative of a compressor mechanical power between 4 and 6 MW, with a thermal power delivered to the dryer in the range of 8 to 15 MW. These considerations are based on the predicted volumetric flow rate and computed pressure ratio of the compressor of the HTHP, being a consequence of the thermodynamic characteristics of the $CO_2$+$C_2Cl_4$ mixture at the composition and conditions investigated in this work.

The cycle thermodynamics is represented clearly in the P-T and T-Q diagrams of Figure 9, along with the plant layout of the simple recuperative cycle. In these circumstances, the mixture conditions at the inlet of the evaporator are computed with a highly dominant mass fraction of the liquid phase, limiting possible problems of two-phases maldistribution at the inlet of the evaporator manifolds. Moreover, in the T-Q diagrams it is visible that an internal pinch of around 5°C is found at the heat sink HX (the supercritical cooler), while the evaporator is pinched both at the cold end and the hot end, with the working fluid absorbing most of the heat at a temperature below 40°C. In conclusion, the investigated mixture is found to be perfectly suitable as working fluid of very high temperature heat pumps for applications, such as spray dryers, characterized by a marked temperature variation of both the sink and the cold source and a large temperature lift.

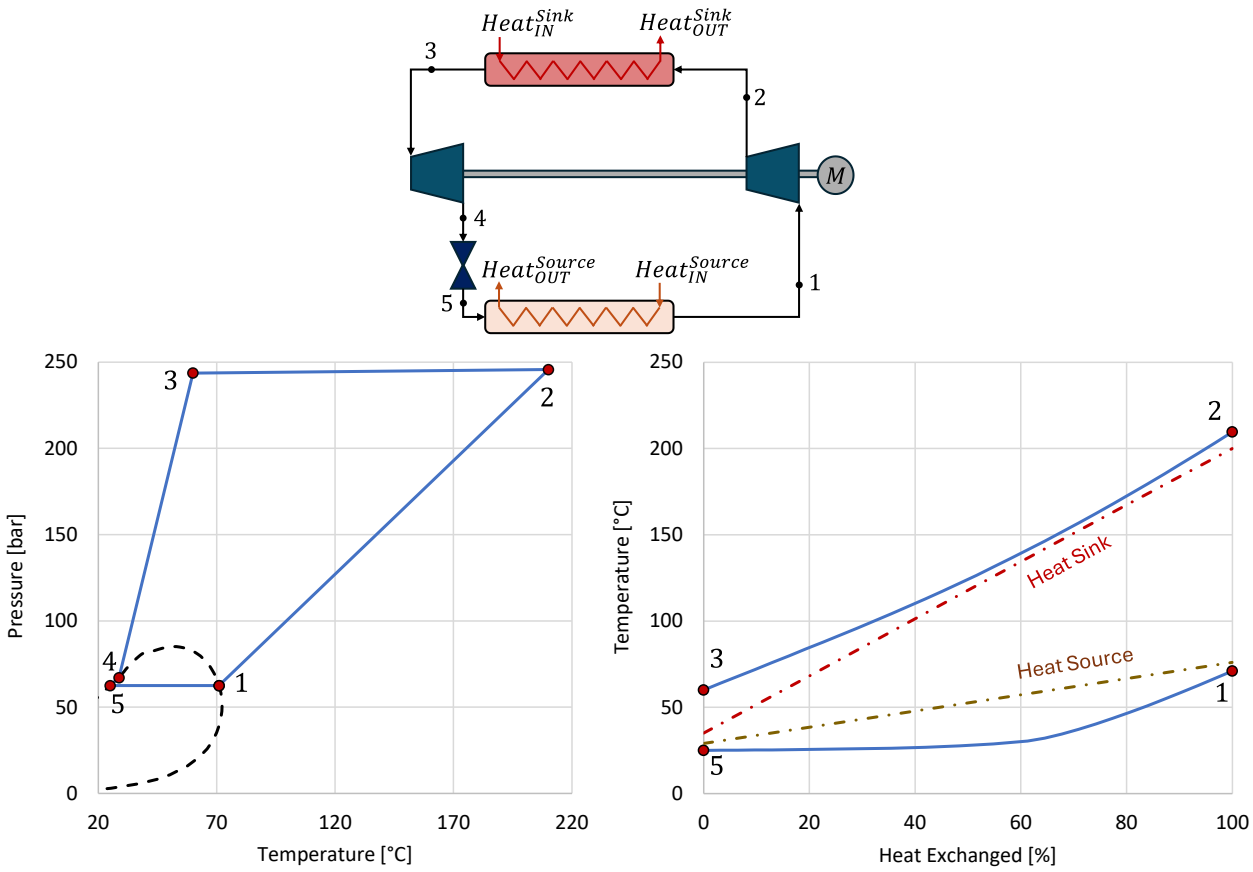


*Figure 9. Plant layout, Pressure-Temperature and Temperature-Heat Exchanged diagrams of the transcritical HTHP with the $CO_2$+$C_2Cl_4$ mixture (96%wt $CO_2$) proposed in this work for a spray drying plant. The T-Q diagrams evidence both the heat exchange process in the gas cooler and in the evaporator.*

## 5.1 Case study results: Comparison with HTHP working with pure fluids

The case study proposed in the previous section demonstrates that the $CO_2$+$C_2Cl_4$ mixture can achieve high efficiencies with an effective exploitation of the heat source, available at 76°C and cooled down by 47°C, to 29°C.

The comparative analysis between the results of the HTHP with the mixture and the conventional working fluid is carried out for each of the pure-fluid HTHP by fixing the cycle minimum pressure as the evaporation pressure at 24°C, coherently with the HTHP adopting the $CO_2$+$C_2Cl_4$ mixture, with a 5°C temperature difference at the cold end of the evaporator.

Results are listed in Table 2 for all fluids considered: it is evident that the most promising pure fluid for this plant can be considered propane, mainly for the limited compressor pressure ratio, the attractive VHC and the good COP. Consequently, for this case study, the $CO_2$-mixture shows the most promising results: with highest values of COP and second law efficiency, a minimum pressure above the atmospheric value, a compressor ratio around 4 and volumetric ratio below 3. Additionally, the fluid has also favorable characteristics in terms of flammabilty, toxicity and environmental impact. Accordingly, a visualization of the T-s diagrams of the heat pumps with the two working fluids, propane and the mixture, is also shown in Figure 10, evidencing the temperature profile of both the source and the sink of the cycle. In the diagrams the cold source and the heat sink are clearly marked: a visible difference between the two cycles is the different matching of the temperature profile of the working fluid in the evaporator. Most importantly, while the compressor inlet for the $CO_2$-mixture is defined univocally at saturated vapor conditions, by properly varying the mixture composition, for the pure fluid a large superheating is necessary, from the two-phase conditions, reaching the desired compressor inlet temperature.

Comparing the mixture performance to the one of all the pure fluids, including propane, it is possible to notice that pure fluids allow for HTHP with VHC of an order of magnitude lower than the one computed for the cycle with the $CO_2$+$C_2Cl_4$ mixture. Moreover, all pure fluids present pressure and volumetric ratios of the compressor around one order of magnitude higher than the one of the mixture, drastically compromising the manufacturing, the operation and the achievable efficiencies of the compressor, that in this case study are assumed constant for all working fluids, as a conservative choice.

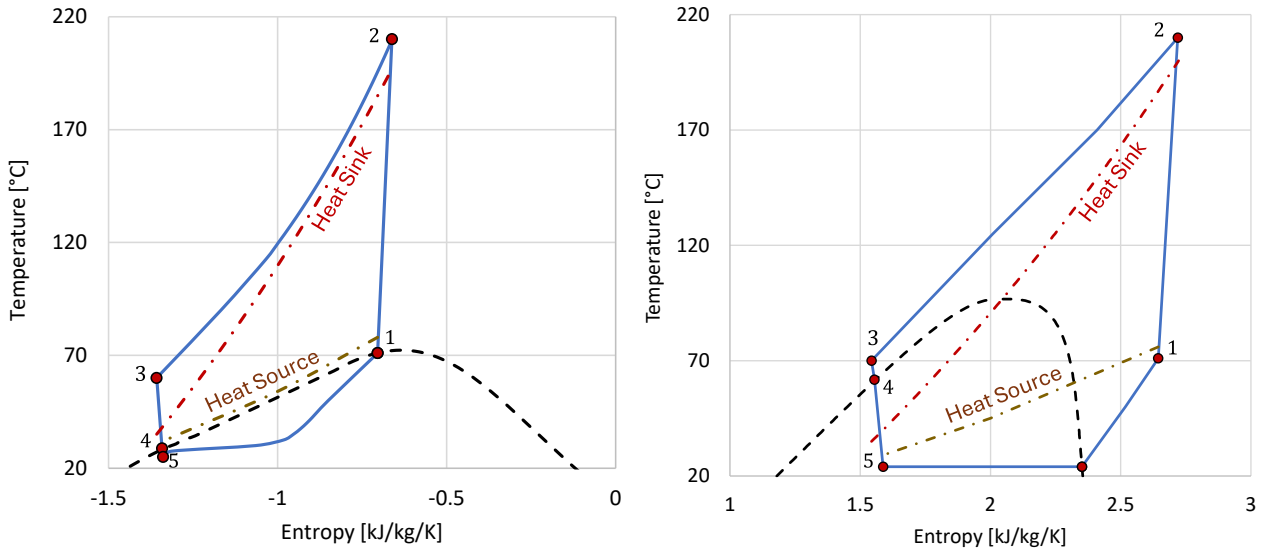


*Figure 10. Comparison between the transcritical HTHP proposed in this work for a spray dryer plant with the $CO_2$+$C_2Cl_4$ mixture (left) and propane (right).*

*Table 2. Performance comparison between the HTHP with the $CO_2$+$C_2Cl_4$ mixture and a conventional configuration for HTHP working with commercial refrigerants for a spray dryer plant*

| **Fluid** | **Heat Source** | **Heat Sink** | **COP** | **COP II Law** | **$P_{min}$ [bar]** | **$P_{max}$ [bar]** | **$\beta_{Comp}$** | **$VR_{Comp}$** | **$\rho_{Comp,IN}$ [kg/m³]** | **VHC [MJ/m³]** | **Flammable** | **GWP** |
|---|---|---|---|---|---|---|---|---|---|---|---|---|
| **$CO_2$+$C_2Cl_4$ (96%mass $CO_2$)** | 76-29°C | 35-200°C | 3.39 | 0.738 | 62 | 245 | 3.93 | 2.40 | 131 | 36.2 | No | - |
| n-Pentane | | | 2.86 | 0.623 | 0.7 | 37 | 55.7 | 81.8 | 2 | 0.9 | Yes | 20 |
| R134a | | | 2.99 | 0.652 | 6.5 | 103 | 15.9 | 15.0 | 25 | 6.2 | Yes | 1430 |
| R1234yf | | | 3.01 | 0.657 | 6.6 | 146 | 22.0 | 19.6 | 29 | 6.2 | Yes | < 5 |
| R1234ze | | | 2.97 | 0.648 | 4.8 | 103 | 21.2 | 21.4 | 21 | 4.8 | Yes | 6 |
| Propane | | | 2.94 | 0.641 | 9.3 | 115 | 12.4 | 11.7 | 16 | 7.7 | Yes | < 5 |
| Iso-Pentane | | | 2.90 | 0.631 | 0.9 | 43 | 48.2 | 78.1 | 2 | 1.1 | Yes | 11 |
| R245fa | | | 2.94 | 0.640 | 1.4 | 58 | 40.5 | 47.3 | 7 | 1.8 | No | 1030 |
| R365mfc | | | 2.91 | 0.635 | 0.5 | 43 | 79.6 | 129.5 | 3 | 0.8 | No | 804 |
| R236ea | | | 2.98 | 0.650 | 2.0 | 84 | 42.1 | 52.8 | 11 | 2.4 | No | 1330 |
| R236fa | | | 2.98 | 0.648 | 2.6 | 106 | 40.4 | 44.9 | 15 | 3.0 | No | 9810 |

In conclusion, the adoption of $CO_2$-mixtures with large glides during evaporation (as the $CO_2$+$C_2Cl_4$ mixture) is proven to be an effective choice for HTHP that must operate with highly sensible heat sources and heat sinks, outperforming conventional pure fluids in terms of COP and the characteristics of the compression process. On the other hand, any different case study of HTHP with heat sources at constant temperature could not efficiently match the evaporation process of the $CO_2$-mixtures, resulting in poorer performance of the heat pump if compared to a pure-fluid HTHP. The outcome of this comparison hence depicts a subtle but crucial dependency between the characteristics of the sources and sinks of the heat pump for a given application and the thermodynamic characteristics of the most favourable working fluids.

## 5.9 Conclusions

This work proposes an insight into an innovative working fluid for high temperature heat pumps, the $CO_2$+$C_2Cl_4$ mixture, suitable for both current and next-generation heat pumps.

The peculiarity of the working fluid for these systems is to allow the exploitation of a low temperature sensible waste heat, expanding the operative conditions with respect to applications of heat pumps with pure fluids, normally driven by isothermal latent heat at the cold source. To support the analytical considerations on the HTHP with this mixture, an experimental analysis of the working fluid is proposed, providing encouraging evidence for the adoption of this mixture. Long-term static thermal stability stresses demonstrated a good thermal resistance of $C_2Cl_4$, that in a high temperature heat pump can operate above 200°C.

The case study investigated of a $CO_2$+$C_2Cl_4$ mixture heat pump for an industrial application (a spray dryer plant) can demonstrate that the working fluid, and in general the family of $CO_2$-based mixture with large glides adopting a dopant with a low volatility, can achieve optimal results in the main key performance parameters of a high temperature heat pump. The configuration of heat pump shown, with a heat source representative of low-temperature waste heat that is sensibly cooled by around 50°C, shows very high COP (with second law efficiencies around 74%), a low value of pressure ratio between the two pressure sides (below 4) and a very limited volumetric ratio across the compressor (below 2.5), with a volumetric heating capacity above 36.2 MJ/m$^3$. The work also shows that across a pool of common refrigerants, such promising values in performance parameter are not achievable, as they are only possible due to the mixing of two pure fluids with different volatility.

As the innovative $CO_2$ dopant does not pose relevant issues in terms of toxicity, flammability, OPD and it is liquid at ambient conditions, it can be considered an interesting choice for industrial applications of closed thermodynamic cycles, where the working fluid does not enter in contact with the environment under normal operating conditions. Future works on the $CO_2$+$C_2Cl_4$ mixture must include an experimental analysis of the vapor-liquid equilibrium of the mixture, to properly define a more accurate thermodynamic model. Future works on innovative working fluids with large glides for heat pumps must include a sensitivity analysis on possible mixtures and their performances, along with the characterization of the system performances on a case-by-case basis, depending on the sensible heat sources from which the waste heat is recovered, and the sensible heat sinks to provide upgraded heat.

## Nomenclature

### Acronyms

AAD: Average Absolute Deviation

BIP: Binary Interaction Parameter of a mixture

CEEP: Centre for Energy Environment Processes

COP: Heat pump Coefficient of Performance

EoS: Equation of State

GWP: Global Warming Potential of a fluid

HCFO: Hydro-Chloro-Fluoro-Olefins

HFC: Hydro-Fluoro-Carbons

HFO: Hydro-Fluoro-Olefins

HTHP: High temperature heat pump

VHTHP: Very high temperature heat pump

HX: Heat Exchanger

ODP: Ozone Depletion Potential of a fluid

$sCO_2$: Supercritical Carbon Dioxide

VLE: Vapor Liquid Equilibrium of a mixture

VHC: Volumetric Heating Coefficient

VR: Volumetric Ratio across the compressor

VTD: Vibrating Tube Densimeter

### Symbols

$h$: Enthalpy [kJ/kg]
$\dot{m}$: Mass flow rate [kg/s]

$P$: Pressure [bar]

$\Delta P$ : Pressure drop [bar]

$\dot{Q}$: Thermal power [MW]

$T$: Temperature [°C]

$\Delta T$ : Temperature difference [°C]

$\rho$ : Density of the mixture [kg/m$^3$]

$\tau$ : Oscillation period of the VTD [Hz]

$k^*$ : Decomposition rate of the fluid [‰$_{mol}$/s]

$\dot{W}$: Mechanical power [MW]

## Appendix A – Liquid densities of the $CO_2$+$C_2Cl_4$ mixture experimental data and comparison with the proposed EoS results

The liquid densities of the $CO_2$+$C_2Cl_4$ mixture, proposed in Figure 3, are collected in Table A1 in this appendix, along with the expanded uncertainties on temperature, pressure and density, with a coverage factor of 2.

*Table A1. Experimental liquid densities collected on the $CO_2$+$C_2Cl_4$ mixture*

| $x_{CO2}$ | $\underline{T}$ | $P$ | $\rho_{Mix}$ | $u_{Expanded}(T)$ | $u_{Expanded}(P)$ | $u_{Expanded}(\rho)$ |
|---|---|---|---|---|---|---|
| [%] | $[°C]$ | $[bar]$ | $[\frac{kg}{m^3}]$ | $[°C]$ | $[bar]$ | $[\frac{kg}{m^3}]$ |
| 93.25 | 40.27 | 189.19 | 957.6 | 0.06 | 0.04 | 5.9 |
| | | 167.09 | 942.1 | 0.06 | 0.05 | 5.9 |
| | | 143.02 | 921.9 | 0.06 | 0.05 | 5.9 |
| | | 131.75 | 910.6 | 0.06 | 0.04 | 5.9 |
| | | 115.23 | 891.7 | 0.06 | 0.04 | 5.9 |
| | | 124.48 | 901.8 | 0.06 | 0.05 | 5.9 |
| | | 132.52 | 910.4 | 0.06 | 0.05 | 5.9 |
| | | 141.71 | 919.5 | 0.06 | 0.04 | 5.9 |
| | | 156.30 | 932.4 | 0.06 | 0.04 | 5.9 |
| | | 179.62 | 950.4 | 0.06 | 0.05 | 5.9 |
| | | 169.56 | 943.6 | 0.06 | 0.04 | 5.9 |
| | | 160.20 | 936.5 | 0.06 | 0.08 | 5.9 |
| | | 152.26 | 929.8 | 0.06 | 0.06 | 5.9 |
| | | 125.91 | 904.3 | 0.06 | 0.04 | 5.9 |
| 93.25 | 59.98 | 185.20 | 864.8 | 0.06 | 0.08 | 2.4 |
| | | 169.63 | 845.3 | 0.06 | 0.06 | 2.4 |
| | | 160.23 | 831.6 | 0.06 | 0.05 | 2.4 |
| | | 150.00 | 814.5 | 0.06 | 0.05 | 2.4 |
| | | 138.32 | 791.1 | 0.06 | 0.04 | 2.4 |
| | | 124.14 | 753.4 | 0.06 | 0.05 | 2.4 |
| | | 140.62 | 796.9 | 0.06 | 0.04 | 2.4 |
| | | 154.49 | 822.7 | 0.06 | 0.06 | 2.4 |
| | | 171.99 | 848.6 | 0.06 | 0.05 | 2.4 |
| 93.25 | 79.84 | 191.86 | 743.4 | 0.06 | 0.06 | 2.5 |
| | | 170.63 | 700.5 | 0.06 | 0.05 | 2.5 |
| | | 159.19 | 670.1 | 0.06 | 0.05 | 2.5 |
| | 79.99 | 154.63 | 657.1 | 0.06 | 0.05 | 2.5 |

| | | | | | | |
|---|---|---|---|---|---|---|
| | | 178.24 | 718.5 | 0.06 | 0.04 | 2.5 |
| | | 187.58 | 736.7 | 0.06 | 0.04 | 2.5 |
| | | 183.82 | 730.2 | 0.06 | 0.05 | 2.5 |
| 83.82 | 40.08 | 171.61 | 1065.6 | 0.06 | 0.05 | 5.9 |
| | | 158.41 | 1058.4 | 0.06 | 0.05 | 5.9 |
| | | 134.50 | 1044.1 | 0.06 | 0.05 | 5.9 |
| | | 116.23 | 1031.3 | 0.06 | 0.05 | 5.9 |
| | | 99.21 | 1017.6 | 0.06 | 0.04 | 5.9 |
| | | 90.08 | 1009.3 | 0.06 | 0.06 | 5.9 |
| 90.80 | 40.22 | 162.38 | 977.0 | 0.07 | 0.05 | 5.9 |
| | | 149.77 | 967.8 | 0.07 | 0.04 | 5.9 |
| | | 139.22 | 959.3 | 0.07 | 0.04 | 5.9 |
| | | 118.93 | 941.0 | 0.07 | 0.04 | 5.9 |
| | | 101.31 | 921.8 | 0.07 | 0.05 | 5.9 |
| | | 130.06 | 951.4 | 0.07 | 0.05 | 5.9 |
| | | 156.08 | 972.4 | 0.07 | 0.04 | 5.9 |
| 85.69 | 40.17 | 160.87 | 1056.5 | 0.06 | 0.05 | 5.9 |
| | | 140.88 | 1045.1 | 0.06 | 0.05 | 5.9 |
| | | 120.58 | 1031.9 | 0.06 | 0.05 | 5.9 |
| | | 99.97 | 1016.4 | 0.06 | 0.04 | 5.9 |
| | | 110.20 | 1024.0 | 0.06 | 0.07 | 5.9 |
| | | 129.81 | 1037.6 | 0.06 | 0.05 | 5.9 |
| | | 183.83 | 1068.1 | 0.06 | 0.11 | 5.9 |
| 85.69 | 59.96 | 197.11 | 1013.8 | 0.06 | 0.05 | 2.4 |
| | | 169.79 | 993.9 | 0.06 | 0.09 | 2.4 |
| | | 149.54 | 976.1 | 0.06 | 0.05 | 2.4 |
| | | 125.13 | 949.4 | 0.06 | 0.05 | 2.4 |
| | | 138.22 | 964.7 | 0.06 | 0.05 | 2.4 |
| | | 159.80 | 985.3 | 0.06 | 0.04 | 2.4 |
| | | 184.28 | 1004.5 | 0.06 | 0.12 | 2.4 |
| 85.69 | 79.95 | 220.43 | 929.7 | 0.09 | 0.05 | 2.5 |
| | | 200.09 | 911.5 | 0.09 | 0.07 | 2.5 |
| | | 180.18 | 890.4 | 0.09 | 0.12 | 2.5 |
| | | 170.03 | 877.6 | 0.09 | 0.05 | 2.5 |
| | | 149.72 | 846.4 | 0.09 | 0.05 | 2.5 |
| | | 160.92 | 864.7 | 0.09 | 0.04 | 2.5 |

| | | | | | | |
|---|---|---|---|---|---|---|
| | | 188.22 | 899.0 | 0.09 | 0.04 | 2.5 |
| | | 133.41 | 808.0 | 0.09 | 0.04 | 2.5 |
| | | 131.43 | 800.8 | 0.09 | 0.04 | 2.5 |
| 70.31 | 40.18 | 160.30 | 1227.3 | 0.06 | 0.13 | 5.9 |
| | | 140.07 | 1220.5 | 0.06 | 0.04 | 5.9 |
| | | 119.36 | 1213.1 | 0.06 | 0.26 | 5.9 |
| | | 99.15 | 1205.3 | 0.06 | 0.08 | 5.9 |
| | | 76.84 | 1196.1 | 0.06 | 0.11 | 5.9 |
| | | 91.41 | 1202.1 | 0.06 | 0.23 | 5.9 |
| | | 110.05 | 1209.5 | 0.06 | 0.22 | 5.9 |
| | | 128.87 | 1216.4 | 0.06 | 0.12 | 5.9 |
| 70.31 | 59.93 | 193.95 | 1197.5 | 0.07 | 0.05 | 2.4 |
| | | 179.32 | 1191.7 | 0.07 | 0.05 | 2.4 |
| | | 150.66 | 1179.5 | 0.07 | 0.07 | 2.4 |
| | | 119.12 | 1164.1 | 0.07 | 0.04 | 2.4 |
| | | 95.24 | 1150.7 | 0.07 | 0.04 | 2.4 |
| | | 103.96 | 1155.6 | 0.07 | 0.10 | 2.4 |
| | | 137.78 | 1172.9 | 0.07 | 0.08 | 2.4 |
| | | 160.41 | 1183.2 | 0.07 | 0.12 | 2.4 |
| 70.47 | 40.28 | 147.49 | 1224.2 | 0.06 | 0.23 | 5.9 |
| | | 130.59 | 1218.2 | 0.06 | 0.16 | 5.9 |
| | | 105.17 | 1208.8 | 0.06 | 0.27 | 5.9 |
| | | 73.95 | 1195.9 | 0.06 | 0.14 | 5.9 |
| | | 87.61 | 1201.7 | 0.06 | 0.07 | 5.9 |
| | | 114.76 | 1212.4 | 0.06 | 0.06 | 5.9 |
| | | 162.66 | 1229.3 | 0.06 | 0.09 | 5.9 |
| 70.47 | 59.97 | 164.90 | 1187.0 | 0.06 | 0.05 | 2.4 |
| | | 145.58 | 1178.6 | 0.06 | 0.05 | 2.4 |
| | | 125.33 | 1168.8 | 0.06 | 0.13 | 2.4 |
| | | 97.89 | 1153.9 | 0.06 | 0.12 | 2.4 |
| | | 103.68 | 1157.2 | 0.06 | 0.11 | 2.4 |
| | | 115.00 | 1163.4 | 0.06 | 0.18 | 2.4 |
| | | 134.86 | 1173.5 | 0.06 | 0.14 | 2.4 |
| | | 152.43 | 1181.6 | 0.06 | 0.07 | 2.4 |
| | | 173.68 | 1190.8 | 0.06 | 0.04 | 2.4 |
| 70.47 | 79.91 | 199.36 | 1117.2 | 0.06 | 0.07 | 2.5 |

| | | | | | | |
|---|---|---|---|---|---|---|
| | | 180.92 | 1107.8 | 0.06 | 0.04 | 2.5 |
| | | 161.74 | 1097.3 | 0.06 | 0.13 | 2.5 |
| | | 140.29 | 1084.0 | 0.06 | 0.08 | 2.5 |
| | | 120.79 | 1069.9 | 0.06 | 0.05 | 2.5 |
| | | 129.32 | 1076.3 | 0.06 | 0.04 | 2.5 |
| | | 148.13 | 1089.1 | 0.06 | 0.05 | 2.5 |
| | | 167.22 | 1100.5 | 0.06 | 0.05 | 2.5 |
| | | 183.50 | 1109.3 | 0.06 | 0.08 | 2.5 |

The densities are also reported along with the calculations of the Peng Robinson EoS with $k_{ij} = 0.10$ in Figure A1, as discussed in Chapter 3.1: the comparison between the modelled values and the experimental data demonstrate the effective capability of the EoS to properly compute the densities of the mixture in the liquid region.

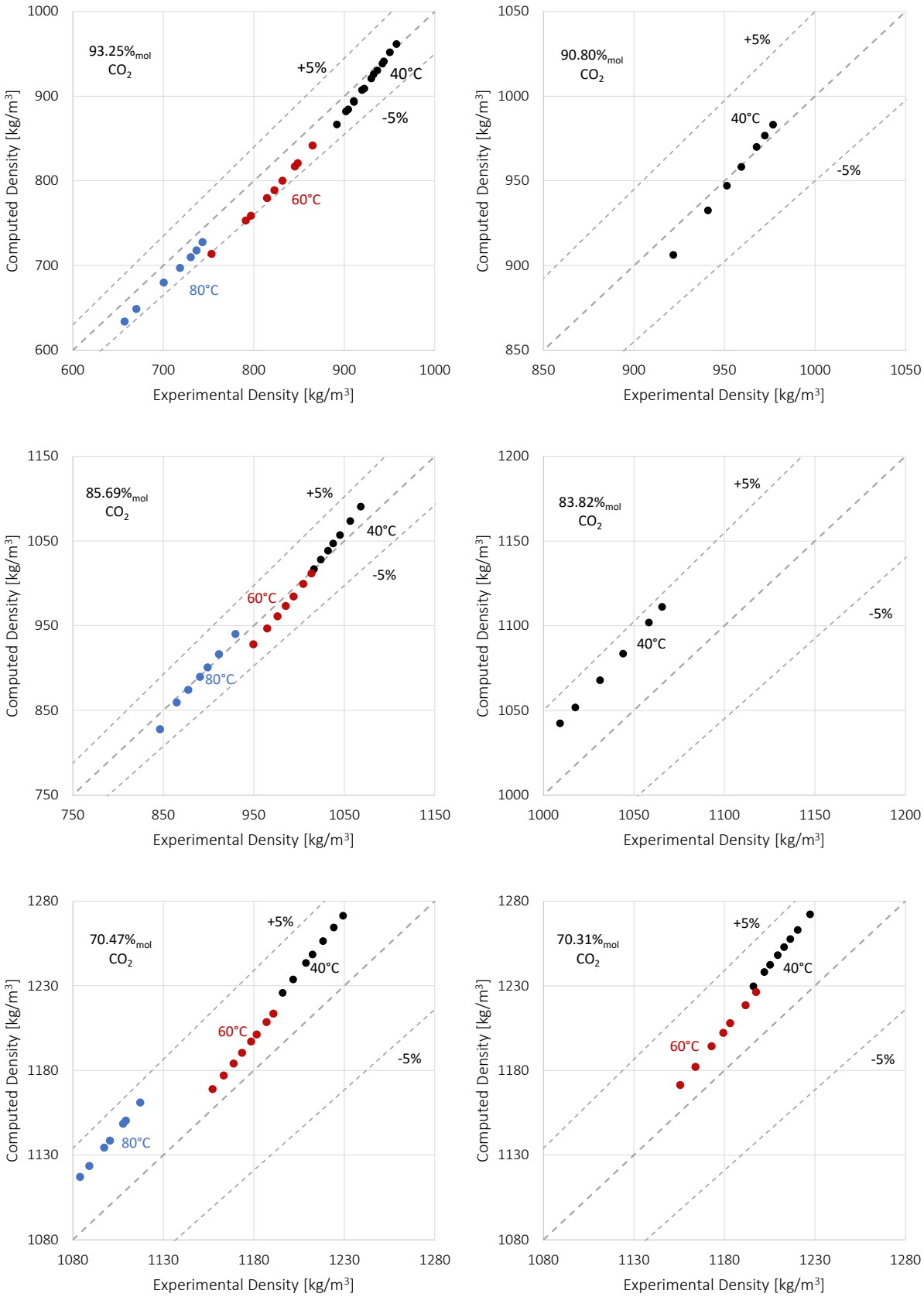


*Figure A1. Comparison between the experimental liquid densities of the $CO_2$+$C_2Cl_4$ mixture and the values predicted by the EoS in this work (PR EoS with $k_{ij} = 0.1$)*

## 5.10 Bibliography

[1] A.H. Hassan, J.M. Corberán, M. Ramirez, F. Trebilcock-Kelly, J. Payá, A high-temperature heat pump for compressed heat energy storage applications: Design, modeling, and performance, Energy Reports 8 (2022) 10833–10848. https://doi.org/10.1016/J.EGYR.2022.08.201.

[2] T. El Samad, A. Żabnieńska-Góra, H. Jouhara, A.I. Sayma, A review of compressors for high temperature heat pumps, Thermal Science and Engineering Progress 51 (2024) 102603. https://doi.org/10.1016/J.TSEP.2024.102603.

[3] B. Zühlsdorf, F. Bühler, M. Bantle, B. Elmegaard, Analysis of technologies and potentials for heat pump-based process heat supply above 150 °C, Energy Conversion and Management: X 2 (2019) 100011. https://doi.org/10.1016/J.ECMX.2019.100011.

[4] A. Marina, S. Spoelstra, H.A. Zondag, A.K. Wemmers, An estimation of the European industrial heat pump market potential, Renewable and Sustainable Energy Reviews 139 (2021) 110545. https://doi.org/10.1016/J.RSER.2020.110545.

[5] K.J. Chua, S.K. Chou, W.M. Yang, Advances in heat pump systems: A review, Appl Energy 87 (2010) 3611–3624. https://doi.org/10.1016/J.APENERGY.2010.06.014.

[6] C. Arpagaus, F. Bless, M. Uhlmann, J. Schiffmann, S.S. Bertsch, High temperature heat pumps: Market overview, state of the art, research status, refrigerants, and application potentials, Energy 152 (2018) 985–1010. https://doi.org/10.1016/J.ENERGY.2018.03.166.

[7] A. Jaatinen-Varri, J. Tiainen, J. Honkatukia, A. Uusitalo, T. Turunen-Saaresti, Design considerations for a high-temperature heat pump centrifugal compressor, in: Proceedings of 15th European Conference on Turbomachinery Fluid Dynamics & Thermodynamics ETC, 2023.

[8] C. Mateu-Royo, C. Arpagaus, A. Mota-Babiloni, J. Navarro-Esbrí, S.S. Bertsch, Advanced high temperature heat pump configurations using low GWP refrigerants for industrial waste heat recovery: A comprehensive study, Energy Convers Manag 229 (2021) 113752. https://doi.org/10.1016/J.ENCONMAN.2020.113752.

[9] J. Liu, L. Zhou, Z. Lin, X. Zhang, Performance evaluation of low GWP large glide temperature zeotropic mixtures applied in air source heat pump for DHW production, Energy Convers Manag 274 (2022) 116457. https://doi.org/10.1016/J.ENCONMAN.2022.116457.

[10] MAN Heat Pump, https://www.man-es.com/docs/default-source/document-sync/man-heat-pump-hpu328c592b5d584f9eba47f4b6bed3574e.pdf?sfvrsn=9bd416fb_3 (accessed February 20, 2024).

[11] J. Li, Z. Yang, H. Li, S. Hu, Y. Duan, J. Yan, Optimal schemes and benefits of recovering waste heat from data center for district heating by CO2 transcritical heat pumps, Energy Convers Manag 245 (2021) 114591. https://doi.org/10.1016/J.ENCONMAN.2021.114591.

[12] J. Wang, M. Belusko, M. Liu, H. Semsarilar, R. Liddle, A. Alemu, M. Evans, C. Zhao, J. Hudson, F. Bruno, A comprehensive study on a novel transcritical CO2 heat pump for simultaneous space heating and cooling – Concepts and initial performance, Energy Convers Manag 243 (2021) 114397. https://doi.org/10.1016/J.ENCONMAN.2021.114397.

[13] M. Luberti, R. Gowans, P. Finn, G. Santori, An estimate of the ultralow waste heat available in the European Union, Energy 238 (2022) 121967. https://doi.org/10.1016/J.ENERGY.2021.121967.

[14] E. Macchi, M. Astolfi, Organic Rankine Cycle (ORC) Power Systems - Technologies and applications, Elsevier, 2017. https://doi.org/10.1016/C2014-0-04239-6.

[15] S. Brückner, S. Liu, L. Miró, M. Radspieler, L.F. Cabeza, E. Lävemann, Industrial waste heat recovery technologies: An economic analysis of heat transformation technologies, Appl Energy 151 (2015) 157–167. https://doi.org/10.1016/J.APENERGY.2015.01.147.

[16] S.S.M. Shamsi, S. Barberis, S. Maccarini, A. Traverso, Large scale energy storage systems based on carbon dioxide thermal cycles: A critical review, Renewable and Sustainable Energy Reviews 192 (2024) 114245. https://doi.org/10.1016/J.RSER.2023.114245.

[17] M. Mercangöz, J. Hemrle, L. Kaufmann, A. Z'Graggen, C. Ohler, Electrothermal energy storage with transcritical CO2 cycles, Energy 45 (2012) 407–415. https://doi.org/10.1016/J.ENERGY.2012.03.013.

[18] L. Sanz Garcia, E. Jacquemoud, P. Jenny, Thermo-economic heat exchanger optimization for Electro-Thermal Energy Storage based on transcritical CO2 cycles, 3rd European Conference on Supercritical CO2 (SCO2) Power Systems 2019: 19th-20th September 2019 (2019) 353–362. https://doi.org/10.17185/DUEPUBLICO/48917.

[19] ETES System Overview | Echogen Power Systems, https://www.echogen.com/energy-storage/etes-system-overview (accessed February 13, 2024).

[20] H. Abedini, E. Vieren, T. Demeester, W. Beyne, S. Lecompte, S. Quoilin, A. Arteconi, A comprehensive analysis of binary mixtures as working fluid in high temperature heat pumps, Energy Convers Manag 277 (2023) 116652. https://doi.org/10.1016/J.ENCONMAN.2022.116652.

[21] E. Vieren, T. Demeester, W. Beyne, A. Arteconi, M. De Paepe, S. Lecompte, The thermodynamic potential of high-temperature transcritical heat pump cycles for industrial processes with large temperature glides, Appl Therm Eng 234 (2023) 121197. https://doi.org/10.1016/J.APPLTHERMALENG.2023.121197.

[22] D. Wu, B. Ma, J. Zhang, Y. Chen, F. Shen, X. Chen, C. Wen, Y. Yang, Working fluid pair selection of thermally integrated pumped thermal electricity storage system for waste heat recovery and energy storage, Appl Energy 371 (2024) 123693. https://doi.org/10.1016/J.APENERGY.2024.123693.

[23] E. Morosini, D. Alfani, M. Renzoni, G. Manzolini, Thermally integrated innovative Carnot batteries to upgrade and dispatch low temperature sensible waste heat, in: ATI Annual Congress (ATI 2024), Under Review, IOP Publishing, 2024.

[24] J. Liu, F. Zhou, N. Lyu, H. Fan, X. Zhang, Analysis of low GWP ternary zeotropic mixtures applied in high-temperature heat pump for waste heat recovery, Energy Convers Manag 292 (2023) 117381. https://doi.org/10.1016/J.ENCONMAN.2023.117381.

[25] B. Dai, P. Zhao, S. Liu, M. Su, D. Zhong, J. Qian, X. Hu, Y. Hao, Assessment of heat pump with carbon dioxide/low-global warming potential working fluid mixture for drying process: Energy and emissions saving potential, Energy Convers Manag 222 (2020) 113225. https://doi.org/10.1016/J.ENCONMAN.2020.113225.

[26] Tetrachloroethylene | The Observatory of Economic Complexity, https://oec.world/en/profile/hs/tetrachloroethylene-perchloroethylene (accessed February 20, 2024).

[27] T. Claxton, R. Hossaini, O. Wild, M.P. Chipperfield, C. Wilson, On the Regional and Seasonal Ozone Depletion Potential of Chlorinated Very Short-Lived Substances, Geophys Res Lett 46 (2019) 5489–5498. https://doi.org/10.1029/2018GL081455.

[28] R.R. Dreisbach, R.A. Martin, Physical Data on Some Organic Compounds, Ind Eng Chem 41 (1949) 2875–2878. https://doi.org/10.1021/IE50480A053.

[29] A. Krishnaiah, K.N. Surendranath, Densities, Speeds of Sound, and Viscosities of Mixtures of Oxolane with Chloroethanes and Chloroethenes, J Chem Eng Data 41 (1996) 1012–1014. https://doi.org/10.1021/JE950304E.

[30] E. Lynge, H. Tinnerberg, L. Rylander, P. Romundstad, K. Johansen, M.L. Lindbohm, P. Heikkilä, H. Westberg, L.B. Clausen, A. Piombino, B.L. Thorsted, Exposure to Tetrachloroethylene in Dry Cleaning Shops in the Nordic Countries, Ann Occup Hyg 55 (2011) 387–396. https://doi.org/10.1093/ANNHYG/MEQ101.

[31] L.S. Gold, A.J. De Roos, M. Waters, P. Stewart, Systematic Literature Review of Uses and Levels of Occupational Exposure to Tetrachloroethylene, J Occup Environ Hyg 5 (2008) 807–839. https://doi.org/10.1080/15459620802510866.

[32] A. Yasuhara, Thermal decomposition of tetrachloroethylene, Chemosphere 26 (1993) 1507–1512. https://doi.org/10.1016/0045-6535(93)90218-T.

[33] G. Di Marcoberardino, E. Morosini, D. Di Bona, P. Chiesa, C. Invernizzi, P. Iora, G. Manzolini, Experimental characterisation of CO2 + C6F6 mixture: Thermal stability and vapour liquid equilibrium test for its application in transcritical power cycle, Appl Therm Eng 212 (2022). https://doi.org/10.1016/J.APPLTHERMALENG.2022.118520.

[34] H. Guo, M. Gong, X. Qin, Performance analysis of a modified subcritical zeotropic mixture recuperative high-temperature heat pump, Appl Energy 237 (2019) 338–352. https://doi.org/10.1016/J.APENERGY.2018.12.094.

[35] M. Nazeri, A. Chapoy, A. Valtz, C. Coquelet, B. Tohidi, New experimental density data and derived thermophysical properties of carbon dioxide – Sulphur dioxide binary mixture (CO2 - SO2) in gas, liquid and supercritical phases from 273 K to 353 K and at pressures up to 42 MPa, Fluid Phase Equilib 454 (2017) 64–77. https://doi.org/10.1016/j.fluid.2017.09.014.

[36] M. Doninelli, E. Morosini, G. Di Marcoberardino, C.M. Invernizzi, P. Iora, M. Riva, P. Stringari, G. Manzolini, Experimental investigation of the CO2+SiCl4 mixture as innovative working fluid for power cycles: Bubble points and liquid density measurements, Energy 299 (2024) 131197. https://doi.org/10.1016/j.energy.2024.131197.

[37] R. Span, W. Wagner, A New Equation of State for Carbon Dioxide Covering the Fluid Region from the Triple-Point Temperature to 1100 K at Pressures up to 800 MPa, J Phys Chem Ref Data 25 (1996) 1509–1596. https://doi.org/10.1063/1.555991.

[38] D.Y. Peng, D.B. Robinson, A New Two-Constant Equation of State, Industrial and Engineering Chemistry Fundamentals 15 (1976) 59–64. https://doi.org/10.1021/i160057a011.

[39] AspenTech, Aspen Plus | Leading Process Simulation Software | AspenTech, https://www.aspentech.com/en/products/engineering/aspen-plus.

[40] M. Pasetti, C.M. Invernizzi, P. Iora, Thermal stability of working fluids for organic Rankine cycles: An improved survey method and experimental results for cyclopentane, isopentane and n-butane, Appl Therm Eng 73 (2014) 764–774. https://doi.org/10.1016/J.APPLTHERMALENG.2014.08.017.

[41] M. Doninelli, G. Di Marcoberardino, P. Iora, M. Gelfi, C.M. Invernizzi, G. Manzolini, Silicon Tetrachloride as innovative working fluid for high temperature Rankine cycles: Thermal Stability, material compatibility, and energy analysis, Appl Therm Eng 249 (2024) 123239. https://doi.org/10.1016/J.APPLTHERMALENG.2024.123239.

[42] C.M. Invernizzi, P. Iora, G. Manzolini, S. Lasala, Thermal stability of n-pentane, cyclo-pentane and toluene as working fluids in organic Rankine engines, Appl Therm Eng 121 (2017) 172–179. https://doi.org/10.1016/J.APPLTHERMALENG.2017.04.038.

[43] M. Doninelli, G. Di Marcoberardino, I. Alessandri, C.M. Invernizzi, P. Iora, Fluorobenzene as New Working Fluid for High-Temperature Heat Pumps and Organic Rankine Cycles: Energy Analysis and Thermal Stability Test, Energy Convers Manag (2024).

[44] C. Invernizzi, M. Binotti, P. Bombarda, G. Di Marcoberardino, P. Iora, G. Manzolini, Water Mixtures as Working Fluids in Organic Rankine Cycles, Energies 2019, Vol. 12, Page 2629 12 (2019) 2629. https://doi.org/10.3390/EN12132629.

[45] J.F. Wang, C. Brown, D.J. Cleland, Heat pump heat recovery options for food industry dryers, International Journal of Refrigeration 86 (2018) 48–55. https://doi.org/10.1016/j.ijrefrig.2017.11.028.

[46] F. Schlosser, S. Zysk, T.G. Walmsley, L. Kong, B. Zühlsdorf, H. Meschede, Break-even of high-temperature heat pump integration for milk spray drying, Energy Convers Manag 291 (2023) 117304. https://doi.org/10.1016/J.ENCONMAN.2023.117304.

[47] H. Fu, J. Shi, J. Yuan, X. Zhang, L. Sun, Heat recovery scheme design and thermodynamic analysis of closed-cycle heat pump drying system, Energy Convers Manag 286 (2023) 117034. https://doi.org/10.1016/J.ENCONMAN.2023.117034.

[48] NIST - National Institute of Standards and Technology, REFPROP - Reference Fluid Thermodynamic and Transport Properties.

[49] A. Zhao, R. Pecnik, J.W.R. Peeters, Thermodynamic analysis and heat exchanger calculations of transcritical high-temperature heat pumps, Energy Convers Manag 303 (2024) 118172. https://doi.org/10.1016/J.ENCONMAN.2024.118172.

[50] A. Romei, P. Gaetani, A. Giostri, G. Persico, The Role of Turbomachinery Performance in the Optimization of Supercritical Carbon Dioxide Power Systems, J Turbomach 142 (2020). https://doi.org/10.1115/1.4046182.

## Supplementary Materials

### Preparation of the mixture from the two separate pure components

In order to determine the exact molar composition of the $CO_2$+$C_2Cl_4$ mixture whose densities are measured in the Vibrating Tube Densimeter (VTD) it was adopted the same methodology reported in literature for a different $CO_2$-based mixture characterized in the same experimental campaign at CEEP experimental platform [1], recollected in this appendix.

The mixture is prepared by precisely weighting both pure components, being filled into a dedicated variable volume cylinder (VVC), on the basis of their respective vapor pressures (starting from the heavier constituent to the lighter one). $CO_2$ represents the most volatile component, stored under two-phase conditions within a gas vessel at ambient temperature (~20 °C) and pressure (~57 bar), while tetrachloroethylene ($C_2Cl_4$) remains in a liquid phase under standard conditions, and it is confined in a separate vessel. The certified purity by the suppliers is at least 99.995% for carbon dioxide, and above 99% for $C_2Cl_4$. Before charging the components, a magnetic stirrer is positioned within the VVC to ensure homogeneity during measurements. Subsequently, a vacuum pump evacuates the VVC down to a pressure below 6 Pa, monitored by a Pirani vacuum gauge at the inlet. Then, the VVC is weighted.

Subsequently, the dopant is manually introduced into the VVC through a sealing cap with a syringe. The VVC is then reweighed to determine the dopant mass. $CO_2$ is introduced afterwards, via an additional variable volume auxiliary cylinder pressurized at 200 bar. After preparing the mixture in the main VVC, its mass is measured for the third time to determine the quantity of $CO_2$ injected through the difference in mass. Finally, the mixture molar fraction is determined knowing the mass

of both components. The measuring device adopted is a Mettler Toledo CC3000 balance with a precision of ±0.0001 g. Once the variable volume cylinder is filled with a known quantity of both fluids, it is moved to the VTD test rig, where the piston of the cylinder is put into contact with a high-pressure nitrogen reservoir at a pressure largely over the expected bubble condition. An electromagnetic field is applied to the external surface of the cylinder to put in motion the internal agitator. After approximately thirty minutes, the composition is assumed to have reached complete homogeneity, and the whole circuit of the VTD is evacuated to create a vacuum before injecting the mixture for pressure difference.

**Uncertainty calculation on the measured densities at the VTD**

Regarding the experimental data on the densities of the liquid $CO_2$+$C_2Cl_4$ mixture, the uncertainty on the values measured is computed as reported in literature [1] for a different mixture belonging to the same experimental campaign, recollected in this appendix.

The uncertainty on the physical quantity "X" (that can be either temperature, pressure or density) is computed as follows, extended with a coverage factor of $k = 2$.

$$u_{Expanded}(X) = k \cdot \sqrt{(u_{Calibration}(X))^2 + (u_{Acquisition}(X))^2} \quad \text{(E1)}$$

Where the two contributions are calculated as reported below:

$$u_{Calibration}(X) = \big(Measured\ (X) - Reference\ (X)\big) \quad \text{(E2)}$$

$$u_{Acquisition}(X) = \sigma(X_{acquisited}) \quad \text{(E3)}$$

The impact of the VTD calibration on the uncertainty calculations is assessed by comparing the instrument calibration curve with a reference value. In this study, the contributions are determined at 0.03 °C for temperature and 0.02 bar for pressure under all the conditions considered. For the density, values vary: 2.95 kg/m$^3$ at 40°C, 1.19 kg/m$^3$ at 60°C, and 1.27 kg/m$^3$ at 80°C. The reference values are based on thermocouples and pressure transducers for temperature and pressure, respectively. The calibration of the density adopts as references the Span and Wagner equations of state, since the VTD calibration used pure $CO_2$ as a reference fluid. The pressure transducer operated is a PAA-35HXTC with a range up to 700 bar, and the temperature sensors are four-wire 100-Ω platinum resistance probes (Pt100). The calibration procedure of the pressure employs a GE Sensing PACE 5000 as the reference pressure transducer. Measurements are conducted using an Agilent HP34970A data acquisition unit for pressure and temperature, and an Anton Paar mPDS 5 transmitter for specific periods. Uncertainties from acquisitions ($u_{Acquisition}$) are determined by the standard deviation of the variable, $\sigma(X_{acquisited})$, calculated directly from the data acquisition unit, based on at least 60 acquisitions with a frequency of 1 Hz.

**Details on the Vibrating Tube Densimeter (VTD) test rig**

The characteristics of the VTD and its operating principles have been described in literature [1] for a different mixture belonging to the same experimental campaign, recollected in this appendix.

To measure the density of the liquid mixture the vibration period of the U-shaped tube is recorded, and it is compared to the vibration period of the vacuum tube. The VTD is submerged in a liquid thermostatic bath to maintain a constant temperature for accurate measurement, controlled by a heat transfer fluid for a stability in temperature of around 0.02°C. Detailed operational instructions are outlined in a previous work [2]: as mentioned in the literature, when the pressure of the fluid decreases during operation, slightly before the advent of the bubble point starting from subcooled liquid conditions, the temperature of the thermostatic bath should be around 0.2°C lower than the heat transfer fluid flowing in the jacket of the densimeter, because the first bubble of $CO_2$-mixture should occur precisely into the densimeter in the vibrating tube, in case of a bubble onset.

The vibration period measured by the VTD can be exactly correlated with the mass into the vibrating tube and thus the density of the fluid contained in the tube. the calibration of the VTD is performed by correlating the known density of a pure fluid to its vibration periods measured in the VTD, establishing a temperature-dependent relationship between vibration period and density. Pressure dependence is neglected. This process requires measuring tube vibration period with the reference fluid at each temperature of interest.

The operational procedure begins with vacuuming the entire circuit up to valves V2 and V4. Then, the nitrogen reservoir is connected to the variable volume cylinder, pushing the mixture into the VTD via piston movement caused by the pressure difference. Once thermal and mechanical equilibrium is reached, the variable volume cylinder is excluded (V4 is closed), and valves V5 and V6 are closed too, during measurements. The variable volume cell, introduced after the VTD outlet, allows manual adjustment of volume and pressure without affecting the primary mixture in the cylinder, crucial for accurately defining the measured fluid composition. The piston position in the variable volume cell is adjusted manually with valve V6 open to match the VTD pressure to the desired value. After equilibrium, valve V6 is closed, enabling further acquisitions at the same temperature but different pressures. This procedure is repeated for each temperature during measurements

**Computed volumes of mixing of the $CO_2$+$C_2Cl_4$ mixture**

In addition to the measurements on the mixture densities, a further set of quantities is also presented in this work to expand the available data on the $CO_2$+$C_2Cl_4$ mixture. In fact, also pseudo experimental volumes of mixing of this mixture are computed and proposed.

Volumes of mixing represent the deviation from ideal mixing volume and describes the effect of pressure on the real behavior of the mixture. They are computed according to their definition, reported in the equation below, starting from all the measured densities of the liquid mixture in the VTD and the volumetric behavior of the pure components at the same temperature and pressure.

$$\Delta v_{Mixing}(T,P,x) = v^{Mix}_{Measured}(T,P,x) - (x_{CO_2,Mix} \cdot v_{CO_2}(T,P) + x_{C_2Cl_4,Mix} \cdot v_{C_2Cl_4}(T,P)) \quad \text{(E4)}$$

For the calculations, pure $CO_2$ is modelled with the Span and Wagner EoS, considered the gold standard for this fluid, and the liquid densities of pure $C_2Cl_4$ are computed according to the PC-SAFT EoS, embedded within ASPEN Plus v.11 [3], optimized on the experimental data of saturated liquid densities, heat capacity, vapor pressure and heat of vaporization available in the ASPEN Plus

database. The result of the optimization procedure of the PC-SAFT EoS and the fitting between experimental and calculated values are reported in the Figure F1 below.

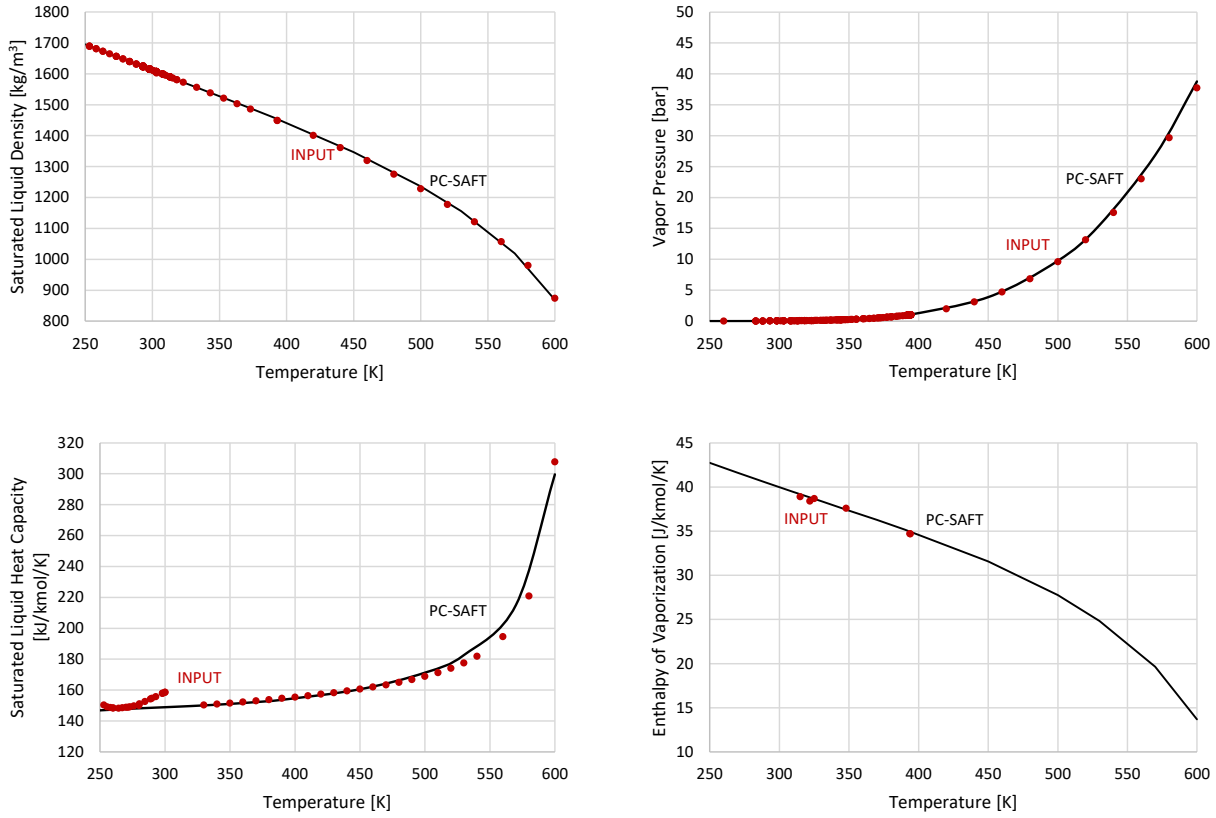


*Figure F1. Comparison between the experimental data of the pure $C_2Cl_4$ (dots) and the predicted values with the PC-SAFT as optimised in this work.*

Results in Table T1 below list the computed values of the volumes of mixing of the $CO_2$+$C_2Cl_4$ mixture at the same temperature, pressure and composition measured in the densimeter.

*Table T1. Volumes of mixing of the $CO_2$+$C_2Cl_4$ mixture at the same conditions in which measurements are carried out in this work*

| $x_{CO2}$ | $\underline{T}$ | $P$ | $\rho_{Mix}$ | $\rho_{CO_2\ (Pure)}$ | $\rho_{C_2Cl_4\ (Pure)}$ | $\Delta v_{Mixing}(\underline{T}, P, x)$ |
|---|---|---|---|---|---|---|
| [%] | [°C] | [bar] | $[\frac{kg}{m^3}]$ | $[\frac{kg}{m^3}]$ | $[\frac{kg}{m^3}]$ | $[\frac{m^3}{mol}]$ |
| 93.25 | 40.27 | 189.19 | 957.6 | 827.75 | 1619.35 | -1.95 |
| | | 167.09 | 942.1 | 802.52 | 1615.96 | -2.62 |
| | | 143.02 | 921.9 | 766.57 | 1612.20 | -3.82 |
| | | 131.75 | 910.6 | 744.45 | 1610.42 | -4.72 |
| | | 115.23 | 891.7 | 699.70 | 1607.79 | -7.04 |
| | | 124.48 | 901.8 | 727.17 | 1609.27 | -5.47 |
| | | 132.52 | 910.4 | 746.13 | 1610.55 | -4.58 |
| | | 141.71 | 919.5 | 764.23 | 1612.00 | -3.84 |

| | | | | | | |
|---|---|---|---|---|---|---|
| | | 156.30 | 932.4 | 787.83 | 1614.28 | -3.00 |
| | | 179.62 | 950.4 | 817.49 | 1617.89 | -2.16 |
| | | 169.56 | 943.6 | 805.63 | 1616.34 | -2.51 |
| | | 160.20 | 936.5 | 793.37 | 1614.89 | -2.88 |
| | | 152.26 | 929.8 | 781.79 | 1613.65 | -3.26 |
| | | 125.91 | 904.3 | 730.83 | 1609.50 | -5.35 |
| 93.25 | 59.98 | 185.20 | 864.8 | 697.86 | 1588.79 | -5.45 |
| | | 169.63 | 845.3 | 663.87 | 1586.20 | -7.08 |
| | | 160.23 | 831.6 | 638.40 | 1584.63 | -8.54 |
| | | 150.00 | 814.5 | 604.34 | 1582.90 | -10.85 |
| | | 138.32 | 791.1 | 553.25 | 1580.91 | -15.23 |
| | | 124.14 | 753.4 | 465.60 | 1578.46 | -25.90 |
| | | 140.62 | 796.9 | 564.64 | 1581.30 | -14.21 |
| | | 154.49 | 822.7 | 620.27 | 1583.66 | -9.74 |
| | | 171.99 | 848.6 | 669.58 | 1586.60 | -6.79 |
| 93.25 | 79.84 | 191.86 | 743.4 | 574.34 | 1560.03 | -8.37 |
| | | 170.63 | 700.5 | 509.27 | 1556.21 | -13.21 |
| | | 159.19 | 670.1 | 466.35 | 1554.12 | -17.26 |
| | 79.99 | 154.63 | 657.1 | 446.77 | 1553.06 | -19.57 |
| | | 178.24 | 718.5 | 533.63 | 1557.36 | -11.40 |
| | | 187.58 | 736.7 | 561.63 | 1559.04 | -9.35 |
| | | 183.82 | 730.2 | 550.75 | 1558.37 | -10.17 |
| 83.82 | 40.08 | 171.61 | 1065.6 | 809.34 | 1616.95 | -2.38 |
| | | 158.41 | 1058.4 | 792.17 | 1614.91 | -2.98 |
| | | 134.50 | 1044.1 | 751.95 | 1611.16 | -4.68 |
| | | 116.23 | 1031.3 | 705.34 | 1608.25 | -7.20 |
| | | 99.21 | 1017.6 | 620.70 | 1605.50 | -13.53 |
| | | 90.08 | 1009.3 | 483.95 | 1604.02 | -29.82 |
| 90.80 | 40.22 | 162.38 | 977.0 | 796.67 | 1615.31 | -3.09 |
| | | 149.77 | 967.8 | 778.27 | 1613.34 | -3.75 |
| | | 139.22 | 959.3 | 760.03 | 1611.68 | -4.49 |
| | | 118.93 | 941.0 | 712.19 | 1608.46 | -6.92 |
| | | 101.31 | 921.8 | 633.65 | 1605.62 | -12.66 |
| | | 130.06 | 951.4 | 741.15 | 1610.23 | -5.36 |
| | | 156.08 | 972.4 | 787.85 | 1614.33 | -3.38 |
| 85.69 | 40.17 | 160.87 | 1056.5 | 794.93 | 1615.14 | -3.98 |

| | | | | | | |
|---|---|---|---|---|---|---|
| | | 140.88 | 1045.1 | 763.49 | 1612.02 | -5.32 |
| | | 120.58 | 1031.9 | 717.56 | 1608.80 | -7.76 |
| | | 99.97 | 1016.4 | 624.73 | 1605.48 | -14.69 |
| | | 110.20 | 1024.0 | 681.98 | 1607.13 | -10.06 |
| | | 129.81 | 1037.6 | 741.01 | 1610.27 | -6.41 |
| | | 183.83 | 1068.1 | 822.68 | 1618.68 | -2.98 |
| 85.69 | 59.96 | 197.11 | 1013.8 | 719.24 | 1590.77 | -6.75 |
| | | 169.79 | 993.9 | 664.39 | 1586.25 | -9.90 |
| | | 149.54 | 976.1 | 602.75 | 1582.84 | -14.61 |
| | | 125.13 | 949.4 | 472.94 | 1578.66 | -30.06 |
| | | 138.22 | 964.7 | 552.94 | 1580.91 | -19.52 |
| | | 159.80 | 985.3 | 637.26 | 1584.58 | -11.79 |
| | | 184.28 | 1004.5 | 696.18 | 1588.66 | -7.94 |
| 85.69 | 79.95 | 220.43 | 929.7 | 637.84 | 1564.89 | -8.20 |
| | | 200.09 | 911.5 | 594.40 | 1561.32 | -11.24 |
| | | 180.18 | 890.4 | 539.97 | 1557.76 | -16.07 |
| | | 170.03 | 877.6 | 506.32 | 1555.93 | -19.72 |
| | | 149.72 | 846.4 | 426.27 | 1552.20 | -31.17 |
| | | 160.92 | 864.7 | 472.39 | 1554.27 | -24.05 |
| | | 188.22 | 899.0 | 563.64 | 1559.21 | -13.79 |
| | | 133.41 | 808.0 | 354.42 | 1549.16 | -45.69 |
| | | 131.43 | 800.8 | 345.71 | 1548.79 | -47.68 |
| 70.31 | 40.18 | 160.30 | 1227.3 | 794.13 | 1615.05 | -4.12 |
| | | 140.07 | 1220.5 | 761.97 | 1611.88 | -5.46 |
| | | 119.36 | 1213.1 | 713.96 | 1608.60 | -7.85 |
| | | 99.15 | 1205.3 | 618.01 | 1605.34 | -14.22 |
| | | 76.84 | 1196.1 | 245.34 | 1601.68 | -89.83 |
| | | 91.41 | 1202.1 | 511.74 | 1604.08 | -24.46 |
| | | 110.05 | 1209.5 | 681.29 | 1607.10 | -9.76 |
| | | 128.87 | 1216.4 | 738.83 | 1610.11 | -6.55 |
| 70.31 | 59.93 | 193.95 | 1197.5 | 714.08 | 1590.29 | -7.34 |
| | | 179.32 | 1191.7 | 686.29 | 1587.88 | -8.81 |
| | | 150.66 | 1179.5 | 607.21 | 1583.08 | -14.08 |
| | | 119.12 | 1164.1 | 428.44 | 1577.66 | -34.55 |
| | | 95.24 | 1150.7 | 262.71 | 1573.47 | -79.40 |
| | | 103.96 | 1155.6 | 315.69 | 1575.01 | -59.90 |

| | | | | | | |
|---|---|---|---|---|---|---|
| | | 137.78 | 1172.9 | 551.01 | 1580.88 | -18.94 |
| | | 160.41 | 1183.2 | 639.32 | 1584.72 | -11.71 |
| 70.47 | 40.28 | 147.49 | 1224.2 | 774.14 | 1612.89 | -5.09 |
| | | 130.59 | 1218.2 | 741.81 | 1610.23 | -6.56 |
| | | 105.17 | 1208.8 | 656.42 | 1606.15 | -11.57 |
| | | 73.95 | 1195.9 | 222.29 | 1601.04 | -103.22 |
| | | 87.61 | 1201.7 | 406.39 | 1603.29 | -40.30 |
| | | 114.76 | 1212.4 | 697.95 | 1607.70 | -8.92 |
| | | 162.66 | 1229.3 | 796.66 | 1615.26 | -4.18 |
| 70.47 | 59.97 | 164.90 | 1187.0 | 651.67 | 1585.42 | -11.10 |
| | | 145.58 | 1178.6 | 586.88 | 1582.15 | -15.93 |
| | | 125.33 | 1168.8 | 474.23 | 1578.68 | -27.99 |
| | | 97.89 | 1153.9 | 277.51 | 1573.88 | -73.55 |
| | | 103.68 | 1157.2 | 313.55 | 1574.90 | -60.89 |
| | | 115.00 | 1163.4 | 396.08 | 1576.88 | -40.61 |
| | | 134.86 | 1173.5 | 534.84 | 1580.32 | -20.81 |
| | | 152.43 | 1181.6 | 613.20 | 1583.32 | -13.82 |
| | | 173.68 | 1190.8 | 673.58 | 1586.89 | -9.74 |
| 70.47 | 79.91 | 199.36 | 1117.2 | 592.94 | 1561.26 | -12.08 |
| | | 180.92 | 1107.8 | 542.59 | 1557.97 | -16.39 |
| | | 161.74 | 1097.3 | 475.93 | 1554.49 | -23.77 |
| | | 140.29 | 1084.0 | 385.23 | 1550.52 | -38.30 |
| | | 120.79 | 1069.9 | 300.36 | 1546.85 | -60.16 |
| | | 129.32 | 1076.3 | 336.72 | 1548.47 | -49.42 |
| | | 148.13 | 1089.1 | 419.70 | 1551.98 | -32.01 |
| | | 167.22 | 1100.5 | 496.58 | 1555.49 | -21.25 |
| | | 183.50 | 1109.3 | 550.37 | 1558.43 | -15.67 |

## Bibliography of Supplementary Materials


[1] M. Doninelli, E. Morosini, G. Di Marcoberardino, C.M. Invernizzi, P. Iora, M. Riva, P. Stringari, G. Manzolini, Experimental investigation of the CO2+SiCl4 mixture as innovative working fluid for power cycles: Bubble points and liquid density measurements, Energy 299 (2024) 131197. https://doi.org/10.1016/j.energy.2024.131197.

[2] Y. FU, A. VALTZ, S. AHAMADA, H. HU, C. COQUELET, Density data for carbon dioxide (CO2) +trans-1,3,3,3-tetrafluoroprop-1-ene (R-1234ze(E)) mixture at temperatures from 283.32 to 353.02K and pressures up to 10MPa, International Journal of Refrigeration 120 (2020) 430–444. https://doi.org/10.1016/J.IJREFRIG.2020.06.006.

[3] AspenTech, Aspen Plus | Leading Process Simulation Software | AspenTech, https://www.aspentech.com/en/products/engineering/aspen-plus.

# *Chapter 6 - New isochoric apparatus for bubble point measurements*

*THIS CHAPTER IS BASED ON THE ARTICLE: "EXPERIMENTAL ISOCHORIC APPARATUS FOR BUBBLE POINTS DETERMINATION: APPLICATION TO $CO_2$ MIXTURES AS ADVANCED WORKING FLUIDS", PUBLISHED IN INTERNATIONAL JOURNAL OF THERMOFLUIDS, ELSEVIER, DOI: HTTPS://DOI.ORG/10.1016/J.IJFT.2024.100742*

**Abstract**

Carbon dioxide binary mixtures are increasingly considered as working fluids in transcritical power cycles, due to the capability to perform liquid-phase compression even at high environmental temperatures. However, a robust thermodynamic model is essential for optimal and reliable design conditions. It is widely recognized that fine-tuning the equation of state with experimental vapor-liquid equilibrium data of the mixture significantly enhances its reliability.

In this work, a new apparatus dedicated to vapour-liquid equilibrium measurements of mixtures is presented. The proposed method consists of a constant-volume system, where bubble points are identified from the divergence of slope of the isochoric lines between the two-phase and liquid regions, in the temperature-pressure plane. The temperature and pressure limits of the apparatus are 503 K and 25 MPa.

Bubble points of $CO_2$ binary mixtures with hexafluorobenzene ($C_6F_6$) and n-pentane ($C_5H_{12}$) have been measured and compared with previous literature data for validation purposes. Then, the $CO_2$ mixture with octafluorocyclobutane (c-$C_4F_8$) is experimentally studied, addressing a literature gap in bubble point data. The data are used to calibrate the thermodynamic model, leading to affordable design conditions of the power cycle compared to the non-optimized thermodynamics scenario, in a concentrated solar power tower plant.

## 6.1 Introduction

Starting from the theoretical conceptualization of supercritical carbon dioxide ($sCO_2$) power cycles, attributed to Angelino [1] and Feher [2], nowadays there is a renewed and growing interest in this technology to replace the state-of-the-art steam Rankine cycle in different sectors. In particular, $sCO_2$ as working fluid is attractive in high-temperature applications such as nuclear [3], solar [4], and high-temperature waste heat [5], due to high thermal efficiency and power density. However, in hot environments, where ambient air easily approaches 308 K, such as in typical locations of concentrated solar power (CSP) plants the minimum cycle temperature in dry-cooling conditions is constrained at values around 323 K. As a result, the compressibility of pure $sCO_2$ at the compressor intake is penalized by the compression step, that is far from the critical point. For this reason, the H2020 Scarabeus [6] and H2020 Desolination [7] projects proposed the adoption of innovative working fluids constituted by binary mixtures where the $CO_2$ is blended with dopants having higher critical temperature [8]. In this way the critical temperature of the $CO_2$ binary mixture can reach higher values compared to pure $CO_2$ by acting on the mixture composition, thus it is possible to fully

condense the working fluid even at high values of minimum cycle temperature. As investigated by Imre and Ahmed [9], the critical temperature has a strong effect on the performance of Rankine cycles. The primary effect is the opportunity to employ liquid-phase compression, bringing two main advantages: lower energy consumption for the compression step, and a less challenging pump design [10] compared to a $sCO_2$ compressor operating near critical conditions. Secondly, as a result of mixing $CO_2$ with a more complex dopant, the heat capacities within the recuperator are more balanced than pure $sCO_2$, reducing the layout complexity from a recompressed cycle to a simple recuperative cycle. The utilization of $CO_2$ mixtures for efficiency improvement is also discussed in the review work of Chowdhury and Eshan [11]. Turja et al. [12] considered the use of a bottoming Organic Rankine Cycle to recover the rejected heat of a $sCO_2$ cycle, showing that at increasing main compressor temperature the $sCO_2$ is largely penalized (lower compressibility) while increases the production of the bottoming ORC. The use of $CO_2$-mixtures as working fluids in that context would penalise less the power production as the compression step can be in liquid phase even at high values of minimum cycle temperature.

The proposed $CO_2$ blended solution, in fact, results in efficiency gains especially at minimum cycle temperatures as high as 323 K, compared to using pure $sCO_2$ [13]. It is worth it to mention that $CO_2$-based mixtures have been considered as working fluid not only for power generation purposes but also in refrigeration systems and heat pumps [14][15] and cogeneration [16].

In general, the accurate knowledge of the phase boundaries of mixtures is crucial for the design and optimization of closed thermodynamic cycles working in direct or inverse Rankine cycles. The evaluation of the power cycle efficiency and reliable design conditions strongly depend on the accuracy of the equation of state (EoS) used to determine the thermodynamic properties of the mixture and its phase behaviour. It is well known that, in case of mixtures, the reliability of the EoS is improved when the binary interaction parameters of the EoS are regressed based on experimental vapour-liquid equilibrium (VLE) data. When these adjustable parameters are tuned on experimental VLE data, the phase boundaries of the mixture are better represented by the EoS, which is crucial from the power cycle point of view. Chen [17] utilized experimental VLE data of $CO_2$ mixtures as input for a prediction model. This model correlates the binary interaction parameter of the Peng Robinson (PR) EoS - with van der Waals mixing rules - to the critical parameters and acentric factor of organic compounds in mixture with $CO_2$. In a similar way, Abdel-Azim [18] used experimental bubble points to train an artificial neural network model capable to predict the bubble pressure of oils.

Generally, VLE data of mixtures are measured with conventional Pressure-Volume-Temperature (PVT) systems and VLE apparatus. In PVT systems, the mixture is transferred into a cell, whose volume is varied with an automated piston under isothermal conditions, and the bubble point is determined from the divergence of the volumetric behaviour in the liquid phase and the two-phase field. A PVT cell has been recently utilized by the authors [19], in the context of H2020 Desolination project, to measure bubble points of a $CO_2$ mixture with $SiCl_4$ for high-temperature Rankine cycle application. Moreover, in the same work, a non-conventional approach has been adopted to measure additional bubble points with a vibrating tube densimeter. In VLE cells, instead, a small sample of fluid, from both liquid and vapour phases, is extracted, vaporized, and analysed with gas chromatography. To avoid dead volumes and large pressure drop within the cell, the adoption of a

capillary rapid on-line sampling injector (ROLSI®) [20] become a practical standard for VLE cells. A VLE apparatus used for the measurement of $CO_2$ binary mixtures is well described in the experimental works of Coquelet and Valtz [21][22][23]. The same concept has been applied by Wu et al. [24] to measure VLE data of $CO_2$+fluoroethane (R161) binary system. A VLE apparatus with ROLSI has been also used by Sadaghiani et al. [25] to measure a $CO_2$ binary mixture with 3,3,3-Trifluoropropene and, subsequently, tune the binary interaction parameters of different EoS.In the context of the project, the $CO_2$ mixture with $C_6F_6$ has been experimentally investigated in terms of vapour-liquid equilibrium measurements [26] by using a VLE cell. Then, the obtained VLE data have been used for the thermodynamic assessment of the mixture and to achieve a reliable thermal efficiency of the power cycle in CSP application at 823 K turbine inlet temperature. Recently, given the outstanding thermal stability of perfluorocarbons, the $CO_2$ mixture with c-$C_4F_8$ have been investigated [27] as potential working fluid in transcritical power cycles in CSP plants with central receiver. However, in the latter reference, no experimental VLE data were available to optimize the thermodynamic model, so the uncertainty in the performance results is not negligible. Additionally, the absence of experimental data on the phase behaviour of the mixture prevents an accurate determination of the minimum cycle pressure, specifically the bubble pressure at the pump inlet's minimum cycle temperature. The presence of even a few VLE points in the mixture enables more precise studies to ascertain its potential in power cycles. This article is intended to present a newly developed apparatus for bubble point measurements, that allows the investigation of new potential $CO_2$ mixtures for thermodynamic cycles with the need for limited equipment compared to traditional VLE and PVT systems abovementioned.

The isochoric apparatus developed in the Fluid Test Laboratory of the University of Brescia [28], which is presented and validated in the following sections. The experimental setup is designed to obtain bubble points of mixtures from the divergence of isochoric behaviour of the mixture between the two-phase VLE region and the single-phase liquid region. The apparatus implemented in our laboratory employs a methodology (isochoric) already established in the literature; however, the proposed isochoric system provides the advantage of a simplified procedure and equipment, resulting in reduced cost.

Hall and Eubank [29] showcased the viability of the isochoric technique for acquiring VLE data of mixtures, employing a sophisticated experimental setup inspired by the Burnett method [30]. The Burnett method is characterized by a series of isothermal expansions performed on the fluid; this technique involves transferring the fluid from an initial volume to a pre-evacuated secondary volume, and pressure measurements are recorded after each expansion. To date, the Burnett method still ranks as one of the most precise techniques for determining PVT behavior. As stated by Hall and Eubank, "a rough PVT apparatus can reproduce conventional VLE data within the accuracy of the latter" [29], referring to a conventional VLE apparatus. Stouffer et al. [31] modified the apparatus described by Hall and Eubank including a small density reduction cell to expand the $CO_2$+hydrogen sulphide mixture from homogeneous liquid condition, and therefore investigating multiple isochores above the critical one. This modification, enabling the exploration of multiple isochores through expansion in the liquid phase, facilitated the acquisition of multiple bubble points for the mixture. Each isochore corresponds, in fact, to a unique bubble point of the mixture. Then, Zhou et al. [32] developed an automated isochoric apparatus for vapour-liquid equilibrium and density

measurements of natural gas-like mixtures. The interesting apparatus is well described in his PhD dissertation [33], however only dew points were measured and, compared to our setup, the procedure required the externally preparation of the mixture to be charged in the cell at each investigated isochore. Also Velez et al. [34] adopted a constant-volume (isochoric) system to obtain phase transition points for methanol + vegetal oils, reacting systems, from the intersection of the isochoric lines. Recently, Goni et al. [35] adopted the isochoric methodology to measure bubble points of binary mixtures of ethane with heavy hydrocarbons (decane, undecane, dodecane and tridecane), proving good agreement between their data and previous isothermal VLE measurements in literature.

Compared to the abovementioned isochoric investigations, the VLE setup, presented in this work, is characterised by a simple design and a reduced number of components (sensors, valves, fittings), making it feasible for less-equipped laboratories, without compromising on flexibility to different binary mixtures and accuracy. Moreover, a straightforward procedure to fill the vessel and change the mixture density without compromising the composition is here discussed. The proposed methodology has been validated through the measurement of bubble points of well-known $CO_2$ binary mixtures with $C_6F_6$ and n-pentane, proving its consistency with previously published experimental VLE data. Afterwards the apparatus has been used to determine experimental bubble of the mixture $CO_2$+c-$C_4F_8$ , never published before, at a composition relevant to transcritical power cycle considerations. Among the various perfluorocarbons investigated in the H2020 Scarabeus project, the $CO_2$+c-$C_4F_8$ mixture was recently examined by Morosini et al. [27] in a CSP plant with central receiver, operating at a turbine inlet temperature of 823 K. However, the referenced study lacked available VLE data, raising concerns about the optimization of the thermodynamic model and the reliability of the design conditions and efficiency values. The thermodynamic model has been fine-tuned based on the obtained experimental data in this work, ensuring a robust evaluation of the power cycle and providing reliable design point for the component manufacturing.

## 6.2 Experimental Investigation

In this section, the experimental setup will be presented, as well as the methodology adopted for the bubble point determination. The mixture preparation procedure will be discussed after a description of the apparatus, as the mixture is directly prepared within the system rather than in an external cylinder.

### 6.2.1 Chemicals

The chemical species that have been experimentally investigated are reported in Table 1, along with their commercial supplier and purity level. The chemicals have been used without further purification.

*Table 1. Investigated chemicals with information about suppliers and purity.*

| Component | CAS number | Supplier | Purity [% mol] | MW [g/mol] |
|---|---|---|---|---|
| $CO_2$ | 124-38-9 | Sol [36] | 99.99 | 44.01 |

| | | | | |
|---|---|---|---|---|
| $C_6F_6$ | 392-56-3 | Alfa Aesar [37] | >99 | 186.06 |
| $C_5H_{12}$ | 109-66-0 | Sigma-Aldrich [38] | 98 | 72.15 |
| c-$C_4F_8$ | 115-25-3 | Abcr GmbH [39] | 99 | 200.03 |

### 6.2.2 Experimental setup

The schematic of the apparatus in its main components is presented in Figure 1. The core of the apparatus consists of a flanged cylinder made of stainless steel SS304, sealed with 8 bolts and an inert graphite gasket ("d" in Figure 1). The cylinder has been designed for a maximum temperature of 503 K and a maximum pressure of 25 MPa. The lowest temperature that can be explored is 228 K, according to the refrigeration limits of the cryostat. The total internal volume, including tubing and other cavities, resulted to be 127.6 mL, evaluated by weighting the cell fully charged with distilled water compared to the empty vessel at vacuum conditions. Before each test, the system undergoes a leak testing with pure $CO_2$ at 4.5 MPa for a prolonged period of time (3 days).

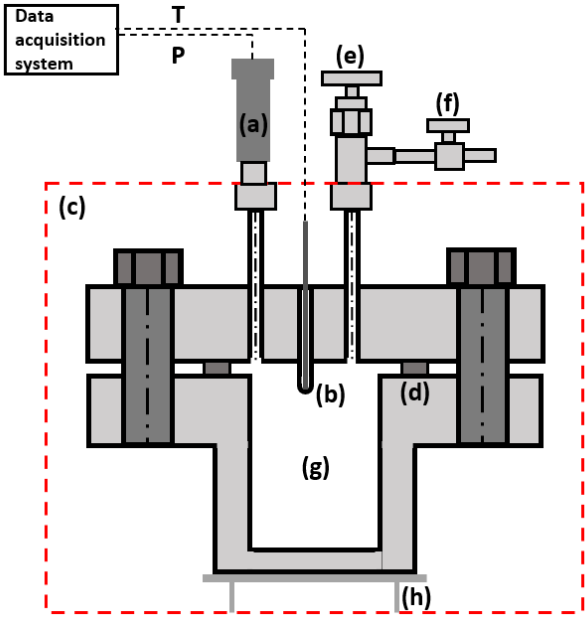


*Figure 1. Schematization of the apparatus adopted for the bubble-points measurements: (a) pressure transducer; (b) thermoresistance well with temperature probe; (c) boundaries of thermal oil - thermostatic bath; (d) graphite gasket; (e) cell main valve; (f) charging/venting valve; (g) cell internal volume; (h) cylinder support.*

The system is placed inside a thermostatic bath (Julabo FP40, represented by red dotted line in Figure 1), to ensure a stable temperature control. The temperature of the bath is set by a PID controller and can be varied from 228 K to 423 K, with a resolution of 0.1 K. A LabVIEW program is used for the acquisition and recording of temperature and pressure signals. The temperature is acquired with a

4-wires thermoresistance Pt100 with tolerance ±0.03 K at 273 K (class 1/10), while ±0.08 K at 100°C, which is inserted in the housing "b" in Figure 1.

The pressure transducer is the model PA-33X manufactured by Keller, with digital interface RS485. The instrument has undergone dedicated calibration within the temperature range of 293-393 K (9 points) to ensure high accuracy across the entire temperature range of interest. An additional calibration was performed by an accredited calibration laboratory. The full scale (FS) of the pressure transmitter is 10 MPa (absolute). The total error band resulting from the calibration procedure ranges from -0.002%FS (293 K) to 0.007%FS (393 K). Moreover, the pressure transmitter also measures the temperature behind its metallic separating diaphragm, with a resolution of ±2°K, but this information is recorded only to ensure that isothermal conditions are reached in all the vertical sections of the apparatus.

Isothermal conditions can be met in the cell thanks to the compact design considering that the internal volume ("g" in Figure 1), thus the investigated the fluid is completely submerged into the thermostatic bath. A metallic support ("h" in Figure 1) has been adopted to regulate the cylinder elevation with respect to thermal oil, in order to prevent the pressure transducer from wetting and the consequent overheating of the electrical components. Then, the top of the system is covered with rockwool to minimize the heat transfer with the environment.

### 6.2.3 Mixture preparation

Following the description of the experimental setup, it is here discussed how the mixture is directly prepared into the cell. Compared to many literature approaches [40], in this procedure there is no need for an external pressurized cylinder above the bubble pressure, at ambient temperature, to maintain the mixture in a homogeneous liquid phase while charging the cell. This approach avoids additional costs and the risk of the pressurizing gas (usually nitrogen) leaking through the piston into the mixture, usually determined by piston seal degradation over time.

The components of the mixture are charged into the cell according to their relative volatility. In case of $CO_2$ binary mixture with higher critical point dopant, the latter is charged first in the cell. Before the loading phase, air is evacuated from the system to around 100 Pa with a DamiCosmos vacuum pump, and the system is weighted with a Mettler-Toledo MS-TS Precision scalewhich has an accuracy of ±0.01 grams. As the cell volume is quite big (approximately 127.6 mL), the typical amount of each component is in the order of tens of grams, then the uncertainty on the composition, given by the weighting, is negligible: the only contribution of composition uncertainty is given by the declared purity of the fluid samples from manufacturer (Table 1).

The desired mass of the first component is introduced into the system, and subsequently the vacuum pump is used for few seconds to remove the potential non-condensable gases dissolved in the fluid sample. The main valve ("e" in Figure 1) is then closed and the confined fluid between valve "e" and "f" is entirely removed with the vacuum pump. The resulting mass of the competent is so determined weighting again the apparatus and deducting the tare measurement. The mass of each component charged into the system is specified in Appendix B.

Then, the $CO_2$ is charged from the bottle with a proper pressure reducer in order to charge the target mass of $CO_2$ at controlled temperature and pressure (then density). The piping that connects the $CO_2$ bottle and the cell is under vacuum conditions before charging, to avoid air intake in the cell. The

weight of the system filled with the mixture is then measured again, and the resulting mixture composition is computed.

The charging procedure starts from the definition of the target composition to be investigated. At the same time, the mass of each component to be charged is constrained to achieve the target value of density in order to investigate an isochoric sufficiently higher than the critical density of the mixture.

### 6.2.4 Methodology description

After the charging procedure is completed, the mixture is in two-phase vapour-liquid equilibrium region, at density higher than the critical one. The physical principle that allows to determine the bubble points of the mixture with this apparatus is the relative change in compressibility between the liquid phase and the two-phase mixture, that in an isochoric system can be visualised as the slope of the pressure against the temperature (dP/dT). As can be seen for a generic binary mixture in the p-T plane in Figure 2, the single-phase liquid mixture is less compressible than the two-phase mixture, leading to high pressure variation as consequence of a temperature variation. Accordingly, the bubble point (bubble pressure and temperature) can be determined by the intersection of the isochoric line both preceding and following the bubble temperature. The same methodology based on the interception between the lines that best fit the experimental points, in the VLE and liquid regions, is adopted also in variable-volume PVT apparatus. In the latter case, compared to an isochoric apparatus, the bubble point is identified as interception point in the pressure-volume plane [40][41]. The same procedure could be used to measure the dew points of a mixture in case the mixture is charged in the cell at a density lower than the critical one.

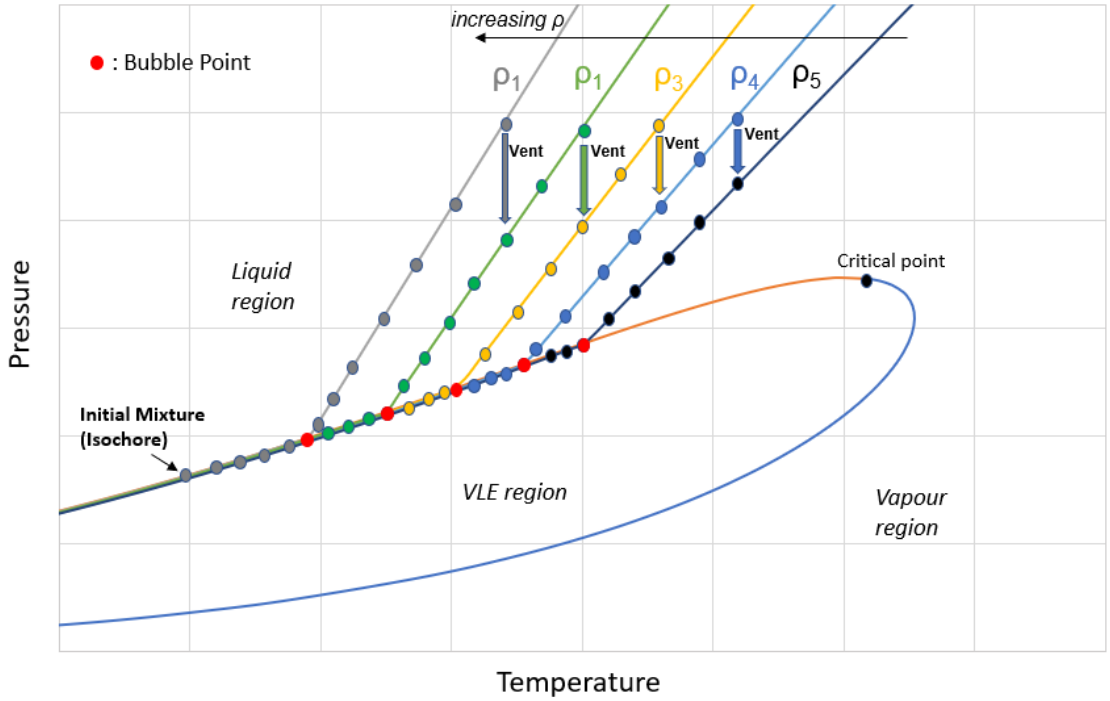


*Figure 2. Conceptual procedure for the bubble point identification of a mixture using an isochoric setup, with dots representing each experimental (P,T) measurement, different colours stand for different series (isochores) measured, and the simulated phase envelope and critical point; the bubble points (red dots) are identified from the drastic change in slope of the isochore between the VLE region and the single-phase liquid region.*

For each isochore investigated, it is possible to obtain one single bubble point of the mixture charged in the cell. For this reason, as presented in Figure 2, a venting of a small portion of the homogeneous liquid mixture is carried out in high-pressure conditions. By actuating the main valve ("e" in Figure 2), the liquid mixture is introduced into the confined piping volume between valves "e" and "f", causing a minor pressure reduction. That volume is around 2 mL (1.5% of the cell volume), then it causes a little pressure drop in the cell, which prevents the mixture from entering the VLE region and undergoing phase separation. Following this, valve "e" is closed, and the small portion of the mixture is evacuated under hood by opening valve "f." This procedure is reiterated until the desired temperature and pressure conditions are achieved for a new isochoric investigation, at a lower mixture density compared to the previous one. This simple technique allows to perform the same concept introduced by Stouffer et al. [31], with their density reduction cell in the modified Burnett apparatus, but in a much simpler manner. Moreover, by adopting this approach, there is no need for an external pressurized cylinder to charge the mixture in the cell at a different density.

Upon achieving equilibrium, the temperature and pressure measurements are typically recorded when the standard deviations for pressure and temperature are below 3 mbar and 0.001°C, respectively, for two minutes recording time.

After acquiring one measurement, the temperature is systematically incremented, and the system is allowed to reach a new equilibrium state (P,T) along the isochoric line.

It must be stressed out that, at high reduced densities ($\varrho \gg \varrho_{cr}$), as evident in Figure 2, each single experimental point (P,T) measured in the VLE region lies very close to the bubble line and could be

considered as a qualitative bubble point of the mixture itself. Even if the difference between the experimental points in the VLE region and the bubble curve is within the experimental uncertainty, in this work only the bubble points obtained from the curves interception are proposed. The earlier assertion is emphasized to underscore that, regardless of the isochoric line's slope in the liquid region, the intersection point invariably aligns with the bubble line. This means that the rigorous mathematical uncertainty detailed in the Appendix A is misleading, as it fails to capture the physics elucidated in this work and the efficacy of the proposed method.

### 6.3 Experimental results, modelling, and discussion

The experimental campaign consists of the determination of the bubble points of three $CO_2$ based binary mixtures identifying the interception between the two-phase and the liquid region at different density and compositions. Two mixtures ($CO_2$+$C_6F_6$ and $CO_2$+$C_5H_{12}$), whose volumetric behaviour is well-known in literature, are selected to validate the proposed apparatus and procedure while VLE data on the blend $CO_2$+c-$C_4F_8$ are here presented for the first time. As already mentioned, the interest on this blend relies on its adoption as working fluid in closed power cycle for CSP or other applications.

The bubble points, measured with the procedure presented in the previous section, are reported in Appendix B, with the associated uncertainty computed as in Appendix A. The results are also presented in graphical form in the next sections.

The validation of the first two blends is performed indirectly comparing the experimental results with suitable thermodynamic model, fitted with previous literature measurements. This expedient Is necessary because the mixture compositions obtained by the loading procedure are close but different from the ones available in literature: it is so important to verify that the experimental results are aligned with the one used to characterise the mixture behaviour in literature.

The original PR EoS [42], as expressed in Equation 1-6, has been considered for the post-processing and comparison of the experimental data, given its simplicity and robustness.

$$P = \frac{RT}{v-b} - \frac{\alpha a}{v(v+b)+b(v-b)} \tag{1}$$

where the alpha function adopted is in its original form [42]:

$$\alpha = \left[1 + k\left(1 - \sqrt{T_r}\right)\right]^2 \tag{2}$$

$$k = 0.37464 + 1.54226\omega - 0.26992\omega^2 \tag{3}$$

$$a = 0.45724\frac{R^2 T_{cr}^2}{P_{cr}} \tag{4}$$

$$b = 0.0778\frac{RT_{cr}}{P_{cr}} \tag{5}$$

Van der Waals mixing rules are then adopted to describe the binary mixture as follows:

$$a_m = \sum_{i=1}^{n_c}\sum_{j=1}^{n_c} x_i x_j \sqrt{a_{ii}a_{jj}}\left(1 - k_{ij}\right) \quad (6)$$

$$b_m = \sum_{i=1}^{n_c} x_i b_i \quad (7)$$

where the binary interaction parameter $k_{ij}=k_{ji}$ must be fitted on available vapour-liquid equilibrium data to improve the accuracy of the EoS in the mixture description.

The BIP regression is performed within the software ASPEN Properties v12 [16], using the maximum likelihood method as numerical optimization method. The Britt–Luecke algorithm [43] with Deming initialization method [44] was applied to regress the parameter. The Average Absolute Deviation percentage (AAD%) is selected as a metric to quantify the Equation of State (EoS) fitting capability for the experimental data. The AAD percentage is computed in this work as shown in Equation (8), where $P_{exp}$ is the measured value, $P_{calc}$ is the value calculated by using the optimised EoS and N is the number of experimental data considered:

$$AAD_{Pbubble}[\%] = \frac{100}{N}\cdot\sum_{i=1}^{N}\left|\frac{P_{exp} - P_{calc}}{P_{exp}}\right| \quad (8)$$

The consistency of bubble points measured in this study is assessed by comparing the AAD percentage of a thermodynamic model tuned with literature data against the bubble points measured here. If the AAD of the model with our data is equal or lower than that with literature data, the bubble points obtained in this work are considered in good agreement with the literature.

The parameters of the chemical species studied in this work that are required by the PR EoS are reported in Table 2.

*Table 2. Parameters adopted by the EoS (default values in Aspen Properties [45]) and the BIPs of the mixtures.*

| Component | $T_{cr}$ [K] | $P_{cr}$ [MPa] | ω [-] | BIP $CO_2$ mixture |
|---|---|---|---|---|
| $CO_2$ | 304.21 | 7.383 | 0.224 | - |
| $C_6F_6$ | 516.73 | 3.273 | 0.396 | $k_{ij}$=0.16297-0.0003951·T [K] [26] |
| $C_5H_{12}$ | 469.7 | 3.37 | 0.252 | $k_{ij}$=0.1222* |
| c-$C_4F_8$ | 388.37 | 2.778 | 0.356 | See Section 3.3 |

**Default value in Aspen Plus database, aligned with [46].*

### 6.3.1 $CO_2$+$C_6F_6$ mixture

The $CO_2$+$C_6F_6$ mixture is one of the two reference mixture here selected for the methodology and procedure validation. According to a previous experimental work of Di Marcoberardino et al. [26], the PR EoS is the EoS that guarantees the lowest average absolute deviation percentage (AAD=2.6%) when compared to experimental bubble pressures of the binary system $CO_2$+$C_6F_6$. The PR EoS as optimized in [26], with a temperature-dependent BIP equal to $k_{ij}$=0.16297-0.0003951·T [K], has been

considered to compare the data obtained in this work with the previous experimental data. The comparison is also available in graphical form in Figure 3.

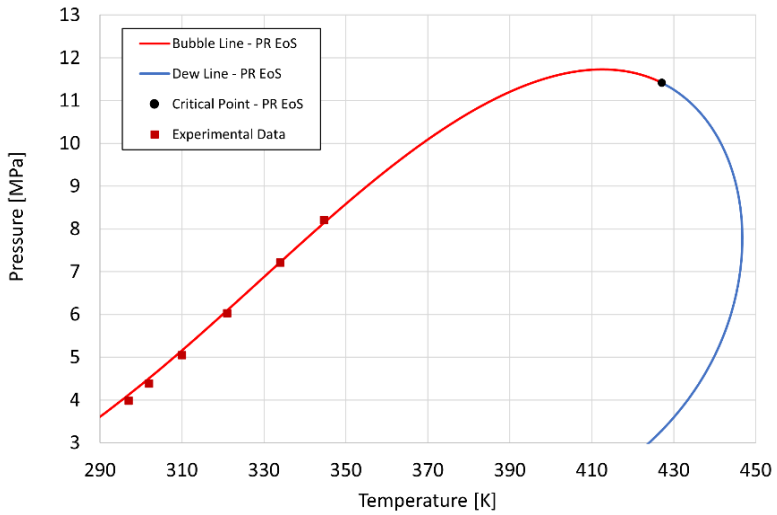


*Figure 3. Phase envelope (solid line) of the $CO_2$+$C_6F_6$ mixture (71.2% molar $CO_2$) simulated with the PR EoS with $k_{ij}$, and the experimental data obtained in this work (red points).*

The mixture is loaded in the experimental apparatus at a 71.2% $CO_2$ molar fraction. This composition aligns with the composition range of interest for the specific mixture in power cycle applications [26] and with available experimental data in the literature.

The experimental bubble points obtained in this work (red dots in Figure 3), have an AAD% equal to 1.76% compared with the PR EoS with $k_{ij}$ as optimized in [26], which is lower than the AAD% reported by the model when compared to the experimental bubble points used in the fitting in the latter work (2.8 %), underscoring an agreement with the literature data.

### 6.3.2 $CO_2$+n-pentane mixture

The $CO_2$+n-pentane mixture has been investigated at two different molar compositions (data in Appendix B) with the aim to validate the procedure as well as to provide new experimental data. Specifically, we have focused on two compositions with molar fractions close to 50%, where mixing effects are more pronounced: the resulting compositions, after the mixture preparation procedure and weighting, consist of a $CO_2$ fraction of 52.2% and 62.3%.

Besserer and Robinson [47] suggested that the earlier VLE data of Poettmann and Katz [48] regarding this binary mixture were inaccurate. They identified a significant discrepancy, exceeding 30%, in the liquid phase compositions between their findings and those of Poettmann. Subsequently, Cheng et al. [46] conducted measurements on the $CO_2$+n-pentane binary system across a broader range of temperature and composition. Since their results were consistent with those of Besserer & Robinson, the data from Poettman and Katz have not been considered in this analysis.

For the $CO_2$+Pentane binary mixture, in Aspen Plus v12 environment, the BIP of the PR EoS is already available at the default value of $k_{ij}$=0.1222, which is a value considered also by Cheng et al. [46]. However, Cheng et al. [46] found out that no cubic EoS (Soave-Rediich-Kwong, Peng-Robinson, Kubic-Martin, and Adachi-Lu-Sugle) was able to correlate the data within the experimental error, even with the use of a BIP. An attempt to improve the capability of the EoS is performed here,

regressing a temperature-dependent BIP on the experimental data of Cheng et al. [46], which resulted to be $k_{ij}(T) = 0.09396 + 0.00007878 \cdot T[K]$.

The predictive capability of the PR EoS for the VLE data measured by Cheng et al. [46] above 20°C is illustrated by the average absolute percentage deviations shown in Figure 4. It is worth noting that the data from Cheng et al. were selected as they constitute the largest dataset available for this mixture. In Figure 4, also the deviations of the Kunz-Wagner EoS [49], as implemented in REFPROP v10 [50], are shown. A marginal improvement in the performance of the EoS is observed with the temperature-dependent BIP proposed here, resulting in an overall percentage AAD percentage of 1.9%, compared to 2.3% with the constant BIP. It's noteworthy that the AAD% reported by the REFPROP model is substantially higher at 4.3%. Additionally, it's important to mention that several experimental points were excluded from the evaluation due to the REFPROP model's failure to converge under specific conditions. The model of REFPROP was applied by Ganesan and Eikevik [51] to analyse the performance of a cascaded high-temperature heat pump adopting $CO_2$+n-pentane mixture as working fluid in the topping cycle. However, the non-negligible error of the model implemented in REFPROP database at calculating the bubble pressure at elevated temperature suggests that it is not the best choice for the design of high-temperature heat pumps operating with $CO_2$+n-pentane binary mixture.

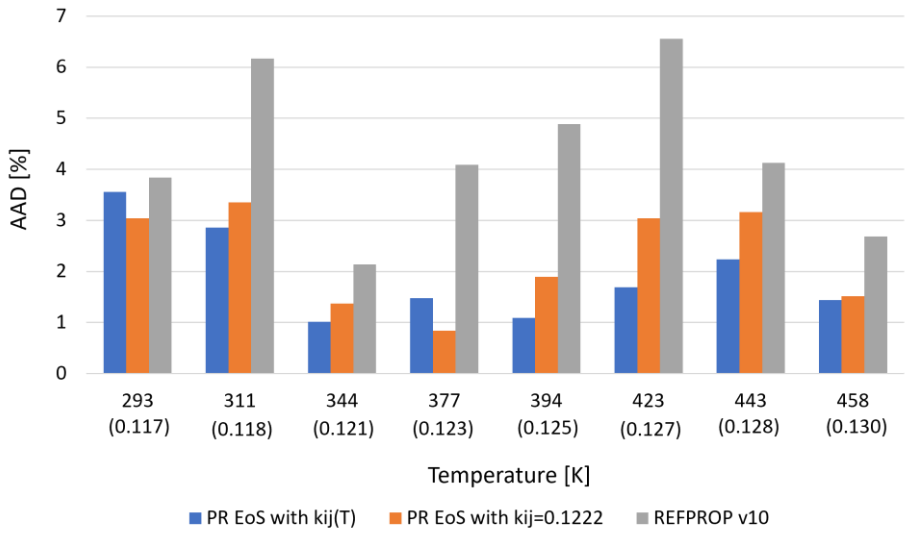


*Figure 4. Average absolute deviation of different EoS compared to the VLE data measured by a previous literature work (Cheng et al. [46]) above 293 K; on the temperature axis, the values of the $k_{ij}(T)$ are reported within brackets.*

The AAD percentage of the PR EoS with temperature-dependent BIP against the bubble points measured in this work is equal to 2.9%, which is aligned with the deviations of the thermodynamic model compared to literature data (see Figure 4).

To enable a visual comparison, points were extrapolated from the obtained bubble lines in this study, aligning them with the same temperatures as other isothermal VLE datasets available in the literature. This comparison is shown in Figure 5. The bubble points, extrapolated from the measured bubble, line are consistent with the data of Cheng et al. [46] and perfectly aligned with the data of

Besserer & Robinson [47]. This provides further evidence of agreement between the data obtained in this study and the data reported in earlier literature works.

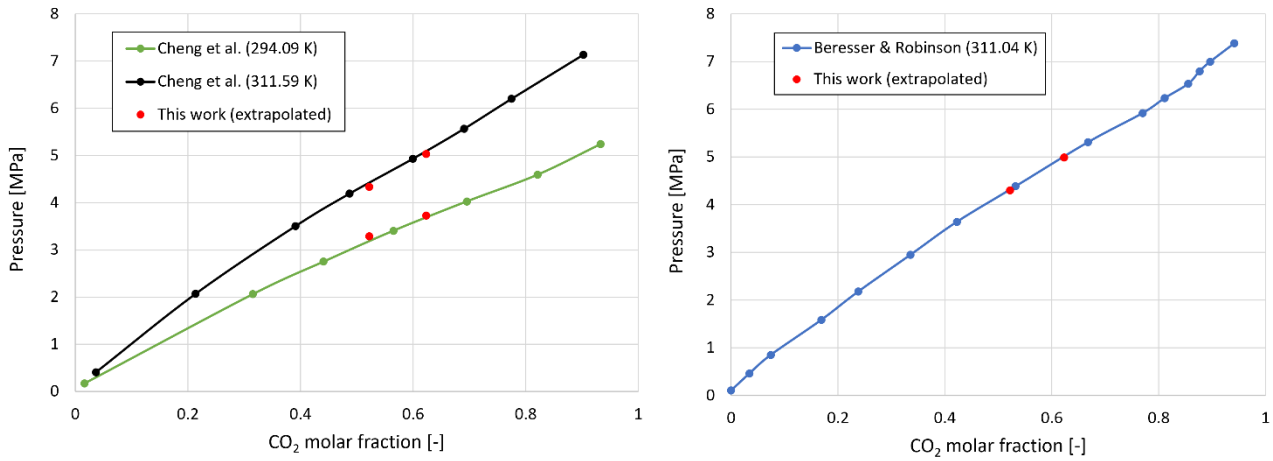


*Figure 5. Bubble points measured by other authors in the literature, and the bubble points extrapolated from the measurements of this work (red dots) at the same temperatures.*

### 6.3.3 $CO_2$+c-$C_4F_8$ bubble points and EoS tuning

After validating the setup and procedure, bubble points of the $CO_2$ mixture with c-$C_4F_8$ have been measured at a composition of interest from the power cycle point of view [27], specifically at 77.25% $CO_2$ molar fraction. The bubble points, along with their uncertainty, are reported in Appendix B. In this case, the experimental measurements are required to calibrate, for the first time, the BIP of a suitable EoS.

Table 3 presents the BIP ($k_{ij}$) acquired through data regression in Aspen Plus v12, along with the AAD percentage computed on the bubble pressure for each temperature. The table also includes an overall average AAD%, which results to be 0.31% for PR EoS with van der Waals mixing rules. For comparison purposes, the same procedure for the BIP regression is carried out for PR EoS with Boston Mathias (PR-BM) alpha function [52], PR EoS with Wong Sandler (PR-WS) mixing rules [53], and Soave-Redlich-Kwong EoS [54]. The deviations compared to experimental data are reported in Table 3.

*Table 3. BIP regressed and AAD% of different EoS vs experimental bubble points of $CO_2$+c-$C_4F_8$ mixture.*

| **EoS** | **$k_{ij}$** | **AAD percentage** | | | | |
|---|---|---|---|---|---|---|
| | | 282.95 K | 295.25 K | 309.75 K | 317.05 K | Average |
| PR-vdW | 0.04070 ±0.00398 | 0.3% | 0.28% | 0.62% | 0.06% | 0.31% |
| PR-BM | 0.03946 ±0.00252 | 0.33% | 0.21% | 0.76% | 0.56% | 0.34% |
| PR-WS | 0.42052 ±0.018511 | 3.09% | 1.53% | 0.68% | 3.79% | 2.27% |

| | | | | | | |
|---|---|---|---|---|---|---|
| SRK | 0.04442 ±0.00389 | 4.34% | 4.44% | 4.91% | 3.75% | 4.33% |

In Figure 6 all the measurements (both in VLE and liquid regions) used to obtain the bubble points are reported. The phase envelope, in Figure 6, calculated with the PR EoS as optimized in this section on the experimental bubble points ($k_{ij}$=0.0407) shows the good agreement with the experimental data. It can be noted, instead, that the phase envelope calculated without EoS optimisation ($k_{ij}$=0) leads to errors in calculating the bubble line, as well as in the estimation of the critical point of the mixture. The lowest isochore investigated in Figure 6 is too close to the critical point to determine with good accuracy the bubble point: the density of the vapour and liquid phase are similar approaching the critical point. For this reason, this bubble point is not considered nor reported in Appendix B.

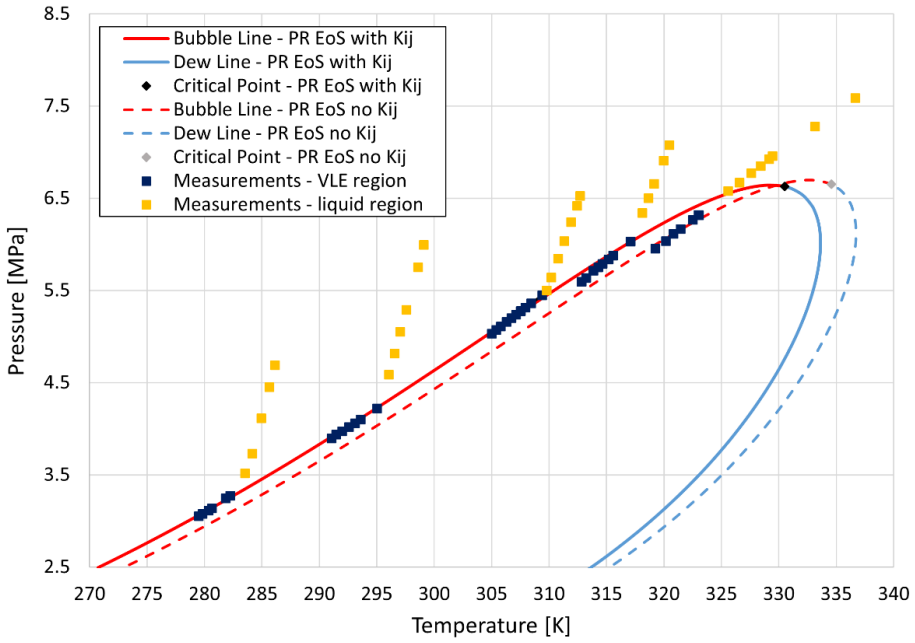


*Figure 6. Experimental measurements of $CO_2$+c-$C_4F_8$ mixture (77.25% molar $CO_2$), and the phase envelope calculated both with the PR EoS optimized on the bubble points ($k_{ij}$=0.0407) and without BIP ($k_{ij}$=0).*

As mentioned in the methodology section, the distance of each experimental point in the VLE region (blue dots in Figure 6) to the bubble line is within the instrumental uncertainty, for the isochores at low reduced temperature. For this reason, each individual point effectively could be considered as a standalone bubble point. However, this perspective is not explored in this study, and the bubble point is reported only as intersection between the VLE and liquid isochoric lines.

## 6.4 Application of the mixture $CO_2$+c-$C_4F_8$: power cycle modelling

In this section, the PR EoS, optimized on the bubble points obtained in this work, will be used to evaluate the performance of the $CO_2$+c-$C_4F_8$ mixture in a CSP tower plant.

Over the last years, perfluorocarbons have been proposed as suitable dopant for blending $CO_2$ as working fluid for CSP tower power block because of the potential high thermal stability related to the C-F bond energy. The mixture $CO_2$+c-$C_4F_8$ was already presented in a previous work [27] showing interesting power cycle efficiency values although it wasn't possible to optimise the property model due to the lack of information in literature about the phase behaviour (i.e. the molecules interaction). The experimental campaign carried out on this mixture aimed at covering this gag: the PR EoS with vdW mixing rules, as optimized in the previous section ($k_{ij}$=0.0407) on the experimental bubble points, is used here for the calculation of the thermodynamic properties of the mixture. The analysis presented here is therefore useful to validate the promising results of the mixture in CSP application.

The $CO_2$+c-$C_4F_8$ mixture operates in a transcritical power cycle in simple-recuperated (SR) and recompression (RC) layouts. The cycle is simulated in Aspen Plus V12 [45] with the assumptions reported in Table 4, which are in agreement with the previous study about this mixture [27]. The turbine inlet temperature (TIT) is equal to 823.15 K, coherently with a state-of-the-art CSP tower plant adopting molten salts as heat transfer and storage fluid.

*Table 4. Power cycles assumptions for $CO_2$+c-$C_4F_8$ mixture cycle.*

| **Power Cycle Parameter** | **Value** |
|---|---|
| Turbine Inlet Temperature [K] | 823.15 |
| Turbine Inlet Pressure [MPa] | 25.3 |
| Cycle Minimum Temperature [°C] | 324.15 |
| Turbine / Pump Isentropic Efficiency [%] | 92 / 88 |
| PCHE Minimum Internal Temperature Difference [K] | 5 |
| Condenser Pressure drop [MPa] | 0.2 |
| PHE Pressure drop [MPa] | 0.4 |
| Recuperator Pressure drop HP / LP [MPa] | 0.05 / 0.1 |

The maximum cycle pressure at the pump outlet is dictated by the assumed turbine inlet pressure and the pressure drops across the heat exchangers on the high-pressure side. At fixed maximum pressure (mostly determined by material integrity at the maximum cycle temperature), the turbine pressure ratio and enthalpy drop at design conditions is determined by the bubble pressure and the design pressure drops in the recuperator (or recuperators) and condenser. In this scenario, the accurate knowledge of the bubble pressure at fixed pump inlet is very relevant for the correct evaluation of the pressure ratio across the turbomachines.

The SR and RC cycle architectures are represented in Figure 7, and the corresponding T-s diagram in Figure 8. The mixture is pumped from the bubble point conditions up to the cycle maximum pressure, then it enters the recuperator to recover the thermal power available from the turbine outlet. After the internal heat recovery process, the mixture enters the primary heat exchanger (PHE) where it is heated up to 823.15 K by the molten salts. Then, the mixture is expanded in the turbine and cooled in the recuperator. In the end, the mixture enters the air-cooled condenser to condensate.

In comparison to the SR architecture, the RC configuration divides the internal heat recovery process into two heat exchangers handling different mass flow rates on the high-pressure side (cold side). Specifically, the turbine outlet stream sequentially passes through the High-Temperature (HT) Recuperator and Low-Temperature (LT) Recuperator before undergoing a separation: a portion enters the compressor, mixing with high-pressure steam at the LT Recuperator outlet, while the rest proceeds for complete condensation, undergoes pumping, and re-enters the LT Recuperator. The recompression layout is adopted to balance the heat capacities, then to reduce the irreversibility in the internal heat recovery process.

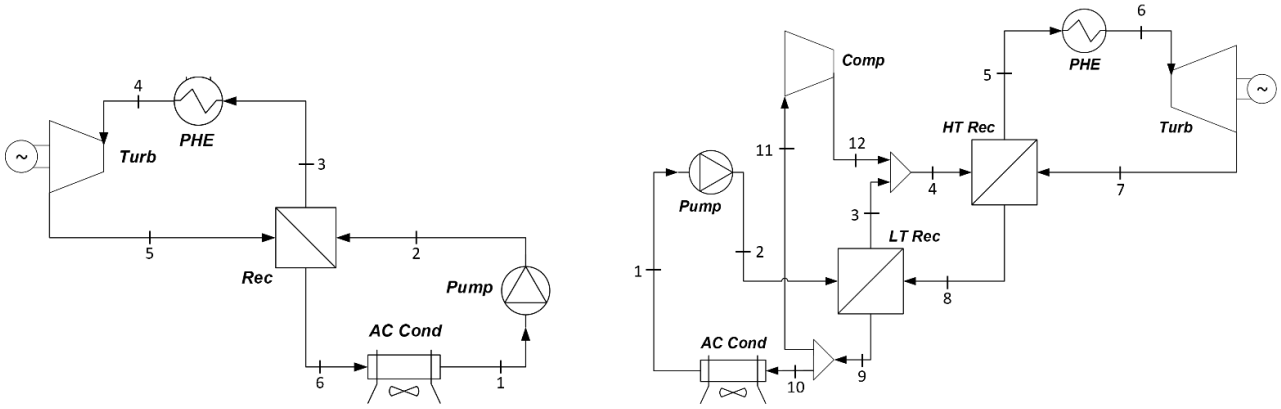


*Figure 7. Simple-recuperated (SR) on the left, and recompression (RC) layout on the right.*

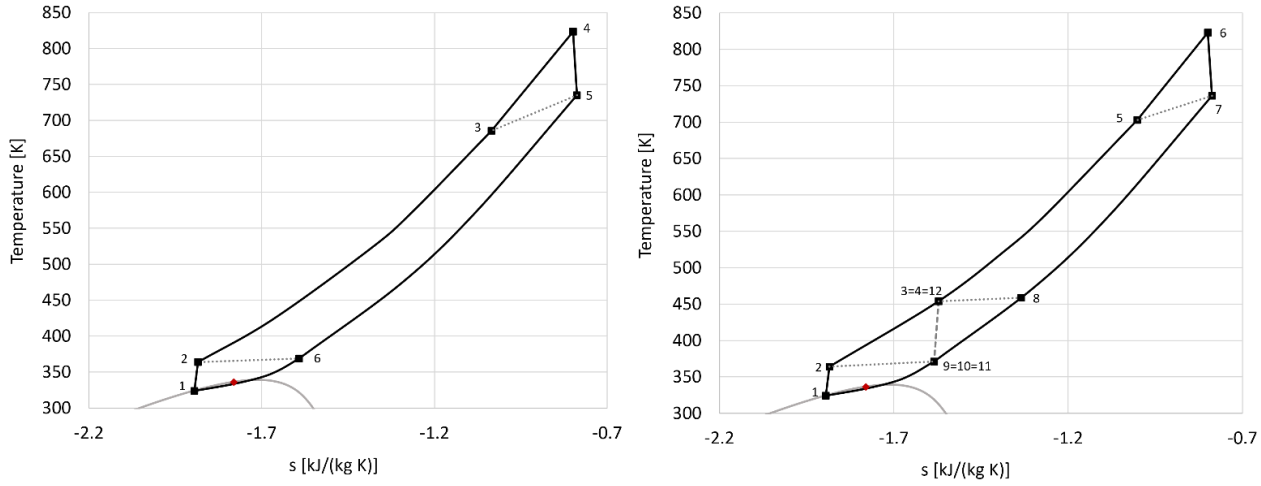


*Figure 8. T-s diagram of the transcritical cycle adopting $CO_2$+c-$C_4F_8$ mixture (27% c-$C_4F_8$ molar fraction) in SR layout (left) and RC layout (right). The critical point of the mixture is represented as a red diamond in the T-s diagram. The internal heat recovery processes (LT and HT Rec) is represented through dotted lines, while the re-compression as dashed line.*

A sensitivity analysis is performed to assess the thermodynamic cycle efficiency at varying $CO_2$ molar content. The thermal efficiency of the simple recuperated (SR) and recompression (RC) cycles are defined according to Eq. 9 and 10, respectively.

$$\eta_{th,SR} = \frac{W_{Turbine} - W_{Pump}}{Q_{in}} \quad (9)$$

$$\eta_{th,RC} = \frac{W_{Turbine} - W_{Pump} - W_{compressor}}{Q_{in}} \quad (10)$$

Results are reported in Figure 9 according to the optimised thermodynamic model (PR EoS with $k_{ij}$) and the non-optimized model (PR EoS with null $k_{ij}$). The optimisation of the thermodynamic model confirms the good efficiency of the mixture under reliable design conditions, outperforming pure $sCO_2$ under the same assumptions and power block [27]. A maximum value of 43% efficiency is reached when approaching the 50% dopant molar content, in a simple recuperated architecture. Instead, the composition that optimise the RC cycle efficiency is around 27% c-$C_4F_8$ molar content, surpassing the 44% thermal efficiency. The thermodynamic model optimisation confirms, then, the good efficiency achieved with the adoption of this mixture.

Although the gap between the calculated design efficiency using an optimized and non-optimized thermodynamic model is low (less than 0.2 percentage points), as evidenced in Figure 9, the difference on the prediction of the mixture density and enthalpy at different operating conditions may lead to notable inconsistencies in the design of each cycle components. Assuming a power block with a target mechanical output of 100 MW, Table 5 shows the impact of the BIP on the different components design with respect to a null kij for the two investigated layouts. The discrepancies highlight the errors that stem from designing components based on a non-optimized thermodynamic model.

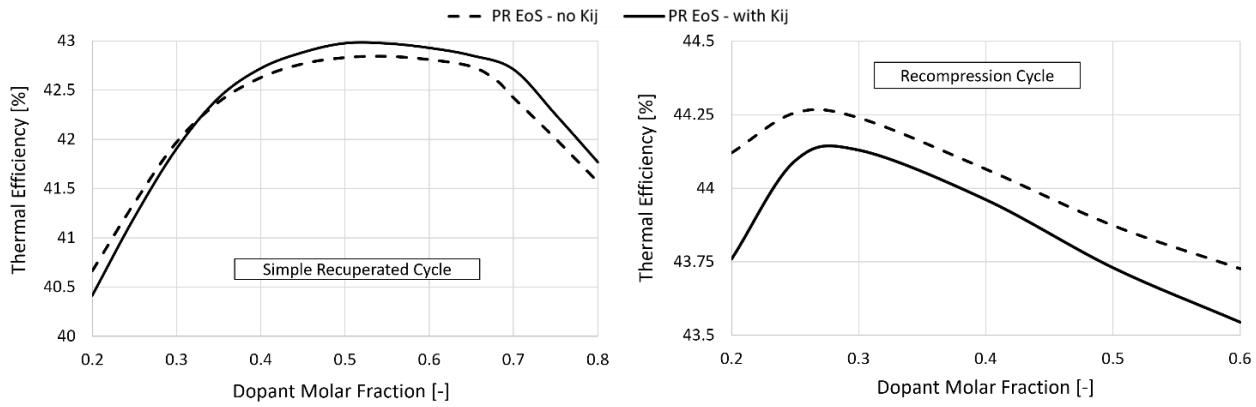


*Figure 9. Thermal efficiency of the $CO_2$+c-$C_4F_8$ cycle calculated both with the PR EoS optimized ($k_{ij}$=0.0407) and without optimisation ($k_{ij}$=0), in simple recuperated layout (left side) and recompression layout (right side).*

*Table 5. Percentage deviations on component design when performed with non-optimised PR EoS ($k_{ij}$=0) compared to the optimized EoS ($k_{ij}$=0.0407)), with 27% dopant molar content and targeting the same mechanical output (100 MW).*

| Parameter | Percentage Deviation (RC cycle) [%] | Percentage deviation (SR cycle) [%] |
|---|---|---|
| $P_{min,cycle}$ | -3.25 | -3.25 |
| PHE Thermal Power | -0.3 | -0.28 |

| | | |
|---|---|---|
| Mass Flow Rate | -3.27 | -3.51 |
| Turbine Power | -1.4 | -1.62 |
| Pump Power | -7.23 | -6.37 |
| Compressor Power | -1.49 | - |
| LT Recuperator Th. Power | -0.68 | -3.08 |
| HT Recuperator Th. Power | -3.85 | - |
| UA LT Recuperator | -2.8 | -2.67 |
| UA HT Recuperator | -6.68 | - |
| Condenser Thermal Power | -0.53 | -0.49 |

Under similar thermal power exchanged in the primary heat exchanger (-0.3%), the inconsistencies on components design are highlighted. Firstly, the minimum cycle pressure is underestimated by 3.25% compared to the actual value required for the complete condensation of the mixture at 324.15 K (minimum cycle temperature). This implies that, in operation, the turbine (and then the other components) must operate under off-design conditions, expanding at a higher pressure to ensure full condensation of the mixture. This has an impact on the turbomachines and cycle efficiency, which can only be assessed through a proper off-design analysis, beyond the scope of this study. The heat exchangers appear as underestimated too: the UA product (representative of the size) of the recuperator, in particular, is noticeably lower (up to 6.7%) than the actual value that guarantee the declared effectiveness, i.e. the 5 K as minimum pinch temperature. As a result, the heat transfer area obtained with incorrect design conditions would be underestimated, which penalizes the effectiveness of the heat exchangers.

Also, the pump power results to be underestimated by 3.25% when the power cycle is designed with null $k_{ij}$ value, which mostly reflects the error in the determination of the correct mass flow rate of the mixture (3.27%).

## 6.5 Conclusions

A novel isochoric apparatus is presented for the measurement of vapor-liquid equilibrium phase boundaries of mixtures. The experimental setup and procedure have been validated by measuring bubble points of $CO_2$ binary mixtures with hexafluorobenzene and n-pentane, characterised in previous literature works. Specifically, the absolute deviation of the PR equation of state, in comparison to the measured bubble points, was similar or even lower than the corresponding deviation observed when using the same thermodynamic model tuned on previous literature data.

Bubble points of the $CO_2$+c-$C_4F_8$ mixture, which have not been experimentally investigated in the literature, have been measured at a composition of interest from a transcritical power cycle perspective. These bubble points were utilized for the refinement of the PR EoS. As a result, the average absolute deviation of the fitted EoS against experimental bubble points resulted to be 0.31%. The calibrated thermodynamic model has been used then to evaluate the transcritical power cycle operating with the mixture as a working fluid in CSP application considering 823.15 K as maximum cycle temperature.

As a matter of facts, the utilization of the EoS without fine-tuning (null binary interaction parameter) tends to overestimate the pressure ratio across turbomachines by 3.25%. Furthermore, in the non-optimized scenario, the design pump power and the UA product of the recuperator are underestimated by more than 6%, thereby impacting the cycle efficiency under actual operating conditions. The thermal efficiency of the mixture overcomes the 44% value in a recompressed architecture, making it a promising candidate for future research.

The experimental isochoric setup introduced in this work will be employed in future studies to measure VLE data of $CO_2$ mixtures for closed power cycles, heat pumps and refrigeration systems.

## Nomenclature

Acronyms

| | |
|---|---|
| A | Heat Transfer Area |
| AAD | Average Absolute Deviation |
| AC | Air Cooled |
| CSP | Concentrated solar power |
| EoS | Equation of state |
| HTF | Heat transfer fluid |
| PHE | Primary Heat Exchanger |
| PR | Peng Robinson |
| REFPROP | Reference Fluid Thermodynamic and Transport Properties |
| RC | Recompressed |
| SR | Simple Recupered |
| TIT | Turbine Inlet Temperature, K |
| U | Overall Heat Transfer Coefficient |
| VLE | Vapour Liquid Equilibrium |

*Symbols*

| | |
|---|---|
| c | Cyclic |
| $\dot{m}$ | Mass flow rate, kg $s^{-1}$ |
| P | Pressure, MPa |
| Q | Thermal duty, MW |
| R | Universal Gas Constant |
| s | Entropy, kJ $kg^{-1}$ $K^{-1}$ |
| T | Temperature, K |
| W | Mechanical power, MW |
| x | Molar fraction, - |

*Greek symbols*

| | |
|---|---|
| $\eta_{th}$ | Cycle Thermal Efficiency, - |
| $\varrho$ | Density, kg $m^{-1}$ |
| $\omega$ | Pitzer acentric factor, - |

Subscripts

| | |
|---|---|
| cr | Critical |
| in | Inlet |
| min | Minimum |
| max | Maximum |

## 6.6 Bibliography


[1] G. Angelino, Carbon Dioxide Condensation Cycles For Power Production, J. Eng. Power. 90 (1968) 287–295. https://doi.org/10.1115/1.3609190.

[2] E.G. Feher, The Supercritical Thermodynamic Power Cycle, Energy Convers. 8.2. (1968) 85–90.

[3] V. Dostal, P. Hejzlar, M.J. Driscoll, High-performance supercritical carbon dioxide cycle for next-generation nuclear reactors, Nucl. Technol. 154 (2006) 265–282. https://doi.org/10.13182/NT154-265.

[4] M. Binotti, M. Astolfi, S. Campanari, G. Manzolini, P. Silva, Preliminary assessment of sCO2 cycles for power generation in CSP solar tower plants, Appl. Energy. 204 (2017) 1007–1017. https://doi.org/10.1016/j.apenergy.2017.05.121.

[5] D. Alfani, M. Binotti, E. Macchi, P. Silva, M. Astolfi, sCO2 power plants for waste heat recovery: Design optimization and part-load operation strategies, Appl. Therm. Eng. 195 (2021) 117013. https://doi.org/10.1016/j.applthermaleng.2021.117013.

[6] M. Binotti, G. Di Marcoberardino, P. Iora, C. Invernizzi, G. Manzolini, Scarabeus: Supercritical carbon dioxide/alternative fluid blends for efficiency upgrade of solar power plants, AIP Conf. Proc. 2303 (2020). https://doi.org/10.1063/5.0028799.

[7] DESOLINATION – Sustainable desalination from Concentrated Solar Power., https://desolination.eu/.

[8] G. Di Marcoberardino, C.M. Invernizzi, P. Iora, A. Ayub, D. Di Bona, P. Chiesa, M. Binotti, G. Manzolini, Experimental and analytical procedure for the characterization of innovative working fluids for power plants applications, Appl. Therm. Eng. 178 (2020) 115513. https://doi.org/10.1016/j.applthermaleng.2020.115513.

[9] A.R. Imre, A.M. Ahmed, Effect of the working fluids critical temperature on thermal performance for trilateral flash cycle and organic Rankine cycle, Int. J. Thermofluids. 20 (2023) 100417. https://doi.org/10.1016/j.ijft.2023.100417.

[10] O.A. Terracciano, F. De Francesco, R. Brizzi, F. Annese, M. Doninelli, L. Putelli, M. Gelfi, An Advanced Desalination System with an Innovative CO2 Power Cycle Integrated with Renewable Energy Sources, in: 2023: p. D011S017R002. https://doi.org/10.2118/215993-MS.

[11] A.S. Chowdhury, M.M. Ehsan, A Critical Overview of Working Fluids in Organic Rankine, Supercritical Rankine, and Supercritical Brayton Cycles Under Various Heat Grade Sources, Int. J. Thermofluids. 20 (2023) 100426. https://doi.org/10.1016/j.ijft.2023.100426.

[12] A.I. Turja, K.N. Sadat, M.M. Hasan, Y. Khan, M.M. Ehsan, Waste Heat Recuperation in Advanced Supercritical CO2 Power Cycles with Organic Rankine Cycle Integration & Optimization Using

Machine Learning Methods, Int. J. Thermofluids. 22 (2024) 100612. https://doi.org/10.1016/j.ijft.2024.100612.

[13] F. Crespi, G.S. Martínez, P.R. De Arriba, D. Sánchez, F. Jiménez-Espadafor, Influence of working fluid composition on the optimum characteristics of blended supercritical carbon dioxide cycles, Proc. ASME Turbo Expo. 10 (2021) 1–11. https://doi.org/10.1115/GT2021-60293.

[14] B. Dai, C. Dang, M. Li, H. Tian, Y. Ma, Thermodynamic performance assessment of carbon dioxide blends with low-global warming potential (GWP) working fluids for a heat pump water heater, Int. J. Refrig. 56 (2015) 1–14. https://doi.org/10.1016/j.ijrefrig.2014.11.009.

[15] J. Gómez-Hernández, R. Grimes, J. V. Briongos, C. Marugán-Cruz, D. Santana, Carbon dioxide and acetone mixtures as refrigerants for industry heat pumps to supply temperature in the range 150–220 oC, Energy. 269 (2023). https://doi.org/10.1016/j.energy.2023.126821.

[16] M. Doninelli, E. Morosini, G. Gentile, L. Putelli, G. Di Marcoberardino, M. Binotti, G. Manzolini, Thermal desalination from rejected heat of power cycles working with CO2-based working fluids in CSP application: A focus on the MED technology, Sustain. Energy Technol. Assessments. 60 (2023) 103481. https://doi.org/https://doi.org/10.1016/j.seta.2023.103481.

[17] C. Chen, W. Su, L. Xing, X. Lin, D. Ji, N. Zhou, A prediction model for the binary interaction parameter of PR-VDW to predict thermo-physical properties of CO2 mixtures, Fluid Phase Equilib. 565 (2023) 113634. https://doi.org/10.1016/j.fluid.2022.113634.

[18] R. Abdel-Azim, Estimation of bubble point pressure and solution gas oil ratio using artificial neural network, Int. J. Thermofluids. 14 (2022) 100159. https://doi.org/10.1016/j.ijft.2022.100159.

[19] M. Doninelli, E. Morosini, G. Di Marcoberardino, C.M. Invernizzi, P. Iora, M. Riva, P. Stringari, G. Manzolini, Experimental investigation of the CO2+SiCl4 mixture as innovative working fluid for power cycles: Bubble points and liquid density measurements, Energy. 299 (2024) 131197. https://doi.org/10.1016/j.energy.2024.131197.

[20] P. Guilbot, A. Valtz, H. Legendre, D. Richon, Rapid on-line sampler-injector: A reliable tool for HT-HP sampling and on-line GC analysis, Analusis. 28 (2000) 426–431. https://doi.org/10.1051/analusis:2000128.

[21] K. Djebaili, E. El Ahmar, A. Valtz, A.H. Meniai, C. Coquelet, Vapor-Liquid Equilibrium Data for the Carbon Dioxide (CO2) + 1,1,1,3,3-Pentafluorobutane (R365mfc) System at Temperatures from 283.15 to 337.15 K, J. Chem. Eng. Data. 63 (2018) 4626–4631. https://doi.org/10.1021/acs.jced.8b00683.

[22] H. Madani, A. Valtz, C. Coquelet, A.H. Meniai, D. Richon, (Vapor + liquid) equilibrium data for (carbon dioxide + 1,1-difluoroethane) system at temperatures from (258 to 343) K and pressures up to about 8 MPa, J. Chem. Thermodyn. 40 (2008) 1490–1494. https://doi.org/10.1016/j.jct.2008.06.002.

[23] N. Juntarachat, A. Valtz, C. Coquelet, R. Privat, J.N. Jaubert, Experimental measurements and correlation of vapor-liquid equilibrium and critical data for the CO2 + R1234yf and CO2 + R1234ze(E) binary mixtures, Int. J. Refrig. 47 (2014) 141–152. https://doi.org/10.1016/j.ijrefrig.2014.09.001.

[24] Z. Wu, R. Sun, L. Shi, P. Hu, H. Tian, X. Wang, G. Shu, Vapor-liquid equilibrium measurement and critical line prediction for carbon dioxide (CO2) + fluoroethane (R161) binary mixtures, J. Supercrit. Fluids. 207 (2024) 106205. https://doi.org/10.1016/j.supflu.2024.106205.

[25] M.S. Sadaghiani, A. Arami-Niya, B. Marsh, S.Z.S. Al Ghafri, E.F. May, Vapor-Liquid Equilibria for Carbon Dioxide + 3,3,3-Trifluoropropene Binary Mixtures at Temperatures between (288 and 348) K, J. Chem. Eng. Data. 66 (2021) 4044–4055. https://doi.org/10.1021/acs.jced.1c00297.

[26] G. Di Marcoberardino, E. Morosini, D. Di Bona, P. Chiesa, C. Invernizzi, P. Iora, G. Manzolini, Experimental characterisation of CO2 + C6F6 mixture: Thermal stability and vapour liquid equilibrium test for its application in transcritical power cycle, Appl. Therm. Eng. 212 (2022) 118520. https://doi.org/10.1016/j.applthermaleng.2022.118520.

[27] E. Morosini, E. Villa, G. Quadrio, M. Binotti, G. Manzolini, Solar tower CSP plants with transcritical

cycles based on CO2 mixtures: A sensitivity on storage and power block layouts, Sol. Energy. 262 (2023) 111777. https://doi.org/https://doi.org/10.1016/j.solener.2023.05.054.

[28] University of Brescia, ERGO - Fluid Test Laboratory, https://ergo.unibs.it/research/fluid-test-laboratory.

[29] K.R. Hall, P.T. Eubank, A.S. Myerson, W.E. Nixon, A new technique for collecting binary vapor-liquid equilibrium data without measuring composition: The method of intersecting isochores, AIChE J. 21 (1975) 1111–1114. https://doi.org/10.1002/aic.690210610.

[30] E.S. Burnett, Compressibility Determinations Without Volume Measurements, J. Appl. Mech. 3 (2021) A136–A140. https://doi.org/10.1115/1.4008721.

[31] C.E. Stouffer, S.J. Kellerman, K.R. Hall, J.C. Holste, B.E. Gammon, K.N. Marsh, Densities of Carbon Dioxide + Hydrogen Sulfide Mixtures from 220 K to 450 K at Pressures up to 25 MPa, J. Chem. Eng. Data. 46 (2001) 1309–1318. https://doi.org/10.1021/je000182c.

[32] J. Zhou, P. Patil, S. Ejaz, M. Atilhan, J.C. Holste, K.R. Hall, (p, Vm, T) and phase equilibrium measurements for a natural gas-like mixture using an automated isochoric apparatus, J. Chem. Thermodyn. 38 (2006) 1489–1494. https://doi.org/10.1016/j.jct.2005.12.011.

[33] J. Zhou, K.R. Hall, J.C. Holste, Automated isochoric apparatus for pVT and phase equilibrium studies of natural gas mixtures, AIChE Annu. Meet. Conf. Proc. (2004) 3477–3480.

[34] A. Velez, P. Hegel, G. Mabe, E.A. Brignole, Density and conversion in biodiesel production with supercritical methanol, Ind. Eng. Chem. Res. 49 (2010) 7666–7670. https://doi.org/10.1021/ie100670r.

[35] M.U. Goni, R. Burgass, A. Chapoy, P. Ahmadi, Isochoric bubble point data for binary systems of 1 (ethane) in 2 (decane, undecane, dodecane and tridecane), Fluid Phase Equilib. 577 (2024) 113968. https://doi.org/10.1016/j.fluid.2023.113968.

[36] Sol Group, https://www.sol.it/it (accessed February 28, 2024).

[37] ThermoFisher Scientific (ex Alfa Aesar), https://www.thermofisher.com/it/en/home.html (accessed February 28, 2024).

[38] Sigma Aldrich, https://www.sigmaaldrich.com/IT/it (accessed February 28, 2024).

[39] abcr GmbH, https://abcr.com/ (accessed February 28, 2024).

[40] E. Neyrolles, A. Valtz, C. Coquelet, A. Chapoy, On the phase behaviour of the CO2 + N2O4 system at low temperatures, Chem. Eng. Sci. 258 (2022) 117726. https://doi.org/https://doi.org/10.1016/j.ces.2022.117726.

[41] C. Coquelet, A. Valtz, P. Théveneau, Experimental Determination of Thermophysical Properties of Working Fluids for ORC Applications, in: 2019. https://doi.org/10.5772/intechopen.87113.

[42] D.Y. Peng, D.B. Robinson, A New Two-Constant Equation of State, Ind. Eng. Chem. Fundam. 15 (1976) 59–64. https://doi.org/10.1021/i160057a011.

[43] H.I. Britt, R.H. Luecke, The estimation of parameters in nonlinear, implicit models, Technometrics. 15 (1973) 233 – 247. https://doi.org/10.1080/00401706.1973.10489037.

[44] W.E. Deming, Statistical Adjustment of Data, Dover Publication Inc., New York, 1943.

[45] Aspen Technology Inc., Aspen Plus®, Version V12.1, (2022).

[46] H. Cheng, M.E. Pozo De Fernández, J.A. Zollweg, W.B. Streett, Vapor-Liquid Equilibrium in the System Carbon Dioxide + n-Pentane from 252 to 458 K at Pressures to 10 MPa, J. Chem. Eng. Data. 34 (1989) 319–323. https://doi.org/10.1021/je00057a018.

[47] G.J. Besserer, D.B. Robinson, Equilibrium-Phase Properties of n-Pentane-Carbon Dioxide System, J. Chem. Eng. Data. 18 (1973) 416–419. https://doi.org/10.1021/je60059a020.

[48] F.H. Poettmann, D.L.V. Katz, Phase Behavior of Binary Carbon Dioxide-Paraffin Systems, Ind. \& Eng. Chem. 37 (1945) 847–853. https://api.semanticscholar.org/CorpusID:98720285.

[49] O. "Kunz, R. "Klimeck, W. [Ruhr-U.B. (Germany)]" "Wagner, M. [E. O.R.A.G. "Jaeschke Dorsten (Germany)]," The GERG-2004 wide-range equation of state for natural gases and other mixtures, VDI-Verlag, Duesseldorf (Germany), Germany, 2007. https://doi.org/https://doi.org/.

[50] E. W. Lemmon and and Ian H. Bell and M. L. Huber and M. O. McLinden, NIST Standard Reference Database 23: Reference Fluid Thermodynamic and Transport Properties-REFPROP, Version 10.0, National Institute of Standards and Technology, (2018). https://doi.org/https://doi.org/10.18434/T4/1502528.

[51] P. Ganesan, T.M. Eikevik, New zeotropic CO2-based refrigerant mixtures for cascade high-temperature heat pump to reach heat sink temperature up to 180 °C, Energy Convers. Manag. X. 20 (2023). https://doi.org/10.1016/j.ecmx.2023.100407.

[52] J.F. Boston, P. Mathias, Phase Equilibria in a Third-Generation Process Simulator, EFCE Publ. Ser. (European Fed. Chem. Eng. (1980) 823–849.

[53] D.S.H. Wong, S.I. Sandler, A theoretically correct mixing rule for cubic equations of state, AIChE J. 38 (1992) 671–680. https://doi.org/https://doi.org/10.1002/aic.690380505.

[54] G. Soave, Equilibrium constants from a modified Redlich-Kwong equation of state, Chem. Eng. Sci. 27 (1972) 1197–1203. https://doi.org/10.1016/0009-2509(72)80096-4.

## Appendix A: Uncertainty calculation

A rigorous procedure is adopted to determine the uncertainty of each bubble point computed from the inserseption of the isochoric line in the two-phase and liquid-phase regions.

The uncertainty on the bubble temperature and pressure is computed as in Equations E1-4, multiplied with a coverage factor of $k = 2$ in order to extend it to a confidence interval of 95%:

$$u_{Expanded}(\pi_{bub}) = k \cdot \sqrt{(u_{Calibration}(\pi))^2 + (u_{Acquisition}(\pi))^2 + (u_{Repetition}(\pi))^2 + (u_{Fitting}(\pi))^2} \quad \text{(E1)}$$

where the generic $\pi_{bub}$ stands for the bubble pressure ($P_{bub}$) and bubble temperature ($T_{bub}$).

The contributions of the uncertainty are calculated as follows:

$$u_{Calibration}(\pi) = \max\big(Measured\ (\pi) - Reference\ (\pi)\big) \quad \text{(E2)}$$

$$u_{Acquisition}(\pi) = \sigma(\pi_{acquisited}) \quad \text{(E3)}$$

$$u_{Repetition}(\pi) = \frac{\sigma(\pi_{measured})}{\sqrt{n}} \quad \text{(E4)}$$

The contribution of the calibration in the uncertainty calculations is evaluated accounting for the calibration curve of the instrument compared with a reference value. The pressure transducer has undergone dedicated calibration within the temperature range of 293-393 K, utilizing 9 calibration points. This calibration process ensures the attainment of high accuracy throughout the entire temperature range of interest. The pressure transmitter operates with a full scale (FS) of 100 bar (absolute). The total error band, derived from the calibration procedure, spans from -0.002%FS at 293 K to 0.007%FS at 393 K. The contribution of calibration is then considered to vary linearly from with the temperature as represented in Figure A.1.

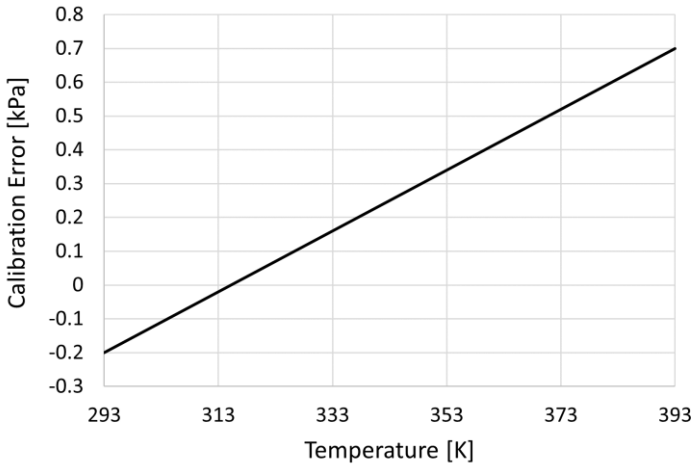


*A. 1. Uncertainty contribution of the bubble pressure due to calibration procedure as function of temperature.*

The contribution of the acquisitions to the uncertainties is accounted according to the standard deviation of the variable, $\sigma(\pi_{acquisited})$, directly computed with the data acquisition unit, in a wide range of at least 120 acquisitions with a frequency of one acquisition per second (2 minutes). Considering that the standard deviation of the single point acquired (over 2 minutes acquisition) is usually lower than 100 Pa and 0.0003 K, this uncertainty contribution is almost negligible. This is the result of the carefulness exercised in capturing each individual data point, allowing for the mixture to stabilize at the required temperature and pressure for the necessary duration.

The contribution of the repetition of each measurement to the final value reported (as an average) is accounted for the standard deviation of all the measured data $\sigma(\pi_{measured})$ divided by the square root of the number of data recorder at the same conditions (T,P,x).

Finally, it is introduced the fitting contribution ($u_{fitting}(\pi)$) related to the methodology used to obtain the bubble point ($T_{bubble}$,$P_{bubble}$) from the inserseption of the isochoric lines fitting the measurements in the VLE and liquid regions. This contribution is calculated with the same rigorous mathematical procedure presented by Goni et al. [35] (in Appendix).

**Appendix B: Experimental data**

The bubble point data for the $CO_2$ mixtures, obtained through measurements using the isochoric apparatus in this study, are detailed in Tables T1-3. These tables include information on the liquid molar fraction of $CO_2$, alongside the corresponding bubble temperatures and pressures, along with their expanded uncertainties. In Table T4 are reported the masses of each component charged into the cell along with its temperature during the $CO_2$ charging. The pressure at which the $CO_2$ is throttled during the transfer from its main bottle is also reported in Table T4. After charging, homogenization of the mixture is ensured by waiting for at least 34 hours. Then, the temperature is increased and venting in homogeneous liquid conditions is carried out up to the temperatures of interest in this work (above 280 K).

*Table T1. experimental bubble points for $xCO_2+(1-x)C_6F_6$ mixture.*

| **$CO_2$ Molar Fraction [%]** | **T [K]** | **U(T) [K]** | **P [MPa]** | **U(P) [MPa]** |
|---|---|---|---|---|
| 71.2% | 297 | 0.08 | 3.987 | 0.015 |
| | 301.97 | 0.11 | 4.388 | 0.019 |
| | 310.04 | 0.08 | 5.049 | 0.011 |
| | 321.01 | 0.15 | 6.028 | 0.028 |
| | 334.01 | 0.15 | 7.211 | 0.034 |
| | 344.65 | 0.19 | 8.204 | 0.037 |

*Table T2. experimental bubble points for $xCO_2+(1-x)C_5H_{10}$ mixture.*

| **$CO_2$ Molar Fraction [%]** | **T [K]** | **U(T) [K]** | **P [MPa]** | **U(P) [MPa]** |
|---|---|---|---|---|
| 62.3% | 298.85 | 0.17 | 4.098 | 0.041 |
| | 312 | 0.21 | 5.028 | 0.036 |
| | 327.47 | 0.62 | 6.225 | 0.096 |
| 52.2% | 299.19 | 0.20 | 3.601 | 0.049 |
| | 312.68 | 0.19 | 4.389 | 0.031 |
| | 329.5 | 0.28 | 5.478 | 0.054 |

*Table T3. experimental bubble points for $xCO_2+(1-x)c\text{-}C_4F_8$ mixture.*

| **$CO_2$ Molar Fraction [%]** | **T [K]** | **U(T) [K]** | **P [MPa]** | **U(P) [MPa]** |
|---|---|---|---|---|
| 77.25% | 282.97 | 0.07 | 32.96 | 0.033 |
| | 295.3 | 0.05 | 42.38 | 0.011 |
| | 309.73 | 0.07 | 54.77 | 0.005 |
| | 317.09 | 0.17 | 60.25 | 0.27 |

*Table T4. Masses of components charged for the preparation of the mixtures investigated.*

| **Mix** | **x [molar %]** | **Mass $CO_2$ [g]** | **Mass [g]** | **Cell temperautre while charging $CO_2$ [K]** | **Pressure of $CO_2$ while charging [MPa]** |
|---|---|---|---|---|---|
| $xCO_2+(1-x)C_6F_6$ | 71.2 | 56.05 | 95.83 | 258 | 2.5 |
| $xCO_2+(1-x)C_5F_{12}$ | 62.3 | 48.350 | 47.960 | 263 | 2.85 |

| | | | | | |
|---|---|---|---|---|---|
| $xCO_2+(1-x)C_5F_{12}$ | 52.2 | 37.34 | 56.02 | 263 | 2.85 |
| $xCO_2+(1-x)c\text{-}C_4F_8$ | 77.25 | 59.74 | 79.98 | 283 | 5.0 |

# PART 3:
# Transport properties modelling of $CO_2$ mixtures

*This Part of the thesis discusses about the transport properties modelling of $CO_2$ mixtures, focusing on dynamic viscosity and thermal conductivity. The reason behind the study is that such properties are essential for the design of the components of the power block, in particular heat exchangers.*

*In Chapter 7, a survey of models available for the prediction of transport properties of mixtures is carried out, assessing their capability against the few experimental data available of $CO_2$ binary mixtures with complex compounds. The non-conformability (i.e. different size, shape, volume) of such chemicals in comparison with $CO_2$ leads to inaccuracies by conventional methods, especially in dense phase.*

# *Chapter 7 - Transport properties of $CO_2$ complex mixtures*

*THIS CHAPTER IS BASED ON THE ARTICLE: "ON THE DESIGN OF RECUPERATOR FOR TRANSCRITICAL CYCLE ADOPTING $CO_2$-BASED MIXTURE AS WORKING FLUID: A FOCUS ON TRANSPORT PROPERTIES PREDICTION", PUBLISHED IN ENERGY TECHNOLOGY, WILEY, DOI: HTTPS://DOI.ORG/10.1002/ENTE.202300677*


**Abstract**

Transcritical cycles working with $CO_2$-based mixtures gained considerable attention due to thermodynamic efficiency gain compared to pure $sCO_2$ in hot-environments. Previous literature works proved that the adoption of $CO_2$ mixtures provides a reduction of the levelized cost of electricity in concentrated solar power applications and medium-high temperature heat recovery. However, for techno-economic analysis and heat exchanger design, proper evaluation of transport properties of the $CO_2$-based mixtures in power cycle conditions is necessary. This work deals with the analysis of the proper transport properties models for $CO_2$ mixtures to assess their actual thermal behaviour. A literature review on transport properties models, and their validation with available experimental data, proves that the friction theory is suitable for $CO_2$ blended with dopants having high molecular complexity. The impact of the different model selection on the recuperator sizing, considering optimized power cycle conditions, is assessed on the $CO_2$ mixtures with Hexafluorobenzene and Decane: the TRAPP and Chung-Lee-Starling models are imported from Aspen Plus, while the friction-theory model is implemented and calibrated in an in-house Matlab code. The optimal design of the recuperator for the $CO_2$+$C_6F_6$ mixture in a 100 $MW_{el}$ power block coupled with a solar tower plant located in Sevilla is carried out.


## 7.1 Introduction

The EU aims to be climate neutral within 2050 with a long-term strategy, and there is need for high-efficient technologies to meet such ambitious goal. In this context, concentrating solar power (CSP) is one of the most attractive technologies since it can provide dispatchable electricity to the grid when coupled with thermal energy storage (TES) system, although a large-scale development is limited by significant capital costs which negatively affect the Levelized Cost of Electricity (LCOE).

CSP is expected to deliver up to 12% of the global electricity by year 2050 [1]. To achieve this ambitious goal, many programmes have been launched from Europe (H2020) and from the USA (SunShot) aiming at achieving higher power-block thermal efficiencies and lowering capital costs. Particular attention is given to alternative working fluids in order to reduce the system complexity and size. Supercritical $CO_2$ power cycles are expected to be the primary choice for next-generation power plants, but they are penalized by dry-cooling in high-temperature environments, typical of CSP locations. In fact, at high values of minimum cycle temperature, the benefit related to the exploitation of real gas effect is mitigated. The H2020 SCARABEUS project [2] introduced the adoption of innovative $CO_2$ mixtures, using dopants with higher critical temperature than $CO_2$,

allowing transcritical Rankine cycles even in hot and arid regions, then exploiting the benefit of liquid-phase compression. As additional benefit, $CO_2$ mixtures typically possess good thermodynamic efficiency even in a simple-recuperated layout, thus requiring less components and minor management complexity in comparison with a recompressed $sCO_2$ cycle. The adoption of $CO_2$ mixtures could be advantageous also in the medium-high temperature heat recovery applications [3]. The temperature glide occurring during mixture's condensation could be exploited for cogeneration scopes. The $CO_2$ mixture with Hexafluorobenzene ($C_6F_6$) has been extensively studied both theoretically [4][5] and experimentally [6] as innovative working fluid in CSP tower plant with 550°C turbine inlet temperature, with solar salts as heat transfer fluid. Many other dopants have been considered in the high-temperature CSP context, such as $SO_2$ [7], $TiCl_4$ and $N_2O_4$ [8]. Even if $CO_2$ mixtures have been investigated from the thermodynamic point of view, no studies have been carried out in the non-equilibrium field. On the contrary, the relevance of transport properties in heat exchangers design and rating, as well as the in the transient behaviour of the mixture is well recognized, and this work is intended to provide insight into the appropriate modelling of viscosity and thermal conductivity of $CO_2$ mixtures in power cycle conditions.

Many experimental dynamic viscosity data are available for mixtures of carbon dioxide with impurities involved in the carbon capture and storage (CCS) processes, as well as with methane due to industrial interest in natural gas. Li et al. [9] collected experimental data of $CO_2$-rich mixtures with impurities relevant for CCS and validated the most adequate models for that purpose. Nazeri and Chapoy [10] tested the viscosity of several $CO_2$-rich mixtures, and recommended the most appropriate models to be adopted, but the study regarded only $CO_2$ mixtures with lightweight and simple components involved in CCS processes. In contrast, in the application of interest here, the dopant to be mixed with $CO_2$ is typically a compound characterized by high molecular complexity, which helps to balance the heat capacities within the recuperator. Due to this literature gap, this work is aimed to assess the appropriate transport properties models for $CO_2$ mixtures with complex compounds. Few experimental viscosities and thermal conductivities of $CO_2$ mixtures with heavy and complex hydrocarbons, from enhanced oil recovery sector, proved fundamental to validate the reliability of the investigated models in the next sections. The scarcity of experimental thermal conductivity data highlights the need to perform more experimental activity in this field.

It is worth is to mention that the adoption of transcritical $CO_2$-based cycles was proven to be an interesting solution not only for power generation purposes, but also for energy storage systems. In fact, Liu et al. [11] proposed a two-stage transcritical compressed $CO_2$ energy storage system that outperforms conventional compressed air energy storage (CAES) in terms of overall efficiency. The adoption of transcritical $CO_2$-based mixtures instead of pure $CO_2$ could provide further advantages, and the present paper provides useful guidelines to model transport properties for components design and rating.

In the first section, several transport properties models available from the literature which are capable of describing both dense liquid and vapour phases are briefly presented. Afterwards, the comparison with few experimental data in high-density conditions indicates that the recent friction theory model has improved ability to reproduce transport properties of dense $CO_2$ complex mixtures compared to conventional one-fluid theories. Then, the friction theory models for viscosity and thermal conductivity have been optimized for two mixtures of interest of this work. Specifically, the

dopants considered here are: hexafluorobenzene ($C_6F_6$) that has been extensively investigated as promising dopant in previous works, and n-decane ($C_{10}H_{22}$) because it is a heavy and complex compound (as $C_6F_6$) with $CO_2$ mixture transport property data available in literature in a wide range of pressures and temperatures. Thus, the primary interest of this work is the transport property characterisation of the $CO_2$/ $C_6F_6$ mixture, then the $CO_2$/ $C_{10}H_{22}$ is primarily investigated to assess the influence of the model selection on a mixture whose transport properties are well known. Once assessed that the friction-theory models for viscosity and thermal conductivity has superior predictivity in complex mixtures compared to other literature models available in commercial software, the coefficients required by the friction-theory models are regressed for the mixtures investigated, and the influence of the transport model used is studied in real case studies. The $CO_2$/ $C_6F_6$ mixture is applied as working fluid in a concentrated power plant with solar salt as heat transfer fluid (HTF), then 550°C as maximum cycle temperature, a thermal level compatible with the thermal stability of the fluid [6]. The $CO_2$/ $C_{10}H_{22}$ mixture is simulated in a concentrated solar plant with parabolic through, with maximum cycle temperature equal to 350°C, compatible with the state-of-the-art thermal oil level (around 390°C). The composition and the operating conditions are optimized for the considered case studies. Then, the printed circuit heat exchanger (PCHE) recuperator has been designed with different transport property methods to highlight their influence on the size prediction and to assess whether a method easily available from commercial software could be suitable for this scope and then, for a realistic cost assessment and sizing. The PCHE is the particular heat exchanger selected for design for several reasons: (i) the working fluid mixture flows in both hot and cold sides, then the impact of transport properties estimate is enhanced; (ii) a wide range of density conditions are encountered in the PCHE recuperator of the transcritical cycle, from high-pressure liquid to supercritical gas conditions; (iii) few models are capable of describing with good accuracy and with continuity the transcritical transition; (iv) it represents the most cost expensive component of the power block, then a reliable sizing is necessary; (v) the recuperator effectiveness has great impact on the cycle efficiency, then an incorrect design would lead to inefficiencies.

Particular attention has been given to the selection of the most appropriate models to determine the heat transfer coefficient of the mixture. As a peculiarity of the transcritical cycles working with complex dopants is that partial condensation occurs near the recuperator cold-end, then there is need to describe the mixture's behaviour both in single-phase vapour and two-phase regions.

To date, PCHEs were experimentally and numerically studied with single-phase working fluids such as helium, water, and carbon dioxide; the results are well summarized in the work of Chai and Tassou [12]. Few efforts have been made in the two-phase field [13]. As regards mixtures, Kim et al. [14] investigated the thermal–hydraulic performance of PCHE experimentally and numerically with He/$CO_2$ mixture.

The PCHE recuperator has been sized with different transport properties models, starting from optimized power cycle conditions, for the $CO_2$ mixtures with Hexafluorobenzene and Decane: the TRAPP and Chung-Lee-Starling models were imported from Aspen Plus environment, since they are models applicable in a wide density domain, while the friction-theory model was implemented (and calibrated) in an in-house Matlab code.

Once the most appropriate methods are selected, the optimal PCHE design is carried out by minimizing the Levelized Cost of Electricity (LCOE) for a CSP field designed in Sevilla (Spain).

## 7.2 Transport properties models for $CO_2$ mixtures

Viscosity is a physical property that measures the internal friction among fluid layers, and it is related to the rate of momentum diffusion due to existing velocity gradient. In the same way, thermal conductivity is correlated to the rate of heat flux resulting from a temperature gradient. Both viscosity and thermal conductivity are functions of temperature and pressure or density.

The starting point of the theoretical basis for the calculation of both viscosity and thermal conductivity at "zero-density" conditions is the elementary kinetic theory of gases [15]. In this work, the Chung et al. model [16] is the kinetic-theory based method selected for the evaluation of viscosity (Eq. 1) and thermal conductivity (Eq. 4) of the pure components. This method has been chosen because it is the most faithful to Chapman-Enskog theory, but also it employs the acentric factor (ω) and the dipole moment (μ) to account for the molecular shape, the polarity, and anisotropic intermolecular forces. In dilute-gas conditions, the mean expected deviations is lower than 1.5% for nonpolar gases and up to 4% for polar gases [17]. Whilst rigorous theoretical methods are not suitable for the mixtures, so semi-empirical mixing rules has to be adopted. Wilke [18] proposed a semi-empirical formula for the evaluation of the binary mixture viscosity (Eq. 2-3), reporting an average deviation of less than 1% in comparison with experimental data of 17 mixtures [18]. Many methods have been proposed for the thermal conductivity of dilute-gas mixtures [17], but the most commonly used is the empirical model proposed by Wassiljewa [19], in Eq.5, where the function $A_{ij}$ can be calculated as proposed by Mason and Saxena (Eq. 6) [20].

"zero-density" viscosity

$$\mu_{i,0} = 40.785\,\frac{F_C\,(MT)^{\frac{1}{2}}}{V_C^{\frac{2}{3}}\,\Omega^{(2,2)}} \quad (1) \qquad \mu_{m,0} = \sum_{i=1}^{n}\frac{y_i\,\mu_{i,0}}{\sum_{j=1}^{n} y_i\,\Phi_{ij}} \quad (2) \qquad \Phi_{ij} = \frac{\left[1+\left(\frac{\mu_i}{\mu_j}\right)^{\frac{1}{2}}\left(\frac{M_j}{M_i}\right)^{\frac{1}{4}}\right]^2}{\left[8\left(1+\frac{M_i}{M_j}\right)\right]^{\frac{1}{2}}} \quad (3)$$

"zero-density" Th. conductivity

$$\frac{\lambda_{i,o}\,M'}{\mu_{i,0}\,C_v} = \frac{3.75\,\psi}{C_v/_R} \quad (4) \qquad \lambda_{m,0} = \sum_{i=1}^{n}\frac{y_i\lambda_{i,0}}{\sum_{j=1}^{n} y_j A_{ij}} \quad (5) \qquad A_{ij} = \frac{\left[1+\left(\frac{\lambda_{tr,i}}{\lambda_{tr,j}}\right)^{1/2}\left(\frac{M_i}{M_j}\right)^{1/4}\right]^2}{\left[8\left(1+\frac{M_i}{M_j}\right)\right]^{1/2}} \quad (6)$$

While the transport properties models at low-density have a solid theoretical basis, all methods practically used for dense gases and liquids are empirical or semi-theoretical [17]. In this scenario, the common approach considers the generic transport property $\pi$ at high-density as a sum of a "zero-density" term ($\pi_0$) and a pressure/density effect contribution $\Delta\pi(T,p)$ known as the "excess property" or "residual property".

$$\pi(T,p) = \pi_0(T) + \Delta\pi(T,p) \quad (7)$$

The zero-density term $\pi_0(T)$ is evaluated with the methods described previously, while each model distinguishes on how the residual term $\Delta\pi(T,p)$ is treated. The residual property can be defined with an empirical correlation, of density and temperature, regressed from experimental data, or it can be derived from an extension of the kinetic theory (such as the extension of the Chung-Lee-Starling model for the viscosity of dense gases [21]).

The most successful approaches are based on the corresponding state principle. According to this principle, it is possible to evaluate the residual property of a pure fluid or mixture from the well-known available property of a reference fluid, that is evaluated in a corresponding state $(T_0, \rho_0) = \left(\frac{T}{f_i}, \rho\, h_i\right)$ with respect to a pure fluid "i" of interest. The scaling factors $f_i$ and $h_i$ which are related to the ratios between the intermolecular potential function parameters (the depth of the potential well ε and the equilibrium distance σ), that are in turn proportional to the critical parameters ($T_c$, $V_c$) ratios from a macroscopic point of view. Thus:

$$f_i = \frac{\varepsilon_i}{\varepsilon_{ref}} = \frac{T_{c,i}}{T_{c,ref}} \tag{8}$$

$$h_i = \frac{\sigma_i^3}{\sigma_{ref}^3} = \frac{V_{c,i}}{V_c^{ref}} \tag{9}$$

In case of mixtures, simple mixing rules are applied to the pure component factors for the calculation of the scaling factors $f_m$ and $h_m$, considering that the properties of a mixture are consistent with the behaviour of a hypothetical pure fluid which is conformal with the reference fluid. Since the straight application of the corresponding states is accurate only for similar molecules (said "conformal") [22] having similar intermolecular potential, Leach and co-workers [23] suggested the use of "shape factors" ϕ and θ to correct the reducing ratios, as described below. The authors suggested temperature-dependent correlations for the shape factors in terms of the Pitzer acentric factor and the critical compressibility factor.

$$f_i = \frac{T_{c,i}}{T_c^{ref}}\,\theta_i \tag{10}$$

$$h_i = \frac{V_{c,i}}{V_c^{ref}}\,\emptyset_i \tag{11}$$

The use of shape factors distinguishes the so-called "extended corresponding states" (ECS) methods. An example of a ECS method is the one used in the software Refprop [24] or in the method of Ely & Huber [25]. Exact shape factors can be obtained by solving the simultaneous equality of the residual dimensionless Helmholtz free energy and the residual compressibility factors, then the resolution of a non-linear system. Thus, Monnery [26] suggested to retrieve correlations for the shape factors directly from experimental data instead of thermodynamics.

Anyway, the one-fluid theory fails because the density effects are not well addressed when dealing with mixtures of components having high difference in size (especially for high molar volume ratios) since the real local composition of the mixture is different than the bulk and it is dominated by the larger component.

The improvement on model reliability for these specific mixtures follows two paths: the use of a more "conformal" reference fluid, or another physically sound approach. In this work, $CO_2$ was adopted as reference fluid to improve the conformability between the reference fluid and the $CO_2$-rich mixtures of interest in ECS methods. Moreover, the recent friction theory model [27] is investigated here. In the friction theory model, an EoS is used to compute the attractive and repulsive intermolecular interactions, in terms of attractive and repulsive pressure or entropy, that are used as input for the model to predict the transport property in a wide range of conditions. Since an EoS is capable of describing the interactions in a binary mixture in a wide range of thermodynamic conditions, it is a solid basis for a transport property model capable of describing even complex mixtures. In the following subsections, the most interesting models for dense $CO_2$ mixtures are discussed.

### 7.2.1 The TRAPP method for viscosity and thermal conductivity

The TRAPP (TRAnsport Property Prediction) method was presented by Ely and Hanley in 1981 as an extended corresponding states-based computer program for the prediction of viscosity and thermal conductivity in hydrocarbon mixtures [28] in both gas and liquid phases, using methane as reference fluid. Then, propane has been used in the more recent SUPERTRAPP model [29]. The residual property of the mixture $\Delta\eta_m$ is related to that of the reference fluid through appropriate mixing rules, as illustrated below.

$$\Delta\eta_m(T,\rho) = \eta_m(T,\rho) - \eta_m^0(T) = F_{\eta m}\,(\eta^R - \eta_0^R) + \Delta\eta_m^{ENSKOG} \tag{12}$$

$$F_{\eta m} = (M^R)^{-0.5}(h_m)^{-2}\sum_i\sum_j y_i y_j \left(f_{ij}M_{ij}\right)^{0.5}\left(h_{ij}\right)^{4/3} \tag{13}$$

where $h_m = \sum_i\sum_j y_i y_j h_{ij}$ and $f_m h_m = \sum_i\sum_j y_i y_j f_{ij} h_{ij}$.

In case of viscosity an Enskog term $\Delta\eta^{ENSKOG}$ [30] was introduced to improve the accuracy of the relation when the size difference of the two components in the binary mixture become large (absent for thermal conductivity). This is because the concentration of the larger component is locally higher than the bulk, and it controls the value of viscosity (since viscosity is dominated by short-range forces).

The "$CO_2$-SUPERTRAPP" [10] model has been also considered: the approach is the same as in the TRAPP method, but $CO_2$ is used as reference fluid with the polynomial correlation of Huber et al. [31]. The $CO_2$-SUPERTRAPP model has not been used for the viscosity estimate since it does not provide a general improvement compared to the SUPERTRAPP model: the first overpredicts the property values while the latter typically underpredicts them, as stated by [10].

### 7.2.2 The Pedersen & Christensen model for viscosity

The model of Pedersen and Christensen ([22],[23],[24]) for viscosity evaluation lays its fundamentals on the work of Christensen (1980, [32]). The final formulation is:

$$\mu_m(P,T) = \left(\frac{T_{C,mix}}{T_{C,0}}\right)^{-\frac{1}{6}} \left(\frac{P_{C,mix}}{P_{C,0}}\right)^{\frac{2}{3}} \left(\frac{M_{mix}}{M_0}\right)^{-\frac{1}{2}} \left(\frac{\alpha_{mix}}{\alpha_0}\right) \mu_0(T_0, P_0) \tag{14}$$

where the reference fluid, with the subscript "0", is evaluated at $T_0 = \frac{T}{\frac{T_{C,mix}}{T_{c,0}} \frac{\alpha_{mix}}{\alpha_0}}$ and $P_0 = \frac{P}{\frac{P_{C,mix}}{P_{c,0}} \frac{\alpha_{mix}}{\alpha_0}}$.

The $\alpha_{mix}$ and $\alpha_0$ parameters are evaluated as:

$$\alpha = 1 + 7.378 \cdot 10^{-3}\, {\rho_R}^{1.847}\, M^{0.5173} \tag{15}$$

The authors of this model suggest mixture's pseudo-critical parameters to be used, with simple mixing rules from the van der Waals one-fluid approximation. Although the reference fluid in the original model is methane, in this work carbon dioxide is chosen as reference fluid: the resulting so-called $CO_2$-Pedersen model has been used by Nazeri et al. (2016, [10]) for the estimation of $CO_2$ mixtures properties. An advantage of this model is that is does not require the density as input. However, high deviations are expected with complex compounds since mixture's critical properties are estimated with simple vdW mixing rules.

### 7.2.3 The friction theory model for viscosity

The friction theory model was developed by Quiñones-Cisneros et al. [27] implementing the residual viscosity term from a mechanical point of view. In analogy with the well-known Amontons–Coulomb friction law, the residual term (friction viscosity $\eta_f$) is related to the attractive and repulsive pressure terms by means of friction coefficients, as described in Eq. 16.

$$\eta = \eta_0 + \eta_f = \eta_0 + \sum_{i=1}^{n_a} k_{a,i}\, p_a^i + \sum_{i=1}^{n_r} k_{r,i}\, p_r^i \tag{16}$$

where $k_{r,i}$ and $k_{a,i}$, are the friction coefficient of the pure fluid, $\eta_0$ is the zero-density viscosity, $p_a^i$ and $p_r^i$ are the i-th order attractive and repulsive pressure deriving from an EoS.

At high pressure conditions, the intermolecular distance between the fluid layers decreases and the short-range intermolecular forces predominate over the long-range attractive forces. For this reason, a second order truncation of the repulsive term ($n_r = 2$) is suggested, while a first-order truncation is sufficient for the attractive pressure term ($n_a = 1$) [33]. Thus, the resulting quadratic equation of the friction theory model is shown in Eq. 17.

$$\eta = \eta_0 + k_r p_r + k_a p_a + k_{rr} {p_r}^2 \tag{17}$$

In case of mixtures, the residual friction term is calculated in the same way, but mixing rules are applied for the mixture friction coefficients:

$$k_j = \sum_i^n z_i\, k_{j,i} \qquad with\ j = a, r, rr \tag{18}$$

$$z_i = \frac{x_i}{M_i^{\epsilon} \cdot \sum_i \frac{x_i}{M_i^{\epsilon}}} \tag{19}$$

where $k_{r,i}$, $k_{a,i}$, $k_{rr,i}$ are the friction coefficient of the n pure components in mixture having mole fraction $x_i$ and molecular weight $M_i$; the exponent $\varepsilon$ is typically assumed equal to 0.30 [27].

The pure fluid friction coefficients are obtained fitting the experimental residual viscosities: friction coefficients for many alkanes, but also for carbon dioxide and nitrogen, can be found in the work of Quiñones-Cisneros and Deiters [33]. If friction coefficients cannot be retrieved due to the lack of experimental data for specific chemical compounds in a wide range of temperatures and pressures, the general corresponding states-based friction theory model can be used. In the general one-parameter friction theory model, the friction viscosity is expressed in a reduced form: the friction viscosity (residual) term $\eta_f$ can be calculated from the reduced friction viscosity $\hat{\eta}_f$ and a characteristic critical viscosity $\eta_c$, which is the only one parameter of the model that has to characterized for each component in the mixture.

$$\hat{\eta}_f = \frac{\eta_f}{\eta_c} = \hat{\eta}_{f,r} + \hat{\eta}_{f,a} \tag{20}$$

By adopting the general one-parameter model, the reduced friction viscosity $\hat{\eta}_f$ is calculated in the same way as in Eq. 16, but with the pure-component friction factors $k_{j,i}$ described as:

$$k_{j,i} = \frac{\eta_{c,i}\ \hat{k}_{j,i}}{P_{c,i}} \tag{21}$$

$$\hat{k}_{j,i} = \hat{k}_{j,c} + \Delta\hat{k}_{j,i} \tag{22}$$

where the critical isotherm contribution, with the subscript "c", depends on the selected EoS, while the residual temperature dependent contribution depends also on the pure-component critical temperature.

The characteristic critical viscosity of the pure compounds $\eta_{c,i}$ is the only real degree of freedom of the model, resulting in the choice of the cubic EoS: in this work, the PR and SRK EoS have been evaluated for this purpose. As the results provided from these cubic EoS are very similar, the PR-EoS, and the corresponding model is then called f-PR model.

### 7.2.4 The friction theory model for thermal conductivity

Whereas the friction theory model for viscosity has a direct derivation from mechanical considerations on the shear stress among fluid layers, the relationship between thermal conductivity and thermodynamic caloric properties is not as intuitive. In similarity with the f-theory model for viscosity (eq. 16), Quiñones-Cisneros et al. [34] developed the friction theory model as follows:

$$\lambda = \lambda_0 + \lambda_f + \lambda_c = \lambda_0 + \sum_{i=1}^{n_a} \phi_{a,i}\ s_a^i + \sum_{i=1}^{n_r} \phi_{r,i}\ s_r^i + \lambda_c \tag{23}$$

where $\phi_{r,i}$ and $\phi_{a,i}$, are the friction coefficients of the pure fluid, $\eta_0$ is the zero-density viscosity, $s_a^i$ and $s_r^i$ are the i-th order attractive and repulsive residual entropy terms which can be derived from an EoS. The critical enhancement term is reported to be:

$$\lambda_c = \phi_c\ \rho^3 / \left(\frac{\partial p}{\partial v}\right)_T \tag{24}$$

The authors suggested a second-order truncation, so the formulation can be made explicit, as:

$$\lambda = \lambda_0 + \lambda_c + \phi_{a,1} s_a + \phi_{a,2} {s_a}^2 + \phi_{r,1} s_r + \phi_{r,2} {s_r}^2 \tag{25}$$

The friction coefficients can be defined with the following expressions:

$$\phi_{a,1} = a_0 \, exp\left[ a_1 \left( \frac{T_c}{T} - 1 \right) + a_2 \left( \left( \frac{T_c}{T} \right)^2 - 1 \right) \right] \tag{26}$$

$$\phi_{r,1} = b_0 \, exp\left[ b_1 \left( \frac{T_c}{T} - 1 \right) + b_2 \left( \left( \frac{T_c}{T} \right)^2 - 1 \right) \right] \tag{27}$$

$$\phi_{a,2} = A_0 \tag{28}$$

$$\phi_{r,2} = B_0 \tag{29}$$

Thus, nine coefficients ($a_i$, $b_i$, $A_0$, $B_0$, $\phi_c$) need to be regressed for each chemical species using experimental thermal conductivity data of the pure fluid. Friction coefficients are already available in [34] for many compounds including $CO_2$ and some hydrocarbons. In this work, the PR-EoS is used to obtain the residual attractive and repulsive entropy terms.

In case of mixtures, simple mass fraction-based mixing rules are applied to the friction coefficients as suggested by Quiñones-Cisneros. The validation of the model for mixtures is still an open point due to very few reliable experimental data are available. For this reason, a general one-parameter f-theory model for thermal conductivity is still missing. However, the model is reported to be satisfactory for most of the mixtures evaluated [34].

### 7.3 Transport properties models validation with CO2 mixtures experimental data

The transport properties models described in the previous section were implemented in MATLAB environment [35] for their validation with proper $CO_2$ mixtures experimental data. A survey of available $CO_2$ mixtures experimental data was carried out. Looking at the application in transcritical cycle, particular attention was given to dataset in the dense region (high operating pressure) and to mixtures with heavy and complex dopants. The few experimental data available for $CO_2$ mixtures mainly comes from the CCS sector where most of them concern the gas field at room pressure [9]. The selected pure fluid are $N_2$ and some lightweight ($CH_4$, $C_2H_6$) and heavy hydrocarbons ($C_{10}H_{22}$, $C_{12}H_{26}$). Their molecular parameters are reported in

Table 1 together with the values of pure $CO_2$. Although the main investigated dopant is a perfluorocarbon, the n-decane can be used as a reference fluid for the transport properties validation due to its molecular mass and complexity. The comparison with the data available in the gas phase at ambient pressure was excluded because they are outside the range of interest and typically the zero-density properties models are particularly accurate (with an average error typically below 3-4% [17]). The models accuracy is represented by the percentage average absolute deviation (AAD%), between the calculated and the experimental values weighted on the number of available data (see

Eq.30). Table 2 reports the AAD% of the models in comparison with the experimental viscosity in gas or liquid phase at various molar compositions.

$$AAD\% = \sum_i \frac{|\eta_i - \eta_{i,exp}|}{N_{points}} \cdot 100 \tag{30}$$

*Table 1. Main characteristics of pure components*

| Species | $MW$ [kg/kmol] | $P_C$ [bar] | $T_C$ [K] | $V_C$ [cm³/mol] |
|---|---|---|---|---|
| $CO_2$ | 44.010 | 74.74 | 304.12 | 94.07 |
| N2 | 28.010 | 33.98 | 126.20 | 90.10 |
| $CH_4$ | 16.043 | 45.99 | 190.56 | 98.6 |
| $C_2H_6$ | 30.07 | 48.72 | 305.32 | 145.5 |
| $C_{10}H_{22}$ | 142.285 | 21.10 | 617.70 | 624 |
| $C_{12}H_{26}$ | 170.338 | 18.20 | 658.00 | 754 |

*Table 2. Viscosity models comparison with experimental data*

| Mixtures | Phase | Ref. | NP | T [K] | P [bar] | AAD % f-theory | AAD % SUPERTRAPP | AAD % $CO_2$-Pedersen |
|---|---|---|---|---|---|---|---|---|
| $CO_2$+$N_2$ | G | [36] | 35 | 293 | 1-22 | 2.57 | 2.45 | 0.6 |
| $CO_2$+$CH_4$ | G | [37] | 88 | 323-473 | 3.3-69.7 | 4.58 | 4.55 | 2.77 |
| $CO_2$+$C_2H_6$ | G-L | [38] | 70 | 280-320 | 21-348 | 7.12 | 9.4 | / |
| $CO_2$+$C_{10}H_{22}$ | L | [39] | 70 | 311-403 | 69-347 | 7.1 | 17.3 | / |
| $CO_2$+$C_{12}H_{26}$ | L | [40] | 20 | 284-351 | 14-142 | 9.9 | 24.2 | / |

As stated by Nazeri et al. [10], the $CO_2$-Pedersen represents the best model of viscosity for $CO_2$ mixtures in CCS application, i.e. with lightweight and simple compounds. However, since the methods implements simple mixing rules for the mixture's critical parameters, it is not reliable with complex mixtures and for this reason its results are reported only for two datasets in Table 2.

Even if the TRAPP method is extendable into the liquid region, the density effects are very influenced by mass and molecular size differences between the reference fluid (propane in the SUPERTRAPP) and the component in the binary mixture. These discrepancies are evident the more the critical volume of the component increases compared to the critical volume of the reference fluid, which is representative of high size differences:

$$\left(\frac{\sigma_i}{\sigma_0}\right)^3 \cong \frac{\rho_o^c}{\rho_i^c} = \frac{V_o^c}{V_i^c}$$

The local size differences especially affect the viscosity estimation considering that, at high densities, the momentum transport takes place predominantly by intermolecular forces rather than collisions between molecules in free flight. A second-order effect of the repulsive intermolecular forces is considered into the friction theory model for viscosity, making it physically consistent.

As it can be noted, when the complexity of the mixture increases, the one-fluid theory lead to high errors (more than 15%). Figure 1 shows, as an example, the comparison between the experimental viscosities of the $CO_2$/n-dodecane mixture and the estimated values. This particular dataset have been also evaluated in the literature with specific models for liquids based on the Eyring theory [40], but without success: the reported AAD of the Grunberg and Nissan model was 63%, while the Katti and Chaudri model achieves an AAD equal to 43%. So it is possible to conclude that the friction theory model has the largest potential of providing accurate estimate when dealing with complex and dense mixtures.

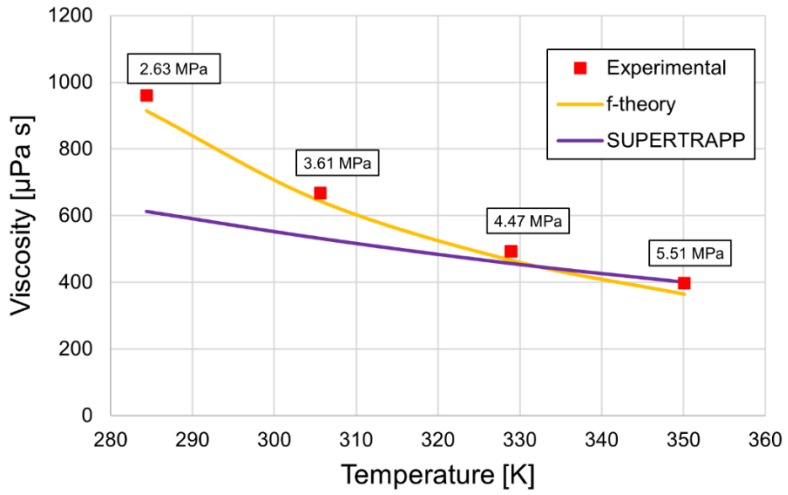


*Figure 1. Experimental and calculated viscosities comparison for 40%$CO_2$+n-dodecane mixture at different temperature and pressure*

As regards the thermal conductivity, the comparison between the scarce experimental data from the literature and the considered models is illustrated in Table 3. The recent data of Patek et al. [41] has been selected for the comparison of the $CO_2$+$CH_4$ mixture in the gas phase, while the recent data of Kim et al. [42] have been used for the dense-liquid phase.

*Table 3. Thermal conductivities models comparison with experimental data*

| Mixtures | Phase | Ref. | NP | T [K] | P [bar] | AAD % f-theory | AAD % SUPER TRAPP | CO2-SUPER TRAPP |
|---|---|---|---|---|---|---|---|---|
| $CO_2$+$CH_4$ | G | [41] | 180 | 300-425 | 7.27-119.7 | 3.13 | 8.66 | 1.34 |

| | | | | | | | | |
|---|---|---|---|---|---|---|---|---|
| $CO_2$+$CH_4$ | L | [42] | 8 | 223.7-295.6 | 71.4-198.5 | 5.16 | 5.17 | 5.01 |
| $CO_2$+$N_2$ | L-SC | [42] | 11 | 223.8-308.4 | 54.5-201.5 | 4.72 | 5.05 | 5.68 |
| $CO_2$+$N_2$ | G | [43] | 22 | 321.4-381.8 | 11-250 | 1.74 | 9.84 | 2.2 |
| $CO_2$+$N_2O$ | G | [44] | 33 | 300.65 | 8-42.5 | 1.2 | 1.3 | 2.28 |
| $CO_2$+$C_{10}H_{22}$ | L | [45] | 23 | 298.15-328.15 | 11.3-105 | 4.03 | 21.1 | 22.3 |

An improvement in the thermal conductivity prediction can be noted when carbon dioxide is used as reference fluid ($CO_2$-SUPERTRAPP) with respect to propane. However, regarding the $CO_2$+n-decane mixture, the comparison with the data in [45] shows how the corresponding states-based models fails when dealing with complex mixture, especially in the dense-liquid phase. Instead, the adoption of the friction theory model, with optimised friction coefficients (as explained in the following section), yields reasonably good results with an AAD of about 4%.

This preliminary analysis confirms that the f-theory has the largest potential of providing reliable results even for asymmetric mixtures in a wide range of operating conditions, thus it will be used to estimate the transport properties for the PCHE recuperator design of the two case-studies.

### 7.4 Friction-theory models optimisation for the case-studies

The friction-theory models for viscosity and thermal conductivity are here optimised for the two selected $CO_2$ blends, $CO_2$+$C_{10}H_{22}$ and $CO_2$+$C_6F_6$. The model predictions are compared with two models identified in Aspen Plus® environment [46], valid in both gas and liquid fields: the Chung-Lee-Starling and TRAPP methods. The friction-theory models are fitted with selected experimental data of the pure components of the mixture. Data in dense conditions are crucial for a proper characterisation of the residual property (friction term). About the critical characteristic viscosity of the pure compound compounds $\eta_{c,i}$, only one parameter has to be fitted. On the other hand, nine coefficients ($a_i$, $b_i$, $A_0$, $B_0$, $\phi_c$) need to be regressed in the friction-theory model for thermal conductivity. The regression is carried out in MATLAB environment by using a non-linear least-squares optimization with Levenberg-Marquardt algorithm. The results of the fitting procedure is presented in Table 4.

*Table 4. optimised parameters for the friction coefficients of the f-theory thermal conductivity model*

| | $a_0$ | $a_1$ | $a_2$ | $b_0$ | $b_1$ | $b_2$ | $A_0$ | $B_0$ | $\Phi_c$ |
|---|---|---|---|---|---|---|---|---|---|
| $CO_2$ | -0.3868 | 35.6309 | -15.9827 | -3.6295 | 2.6629 | -2.6629 | 0.2274 | 0.3120 | -0.6579 |
| $C_{10}H_{22}$ | 0.0330 | 11.6087 | -2.6466 | -1.5481 | 20.00 | -10.3860 | 0.0616 | 0.0171 | -0.0072 |
| $C_6F_6$ | -0.9287 | 5.5583 | -1.8031 | -0.0344 | 0.0022 | 0 | 0.0142 | 0.0018 | -0.0408 |

### 7.4.1 $CO_2$+n-decane mixture: viscosity and thermal conductivity assessment

For the reference mixture, the general one-parameter f-theory model for viscosity (Eq.16-22) is available in literature with the characteristic critical viscosities optimized both for $CO_2$ [47] and n-decane [27]: $\eta_{c,CO2}$=376.872 μP and $\eta_{c,C10H22}$=257.928 μP. As already presented in Table 2, these coefficients allow the estimation of the viscosity with reasonably good results (with an AAD of 7%). As an example, Figure 2 shows the calculated viscosities with the three models compared with liquid experimental measurements at 311 K and a $CO_2$ molar content of 15%. The TRAPP and the Chung-Lee-Starling models are far from the real mixture behaviour, overestimating and underestimating the experimental dynamic viscosities respectively with a minimum AAD of 19%.

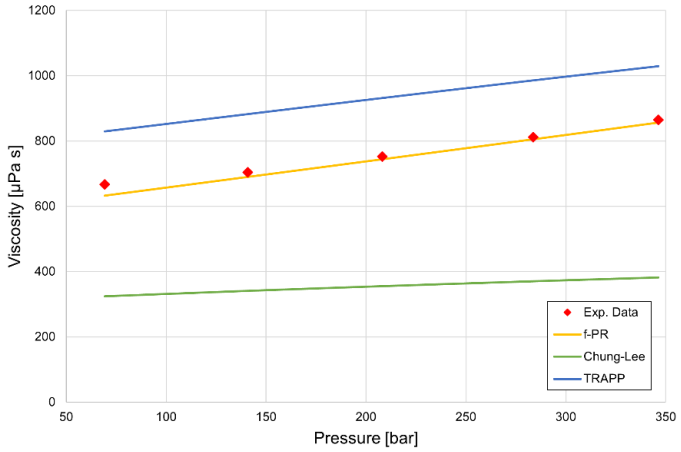


*Figure 2. Comparison among viscosity models, 15%$CO_2$+n-decane mixture (T=311 K)*

The thermal conductivity of the mixture has been modelled with the friction theory model for thermal conductivity (eq.23-29). The nine coefficients, reported in Table 4, of the pure $CO_2$ are taken from the original model [34]. On the other hand, the friction coefficients of pure n-decane, proposed in [34], lead to large deviations when they are adopted for the mixture, even if the agreement with pure n-decane experimental data was very good. For this reason, the parameters of the pure n-decane were here regressed against the recent experimental data of Zheng et al. [48] providing an AAD=0.87%. To obtain f-theory coefficients that provide good results also for the mixture, some constraints have been imposed in the regression to have sign concordance of the coefficients ($A_0$, $B_0$) of both n-decane and $CO_2$ associated to the quadratic residual entropy. As reported in Table 3, the f-PR model with the coefficients in Table 4 has an AAD equal to 4.03% while the corresponding states models have deviations over 15%. In Figure 3, some experimental thermal conductivities at different mixture compositions [45] are compared with the calculated values with the three models. The measurements are characterised by two different temperature (298 and 328 K) and a pressure range of 1–10 MPa. Results agree with the viscosity outcome: the TRAPP model overestimates the thermal conductivity of the mixture especially at high carbon dioxide fractions (AAD=18.4%), while the Chung-Lee gives the opposite trend with a similar AAD (17.1%).

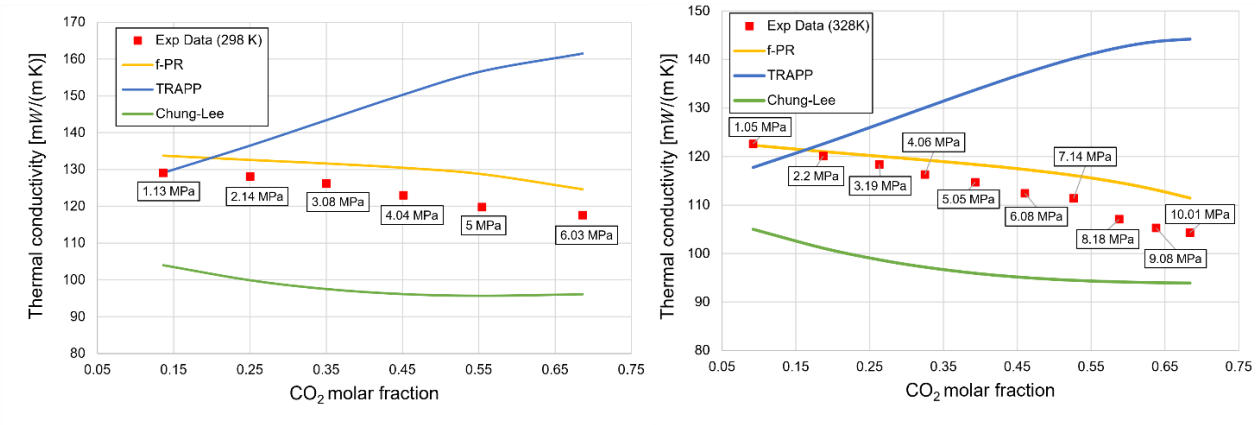


*Figure 3. comparison between models and experimental data (298 K left, 328 K right) of $CO_2$+n-decane.*

### 7.4.2 $CO_2$+$C_6F_6$ mixture: viscosity and thermal conductivity assessment

To calibrate the general one-parameter f-theory model for viscosity in case of pure $C_6F_6$, the relatively recent experimental liquid viscosities of Freire et al. [49] has been mainly used. As mentioned by Freire et al., viscosities measurements of fluorocarbons in literature are scarce and often discordant. Moreover the viscosity of fluorinated compounds is remarkably higher than their homologous hydrocarbons [49]; and the viscosity increases from linear structures to cyclic and aromatic structures (i.e. $C_6F_6$). Even if only five data points are available for the $C_6F_6$ in the temperature range 298.15–318.15 K, they are crucial to assess the behaviour of its viscosity at high densities (liquid phase region), and then to characterize the residual term. Some experimental data of Dymond et al. [50] are also used for a better regression at higher temperature (up to 323.2 K) and pressure (0.1-47.7 MPa). Some data are excluded from the evaluation since there are some inconsistences: for example, at atmospheric pressure, there are liquid viscosities data above the normal boiling temperature. The regressed value of critical characteristic viscosity is $\eta_{c,C6F6}$=640.76 μP, which guarantee a mean absolute deviation of 6.1% that is satisfactory for the scope of this work, as can be seen in Figure 4 (left). Results of the TRAPP and Chung-Lee-Starling models, in Figure 4 (right), show large deviations from the experimental data.

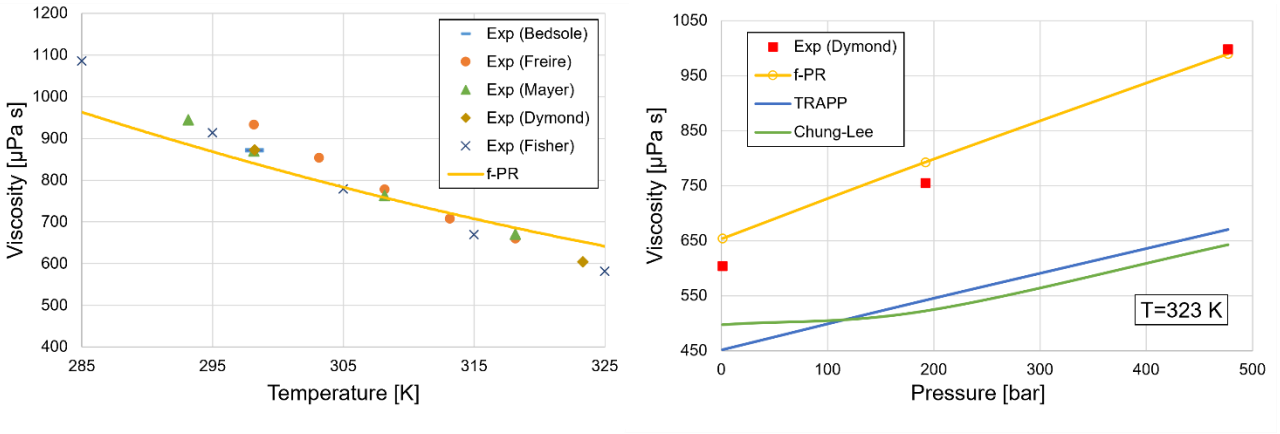


*Figure 4. f-PR vs experimental liquid viscosity of pure $C_6F_6$ at ambient pressure (left); comparison with isothermal data at high pressure (right).*

The f-theory model for thermal conductivity has been optimised by regressing the friction coefficients on the only three liquid data at ambient pressure available for $C_6F_6$ from Irving et al. [51]. Additional data obtained by the interpolation of the Irving experimental data were needed to find the 9 friction coefficients. For a better fitting procedure, more experimental points would be necessary. However, even few data in the liquid phase are helpful in the characterization of the residual friction term since the residual attractive and repulsive entropies are high in the liquid phase. The regressed parameters that describe the friction coefficients in Eq.23-29 are reported in In conclusion, the resulting mixture behaviour in terms of transport properties cannot be validated because no experimental measurements has been found in literature for this specific dopant. The comparison of the models with the experimental data, in Figure 5, shows that the results of the TRAPP and Chung-Lee models overestimate the measurements.

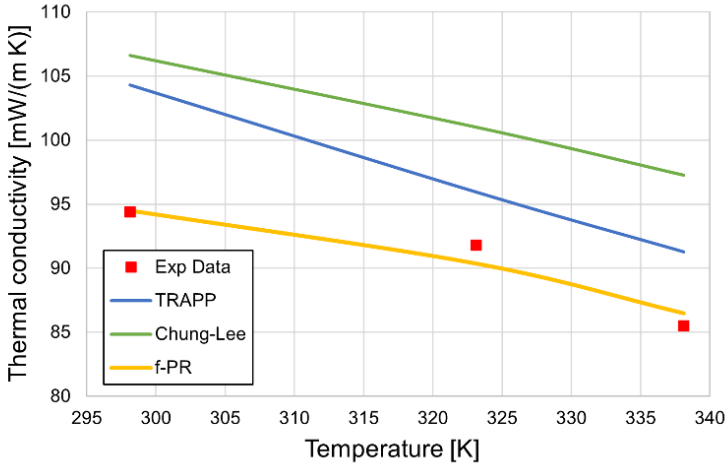


*Figure 5. liquid thermal conductivity of pure $C_6F_6$ at ambient pressure (Irving et al.) vs models*

As reported by Irving, the thermal conductivity of fluorinated hydrocarbons is lower than that of the corresponding hydrocarbons. The more the fluorine atoms in the molecule, the lesser is the thermal conductivity if compared to the same hydrocarbon structure. As it can be noted, in fact, the

thermal conductivity of pure $C_6F_6$ is relatively low considering that it is in the liquid phase at medium-low reduced temperatures (0.56-0.65), where the density is very high (1614 kg/m$^3$ at 298 K and 1 atm according to Counsell et al. [52]) if compared to benzene whose thermal conductivity is about 150% higher in the same conditions. In conclusion, the resulting mixture behaviour in terms of transport properties cannot be validated because no experimental measurements has been found in literature for this specific dopant.

## 7.5 PCHE recuperator design methodology

The transport properties are implemented into a PCHE design code to define the heat transfer coefficients and its size. PCHEs are composed by an alternation of overlapping hot and cold plates (in which minichannels are chemically etched) that are joined by means of a diffusion bonding process. A stack of plates (Figure 6) is jointed to form a core block of the desired geometry, called unit. The total PCHE volume consists of blocks with dimensions up to 0.6x0.6x1.5 m. If larger heat exchangers are required, multiple blocks can be welded together. The width $L_x$ of a single plate is limited to 0.6 m, and a stack of plates $L_y$ equal to 0.6 m is usually used in the diffusion bonding procedure, while the maximum axial length of the block is fixed by the maximum plate length of 1.5 m [53]. In this work, the most applied configuration with counter-current flow in 2 mm width straight minichannels is considered with channel pass equal to 2.4 mm and a plate thickness $t_p$ equal to 1.5 mm. The mechanical integrity of the PCHE with the considered channel geometry is verified as in [54].

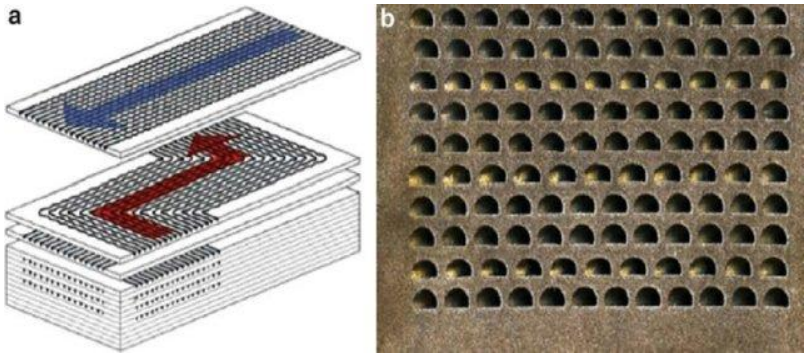


*Figure 6. PCHE: (a) plate stack, (b) module cross section [55].*

A segment-by-segment method is implemented to catch the local variations of the mixture thermophysical properties. The PCHE recuperator has been discretized along the axial direction into N segments (sub-heat exchangers), as shown in Figure 7, characterised by the same exchanged thermal duty, following the approach proposed by Jiang et al. [56].

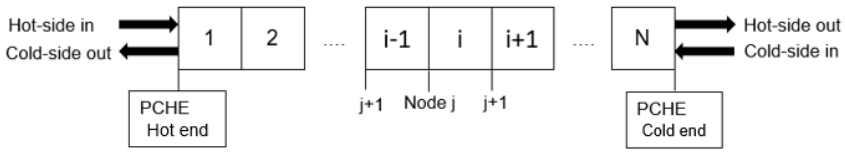


*Figure 7. segmentation procedure adopted for the PCHE design.*

The thermophysical properties of the mixture are calculated locally at the segment temperature and at its pressure level (considering the pressure drop in the segment). The axial length $L_{z,i}$ of the PCHE segment is evaluated with LMTD method once the local convective heat transfer coefficients of both sides $h_{hot,i}$ and $h_{cold,i}$ are estimated with appropriate models. Convergency is reached on the free-flow-area to guarantee the design with desired % pressure drop in the low-pressure side.

The number of channels per plate $N_{ch,P}$ and the number of plates $N_P$ in a block are obtained from Eq, 31 and 32 respectively. Each block has side margins (depending on header thickness and the attachment welds) and block ends that do not accommodate channels; a side margin $\Delta\delta$ of 50 mm and end plates $\Delta y$ of 5 mm are assumed here.

$$N_{ch,P} = int\left(\frac{L_x - 2 \cdot \Delta\delta}{pass}\right) \tag{31}$$

$$N_P = int\left(\frac{L_y - 2 \cdot \Delta y}{t_p}\right) \tag{32}$$

The recuperator is made by SS316 since it is compatible with the operating conditions of interest [57]. The metal thermal conductivity is considered as in [58] and the roughness of the channel is assumed to be 10 μm. Dewson and Gray reported a cost of 30 $/kg in 2003 [59] based on the weight of the delivered SS316-based PCHE. The cost per kg is actualized by using the medium CEPCI of the period January-April 2022 [60]. The final value is then 66 $/kg. Thus, the recuperator capital cost is estimated as:

$$PCHE_{cost} = (V - V_{channels})\, \rho_{SS316}\, C_{SS316} \tag{33}$$

$$V_{channels} = A_{ch}\, N_{ch,tot}\, L_z \tag{34}$$

where $\varrho_{SS316}$ is equal to 7980 kg/m$^3$. This correlation comes from commercial practice for the cost evaluation based on the real PCHE weight, subtracting the volume occupied by channels [61].

For the calculation of the local (each segment) heat transfer coefficients and pressure drop, models valid for both single-phase and two-phase flow are considered as partial condensation occurs in the low-pressure side. The heat transfer coefficient has been computed with accurately selected models in both single-phase region and two-phase region, since partial condensation occurs inside the PCHE recuperator for the $CO_2$-based mixtures considered. The Gnielinski correlation can provide a good match between simulated and experimental results in case of straight channels PCHE, as in this work, with a maximum error of 5% [62]. Moreover, as there are no experimental works on two-phase flows in PCHEs, we adopted a heat transfer coefficient model for two-phase mixtures that we have validated in a previous experimental work on a $CO_2$ mixture [63]. The correlations are discussed in detail in the Supporting Information section.

## 7.6 Power cycle application: PCHE design and impact

The assessment of the two $CO_2$-based power cycles applied in CSP context is carried out to show the impact of the transport properties prediction on the design of the PCHE recuperator as well as on the cycle performance. The mixture with n-decane is here considered as a reference $CO_2$ blend with

heavy compounds due to the well-known thermo-physical mixture properties. The cycle results and the thermodynamic input parameters for the PCHE design are obtained in the Aspen Plus®. The simple recuperative cycle layout and its representation in the T-s diagram are reported in Figure 8. In this configuration, the fluid is typically in the two-phase region at the outlet of the recuperator low-pressure side (6). The condensation of the mixture is completed in the condenser (6-1). The design of the PCHE has been carried out starting from a base case of 1% pressure drop across the low-pressure side ($\Delta P_{H,rec}$), and then increasing the values (up to 4%) to highlight the impact of the design on the capital costs and the cycle performance.

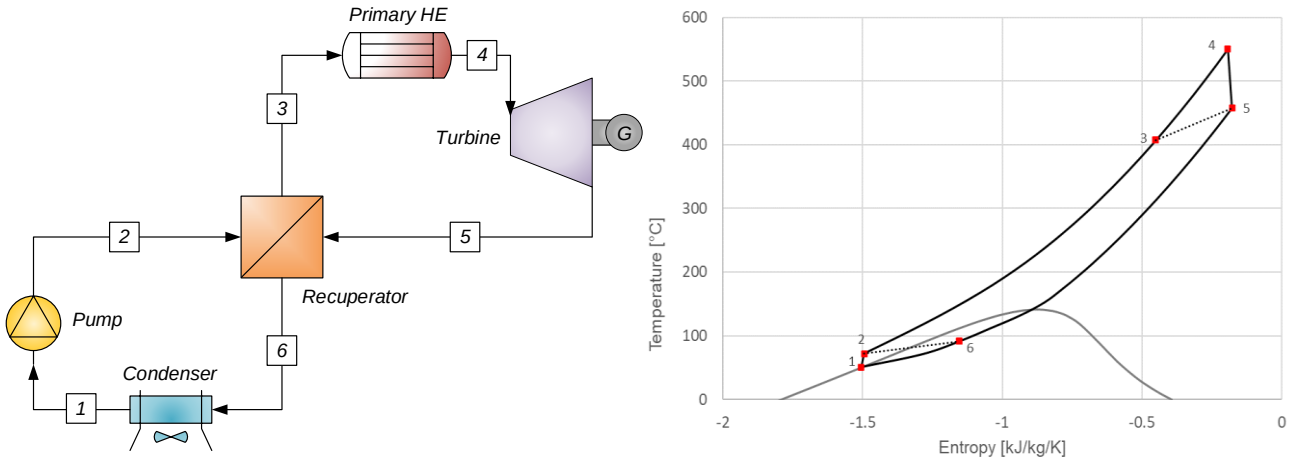


*Figure 8. Plant layout of the cycle working with $CO_2$ mixtures (left). T-s diagrams of transcritical $CO_2$+$C_6F_6$ mixture with $x_{CO2}$ = 84% molar (right); the regeneration is highlighted by dashed lines.*

The main assumptions of the power cycles are summarized in Table 5: most of the values are taken from previous studies [8,64–66]. The maximum temperature depends on the mixture thermal stability and, as a consequence, on the related CSP technology: for the $CO_2$+$C_6F_6$ mixture, the power cycle can be coupled with a CSP-tower plant configuration with molten salts as HTF, while, for the $CO_2$+$C_{10}H_{22}$ mixture, a Linear Fresnel Reflector with commercial HTFs is considered. However long-term thermal stability of the latter should be investigated: the selected temperature level (350 °C) is in line with the upper limit range for thermal stability of hydrocarbons and n-Decane experimental data availability range (up to 402°C).

*Table 5. Assumptions for the power cycle simulations*

| | | **$CO_2$+$C_{10}H_{22}$** | **$CO_2$+$C_6F_6$** |
|---|---|---|---|
| Parameters | units | Values | Values |
| $T_{min,cycle}$ | °C | 51 | |
| $T_{in,turb}$ | °C | 350 | 550 |
| $P_{in,turb}$ | bar | 250 | |
| $\Delta T_{min,rec}$ | °C | 5 | |

| | | | |
|---|---|---|---|
| $\Delta P_{H,rec}$ | % | 1 | 1 |
| | (bar) | (1.1) | (0.81) |
| $\Delta P_{C,rec}$ | bar | 0.45[a] | 0.23[a] |
| $\Delta P_{PHE}$ | % | 2 | |
| $\Delta P_{COND}$ | % | 2 | |
| Turbine / pump Isentropic Efficiency | % | 92 / 88 | |

[a] *The pressure drop in the HP side is in accordance with the design results*

The composition of the mixture is optimized to achieve the maximum cycle efficiency at the selected operating conditions. The evaluation of the power cycle performance at the various PCHE design will include the cycle thermodynamic efficiency and the effectiveness of the recuperator, defined in Eq. 35 and Eq. 36 respectively.

$$\eta_{Cycle} = \frac{W_{Turbine} - W_{Pump}}{Q_{in}} \tag{35}$$

$$\varepsilon_{\mathrm{Rec}} = \frac{Q_{Recuperated}}{Q_{\infty}} = \frac{h(T_3, P_3) - h(T_2, P_2)}{h(T_5, P_5) - h(T_2, P_6)} \tag{36}$$

A detailed descriptions of the results of the recuperator can be found in the section of the $CO_2$+$C_6F_6$ mixture, while the section of the $CO_2$+$C_{10}H_{22}$ mixture is aimed to highlight the relevance of the properties estimation for a mixture with accessible experimental data on transport properties.

### 7.6.1 $CO_2$ + n-Decane mixture

The power cycle is evaluated for a net power output of 50 MW. The PR EoS with an optimized binary interaction parameter $k_{ij}$=0.1141 [67] is used. From a preliminary analysis, the mixture composition that maximise the cycle efficiency corresponds to a $CO_2$ molar fraction of 89%, as shown in Figure 9. Table 6 collect the main operating conditions of the cycle for this composition, while the cycle power balance and the main PCHE features at design condition (base case with 1% $\Delta P_{H,rec}$) are reported in Table 7. It can be noticed that the amount of recovered heat power in the recuperator is remarkably high for this working fluid, if compared to the net mechanical power and the thermal power input. The T-Q diagram of the PCHE recuperator is shown in Figure 10. The minimum internal temperature approach (5°C) is encountered at 28% of the total exchanged thermal duty near the recuperator hot-end, where the dew point occurs (around 224 °C), thus the heat transfer mostly falls in the two-phase region for the hot side. The well-balanced heat capacities of the two streams inside the recuperator yield a good thermodynamic efficiency of the cycle although the turbine inlet temperature is 350 °C.

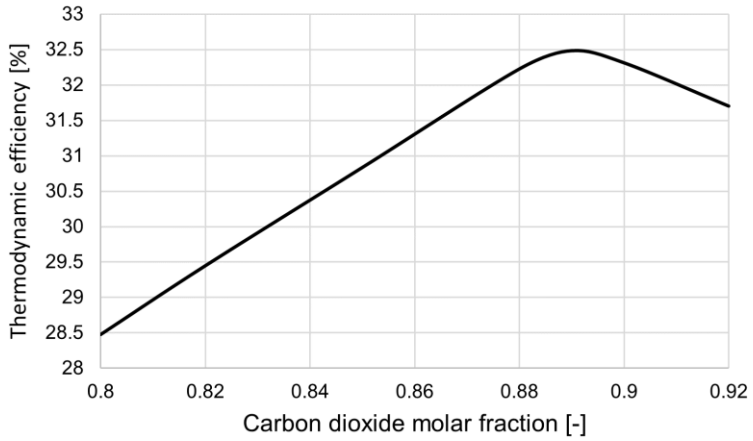


*Figure 9. Mixture $CO_2$+$C_{10}H_{22}$: Cycle thermodynamic efficiency as function of the mixture composition*

*Table 6. Mixture $CO_2$+$C_{10}H_{22}$: main thermodynamic conditions (base case 1% ΔPH,rec)*

| Streams | T [°C] | P [bar] | $x_{vap}$ [-] |
|---|---|---|---|
| 1 | 51 | 106.3 | 0 |
| 2 | 68.2 | 255.6 | 0 |
| 3 | 282.4 | 255.1 | 1 |
| 4 | 350 | 253 | 1 |
| 5 | 294.9 | 109.5 | 1 |
| 6 | 75.9 | 108.4 | 0.6 |

*Table 7. Mixture $CO_2$+$C_{10}H_{22}$: Cycle performance at design conditions (base case 1% ΔPH,rec)*

| Parameter | units | value |
|---|---|---|
| $\dot{m}$ | kg/s | 1200.7 |
| $W_{pump}$ | MW | 28.7 |
| $Q_{rec}$ | MW | 516.9 |
| $Q_{PHE}$ | MW | 154.1 |
| $W_{turb}$ | MW | 78.7 |
| $Q_{cond}$ | MW | 104.1 |
| $UA_{rec}$ | MW/K | 70.7 |
| $\varepsilon_{rec}$ | % | 96.2 |
| $\eta_{cycle}$ | % | 32.5 |

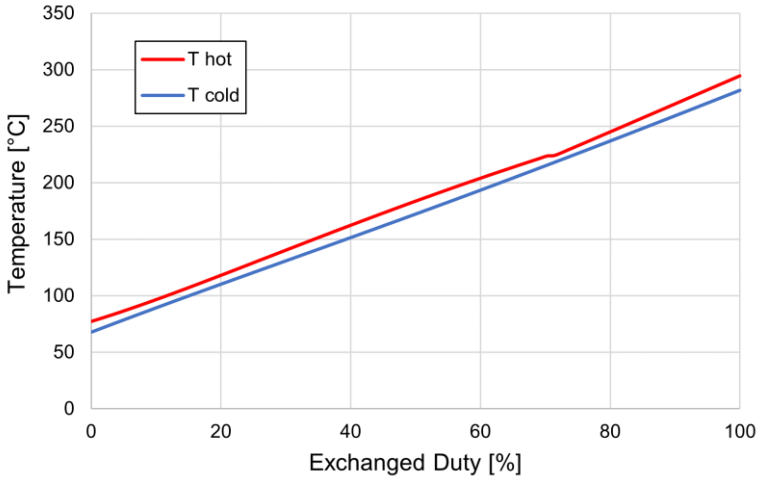


*Figure 10. Mixture $CO_2$+$C_{10}H_{22}$: T-Q diagram of the recuperator (base case 1% ΔPH,rec)*

The design of the PCHE recuperator is carried out with three different models for the prediction of the transport properties: the TRAPP model, the Chung-Lee-Starling model, and the friction theory model (f-PR). The trend of the dynamic viscosity and thermal conductivity of the mixture at the upper and lower (two-phase field) isobars in the heat exchanger temperature range is represented in Figure 11. The differences between the models are quite evident, especially at low temperatures in the HP side and in the liquid phase at low pressure. On the other hand, the values of the vapour phase at low pressure are quite in agreement. It is evident that the TRAPP model results are higher with respect to those of the f-PR model: this is in accordance with the experimental data comparison shown in Figure 2.

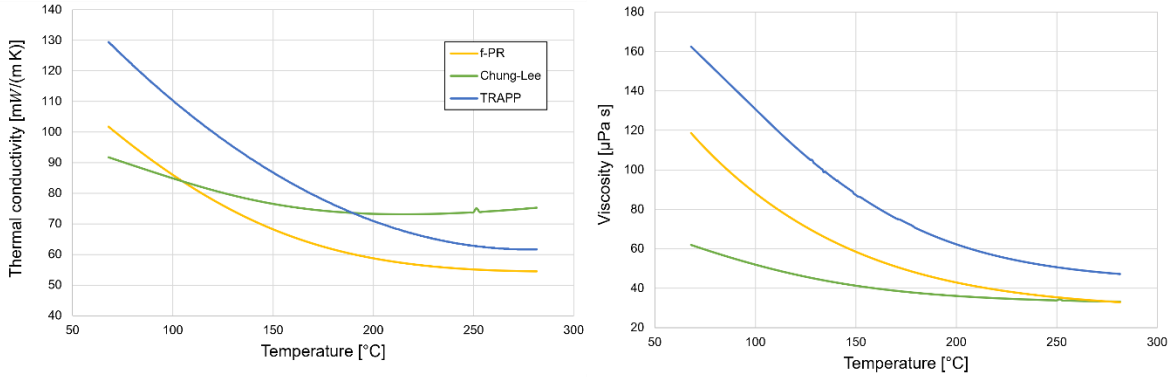

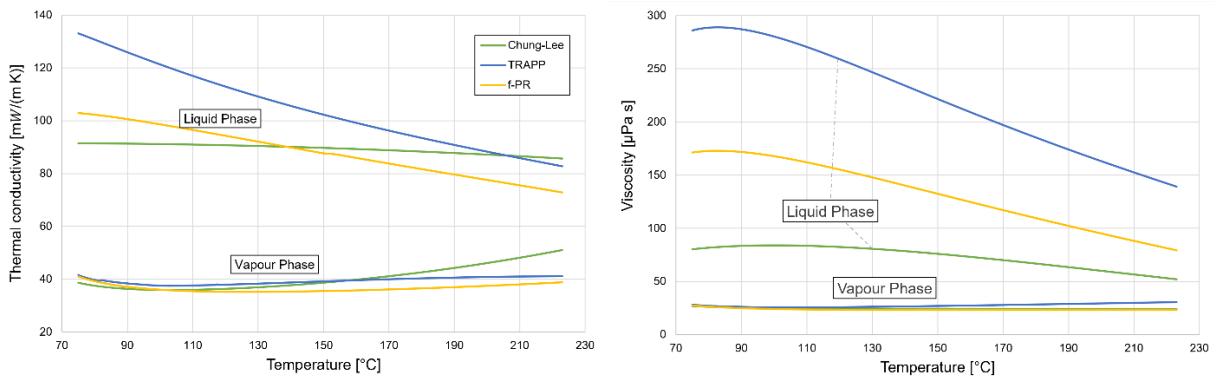


*Figure 11. Mixture $CO_2$+$C_{10}H_{22}$: thermal conductivity and viscosity calculated with different models in the HP side (top) and in the two-phase region LP side (bottom) of the recuperator.*

The trend of the overall heat transfer coefficient U along the heat exchanger is illustrated in Figure 12. It is possible to conclude that the heat transfer area obtained with TRAPP and friction theory models are similar even if the transport properties are differently predicted: an overestimation of the viscosity by the TRAPP model leads to lower Reynolds and Nusselt numbers, but this is compensated by an overestimation of the thermal conductivity in the calculation of the heat transfer coefficient.

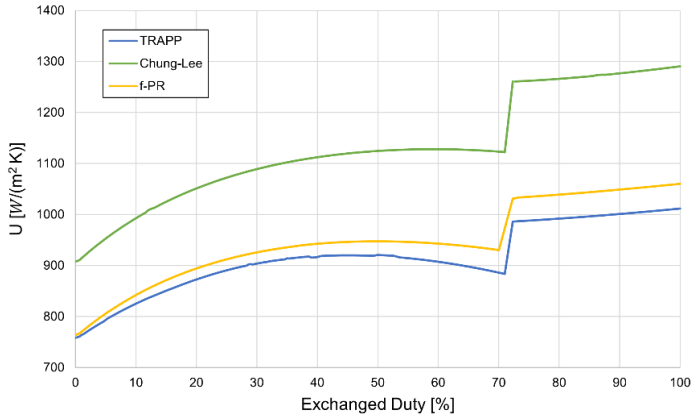


*Figure 12. Mixture $CO_2$+$C_{10}H_{22}$: U along the PCHE for $CO_2$+n-decane, model comparison (base case 1% ΔPH,rec)*

The results of the design using the different models is reported in Table 8. Since the Chung-Lee-Starling method seems to underestimate the viscosity of this mixture (as proved by the experimental comparison in Figure 2) without penalising the thermal conductivity, the high Reynolds numbers favour the heat transfer, and the heat exchanger results more compact.

*Table 8. Mixture $CO_2$+$C_{10}H_{22}$: PCHE design results (base case 1% ΔPH,rec) with different transport properties models*

| | **TRAPP** | **f-PR** | **Chung-Lee** |
|---|---|---|---|
| G [kg/(sm²)] | 403 | 396 | 428 |
| $N_{ch,hot/cold}$x$10^6$ | 1.897 | 1.93 | 1.79 |
| $L_z$ [m] | 8.36 | 7.95 | 7.22 |
| A [m²] | 81523 | 78904 | 66301 |
| V [m³] | 164.8 | 159.5 | 134 |
| Cost [M$] | 60.6 | 58.6 | 49.2 |

### 7.6.2 $CO_2$ + $C_6F_6$ mixture

The power cycle is evaluated for a net mechanical power output of 100 MW and properties assessment is carried out with the PR EoS, by using an optimised BIP from [6]. A mixture composition with a $CO_2$ molar content of 84% is chosen according to the same work [6] to maximize the gross cycle efficiency (around 42%). The most relevant thermodynamic points of the cycle are summarized in Table 9 for the base case. To see the impact of the PCHE design on the cycle performance, the hot-side pressure drops have been varied from 1 to 4% (corresponding to 0.81÷3.2 bar). The cycle power balance and the main PCHE features at design condition reported in Table 11.

*Table 9. Mixture $CO_2$+$C_6F_6$: main thermodynamic conditions (base case 1% ΔPH,rec)*

| Streams | T [°C] | P [bar] | $x_{vap}$ [-] |
|---|---|---|---|
| 1 | 51 | 77.7 | 0 |
| 2 | 71.9 | 255.5 | 0 |
| 3 | 406 | 255.1 | 1 |
| 4 | 550 | 250 | 1 |
| 5 | 457.5 | 80.1 | 1 |
| 6 | 90.1 | 79.3 | 0.53 |

The T-Q diagram of the PCHE recuperator is shown in Figure 13, where the internal pinch point is identified at the dew point near the cold-end. The values of the dynamic viscosity and thermal conductivity of the mixture along the upper and lower (two-phase field) isobars in the heat exchanger temperature range, calculated with the three investigated transport properties models, is represented in Figure 14. Moreover Figure 15 shows the same properties in the single-phase LP side of the recuperator.

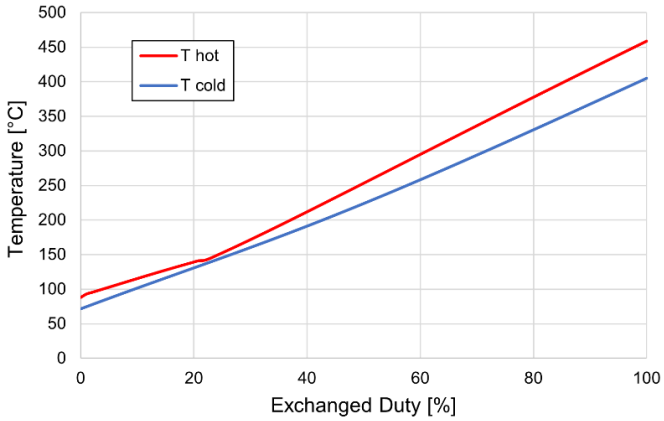


*Figure 13. Mixture $CO_2$+$C_6F_6$: T-Q diagram of the PCHE (base case 1% ΔPH,rec).*

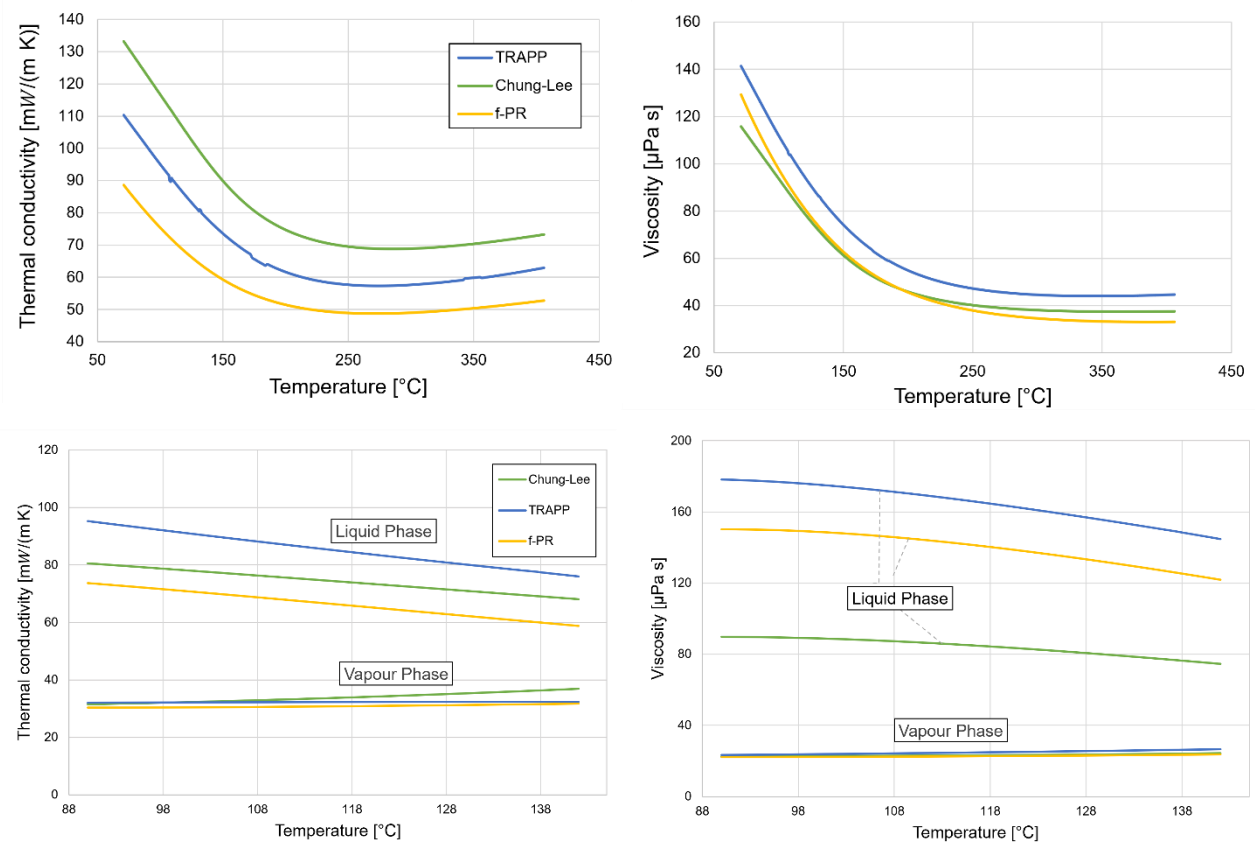


*Figure 14. Mixture $CO_2$+$C_6F_6$: thermal conductivity and viscosity calculated with different models in the HP side (top) and in LP side two-phase region (bottom) of the recuperator in the heat exchanger temperature range.*

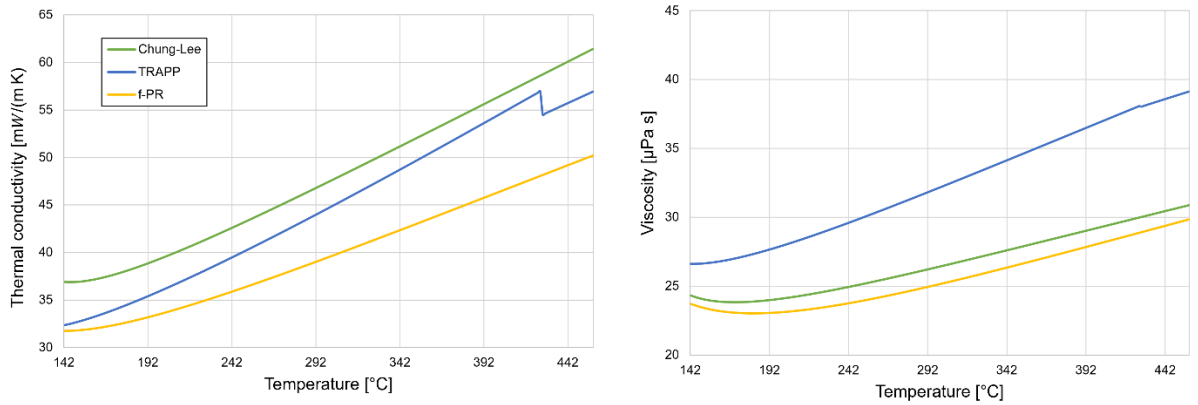


*Figure 15. Mixture $CO_2$+$C_6F_6$: transport properties in the single-phase LP side with different models.*

It can be noted that the thermal conductivity predicted with the f-PR model is lower if compared to the other two models as shown in Figure 5 where both TRAPP and Chung-Lee models overestimate the experimental data of pure $C_6F_6$. The overall heat transfer coefficient is reported in Figure 17. In the HP stream, the viscosity increases about four times from the hot-end to the cold-end: this enhancement across critical conditions entails a drastic variation of the Reynolds number. Consequently, there is a reduction of the convective heat exchange performance at the cold-end that is only partially relieved by the increase of the thermal conductivity in that region. The

counterbalanced trends of viscosity and thermal conductivity in the cold-side are well represented by the Prandtl numbers and the Reynolds number in Figure 16.

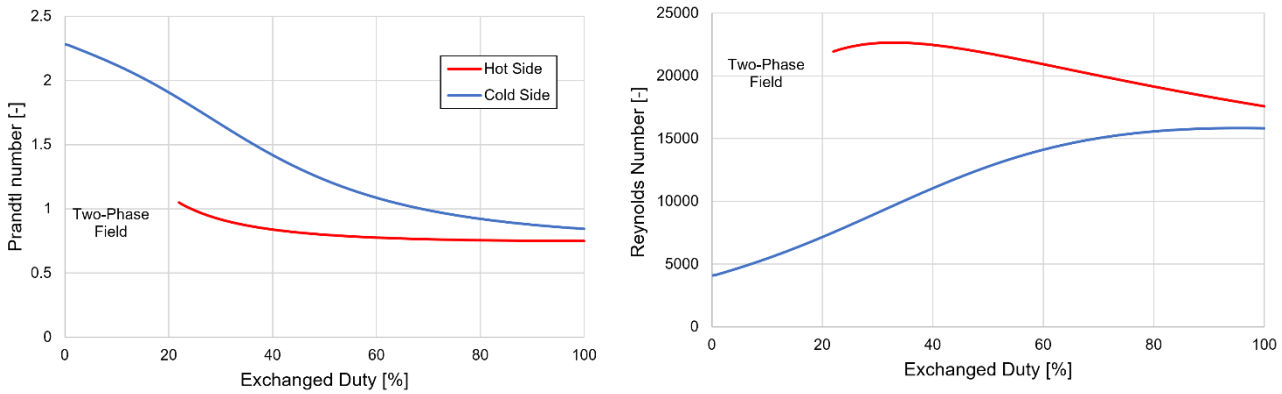


*Figure 16. Mixture $CO_2$+$C_6F_6$: Prandtl and Reynolds numbers trend along the PCHE*

In the LP stream, the Reynolds number increases due to a reduction of the viscosity between the hot-end and the condensation onset, thus enhancing even the Nusselt number. However, the marked decrease of the thermal conductivity, from the hot-in to the pinch-point, determines an overall progressive reduction of the convective heat transfer coefficient in the LP side. On the other hand, the TRAPP model provides a higher thermal conductivity but at the same time higher viscosity compared with the fitted f-PR model. As a consequence, the resulting heat transfer coefficients are quite similar using the two models especially in the single-phase region, while notable difference can be seen in the two-phase region. In the end, the resulting recuperator design with the two models is very similar because the two-phase field corresponds only at about 20% of the total exchanged thermal power. Whilst the Chung-Lee-Starling model estimates a higher thermal conductivity and, at the same time, a similar or even lower viscosity compared to the f-PR model, leading to a more compact PCHE. The design results are reported in Table 10.

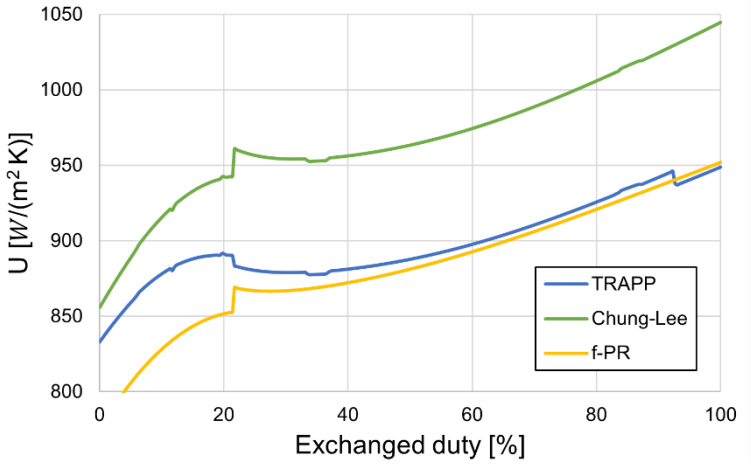


*Figure 17. Mixture $CO_2$+$C_6F_6$: U along the PCHE, model comparison (base case)*

*Table 10. Mixture $CO_2$+$C_6F_6$: PCHE design results (base case)*

| | **TRAPP** | **f-PR** | **Chung-Lee** |
|---|---|---|---|
| G [kg/(s m²)] | 432 | 429 | 449 |
| $N_{ch,hot/cold}$ x $10^6$ | 1.8 | 1.82 | 1.74 |
| $L_z$ [m] | 4.07 | 4.15 | 3.97 |
| A [m²] | 37'800 | 38'780 | 35'267 |
| V [m³] | 76.4 | 78.4 | 71.3 |
| Cost [M$] | 28.1 | 28.8 | 26.2 |

The cycle power balance and PCHE design, using f-PR, at different hot-side percentage pressure drop, keeping a constant net mechanical output, is reported in Table 11. The different PCHE design affects both the upper and the lower isobars. The pump inlet pressure is fixed to achieve saturation conditions at 51°C while the pressure at turbine inlet is set as constant parameter at 250 bar. Thus, the different pressure drops in the HP and LP streams of the recuperator affect both the pump outlet and the turbine outlet conditions. When the allowable pressure drop in the PCHE channel increases, the channel length increases due to more duty exchanged in the single channel, even if the heat transfer coefficients are higher.

*Table 11. Mixture $CO_2$+$C_6F_6$: cycle performance at different PCHE pressure drop using f-PR as transport properties model.*

| **Parameter** | **units** | ***1% $\Delta P_{H,rec}$*** | ***2% $\Delta P_{H,rec}$*** | ***3% $\Delta P_{H,rec}$*** | ***4% $\Delta P_{H,rec}$*** |
|---|---|---|---|---|---|
| $\Delta P_{C,rec}$[a] | bar | 0.23 | 0.45 | 0.68 | 0.92 |
| $\dot{m}$ | kg/s | 1224.7 | 1237.7 | 1251.3 | 1265.3 |
| $W_{pump}$ | MW | 25.4 | 25.7 | 26.0 | 26.4 |
| $Q_{rec}$ | MW | 609.4 | 617.0 | 624.9 | 629.1 |
| $Q_{TH,in}$ | MW | 237.7 | 239.1 | 240.5 | 242.0 |
| $W_{turb}$ | MW | 125.4 | 125.7 | 126.0 | 126.4 |

| | | | | | |
|---|---|---|---|---|---|
| $Q_{cond}$ | MW | 137.7 | 139.1 | 140.5 | 142 |
| $UA_{PCHE}$ | MW/K | 33.3 | 33.7 | 34.1 | 34.5 |
| $\varepsilon_{rec}$ | % | 92.85 | 92.88 | 92.92 | 92.96 |
| $\eta_{cycle}$ | % | 42.1 | 41.8 | 41.6 | 41.3 |
| G | kg/(sm$^2$) | 429 | 602 | 737 | 850 |
| $N_{ch,\ hot/cold} x10^6$ | - | 1.82 | 1.31 | 1.08 | 0.95 |
| $L_z$ | m | 4.15 | 4.49 | 4.65 | 4.76 |
| A | m$^2$ | 35'267 | 30'218 | 25'836 | 23'193 |
| V | m$^3$ | 78.4 | 61.1 | 52.2 | 46.9 |
| Cost | M$ | 28.8 | 22.4 | 19.2 | 17.2 |

[a] *The pressure drop in the cold-side of the recuperator is in accordance with the results of the design*

The LCOE is so computed to see the impact of the PCHE design at different pressure drops on the overall CSP plant. The cost functions to assess the capital costs of the power block are taken from Weiland et al. [68] for turbine, pump, motor and generator, whereas Thermoflex has been used to determine the cost of the PHE. The economic analysis is carried out installing the power block and the CSP tower in Sevilla (Spain). The cost functions of the solar tower, receiver, HTF pump and piping are taken from Kelly at al. [69] while the solar field cost is assumed equal to 145 \$/m$^2$ of heliostat area as suggested in SAM [70]. A 8-hours TES, that consists of two molten salts tanks, is assumed computing the related cost from the work of Manzolini et al [71]. The design of the solar field, for a thermal input of 717 $MW_{th}$ at the receiver, as well as additional financial and operating expenses related to the CSP plant are presented in [72]. The LCOE is calculated as:

$$LCOE\left[\frac{\$}{MWh_{el}}\right] = \frac{CSP\ Plant\ CAPEX \cdot CRF + CSP\ Fixed\ OPEX}{Yearly\ Net\ Electric\ Energy\ Produced} + CSP\ Variable\ OPEX \qquad (37)$$

Table 12 reports the capital cost related to the components of the power block. The overall power block cost decreases as the allowable pressure drop across the PCHE increases, but at the same time the size of the other power block components slightly increases at fixed 100 MW electrical output. The solar field and the tower are fixed, while the TES size is computed for each power cycle based on the optimal LCOE condition. An optimal TES size of 8 hours is found, and the dimensions of the tanks to provide the design thermal have a low impact on the capital costs from one case to another. The results of the annual analysis considering Sevilla as location of the CSP plants with different power block and TES design are represented in Table 13.

*Table 12. Mixture $CO_2$+$C_6F_6$: Power block capital costs at different PCHE recuperator design*

| **PB costs** | **units** | ***1% $\Delta P_{H,rec}$*** | ***2% $\Delta P_{H,rec}$*** | ***3% $\Delta P_{H,rec}$*** | ***4% $\Delta P_{H,rec}$*** |
|---|---|---|---|---|---|
| Pump | M$ | 4.85 | 4.89 | 4.94 | 5 |
| Turbine | M$ | 3 | 3.02 | 3.04 | 3.07 |
| PHE | M$ | 24.2 | 24.5 | 24.7 | 25 |

| | | | | | |
|---|---|---|---|---|---|
| Condenser | M$ | 8.78 | 8.86 | 8.91 | 9 |
| Power Block | M$ | 74.5 | 68.6 | 65.8 | 64.3 |
| PCHE/PowerBlock | % | 38.6 | 32.7 | 29.1 | 26.7 |

*Table 13. Mixture $CO_2$+$C_6F_6$: Annual analysis of the CSP plant at different recuperator design*

| **CSP Plant results** | **units** | ***1% $\Delta P_{H,rec}$*** | ***2% $\Delta P_{H,rec}$*** | ***3% $\Delta P_{H,rec}$*** | ***4% $\Delta P_{H,rec}$*** |
|---|---|---|---|---|---|
| Yearly Electric Energy | $GWh_{el}$/year | 407.5 | 405.45 | 404.07 | 401.98 |
| Equivalent Hours of Defocusing | h/year | 77 | 68 | 61 | 52 |
| Solar Multiple | - | 2.52 | 2.5 | 2.49 | 2.47 |
| TES Cost | M$ | 60.11 | 60.5 | 60.76 | 61.16 |
| Solar Field Cost | M$ | 183 | 183 | 183 | 183 |
| Tower Cost | M$ | 24 | 24 | 24 | 24 |
| Specific CSP CAPEX | $/$kW_{el}$ | 5330 | 5262 | 5231 | 5218 |
| PCHE % Investment Cost | - | 5.5 | 4.3 | 3.7 | 3.4 |
| LCOE | $/$MWh_{el}$ | 133.9 | 133.1 | 132.9 | 133.3 |

As highlighted in Figure 18, a local minimum of the LCOE is found around a hot-side pressure drop of 3% due to a more compact PCHE with respect to the base case without affecting much the cycle efficiency (Table 11). The LCOE local minimum is not very significative, but it is relevant for many aspects: lower investment cost compared to the base case, lower number of PCHE modules operating in parallel reducing the risks of maldistribution, lower block welding and associated labor, lower maintenance costs. When the available solar power exceeds the power block thermal input, the TES stores the exceeding energy until its capacity is saturated and the defocusing of the heliostats is practiced. The adoption of a more compact PCHE recuperator represents a good solution also because defocusing hours are reduced.

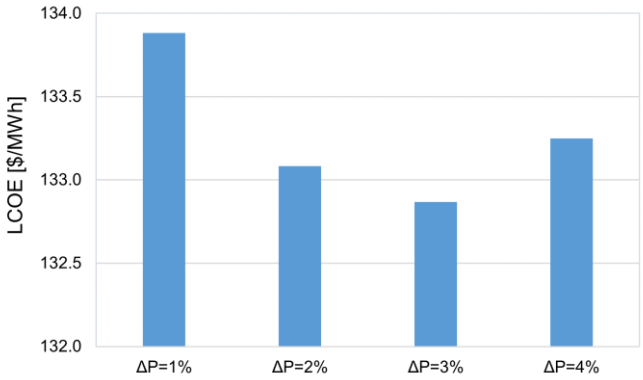


*Figure 18. Mixture $CO_2$+$C_6F_6$: LCOE of simple recuperated 100 MW cycle at different PCHE design conditions.*

## 7.7 Conclusions

Over the last years, new closed power cycle configurations adopting $CO_2$-based mixtures as innovative working fluid are considered as promising alternative to $sCO_2$ cycles when dry-cooling in hot environments is performed. . In particular, some works suggested the use of $CO_2$ mixture with heavy and complex compounds, such as $CO_2$+$C_6F_6$, in simple recuperative transcritical power cycle. Although preliminary analysis highlighted the benefits of this solution, a detailed design of the power block components requires the knowledge of the thermophysical properties of binary mixtures of interest. Previous literature works focused only on thermodynamic assessment of the $CO_2$-based mixture, but no theoretical neither experimental studies on the transport properties have been performed Starting from an extensive literature review, this work explored the adoption of suitable transport properties models for the design of the heat exchangers of the cycle, focusing on the PCHE recuperator of the transcritical power cycle with the $CO_2$+$C_6F_6$ and $CO_2$+$C_{10}H_{22}$ mixtures.

In general, the comparison of most appropriate models with available experimental data of $CO_2$-based mixtures highlights the shortcomings of the properties in the non-equilibrium field with respect to thermodynamics. On the other hand, the adoption of the recent friction theory model results to be a valid tool for modelling the transport properties from the dilute region to dense fluid states, even for asymmetric mixtures, compared to corresponding states-based models models available in commercial software. Moreover, the f-theory models can be optimised on the pure component experimental data, without needing for binary interaction parameters, and this is a great benefit since experimental data of $CO_2$-mixtures are scarce especially in the high-pressure conditions of a transcritical power cycle.

As there are no experimental data on the investigated $CO_2$+$C_6F_6$ mixture, an additional $CO_2$ blend with a heavy dopant, $CO_2$+n-decane, whose transport properties are well known, is selected to prove this concept. The two $CO_2$ mixtures have been investigated in optimized cycle conditions in concentrated solar power plants. The $CO_2$ mixture with n-decane showed very high thermodynamic efficiency (32.5%) at 350°C maximum temperature due to well-balanced heat capacities within the recuperator, in a simple-recuperated layout. On the other hand, the low mean temperature difference along the PCHE recuperator leads to a large heat transfer area and volume. Compared to TRAPP and Chung-Lee-Starling models, imported from commercial software, the adoption of the optimized friction theory model, implemented in an in-house code, proved to be effective in describing the heat transfer behaviour of the mixture.

In case of the $CO_2$+$C_{10}H_{22}$ mixture, the use the Chung-Lee model overpredicts the global heat transfer coefficient (around +16%), due to an underestimate of the dynamic viscosity. Instead, the heat transfer area obtained by the TRAPP method is similar to that obtained by the friction-theory model (representative of real mixture behaviour), even if the deviations in the transport properties prediction are marked: an overestimate of the viscosity by the TRAPP method entails lower Reynolds and Nusselt numbers, but it is compensated at the same time by an overestimate of thermal conductivity. This leads to comparable areas and volumes predicted by TRAPP and friction theory models.

The same outcome can be observed for the PCHE recuperator of the $CO_2$+$C_6F_6$ mixture: compared to the optimized f-theory model, the TRAPP overestimate both viscosity and thermal conductivity, providing a similar heat transfer area and volume.Even if the TRAPP and Chung-Lee models are

recognized as equally valid in a wide density domain, this research shows that the TRAPP model provides reasonable results for the $CO_2$-based mixtures investigated in terms of heat transfer area and volumes, even if the transport property prediction is questionable as evidenced by the comparison with experimental data of the case-studies. Obviously, the use of the latter model could be not suitable, for example, in the calculation of pressure losses in the pipes of the power plant. In any case, dedicated analysis should be performed for each specific $CO_2$ mixture investigated, and the use of the optimized friction theory model results to be a useful tool to improve the reliability of the design results.

A better understanding of the heat transfer behavior of $CO_2$ binary mixtures is crucial for the cycle design, but also to predict the off-design performance, and this work provides useful guidelines when dealing with the design of the heat exchangers of a transcritical $CO_2$-based cycle.

The optimal design of the PCHE of the transcritical power cycle working with $CO_2$+$C_6F_6$ applied in a CSP located in Sevilla is found to be around 3% hot-side pressure drop, a solution that allows more compactness (lower capital costs) without affecting much the cycle efficiency and reducing the maldistribution risks too.

**Nomenclature**

Acronyms

| | |
|---|---|
| BIP | Binary interaction parameter, - |
| CFC | Chlorofluorocarbon |
| CSP | Concentrated solar power |
| ECS | Extended Corresponding States |
| EoS | Equation of state |
| HTF | Heat transfer fluid |
| LCOE | Levelized cost of electricity, \$ $MWh^{-1}$ |
| LMTD | Logarithmic Mean Temperature Difference |
| PB | Power Block |
| PR | Peng Robinson EoS |
| PCHE | Printed circuit heat exchanger |
| Refprop | Reference Fluid Thermodynamic and Transport Properties |
| TES | Thermal Energy Storage |
| TRAPP | TRAnsport Property Prediction |

Symbols

| | |
|---|---|
| ΔP | Pressure drop, bar |
| $\Delta\pi_{residual}$ | Residual property π |
| h | Enthalpy, kJ/kg |

| | |
|---|---|
| $k_{i,j}$ | Cubic EoS binary interaction parameter, - |
| $\dot{m}$ | Mass flow rate, kg $s^{-1}$ |
| MW | Molar mass, kg $kmol^{-1}$ |
| P | Pressure, bar |
| Q | Thermal duty, MW |
| $\varrho$ | Density, kg $m^{-3}$ |
| s | Entropy, kJ $kg^{-1}$ $K^{-1}$ |
| T | Temperature |
| V | Molar Volume |
| $x_i$ | Species i molar fraction, - |
| W | Mechanical work, MW |
| Z | Compressibility factor, - |

Greek symbols

| | |
|---|---|
| $\eta$ | Efficiency, - |
| $\varepsilon_{Rec}$ | Recuperator effectiveness, - |
| $\omega$ | Pitzer acentric factor, - |

Subscripts

| | |
|---|---|
| a | Attractive |
| c | Critical |
| ch | Channel |
| el | Electrical |
| f | Friction term |
| i,j | Species |
| m | Mixture |
| o | Zero-density |
| P | Plates |
| r | Repulsive |
| th | Thermal |

Superscripts

| | |
|---|---|
| r | Residual |
| ref | Reference flud |

## 7.8 Bibliography

[1] Greenpeace, Solar Thermal Electricity. Global Outlook 2016. Available at: https://www.greenpeace.org/archive-

international/Global/international/publications/climate/2016/Solar-Thermal-Electricity-Global-Outlook-2016.pdf, (2016).

[2] SCARABEUS, Supercritical Carbon dioxide/Alternative fluids Blends for Efficiency Upgrade of Solar power plants, (2019).

[3] E. Morosini, M. Doninelli, D. Alfani, M. Astolfi, G. Di Marcoberardino, G. Manzolini, Analysis of the Potential of Co2 Based Mixtures To Improve the Efficiency of Cogenerative Waste Heat Recovery Power Plants, Conf. Proc. Eur. SCO2 Conf. (2023) 169–178. https://doi.org/10.17185/duepublico/77287.

[4] G. Di Marcoberardino, E. Morosini, G. Manzolini, Preliminary investigation of the influence of equations of state on the performance of CO2 + C6F6 as innovative working fluid in transcritical cycles, Energy. 238 (2022) 121815. https://doi.org/10.1016/j.energy.2021.121815.

[5] E.M. S. Lasala, P. Chiesa, Binary mixtures of carbon dioxide and fluorocarbons as working fluids for power production applications, Conf. Proc. JEEP2014 – 40ième Journées d'Etudes Des Equilibres Entre Phases. (2014) 10–11. https://doi.org/10.13140/RG.2.2.14853.58084.

[6] G. Di Marcoberardino, E. Morosini, D. Di Bona, P. Chiesa, C. Invernizzi, P. Iora, G. Manzolini, Experimental characterisation of CO2 + C6F6 mixture: Thermal stability and vapour liquid equilibrium test for its application in transcritical power cycle, Appl. Therm. Eng. 212 (2022) 118520. https://doi.org/10.1016/j.applthermaleng.2022.118520.

[7] E. Morosini, A. Ayub, G. di Marcoberardino, C.M. Invernizzi, P. Iora, G. Manzolini, Adoption of the CO2 + SO2 mixture as working fluid for transcritical cycles: A thermodynamic assessment with optimized equation of state, Energy Convers. Manag. 255 (2022). https://doi.org/10.1016/j.enconman.2022.115263.

[8] G. Manzolini, M. Binotti, D. Bonalumi, C. Invernizzi, P. Iora, CO2 mixtures as innovative working fluid in power cycles applied to solar plants. Techno-economic assessment, Sol. Energy. 181 (2019) 530–544. https://doi.org/10.1016/J.SOLENER.2019.01.015.

[9] H. Li, Ø. Wilhelmsen, Y. Lv, W. Wang, J. Yan, Review of available experimental data and models for the transport properties of CO 2-mixtures relevant for CO 2 capture , transport and storage, in: 2011.

[10] M. Nazeri, A. Chapoy, R. Burgass, B. Tohidi, Viscosity of CO2-rich mixtures from 243 K to 423 K at pressures up to 155 MPa: New experimental viscosity data and modelling, J. Chem. Thermodyn. 118 (2018) 100–114. https://doi.org/10.1016/j.jct.2017.11.005.

[11] Z. Liu, B. Liu, J. Guo, X. Xin, X. Yang, Conventional and advanced exergy analysis of a novel transcritical compressed carbon dioxide energy storage system, Energy Convers. Manag. 198 (2019) 111807. https://doi.org/10.1016/j.enconman.2019.111807.

[12] L. Chai, S.A. Tassou, A review of printed circuit heat exchangers for helium and supercritical CO2 Brayton cycles, Therm. Sci. Eng. Prog. 18 (2020) 100543. https://doi.org/10.1016/j.tsep.2020.100543.

[13] S. Li, Z. Zhao, Y. Zhang, H. Xu, W. Zeng, Experimental and numerical analysis of condensation heat transfer and pressure drop of refrigerant r22 in minichannels of a printed circuit heat exchanger, Energies. 13 (2020). https://doi.org/10.3390/en13246589.

[14] I.H. Kim, H.C. NO, Thermal-hydraulic physical models for a Printed Circuit Heat Exchanger covering He, He-CO2 mixture, and water fluids using experimental data and CFD, Exp. Therm. Fluid Sci. 48 (2013) 213–221. https://doi.org/10.1016/j.expthermflusci.2013.03.003.

[15] Transport phenomena, R. B. Bird, W. E. Stewart, and E. N. Lightfoot, John Wiley and Sons, Inc., New York (1960). 780 pages. \$11.50, AIChE J. 7 (1961) 5J-6J. https://doi.org/https://doi.org/10.1002/aic.690070245.

[16] T.H. Chung, L.L. Lee, K.E. Starting, Applications of Kinetic Gas Theories and Multiparameter Correlation for Prediction of Dilute Gas Viscosity and Thermal Conductivity, Ind. Eng. Chem. Fundam. 23 (1984) 8–13. https://doi.org/10.1021/i100013a002.

[17] B.E. Poling, J.M. Prausnitz, The Properties of Gases and Liquids, 2001.

[18] C.R. Wilke, A viscosity equation for gas mixtures, J. Chem. Phys. 18 (1950) 517–519. https://doi.org/10.1063/1.1747673.

[19] A. Wassiljewa, No Title, Phys. Z. 5 (1904) 737–742.

[20] E.A. Mason, S.C. Saxena, Thermal Conductivity of Multicomponent Gas Mixtures. II, J. Chem. Phys. 31 (1959) 511–514. https://doi.org/10.1063/1.1730386.

[21] T.H. Chung, M. Ajlan, L.L. Lee, K.E. Starling, Generalized multiparameter correlation for nonpolar and polar fluid transport properties, Ind. \& Eng. Chem. Res. 27 (1988) 671–679. https://doi.org/10.1021/ie00076a024.

[22] D. Browarzik, J.P.M. Trusler, I.G. Economou, J. Ely, C. McCabe, A. Galindo, M.A. Anisimov, M.C. Kroon, E. Lemmon, S. Bottini, E. Brignole, S. Pereda, S. Kjelstrup, D. Bedeaux, S.I. Sandler, Applied Thermodynamics of Fluids, The Royal Society of Chemistry, 2011. https://doi.org/10.1039/9781849730983.

[23] J.W. Leach, P.S. Chappelear, T.W. Leland, Use of molecular shape factors in vapor-liquid equilibrium calculations with the corresponding states principle, AIChE J. 14 (1968) 568–576. https://doi.org/10.1002/aic.690140407.

[24] E. W. Lemmon and and Ian H. Bell and M. L. Huber and M. O. McLinden, NIST Standard Reference Database 23: Reference Fluid Thermodynamic and Transport Properties-REFPROP, Version 10.0, National Institute of Standards and Technology, (2018). https://doi.org/https://doi.org/10.18434/T4/1502528.

[25] M.L. Huber, D.G. Friend, J.F. Ely, Prediction of the Thermal Conductivity of Refrigerants and Refrigerant Mixtures, Fluid Phase Equilib. 80 (1992) 249–261.

[26] W.D. Monnery, A.K. Mehrotra, W.Y. Svrcek, Modified shape factors for improved viscosity predictions using corresponding states, Can. J. Chem. Eng. 69 (1991) 1213–1219. https://doi.org/https://doi.org/10.1002/cjce.5450690523.

[27] S.E. Quiñones-Cisneros, C.K. Zéberg-Mikkelsen, E.H. Stenby, One parameter friction theory models for viscosity, Fluid Phase Equilib. 178 (2001) 1–16. https://doi.org/10.1016/S0378-3812(00)00474-X.

[28] J.F. Ely, H.J.M. Hanley, A Computer Program for the Prediction of Viscosity and Thermal Conductivity in Hydrocarbon Mixtures, (1981).

[29] B.A. Younglove, J.F. Ely, Thermophysical Properties of Fluids. II. Methane, Ethane, Propane, Isobutane, and Normal Butane, J. Phys. Chem. Ref. Data. 16 (1987) 577–798. https://doi.org/10.1063/1.555785.

[30] J.F. Ely, an Enskog Correction for Size and Mass Difference Effects in Mixture Viscosity Prediction., J. Res. Natl. Bur. Stand. (United States). 86 (1981) 597–604. https://doi.org/10.6028/jres.086.028.

[31] M.L. Huber, E.A. Sykioti, M.J. Assael, R.A. Perkins, Reference correlation of the thermal conductivity of carbon dioxide from the triple point to 1100 K and up to 200 MPa, J. Phys. Chem. Ref. Data. 45 (2016). https://doi.org/10.1063/1.4940892.

[32] P.L. Christensen, A.A. Fredenslund, A corresponding states model for the thermal conductivity of gases and liquids, Chem. Eng. Sci. 35 (1980) 871–875. https://doi.org/https://doi.org/10.1016/0009-2509(80)85073-1.

[33] S.E. Quiñones-Cisneros, U.K. Deiters, Generalization of the friction theory for viscosity modeling, J. Phys. Chem. B. 110 (2006) 12820–12834. https://doi.org/10.1021/jp0618577.

[34] S.E. Quiñones-Cisneros, S. Pollak, K.A.G. Schmidt, Friction Theory Model for Thermal Conductivity, J. Chem. Eng. Data. 66 (2021) 4215–4227. https://doi.org/10.1021/acs.jced.1c00400.

[35] The MathWorks Inc., MATLAB. (2022a).

[36] J. Leidenfrost, Brown University, Providence, R.I., U.S.A., (1959).

[37] K.J. Dewitt, G. Thodos, Viscosities of binary mixtures in the dense gaseous state: The methane-carbon dioxide system, Can. J. Chem. Eng. 44 (1966) 148–151. https://doi.org/10.1002/cjce.5450440305.

[38] D.E. Diller, L.J. Van Poolen, F. V. dos Santos, Measurements of the Viscosities of Compressed Fluid and Liquid Carbon Dioxide + Ethane Mixtures, J. Chem. Eng. Data. 33 (1988) 460–464. https://doi.org/10.1021/je00054a020.

[39] A.S. Culllck, M.L. Mathis, Densities and Viscosities of Mixtures of Carbon Dioxide and n-Decane from 310 to 403 K and 7 to 30 MPa, J. Chem. Eng. Data. 29 (1984) 393–396. https://doi.org/10.1021/je00038a008.

[40] F.F. Czubinski, C.J. Noriega Sanchez, A.K. Da Silva, M.A. Marcelino Neto, J.R. Barbosa, Phase Equilibrium and Liquid Viscosity of CO2 + n-Dodecane Mixtures between 283 and 353 K, J. Chem. Eng. Data. 64 (2019) 3375–3384. https://doi.org/10.1021/acs.jced.9b00187.

[41] J. Pátek, J. Klomfar, L. Čapla, P. Buryan, Thermal Conductivity of Carbon Dioxide–Methane Mixtures at Temperatures Between 300 and 425 K and at Pressures up to 12 MPa, Int. J. Thermophys. 26 (2005) 577–592. https://doi.org/10.1007/s10765-005-5566-6.

[42] D. Kim, S.W. Løvseth, A. Arami-Niya, E.F. May, Liquid and Dense Phase Thermal Conductivity Measurements of CO 2 + N 2 and CO 2 + CH 4 Mixtures at Temperatures from 223 K to 308 K and Pressures up to 20 MPa , J. Chem. Eng. Data. (2021). https://doi.org/10.1021/acs.jced.1c00270.

[43] A.I. Johns, A.C. Scott, J.T.R. Watson, D. Ferguson, A.A. Clifford, Measurement of the Thermal Conductivity of Gases by the Transient Hot-Wire Method, Philos. Trans. R. Soc. London. Ser. A, Math. Phys. Sci. 325 (1988) 295–356.

[44] N. Imaishi, J. Kestin, W.A. Wakeham, R. Island, 1. Introduction, (1984) 50–71.

[45] K. Kian, A.M. Scurto, Heat Transport Properties of CO2-Expanded Liquids: N-Hexane, n-Decane, and n-Tetradecane, Ind. Eng. Chem. Res. 56 (2017) 12822–12832. https://doi.org/10.1021/acs.iecr.7b03513.

[46] Aspen Technology Inc., Aspen Plus®, Version V12.1, (2022).

[47] C.K. Zeberg-Mikkelsen, E.H. Stenby, Viscosity Study of Hydrcarbon Fluids at Reservoir Conditions Modeling and Measurements, (2001).

[48] X. Zheng, D. Qu, F. Zhang, Y. Liu, G. Qin, Measurements and calculations of thermal conductivity for liquid n-octane and n-decane, Fluid Phase Equilib. 533 (2021) 112940. https://doi.org/10.1016/j.fluid.2021.112940.

[49] M.G. Freire, A.G.M. Ferreira, I.M.A. Fonseca, I.M. Marrucho, J.A.P. Coutinho, Viscosities of liquid fluorocompounds, J. Chem. Eng. Data. 53 (2008) 538–542. https://doi.org/10.1021/je700632z.

[50] J.H. Dymond, J. Robertson, J.D. Isdale, Transport properties of nonelectrolyte liquid mixtures-IV. Viscosity coefficients for benzene, perdeuterobenzene, hexafluorobenzene, and an equimolar mixture of benzene + hexafluorobenzene from 25 to 100°c at pressures up to the freezing pressure, Int. J. Thermophys. 2 (1981) 223–236. https://doi.org/10.1007/BF00504186.

[51] J.B. Irving, D.T. Jamieson, Thermal conductivity of 13 fluorocarbon liquids, J. Fluor. Chem. 5 (1975) 449–456. https://doi.org/https://doi.org/10.1016/S0022-1139(00)82503-8.

[52] J.F. Counsell, J.H.S. Green, J.L. Hales, J.F. Martin, Thermodynamic properties of fluorine compounds. Part 2.—Physical and thermodynamic properties of hexafluorobenzene, Trans. Faraday Soc. 61 (1965) 212–218. https://doi.org/10.1039/TF9656100212.

[53] R. Le Pierres, D. Southall, S. Osborne, Impact of mechanical design issues on printed circuit heat exchangers, Proc. SCO2 Power Cycle Symp. (2011) 24–25.

[54] A.P. Simanjuntak, J.Y. Lee, Mechanical integrity analysis of a printed circuit heat exchanger with channel misalignment, Appl. Sci. 10 (2020). https://doi.org/10.3390/app10062169.

[55] B. Zohuri, Compact heat exchangers: Selection, application, design and evaluation, 2016. https://doi.org/10.1007/978-3-319-29835-1.

[56] Y. Jiang, E. Liese, S.E. Zitney, D. Bhattacharyya, Design and dynamic modeling of printed circuit heat exchangers for supercritical carbon dioxide Brayton power cycles, Appl. Energy. 231 (2018) 1019–1032. https://doi.org/10.1016/j.apenergy.2018.09.193.

[57] ASME, An International Code 2015 ASME Boiler & Pressure Vessel Code Section III. Rules for Construction of Nuclear Facility Components Division 5 High Temperature Reactors, New York, USA, 2015.

[58] T.W. Watson, H.E. Robinson, Thermal Conductivity of a Sample of SS 316, (1963).

[59] S.J. Dewson, C. Grady, HEATRIC™ Workshop at MIT.

[60] Chemical Engineering Magazine, https://www.chemengonline.com/.

[61] V. Dostal, P. Hejzlar, M.J. Driscoll, High-performance supercritical carbon dioxide cycle for next-generation nuclear reactors, Nucl. Technol. 154 (2006) 265–282. https://doi.org/10.13182/NT154-265.

[62] S. Chung, S.W. Lee, N. Kim, S.M. Shin, M.H. Kim, H.J. Jo, Experimental study of printed-circuit heat exchangers with airfoil and straight channels for optimized recuperators in nitrogen Brayton cycle, Appl. Therm. Eng. 218 (2023) 119348. https://doi.org/10.1016/j.applthermaleng.2022.119348.

[63] V. Illyés, E. Morosini, M. Doninelli, P.-L. David, X. Guerif, A. Werner, G. Di Marcoberardino, G. Manzolini, Design of an Air-Cooled Condenser for CO2-Based Mixtures: Model Development, Validation and Heat Exchange Gain with Internal Microfins, in: 2022: p. V009T28A016. https://doi.org/10.1115/GT2022-82438.

[64] F. Crespi, P. Rodríguez de Arriba, D. Sánchez, A. Ayub, G. Di Marcoberardino, C.M. Invernizzi, G.S. Martínez, P. Iora, D. Di Bona, M. Binotti, G. Manzolini, Thermal efficiency gains enabled by using CO2 mixtures in supercritical power cycles, Energy. 238 (2022) 121899. https://doi.org/10.1016/j.energy.2021.121899.

[65] F. Crespi, G.S. Martínez, P.R. De Arriba, D. Sánchez, F. Jiménez-Espadafor, Influence of working fluid composition on the optimum characteristics of blended supercritical carbon dioxide cycles, Proc. ASME Turbo Expo. 10 (2021) 1–11. https://doi.org/10.1115/GT2021-60293.

[66] O.A. Aqel, M.T. White, M.A. Khader, A.I. Sayma, Sensitivity of transcritical cycle and turbine design to dopant fraction in CO2-based working fluids, Appl. Therm. Eng. 190 (2021) 116796. https://doi.org/https://doi.org/10.1016/j.applthermaleng.2021.116796.

[67] H. "Knapp, S. "Zeck, R. [Technische U.B. (Germany "Langhorst F.R.). Inst. fuer Thermodynamik und Anlagentechnik]," Vapor-liquid equilibria for mixtures of low boiling substances. Pt. 3. Ternary systems, Frankfurt am Main, Germany, F.R.; DECHEMA, Germany, 1989. https://doi.org/https://doi.org/.

[68] N.T. Weiland, B.W. Lance, S.R. Pidaparti, sCO2 Power Cycle Component Cost Correlations From DOE Data Spanning Multiple Scales and Applications, in: 2019. https://doi.org/10.1115/GT2019-90493.

[69] B. Kelly, M. Izygon, L. Vant-Hull, Advanced Thermal Energy Storage for Central Receivers with supercritical coolants, SolarPaces Conf. (2010). https://doi.org/10.2172/981926.

[70] System Advisor Model (SAM), https://sam.nrel.gov/.

[71] G. Manzolini, G. Lucca, M. Binotti, G. Lozza, A two-step procedure for the selection of innovative high temperature heat transfer fluids in solar tower power plants, Renew. Energy. 177 (2021) 807–822. https://doi.org/10.1016/j.renene.2021.05.153.

[72] M. Doninelli, E. Morosini, G. Gentile, L. Putelli, G. Di Marcoberardino, M. Binotti, G. Manzolini, Thermal desalination from rejected heat of a transcritical cycle working with a CO2-based mixture in CSP application: a focus on the MED technology, Sustain. Energy Technol. Assessments. (2023).

# PART 4:
# Applications

*The Part 4 of this thesis collects the published articles on the system design and annual evaluation of the performance.*

*Chapter 8 deals with the analysis of the coupling between a $CO_2$-based power cycle in CSP plant and a thermal desalination unit (multi-effect desalination system) through the heat rejection unit of the cycle. The*

*Chapter 9 explores the use of $SiCl_4$, treated in previous Parts as both pure fluid and in mixture with $CO_2$, as working fluid for biomass-fired plant serving a local district heating network, thus providing combined heat and power. The design and off-design of the plant are explored to assess the economic performance of the proposed system. The research is funded by HICLOPS and COFFEE projects.*

# *Chapter 8 - Thermal desalination driven by $CO_2$ based power cycles*

*THIS CHAPTER IS BASED ON THE ARTICLE: "THERMAL DESALINATION FROM REJECTED HEAT OF POWER CYCLES WORKING WITH $CO_2$-BASED WORKING FLUIDS IN CSP APPLICATION: A FOCUS ON THE MED TECHNOLOGY", PUBLISHED IN SUSTAINABLE ENERGY TECHNOLOGIES AND ASSESSMENTS, ELSEVIER, DOI: HTTPS://DOI.ORG/10.1016/J.SETA.2023.103481*


**Abstract**

This work analyses the integration of concentrated solar power plants based on innovative $sCO_2$ cycles and transcritical $CO_2$-based mixtures cycles with thermal desalination plants adopting the conventional MED technology. In these cogeneration plants, all heat rejected from the cycle is exploited by the desalination system, avoiding any parasitic electric consumption of the fans of the air-cooled heat rejection unit. The MED layout proposed exploits both latent effects, from 3 to 8, and sensible effects, to match at best the temperature level at which the heat is available from the power cycles, delivered to the desalination plant through an intermediate loop of demineralized water.

The cogenerative solution is designed in all its components and proposed in this work as a 100 $MW_{el}$ solar tower CSP plant located in Sevilla, resulting in a yearly production of around 400 $GWh_{el}$/year and between 3.5 and 4.2 $Mm^3$ of freshwater produced, depending on the configuration analysed. Various power cycle layouts are investigated, working with both $sCO_2$ and the innovative $CO_2$+$C_6F_6$ mixture as working fluids. Regarding the solar plant, detailed models for the solar field optical analysis and the receiver thermal analysis are adopted. The seawater desalination plant, when coupled with this category of CSP plants, presents a thermal consumption between 180 and 140 kWh/$m^3$. Finally, the cogenerative plants performances are compared in terms of levelized cost of electricity, with a slight edge for the innovative mixture cycles, and levelized cost of water, in a range between 1 and 2 \$/$m^3$.


## 8.1 Introduction

The global water demand for all uses in the 2010s was about 4600 $km^3$ per year, with an estimated growth by 20-30% in 2050, up to 5500-6000 $km^3$ per year [1]. Today, 3.6 billion people live in areas with shortage of potable water at least one month per year, and this number is expected to increase to 4.8–5.7 billion by 2050 [2]. Desalination of seawater is a well-established technology adopted to reduce the mismatch between local clean water demand and the limited access to conventional water resources, but also to improve the quality of existing brackish water. In 2020 there were 16876 installed desalination plants around the world (20971 including the ones under construction), representing an installed capacity of 97.2 million $m^3$/day [3]. Whilst desalination has great potential, there are barriers that limit its diffusion, such as capital costs, the related greenhouse gases emissions and the management of the produced brine.

Nowadays, the market share of thermal desalination technologies is about 33% of the total, while the membrane-based reverse osmosis (RO) dominates almost the rest of the market [4]. However, thermal desalination is the most applied technology in the Arabian Gulf countries covering about 68% of the installed facilities, due to its reliability in handling critical seawater conditions of high temperature and salinity [5]. The adoption of a thermal based technology avoids the necessity to periodically replace membranes, massively pre-treat the seawater and to shut down the plant for months in case of red tide phenomena [6]. The dominant thermal desalination technologies are multi-stage flash (MSF) and multi-effect distillation (MED), with MED normally preferred for the lower thermal and auxiliary electric energy consumption. The thermal energy consumption of a typical MED process powered by latent heat is 64 kWh/m$^3$ at a first effect temperature of 67°C, whereas the MSF would require at least 105°C to have the same specific energy consumption [7]. Nevertheless, the main issue related to MED processes are scaling phenomena that limit the top brine temperature under 70°C, effectively narrowing the admissible operational temperature range.

Various MED plants are studied in literature adopting conventional steam Rankine cycles to deliver latent heat to the desalination system, usually through bleedings from the turbine, effectively leading to a parasitic load that reduces the electric efficiency of the power block itself. Under this perspective, a feasible application of Rankine cycles within the renewable energy spectrum is concentrated solar power (CSP).

As a matter of fact, among the many renewable energy technologies, CSP with thermal energy storage (TES) can be identified as one of the most interesting technologies to provide dispatchable and flexible electricity to the grid [8]. In particular, CSP plants based on the tower concept (i.e., solar tower) are particularly promising due to the high maximum temperature that can be reached by the heat transfer fluid (HTF). At the current state-of-the-art of solar tower plants, steam Rankine cycles are adopted to convert the thermal energy into electricity. Alternatively, supercritical $CO_2$ cycles ($sCO_2$) have been widely studied in literature to enhance the CSP competitiveness thanks to their smaller weight and volume and to simpler power block layouts [9]. However, a suitable power cycle for CSP applications should operate with high efficiency at high minimum temperatures of the cycle, especially if an air-cooled heat rejection unit is adopted: this key characteristic cannot be necessarily guaranteed with $sCO_2$ cycles due to their drop in cycle efficiency when the compression step is far from the critical point of the working fluid (around 31°C). A possible solution, investigated in the H2020 SCARABEUS project [10], can be the adoption of $CO_2$-based mixtures as working fluids to turn the supercritical cycle into a transcritical one. Mixing carbon dioxide with a dopant that has a higher critical temperature compared with pure $CO_2$ (31°C) allows having transcritical cycles also at high values of minimum temperature (above 50°C), ensuring benefits in terms of efficiency and simplicity of the power block layouts [11]. Among the many possible mixtures for this purpose, $CO_2$+$C_6F_6$ has been already considered for power cycles, in particular for CSP applications within the SCARABEUS project [12]. Moreover, the mixture has been safely proved to be thermally stable above 550°C from an experimental perspective [13], a temperature level coherent with the current state of the art solar tower CSP plant with solar salts as HTF.

This work aims at evaluating the potentiality of a CSP+MED cogeneration system for the simultaneous production of electric energy and demineralized water, where a $CO_2$-binary mixture is adopted as working fluid in the power cycle. After the modelling of all the components at design

conditions, an annual analysis is carried out to compare the performance of difference cycle layouts and the results of a pure $sCO_2$-based cycle. Differently from this work, literature works typically provide techno-economic analyses of CSP+D systems not based on yearly analysis, but only considering the design conditions. Performance maps of the specific thermal energy consumption of a MED plant powered by a low-temperature sensible heat source are also provided, which could be useful to assess the potentiality of a coupling between a different sensible waste heat source (such as heat recovery before the stack of a combined cycle in the range above 45°C). As a matter of fact, in this work the low-grade heat is introduced in the MED system with an intermediate water loop of demineralized water above 45°C, which is the minimum value compatible with the MED technology, since the last MED effect is typically at a temperature around 40-44°C. Economic results are also provided, with maps of the levelized cost of water (LCOW) as function of MED layout, the temperature of the sensible heat source and plant capacity factor, which could be useful for the performance assessment in other locations.

Compared to other literature works, in this analysis the rejected heat from the cycle is fully exploited in the desalination unit, thus avoiding both the electrical consumption of an additional air-cooled condenser and avoiding any electrical production losses, that would be unavoidable with steam Rankine cycles due to the bleeding from the low-pressure steam turbine that feed the MED plant.

The complete and detailed modelling of the entire CSP+D system, including the MED system, the solar field, the thermal receiver, the consumption of the HTF pump and the power cycle is a key factor to accurately estimate the LCOW based on real total equivalent annual operating hours. Ultimately, this work will present the performances of a CSP+MED plant in terms of levelized cost of energy (LCOE) and LCOW considering Sevilla (Spain) as a suitable location, since it is representative of a of a European location with high irradiance, for a power plant with an electric output of 100 $MW_{el}$.

## 8.2 Literature review on the coupling between CSP and MED systems

The coupling between a low-grade renewable heat source and MED systems has been studied in the literature, not only through the integration with power cycles but also with salt gradient solar ponds [14] or with solar collectors and thermal energy storage systems [15] proving to be an effective solution in semi-arid regions. In their review, Ahmed et al. [16] emphasized the need for comprehensive studies on hybrid CSP power systems and desalination plants, also underlining the importance of using available waste heat to improve the economic performance of the plants. An integrated and cogenerative CSP and desalination system (CSP+D) has been proposed and described by Moser et al. [17] from a financial and environmental point of view. Palenzuela [18] carried out a techno-economic comparison between CSP+MED and CSP+RO systems in Mediterranean and MENA regions, and the integration between MED and CSP resulted to be the most favourable in dry cooling conditions. Sankar [19] studied the carbon black industry where both electricity and freshwater are required, concluding that the coupling between CSP and MED yields higher economic benefits and ensures production continuity compared to the round the clock production of the CSP+RO system. In another work, Olwig [20] compared two hybrid CSP+TVC+MED and CSP+RO systems operating with 42 MW steam Rankine cycles powered by a parabolic through CSP plant, resulting in better economic performance for the CSP+RO configuration, with LCOW of about 1\$/$m^3$ computed with feed-in-tariff of 240\$/$MWh_{el}$ for the electricity share. It is nevertheless

necessary to underline that the LCOW, in case of the CSP+RO hybrid system, is strongly dependent on the electricity price. Askari [21] studied a linear Fresnel powered steam Rankine cycle integrated with either MED, RO, TVC+MED and the separate freshwater production by coupling directly MED and TVC+MED with the solar field: the LCOW computed was around \$1.6/$m^3$ for the CSP+MED cogeneration plant and \$3.1/$m^3$ for the separate production. Finally, the attractivity of this cogenerative solution has been demonstrated not only in CSP hybrid plants: for example Moradi et al. [22] studied a hybrid system for combined electric power and freshwater production where the heat from a solid oxide fuel cell is recovered by a Stirling engine providing steam for a multi-effect desalination unit.

As mentioned, in traditional power plants coupled with MED plants, steam is expanded in backpressure turbines with associated power loss of about 3 $kWh_{el}/m^3$ of freshwater [23]. Sharaf et al. [24] analysed a hybrid system composed by a solar ORC and a MED-VC (vapour compression), where the thermal or mechanical compression of the vapour feeding the first effect of the MED improves its thermal energy consumption and increases the water production rate. However, both the systems have drawbacks: the ejector of the thermal vapour compressor requires feeding motive steam that must be generated in a separate boiler by scarifying thermal energy collected from the solar field, while the mechanical vapour compression requires the use of electrical power generated by the solar ORC to power a compressor. The option of increasing the minimum cycle temperature of the ORC to directly reject the latent heat of condensation to the MED unit is totally counterproductive from the efficiency point of view.

Moving from steam cycles to innovative cycles, both for $sCO_2$ and $CO_2$-based mixtures power cycles in CSP applications the heat is rejected at a relatively high temperature (above 80°C, depending on the mixture and the assumptions on the cycle characteristics). This large contribution of thermal power, released to the environment with air cooled heat rejection unit (HRU), can be instead used under a cogenerative perspective in a thermal desalination plant for potable water production: in fact, the non-isothermal heat rejection fits the needs of the thermal level required by the desalination plant, without the need to compromise the net electrical power output. The coupling between the cycle HRU and the MED unit can be achieved with a closed loop of demineralized water that absorbs the heat from the cycle and releases it to the MED system. The coupling between CSP and MED has a twofold beneficial effect: the exploitation of the cycle wasted heat to produce fresh water and the adoption of a water-cooled HRU instead of an air cooled one, with a consequent reduction of the capital and operating cost (avoiding the consumption of auxiliary fans for dry cooling).

In recent years, the study of $sCO_2$ cycles coupled with MED plants has been carried out by a series of authors in the literature ([7], [25], [26]): in those cases, the cycle minimum temperature considered was around the critical temperature of $CO_2$, to exploit real gas effects and optimize the cycle efficiency. Under this assumption: i) not all the available wasted heat from the cycle could be exploited by the desalination plant, since the temperature of the heat introduction to the MED system is limited above 40°C by the seawater temperature preheated in the down-condenser, ii) the design and operation of the compressor of the $sCO_2$ cycle becomes critical [27]. In contrast, a higher value of minimum cycle temperature (51°C) is assumed in this work: this temperature is suitable to describe high ambient temperature locations, enabling to maximize the cogeneration production of

the CSP+D plant, and at the same time to explore the potentiality of $CO_2$-mixtures as working fluid in transcritical cycles for electrical and potable water production.

## 8.3 Methodology: MED system

As discussed, MED plants are a flexible and reliable solution for seawater desalination in case low-grade heat is available. The layout of the process is ideally composed of a cascade of effects (or stages) where a sequence of simultaneous evaporation and condensation processes occurs, obtained by spraying preheated seawater on the top of a tube bundle in which the condensation of the vapour formed in the previous effect takes place.

The specific MED layout and the coupling between the power cycle HRU and the MED are depicted in Figure 1, assumed according to literature [26] for this application and composed of a series of latent and sensible effects. As already mentioned, the heat transferred to the desalination plant is the totality of the rejected heat from the power cycle enabling an efficient coupling between the two systems. The thermal power is exchanged through an intermediate closed loop of demineralized water that represents the cold sink for the cycle and at the same time the hot source for the MED. The demineralized water enters the heat rejection unit (HRU) at 45°C and exits at a temperature that depends on the power cycle characteristics, but always higher than 70°C. The intake seawater enters the down-condenser, acting as a coolant, to allow the condensation of the distilled water vapour produced in the last ($N^{th}$) effect assumed at 44°C (last effect temperature, bottom brine temperature). The necessary seawater to completely condense, in the down-condenser, the water evaporated in the last latent effect is higher than the seawater that can be treated in the MED: hence, a part of it is discharged after the down-condenser. The other stream of seawater feeds the MED unit. In particular, it is preheated to saturated conditions by the demineralized water in the last ($N^{th}$) preheater. After that, a fraction of preheated seawater enters both the last effect ($N^{th}$) and the last sensible effect ($N\text{-}1^{th}$) to evaporate. In particular, the preheated seawater is evaporated in the sensible intermediate effect due to the heat released by the sensible demineralized water loop (with pinch point temperature difference as reported in Table *1*), while in the main effect evaporation occurs through the latent heat of condensation of the vapour formed in the previous effect. The desalinated water vapour produced in both the last sensible and main latent effects are then condensed in the down-condenser. The other fraction of preheated seawater, that is not sent to the last stage, is further preheated to reach saturation conditions at a temperature higher than the one in the previous preheater. As before, a fraction of seawater is evaporated in the sensible and latent effects, while a part is sent to the next preheater. The difference between the last effect and the previous ones is that the steam produced in the previous effects is not condensed with seawater in the down-condenser but is condensed into the subsequent latent effects. In fact, in the latent effects occur simultaneously the condensation of this steam and the evaporation of preheated seawater.

The operating principle is repeated in each effect except for the first effect, where evaporation of seawater (at the maximum temperature, the top brine temperature, limited under 70°C due to scaling issues) occurs exclusively by means of heat transfer from the demineralized water loop.

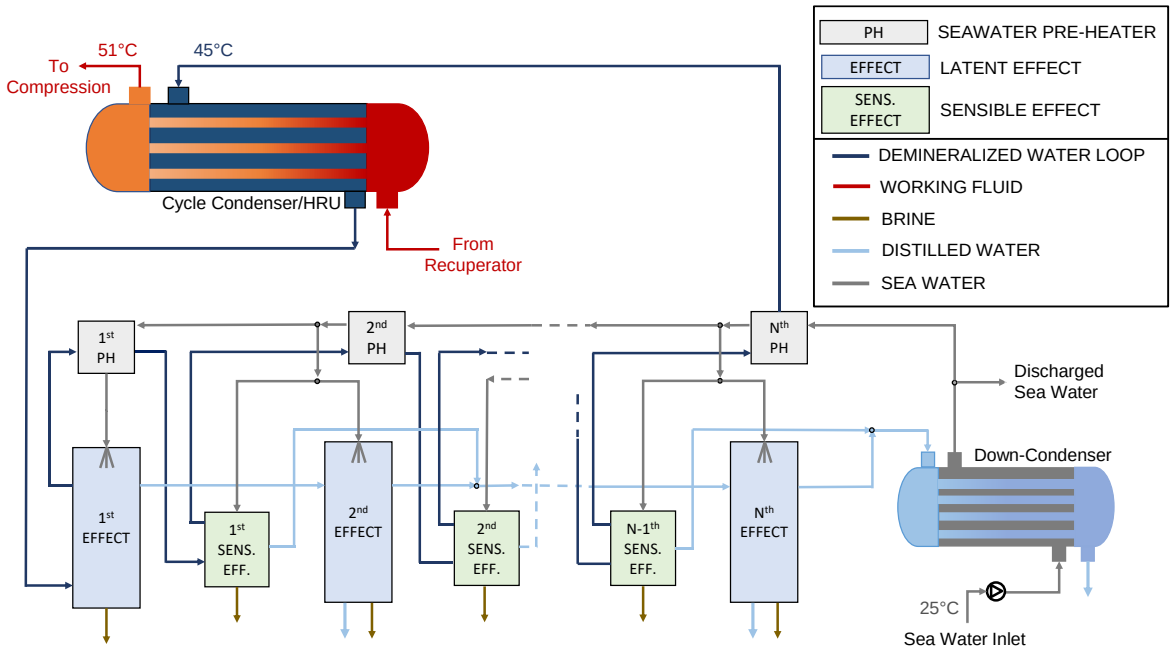


*Figure 1. Plant layout of the MED plant adopted in this work*

The temperature of the vapour formed in the first effect depends on the number of effects considered. In this study, MED units from 3 to 8 effects are considered, with a temperature difference of 3°C and 4°C between each latent effect.

The thermodynamic performances and the economic analysis of various configurations of MED plants, under different conditions and number of effects, have been evaluated under the assumptions of Table 1. The salinity of the rejected brine and the other operating parameters and constraints are controlled by including upper bounds. To avoid scaling issues, the salinity of the rejected brine is limited by the vapor quality imposed at 50% at the outlet of each latent effect: the evaporated half fraction (salt-free) is condensed in the subsequent latent effect, while the other half liquid stream (with a salinity of two times the seawater) is directly rejected, called brine. The split ratio after each preheater (controlling the seawater entering the latent effect, sensible effect and subsequent preheater) is calculated iteratively to simultaneously meet the constraints on the pinch temperature difference in the sensible effect and on the vapour fraction in the latent effect.

*Table 1. Assumptions on the seawater conditions and the MED plant*

| **Parameter** | **Value** |
|---|---|
| Seawater salinity [$g_{SALT}/kg_{WATER}$] | 35 |
| Seawater temperature [°C] | 25 |
| Rejected brine salinity [$g_{SALT}/kg_{BRINE}$] | 70 |
| Last effect temperature [°C] | 44 |
| Demineralized water inlet temperature [°C] | 45 |
| Pinch point between sensible effects [°C] | 3 |
| ΔT between latent effects [°C] | 3 - 4 |

Sharan et al. [26] demonstrated that the adoption of intermediate sensible evaporators in a MED unit powered by a sensible heat source is beneficial to increase the distillate production. This solution has been applied in this work because it allows to cool the demineralized water loop down to 45°C, as required considering the characteristics of the power cycles.

The MED system and its coupling with the sensible heat source (demineralized water) are simulated in Aspen Plus V12 [28] as already done in the literature [29]. The thermodynamic properties of the seawater, treated as a mixture of water and sodium chloride (NaCl), are modelled with the electrolyte Non-Random Two-Liquid (NRTL) model with Redlich-Kwong equation of state.

Additional details on the plant proposed in Figure 1 for a case specific condition, representative of a real plant, are proposed Appendix A, along with some considerations on the technology adopted for the effects and heat exchangers of the MED plant.

## 8.4 Methodology: CSP plant modelling

The MED system is assumed to be coupled with a 100 $MW_{el}$ CSP plant based on a solar tower receiver and located in Sevilla, Spain. The solar field, which is fixed for all the power cycles considered in this work, is generated through SolarPilot [30] assuming a design thermal input to the receiver of 717 $MW_{th}$ and considering the same tower height, heliostats dimensions, receiver height and receiver diameter of the Crescent Dunes power plant, located in Tonopah (NV, USA) [31]. Appendix B reports some of the details on the methodology adopted for the design and simulation of the CSP Plant. The solar field aerial view and the optical efficiency of each heliostat is depicted in Figure 2 (left), while the obtained heat flux map on the receiver at design conditions (summer solstice, solar noon, DNI of 950 W/m²) is shown in Figure 2 (right).

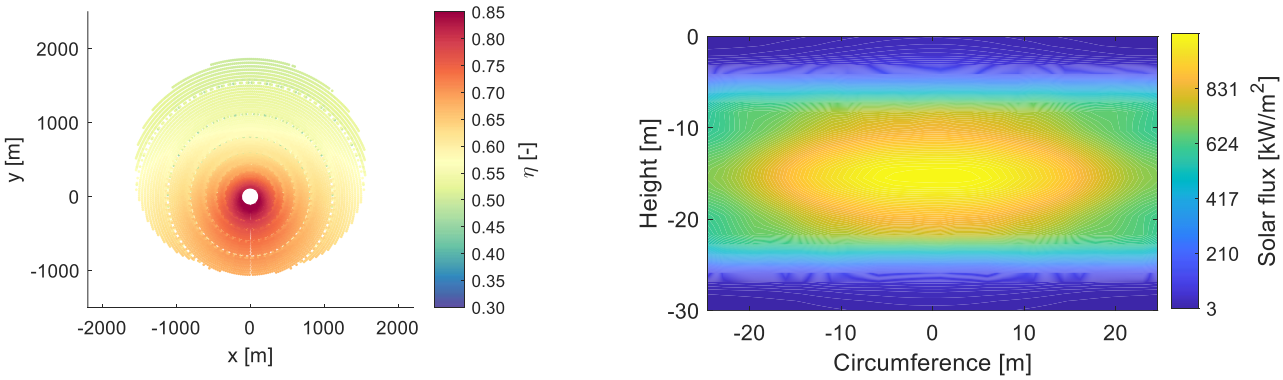


*Figure 2. Planar view of the solar field from SolarPilot: heliostats optical efficiency characterization (left). Thermal flux on the receiver at design conditions (right).*

Regarding the receiver design, two different conditions are considered at constant receiver height and diameter and assuming two separate flow paths of the HTF (one on the east side, the other on the west side). The first design, considered for the scenario with HTF temperature at the receiver inlet equal to 290 °C, has the same characteristics of the Crescent Dunes receiver; the second design,

that is adopted for the cases with HTF temperature at the receiver inlet in the range 415°C – 432 °C, much higher than in the Crescent Dunes plant, has the same receiver height and diameter of the first one, but with different tubes dimensions and arrangement. Once the geometry of the receiver and the solar field are determined, the receiver thermal efficiency is computed with the Modelica package SolarReceiver2D [32]. Additional details on this thermal analysis and the modelling of the receiver circuitation for the second receiver are available in Appendix B. The performance of the receiver in both conditions are reported in Table 2, along with the main assumptions on the receiver geometry, the tube materials, spacing, absorptivity and emissivity.

*Table 2. Receiver dimensions and tube circuitations of the two configurations of tubular receiver considered in this work, adopting solar salts as HTF*

| | **Low HTF inlet temperature** | **High HTF inlet temperature** |
|---|---|---|
| HTF inlet/outlet temperature [°C] | 290 / 565 | 420 / 565 |
| HTF | Solar Salts | |
| Receiver height [m] | 30.5 | |
| Receiver diameter [m] | 15.8 | |
| Design thermal input ($\dot{Q}_{in,rec}$) [$MW_{th}$] | 717 | |
| Coating absorptivity [%], emissivity [%] | 93, 87 | |
| Tubes material | Haynes 230 | |
| Tubes spacing [mm] | 2 | |
| Tube outer diameter / thickness [mm] | 51.5 / 1.65 | 75.5 / 2.1 |
| Tubes per panel / panels per flow path [-] | 66 / 7 | 40 / 8 |
| | **Performances on design conditions** | |
| HTF mass flow rate [kg/s] | 717 | 1350 |
| Pressure drop on the receiver [bar] | 16.7 | 30 |
| HTF pump consumption [$MW_{el}$] | 2.54 | 6.05 |
| Receiver thermal efficiency [%] | 85.44 | 85.37 |

To carry out the yearly analysis, the thermal efficiency in off-design conditions is only determined by the thermal power on the receiver, as suggested in literature [9]. The calculations in off-design are carried out with the same thermal model adopted for the design calculations, scaling the input heat flux map. Figure 3 reports the trends of receiver thermal efficiency and HTF pump electric consumption as function of the ratio between receiver thermal input ($\dot{Q}_{in\ rec}$) and design thermal input ($\dot{Q}_{in\ rec,design}$).

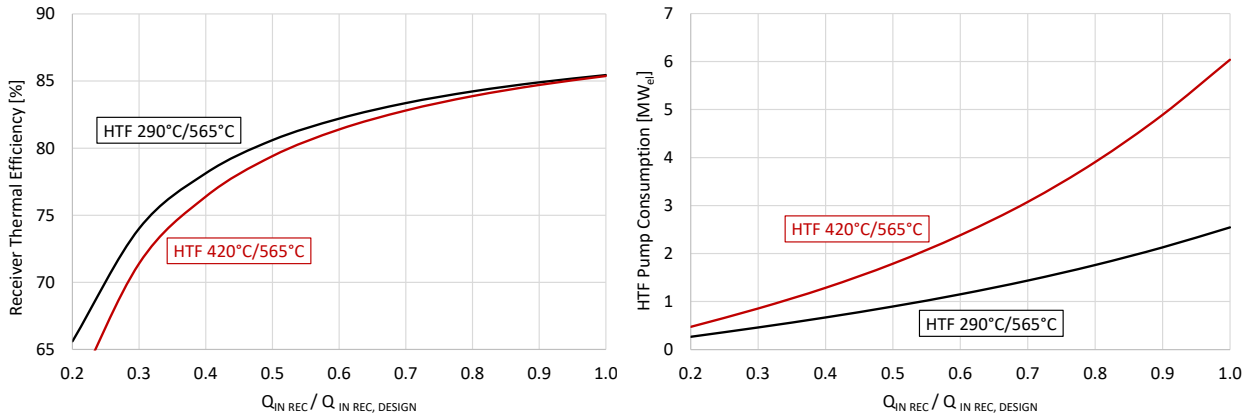


*Figure 3. Receiver thermal efficiency for the two circuitations presented in Table 2 (left). HTF electric pump consumption for the same conditions (right)*

## 8.5 Methodology: Power cycles simulations

In recent years, $sCO_2$ cycles have been studied for application in CSP plants in various configurations, evidencing the recompression layout as optimal for the coupling with CSP, mainly due to the high cycle efficiency [33]. Nevertheless, considering the state-of-the-art HTF (solar salts) with maximum temperature of 565°C, $sCO_2$ cycles are not particularly competitive with respect to steam cycles, mainly due to the limited temperature difference across the primary heat exchanger, leading to HTF temperature differences in the order of 150°C [34]. The adoption of $CO_2$-based mixtures in transcritical cycles helps shifting this paradigm: due to a lower compression outlet temperature and more balanced heat capacities in the recuperator, they present a more limited drop in cycle efficiency at lower heat introduction temperatures than $sCO_2$ cycles. For this reason, in this work the $CO_2$+$C_6F_6$ mixture is adopted both in plant layouts with high cycle efficiency and in the cascade layout, a specific configuration adopted to increase the heat recovery capability of the simple recuperative cycle.

The various cycle layouts considered are represented in Figure 4. The cascade (CAS), the simple recuperative (SIM) and the precompression (PRE) cycles are analysed for the $CO_2$-mixture, already shown very promising for the selected working fluid in literature, particularly in CSP applications [35]. In addition, as reference case, the recompressed (REC) cycle is also investigated with sCO2, since it is the most studied layout for CSP applications. Details on the power block layouts and simulations are discussed in Appendix C, while the necessary assumptions on the cycle non-idealities are shown in Table 3. In the simulations, the gross mechanical power is always set at 100 MW, the turbine inlet temperature is set to a typical value for the CSP plants using solar salts, while the minimum cycle temperature is assumed to be higher than 50°C, consistently with dry cooling in hot environments and to enable an efficient coupling with the MED plant, as shown in Figure 1. The assumptions on the turbomachinery and heat exchangers are aligned with previous works and with the state-of-the-art technologies [36]. The Span-Wagner equation of state [37] is used for the thermodynamic properties assessment of the $sCO_2$, while the PC-SAFT equation of state with optimized interaction parameters is considered from literature [38], used to describe the thermodynamics of the $CO_2$+$C_6F_6$ mixture.

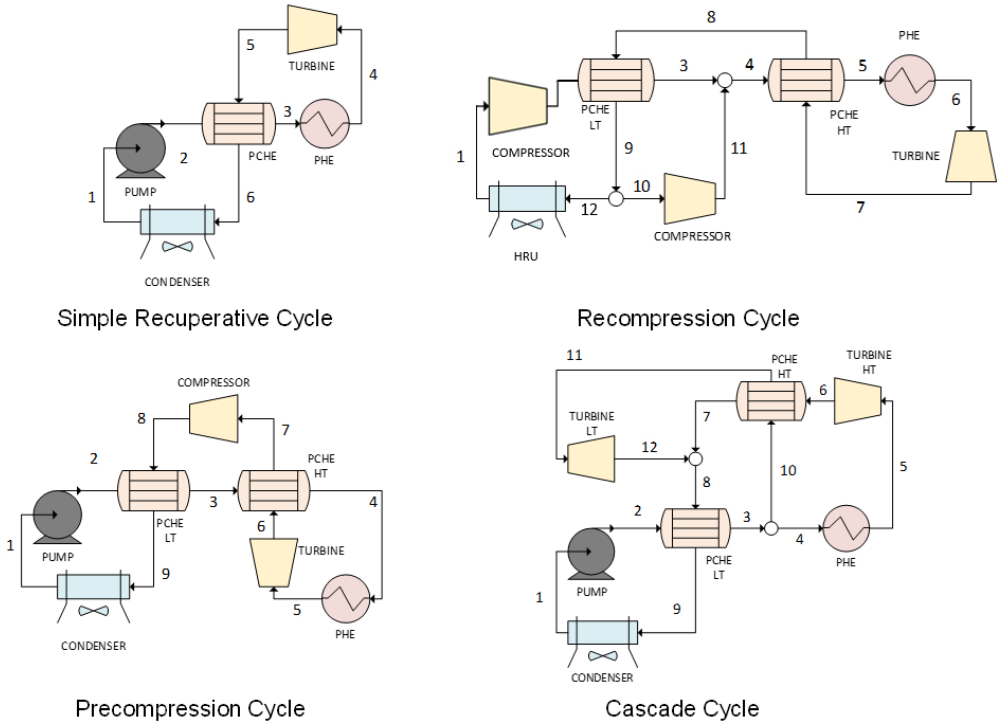


*Figure 4. Power block layouts considered in this work for the $CO_2$-based cycles*

*Table 3. Power cycles assumptions and non-idealities*

| **Power Cycle Parameter** | **Value** |
|---|---|
| Turbine Inlet Temperature [°C] | 550 |
| Turbine Inlet Pressure [bar] | 250 |
| Compression Inlet Temperature [°C] | 51 |
| Turbine / Compression Isentropic Efficiency [%] | 92 / 88 |
| PCHE Minimum Internal Temperature Difference [°C] | 5 |
| Condenser/ HRU Pressure loss [bar] | 2 |
| PHE Pressure loss [bar] | 4 |
| PCHE Pressure loss HP / LP [bar] | 0.5 / 1 |

As previous works evidenced [39], the advantage in term of economic performances of transcritical simple-recuperated $CO_2$-mixture cycles with respect to the recompressed $sCO_2$ cycles are evident especially at high minimum temperature, where pure $CO_2$ is far from the critical point and the compressibility factor sharply increases. The mixture composition, reported in Table 5, is selected optimizing the thermodynamic efficiency for each plant layout adopting the $CO_2$+$C_6F_6$ mixture. The minimum pressure of the transcritical cycles working with the $CO_2$ mixture is the bubble pressure at pump inlet conditions, while it is an optimised parameter in case of $sCO_2$.

As the possibility to employ an efficient simple recuperated layout represents one of the most attractive features of $CO_2$ mixtures compared to $sCO_2$, Figure 5 and Table 4 represent an insight on the comparison between the simple recuperative $CO_2$+$C_6F_6$ cycle and the recompressed $sCO_2$ cycle, for a gross mechanical power of 100 MW.

*Table 4. Performance of two representative power cycles investigated in this work, including the thermal and mechanical power balance*

| Variable | $sCO_2$ Cycle | $CO_2$+$C_6F_6$ Cycle |
|---|---|---|
| Plant layout | Recompressed | Simple Recuperative |
| Mass Flow Rate [kg/s] | 1410 | 1218 |
| Specific Work [kJ/kg] | 71.5 | 82.1 |
| Pump/Main Compressor Power [MW] | 31.0 | 25.0 |
| Recompressor Power [MW] | 22.6 | - |
| Turbine Power [MW] | 153.6 | 125.0 |
| Recuperator Thermal Power [MW] | 163 (LT) - 436 (HT) | 623 |
| PHE Thermal Power [MW] | 237.8 | 238 |
| HRU Thermal Power [MW] | 137.8 | 138 |
| $UA_{PCHE}$/PHE Thermal Power ratio [1/K] | 0.22 | 0.15 |
| Working fluid inlet PHE Temperature [°C] | 416.6 | 401.1 |
| Working fluid inlet HRU Temperature [°C] | 100.4 | 81.7 |
| Gross Cycle Efficiency [%] | 42.8 | 42 |
| Electromechanical losses [$MW_{el}$] | 2 | 1.5 |
| Cycle Electric Efficiency [%] | 42.0 | 41.4 |

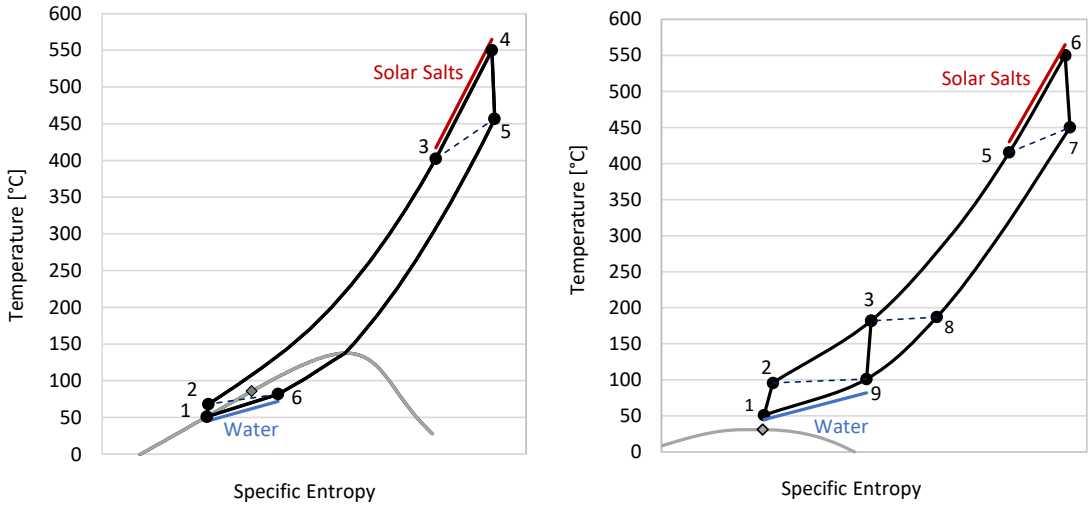


*Figure 5. T-s diagrams of the two power cycles proposed in Table 4: simple cycle with $CO_2$+$C_6F_6$ mixture (left), $sCO_2$ recompressed cycle (right)*

In Table 5 are listed the key performance indicators of the various power block investigated in this work, along with the maximum temperature reached by the demineralized water in the hot side of the condenser, assuming a pinch point of 3°C between the working fluid and the cooling flow of demineralized water. The heat rejection process from the power cycle to the closed loop (in the top left of Figure 1) under these constraints is shown in the T-Q diagrams of Figure 6, again for the simple recuperative cycle with the $CO_2$+$C_6F_6$ mixture and the recompressed $sCO_2$ cycle: from the figure it is clearly visible that higher maximum temperatures of the demineralized water intermediate flow are possible with $sCO_2$ cycles, allowing for a more performant coupling between the power cycle and the bottom desalination plant.

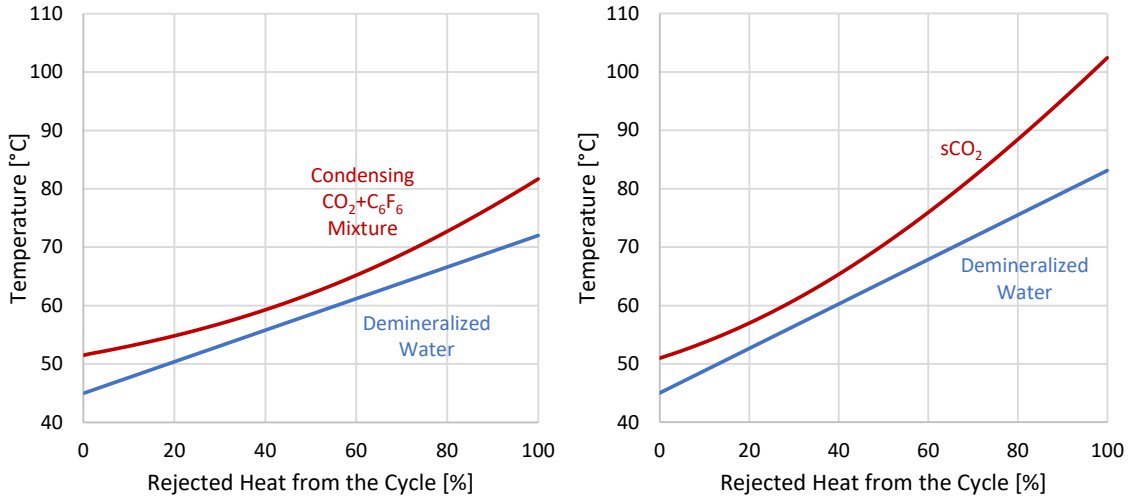


*Figure 6. T-Q diagrams of the HRU of the two power cycles presented in Table 4*

*Table 5. Cycles investigated in this work: focus on the heat introduction (by the HTF) and heat rejection (in the HRU) processes*

| | Dopant molar fraction [%] | Cycle gross efficiency [%] | HTF temperatures [°C] | Working fluid at HRU inlet [°C] | Temperature range demineralized water [°C] |
|---|---|---|---|---|---|
| SIM cycle | 13% $C_6F_6$ | 42.0 | 420 – 565 | 81.9 | 45 – 72.0 |
| PRE cycle | 12% $C_6F_6$ | 43.3 | 415 – 565 | 81.4 | 45 – 71.3 |
| CAS cycle | 12% $C_6F_6$ | 39.5 | 288 – 565 | 82.7 | 45 – 72.7 |
| REC cycle | Pure $CO_2$ | 42.8 | 432 – 565 | 100.4 | 45 – 82.2 |

## 8.6 Methodology: Yearly analysis

Once the methodology to model the CSP+D plant is presented, the yearly analysis is also detailed and described in this chapter, as the focus of this work is to determine the yearly performances of the cogenerative plants.

Since the cycles and the MED plant are decoupled by the demineralized water loop, the inlet and outlet conditions of the working fluid across the HRU are assumed to be always constant, in order

not to influence the specific freshwater production. To do so, the power cycles must run always at constant load (full load), when thermal input is available in the HTF from the solar field, and always at constant cycle minimum temperature. In fact, a partial load condition would: i) penalize the cycle efficiency with respect to a full load condition, reducing the electric power produced, ii) decrease the inlet temperature of the working fluid in the HRU, meaning that not all the heat rejected would be available at a temperature range above 45°C in the demineralized water loop. Since running the cycle in part load and decreasing the cycle minimum temperature would negatively affect the specific thermal consumption of the MED system, these two conditions are not considered.

An overview of the yearly analysis carried out in this work is represented in Figure 7: starting from the hourly DNI data (available in the SolarPilot database for Sevilla and detailed in Appendix D), the optical efficiency of the solar field is evaluated for each sun position (reported in Appendix D). Then, according to the thermal model already presented and the results of the receiver thermal efficiency in Figure 3, the thermal power absorbed by the HTF is computed for each hour of the year. Adopting a simplified TES operating strategy, the thermal power fed to the power cycle is computed: in case the power block is running at full load and the hot tank of the TES is full, a partial defocusing of some heliostats is assumed, to reduce the receiver thermal input. The TES size, on the other hand, is computed for each power cycle based on the optimal LCOE condition.

Ultimately, it is carried out an hourly analysis of the electric energy and the thermal energy rejected to the MED system. Coupling each power cycle with the intermediate loop of demineralized water, as presented in Table 5, allows to define the specific thermal consumption of the MED, univocally determined for each demineralized water maximum temperature and number of MED effects, as evidenced in the next section. Accordingly, the yearly overall energy produced and the yearly overall freshwater produced are determined for each power cycle investigated, with the solar plant proposed in this work.

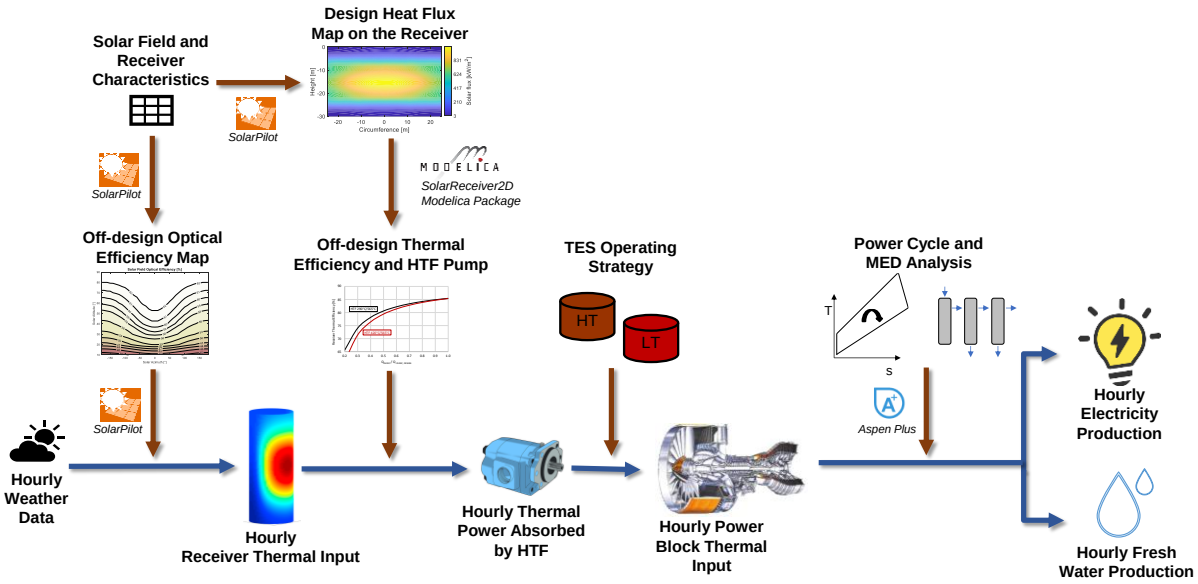


*Figure 7. Flowchart of the yearly analysis proposed in this work on an hourly basis*

## 8.7 Economic analysis

To correctly estimate the techno-economic performances of the cogenerative CSP+D plants, capital cost functions must be selected from literature. The euro-to-dollar conversion is applied, if necessary, with the average conversion factor of 2021. Costs functions are actualised to 2021 considering the Chemical Engineering Plant Cost Index (CEPCI) index. About the MED plant, the LCOW has been evaluated considering both the capital (CAPEX) and operating (OPEX) costs under the different operating conditions (heat source temperature, number of effects, heat input) according to Equation (1).

$$LCOW\left[\frac{\$}{m^3}\right] = \frac{MED\ Plant\ CAPEX \cdot CRF + MED\ Fixed\ OPEX}{Yearly\ Fresh\ Water\ Produced} \quad (1)$$

The correlation developed by Kosmadakis et al. [40], fitted on over 28 existing MED plants, has been used to evaluate the CAPEX of the MED system as a function of the daily distillate product and the evaporator/condenser area. The estimation of the heat transfer area is relevant for the capital cost assessment, since the evaporator/condenser bundles consist of a large portion of plant's cost. A 20% increment factor has been applied to the calculated area of the latent effects to consider the realistic mean temperature difference due to thermodynamic losses that have been estimated under the geometry assumptions for the tube bundle in Appendix A.

The annual operating costs are evaluated considering the total equivalent operating hours of the CSP plant, including the characteristics of Table 6, such as: the cost of chemicals necessary to pre-treat the seawater, the direct labour cost and the electricity pumping cost of the seawater from the intake (assuming a total head developed of 3.5 bar), of the brine and distillate products, and of the demineralized water in the closed loop (assuming a pressure drop of 1 bar across the MED plant).

*Table 6. Economic assumptions for the cost model of the MED system*

| Parameter | Value |
|---|---|
| Discount rate / CRF [41] | 8% / 8.88% |
| MED Plant lifetime | 30 years |
| Electric energy cost | 150 $/MWh$_{el}$ |
| Chemicals cost [42] | 0.024 $/m$^3_{seawater}$ |
| Labour cost [42] | 0.05 $/m$^3_{seawater}$ |

Regarding the CSP plant, the LCOE is computed accounting for the formulation of Equation (2):

$$LCOE\left[\frac{\$}{MWh_{el}}\right] = \frac{CSP\ Plant\ CAPEX \cdot CRF + CSP\ Fixed\ OPEX}{Yearly\ Net\ Electric\ Energy\ Produced} + CSP\ Variable\ OPEX \quad (2)$$

To estimate the LCOE, specific cost functions are necessary for each of the plant components. For the power block, the cost of turbines, pumps, compressors, and recuperators are taken from Weiland [43], while for both PHE and water-cooled condensers/HRU the cost functions from Weiland are not applicable. To estimate their costs, the two heat exchangers are modelled in Thermoflex [44] as shell

and tube HX fitting the pressure drops of Table 3, adopting Inconel 617 for the tubes of the PHE and carbon steel for the tubes of the HRU, since the HX capital cost are provided by the tool.

The cost functions of the solar tower, receiver, HTF pump and HTF piping are taken from Kelly at al [45], actualized with the CEPCI index at the year 2021, and resulting in capital costs very similar to the ones proposed by System Advisor Model (SAM) [46]. The solar field cost, instead, is assumed equal to 140 $/m$^2$ of heliostat area as suggested in SAM. The TES cost, modelled as a direct two tanks solar salts system, is computed considering the cost analysis presented in Manzolini et al [47].

Additional financial assumptions and OPEX related to the CSP plant are listed in Table 7, mainly assumed from SAM.

*Table 7. Financial assumptions for the cost model of the CSP plant*

| Parameter | Value |
|---|---|
| Discount rate / CRF | 8% / 8.88% |
| CSP Plant lifetime | 30 years |
| Fixed OPEX [$/kW/year] | 66 $/kW/year |
| Variable OPEX [$/MWhel] | 3.5 $/MWhel |
| CSP Indirect + Contingency Costs | 20% of the overall CSP CAPEX |

## 8.8 Results

In this chapter the thermodynamic and economic performances of the cogenerative CSP+D plants based on solar tower CSP plants are evidenced and discussed.

At first, the specific thermal consumption of the investigated MED system, proposed in Figure 1, is shown in Figure 8 as function of the number of latent effects and the maximum temperature of the demineralized water: the results assumed a 3°C temperature difference between the latent effects as this condition is considered preferable (by around -15%) with respect to the one with 4°C of temperature difference between latent effects.

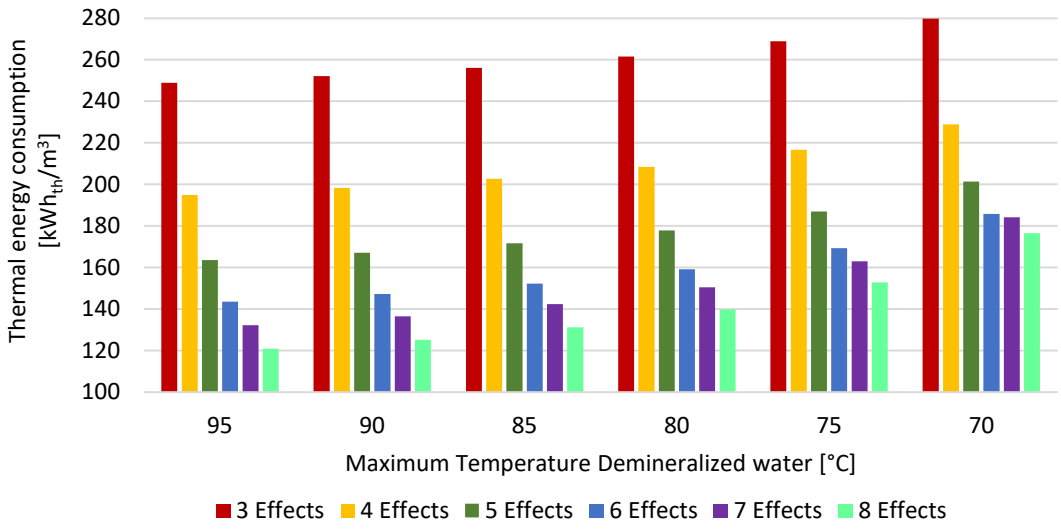


*Figure 8. Specific thermal energy consumption per unit of freshwater (m³) produced with the MED plant described in this work*

Accordingly, the temperature of the demineralized water (heat source for the MED plant) considerably affects the thermal energy consumption and, thus, the instantaneous and annual production of freshwater. Fixing the number of effects, the thermal consumption decreases with the increase of the temperature of the heat source due to a larger percentage of heat introduced in in the first latent effect, whose steam product drives the evaporation of the seawater in the following stages.

On the other hand, the total equivalent annual operating hours (EOH) of the CSP power plant plays a significant role for the annual analysis. In a CSP plant, the annual EOH depends mainly on the weather data and the design choices of TES size and solar multiple. Since the LCOW, as expressed in Equation (1), is strictly related to the annual fresh water produced, its value depends on the location in which the solar plant is installed. To increase the generalisation of the study, the LCOW has been calculated at three annual EOH which can be representative of both peaker plants and baseload plants, or to make possible the evaluation at different geographical locations and solar field design. The results of LCOW at different annual EOH are presented in Figure 9 for the case with 3°C of temperature difference between effects, and in Figure 10 for the case of 4°C effects temperature difference. From the results it is possible to notice a strong dependence of the LCOW on the EOH.

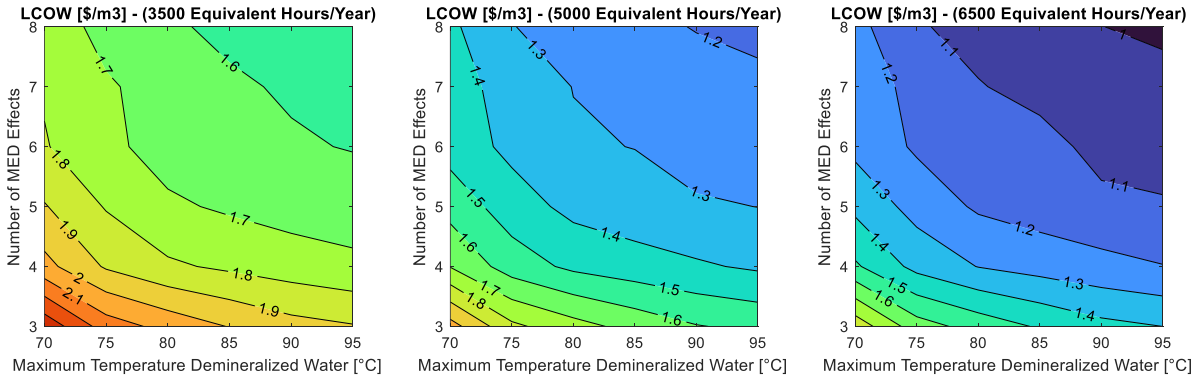


*Figure 9. LCOW [$/m³] of freshwater produced with the MED plant in Figure 1, as function of the number of MED effects and maximum temperature of demineralized water. Results for* $\Delta T_{effects} = 3°C$

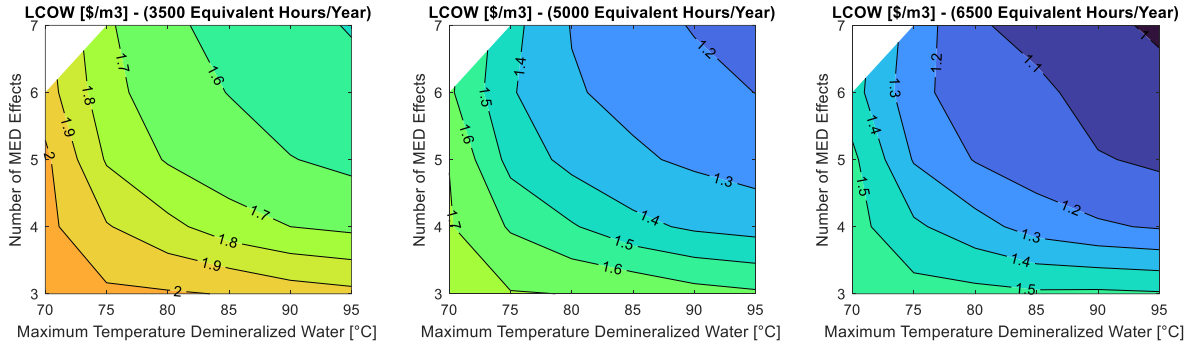


*Figure 10. LCOW [$/m³] of freshwater produced with the MED plant in Figure 1, as function of the number of MED effects and maximum temperature of demineralized water. Results for* $\Delta T_{effects} = 4°C$

For the specific analysis of this work, the MED plants are proposed with 8 effects and an average apparent difference between the latent effects of 3°C, representing the most favourable configuration for the LCOW. According to the LCOE analysis, the optimal TES size is obtained at 8 equivalent hours, for all the power cycle configurations. The yearly results are proposed in Table 8 in terms of electric energy produced (accounting for the generators and motors electromechanical efficiency of 99%, as showed in Table 4), thermal rejected energy to the desalination plant and some other key performance parameters of the CSP plant. Considering the nature of the cogenerative plant, the resulting energy produced does not include any electric consumption related to the power cycle heat rejection system (it is allocated to the operating costs of the MED), but includes the yearly energy absorbed by the HTF pump, computed according to the results of Figure 3, and specific to each HTF temperature range of Table 5. As the resulting performances of the MED plant are strictly related to the operating conditions of the CSP plant (in terms of yearly rejected energy, annual EOH, temperature of the demineralized water/heat source), they are also presented in the bottom of Table 8.

*Table 8. Techno-Economic results of the CSP+D plants proposed in this work*

| | $CO_2$+$C_6F_6$ Simple | $CO_2$+$C_6F_6$ Precompressed | $CO_2$+$C_6F_6$ Cascade | $sCO_2$ Recompressed |
|---|---|---|---|---|
| | | **CSP plant results** | | |

| | | | | |
|---|---|---|---|---|
| Yearly Electric Energy [$GWh_{el}$/year] | 407.9 | 414.9 | 395.5 | 404.0 |
| Yearly Energy to MED [$GWh_{th}$/year] | 581.1 | 562.9 | 620.2 | 576.5 |
| TES Size [h] | 8 | 8 | 8 | 8 |
| Equivalent Hours of Defocusing [h/year] | 74 | 122 | 14 | 83 |
| Solar Multiple | 2.51 | 2.59 | 2.36 | 2.53 |
| Specific CSP CAPEX [$/$kW_{el}$] | 5158 | 5265 | 5035 | 5530 |
| LCOE [$/$MWh_{el}$] | 131 | 131 | 132 | 139 |
| | **MED plant results (8 effects, $\Delta T_{effects} = 3°C$)** | | | |
| EOH [h/year] | 4069 | 4149 | 3955 | 4040 |
| LCOW [$/m$^3$] | 1.56 | 1.56 | 1.58 | 1.44 |
| Annual fresh water [$Mm^3$/year] | 3.58 | 3.54 | 3.74 | 4.22 |

From an energetic perspective, the transcritical cycle with the $CO_2$+$C_6F_6$ mixture (particularly in the precompression layout) shows higher electric performances than the $sCO_2$ counterpart, with +3% in energy production and a lower specific CAPEX, with LCOE reductions up to 6%. Regarding the freshwater production, the $sCO_2$ cycle can definitely benefit from a lower thermal specific consumption: a value around 135 kWh/$m^3$, 10% lower than the one of the $CO_2$+$C_6F_6$ mixture (near 150 kWh/$m^3$). Accordingly, the freshwater production for the $sCO_2$ plant is higher on a yearly basis, and lower LCOW are computed (1.44 \$/$m^3$ against the 1.56 \$/$m^3$ of the mixture power plant). In fact, the different heat rejection temperature from the HRU of the two power cycles is the consequence of these results, benefiting the $sCO_2$ power cycle. Additional comments to the results and few comparisons with literature results are available in Appendix E.

## 8.9 Conclusions

By adopting a cogenerative CSP+D system based on the MED technology and innovative $CO_2$-based power cycles it is possible to fully exploit the rejected heat from a high-minimum temperature closed power cycle without affecting its thermal efficiency, avoiding the parasitic electric consumptions of air-cooled HRU: this approach marks a significant difference with respect to the state of the art of CSP+D plants based on steam cycles, that feed the MED through bleeding from the steam turbine. Differently from the literature exploring $sCO_2$ power blocks, in this work the totality of the heat rejected from the power cycle of a CSP plant is introduced in the desalination plant, due to the high value of minimum temperature of the power cycle at design, a condition in which $CO_2$-mixtures have electrical performances higher than $sCO_2$ cycles.

With respect to other solar desalination systems (like RO coupled with photovoltaic plants), with a CSP+MED system the waste product of the power production section can be adopted as input to the desalination plant, evidencing the inherent excellent integration capability of these two systems. As results, specific thermal energy consumptions around 130-150 kWh/$m^3$ are computed with $CO_2$-

based cycles, per unit of desalinated water: these levels are twice the range achieved with steam cycles, but are obtained without electric power loss from the electric side, as no bleedings are foreseeable in $CO_2$ plants.

An annual analysis of a CSP plant with a state-of-the-art solar tower and solar salts as HTF is carried out, adopting specific tools, selecting Sevilla (Spain) as a reference European location with high solar irradiation. According to this analysis, designing the solar plant and fixing the power cycle to a reference size of 100 $MW_{el}$, annual equivalent hours in the order of 4000 h/year are achievable: these values are tied to promising ranges of LCOE (around 130 $/MWh$_{el}$) and specific CAPEX of the overall CSP plants (in the order of 5000 $/kW$_{el}$).

Regarding the power cycle analysis, the innovative $CO_2$ mixture in transcritical cycles proved to be effective in the reduction of the LCOE of a CSP tower plant by about 6%, with a much simpler cycle layout if compared to the recompressed $sCO_2$, suggesting an easier control and operation of the plant. On the other hand, looking at the MED process, the pure $CO_2$ plant outperformed the $CO_2$ mixture in terms of both LCOW and annual distillate production due to the lower thermal energy consumption.

In the scenario analyzed, LCOW in the order of 1.4-1.6 $/m$^3$ are obtained, but LCOW around 1.1-1.2 $/m$^3$ are foreseeable with plants designed in locations characterized by a higher annual radiation and TES capacity, by exploiting capacity factors of the solar plant in the order of 70%.

Future works will develop and asses coupling between another CSP+D technology, not based on the MED but on the forward osmosis, as part of the research on this topic.

## Nomenclature

**Acronyms/Abbreviations**

| | | | |
|---|---|---|---|
| BPE | Boiling Point Elevation | LCOW | Levelized Cost of Water |
| CAPEX | Capital Expenditure | LP | Low pressure |
| CEPCI | Chemical Engineering Plant Cost Index | LT | Low temperature |
| CRF | Capital Recovery Factor | MED | Multi-Effect Distillation |
| CSP | Concentrated Solar Power | MSF | Multi-Stage Flash Distillation |
| D | Desalination | OPEX | Operational Expenditure |
| DNI | Direct Normal Irradiance | PCHE | Printed Circuit Heat Exchanger |
| EOH | Equivalent Operating Hours | PHE | Primary Heat Exchanger |
| h | Hours | PRE | Precompression |
| HP | High pressure | Q | Thermal duty |
| HT | High temperature | RC | Recompression |
| HTF | Heat transfer fluid | RO | Reverse Osmosis |
| HX | Heat exchanger | SR | Simple Recuperated |
| LCOE | Levelized Cost of Electricity | T | Temperature |

**Symbols**

| | |
|---|---|
| η | Efficiency |
| ΔT | Temperature difference |

**Subscripts and superscripts**

| | |
|---|---|
| el | Electric |
| Rec | Receiver |

## Appendix A: Details on the MED modelling

In this appendix are described some of the hypothesis done in the modelling of the MED plant, along with a focus on a specific condition of MED plant, selected as representative of the technology.

The T-Q diagram proposed in Figure 11 helps in visualizing the heat transfer process from the demineralized water loop side, assuming an arbitrary configuration of the MED plant, with 4 latent effects and the maximum temperature of the hot source at 85°C: in the first latent effect, the demineralized water releases most of its energy content to a feed seawater stream allowing it to partially evaporate, with an approach temperature of 3°C. Then, the temperature of the sensible heat source defines the top brine temperature and the numbers of effects of the MED plant. The rest of thermal energy available from the heat source is then transferred through the feed preheaters and the sensible intermediate effects. The vapour formed in the latent first effect passes through a mesh-wire demister entering the second latent effect and act as a heat source for the subsequent stage, by releasing its latent heat of condensation. Starting from the second latent effect, the main driving force is the temperature difference between the latent effects. The condensed freshwater streams produced in each effect by the sub-atmospheric condensation of the vapour formed in the previous stage are then pumped and collected.

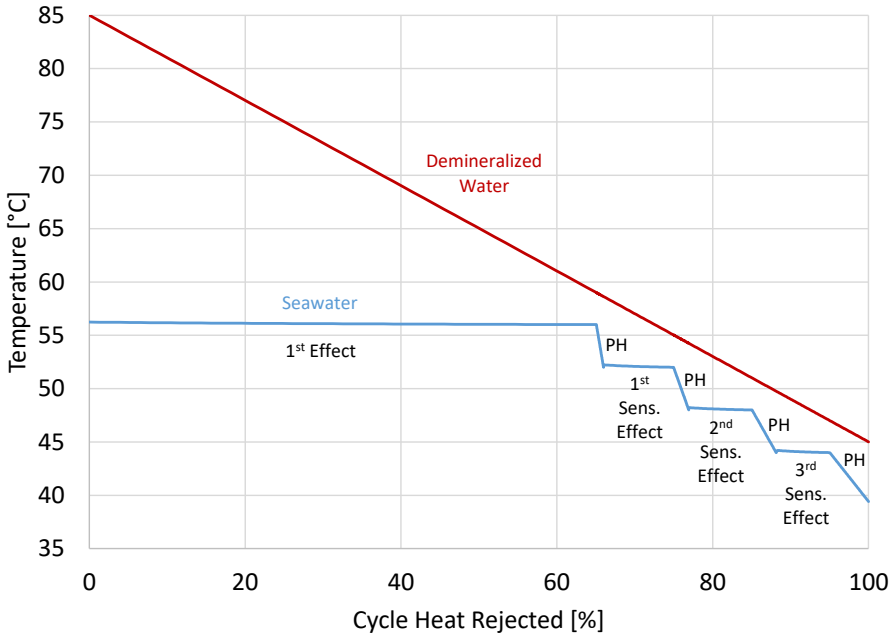


*Figure 11. T-Q diagram of the MED layout proposed in Figure 1, assuming 4 effects and a maximum temperature of the demineralized water of 85°C*

The core of the main effects consists of a horizontal falling-film evaporator/condenser tube bank where the condensing steam from the previous effect is condensed inside the tubes and the preheated seawater feed is sprayed on the outer surface of the tubes to evaporate from a liquid film. Other characteristics of the single stage are a bottom un-evaporated brine pool, and a mesh-wire demister for the vapour entering the next effect. Once it is formed, the vapour is subject to a series of pressure drop trough the bundle, the mesh-wire demister, and during in-tube condensation in the next effect. These pressure drops represent thermodynamic losses, since pressure and temperature are strictly related during phase change, which causes a temperature drop during condensation. The total pressure drop in each stage have been computed considering the geometric parameters of a typical low temperature-MED plant [49] to assess the realistic mean temperature difference between the two sides of the evaporator/condenser. The total vapour pressure drop (and then the corresponding temperature drop) is calculated as the sum of the three terms: the pressure drop through the tube bundle, the one in the mesh-wire demister (considering a velocity of the vapour that avoids entrainment [50]), and an average pressure drop during in-tube condensation in the next effect. The correlations adopted are described in the work of Zhou et al. [49]. While the vapour encounters a temperature depression, the temperature of the evaporating sea water sprayed on the bundle undergoes an increase due to boiling point elevation (BPE) that reduces the available mean temperature difference, increasing the area necessary for the evaporator/condenser.

In this work, it is decided not to recirculate the brine since the steam obtainable from its flashing at the entrance to the next stage is computed to be in the order of 1% of the total distillate. Non-equilibrium allowance effects are therefore not treated, even for the absence of flashing boxes. Thus, a brine pool is maintained just to reduce the thermal losses to the environment improving the thermal efficiency of the effect, but the exceeding brine is mixed to the discharged fraction of seawater after the down condenser. Since the amount of discarded seawater is much larger than the amount of brine collected in each effect, this allows to reject into the sea a medium-low temperature water (at about 38°C) with a low salts content (near the seawater salinity), reducing the environmental impact of the rejected stream.

**Appendix B: Additional information on the design of the CSP plant**

The design of the solar field is carried out with the tool SolarPilot. The main solar field characteristics are provided in Table 9. The heliostats aiming strategy "Image Size Priority" with a maximum offset factor of 4 is adopted for the solar field simulation, as it ensures a good compromise between homogeneity of the flux distribution and optical efficiency [51], considering the fixed dimensions of the receiver; the maximum offset is chosen in order to meet a peak heat flux on the receiver of 1 MW/m$^2$. The simulation in SolarPilot are carried out assuming the sun position at the solar noon of the summer solstice.

*Table 9. Main solar field characteristics modelled in SolarPilot*

| Parameter | Value |
|---|---|
| Heliostats dimensions [m] | 11.3 x 10.4 |
| Heliostats number | 10924 |
| Tower height (including the receiver) [m] | 195 |
| Heliostats reflectivity / fouling factor [%] | 95 / 95 |

| | |
|---|---|
| Heliostats surface slope error [mrad] | 1.53 |

As mentioned in the manuscript and reported in Table 2, a receiver circuitation different from the one in Crescent Dunes is studied, for an HTF temperature range of 565-420°C. Since no existing CSP plant has these characteristics, the receiver circuitation is obtained through a simplified optimization procedure based on the receiver thermal and hydrodynamic performances at design conditions, already adopted in literature by the authors [52]. In detail, the number of tubes per panel, the number of panels per flow path, and the tubes outer diameter are varied aiming at maximizing the so called fictitious thermal power ($\dot{Q}_{fictitious}$). The latter is the thermal power absorbed by the HTF at design conditions depurated from the thermal power required by the power block to produce the electricity needed to run the HTF pumps. For each combination of tubes outer diameter and number of panels per flow path, the number of parallel tubes is determined assuming a distance between the adjacent tubes of 2 mm; then, $\dot{Q}_{fictitious}$ is computed through Equation (3) where $\dot{Q}_{in\,rec,design}$ is the receiver thermal input, $\eta_{th}$ is the receiver design thermal efficiency, $P_{HTF,pump}$ is the electric power consumed by the HTF circulation pump at design conditions (assuming a pump efficiency of 80%), and $\eta_{cycle}$ is the power cycle nominal efficiency.

$$\dot{Q}_{fictitious} = \dot{Q}_{in\,rec,design} \cdot \eta_{th} - \frac{P_{HTF,pump}}{\eta_{cycle}} \quad (3)$$

For each combination of tubes diameters and number on panels, $\eta_{th}$ and $P_{HTF,pump}$ are obtained, assuming an HTF temperature at the receiver inlet of 420°C, through the Modelica package SolarReceiver2D [32], that computes also the HTF pressure drop across the receiver. The latter is a two-dimensional dynamic thermal model that allows simulation of any type of external cylindrical receiver. $\eta_{cycle}$ is assumed equal to 42% that represents the average value of the power cycle efficiencies computed in this work for the configurations adopting the HTF temperature range of 420-565°C. The thermal model is run assuming a wind speed of 5.8 m/s, which is an average value on the top of the tower in the plant location [53]. The resulting receiver characteristics are reported in Table 2, highlighting that a low temperature variation of the HTF within the receiver makes convenient the adoption of a lower number of tubes per panel, with a larger tube diameter. Despite the receiver design optimization is carried considering a HTF temperature at the receiver inlet of 420°C, the obtained receiver characteristics are adopted also for the cases with inlet temperature 415°C and 432°C (see Table 6).

**Appendix C: Description of the power block layouts**

The computational tool adopted in this work for the simulations of the power cycle performances is Aspen Plus, a commercial software applied for modelling chemical processes and power cycles for several applications, which integrates mass and energy balances with dedicated equations of state as well as several specific component parameters starting from a component library or user-defined components model.

As mentioned, the CSP plant adopts a direct storage system, meaning that the HTF and the storage fluid coincide with the same heat transfer medium (solar salts). Four power block layouts are considered for the simulation of the innovative $CO_2$-based cycles: the simple recuperative cycle, the recompressed cycle, the precompressed cycle and the cascade cycle, depicted in Figure 4. As a matter

of fact, a previous literature work developed within the SCARABEUS project evidenced that all these power block layouts present similar techno-economic effectiveness, when implemented in a CSP plant with a CO2-based working fluid [35].

The simple recuperative cycle consists of a compression step to increase the pressure of the mixture from saturated liquid conditions to the maximum cycle pressure (from 1 to 2), followed by the working fluid preheating in the recuperator (PCHE) (from 2 to 3), reaching the maximum cycle temperature after the primary heat exchanger (PHE) (point 4). The mixture is then expanded in the turbine (from 4 to 5) and partially cooled down in the recuperator, where it can also partially condense (from 5 to 6), before entering the condenser (COND). An example of the T-s (Temperature-Entropy) diagram for a selected mixture is reported in Figure *5*.

In the benchmark layout, the recompression cycle (REC), with pure $sCO_2$ the pump is replaced by a compressor and the pre-heating section is split in two recuperators that works at different temperature (LT and HT PCHE) and with a different mass flow rate to compensate the effects of the unbalanced heat capacities of CO2-based fluid across the low-pressure side of the recuperator, at low temperature. The $sCO_2$ is compressed (from 1 to 2) to reach the maximum cycle pressure and enters the LT recuperator to preheat (from 2 to 3) and mixed (from 3 to 4) with the fraction of $CO_2$ that is re-compressed (from 10 to 11). After mixing, $sCO_2$ is preheated in the HT PCHE recuperator, reaching the maximum temperature in the PHE, before the expansion that occurs in the turbine (from 6 to 7). The turbine outlet flow is used to preheat the high-pressure side in the HT and LT PCHE recuperator, then it is split: a fraction is compressed (from 10 to 11), while the other fraction is cooled in the HRU (from 12 to 1) up to the minimum cycle temperature.

The other two layouts (precompression and cascade) have been already presented for $CO_2$ mixtures in previous works as an alternative to the simple transcritical cycle [39],[34]. The cascade is characterized by a partial preheating phase of the working fluid (from 2 to 3), which allows a low temperature at the PHE inlet (point 4) and, consequently, a higher temperature difference across the PHE (from 4 to 5) to reach the designed turbine inlet temperature. This is reflected in a higher temperature difference of the HTF, as reported in Table *5*: the cascade layout aims at the maximization of the heat recovery from the heat source. In the precompression cycle, the turbine outlet pressure (point 6) is the one that optimize the cycle efficiency. The turbine outlet flow preheats the high-pressure side in the HT recuperator (from 6 to 7), then the flow is compressed (from 7 to 8) to a pressure that is compatible with the bubble pressure at 51°C (point 1) and the pressure losses within the LT recuperator and condenser.

One of the best features of the adoption of a $CO_2$-based mixture is the capability to operate with good cycle efficiency even in a simple recuperative layout, where only one Printed Circuit Heat Exchanger (PCHE) recuperator and one compression step are necessary, thanks to the well-balanced heat capacities in the recuperator.

**Appendix D: Results on solar plant annual analysis**

The results in this appendix refer to the off-design and yearly analysis of the CSP plant located in Sevilla. In particular, in Figure 12 it is reported the trend of the solar field optical efficiency for any sun position: according to the design criteria, the solar field is sized at the solar noon of the summer solstice. From the optical efficiency map it is possible to notice that an optical efficiency of around

62% at design is computed for this CSP plant. The results of Figure *13*, instead, show the solar resources of the location, as a daily average for each month, for a representative year. In addition, the daily average across each month of the thermal power delivered to the HTF is also shown, computed according to the methodology of Figure *7*.

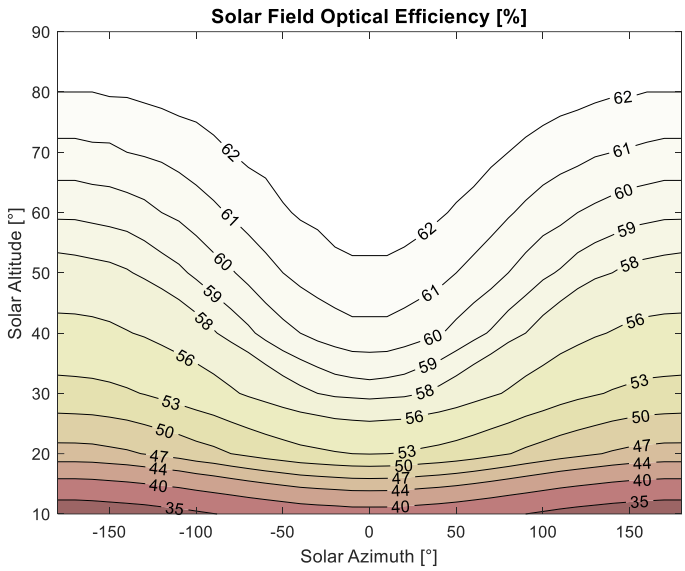


*Figure 12. Off-design map of the optical efficiency of the solar field proposed in this work in Figure 2*

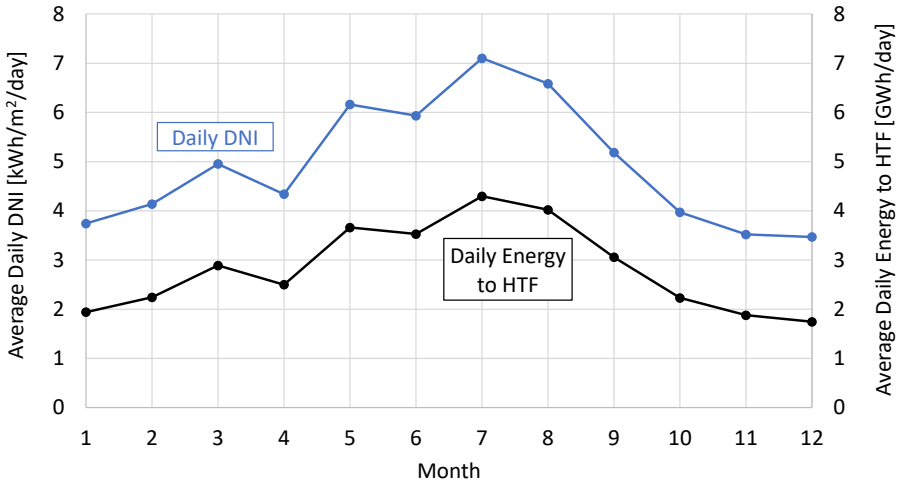


*Figure 13. Average monthly DNI data of Sevilla (Spain) taken from the SolarPilot database, with an yearly average value of 4.92 kWh/m²/day. Average monthly thermal energy transferred to the HTF from the solar plant considered*

## Appendix E: Additional results discussion

This appendix is dedicated to an additional analysis of the results of this work, proposed in Table 8. For comparison purposes, Hoffmann [48] analysed a state-of-the-art 100 $MW_{el}$ CSP+MED tower plant with the MED unit driven by the condenser of the steam Rankine cycle at different condensation temperatures (60-75°C) with LCOW in the range 3.6-2.6 \$/$m^3$ and the LCOE within the range 152-160 \$/$MWh_{el}$, which are numbers not as profitable as the one of this work, even if the

location (Arandis, Namibia) is characterized by higher annual DNI (2528 kWh/m$^2$/year). Moreover, Hoffmann concluded that the proposed CSP+MED solution could not be competitive against grid-powered RO option (1.78 \$/m$^3$) in his case-study. In the state-of-the-art CSP+MED solution, the heat is provided to the MED system by bleeding a fraction of the steam from the turbine or by the condenser (raising the cycle minimum temperature to 60-75°C) with associated electrical production loss. Instead, in the proposed technology there is no need to compromise the electrical production (and the LCOE) to achieve good results for the desalinated water production, since the heat introduced in the MED is the total amount of the heat naturally rejected from the cycle in the HRU. The results of this work can be also compared to conditions of $sCO_2$ cycles applied in CSP+MED cogenerative plants with a lower value of minimum temperature of the cycle temperature: in fact, the choice of this work to adopt a higher value of compression inlet temperature (more representative of hot environments) allows the 100% conversion of the thermal duty entering the power block for electrical and desalinated water productions. Under this perspective, Sharan et al. [26] reported that a 6-effects CSP+MED plant with pure $sCO_2$ can reach a distillate production of 4'472 m$^3$/day at similar thermal duty available, which is remarkably lower than the annual freshwater production of 4.22 million m$^3$/year obtained in this work for pure $sCO_2$ (Table 8), where the equivalent daily production would be 11'562 m$^3$/day. Without discussing the cost assumptions that could differ from previous research works, and considering that the CAPEX of the MED system in inversely proportional to the distillate production [40], the solution proposed in this work seems more cost-effective.

## 8.10 Bibliography


[1] P. Burek *et al.*, "The Water Futures and Solutions Initiative of IIASA," pp. 23–26, 2016.

[2] UNESCO, "The United Nations World Water Development Report 2018: Nature-Based Solutions for Water," 2018.

[3] J. Eke, A. Yusuf, A. Giwa, and A. Sodiq, "The global status of desalination : An assessment of current desalination technologies , plants and capacity," *Desalination*, vol. 495, no. March, p. 114633, 2020, doi: 10.1016/j.desal.2020.114633.

[4] A. N. Mabrouk and H. E. S. Fath, "Technoeconomic study of a novel integrated thermal MSF-MED desalination technology," *Desalination*, vol. 371, pp. 115–125, 2015, doi: 10.1016/j.desal.2015.05.025.

[5] Y. Almulla, "Gulf Cooperation Council (GCC) countries 2040 energy scenario for electricity generation and water desalination Yousef Almulla-Almulla@kth.se Student MSc Sustainable Energy Engineering," 2014.

[6] L. O. Villacorte, S. A. A. Tabatabai, D. M. Anderson, G. L. Amy, J. C. Schippers, and M. D. Kennedy, "Seawater reverse osmosis desalination and (harmful) algal blooms," *Desalination*, vol. 360, pp. 61–80, 2015, doi: 10.1016/j.desal.2015.01.007.

[7] A. M. Delgado-Torres and L. García-Rodriguez, "Solar Desalination Driven by Organic Rankine Cycles (Orc) and Supercritical CO 2 Power Cycles: An Update," *Processes*, 2022, doi: https://doi.org/10.3390/pr10010153.

[8] G. Gentile and G. Manzolini, "The Value of CSP with Thermal Energy Storage in Providing Flexible Electric Power," in *Sustainable Energy Development and Innovation: Selected Papers from the World Renewable Energy Congress (WREC) 2020*, Springer NATURE, 2022, pp. 103–109. doi: 10.1007/978-3-030-76221-6_15.

[9] M. Binotti, M. Astolfi, S. Campanari, G. Manzolini, and P. Silva, "Preliminary assessment of sCO2 cycles for power generation in CSP solar tower plants," *Appl Energy*, vol. 204, pp. 1007–1017, Oct. 2017, doi: 10.1016/J.APENERGY.2017.05.121.

[10] SCARABEUS, "No Title," *Supercritical Carbon dioxide/Alternative fluids Blends for Efficiency Upgrade of Solar power plants*, 2019. https://www.scarabeusproject.eu/

[11] M. Binotti, G. Di Marcoberardino, P. Iora, C. Invernizzi, and G. Manzolini, "Scarabeus: Supercritical carbon dioxide/alternative fluid blends for efficiency upgrade of solar power plants," *AIP Conf Proc*, vol. 2303, no. December, 2020, doi: 10.1063/5.0028799.

[12] G. Manzolini *et al.*, "Adoption of CO2 blended with C6F6 as working fluid in CSP plants," in *AIP Conference Proceedings*, AIP Publishing LLCAIP Publishing, May 2022, p. 090005. doi: 10.1063/5.0086520.

[13] G. Di Marcoberardino *et al.*, "Experimental characterisation of CO2 + C6F6 mixture: Thermal stability and vapour liquid equilibrium test for its application in transcritical power cycle," *Appl Therm Eng*, vol. 212, Jul. 2022, doi: 10.1016/J.APPLTHERMALENG.2022.118520.

[14] S. Masoud Parsa *et al.*, "Thermodynamic, economic, and sensitivity analysis of salt gradient solar pond (SGSP) integrated with a low-temperature multi effect desalination (MED): Case study, Iran," *Sustainable Energy Technologies and Assessments*, vol. 47, no. June, p. 101478, 2021, doi: 10.1016/j.seta.2021.101478.

[15] D. P. S. Cunha and K. V. Pontes, "Desalination plant integrated with solar thermal energy: A case study for the Brazilian semi-arid," *J Clean Prod*, vol. 331, no. November 2021, p. 129943, 2022, doi: 10.1016/j.jclepro.2021.129943.

[16] F. Ahmed, M. Sharizal Abdul Aziz, P. Palaniandy, and F. Shaik, "A review on application of renewable energy for desalination technologies with emphasis on concentrated solar power," *Sustainable Energy Technologies and Assessments*, vol. 53, no. PD, p. 102772, 2022, doi: 10.1016/j.seta.2022.102772.

[17] M. Moser, F. Trieb, and T. Fichter, "Potential of concentrating solar power plants for the combined production of water and electricity in MENA countries," *Journal of Sustainable Development of Energy, Water and Environment Systems*, vol. 1, no. 2, pp. 122–140, 2013, doi: 10.13044/j.sdewes.2013.01.0009.

[18] P. Palenzuela, D. C. Alarcón-Padilla, G. Zaragoza, and J. Blanco, "Comparison between CSP+MED and CSP+RO in Mediterranean Area and MENA Region: Techno-economic Analysis," *Energy Procedia*, vol. 69, pp. 1938–1947, 2015, doi: 10.1016/j.egypro.2015.03.192.

[19] D. Sankar, N. Deepa, S. Rajagopal, and K. M. Karthik, "Solar power and desalination plant for carbon black industry: Improvised techniques," *Solar Energy*, vol. 119, pp. 243–250, 2015, doi: 10.1016/j.solener.2015.07.001.

[20] R. Olwig *et al.*, "Techno-economic analysis of combined concentrating solar power and desalination plant configurations in Israel and Jordan," *Desalination Water Treat*, vol. 41, no. 1–3, pp. 9–25, 2012, doi: 10.1080/19443994.2012.664674.

[21] I. B. Askari, M. Ameri, and F. Calise, "Energy, exergy and exergo-economic analysis of different water desalination technologies powered by Linear Fresnel solar field," *Desalination*, vol. 425, no. July 2017, pp. 37–67, 2018, doi: 10.1016/j.desal.2017.10.008.

[22] M. Moradi, B. Ghorbani, R. Shirmohammadi, M. Mehrpooya, and M. H. Hamedi, "Developing of an integrated hybrid power generation system combined with a multi-effect desalination unit," *Sustainable Energy Technologies and Assessments*, vol. 32, no. November 2018, pp. 71–82, 2019, doi: 10.1016/j.seta.2019.02.002.

[23] C. Sommariva, "Desalination and advanced water treatment : economics and financing," 2010.

[24] M. A. Sharaf, A. S. Nafey, and L. García-Rodríguez, "Thermo-economic analysis of solar thermal power cycles assisted MED-VC (multi effect distillation-vapor compression) desalination processes," *Energy*, vol. 36, no. 5, pp. 2753–2764, 2011, doi: 10.1016/j.energy.2011.02.015.

[25] L. Yuan, Q. Zhu, T. Zhang, R. Duan, and H. Zhu, "Performance evaluation of a co-production system of solar thermal power generation and seawater desalination," *Renew Energy*, vol. 169, pp. 1121–1133, 2021, doi: 10.1016/j.renene.2021.01.096.

[26] P. Sharan, T. Neises, and C. Turchi, "Thermal desalination via supercritical CO 2 Brayton cycle : Optimal system design and techno-economic analysis without reduction in cycle efficiency," *Appl Therm Eng*, vol. 152, no. December 2018, pp. 499–514, 2019, doi: 10.1016/j.applthermaleng.2019.02.039.

[27] S. S. Saravi and S. A. Tassou, "An investigation into sCO2 compressor performance prediction in the supercritical region for power systems," in *Energy Procedia*, 2019. doi: 10.1016/j.egypro.2019.02.098.

[28] Aspen Technology Inc., "Aspen Plus®, Version V12.1." 2022.

[29] A. Baccioli, M. Antonelli, U. Desideri, and A. Grossi, "Thermodynamic and economic analysis of the integration of Organic Rankine Cycle and Multi-Effect Distillation in waste-heat recovery applications," *Energy*, vol. 161, pp. 456–469, 2018, doi: 10.1016/j.energy.2018.07.150.

[30] M. J. Wagner and T. Wendelin, "SolarPILOT: A power tower solar field layout and characterization tool," *Solar Energy*, vol. 171, 2018, doi: 10.1016/j.solener.2018.06.063.

[31] SolarReserve, "Crescent Dunes Solar Energy Plant," 2014.

[32] G. Gentile, G. Picotti, F. Casella, M. Binotti, M. E. Cholette, and G. Manzolini, "SolarReceiver2D: a Modelica Package for Dynamic Thermal Modelling of Central Receiver Systems," *IFAC-PapersOnLine*, vol. 55, no. 20, pp. 259–264, 2022, doi: 10.1016/j.ifacol.2022.09.105.

[33] D. Alfani, M. Astolfi, M. Binotti, P. Silva, and E. Macchi, "Off-design Performance of CSP Plant Based on Supercritical CO2 Cycles," *AIP Conf Proc*, vol. 2303, no. December, 2020, doi: 10.1063/5.0029801.

[34] E. Morosini, A. Ayub, G. di Marcoberardino, C. M. Invernizzi, P. Iora, and G. Manzolini, "Adoption of the CO2 + SO2 mixture as working fluid for transcritical cycles: A thermodynamic assessment with optimized equation of state," *Energy Convers Manag*, vol. 255, p. 115263, 2022, doi: 10.1016/j.enconman.2022.115263.

[35] E. Morosini, E. Villa, G. Quadrio, M. Binotti, and G. Manzolini, "Solar tower CSP plants with transcritical cycles based on CO2 mixtures: A sensitivity on storage and power block layouts," *Solar Energy*, vol. 262, Sep. 2023, doi: 10.1016/J.SOLENER.2023.05.054.

[36] F. Crespi *et al.*, "Thermal Efficiency Gains Enabled by Using CO2 Mixtures in Supercritical Power Cycles," *Energy*, vol. 238, p. 121899, 2021, doi: 10.1016/j.energy.2021.121899.

[37] R. Span and W. Wagner, "A New Equation of State for Carbon Dioxide Covering the Fluid Region from the Triple-Point Temperature to 1100 K at Pressures up to 800 MPa," *J Phys Chem Ref Data*, vol. 25, no. 6, pp. 1509–1596, 1996, doi: 10.1063/1.555991.

[38] G. Di Marcoberardino, E. Morosini, and G. Manzolini, "Preliminary investigation of the in fluence of equations of state on the performance of CO2 + C6F6 as innovative working fluid in transcritical cycles," *Energy*, vol. 238, p. 121815, 2022, doi: 10.1016/j.energy.2021.121815.

[39] F. Crespi *et al.*, "Thermal efficiency gains enabled by using CO2 mixtures in supercritical power cycles," *Energy*, vol. 238, p. 121899, 2022, doi: 10.1016/j.energy.2021.121899.

[40] M. Papapetrou, G. Kosmadakis, A. Cipollina, U. La Commare, and G. Micale, "Industrial waste heat: Estimation of the technically available resource in the EU per industrial sector, temperature level and country," *Appl Therm Eng*, vol. 138, no. July 2017, pp. 207–216, 2018, doi: 10.1016/j.applthermaleng.2018.04.043.

[41] M. Hasan, K. Manesh, R. S. Ghadikolaei, and H. V. Modabber, "Integration of a Combined Cycle Power Plant with MED-RO Desalination Based on Conventional and Advanced Exergy ," 2021.

[42] P. Druetta, P. Aguirre, and S. Mussati, "Minimizing the total cost of multi effect evaporation systems for seawater desalination," *Desalination*, vol. 344, pp. 431–445, 2014, doi: 10.1016/j.desal.2014.04.007.

[43] N. T. Weiland, B. W. Lance, and S. R. Pidaparti, "sCO2 Power Cycle Component Cost Correlations From DOE Data Spanning Multiple Scales and Applications," in Turbo Expo: Power for Land, Sea, and Air, vol. Volume 9: 2019. doi: 10.1115/GT2019-90493.

[44] "Thermoflow Inc., Thermoflex, (2021)."

[45] B. Kelly, M. Izygon, and L. Vant-Hull, "Advanced Thermal Energy Storage for Central Receivers with supercritical coolants," *SolarPaces Conference*, 2010, doi: 10.2172/981926.

[46] "System Advisor Model (SAM)." https://sam.nrel.gov/.

[47] G. Manzolini, G. Lucca, M. Binotti, and G. Lozza, "A two-step procedure for the selection of innovative high temperature heat transfer fluids in solar tower power plants," *Renew Energy*, vol. 177, pp. 807–822, 2021, doi: 10.1016/j.renene.2021.05.153.

[48] J. E. Hoffmann and E. P. Dall, "Integrating desalination with concentrating solar thermal power: A Namibian case study," *Renew Energy*, vol. 115, pp. 423–432, 2018, doi: 10.1016/j.renene.2017.08.060.

[49] S. Zhou, Y. Guo, X. Mu, and S. Shen, "Effect of design parameters on thermodynamic losses of the heat transfer process in LT-MEE desalination plant," *Desalination*, vol. 375, pp. 40–47, 2015, doi: 10.1016/j.desal.2015.07.015.

[50] H. T. El-Dessouky, I. M. Alatiqi, H. M. Ettouney, and N. S. Al-Deffeeri, "Performance of wire mesh mist eliminator," *Chemical Engineering and Processing: Process Intensification*, vol. 39, no. 2, pp. 129–139, 2000, doi: 10.1016/S0255-2701(99)00033-1.

[51] G. Gentile, G. Picotti, M. Binotti, M. E. Cholette, and G. Manzolini, "Dynamic thermal analysis and creep-fatigue lifetime assessment of solar tower external receivers," *Solar Energy*, vol. 247, pp. 408–431, 2022, doi: 10.1016/j.solener.2022.10.010.

[52] E. Morosini, G. Gentile, M. Binotti, and G. Manzolini, "Techno-economic assessment of small-scale solar tower plants with modular billboard receivers and innovative power cycles," in *Journal of Physics: Conference Series*, IOP Publishing, Dec. 2022, p. 012109. doi: 10.1088/1742-6596/2385/1/012109.

[53] "Global wind atlas," *Global Wind Atlas*, 2022. https://globalwindatlas.info/en/

# *Chapter 9 - Biomass -fired plant with $SiCl_4$ working fluid*

*THIS CHAPTER IS BASED ON THE ARTICLE: "AN EFFICIENT SMALL-SCALE BIOMASS COGENERATION PLANT WITH SILICON TETRACHLORIDE AS WORKING FLUID: TECHNO-ECONOMIC ANALYSIS", UNDER REVIEW IN RENEWABLE ENERGY, ELSEVIER.*


**Abstract**

Biomass-fired Organic Rankine Cycles are a well-established solution for combined heat and power, particularly suited for small, decentralized communities. However, compared with other renewable systems, biomass facilities have not benefited from reduced energy costs over time due to high capital and biomass fuel costs. To address this issue, Silicon Tetrachloride ($SiCl_4$) has been recently proposed as an innovative working fluid in high-temperature Rankine cycles, offering significant efficiency gains due to outstanding thermal stability, compared to typical organic fluids.

This work explores the techno-economic feasibility of coupling a 1 MW gross electric $SiCl_4$ cycle with a decentralized biomass boiler. By utilizing commercial molten salts as the heat carrier, instead of traditional thermal oil, the system operates at a turbine inlet temperature of 525°C. The annual performance of the proposed CHP plant is assessed under both baseload and load-following scenarios within an existing district heating network. The cycle's off-design behavior is analysed at part-load and full-electric conditions. With a condensing temperature of 100°C, the gross cycle efficiency reaches 32.3% at nominal power, significantly overcoming state-of-the-art ORC systems. The baseload plant demonstrates a discounted payback period of less than four years under current Italian conditions, highlighting the industrial potential of the proposed solution.


## 9.1 Introduction

The utilization of biomass for energy, commonly known as bioenergy, represents the primary renewable energy source in the EU covering approximately 59% of renewable energy consumption in 2021, as reported by the EU Commission on bioenergy sustainability [1]. Over the last decades, many biomass combustion plants have been installed to produce Combined Heat and Power (CHP). CHP plants fuelled by the combustion of solid biomass mainly relies on two technologies for the power unit: conventional steam Rankine and Organic Rankine Cycle (ORC) systems. Within the 200-2000 $kW_{el}$ range, the ORC technology has demonstrated techno-economic advantages compared to steam cycles [2], and are gaining attraction up to 10 $MW_{el}$ output due to lower required maintenance and technical personal involvement, and better part-load performance. Easy-accessible feed-in-tariff, especially for electrical output below 1 $MW_{el}$, promoted the installation of many biomass-fired ORC systems coupled with district heating networks starting from the 90's [3] [4].

Despite the considerable incentives and the benefit of working with a dispatchable renewable source, biomass plants have shown minimal improvement in the levelized cost of electricity

production, when compared to other renewable energy sources like solar or wind. This stagnation primarily stems from the unique characteristics of biomass-fired plants, which entail significant capital costs associated with biomass boilers and abatement systems, power units, and operational expenses (biomass cost). Progress in enhancing the efficiency of biomass-driven ORCs has been limited, resulting in low electrical efficiencies, around 15% for CHP plants [5].

Noussan et al. [6] assessed the economics of biomass-fired ORC-CHP systems for district heating in Italy, finding payback periods exceeding 8 years. Their research suggests that year-round operation with summer heat dissipation is only advisable if incentives justify it, due to the low electrical efficiency of ORC systems making it economically unviable to operate when heat cannot be utilized or sold. Braimakis et al. [7] also indicated that the economic viability of small-scale ORC biomass-fired CHP plants is limited, requiring a combination of favourable conditions such as high electricity and heat prices, along with low biomass costs, and extended operating hours to achieve discount payback periods of 5–7 years.

Kalina and Świerzewski [8] developed a model, calibrated on real operational data, to monitor and predict the performance of state-of-the-art biomass-fired ORCs connected to municipal heating networks. They also found that profitability of biomass-fired ORC-CHP units in retrofitting district heating plants is rather low, subject to market volatility and financial assistance, with feasible projects now averaging a 12-year discounted payback period [9]. In the techno-economic optimisation of Świerzewski et al. [10], ethylbenzene was found as the most efficient working fluid, enabling a discounted payback time of 10 years. Taljan et al. [11] explored the financial viability of small ORC CHP units coupled with storage tank, demonstrating that the solution without storage has a higher internal rate of return, reaching 10% at a biomass price of 17 €/MWh$_{LHV}$. It must be noted that such rate of return is lower than the hurdle rate, which is the minimum rate of return required for an investment to be considered worthwhile, typically set at around 12% for biomass CHP plants [12]. Tańczuk [13] stated that the integration of ORC in biomass-fired CHP plants in small district heating networks is not profitable in current Polish economy despite 30% of investment subsidy. The study of Uris et al. [14] demonstrates that state-of-the-art biomass-ORC systems are economically viable when operated for a large number of hours to meet base thermal load demands, coupled with low biomass costs.

Regarding the power block, there is little room for improvement the thermal-to-electric efficiency of these small-scale ORC systems because the technology has been well-established for decades. However, this goal can be pursued by introducing a working fluid that stands out from the state-of-the-art fluids currently in use. As stated by Feng et al. [15] in their parameter analysis of biomass-fired ORC, the working fluid has a significant impact on the performance of the system. Silicon tetrachloride ($SiCl_4$) has been recently proposed by the authors as innovative working fluid in very-high temperature Rankine cycle, as pure fluid [16] and in mixture with $CO_2$ [17], with an outstanding thermal stability demonstrated above 650°C in contact with a common stainless-steel alloy (AISI 316L). In this work, a $SiCl_4$ cycle is coupled with a biomass boiler through a heat transfer loop constituted by commercial molten salts. The molten salts enable a maximum cycle temperature of 525°C and, as a consequence, an increase in the electric efficiency compared to state-of-the-art ORCs operating below 300-330°C [18][19]. The use of molten salts instead of conventional thermal oil as heat carrier in biomass plants has already been considered in the literature. In the recent past, ENEA

carried out a research activity on the use of molten salts as heat carrier in biomass boiler coupled with innovative power cycles [20]. Molten salts can act not only as heat carrier but also as energy storage system. Sorrentino et al. [21] proposed a biomass fired ORC CHP system with two-tank molten salts thermal energy storage (TES) system to improve the flexibility and reduce the boiler size. Moreover, the presence of TES enhances the flexibility of the biomass plant during transients [22].

This work investigates the techno-economic potentialities of $SiCl_4$ as working fluid in small-scale CHP plants. The design of each component of the power block is carried out for a 1 MW gross mechanical output. The designed power unit is intended to serve a decentralized district heating network (DHN), for which the heat load duration curve is available. Two scenarios are considered: baseload operation and load-following mode. The off-design performance of the power cycle is then evaluated to determine plant efficiency at part-load and in full-electric mode (off-heating). Compared to literature works, the complete annual analysis – comprising design and off-design evaluation of the plant - is carried out to enable a reliable economic evaluation of the CHP plant. The findings are expected to provide valuable insights for the development and optimization of future biomass CHP plants, contributing to the broader adoption of renewable energy technologies.

## 9.2 CHP plant with $SiCl_4$ as working fluid: layout definition

Biomass-driven ORC systems typically use fluids like siloxanes and toluene for their high thermal stability and critical temperature. A common configuration [23][24] includes a split thermal oil loop characterized by a high-temperature loop (310/250°C) and a low-temperature loop (250/130°C). This setup maximizes biomass exploitation [18], achieving boiler efficiencies of up to 88% [25]. In this study, the same architecture of a split ORC unit, reported in Figure 1, is adopted, but the high-temperature heat transfer loop is constituted by molten nitrate salts. In particular, the commercially-mature "Solar Salt" mixture (60% $NaNO_3$-40% $KNO_3$) has been considered. The reason to adopt molten salts in the HT loop is because of the low thermal stability of thermal oils. As an example, Therminol VP-1 is thermally stable up to 400°C (bulk temperature). Moreover, compared to thermal oil, molten salts have also no fire risks and environmental impacts. The temperatures of the molten salts loop across the primary heat exchanger (PHE) are set at 550/290°C (in/out). The minimum molten salt temperature is set at 290°C to keep a safety margin on the freezing point of the salts (around 228°C). The maximum salts temperature is selected around 550°C to keep a safety margin from the decomposition occurring around 600°C [26].

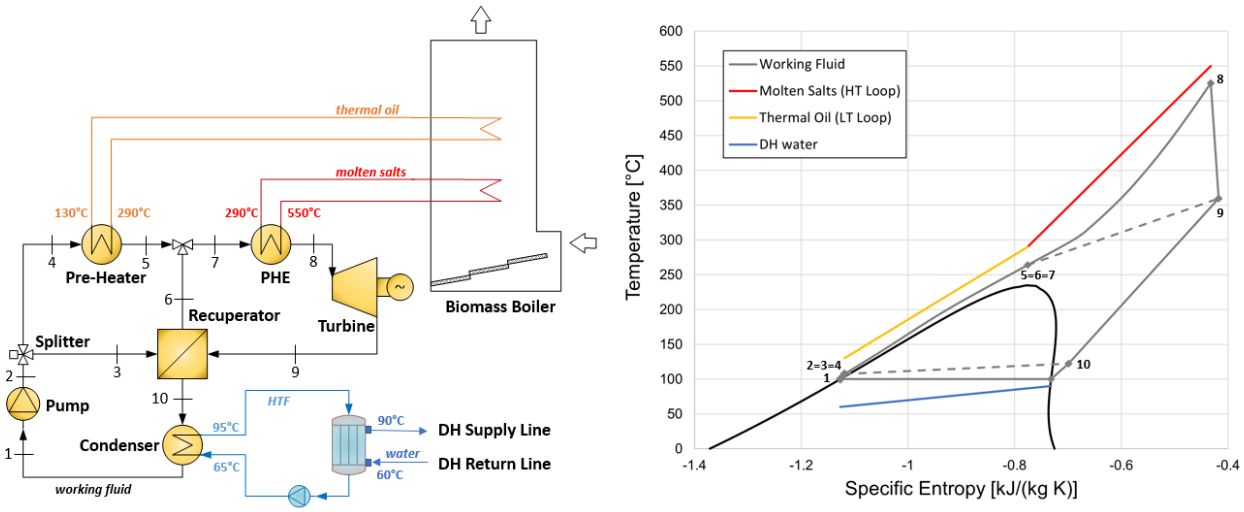


*Figure 1. $SiCl_4$ power cycle in split layout coupled with biomass boiler and thermal user (left); the $SiCl_4$ cycle represented in the T-s diagram including the heat sources (right).*

The cycle maximum temperature, i.e. the turbine inlet temperature (TIT), is assumed to be 525°C for $SiCl_4$, considering 25°C as temperature difference at the PHE hot-end. The cycle maximum pressure is selected equal to 60 bar, according to the preliminary cycle evaluation carried out in a previous work [16]. The minimum cycle temperature (condensation temperature) is equal to 100°C for cogeneration purpose. The thermal power rejected from the cycle, through the condenser, is transferred to an intermediate heat transfer oil loop (65/95°C), that release it to the water loop (60/90°C) of a district heating network. The intermediate HTF loop avoids water-cooled condensation of $SiCl_4$, for safety reasons, given its tendency to hydrolyse in contact with water. Therminol LT has been considered as heat carrier for both the condenser (65/95°C) and the LT-loop (130/290°C) since it has low vapour pressure and good transport properties.

## 9.3 Power Block Design

The cogeneration plant presented in Figure 1 adopting $SiCl_4$ as working fluid is designed for a gross mechanical output of 1 MW in each key component to provide a reliable techno-economic assessment. The selected size is coherent with small-decentralized district heating network. The Peng Robinson equation of state, as validated in a previous work for this fluid [16], is used in Aspen Plus V12 [27] software for the calculation of the thermodynamic properties.

The resulting design of each component is presented in Supplementary Materials section. After the design of each component, the power cycle performance have been evaluated considering the actual pressure drops and turbomachines efficiency. The design operating conditions of the power block are reported in detail in Table 1 and Table 2. The cycle thermal efficiency (first principle) of the power block ($\eta_c$), defined as in Eq. 1, is reported in Table 1. The net electrical efficiency ($\eta_{c,el}$) in Eq. 2 considers the electro-mechanical losses related to the pump and turbine (listed in Table 1).

$$\eta_c = \frac{\dot{W}_T - \dot{W}_P}{\dot{Q}_{in}} = \frac{\dot{W}_T - \dot{W}_P}{\dot{Q}_{PHE} + \dot{Q}_{PH}} = \frac{\dot{m}(h_8 - h_9) - \dot{m}(h_2 - h_1)}{\dot{m}(h_8 - h_7) + \dot{m}_{PH}(h_5 - h_4)} \quad (1)$$

$$\eta_{c,el} = \frac{\dot{W}_T \, \eta_m \, \eta_{gearbox} \, \eta_{gen} - \dfrac{\dot{W}_P}{\eta_m \eta_{motor}}}{\dot{Q}_{in}} = \frac{\dot{W}_{el,net}}{\dot{Q}_{in}} \quad (2)$$

*Table 1. Summary of 1 MWgross $SiCl_4$ cycle final design conditions.*

| Parameters | units | Values |
|---|---|---|
| Minimum Temperature (at pump inlet) | °C | 100 |
| Turbine inlet temperature | °C | 525 |
| Maximum Cycle Pressure | bar | 60 |
| $\Delta T_{min}$ in the Recuperator | °C | 15 |
| $\Delta P_{rec}$ cold/hot side | bar | 0.53/0.019 |
| $\Delta P_{PHE}$ | bar | 0.11 |
| $\Delta P_{cond}$ | bar | 0.011 |
| Turbine Isentropic Efficiency | % | 90.1 |
| Pump Isentropic Efficiency | % | 61.2 |
| Mass Flow Rate $\dot{m}$ | kg/s | 13.05 |
| Split Ratio ($\dot{m}/\dot{m}_{PH}$) | - | 0.89 |
| $\dot{W}_p$ | kW | 92.6 |
| $\dot{W}_t$ | kW | 1092.6 |
| $\dot{Q}_{PHE}$ | kW | 2865.9 |
| $\dot{Q}_{PH}$ | kW | 228.1 |
| $\dot{Q}_{cond}$ | kW | 2094 |
| $\eta_c$ | % | 32.3 |
| $\eta_m$ | % | 98 |
| $\eta_{gearbox}$ | % | 97 |
| $\eta_{motor}$ | % | 98 |
| $\eta_{gen}$ | % | 98 |
| $\dot{W}_{el,net}$ | kW | 920.4 |
| $\eta_{c,el}$ | % | 29.7 |

*Table 2. Thermodynamic states of $SiCl_4$ cycle at design conditions (state diagram in Figure 1).*

| Streams | T [°C] | P [bar] | $x_{vap}$ [-] |
|---|---|---|---|
| 1 | 100 | 3.34 | 0 |
| 2,3,4 | 107.4 | 60 | 0 |
| 5,6,7 | 263.1 | 59.47 | 1 |
| 8 | 525 | 59.34 | 1 |
| 9 | 358.1 | 3.38 | 1 |

| | | | |
|---|---|---|---|
| 10 | 122.4 | 3.36 | 1 |

Even though the working fluid is compressed up to supercritical pressure, the required pump power is rather low (8.5%) compared to the turbine power, due to low compressibility of $SiCl_4$ even at 100°C (well below its critical temperature of 235°C). The split ratio in Table 1, which determines the mass flow rate that enters the recuperator compared to that pre-heated by the LT oil loop, has been selected in order to have a PHE temperature inlet below 265°C, thus guaranteeing at least 25°C of temperature difference at the cold-end of the PHE and at the hot-end of the preheater (PH).

The thermal efficiency of the power unit, at design conditions for cogeneration, is 32.3%. As a comparison, state of the art 1 MW gross biomass-ORC (split) plants present around 16-18% gross efficiency [18]. Considering the electro-mechanical losses (listed in Table 1) for the expander and pump, the resulting net electrical efficiency reduces to 29.7%.

### 9.3.1 Summary of components design

The design results for the 1 $MW_{gross}$ $SiCl_4$ power cycle are resumed in this section, with comprehensive details on component specifications provided in the Supplementary Material section.

All heat exchangers were designed as Shell and Tube types, with high-pressure flow through the tubes. The most economical configurations were selected based on flow arrangement and tube size. For example, the recuperator has 816 tubes (13 mm OD) in a 30° triangular pattern with a heat transfer area of 1994.3 $m^2$. Stainless steel SS316 was used, except for the condenser, which employed carbon steel due to lower temperature conditions.

The axial-flow turbine was designed with four stages, as the high-temperature potential of this fluid justifies a greater investment cost compared to typical ORC systems. The turbine's rotational speed is 30,581 rpm, and its total-to-static efficiency reaches 90.1%. The selected feed pump (Garbarino [29] 50 GHB10) handles a flow rate of 36.1 $m^3/h$ with a 442.9 m head and 61.2% efficiency. Its impeller is made of AISI 316L.

An air cooler for off-heating periods includes 154 tubes per bundle, with a finned surface area of 5147.4 $m^2$ and three 5.85 kW fans.

## 9.4 Heat load duration curve

State-of-the-art small-scale decentralized biomass-fired CHP plants are economically viable only when they exceed 5'000 hours equivalent annual operating hours [30]. In this work, a heat load demand of an existing DHN that fits well the thermal power output of the designed $SiCl_4$ plant has been considered. The investigated power block has a nominal electric and thermal power output of 920.4 $kW_{el}$ and 2094 $kW_{th}$ ($Q_{cond}$ in Table 1) respectively.

In particular, the demand curve of the DHN presented by Tańczuk and Ulbrich [5] - and considered as case study by Capra and Martelli [31] - is used here. The heat load demand is represented in Figure 2 along with the two different scenarios considered for the designed $SiCl_4$ plant: baseload or load-following. A technical operating limit of 20% of the nominal thermal load of the boiler is applied.

During partial load operations, to meet the hourly DHN thermal demand the boiler load must be adjusted in order to satisfy Equation 3:

$$\dot{Q}_{boiler,i}\,\eta_{boiler,i}\,(1-\eta_{c,i}) = \dot{Q}_{DHN,i} \tag{3}$$

where the hourly cycle thermal efficiency $\eta_{c,i}$ depends on the boiler thermal load itself. For this reason, the cycle efficiency at different biomass boiler load will be explored in the next sections. The hourly biomass boiler efficiency $\eta_{boiler,i}$, at varying load, is computed according to the work of Świerzewski and Kalina [9], showing 85.4% at full thermal load.

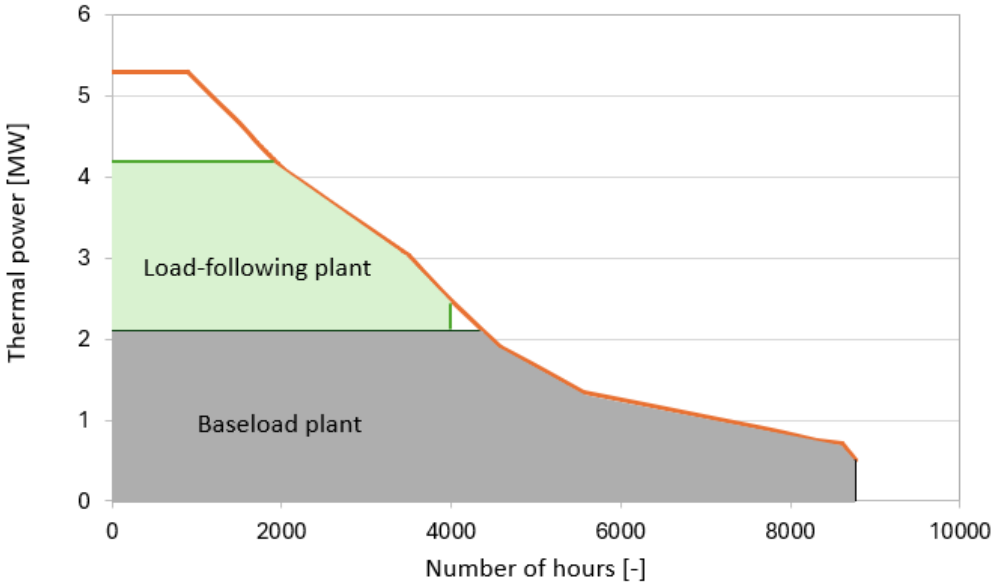


*Figure 2. Heat load demand curve of the DHN [5] and the two different scenarios for the designed $SiCl_4$ CHP plant (baseload or load-following).*

In the load-following scenario, the plant is installed in a DHN where the base load is already covered by other plants. As a consequence, the load-following plant operates in CHP mode for a limited hours of the year (around 4000, see Figure 2), while the rest it works in full-electric mode (decreasing the condensation temperature and dissipating thermal power to the environment). This scenario is rational due to the high electrical efficiency of the $SiCl_4$ plant, whilst it is not for state-of-the-art ORCs due to low electrical efficiency.

Calculating the electrical and thermal power generation throughout the year necessitates a thorough analysis of the off-design behavior of the power unit, which will be the focus of the upcoming sections.

## 9.5 Off-design of the $SiCl_4$ power block

In this Section, the off-design strategies and performance of the $SiCl_4$ power unit are evaluated. According to the discussion of the previous Section, the off-design conditions explored are: i) partial loads behaviour to follow the heat load demand keeping the condensing temperature at 100°C in the range 20-100% of the full electric power; ii) full-electric mode when heat is not required (dissipated) in a certain period of the year.

The off-design evaluation algorithm for the cycle, shown in Figure 3, begins by setting fixed parameters: condensation temperature, working fluid flow rate, and molten salts temperature at 550°C. The turbine is analysed first. Using Stodola's cone law, the turbine inlet pressure is calculated based on condensation temperature, assumed pressure losses in the LP side, and an initial TIT. This determines the turbine's off-design efficiency and outlet conditions. The pump's isentropic efficiency is kept constant, given its minor impact on overall cycle efficiency compared to the turbine. With the turbine inlet pressure set, the pump outlet pressure is calculated, factoring in HP side pressure drops. The recuperator's off-design analysis then provides the inlet conditions for the PHE, followed by evaluating the PHE's performance to adjust the TIT, molten salts flow rate, and outlet temperature. A decision step checks for deviations in TIT, total pressure losses, and the inlet/outlet temperatures of each component, recalculating the necessary components if deviations exceed 1 mbar for pressure losses or 0.5°C for inlet/outlet temperatures. This iterative process continues until all conditions converge, at which point the off-design calculation is complete.

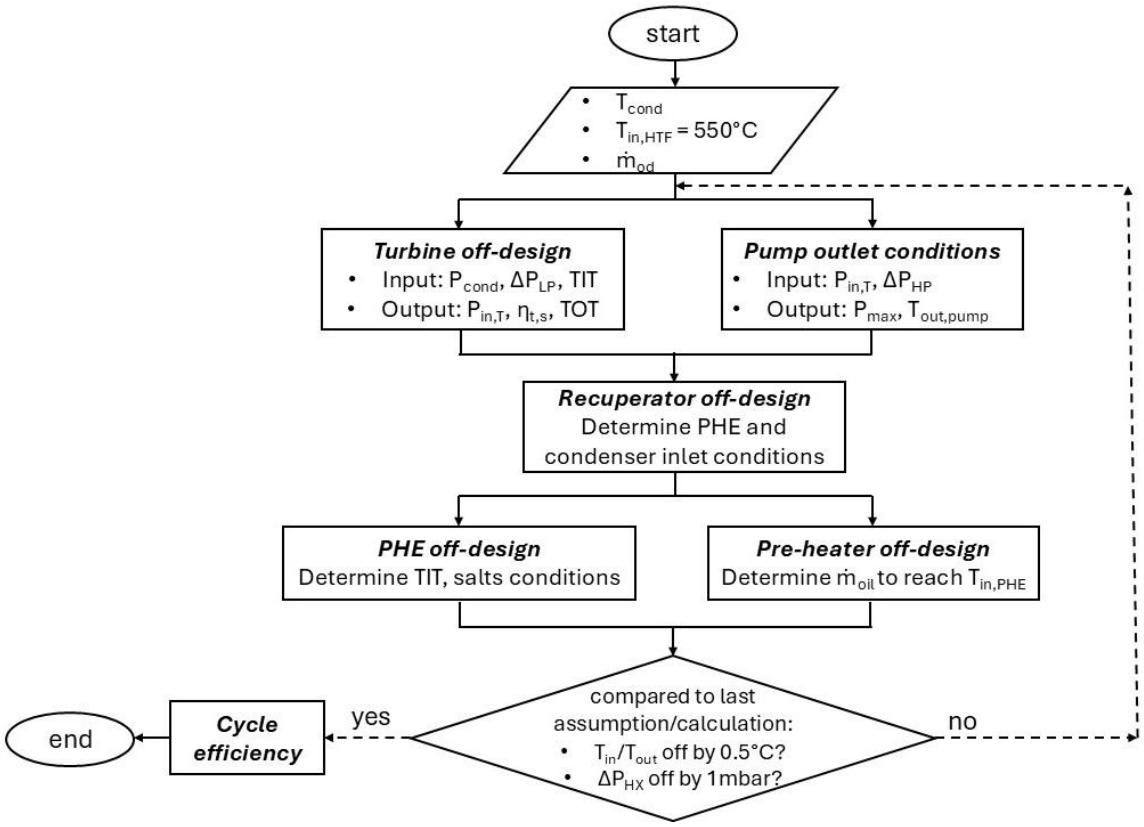


*Figure 3. off-design algorithm adopted in this work; starting from a pre-defined mass flow rate and condensation temperature (depending on cogeneration or full-electric operation), the off-design of each component is iterated until pressure drops and inlet/outlet temperatures are within a defined tolerance.*

### 9.5.1 Off-design: part-load strategy

The power block does not run always at full load, but there is a consistent number of annual hours where the thermal power request by the DHN is lower than the design value. The part-load strategy

is investigated from 100% down to 20% of the nominal load where the variation of the working fluid mass flow rate has been evaluated accordingly.

The non-dimensional flow rate $\Phi_t$ is related to the turbine's characteristic law, that is considered to be in accordance with Stodola's law of the Ellipse [32], as defined in Eq. (4):

$$\Phi_t = \frac{\dot{m}_{in,t}\sqrt{\gamma\, R\, T_{in,t}\, Z_{in,t}}}{P_{in,t}\, A_{in,t}} = f_{Stodola}(\beta_t) \tag{4}$$

Where $\dot{m}_{in,t}$ is the mass flow rate at turbine inlet, $\gamma$ is the heat capacity ratio, Z is the compressibility factor, $T_{in,T}$ is the turbine inlet temperature (TIT), $A_{in,T}$ is the turbine admission area, $P_{in,T}$ is the total pressure at turbine inlet. In this study, a sequential valve vapour chest with variable admission governing stage is not adopted. Consequently, a fixed area and reaction stage are considered at turbine inlet. The same approach has been used by Capra et al. [33] in analysing off-design performance of ORC system in biomass plant.

As a consequence, from a given mass flow rate at part-load and fixed turbine pressure outlet (by condensation temperature), the turbine inlet pressure must be determined. There are three possible control strategies to reduce the turbine inlet pressure in different ways. The sliding-pressure approach decreases the maximum cycle pressure by adjusting the feed-pump pressure head. In the throttling method, the pump outlet pressure remains constant at the full-load or design value, and a valve at the turbine admission is partially closed to achieve the desired pressure reduction. The hybrid strategy combines both sliding-pressure and throttling techniques.

In this particular case, a hybrid approach has been adopted: i) the sliding-pressure mode has been adopted at part-load until the maximum cycle pressure is above 1.1 $P_{cr}$ of the working fluid (above 40 bar); ii) the throttling mode is operated at maximum cycle pressure below 1.1 $P_{cr}$. This control strategy allows to operate in supercritical operating conditions, avoiding two-phase transition in the tubes of the PHE.

The turbine isentropic efficiency in off-design conditions has been evaluated through the correlation reported in the works of Ghasemi [34] and Capra [33]. According to the previous works, the isentropic efficiency of the turbine in off-design conditions ($\eta_{t,od}$) can be expressed as:

$$\eta_{t,od} = \eta_{t,d}\, r_h\, r_v \tag{5}$$

where $\eta_{t,d}$ is the turbine efficiency at design conditions (90.1%), while $r_h$ and $r_v$ are:

$$r_h = ([(1.398\, r_T - 5.425\,)\, r_T + 6.274]\, r_T - 1.886)\, r_T + 0.619 \tag{6}$$

$$r_v = ([(-0.21\, r_{VT} - 1.117)\, r_{VT} - 2.533]\, r_{VT} + 2.588)\, r_{VT} + 0.038 \tag{7}$$

The ratios of the outlet volumetric flow rate ($r_{VT}$) and of the turbine enthalpy drop, used in the relations above, are defined as:

$$r_T = \sqrt{\frac{\dot{V}_{t,out,od}}{\dot{V}_{t,out,d}}} \tag{8}$$

$$r_{VT} = \sqrt{\frac{\Delta h_{t,od}}{\Delta h_{t,d}}} \tag{9}$$

The resulting isentropic efficiency of the turbine and the turbine inlet pressure at partial load conditions are reported in Figure 4.

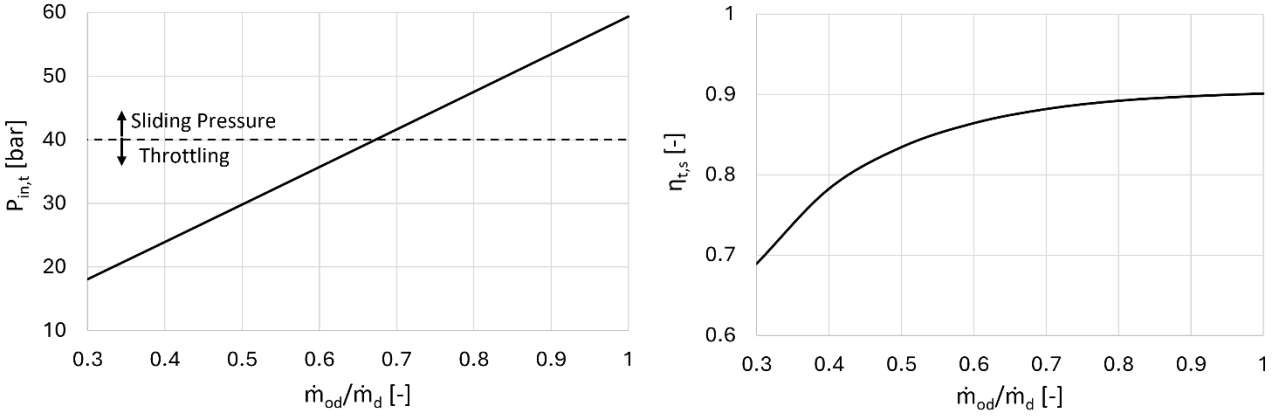


*Figure 4. on the left, the turbine inlet pressure at part-load conditions and the resulting off-design strategies: sliding pressure over 40 bar and a combination of sliding pressure and throttling below 40 bar.*

At part-load, both the turbine's inlet pressure and efficiency (Figure 4) are reduced compared to the design conditions: a steep decrease can be seen below 60% of the nominal load due to transition from sliding pressure to hybrid-throttling operations. The combination of these two effects penalises the cycle thermal efficiency, as shown in Figure 5.

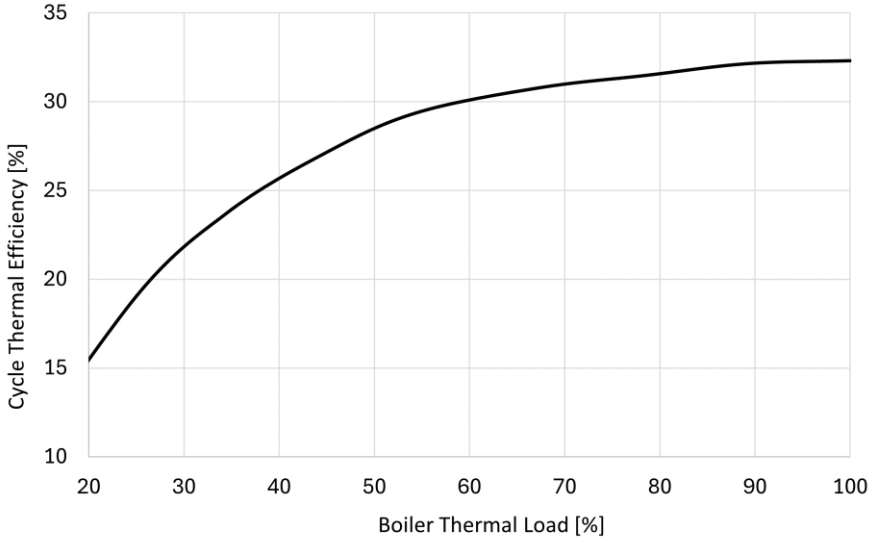


*Figure 5. Cycle thermal efficiency at partial loads of the 1 MW $SiCl_4$ cycle condensing at design temperature (100°C); a steep decrease in cycle efficiency is evident below 60% load due to transition from sliding pressure to hybrid-throttling operations.*

Compared to steam cycles, both state-of-the-art ORC and $SiCl_4$ cycle do not have blade erosion issues at partial load conditions, thus the possibility to span in a wide range of loads.

### 9.5.2 Off-design: full-electric mode

In case of limited number of operating hours in combined heat and power mode, such as for the load-following plant in Figure 2, it is necessary to determine the optimal off-design conditions for full-electric operations. In this scenario, during off-heating hours, the cycle's rejected thermal power is dissipated through an air cooler because the condensation temperature becomes a key variable to optimize for maximizing electrical output. The design of this additional component is presented in the Supplementary material in order to include its cost in the economic analysis of this scenario.

Although lower condensation temperatures can enhance cycle efficiency, they also force the turbine into significant off-design conditions. As the turbine's outlet pressure drops, the enthalpy drop across the turbine increases, leading to higher gas velocity and greater losses in each stage. Additionally, the volumetric flow rate at the turbine outlet increases due to the lower density, further reducing its performance.

As a consequence, the turbine has been evaluated in off-design conditions by varying the condensation temperature/pressure, considering also different cycle mass flow rates. The most significant results are reported in Figure 6.

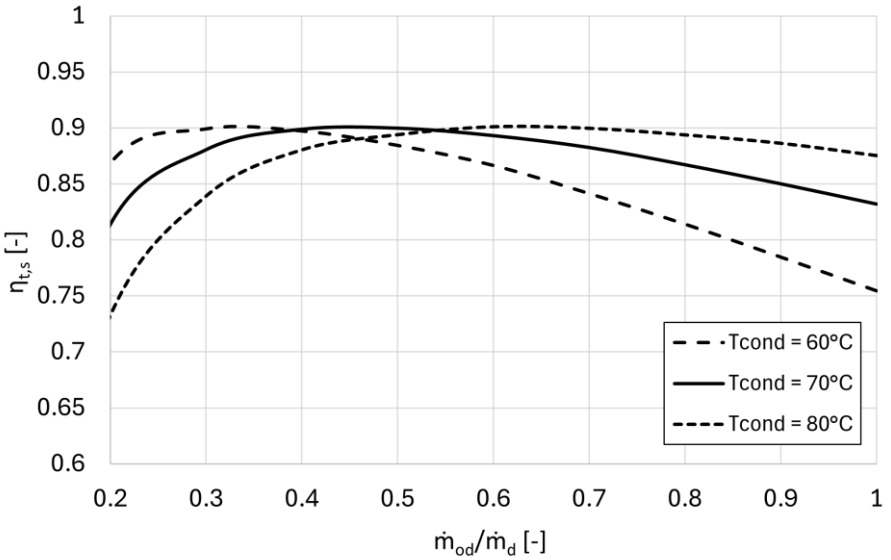


*Figure 6. Turbine isentropic efficiency at different loads, in off-design conditions, when switching to full-electric mode decreasing the condensation temperature compared to design (100°C). The lowest condensation temperature penalises the turbine efficiency. A lower mass flow rate (load) leads to reduced turbine inlet pressure, and efficiency peaks when the off-design enthalpy drop reaches the design value.*

From the results in Figure 6, at design mass flow rate, the case of lowest value of condensation temperature explored (60°C) is the one with the highest penalisation of the turbine's efficiency due to higher enthalpy drop across the turbine with respect to design conditions (100°C condensation). When decreasing the cycle mass flow rate (i.e. the biomass boiler load), the turbine's inlet pressure must be reduced according to the turbine's characteristics (Figure 5); as a consequence, the pressure

ratio and enthalpy drop across the turbine reduces and approaches the design value. For this reason, the off-design efficiency of the turbine reaches approximately the design value in Figure 6 at lower load. However, it is not convenient to run the power block at reduced load due to low cycle efficiency (Figure 5), but also for the low revenues associated with low power production.

The results of the off-design evaluation at different condensation temperatures, at full boiler load, is reported in Figure 7. The optimal solution is to decrease the condensation temperature from 100°C to 70°C during full-electric operations: temperatures below 70°C reduce the advantages of lowering the condensing temperature because the turbine efficiency is too penalised by large enthalpy drop and volume ratio. Reducing the condensation temperature from 70°C to 60°C results in an increase in the volumetric ratio across the turbine, rising from 28 to 38. At 70°C condensation temperature, the cycle thermal efficiency approaches the 35% value, increasing around 3% points compared to design conditions.

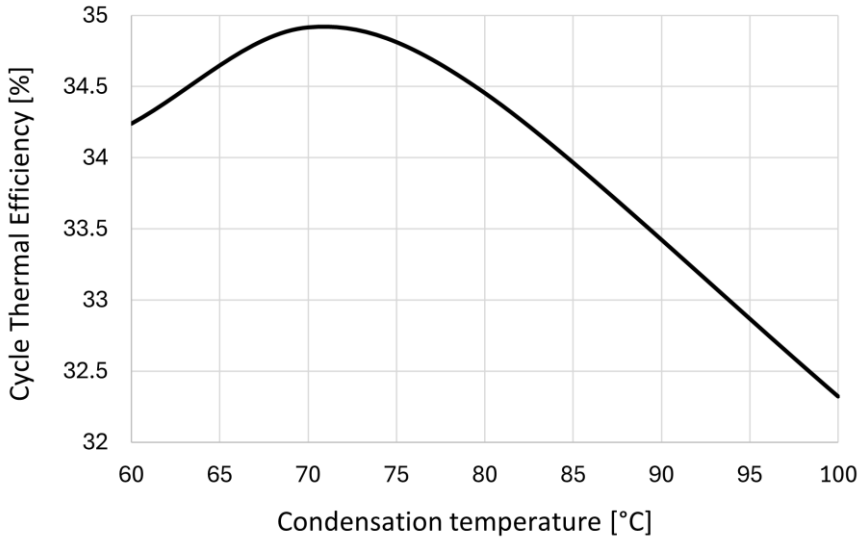


*Figure 7. Cycle thermal efficiency at different condensation temperature in off-design conditions (full-electric mode) of the $SiCl_4$ power unit designed for 100°C condensation temperature; the biomass boiler is operated at full load; the gross cycle efficiency reaches the optimum at around 35% in off-design conditions at 70°C, while further decreasing the condensation temperature implies an efficiency reduction due to turbine's losses.*

The optimal off-design point to operate during the off-heating hours is reported in the T-s diagram of Figure 8 and Table 3.

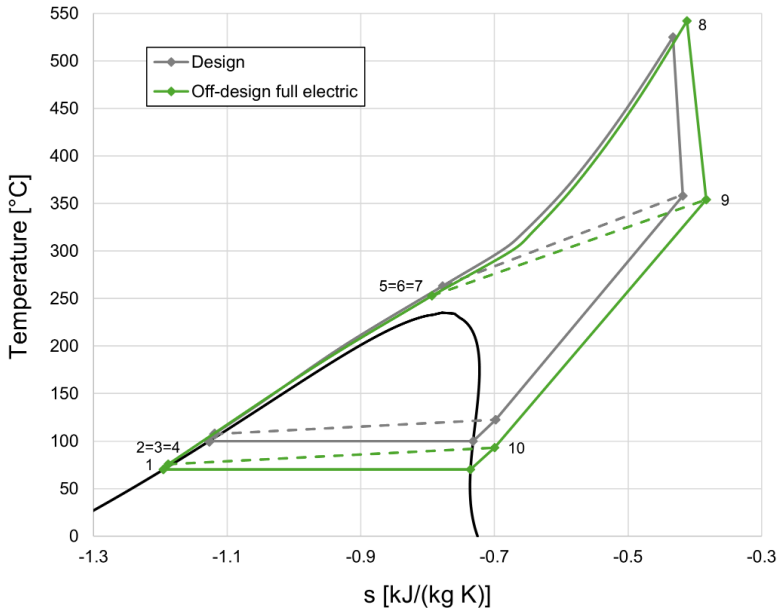


*Figure 8. State diagram of the off-design conditions (green lines) in full-electric mode at 70°C condensation temperature, compared to design conditions (grey lines).*

*Table 3. Thermodynamic states of $SiCl_4$ cycle at full-electric off-design conditions (state diagram in Figure 8).*

| Streams | T [°C] | P [bar] | $x_{vap}$ [-] |
|---|---|---|---|
| 1 | 70 | 1.51 | 0 |
| 2,3,4 | 75.8 | 53.88 | 0 |
| 5,6,7 | 251.3 | 53.47 | 1 |
| 8 | 538.1 | 53.36 | 1 |
| 9 | 350.4 | 1.56 | 1 |
| 10 | 93..2 | 1.53 | 1 |

*Table 4. Conditions of the $SiCl_4$ cycle at full-electric off-design conditions (state diagram in Figure 8).*

| Parameters | units | Values |
|---|---|---|
| Mass Flow Rate $\dot{m}$ | kg/s | 11.75 |
| Split Ratio ($\dot{m}/\dot{m}_{PH}$) | - | 0.89 |
| $\dot{W}_p$ | kW | 73.1 |
| $\dot{W}_t$ | kW | 1150.3 |
| $\dot{Q}_{PHE}$ | kW | 2864.3 |
| $\dot{Q}_{PH}$ | kW | 220.7 |
| $\dot{Q}_{rec}$ | kW | 1789.8 |
| $\dot{Q}_{cond}$ | kW | 1861.6 |
| $\eta_c$ | % | 34.9 |

Compared to design conditions, the maximum cycle pressure is lower according to the turbine's characteristic (Figure 4). At full load of the biomass boiler, the mass flow rate of the working fluid

reaches 90% of the design value (11.75 kg/s), resulting from lowering the condensation temperature to 70°C. The turbine outlet temperature is lower than in design conditions due to the increased expansion ratio, although this is slightly mitigated by reduced turbine efficiency. Consequently, the cold flow entering the recuperator, now at a lower temperature than designed, is preheated to a lower level. With the molten salts temperature fixed at 550°C and the PHE's thermal power maintained at the design value, the cold-end temperature difference of the PHE increases. The overall heat transfer coefficient is only moderately impacted by the 90% mass flow rate, and the slightly higher logarithmic mean temperature difference (LMTD) compared to design conditions results in a modest increase in TIT, from 525°C to 538°C.

## 9.6 Annual energy production

The yearly net electrical and thermal energy production from the designed $SiCl_4$ CHP plant, in the two scenarios delineated in Figure 2, are here discussed. The availability of biomass-ORC plants is usually very high, around 98% for the power block and 98% for the biomass boiler [35], resulting in 8410 operating hours per year. The yearly energy generated by the $SiCl_4$ power block in the two scenarios is reported in Table 6. Heat losses in the HTF circuits have been considered as negligible in this study. A portion of the electrical energy produced is not sent to the grid but used to cover the on-site consumptions of the auxiliaries. The assumptions on the average specific consumption of the auxiliaries of the plant are reported in Table 5.

*Table 5. Assumptions about the average captive consumption of the plant auxiliaries.*

| Auxiliary | Unit | Value |
|---|---|---|
| Biomass handling | $kW_{el}/MW_{th,boiler}$ | 3 [35] |
| HTF pumps | $kW_{el}/MW_{th,boiler}$ | 7 [35] |
| Combustion air fans | $kW_{el}/MW_{th,boiler}$ | 7 [35] |
| Exhaust gas fan | $kW_{el}/MW_{th,boiler}$ | 7 [35] |
| Air-cooler condenser fans* | $kW_{el}$ | 17.6 |

**The consumption of the fans is based on the design (Suppl. Material), to be considered in only-electric mode.*

The baseload CHP plant produces more thermal energy than the load following plant, which is beneficial from the economic standpoint, while the latter operates more hours in full-electric mode rather than in CHP mode. As the load following plant operates less hours at part load, the annual biomass consumption is higher than the baseload scenario.

From the yearly energy production, the Primary Energy Savings (PES) index can be calculated according to Eq. 10:

$$PES\ [\%] = 100 \cdot \left( 1 - \frac{1}{\frac{E_{th,CHP}}{\eta_{th,ref}\ F_{CHP}} + \frac{E_{el,CHP}}{\eta_{th,ref}\ F_{CHP}}} \right) \tag{10}$$

Where:

- $E_{el,CHP}$ and $E_{th,CHP}$ are, respectively, the net electrical and thermal energy produced by the CHP plant.
- $F_{CHP}$ is the primary energy consumed by the CHP plant.
- $\eta_{el,ref}$ and $\eta_{th,ref}$ are, respectively, the reference electrical and thermal efficiency for the separate production of electrical and thermal energy – from biomass - according to the legislation. The harmonized reference efficiency for separate production by solid dry biomass are $\eta_{th,ref}$ =0.86 and $\eta_{el,ref}$ =0.33, starting from 2024 (Commission Delegated Regulation (EU) 2023/2104) [36].

The PES of the cogeneration unit is strictly linked to the incentives: in case the PES is equal or above 10%, or above 0% in case of small cogeneration units (below 1 $MW_{el}$), the plant can be classified as high-efficiency cogeneration and receives incentives (Directive 2012/27/EU of the European Parliament). In many EU countries, incentives are available as Energy Efficiency Certificates (EEC, also called "white certificates") which are proportional to the primary energy saving realized by the CHP plant (in Table 6). The amount of EEC is calculated according to Equations 11-12:

$$Saving\ [MWh] = \frac{E_{el,CHP}\ [MWh]}{\eta_{el,ref}} + \frac{E_{th,CHP}[MWh]}{\eta_{th,ref}} - F_{CHP}[MWh] \quad (11)$$

$$EEC = Saving\ [MWh] \cdot 0.086 \cdot K \quad (12)$$

where K is a harmonisation factor equal to 1.4 for units below 1 $MW_{el}$, and 1.3 in the 1-10 $MW_{el}$ range.

The PES of the CHP plant results equal to 27%. Each EEC corresponds to one ton of oil equivalent (toe) and can be traded on the energy market. The price of one EEC, in Italy, fluctuates between 245 and 260 €/EEC. For the economic analysis in the next section, a value of 250 €/EEC [37] has been assumed.

*Table 6. Annual results for the cogeneration 1 $MW_{gross}$ $SiCl_4$ cycle in the two different scenarios of Figure 2.*

| Parameter | Units | Baseload scenario | Load following scenario |
|---|---|---|---|
| Number of boiler operating hours | h/year | 8410 | 8410 |
| Number of operating hours CHP | h/year | 8410 | 3988 |
| Number of hours full load CHP | h/year | 4391 | 1945 |
| Number of hours full-electric | h/year | 0 | 4422 |
| Electrical energy production | $MWh_{el}$/year | 5'902.9 | 7'260.9 |
| Auxiliary electrical energy consumption | $MWh_{el}$/year | 731 | 1'083.2 |
| Thermal energy production | $MWh_{th}$/year | 14'096.7 | 6'745.1 |
| Biomass consumption | $MWh_{th}$/year | 23'876.3 | 26'872.6 |
| Saving (of primary energy) | $MWh_{th}$/year | 9'063.5 | 4068.7 |
| PES | % | 26.2 | 26.2 |
| EEC | - | 1'091.2 | 489.9 |

## 9.7 Economic analysis

In this section, the economic analysis of the CHP plant, in the baseload and load-following scenarios, in presented.

The main assumptions and correlations used for the economic analysis are listed in Table 7 and discussed here. Costs functions are actualised, if necessary, to 2024 considering the Chemical Engineering Plant Cost Index (CEPCI) index. The specific biomass cost of 30.7 €/MWh in Table 7 is calculated based on the indications provided by a 2023 report of ARERA [38]. This price includes raw material, management, disposal, and transport costs. The wood chip price averages 63.49 €/ton (23.78 €/MWh assuming a LHV of 2.67 MWh/ton), with an ash disposal cost of 1.40 €/MWh and transportation costing 5.52 €/MWh for a 100 km round trip.

*Table 7. Assumptions and correlations for the economic analysis of the biomass CHP plant.*

| | Unit | Value/correlation |
|---|---|---|
| Variable OPEX - Biomass | €/MWh$_{th}$ | 30.7 |
| Biomass boiler | k€ | 3500 [$Q_{boiler}$(MW)/5]$^{0.67}$ |
| HTF boiler + circuit | €/MW$_{LHV}$ | 0.25 |
| Turbine | € | 24'000 [$W_t$(MW)]$^{0.99}$+61'750 [SP/0.18]$^{0.6}$+[$n_{stages}$]$^{1.18}$ |
| Generator | € | 1'850'000 [$W_{el,net}$/11800]$^{0.94}$ |
| Thermal oil | €/kg | 3.1 |
| Molten salts | €/kg | 0.8 |
| BOP | - | 30% of total fixed costs |
| Fixed OPEX - O&M | €/kW$_{el,net}$/year | 100 |
| Fixed OPEX - operators | k€/year | 105 |
| Power block heat exchangers | - | From design – Aspen EDR |

The cost of the biomass boiler is calculated in accordance with the indications of ENEA [39], where the cost of a 5 MW$_{th}$ biomass boiler is considered equal to 3500 k€, with a scale-factor of 0.67 applied. Even if molten salts have higher thermal conductivity and density compared to thermal oil, i.e. lower heat exchange area, it is decided to conservatively consider the same cost of a thermal oil boiler and circuit. In particular, the cost of the HTF boiler (and circuit) is assumed from the indications of Ref. [35] derived from manufacturer's experience.

The correlation presented by Astolfi [40] is used to assess the axial turbine cost. The generator cost is computed with the same correlation used by Wang et al. [41], which is referred to material costs of 2009, then actualized at 2024 through the CEPCI index (+54%).

The cost of the $SiCl_4$ working fluid depends on its purity and the quantity ordered; from a private discussion with a supplier, the cost is fixed at 10 €/kg for an order quantity of 1 ton. The cost of the solar salt is reported to be 0.8 €$/kg [42], while for the thermal oil (Therminol LT), applied in the LT-Loop and in the condenser loop, we assumed the same cost of the similar Therminol VP-1 of 3.1 $/kg [43]. The quantity of $SiCl_4$ is estimated by the volumes of the heat exchangers, while the quantity of

the HTFs is estimated as three time the quantity present in the power block heat exchangers (accounting for all the circuit). The annual operation and maintenance cost (O&M) of the CHP plants is assumed 100€/$kW_{el}$ [44]. Three operators are considered at an annual cost of 35 k€ each.

As regards the heat exchangers of the power block, their cost derives from Aspen Plus EDR, applying the CEPCI correction (+33.4%, from 2020 to 2024). The cost of the pump (including the pump motor) has been provided by the manufacturer [29]. The balance of plant is assumed to be the 30% of the fixed costs associated to the entire biomass plant.

The fixed costs of the CHP plant are presented in Table 8.

*Table 8. Capital cost of the CHP plant.*

| | **Value [k€]** |
|---|---|
| Biomass boiler | 2'819.9 |
| HTF boiler + circuit | 879 |
| Turbine | 426 |
| Generator | 256.2 |
| Condenser | 60.5 |
| Recuperator | 111.5 |
| PHE | 68.2 |
| Pre-Heater | 45.2 |
| DH-HX | 23.3 |
| Air-cooler* | 105.8 |
| Pump (with motor) | 37 |
| Working fluid | 9.5 |
| Molten salts | 1.8 |
| Thermal oil | 19 |
| BOP (baseload plant) | 1'435.1 |
| BOP (load-following plant) | 1'466.8 |
| Total power block (baseload) | 2'470 |
| Total CHP plant (baseload) | 6'218.7 |

*To be considered only for load-following plant scenario.

The load-following scenario differs from the baseload one by the installation of an auxiliary air-cooler which dissipates to the environment the heat rejected by the cycle at the condenser.

The specific capital cost of the $SiCl_4$-based power block module resulted to be around 2500 €/kW, which is aligned with the findings of Quoilin [45] and Taljan et al. [11] for ORCs at equal power output.

For the investment analysis, additional financial assumptions adopted for the CHP plant are listed in Table 9.

*Table 9. Financial assumptions for investment analysis of the CHP plant.*

| Parameter | Value |
|---|---|
| Discount rate r | 6% |
| Plant lifetime | 20 years |
| Amortisation time | 10 years |
| Tax rate | 27.9% |
| Heat selling price | 140.1 €/MWh$_{th}$ |
| **Context: quota-system (certificates)** | |
| Electricity selling price | 126.9 €/MWh$_{el}$ |
| EEC | 250 €/EEC |
| EEC time | 15 years |
| **Context: current Italian conditions (2024)** | |
| Capital expense discount | 40% |
| Electricity selling price (20 years) | 162.8 €/MWh$_{el}$ |

An income tax rate of 27.9% is considered as the sum of Italian IRES (Corporate Income Tax, 24%) and IRAP (Regional Tax on Productive Activities, 3.9% on average).

Many operators set district heating prices based on the cost users would face with alternative heating systems, including the variation of the fuel cost over time. In areas served by natural gas, this reference is typically a gas boiler, and the resulting avoided cost for hot domestic water is around 120 €/MWh [37]. However, for decentralized biomass CHP plant in areas that are not connected to the natural gas grid, the reference is the liquefied petroleum gas (LPG), which is more expensive than natural gas. According to a report of GSE, the heat selling price is assumed in this study equal to 140.1 €/MWh$_{th}$ [46].

As regards the revenues from the electrical energy production, two scenarios have been considered (Table 9): i) a selling price of 126.9 €/MWh$_{el}$, equal to the average value of the Italian PUN ("Prezzo Unico Nazionale", i.e. Single National Price) in 2023, plus the revenues coming from the quota-system mechanism of the white certificates; ii) the current Italian conditions under "FER2" decree, which offers a guaranteed tariff of 185 €/MWh$_{el}$ for 20 years to new biomass plants under 1 MWel, with a 3% annual reduction for future installations. In the latter scenario, a capital grant covering up to 40% of the investment is available, but receiving the full grant reduces the tariff to 162.8 €/MWh$_{el}$.

The net Present Value (NPV) is the current value of all future cash flows (CF), both positive and negative, discounted back to the present time, according to Equation 13:

$$NPV = \sum_{t=1}^{N} \frac{CF_t}{(1+r)^t} - I_0 \quad (13)$$

The trend of the NPV along the lifetime of the plant is shown in Figure 9. No power production is considered within the first year due to manufacturing and installation of the plant. The discounted payback time (DPBT) is the number of years required to reach a NPV equal to zero. The DPBT is 5.5 years for the baseload scenario under the incentivisation scheme of EEC, while it is lower than 4

years under the actual Italian conditions of "FER2" decree. The load-following scenario results to be profitable, with 7 years DPBT, only under current Italian tariff.

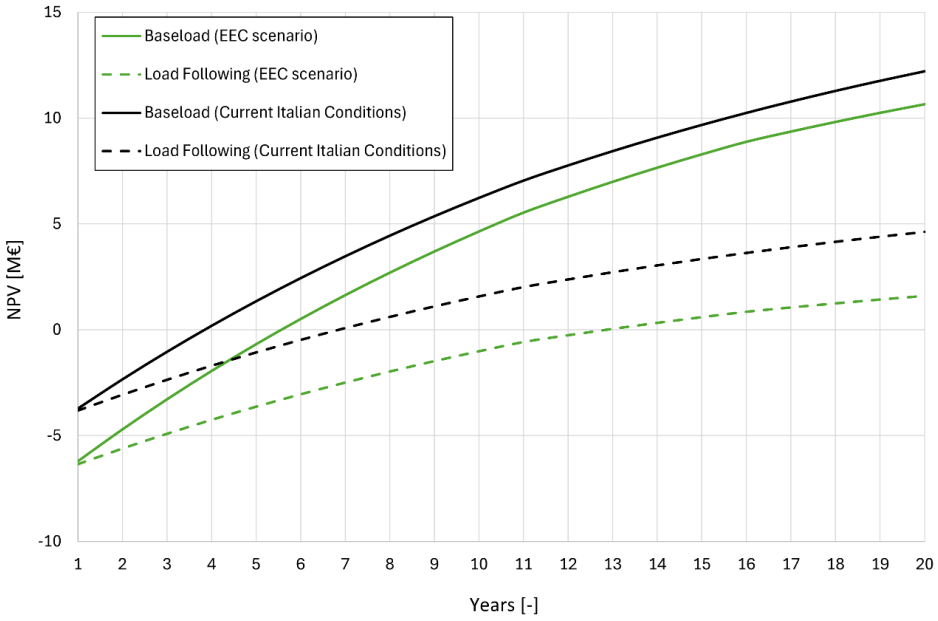


*Figure 9. Actualised cash flow along 20 years CHP plant lifetime in the two different scenarios (baseload and load following); a discounted payback period below four years is found for the baseload plant. The economic analysis is carried out with the financial assumptions of Table 9 (both quota-system scheme based on ECC and guaranteed tariff under current Italian conditions). The lower initial investment cost for the current Italian situation (black curves) is due to 40% of capital expense discount foreseen by legislation (Table 9).*

The internal rate of return (IRR), i.e. the discount rate r for which the value of NPV becomes equal to zero at 20$^{th}$ year, results equal to 39% for the baseload CHP plant under current Italian tariff, proving the profitability of the proposed solutions. The load following scenario is less profitable due to lower thermal power production along the year, showing an IRR of 19.6%. Considering the quota-system scheme based on ECC, the IRR of both base-load and load-following plants decreases to 24.9% and 9.2% respectively.

All the previous calculations consider a heat selling price with is adequate for decentralized plants. Considering instead a heat selling price of 120 €/MWh$_{th}$ [37], which is more aligned with non-decentralized DHN, the DPBT increases to 4.5 years for the baseload plant under current Italian conditions for the electricity price. This result demonstrates the economic profitability of the plant under current conditions in Italy, helping to reduce the reliance of biomass CHP systems on incentives.

## 9.8 Conclusions

In this study, a 1 MW $SiCl_4$ power cycle was integrated into a biomass cogeneration plant. $SiCl_4$'s advanced thermo-chemical stability allows for a notable increase in electrical efficiency, achieving around 30% net electrical efficiency at a turbine inlet temperature of 525°C in combined heat and power mode. The cycle's performance was analysed for both part-load and full-electric operations.

Results indicate that the $SiCl_4$ cycle offers higher efficiency compared to similar-sized commercial ORC systems. Efficiency drops below 60% of nominal load due to throttling losses, but the system performs well in partial load conditions. Lowering the condensation temperature from 100°C to 70°C improves performance in full-electric mode, achieving a thermal efficiency near 35%, about 3 percentage points higher than at design conditions.

For an existing district heating network, the CHP plant's annual production was evaluated in baseload and load-following modes. In baseload, the plant saves 9.1 GWh of primary energy annually, with a primary energy saving index of 26.2%. The $SiCl_4$ power block costs approximately €2,500 per kW, leading to a total investment of around six million euros for the entire CHP plant.

With current Italian renewable energy conditions, including a guaranteed tariff for electricity, the CHP plant has a discounted payback period of under four years for baseload and nearly six years for load-following. The baseload plant's internal rate of return is 39%, highlighting the technology's potential. It is important to note that the analysis of CHP cycle efficiency under both design and off-design conditions has general applicability. However, the economic analysis conducted in this study is specific to the economic conditions of the selected case study (Italy), including factors such as electricity and heat selling prices and biomass costs.

## Nomenclature

**Acronyms/Abbreviations**

| | | | |
|---|---|---|---|
| BOP | Balance of Plant | HX | Heat exchanger |
| CEPCI | Chemical Engineering Plant Cost Index | LT | Low Temperature |
| CHP | Combined Heat and Power | ORC | Organic Rankine Cycle |
| DH | District Heating | PES | Primary Energy Saving |
| DHN | District Heating Network | PH | Pre-Heater |
| EEC | Efficiency Energy Certificate | PHE | Primary Heat Exchanger |
| EU | European Union | PHE | Primary Heat Exchanger |
| HT | High temperature | TIT | Turbine Inlet Temperature |
| HTF | Heat transfer fluid | | |

**Symbols**

| | | | |
|---|---|---|---|
| $\beta$ | Pressure Ratio | T | Temperature |
| h | Specific Mass Enthalpy | x | Mass Fraction |
| P | Pressure | W | Mechanical Power |
| Q | Thermal Duty | Z | Compressibility Factor |
| r | Discount Rate | $\eta$ | Efficiency |
| $\gamma$ | Heat Capacity Ratio | $\Delta$ | Difference |
| R | Universal Gas Constant | | |

**Subscripts and superscripts**

| | | | |
|---|---|---|---|
| c | Cycle | max | Maximum |

| | | | |
|---|---|---|---|
| cond | Condensation | od | Off Design |
| d | Design | out | Outlet |
| el | Electric | p | Pump |
| gen | Generator | t | Turbine |
| in | Inlet | th | Thermal |
| m | Mechanical | vap | Vapour |
| min | Minimum | | |

## 9.9 Bibliography


[1] Camia A, Giuntoli, J. Jonsson, R. Robert, The use of woody biomass for energy production in the EU and impacts on forests The use of woody biomass for energy production in the EU, 2021. https://doi.org/10.2760/831621.

[2] I. Obernberger, G. Thek, COMBUSTION AND GASIFICATION OF SOLID BIOMASS FOR HEAT AND POWER PRODUCTION IN EUROPE – STATE-OF-THE- ART AND RELEVANT FUTURE DEVELOPMENTS, (2008) 1–24.

[3] A. Duvia, M. Gaia, ORC plants for power production from biomass from 0.4 MWe to 1.5 MWe: technology, efficiency, practical experiences and economy, in: Proc. 7th Holzenergie Symopsium, Zurich, 2002.

[4] I. Obernberger, P. Thonhofer, E. Reisenhofer, Description and evaluation of the new 1,000 kWel organic rankine cycle process integrated in the biomass CHP plant in Lienz, Austria, Euroheat and Power. 10 (2002) 1–17. https://api.semanticscholar.org/CorpusID:56093527.

[5] M. Tańczuk, R. Ulbrich, Implementation of a biomass-fired co-generation plant supplied with an ORC (Organic Rankine Cycle) as a heat source for small scale heat distribution system - A comparative analysis under Polish and German conditions, Energy. 62 (2013) 132–141. https://doi.org/10.1016/j.energy.2013.09.044.

[6] M. Noussan, G. Cerino Abdin, A. Poggio, R. Roberto, Biomass-fired CHP and heat storage system simulations in existing district heating systems, Appl. Therm. Eng. 71 (2014) 729–735. https://doi.org/10.1016/j.applthermaleng.2013.11.021.

[7] K. Braimakis, A. Charalampidis, S. Karellas, Techno-economic assessment of a small-scale biomass ORC-CHP for district heating, Energy Convers. Manag. 247 (2021) 114705. https://doi.org/10.1016/j.enconman.2021.114705.

[8] J. Kalina, M. Świerzewski, Identification of ORC unit operation in biomass-fired cogeneration system, Renew. Energy. 142 (2019) 400–414. https://doi.org/https://doi.org/10.1016/j.renene.2019.04.080.

[9] M. Świerzewski, J. Kalina, Optimisation of biomass-fired cogeneration plants using ORC technology, Renew. Energy. 159 (2020) 195–214. https://doi.org/10.1016/j.renene.2020.05.155.

[10] M. Świerzewski, J. Kalina, A. Musiał, Techno-economic optimization of ORC system structure, size and working fluid within biomass-fired municipal cogeneration plant retrofitting project, Renew. Energy. 180 (2021) 281–296. https://doi.org/10.1016/j.renene.2021.08.068.

[11] G. Taljan, G. Verbič, M. Pantoš, M. Sakulin, L. Fickert, Optimal sizing of biomass-fired Organic Rankine Cycle CHP system with heat storage, Renew. Energy. 41 (2012) 29–38. https://doi.org/10.1016/j.renene.2011.09.034.

[12] N.E. Consulting, Electricity Generation Costs and Hurdle Rates Lot 1: Hurdle Rates update for Generation Technologies Prepared for the Department of Energy and Climate Change (DECC), 2015.

[13] M. Tańczuk, Reconfiguration of a small, inefficient district heating systems by means of biomass

Organic Rankine Cycle cogeneration plants – Polish and German perspective after 2035, Renew. Energy. 211 (2023) 452–458. https://doi.org/https://doi.org/10.1016/j.renene.2023.05.032.

[14] M. Uris, J.I. Linares, E. Arenas, Techno-economic feasibility assessment of a biomass cogeneration plant based on an Organic Rankine Cycle, Renew. Energy. 66 (2014) 707–713. https://doi.org/https://doi.org/10.1016/j.renene.2014.01.022.

[15] Y. Feng, F. Zhang, J. Xu, Z. He, Q. Zhang, Parametric analysis and multi-objective optimization of biomass-fired organic Rankine cycle system combined heat and power under three operation strategies, Renew. Energy. 208 (2023) 431–449. https://doi.org/10.1016/j.renene.2023.03.053.

[16] M. Doninelli, G. Di Marcoberardino, P. Iora, M. Gelfi, C.M. Invernizzi, G. Manzolini, Silicon Tetrachloride as innovative working fluid for high temperature Rankine cycles: Thermal Stability, material compatibility, and energy analysis, Appl. Therm. Eng. 249 (2024) 123239. https://doi.org/10.1016/j.applthermaleng.2024.123239.

[17] M. Doninelli, E. Morosini, G. Di Marcoberardino, C.M. Invernizzi, P. Iora, M. Riva, P. Stringari, G. Manzolini, Experimental investigation of the CO2+SiCl4 mixture as innovative working fluid for power cycles: Bubble points and liquid density measurements, Energy. 299 (2024) 131197. https://doi.org/10.1016/j.energy.2024.131197.

[18] A. Salogni, D. Alberti, M. Metelli, R. Bertanzi, Operation and maintenance of a biomass fired - Organic Rankine Cycle - CHP plant: The experience of Cremona, Energy Procedia. 129 (2017) 668–675. https://doi.org/10.1016/j.egypro.2017.09.141.

[19] Q. Eppinga, S. Ganassin, J. Van Buijtenen, Application and operation of 40+ Triogen ORC plants, Energy Procedia. 129 (2017) 684–691. https://doi.org/10.1016/j.egypro.2017.09.145.

[20] M. Caldera, R.Ł Roberto, Analysis of the performance of biomass - fired boilers coupled with high - temperature CHP cycles, 2013 (2013) 483368.

[21] A. Sorrentino, A.M. Pantaleo, C.N. Markides, G. Braccio, E. Fanelli, S.M. Camporeale, Energy performance and profitability of biomass boilers in commercial sector: The case study of Sainsbury's stores in the UK, Energy Procedia. 148 (2018) 639–646. https://doi.org/10.1016/j.egypro.2018.08.152.

[22] A. Mugnini, G. Comodi, D. Salvi, A. Arteconi, Energy flexible CHP-DHN systems: Unlocking the flexibility in a real plant, Energy Convers. Manag. X. 12 (2021) 100110. https://doi.org/https://doi.org/10.1016/j.ecmx.2021.100110.

[23] A. Foresti, Turboden : ORC Solutions for Cogeneration and District Heating, 2015.

[24] A. Salogni, D. Alberti, M. Metelli, R. Bertanzi, Operation and maintenance of a biomass fired - Organic Rankine Cycle - CHP plant: The experience of Cremona, Energy Procedia. 129 (2017) 668–675. https://doi.org/10.1016/j.egypro.2017.09.141.

[25] R. Bini, State of the Art of Orc Technology for Biomass Plants, IEA Bioenergy Work. Small Scale Biomass Co-Generation Technol. (2010). http://www.ieabcc.nl/workshops/task32_Copenhagen/06 Bini -Turboden.pdf.

[26] J. Coventry, C. Andraka, J. Pye, M. Blanco, J. Fisher, A review of sodium receiver technologies for central receiver solar power plants, Sol. Energy. 122 (2015) 749–762. https://doi.org/10.1016/j.solener.2015.09.023.

[27] Aspen Technology Inc., Aspen Plus®, Version V12.1, (2022).

[28] The MathWorks Inc., MATLAB. (2022a).

[29] Pompe Garbarino S.p.A, https://pompegarbarino.com/it/ (accessed February 1, 2024).

[30] IEA, Combined Heat and Power, 2008. https://www.iea.org/reports/combined-heat-and-power.

[31] E. Martelli, F. Capra, S. Consonni, Numerical optimization of Combined Heat and Power Organic Rankine Cycles – Part A: Design optimization, Energy. 90 (2015) 310–328. https://doi.org/https://doi.org/10.1016/j.energy.2015.06.111.

[32] D.H. Cooke, On prediction of off-design multistage turbine pressures by stodola's ellipse, J. Eng. Gas Turbines Power. 107 (1985) 596–606. https://doi.org/10.1115/1.3239778.

[33] F. Capra, E. Martelli, Numerical optimization of combined heat and power Organic Rankine Cycles - Part B: Simultaneous design & part-load optimization, Energy. 90 (2015) 329–343. https://doi.org/10.1016/j.energy.2015.06.113.

[34] H. Ghasemi, M. Paci, A. Tizzanini, A. Mitsos, Modeling and optimization of a binary geothermal power plant, Energy. 50 (2013) 412–428. https://doi.org/10.1016/j.energy.2012.10.039.

[35] A. Guercio, R. Bini, Biomass-fired Organic Rankine Cycle combined heat and power systems, Elsevier Ltd, 2017. https://doi.org/10.1016/B978-0-08-100510-1.00015-6.

[36] European Union, Commission Delegated Regulation (EU) 2023/2104 of 4 July 2023 amending Delegated Regulation (EU) 2015/2402 as regards the review of harmonised efficiency reference values for separate production of electricity and heat in application of Directive 2012/27/, 2023.

[37] M. Baiguini, M. Doninelli, E. Morosini, D. Alfani, G. Di Marcoberardino, P. Giulio Iora, G. Manzolini, C. Mario Invernizzi, M. Astolfi, Small scale CO2 based trigeneration plants in heat recovery applications: A case study for residential sector in northern Italy, Appl. Therm. Eng. 255 (2024) 123943. https://doi.org/https://doi.org/10.1016/j.applthermaleng.2024.123943.

[38] E. Patrucco, L. Mazzocchi, Delibera ARERA 129/2023 Costo di generazione dell'energia elettrica da biomassa solida, 2023. https://www.arera.it/fileadmin/allegati/docs/23/601-23rapporto.pdf.

[39] E. Macchi, M. Astolfi, D. Bonalumi, A. Giuffrida, C. Invernizzi, M. Romano, P. Silva, D. Turi, R. Roberto, V. Gerardi, M. Caldera, Valutazione di cicli termodinamici innovativi per applicazioni con caldaie a sali fusi alimentate a biomassa legnosa, (2013). https://re.public.polimi.it/handle/11311/794719.

[40] M. Astolfi, An innovative approach for the techno-economic optimisation of organic Rankine cycle, 2014.

[41] X.Q. Wang, X.P. Li, Y.R. Li, C.M. Wu, Payback period estimation and parameter optimization of subcritical organic Rankine cycle system for waste heat recovery, Energy. 88 (2015) 734–745. https://doi.org/10.1016/j.energy.2015.05.095.

[42] G. Manzolini, G. Lucca, M. Binotti, G. Lozza, A two-step procedure for the selection of innovative high temperature heat transfer fluids in solar tower power plants, Renew. Energy. 177 (2021) 807–822. https://doi.org/10.1016/j.renene.2021.05.153.

[43] J.D. McTigue, J. Castro, G. Mungas, N. Kramer, J. King, C. Turchi, G. Zhu, Hybridizing a geothermal power plant with concentrating solar power and thermal storage to increase power generation and dispatchability, Appl. Energy. 228 (2018) 1837–1852. https://doi.org/10.1016/j.apenergy.2018.07.064.

[44] IEA ETSAP, Technology Brief E05 - Biomass for Heat and Power, (2010) 1–8. https://iea-etsap.org/E-TechDS/PDF/E05-BiomassforHP-GS-AD-gct.pdf.

[45] S. Quoilin, M. Van Den Broek, S. Declaye, P. Dewallef, V. Lemort, Techno-economic survey of organic rankine cycle (ORC) systems, Renew. Sustain. Energy Rev. 22 (2013) 168–186. https://doi.org/10.1016/j.rser.2013.01.028.

[46] GSE, VALUTAZIONE DEL POTENZIALE NAZIONALE DI APPLICAZIONE DELLA COGENERAZIONE AD ALTO RENDIMENTO E DEL TELERISCALDAMENTO EFFICIENTE, 2015.

## 9.10 Supplementary Materials

### 9.10.1 Results of components design for the 1 MW $SiCl_4$ power cycle

In this Section, the results of the component design are outlined for the 1 MW gross power cycle described in Section 1. Aspen Exchanger Design and Rating (EDR) V12 [1] is used for the design and

off-design of the heat exchangers. Regarding the turbomachines, the turbine is designed in MATLAB while the pump is selected based on the recommendations of a manufacturer. The thermodynamic properties of $SiCl_4$ are obtained with the Peng Robinson equation of state, while the transport properties (dynamic viscosity and thermal conductivity) are calculated as in Ref. [2] in MATLAB with the use of the friction-theory model.

### 9.10.2 Heat exchangers

As the maximum absolute pressure in the cycle is 60 bar, an in-tube configuration is preferred for mechanical reasons. Therefore, all the heat exchangers (HX) have been designed as Shell and Tube (S&T) heat exchangers, with the high-pressure $SiCl_4$ flowing in tube. Specifically, bonnet type heads are chosen because they offer the best option when the head doesn't require frequent removal, as in the case of ORCs. For each HX, the most economical configuration in terms of flow arrangement (crossflow, counterflow), tube/shell diameter, and tube type (finned, unfinned) has been identified and outlined in Table 1.

*Table 1. Heat exchangers design results for 1 $MW_{gross}$ $SiCl_4$ cycle designed for CHP ($T_{min}$ 100°C).*

| Parameters | units | REC | Pre-Heater | PHE | Condenser |
|---|---|---|---|---|---|
| Number of Units | - | 1 | 1 | 1 | 1 |
| Type | - | Crossflow-Finned | Counterflow-Multi Tube Hairpin | Counterflow Long-Baffle | Crossflow |
| Fin Frequency | #/meter | 350 | - | - | - |
| Tubes Number | - | 816 | 151 | 545 | 400 |
| Tubes OD/ID/Pitch | mm | 13/12.44/16.25 | 13/12.44/16.25 | 13/12.44/16.25 | 25.4/23.29 /31.75 |
| Tube Length | mm | 5400 | 6096 | 6096 | 6000 |
| Tube Arrangement | - | 30°-Triangular | 30°-Triangular | 60°-Rotated Triangular | 30°-Triangular |
| Tube Passes | - | 8 | 1 | 2 | 4 |
| Shell OD/ID | mm | 991/967 | 273.05/254.51 | 441.3/431.8 | 776/752 |
| HTC Tube | $W/(m^2 K)$ | 1457.2 | 215.8 | 774.5 | 1276.2 |
| HTC Shell | $W/(m^2 K)$ | 471.2 | 499.2 | 2084.6 | 1292.9 |
| Overall Area | $m^2$ | 1994.3 | 79.5 | 132.1 | 191.5 |
| $\Delta P$ tube/shell | bar | 0.532/0.019 | 0.002/0.01 | 0.106/0.092 | 0.21/0.011 |

As already discusses, friction theory models have been used for the thermal conductivity and dynamic viscosity, since Aspen's transport property models provides poor accuracy in comparison with available experimental data for $SiCl_4$, especially in high-density regions [2]. The thermophysical properties of the molten salts mixture used in the PHE design are reported in [3]. Instead, the

properties of Therminol LT, adopted as HTF in the Pre-Heater and in the condenser, are taken by the product datasheet [4].

According to previous thermal stability and material compatibility study [2], the tubes of the heat exchangers are manufactured in stainless steel SS316 material except for the tubes of the condenser that are designed in carbon steel due to low temperature service.

### 9.10.3 Axial turbine

Axial-flow turbines are used in commercial ORC systems with a limited number of stages. Specifically, the cantilever (overhung) configuration is the most commonly employed arrangement for ORC axial turbines, with bearings placed only to one side of the shaft. This configuration imposes a restriction on the number of stages, often limited to 3/4 due to considerations related to rotordynamics.

For the 1 MW $SiCl_4$ system, a 4-stage turbine is being considered instead of the more typical 2 or 3-stage machine. The significant electric efficiency of the $SiCl_4$ cycle justifies a more substantial investment in design efforts.

In this section, the results of the preliminary design and optimization of the 4-stages axial turbine, as performed in MATLAB using the AxialOpt code [5], are presented. Lookup tables are provided as input for the properties of $SiCl_4$ during the expansion. The optimization is carried out with a mean line design considering the Dunham-Came model [6] for the profile, secondary, tip-clearance, and trailing edge losses. A high-speed machine connected to the generator through a speed reduction gearbox is considered as the rotational speed is optimised. The objective function that is maximized is the total-to-static efficiency of the turbine defined as in Equation 1:

$$\eta_{t,ts} = \frac{\Delta h_{0,t}}{\Delta h_{ts,t} - 0.5 \cdot \frac{C_{a,out}^2}{2}} \quad (1)$$

where $\Delta h_{0,t}$ is the total enthalpy drop across the turbine, $\Delta h_{ts,t}$ is the total-to-static enthalpy drop across the turbine, and $C_{a,out}$ is the absolute axial velocity at the exit of the last stage; the coefficient 0.5 indicates that 50% of the kinetic energy is assumed to be recovered by the fixed diffuser.The results of the design are presented in Table 2.

*Table 2. Preliminary 4-stages axial turbine design for 1 MW $SiCl_4$ cycle for CHP ($T_{min}$ 100°C).*

| **Parameters** | **Units** | **Value** | | | |
|---|---|---|---|---|---|
| Medium diameter $D_m$ | mm | 106.1 | | | |
| Stages Number (n) | - | 4 | | | |
| Blade Height | | 1st stage | 2nd stage | 3rd stage | 4th stage |
| | mm | 12.2 | 13.7 | 17.2 | 27.8 |
| Degree of Reaction | - | 0.48 | 0.38 | 0.45 | 0.55 |
| Rotational Speed | rpm | 30'581 | | | |
| Maximum Mach Number | - | 0.95 | | | |
| Total-to-static efficiency | % | 90.1 | | | |

### 9.10.4 Feed Pump

The feed pump inlet pressure is imposed by saturation conditions of $SiCl_4$ at 100°C, which corresponds to 3.34 bar as absolute pressure, while the maximum cycle pressure at design conditions is set as high as 60 bar.

The pump selection was performed with courtesy of the manufacturer Garbarino® [7], a leading company specialized in the production of centrifugal and positive displacement pumps: their multi-stage centrifugal pumps (GH series) can fit the required operating conditions achieving head up to 85 bar and capacities up to 500 $m^3/h$. The specific pump model selected is 50 GHB10, where the main characteristics and performance are reported in Table 3. The materials employed for the impeller is AISI 316L, which is compatible with the working fluid [2].

*Table 3. Pump selected for 1 $MW_{gross}$ $SiCl_4$ cycle.*

| Parameters | Units | Value |
|---|---|---|
| $Q_{des}$ | $m^3/hour$ | 36.1 |
| $H_{des}$ | m | 442.9 |
| Pump Type | - | Horizontal - Multistage |
| DN Suction/Discharge | mm | 80/50 |
| Rotational Speed | rpm | 2950 |
| Impeller Diameter | mm | 179 |
| NPSH required | m | 1.9 |
| Pump Efficiency | - | 0.612 |
| Motor Power (50 Hz) | kW | 110 |

### 9.10.5 Air Cooler

During off-heating hours, the CHP plant can decrease the condensation temperature and reject the heat to the environment with the use of an additional air-cooler. The condensing $SiCl_4$ at 70°C transfers the thermal power to the oil loop (45-65°C), which in turns releases it to the water loop (40-60°C). Eventually, the thermal power is rejected through the air-cooler, assuming an air temperature equal to 25°C. The main characteristics of the additional air-cooler are summarised in Table 4. The assumed air temperature at the bundle exit is equal to 50°C in order to maintain low the fans electric consumption. The tube material considered is carbon steel. As standard air-cooler operation, G-finned tubes with a fin frequency of 433 fins per meter, made of aluminium 1060, have been considered.

*Table 4. Results of the design of the additional air-cooler.*

| Parameters | Units | Value |
|---|---|---|
| Tubes number per bundle | - | 154 |

| | | |
|---|---|---|
| Bundles per Bay | - | 2 |
| Bays Number | - | 1 |
| Bare Area/Bundle | $m^2$ | 109.6 |
| Number of Rows/Passes | - | 7/4 |
| Tube OD/thickness | mm | 25.4/1.65 |
| Fin OD/thickness | mm | 57.15/0.28 |
| Tube Length | m | 9.14 |
| Bundle width | m | 3.0 |
| Face velocity | m/s | 2.72 |
| Finned Surface | $m^2$ | 5147.4 |
| Pressure drop air side | Pa | 165 |
| Pressure drop tube side | bar | 0.24 |
| Fan Diameter | m | 2.13 |
| Number of Fans | - | 3 |
| Single Fan Power | $kW_{el}$/fan | 5.85 |

### 9.10.6 Bibliography


[1] Aspen Technology Inc., Aspen Exchanger Design & Rating, https://www.aspentech.com/en/products/engineering/aspen-exchanger-design-and-rating.

[2] M. Doninelli, G. Di Marcoberardino, P. Iora, M. Gelfi, C.M. Invernizzi, G. Manzolini, Silicon Tetrachloride as innovative working fluid for high temperature Rankine cycles: Thermal Stability, material compatibility, and energy analysis, Appl. Therm. Eng. 249 (2024) 123239. https://doi.org/10.1016/j.applthermaleng.2024.123239.

[3] A.B. Zavoico, Solar Power Tower - Design Basis Document, Tech. Rep. SAND2001-2100. (2001) 148. https://doi.org/10.2172/786629.

[4] Therminol, Therminol LT datasheet, https://www.therminol.com/product/71093466?pn=Therminol-LT-Heat-Transfer-Fluid.

[5] R. Agromayor, L.O. Nord, Preliminary design and optimization of axial turbines accounting for diffuser performance, Int. J. Turbomachinery, Propuls. Power. 4 (2019). https://doi.org/10.3390/ijtpp4030032.

[6] J.B. Dunham, P.M. Came, Improvements to the Ainley-Mathieson Method of Turbine Performance Prediction, J. Eng. Power. 92 (1970) 252–256.

[7] Pompe Garbarino S.p.A, https://pompegarbarino.com/it/ (accessed February 1, 2024).

# *Chapter 10 - Conclusions and remarks*

This research focused on the thermophysical characterization and experimental validation of innovative working fluids aimed at enhancing the performance of high-temperature thermodynamic cycles. The investigation, spanning Organic Rankine Cycles (ORC), high-temperature heat pumps (HTHP), and power cycles for Concentrated Solar Power (CSP) systems, addresses the broader context of improving energy conversion efficiency while contributing to industrial decarbonization efforts.

A primary contribution of this research was the identification and experimental assessment of silicon tetrachloride ($SiCl_4$) as a working fluid suitable for high-temperature power cycles. Unlike conventional ORC fluids, which are typically limited by thermal stability constraints at around 300-350°C, $SiCl_4$ demonstrated stability at much higher temperatures. Experimental testing confirmed that $SiCl_4$ can operate reliably at temperatures up to 650°C, opening new opportunities for energy recovery from high-grade heat sources such as biomass combustion, industrial flue gases, and solar thermal systems. Although the reactivity of the fluid is less severe than with fluids such as titanium tetrachloride ($TiCl_4$), appropriate system design—including maintaining pressures above atmospheric or using a cover gas shield—would be essential to mitigate these risks and ensure safe operation.

The thermodynamic analysis conducted as part of this research highlighted that, under realistic conditions, a $SiCl_4$-based ORC system could achieve an efficiency gain of approximately 10 percentage points compared to state-of-the-art organic fluids.

In addition to $SiCl_4$, the research introduced fluorobenzene as an alternative fluid for both ORC and HTHP systems. Fluorobenzene's favourable environmental profile—characterized by near-zero Global Warming Potential (GWP) and zero Ozone Depletion Potential (ODP)—makes it an attractive option in light of increasing regulatory pressures on traditional high-temperature fluids, such as hydrofluorocarbons (HFCs). The experimental investigation into fluorobenzene's thermal stability confirmed its resilience up to 350°C, positioning it as a competitive candidate for high-temperature ORC units. A unique stability test was performed on fluorobenzene to simulate real operating conditions, including the presence of a non-condensable gases (NCG) removal system commonly used in ORC systems. This stability test involved subjecting fluorobenzene to a prolonged thermal stress at 350°C with intermittent aspiration to simulate the activation of the NCG removal system. The fluid's volumetric behaviour returned to its initial (pre-stress) state after the aspiration, and subsequent FTIR analysis showed no significant formation of degradation products in the liquid phase. This result suggests that, in a practical ORC system, fluorobenzene could maintain its stability and performance over extended use, provided the presence of an effective NCG management system.

Moreover, in the context of high-temperature heat pumps, fluorobenzene demonstrated good performance across a range of industrially relevant conditions, with coefficients of performance (COP) exceeding 3.25 in applications delivering heat at around 180°C with 100°C temperature lift.

The analysis also explored fluorobenzene's suitability for direct heat exchange with flue gases at 390°C, revealing promising efficiency levels in power generation. The net power output achieved

with fluorobenzene was comparable to that of toluene, a widely used ORC fluid, indicating that fluorobenzene could serve as a viable alternative in applications where both environmental and performance criteria are critical. However, while the initial results are promising, the long-term durability of fluorobenzene in industrial applications, particularly in heat pumps, would require further validation, particularly under sustained operating conditions. The analysis also explored fluorobenzene's suitability for direct heat exchange with flue gases at 390°C, revealing promising exergy efficiency.

Apart from pure fluids, the exploration of $CO_2$-based mixtures formed another critical area of this research, with a focus on expanding the application of transcritical power cycles in CSP systems and HTHPs. Among the mixtures investigated, $CO_2$+$SiCl_4$ showed potential in improving the efficiency of CSP systems. It is demonstrated that, in recompression layout, little molar dopant content can be beneficial in net electrical output (+4.2% compared to pure $CO_2$). The reduction in the primary heat exchanger inlet temperature also offers advantages in terms of reducing parasitic energy consumption in the CSP plant.

Another promising $CO_2$-based mixture explored in this study is $CO_2$+$C_2Cl_4$, examined primarily for applications in high-temperature heat pumps. While $C_2Cl_4$ does not stand out for its thermal stability at extremely high temperatures, experimental stability tests on pure $C_2Cl_4$ showed that it presents low degradation rate below 230-250°C. This level of thermal stability is sufficient for applications in HTHPs, with sink temperatures below 200°C. The $CO_2$+$C_2Cl_4$ mixture demonstrated, in spray drying application, a favourable balance between performance metrics such as COP values and a reasonable pressure ratio across the compressor, which are advantageous for efficiently recovering low-grade waste heat.

A significant portion of this research also focused on addressing the challenges associated with the limited experimental data on the vapor-liquid equilibrium (VLE) properties and density measurements of innovative $CO_2$-based mixtures. Accurate VLE and density data are essential for refining thermodynamic models and ensuring that cycle simulations reflect realistic operational behaviour. Specifically, a combination of experimental techniques, including the use of a variable-volume PVT apparatus, allowed for precise VLE measurements of the $CO_2$+$SiCl_4$ mixture. These experiments provided critical phase equilibrium data, enabling accurate calibration of the Peng-Robinson equation of state (PR EoS) for this mixture. By optimizing binary interaction parameters based on experimental VLE data, the model showed a mean absolute deviation (AAD%) of 0.68% with respect to the bubble point data.

In parallel, density measurements for both the $CO_2$+$SiCl_4$ and $CO_2$+$C_2Cl_4$ mixtures were obtained using a vibrating tube densimeter (VTD). These measurements were critical in characterizing the volumetric behaviour of the mixtures, especially given the significant differences in volatility between $CO_2$ and the dopants. The adopted setup of the VTD can be considered as a reference case for future studies on mixtures with significant volatility difference between the components. Incorporating these density data into the PR EoS model further enhanced the accuracy of thermodynamic property predictions across the operational ranges relevant to transcritical cycles. Moreover, an innovative approach has been used allowing the measurement of bubble points of the $CO_2$+$SiCl_4$ mixture with the VTD. The measured data at the VTD were found to be in good agreement with those obtained by higher-fidelity PVT apparatus.

An experimental isochoric apparatus has been developed within this work at the Fluid Test Laboratory of the University of Brescia to measure bubble points of mixtures. The apparatus has been validated on $CO_2$ binary mixtures with hexafluorobenzene ($C_6F_6$) and n-pentane, which are well-characterized in existing literature. The validation results showed that the measured bubble points matched published data, confirming the accuracy and reliability of the apparatus for determining phase equilibrium properties of complex mixtures. In addition to the validation experiments, the isochoric apparatus has been used to obtain new VLE data for the $CO_2$+c-$C_4F_8$ mixture. These data contribute to filling existing knowledge gaps in the thermodynamic behaviour of this mixture, particularly in the context of high-temperature transcritical cycles.

From the modelling point of view, the transport properties, in particular viscosity and thermal conductivity, were investigated for $CO_2$ mixtures using established models. The study employed friction theory (f-theory) models, which showed improved predictive capabilities compared to traditional corresponding states models once tuned on available experimental data of the mixture's component. Such modelling insights are essential for optimizing heat exchanger designs in power cycles, especially at the conditions of transcritical power cycles where properties drastically vary into heat exchangers.

From a practical perspective, studies on the potential implementation of these fluids in real-world systems suggest both technical and economic feasibility. For example, the integration of a 1 MW $SiCl_4$ cycle into a biomass cogeneration plant achieved higher electrical efficiencies compared to conventional ORC systems of similar scale, particularly in combined heat and power (CHP) mode. The economic analysis conducted indicated that the $SiCl_4$ system offers competitive payback periods, especially in regions with supportive policies for renewable energy. Similarly, the CSP+Desalination system proposed in this thesis, which integrates $CO_2$-based power cycles with desalination technologies, demonstrated the potential to utilize rejected heat effectively without compromising the thermal efficiency of the power cycle. This approach, which could be especially beneficial in regions facing both energy and water scarcity, showed promising economic performance, although further optimization of the integration between power and desalination systems would be necessary to maximize benefits.

While the results presented in this thesis provide a groundwork for the potential application of these innovative fluids, several challenges still need to be addressed. The long-term stability of these fluids, especially in environments with possible contaminants like moisture or impurities, warrants further investigation. Additionally, understanding the interaction between these fluids and system materials over extended operating periods is essential to prevent any material compatibility issues that could impact system reliability. Future research should also consider alternative working fluid mixtures and continue refining the experimental methods used to accurately characterize their thermophysical properties.

In conclusion, the research presented in this thesis contributes to the ongoing development of high-temperature thermodynamic cycles by providing new insights into the behaviour and potential applications of innovative working fluids. While the experimental results and modelling efforts offer encouraging prospects, continued research will be needed to address the remaining technical challenges and fully realize the potential of these fluids in next-generation energy system.

# *ACKNOWLEDGMENTS*

I would like to express my gratitude to my parents, Luca and Emi, for the support and love provided me throughout these years of personal growth and for always encouraging my choices. I'm equally thankful to my sister Francesca and to Andrea for their presence and for sharing moments of joy during these years. The acknowledgment extends to my entire family, including my uncles, aunts, and grandparents.

I would like to express my appreciation to my supervisor, Prof. Gioele Di Marcoberardino, for his guidance, dedication, and encouragement during these years. His openness and support allowed me to explore topics of personal interest, creating a space where I felt comfortable pursuing my ideas with confidence. I want to extend my deeply gratitude also to the other professors in our research group ERGO, Paolo Iora and Costante Invernizzi, or their belief in me, consistently supporting my choices and encouraging my insights. Their trust and encouragement have been invaluable, providing me with the confidence to pursue my ideas and grow as a researcher. My thanks also go to Modestino Savoia for his technical assistance in our laboratory.

A special thanks is devoted to Mauro Riva, whose guidance and expertise in laboratory activities during the period abroad in Fontainebleau have greatly enriched my academic journey.

Thanks to all my colleagues of the PhD room, especially Mattia, who shared this journey. My gratitude also goes to my lifelong friends and to Michela, whose presence and warmth have made this experience all the more meaningful.